Thermodynamics and solid state properties of complex oxides involving transition metal, rare earth and actinide oxides

by

MANJULATA SAHU
CHEM012009040011

Bhabha Atomic Research Centre,
Mumbai 400085, India

A thesis submitted to the
Board of studies in Chemical Sciences
in partial fulfillment of the requirements
for the degree of

Doctor of Philosophy
of
Homi Bhabha National Institute

December, 2014

HOMI BHABHA NATIONAL INSTITUTE

Recommendations of the Viva Voce Board

As members of the Viva Voce Board, we certify that we have read the dissertation prepared by **Smt. Manjulata Sahu** entitled **"Thermodynamics and solid state properties of complex oxides involving transition metal, rare earth and actinide oxides. "** and recommend that it may be accepted as fulfilling the dissertation requirement for the Degree of Doctor of Philosophy.

Date:

Chairman –Dr. K. L.Ramakumar

Guide / Convener – Dr. Smruti Dash.

External examiner- Dr. S.R. Dharwadkar

Member 1 – Dr. A. Goswami — Goswami

Member 2 – Dr. Shyamala Bharadwaj — SRBharadwaj

Member 3 –Dr. Renu Aggarwal — Renu Agarwal

Final approval and acceptance of this dissertation is contingent upon the candidate's submission of the final copies of the dissertation to HBNI.

I hereby certify that I have read this dissertation prepared under my direction and recommend that it may be accepted as fulfilling the dissertation requirement.

Date: 16.11.2015

Place: Mumbai

STATEMENT BY AUTHOR

This dissertation has been submitted in partial fulfillment of requirements for an advanced degree at Homi Bhabha National Institute (HBNI) and is deposited in the Library to be made available to borrowers under rules of the HBNI.

Brief quotations from this dissertation are allowable without special permission, provided that accurate acknowledgement of source is made. Requests for permission for extended quotation from or reproduction of this manuscript in whole or in part may be granted by the Competent Authority of HBNI when in his or her judgment the proposed use of the material is in the interests of scholarship. In all other instances, however, permission must be obtained from the author.

Manjulata Sahu

DECLARATION

I, hereby declare that the investigation presented in the thesis has been carried out by me. The work is original and has not been submitted earlier as a whole or in part for a degree / diploma at this or any other Institution / University.

Manjulata Sahu

Dedicated to my
beloved Father
(Late Shri Gadadhara Sahu)

List of Publications

Refereed Journal

1. Thermal expansion and heat capacity of Gd_6UO_{12}(s), **Manjulata Sahu**, K. Krishnan, M.K. Saxena, K.L. Ramakumar, **J. Alloys Compd. 482 (2009) 141–146**

2. Heat capacity and thermal expansion coefficient of $SrCeO_3$(s) and Sr_2CeO_4(s), **Manjulata Sahu**, K. Krishnan. B.K. Nagar. M.K. Saxena, Smruti Dash, **Thermochim. Acta 525 (2011) 167– 176**

3. Characterization and thermo physical property investigations on $Ba_{1-x}Sr_xMoO_4$ (x = 0, 0.18, 0.38, 0.60, 0.81, 1) solid-solutions, **Manjulata Sahu** , K. Krishnan, B.K. Nagar, Dheeraj Jain, M.K. Saxena, C.G.S. Pillai, Smruti Dash, **J. Nucl. Mater. 427 (2012) 323–332**

4. Combustion synthesis and thermal expansion of RE_6UO_{12}(RE =Dy and Tb), **Manjulata Sahu,** K. Krishnan, M. K. Saxena, Smruti Dash, **J Therm Anal Calorim 112 (2013)165–172**

5. Thermo Physico-chemical properties of Cr_2TeO_6(s), Fe_2TeO_6(s) and Ni_3TeO_6(s), **Manjulata Sahu**, Deepak Rawat, Bal Gobind Vats, M. K. Saxena and Smruti Dash, **Thermochim. Acta 585 (2014) 50–56**

6. Thermophysical Properties of $Ba_{1-x}Sr_xMoO_3$(s), **Manjulata Sahu,** K.Krishnan, M.K.Saxena, Smruti Dash, **J. Nucl.Mater 457(2015) 29-35.**

7. Investigation on thermophysical properties of RE_6UO_{12}(s) (RE=La, Pr, Nd, Sm) and affirmation of phase transition in Nd_6UO_{12}(s), **Manjulata Sahu, K.Krishnan, Dheeraj Jain, M.K.Saxena and Smruti Dash, communicated to Thermochim. Acta.**

Symposium

1. Solid Oxide Galvanic Cell for Determination of Gibbs Energy of Formation of Tb_6UO_{12}(s),**Manjulata Sahu** and Smruti Dash, Proceeding of the 19th International Symposium on Thermal analysis(Thermans-2013),held at Training Schoo; Hostel, HomiBhaba National Institute,Anushaktinagar, Mumbai,held during 19-21 December, Pg.62
2. Thermo physical properties of Fe_2TeO_6(s) and Cr_2TeO_6(s), **Manjulata Sahu**, Bal Gobind Vats, M. K. Saxena and Smruti Dash, Proceedings of the 11th binnial DAE-BRNS Nuclear and Radiochemistry symposium (NUCAR-2013), held at Govt Model Science College(Autonomous),R.D. University, Jabalpur,M.P, Feb 19-23, P.275-6.
3. Solid Oxide Galvanic Cell for determination of Gibbs Energy of Formation of Ho_6UO_{12}(s), **Manjulata Sahu** and Smruti Dash, Proceedings of Fifth ISEAC Triennial International Conference on Advances and recent trends in electrochemistry (**ELAC-2013**) Jan 16-20, 2013, Ramoji Film City, Hyderabad P.333-6
4. Combustion synthesis and thermal expansion of RE_6UO_{12} (s) (RE =Pr, Ho and Lu) **Manjulata Sahu**, K.Krishnan and Smruti Dash, Proceedings of 4th DAE-BRNS International Symposium on material chemistry (ISMC-2012), held at Bhaba Atomic Research Centre, Trombay, Mumbai during 11-15 Dec, 2012, Pg. 110-11.

5. Combustion synthesis and thermal expansion of RE_6UO_{12} (s) (RE =Dy and Tb) **Manjulata Sahu**, K.Krishnan and Smruti Dash,Proceeding of the 18th International Symposium on Thermal analysis(Thermans-2012),held at Training Schoo; Hostel,HomiBhaba National Institute,Anushaktinagar, Mumbai,held during 31st January -2nd February, Pg.120-122

6. Oxygen concentration cell for the measurements of standard molar Gibbs Energy of Formation of Nd_6UO_{12}(s),**Manjulata Sahu** and Smruti Dash, Proceedings of the Nuclear and Radiochemistry symposium Vol.2 (NUCAR-2011), held at GITAM Institute of Science,Visakhapatnam, held during 22-26 Feb, 2011, Pg. 585.

7. Solid Oxide Galvanic Cell to determine Thermochemical Data of $Dy_6UO_{12}(s)$ **Manjulata Sahu,** Smruti Dash, B.K. Sen and V. Venugopal, Proceedings of Fourth ISEAC Triennial International Conference on Electro analytical Chemistry and Allied Topics (**ELAC-2010**) March 16-18, 2010, Puri, Orissa P.231

8. Heat capacity of $Dy_6UO_{12}(s)$, **M.Sahu**, B.K.Nagar, M.K.saxena and S.Dash, Proceedings of DAE-BRNS 3rd International Symposium on Material Chemistry,Bhaba Atomic Research Centre, Trombay, Mumbai, held in Dec 7-9, 2010. P.100

9. Studies on gadolinium-uranium-oxygen system, **Manjulata Sahu**, Smruti Dash, S.C. Parida, M.K. Saxena and K.L. Ramakumar, Proceedings of International Conference on Sol-Gel Processes for Advanced Ceramics, (**SGPAC-2009**) October 11-14, 2009, Kalpakkam P.267

Government of India
Bhabha Atomic Research Centre
HUMAN RESOURCE DEVELOPMENT DIVISION
TRAINING SCHOOL COMPLEX, ANUSHAKTI NAGAR, MUMBAI-400094.

Marks in Courses Undertaken during 2009-2010
at BARC Training School, Anushakti Nagar

Name of Candidate : Manjulata Sahu

S.No.	SUBJECT	MAXIMUM MARKS	MARKS OBTAINED
1	Chemical Thermodynamics	100	95

Place : Mumbai

September 2010

M.Ramanamurthi
Head, OCES PI Section

HRDD

Government of India
Bhabha Atomic Research Centre
HUMAN RESOURCE DEVELOPMENT DIVISION
TRAINING SCHOOL COMPLEX, ANUSHAKTI NAGAR, MUMBAI-400094.

Marks in Courses Undertaken during 2008-2009 at BARC Training School, Anushakti Nagar

Name of Candidate : Manjulata Sahu

S.No.	SUBJECT	MAXIMUM MARKS	MARKS OBTAINED
1	Applied Electrochemistry & Chemical Sensors	100	92
2	Materials Characterisation	100	90

Place : Mumbai

September 2009

M.Ramanamurthi
Head, OCES PI Section

Ravinder Puri
(R.R.Puri)
Head, HRDD

ACKNOWLEDGMENTS

I wish to express my sincere gratitude to my guide **Prof. Smruti Dash** for her continuous guidance, encouragement and constant supervision during the progress of my research work. I am highly indebted to her for introducing me both experimental and theoretical aspects of thermodynamics. I feel highly privileged to work under her invaluable guidance. Her enthusiasm continuously amazed me and inspired me. I am grateful to her for her continuous concern, extensive discussions and suggestions throughout my doctoral research work which helped me to accomplish my thesis work.

I would also like to thank members of the doctoral committee: Prof. **K.L. Ramakumar (Chairman)**, **Prof. A.K.Goswami (Member), Prof. Shyamala Bharadwaj (Member)** and **Prof. Renu Aggarwal (Member),** for their valuable advice, encouragement and insightful comments, valuable suggestions and extensive discussions around my research work.

Words fail to express my sincere gratitude to **Shri M.K. Saxena,** who has always supported me in the research work, build my moral by solving my personal problems.

I am also thankful to **Dr. B.S. Tomar** for his encouragement, patience and support during this research work.

I specially thank my lab mates from CC-11C (**Shri S.B. Deb, Shri B.K. Nagar, Shri Ramamohan Rao, Dr. Ankita Rao and Shri Abhijeet Saha**), C-101(**Dr. S.C.Parida, Dr. S.K. Rakshit and Shri Pradeep Samui**) and **Dr. N. Kumar** for being so friendly to me throughout the progress of this research work. I am also thankful to **Dr. Aishwarya Kar, Dr. Ruma Gupta** and **Dr. Santosh Gupta** for their encouragement and help in writing the thesis. I am also thankful to my lunch group as they have always tried to relieve my stress.

I gratefully acknowledge **Dr. K. Krishnan** for helping in XRD, **Dr Rajakishore Lenka** and **Dr. Pankaj Patro** for reduction of samples and SEM and **Shri Dheeraj Jain** for electrical conductivity and Raman spectroscopy measurements without them most of the results described in this thesis would not have been obtained.

I would like to share this achievement with my husband **Sukanta** for his unconditional love, patience and endurance towards me. This achievement would have been impossible without the support of my husband and my two sons (**Sumeet and Samarjeet**).

Above all, I thank the almighty for enabling me to complete the task.

Manjulata Sahu

CONTENTS

Synopsis **I**

List of figures **XIII**

List of tables **XXIII**

CHAPTER-1-Introduction **1**

1.1. General Introduction **2**

1.2. Challenges of reactor development **3**

- 1.2.1. Fuel
- 1.2.3. Structural materials

1.3. Irradiation behavior of Fuel **6**

1.4. Chemical state of Fission products **6**

1.5. Thermophysico-chemical properties in support of prototype fast breeder reactor **8**

1.6. Importance of RE-U-O systems **10**

- 1.6.1. Rare earths and actinides
- 1.6.2. Nuclear perspective (Interaction between fuel and fission products)
- 1.6.3. Non Nuclear applications
- 1.6.4. Literature survey
- 1.6.5. Properties studied

1.7. Importance of Sr-Ce-O system **15**

- 1.7.1. Nuclear perspective (Interaction between fuel and the fission products)
- 1.7.2. Non Nuclear applications
- 1.7.3. Literature survey
- 1.7.4. Properties studied

1.8. Importance of Ba-Sr-Mo-O system **17**

- 1.8.1. Nuclear perspective (Interaction amongst fission Products)
- 1.8.2. Non Nuclear applications
- 1.8.3. Literature survey
- 1.8.4. Properties studied

1.9. Importance of A-Te-O (A= Cr, Fe, Ni) systems **19**

- 1.9.1. Nuclear perspective (Interaction of stainless steel clad with Te)
- 1.9.2. Non Nuclear applications
- 1.9.3. Literature survey
- 1.9.4. Properties studied

CHAPTER-2-Experimental Methods and Techniques **22**

2.1. Synthesis of compounds **23**
  2.1.1 Solid state reaction or ceramic route
  2.1.2 Soft chemistry routes
    2.1.2.1. Gel Combustion synthesis
    2.1.2.2. Complex Polymerisation Method
2.2. Solid Solutions **25**
2.2.1. Substitutional Solid Solutions
  2.2.1.1. Hume Rothery rules for the formation of substitutional solid solutions
2.2.2. Interstitial Solid Solutions
  2.2.2.1.Hume Rothery rules for the formation of interstitial solid solutions
2.3. Materials characterization techniques **27**
  2.3.1. X-ray Diffraction (XRD) **27**
    2.3.1.1. Principle of X-ray diffraction
    2.3.1.2. Source of background radiation- fluorescence
    2.3.1.3. Determination of lattice parameters
  2.3.2. Raman Spectroscopy **34**
  2.3.3. Scanning Electron Microscopy (SEM) **36**
  2.3.4. Inductively Coupled Plasma-Mass Spectrometry (ICPMS). **39**
  2.3.5. Thermo analytical Methods **40**
    2.3.5.1. Simultaneous Thermogravimetry (TG) and Differential Thermal Analysis (DTA)
  2.3.6. Photoluminescence spectroscopy (PL) **41**
    2.3.6.1. Instrumentation: Excitation and emission spectroscopy
2.4. Thermo-physical properties **44**
  2.4.1. Thermal expansion **44**
    2.4.1.1. Theory
    2.4.1.2. Measurements
      2.4.1.2.1. Lattice thermal expansion by high temperature XRD **46**
      2.4.1.2.1.1. Calibration of HTXRD
      2.4.1.2.2. Bulk thermal expansion using Dilatometry **49**
  2.4.2. Heat capacity **50**
    2.4.2.1. Relevance of heat capacity
    2.4.2.2. Theory of heat capacity **51**
      2.4.2.2.1. Dulong and Petit theory of heat capacity
      2.4.2.2.2. Einstein theory of heat capacity
      2.4.2.2.3. Debye theory of heat capacity

2.4.2.3. Various contributing factors to heat capacity **53**

2.5. Calorimetry **55**

2.5.1. Differential Scanning Calorimeter (DSC)

2.5.1.1. Power compensation DSC **57**

2.5.1.2. Heat flux DSC **57**

2.5.1.2.1. Calibration of DSC **60**

2.5.1.2.1.1. Temperature calibration

2.5.1.2.1.2. Heat calibration

2.5.1.2.1.3. Heat flow rate calibration

2.5.1.2.1.4. τ- lag calibration

2.5.1.2.2. Description of DSC used in present investigation

2.5.1.3. Measurement of heat capacity using DSC **64**

2.5.1.3.1. Determination of heat capacity by three step scanning Method

2.5.1.4. Temperature Modulated DSC (TOPEM Software) **68**

2.5.1.4.1. Specialised TOPEM Software

2.5.1.4.2. Determination of heat capacity using TOPEM software **71**

2.5.1.5. Treatment of heat capacity data **73**

2.6. Thermo-chemical properties **73**

2.6.1. Solid-state electrochemical technique using oxide ion conducting **73**

2.6.2.. Conduction mechanism in solid oxide electrolyte

2.6.3. The relationship between defect equilibria and electrical

2.6.4. Electrolytic Domain

2.6.5. Transport properties of solid electrolytes

2.6.6. Relation between Gibbs energy and e.m.f (*E*) **82**

2.6.7. Critical factors in emf measurements **84**

2.6.8. Criteria for selection of reference electrode **85**

2.6.9. Check of reversibility **86**

2.6.10. Description of experimental set up used in this study

2.6.11. E.m.f. data treatment **87**

2.7. Measurement of Vapour Pressure **88**

2.7.1. Transpiration Method **90**

2.7.1.1. Important parameters to consider in transpiration measurements

2.7.1.1.1. Saturation zone

2.7.1.1.2. Effect of flow rate

2.7.1.2. Vapour pressure data treatment **93**

2.8. Calculation of thermodynamic functions **94**

2.8.1. Derivation of thermodynamic functions from heat capacity data.

2.8.2. Derivation of enthalpy and entropy from gibbs energy data

2.8.2.1. The Second-law method

2.8.2.2. The third-law method

2.9. Establishment of chemical potential diagram **97**

2.10. Classifications of Phase transitions **98**

2.10.1. First Order Phase transition

2.10.2. Second Order Phase transition

2.11. Impedance Spectroscopy **102**

CHAPTER-3- RE-U-O system **106**

3.1. Experimental **106**

3.1.1. Synthesis of RE_6UO_{12} (s)

3.2. Results

3.2.1. Characterisation using XRD **107**

3.2.2. Thermal expansion using HT-XRD **112**

3.2.3. Heat capacity measurements using DSC **122**

3.2.4. Emf measurements on solid-state electrochemical cells **132**

3.2.4.1. Standardization of oxide cell setup

3.2.4.2. Standard molar Gibbs energies of formation of RE_6UO_{12}(s) (RE=La, Nd, Sm, Eu, Gd, Tb, Dy, Ho, Tm, Yb, Lu)

3.2.4.2.1. Standard molar Gibbs energies of formation of RE_6UO_{12}(s) (RE=La, Nd, Sm, Eu, Gd, Tb, Dy, Ho, Tm, Yb, Lu) using air as reference **134**

3.2.4.2.2. Standard molar Gibbs energies of formation of RE_6UO_{12}(s) (RE= Nd, Sm, Eu, Gd, Tb, Dy, Ho, Tm, Yb, Lu) using Ni (s)+ NiO(s) as reference electrode **151**

3.2.5. Study of phase transition using electrical conductivity measurement **152**

3.3. Discussion

3.3.1. Thermal expansion using HT-XRD **155**

3.3.2. Heat capacity measurement using DSC **164**

3.3.3. E.m.f. measurements **170**

3.3.4. Electrical conductivity measurements of RE_6UO_{12}(s) (RE= Nd, Gd, Dy, Tb) **174**

3.4. Summary **176**

Chapter-4- Sr-Ce-O system **178**

4.1. Synthesis of Ternary compounds **178**

4.1.1. $SrCeO_3(s)$

4.1.2. $Sr_2CeO_4(s)$

4.2. Characterisation of $SrCeO_3(s)$ and $Sr_2CeO_4(s)$

4.2.1. XRD **179**

4.2.2. Impurity analysis using ICPMS **180**

4.2.3. Thermal Expansion measurements using HT-XRD. **180**

4.2.4. Heat capacity measurement using DSC **180**

4.2.5. Luminescence study of $SrCeO_3(s)$ **182**

4.2.6. Electrical conductivity measurement of $Sr_2CeO_4(s)$ **182**

4.3. Results

4.3.1. Thermal expansion by HT-XRD **182**

4.3.1.1. $SrCeO_3(s)$

4.3.1.2. $Sr_2CeO_4(s)$

4.3.2. Heat capacity measurement by DSC **186**

4.3.2.1. $CeO_2(s)$

4.3.2.2. $SrCeO_3(s)$

4.3.2.3. $Sr_2CeO_4(s)$

4.3.3. Electrical conductivity measurement of $Sr_2CeO_4(s)$ **190**

4.4. Discussion **192**

4.4.1. Heat capacity of $SrCeO_3(s)$. **192**

4.4.2. Confirmation of instability of $SrCeO_3(s)$ by: **192**

4.4.2.1. XRD

4.4.2.2. Luminescence Study

4.4.3. Heat capacity of $Sr_2CeO_4(s)$.

4.4.4. Detection of second order transition in $Sr_2CeO_4(s)$. **194**

4.4.5. Confirmation of second order phase transition in $Sr_2CeO_4(s)$ from the comparison of thermal expansion of $Sr_2CeO_4(s)$ with $SrCeO_3(s)$

4.4.6. Electrical conductivity measurement of $Sr_2CeO_4(s)$ **196**

4.5. Summary **196**

CHAPTER-5- Ba $_{1-x}$Sr$_x$ MoO$_4$ solid solutions **198**

5.1. Experimental. **198**

5.1.1. Synthesis of Ba $_{1-x}$Sr$_x$ MoO$_4$) (x=0, 0.2, 0.4, 0.5, 0.8, 1) solid solutions

5.1.2. Characterisation of Ba $_{1-x}$Sr$_x$ MoO$_4$) (x=0, 0.2, 0.4, 0.5, 0.8, 1) solid solutions **199**

5.1.2.1. Determination of reaction temperature for using TG-DTA

5.1.2.2. Characterisation by XRD

5.1.2.3. Accurate composition analysis by ICPMS

5.1.2.4. Characterisation using Raman spectroscopy
5.1.2.5. Morphology using Scanning Electron microscopy
5.1.2.6. Thermal expansion studies using HT-XRD
5.1.2.7. Heat capacity measurements using DSC
5.2. Results and discussion **200**
5.2.1. Characterisation of Ba $_{1-x}$Sr$_x$ MoO$_4$) (x=0, 0.2, 0.4, 0.5, 0.8, 1) solid solutions
5.2.1.1. TG-DTA of Precursors **200**
5.2.1.2. Characterisation by XRD **201**
5.2.1.3. Characterisation by Raman Spectroscopy **204**
5.2.1.4. Characterisation of SrMoO$_4$ but BaMoO$_4$ by SEM **208**
5.2.1.5. Crystal Structure indexing of Ba $_{1-x}$Sr$_x$ MoO$_4$(s) (x= 0.18, 0.38, 0.60, 0.81) **209**
5.2.1.6. Thermal expansion of Ba $_{1-x}$Sr$_x$ MoO$_4$(s) (x = 0, 0.6, 1) **209**
5.2.1.7. Heat capacity **215**
5.3. Summary **221**
CHAPTER-6- Ba$_{1-x}$Sr$_x$MoO$_3$(s) solid solutions **222**
6.1. Experimental **222**
6.1.1. Synthesis of Ba$_{1-x}$Sr$_x$MoO$_3$(s) (x=0, 0.2, 0.4, 0.5, 0.8, 1) solid solutions
6.1.2. Characterisation by X-Ray Diffractometry
6.1.3. Characterisation by SEM
6.1.4. Analysis of Metalic elements by ICPMS
6.1.5. Oxygen analysis
6.1.6. Thermal expansion using HT-XRD
6.1.7. Heat capacity measurements using DSC
6.2. Results and Discussion **224**
6.2.1. Reduction condition of Ba$_{1-x}$Sr$_x$MoO$_4$(s)(x = 0, 0.2, 0.4, 0.5, 0.8, 1) solid solutions
6.2.2. XRD analysis
6.2.3. SEM characterisation
6.2.4. Thermal expansion of Ba $_{1-x}$Sr$_x$ MoO$_3$(s) (x = 0, 0.4, 0.8 and 1)
6.2.5. Heat capacity measurement using DSC
6.3. Summary **235**

CHAPTER-7- Cr-Te-O, Fe-Te-O and Ni-Te-O system **236**
7.1. Experimental **236**
7.1.1. Synthesis of compounds in A-Te-O (A=Cr, Fe, Ni) system
7.1.2. Characterization using XRD
7.1.3. Thermal Expansion measurements using HT-XRD
7.1.4. Heat capacity measurements using DSC

7.1.5. Measurement of gibbs energy of formation of Fe_2TeO_6(s) and Ni_3TeO_6(s) by Transpiration technique
7.1.6. Generation of chemical potential Diagram of A-Te-O system.
7.2. Results and Discussion **239**
7.2.1. Thermal expansion **239**
7.2.2. Heat capacity **241**
7.2.3. Gibbs energy using Transpiration method **244**
7.2.3.1. (Fe_2TeO_6, s, T)
7.2.3.2. Ni_3TeO_6(s)
7.2.4. Thermodynamic Functions **251**
7.2.5. Chemical potential diagram of A-Te-O (A= Cr, Fe, Ni) system **258**
7.3. Summary **265**

CHAPTER-8- Conclusion and Suggestions for further studies **266**

References **270**

SynopSiS

The nuclear power renewed global interest as it is the most viable option as an alternate energy source to fossil fuel and produces zero carbon emission. In worldwide, the well proven oxide fuel has been used in the commercial nuclear reactor. In order to grow the nuclear capability of India to required level, reprocessed Pu from the pressurized heavy water reactor (PHWR) will be used in prototype fast breeder reactor (PFBR) as a mixed oxide (MOX) fuel. In irradiated MOX fuels, a number of fission products (FPs) and actinides are produced. They take various chemical states depending on the fuel compositions, temperature and oxygen potential [1-3]. The compounds composed of FPs and actinides would affect significantly the fuel characteristics. Therefore, the behavior of FPs and actinides under irradiation and the properties of their compounds are very important for evaluation of the fuel performance. It has been recognized that some FPs such as rare earths (RE) are soluble in the fuel matrix and form solid solutions of $(U, Pu, Ln) O_2$. On the other hand, some FPs such as alkali, alkaline-earth elements form oxides of the form $(Ba,Sr)(U,Zr,Mo)O_3$ and $Ba(Mo,U)O_4$. Molybdenum and platinum-family metals form metallic inclusions such as Mo-Tc-Ru-Rh-Pd alloys, $U\text{-}Me_3$ (Me= Ru,Rh, Pd). It is well-known that oxidation of the stainless steel clad, by the oxide fuel, is considerably influenced by the presence of the fission products, especially, cesium, iodine and tellurium, at the fuel-clad interface [4]. The thermodynamic properties as well as phase relations of the tellurium compounds of the clad components required in great detail. To ensure that the fuel can be subjected to the desired linear heat ratings without the centerline temperature crossing the melting point of the fuel, a number of physico-chemical data are required for the design of reactor. The melting point and thermal conductivity of the fuel determines the power that can be extracted. The presence of solid FP in the fuel can change its melting point and thermal conductivity. Hence, the knowledge of thermal properties of nuclear material is important in predicting the integrity of fuel. The thermal expansion, which arises as a result of lattice anharmonicity, makes it a key quantity in fundamental studies on cohesive forces. If the expansion coefficient of FP will be higher than fuel, it stresses the clad and leads to failure of fuel pin. Thus, thermal expansion data plays a key role in designing reactor code. The thermal conductivity of a material can be derived from heat capacity, density and diffusivity data, so heat capacity is also an important parameter for reactor designers and used in predicting fuel performance inside the reactor. In addition to the above mentioned thermal properties, the knowledge of one of the most fundamental property i.e. Gibbs energy of formation is imperative to predict the formation and stability of the compounds in various physico-chemical environments. This also helps in establishing phase diagrams of various systems. Hence, a number of physicochemical, thermodynamic and mechanical data are required for the design of a nuclear reactor containing MOX fuel. Similar investigations are required for host of other materials including fission product compounds likely to form in the fuel during irradiation, materials that could form matrices for immobilizing the nuclear waste, materials for control of fission. Even with proven oxide fuel, there exist still many points that are doubtful and unclear with regards to the behaviour of FPs and actinides under irradiation. Hence, there is a requirement for R & D to bridge the gap existed in the literature. Apart from it the optical band gap of the oxides is correlated to the microscopic energy calculated from standard enthalpy of formation. The physico-chemical properties of compounds of f-block elements can provide an insight to its chemical bonding. This study is focused on the determination of thermo physical and thermodynamic properties of the mixed oxides in RE-U-O, Sr-Ce-O, Ba-Sr-Mo-O, Fe-Te-O, Cr-Te-O, and Ni-Te-O systems. The following paragraphs provide literature survey on these systems to identify the existed gap in the literature for selecting studies to be conducted for the research project.

The RE-U-O system is characterized with both solid solutions and presence of RE_6UO_{12} (s) type of compounds [5-6]. These solid solutions are important from the point of view of its applications as burnable absorber in oxide fuel. UO_2–Gd_2O_3 fuel has already been used in BWR and earlier rare earths have also been proposed for it. As RE_6UO_{12} (s) exists in RE-U-O system, its $\Delta\mu(O_2)$ is required to predict its formation under normal or off normal operating condition of the reactor. Y_6AnO_{12} (s) and Yb_6AnO_{12} (s) have been studied as host matrix for immobilization of actinides [7]. Apart from it rare earth compounds are the subject of great interest owing to their various applications. In order to correlate physical properties of f-block compounds, thermodynamic properties are required which are scarce. The systematic study of physico-chemical properties of RE_6UO_{12}(s) (RE= La, Pr, Nd, Sm, Eu, Gd, Tb, Dy, Ho, Er, Tm, Yb and Lu) have not been reported in the literature.

In the MOX fuel, Pu can react with fission product Sr to form compounds in Sr-Pu-O system. Ceria is frequently used as a surrogate material for PuO_2 (s) due to its radio-toxicity and Ce also has appreciable fission yield in both ^{235}U and ^{239}Pu fissions. Sr-Ce-O system is characterized with $SrCeO_3$(s) and $SrCeO_4$ (s). In addition to it, $SrCeO_3$(s) is being used as the high temperature proton conducting electrolyte [8], in hydrogen pumps [9] and in solid oxide fuel cell (SOFC) [10] due to its low activation energy for proton conduction than that of oxide ion. Sr_2CeO_4(s) emits a blue–white fluorescence by the excitation either through the X-ray, cathode ray and ultraviolet ray [11]. Therefore, the thermal behaviour of these ternary oxides is relevant for the study.

The solid solutions in $BaMoO_3$ (s)-$SrMoO_3$ (s) and $BaMoO_4$ (s)-$SrMoO_4$ (s) systems are relevant as $BaMO_3$ (M= U, Zr, Mo) and $BaMO_4$ (M= U, Mo) phases have been identified in the irradiated fuel under the oxygen potentials of -500 to -200 kJ/mol. Alkali earth metal molybdates and tungstates with a scheelite-type structure, such as AMO_4(s) (A = Ba, Sr, Ca and M = Mo, W) and their solid solutions, are important materials in photoluminescence and have widely been used in optical fibers, solid-state-optical masers and electrochromic materials [12]. $BaMoO_3$ (s) and $SrMoO_3$ (s) compounds exhibit ferro-electricity, ferromagnetism, superconductivity, piezoelectric, photo-catalytic and thermoelectricity properties [13-14].

The A–Te–O (A = Cr, Fe, Ni) system has been characterized for a number of compounds [15]. The metal rich phase boundaries of binary tellurides or ternary tellurates which exists in equilibrium with the respective metal are important while considering the chemical interaction of Te with the clad. There exist few literature reports on physico-chemical properties of ternary compounds in A–Te–O (A = Cr, Fe, Ni) system [16-20]. In addition to it, Cr_2TeO_6(s) and Fe_2TeO_6(s) possess anti-ferromagnetic properties [21-22]. Fe_2TeO_6(s) is used to catalyze the oxidation of 1-butene to butadiene and propylene to acrolein [23]. Although the Gibbs energy of formation for Fe_2TeO_6(s) and Ni_3TeO_6(s) has been determined by various authors [16-20], they are not consistent and hence are not conclusive. The heat capacity and thermal expansion data for these compounds are not reported.

The results of selected compounds in RE-U-O (RE= La, Pr, Nd, Sm, Eu, Gd, Tb, Dy, Ho, Er, Tm, Yb and Lu), Sr-Ce-O, Ba-Sr-Mo-O and A-Te-O (A=Cr, Fe, Ni) systems were discussed in the following paragraphs starting with their synthesis, characterization and impurity analysis. The physico-chemical properties such as thermal expansion, heat capacity, Gibbs energy, enthalpy, entropy of formation and phase transitions of identified compounds have been discussed.

The compounds RE_6UO_{12} (s) (RE= La, Pr, Nd, Sm, Eu, Gd, Tb, Dy, Ho, Er, Tm, Yb and Lu) were synthesized by citrate nitrate combustion method using U_3O_8 (s) and RE_2O_3 (s) dissolved in nitric acid as oxidants and citric acid as fuel. Er_6UO_{12} (s) was not reported in the literature. The compound was synthesized for the first time in this study. Pr_6UO_{12}(s) could not be synthesized either by solid-state route or by citrate-nitrate gel combustion route. However by changing the reaction atmosphere to reducing Pr_6UO_{12}(s) could be synthesized. $SrCeO_3$(s) was synthesized by gel combustion method and Sr_2CeO_4(s) by solid state method. The complete solid solutions between $BaMoO_4$(s) and $SrMoO_4$(s) were synthesized by complex polymerization method at low synthesis temperature due to high volatility of MoO_3. The method follows the steps of gel combustion synthesis with an additional step of addition of ethylene glycol to reduce the reaction temperature. Perovskite-type oxides of $Ba_{1-x}Sr_xMoO_3$ (s) (x = 0, 0.2, 0.4, 0.5, 0.8, 1) were prepared by reduction of corresponding $Ba_{1-x}Sr_xMoO_4$ (s) (x = 0, 0.2, 0.4, 0.5, 0.8, 1) oxides having scheelite-type structure. In order to optimize the condition of reduction of $SrMoO_4$ (s) and $BaMoO_4$ (s) to $SrMoO_3$ (s) and $BaMoO_3$ (s), the reduction was tried separately with 8% H_2 (g) + Ar (g) mixture, pure H_2 (g) and in presence of carbon under Ar (g) by varying the temperature. The reduction in 8%H_2 (g) + Ar(g) leads to mixture of (Sr/Ba)MoO_4(s) and (Sr/Ba)MoO_3 (s) phases, while carbothermic reduction leads to pure (Sr/Ba)MoO_4 (s) without any change. But the reduction in pure H_2 leads to pure (Sr/Ba)MoO_3 (s). Therefore all the compositions were reduced in pure H_2. However, Cr_2TeO_6(s), Fe_2TeO_6(s) and Ni_3TeO_6(s) were synthesized by solid state method.

The X-ray diffraction technique was used to characterized RE_6UO_{12}(s) (RE= La, Pr, Nd, Sm, Eu, Gd, Tb, Dy, Ho, Er, Tm, Yb and Lu), $SrCeO_3$(s), Sr_2CeO_4(s) and Cr_2TeO_6(s), Fe_2TeO_6(s) and Ni_3TeO_6(s) by comparing 2θ values of the X-ray diffraction (XRD) peaks reported in the JCPDS files. The $Ba_{1-x}Sr_xMoO_4$ (s) (x = 0, 0.2, 0.4, 0.5, 0.8, 1) and $Ba_{1-x}Sr_xMoO_3$(s) (x = 0, 0.2, 0.4, 0.5, 0.8, 1) solid solutions were identified using XRD. The $Ba_{1-x}Sr_xMoO_4$ (s) (x = 0, 0.2, 0.4, 0.5, 0.8, 1) solid solutions were also characterized by Raman spectroscopy.

Er_6UO_{12}(s) was indexed in the higher symmetry hexagonal system as it was having a rhombohedral structure which was confirmed from the matching of XRD to the nearest neighbor Tm_6UO_{12}(s). Lattice parameters of Er_6UO_{12}(s) were determined using computer program written by Wadhawan [24].

In order to check stability of $SrCeO_3$(s) in the reducing atmosphere, various techniques like XRD and fluorescence spectroscopy were used. To find out the influence of Ar (reducing) and oxygen atmosphere on $SrCeO_3$(s), XRD pattern of $SrCeO_3$(s) was taken after heating in high pure Ar at 1123 K for 48 h and latter XRD pattern of the same was taken after heating in air at 1123 K for 2 h. The XRD pattern of the $SrCeO_3$(s) (heated in Ar) showed few extra peaks due to $SrCO_3$(s) and CeO_2(s). $SrCO_3$(s) peaks were observed because of the reaction between SrO (s) and CO_2 (g) in air. It was also observed that intensity of $SrCeO_3$(s) peaks were reduced by heating in Ar. The XRD pattern of $SrCeO_3$(s) (heated in air) showed increase in the intensity of $SrCeO_3$(s) peaks. These observations infer that $SrCeO_3$(s) is not stable as a pure phase in the reducing atmosphere. This observation was additionally confirmed by exciting $SrCeO_3$(s) with NUV/UV light and recording the emission spectrums. The intensity of broad emission band at 400-470 nm range (characteristic Ce^{3+}) found to increase with increase in temperature. It showed $SrCeO_3$(s) to be stable in oxidizing atmosphere.

The complete solid solutions $Ba_{1-x}Sr_xMoO_4$(s) ($x = 0, 0.2, 0.4, 0.6, 0.8, 1$) was characterized using XRD and Raman spectroscopy. The solid solutions were found to obey Vegard's law. Raman spectrum showed the variation of peak widths of a few representative Raman modes with increasing Sr^{2+} concentration. As evident from the trend, the Raman peaks broadened with initial doping of Sr^{2+} in $BaMoO_4$(s) lattices, reached a maxima between 40 and 60 at.% of Sr content and then reduced further while approaching pure $SrMoO_4$(s). The parabolic trend of this broadening can be attributed to the extent of disorder created in the lattice upon Ba/Sr lattice site mixing in these solid solutions which was increasing in initial levels of doping at either end (Sr^{2+} incorporation in $BaMoO_4$(s) or Ba^{2+} incorporation in $SrMoO_4$(s) and reached to a maximum near equal concentration of both the metal cations ($x = 0.50$). The exact stoichiometry of various solid solutions were found out by analyzing Sr, Ba and Mo content by Inductively coupled plasma mass spectrometry (ICPMS).

In order to find out solid solution in $BaMoO_3$(s)-$SrMoO_3$(s) system, the calculated lattice parameters for $Ba_{1-x}Sr_x MoO_3$(s) ($x = 0, 0.2, 0.4, 0.5, 0.8, 1$) at room temperature have plotted as a function of concentration of $SrMoO_3$(s), it showed slight negative deviation from Vegard's law, a test for solid solution. The exact stoichiometry of various solid solutions was found out by analyzing Sr, Ba and Mo content by ICPMS.

The lattice parameters, volume expansion coefficients, percentage volume expansion coefficients and average coefficient of expansions as function of temperature of RE_6UO_{12}(s) (RE= La, Pr, Nd, Sm, Eu, Gd, Tb, Dy, Ho, Er, Tm, Yb and Lu), $SrCeO_3$(s), Sr_2CeO_4(s), $Ba_{1-x}Sr_xMoO_4$(s) ($x = 0, 0.6, 1$), $Ba_{1-x}Sr_xMoO_3$(s) ($x = 0, 0.4, 0.8, 1$), Fe_2TeO_6(s) and Ni_3TeO_6(s) were measured using high temperature X-ray diffraction (HT-XRD) in the temperature range 298.15-1273 K. The experimental procedure is given by Keskar et al. [25].

The measured volume expansion coefficients have been plotted as a function of ionic radii of RE^{3+} were found not to follow a regular trend. Moreover, the expansion coefficient of La_6UO_{12} (s), Gd_6UO_{12} (s) and Lu_6UO_{12} (s) followed a linear relation with ionic radii. The average volume thermal expansion coefficient value was low for higher rare earth compounds which could be related to stronger bonds.

The thermal expansion of RE_6UO_{12} (s) falls in the range of (22-33) × 10^{-6} K^{-1} and can be categorized as high to moderate thermal expansion materials [26-27].

The thermal expansion coefficient of Sr_2CeO_4(s) was found to be higher than $SrCeO_3$(s) which could be due to open and layered structure of Sr_2CeO_4(s). Comparison of the coefficient of volume expansion of $SrCeO_3$(s) and Sr_2CeO_4(s) showed no change in slope of α_v of $SrCeO_3$(s), but α_v of Sr_2CeO_4(s) curve showed a slope change in the temperature range of 673–773 K. In addition, there was no change in slope in unit cell volume but α_v showed a slope change as a function of temperature. Hence, the phase transition in Sr_2CeO_4(s) is second order type.

There is a linear relation between average thermal expansion coefficients of $Ba_{1-x}Sr_xMoO_4$ (s) (x = 0, 0.6, 1) and the no of mole of $SrMoO_4$(s). The average volume thermal expansion coefficient of $Ba_{1-x}Sr_xMoO_4$(s) (x = 0, 0.6 and 1) was found to be 25.59 × 10^{-6}, 33.86 × 10^{-6} and 34.37 × 10^{-6} K^{-1}, respectively. The values of average volume thermal expansion coefficient of $Ba_{1-x}Sr_x MoO_3$(s) (x=0, 0.4, 0.8, 1) solid solution in the present study are close to that of ceramic nuclear fuels [26]. The thermal expansion of $Ba_{1-x}Sr_xMoO_4$(s) is greater than that of $Ba_{1-x}Sr_x MoO_3$ (s). The average volume thermal expansion coefficient of Fe_2TeO_6(s) and Ni_3TeO_6(s) were determined to be 2.46 × 10^{-5} and 3.02 × 10^{-5} K^{-1}, respectively.

The heat capacity of RE_6UO_{12}(s) (RE= La, Pr, Nd, Sm, Eu, Gd, Tb, Dy, Ho, Er, Tm, Yb and Lu), $SrCeO_3$(s), Sr_2CeO_4(s), $Ba_{1-x}Sr_xMoO_4$(s) (x = 0, 0.2, 0.4, 0.6, 0.8, 1), $Ba_{1-x}Sr_xMoO_3$(s) (x = 0, 0.2, 0.4, 0.5, 0.8, 1), Cr_2TeO_6(s), Fe_2TeO_6(s) and Ni_3TeO_6(s) were measured using differential scanning calorimeter (DSC) in the temperature range 300-870 K. The experimental set up used for this study is given by Sahu et al. [28].

The trend follows in the measured heat capacity is Eu_6UO_{12} (s) > Sm_6UO_{12}(s) > Pr_6UO_{12}(s) ≈ Nd_6UO_{12}(s) > Ho_6UO_{12}(s) ≈ Dy_6UO_{12}(s) > Tb_6UO_{12}(s) ≈ Tm_6UO_{12} (s) ≈ Yb_6UO_{12}(s) > Er_6UO_{12}(s) ≈ La_6UO_{12} (s) > Gd_6UO_{12} (s) > Lu_6UO_{12}(s). The trend followed by calculated and measured heat capacity is more or less similar. As rare earths are recognized by 4f orbitals, the number of unpaired electron can be as high as 7 which give rise to large magnetic moment. However, only heat capacity measurements cannot predict different contributions to it. As per theoretical expectations, the contributions of phonons to heat capacity vary in RE_6UO_{12}(s) as La^{3+} >Nd^{3+}>Sm^{3+}>Eu^{3+}>Gd^{3+} …………>Lu^{3+}

because phonon frequencies decrease with mass of the ions so as heat capacity. It is expected that heat capacity should be the least in the case of La^{3+} (no 4f electrons), Gd^{3+} (half filled 4f shell) and Lu^{3+}(completely filled 4f electrons). In Gd^{3+}, a very small magnetic contribution is reported. The observed trend in the variation of heat capacity of RE_6UO_{12} (s) with varying RE could be due to the combined effect of all contributions to heat capacity. The lattice contribution of the other rare earth compounds at any experimental temperature can be found out using the relation between heat capacity of La_6UO_{12}(s), Gd_6UO_{12} (s) and Lu_6UO_{12}(s) as a function of ionic radii of corresponding rare earth ions. Then the excess contributions were found out by subtracting the lattice heat capacity from the total measured heat capacity. The highest heat capacity of Eu_6UO_{12}(s) may be due to presence of both +2 and +3 valencies at high temperature. Existence of +2 valency may be due to loss of oxygen at high temperature.

The heat capacity of $SrCeO_3$(s) and Sr_2CeO_4(s) were measured in O_2 (g) atmosphere. The $C^{o}_{p}(T)$ of Sr_2CeO_4(s) showed a λ -type phase transition at 750 K. The specific heat capacity of $Ba_{1-x}Sr_xMoO_4$(s) (x = 0, 0.18, 0.38, 0.60, 0.81, 1) and $Ba_{1-x}Sr_x MoO_3$(s) (x=0, 0.2, 0.4, 0.5, 0.8, 1) solid solutions were found to increase with increase in $SrMoO_4$(s) and $SrMoO_3$(s) content, respectively. Heat capacity was measured for Cr_2TeO_6(s), Fe_2TeO_6(s) and Ni_3TeO_6(s) using TOPEM software. The heat capacity of TeO_3(s) was derived from the experimental heat capacity data for tellurates reported in the literature along with that measured in this study.

The Gibbs energy of formation of RE_6UO_{12}(s) (RE= La, Nd, Sm, Eu, Gd, Tb, Dy, Ho,Tm, Yb and Lu) were measured for the first time. The $\Delta_f G^{o}(T)$ of Fe_2TeO_6(s) and Ni_3TeO_6(s) were measured to resolve ambiguity in reported values [16-20].

Gibbs energy of RE_6UO_{12}(s) (RE= La, Nd, Sm, Eu, Gd, Tb, Dy, Ho, Tm, Yb and Lu) have been measured only with e.m.f. technique. The e.m.f set up used for this study is given in the literature [29]. The solid electrolyte used for this study was yttria stabilized zirconia(YSZ). As the $\Delta_f G^{o}_{m}(T)$ of RE_6UO_{12} (s) are not reported in the literature to check reliability of measurements, the co-existing equilibrium phase field {U_3O_8(s) +RE_2O_3(s) + RE_6UO_{12}(s)} have been separately taken with air(PO_2=21kPa) and {Ni(s) +NiO(s) } as reference electrodes. E.m.f of the cells was recorded in the temperature range 970 -1260 K. The Gibbs energy of formation data obtained in this study leads to a conclusion that Eu_6UO_{12}(s) is most unstable and the higher rare earth compounds like Ho_6UO_{12}(s) and Tm_6UO_{12} (s) are most stable, which could be due to smaller size of ions and stronger attraction between the RE^{3+} and oxygen.The calculated $\Delta\mu(O_2)$ for the reaction:

$18RE_2O_3(s)+2U_3O_8(s)+O_2(g) = 6RE_6UO_{12}(s)$ have been plotted as a function of temperature along with that of $UO_2(s)$ and $U_3O_8(s)$. It shows that $\Delta\mu(O_2)$ of fuel is much lower, hence formation of $RE_6UO_{12}(s)$ under normal reactor operating condition is not possible. The comparison of oxygen potential of $RE_6UO_{12}(s)$ shows that $Dy_6UO_{12}(s)$ has the lowest and $Eu_6UO_{12}(s)$ has the highest $\Delta\mu(O_2)$.

The $\Delta_f H^o_m$ (298.15 K) and S^o_m (298.15 K) values of $RE_6UO_{12}(s)$ (RE= La, Nd, Sm, Eu, Gd, Tb, Dy, Ho, Tm, Yb and Lu) have been derived in this study using second law method.

The conflicting Gibbs energy of formation values of $Fe_2TeO_6(s)$ and $Ni_3TeO_6(s)$ were resolved from the measured $TeO_2(g)$ vapour pressure over the required equilibrium phase field using transpiration technique given by Sahu et al. [30]. The $\Delta_f H^o_m$ (298.15 K) and S^o_m (298.15 K) values of $Fe_2TeO_6(s)$ and $Ni_3TeO_6(s)$ were derived from the Gibbs energy expression using second law method. An empirical relation between $\Delta_f H^o_m(A_nTeO_6,s,298.15\ K)$ and enthalpy of formation of transition metal oxide has been derived. From the relation, enthalpy of formation of $A_nTeO_6(s)$ (A = Ba, Bi, Ca, Cd, Co, Cr, Cs, Cu, Dy, Er, Eu, Fe, Gd, Ho, K, La, Li, Lu, Mg, Mn, Na, Nd, Ni, Pb, Rb, Sm, Sr, Tb, Tl, Tm, Y, Yb, Pr and Sc) can be estimated with reasonable accuracy.

The Thermodynamic functions like $H^o_m(T)$-$H^o_m(298.15K)$, $S^o_m(T)$ and Gibbs energy functions ($\phi^o_m(T)$) for $SrCeO_3(s)$, $Sr_2CeO_4(s)$, $Ba_{1-x}Sr_xMoO_4(s)$ (x = 0, 0.18, 0.38, 0.60, 0.81, 1) and of $Ba_{1-x}Sr_x MoO_3(s)$ (x=0, 0.2, 0.4, 0.5, 0.8, 1) have been calculated from the measured heat capacities in this study. Similarly, $H^o_m(T)$-$H^o_m(298.15K)$, $S^o_m(T)$,$\phi^o_m(T)$, $G^o_m(T)$, $H^o_m(T)$, $\Delta_f H^o_m(T)$ and $\Delta_f G^o_m(T)$ have been computed for $RE_6UO_{12}(s)$ (RE= La, Pr, Nd, Sm, Eu, Gd, Tb, Dy, Ho, Er, Tm, Yb and Lu), $Cr_2TeO_6(s)$, $Fe_2TeO_6(s)$ and $Ni_3TeO_6(s)$ from the measured heat capacity and derived $\Delta_f H^o_m(T)$ and S^o_m(298.15 K) values from the Gibbs energy data.

In order to predict the Te potential required for corrosion of stainless steel clad, the chemical potential diagram of Cr-Te-O, Fe-Te-O and Ni-Te-O systems were constructed using thermodynamic information of the various binary alloys in Cr-Te, Fe-Te, Ni-Te and binary oxide phases present in Cr-O, Fe-O, Ni-O, Te-O and ternary phases present in Cr-Te-O, Fe-Te-O and Ni-Te-O systems. These diagrams illustrate the stability of various compounds formed between tellurium and the different stainless steel components under various tellurium and oxygen potentials. The study on chemical potential leads to the conclusion that the reaction between stainless steel clad and tellurium can only take place to form $CrTe_{1.1}(s)$ before the formation of Cr_2O_3 (s).

The average thermal expansion coefficient of RE_6UO_{12}(s) (RE= La, Pr, Nd, Sm, Eu, Gd, Tb, Dy, Ho, Er, Tm, Yb and Lu), $SrCeO_3$(s), Sr_2CeO_4(s), Cr_2TeO_6(s), Fe_2TeO_6(s) and Ni_3TeO_6(s) were found to be much higher than that of MOX fuel. However, α_{av} of $Ba_{1-x}Sr_x MoO_3$(s) (x=0, 0.4, 0.8, 1) are close to MOX fuel. The α_{av} of $Ba_{1-x}Sr_xMoO_4$(s) (x = 0, 0.6, 1) is higher than $Ba_{1-x}Sr_xMoO_3$(s) with ABO_3 type of structure. The plot of heat capacity data of RE_6UO_{12}(s) (RE= La, Pr, Nd, Sm, Eu, Gd, Tb, Dy, Ho, Er, Tm, Yb and Lu) as a function of RE^{3+} did not show any systematic trend which was similar as RE_2O_3(s). However $C^o_p(T)$ of La^{3+} (no 4f electrons), Gd^{3+} (half filled 4f shell) and Lu^{3+} (completely filled 4f electrons) follows a straight-line. Hence, the excess $C^o_p(T)$ of RE_6UO_{12}(s) (RE= La, Pr, Nd, Sm, Eu, Gd, Tb, Dy, Ho, Er, Tm, Yb and Lu) might be due to magnetic and other contributions. The RE_6UO_{12}(s) (RE= La, Pr, Nd, Sm, Eu, Gd, Tb, Dy, Ho, Er, Tm, Yb and Lu) did not show any regular trend in physical properties due to presence of f- electrons. The phase transition in Nd_6UO_{12}(s) Sm_6UO_{12}(s) Tb_6UO_{12}(s) and Yb_6UO_{12}(s) and Sr_2CeO_4(s) were found from the determination of physico-chemical properties.

The generated thermodynamic data can be used for making database for computational modeling and thermodynamic reference table. The derived estimation method can be used to determine Δ_fH^o(298.15 K) of corrosive tellurates:A_nTeO_6(s). Some data generated in this study can be used for the reactor. From the chemical potential diagram it was observed that $CrTe_{1.1}$(s) requires least tellurium potential amongst all binary telluride of stainless steel components. The MOX fuel with high Pu content and higher burn up may lead to formation of metal telluride and tellurate formation can be ruled out under normal operating conditions.

This thesis is divided into eight chapters and the content of each chapter is briefed below.

Chapter-1

This chapter gives a brief introduction about the research problems and importance of thermophysico-chemical property measurements of complex oxides. It clearly gives the existing data and why further data is required in the identified systems.

Chapter -2

It gives the experimental methods used in this study. It describes HT-XRD and analysis of XRD data to calculate room temperature and high temperature lattice parameter, from which % volume expansion, volume expansion coefficient and average thermal expansion coefficient can be derived. It describes different calorimetric techniques to measure heat flow curve and its temperature and energy calibrations. It gives various methods of determination of Gibbs energy. It gives e.m.f and transpiration techniques elaborately. It gives 2nd and 3rd law methods for calculations of enthalpy and entropy at 298.15 K from the high temperature $\Delta_f G^o{}_m(T)$. It describes the calculations of thermodynamic functions from $C^o{}_p\ (T)$, $\Delta_f H^o{}_m$ (298.15 K) and $S^o{}_m$(298.15 K). It also describes the characterization methods like Raman spectroscopy and SEM. It described ICPMS technique, which was used for the determination of purity and stoichiometry of compounds. It briefly described the impedance spectroscopy used for confirmation of phase transition.

Chapter -3

It gives the detailed literature survey on RE-U-O system and its method of preparation and characterization. Method of indexing of Er_6UO_{12} (s) is given. It gives calculations of thermal expansions of RE_6UO_{12}(s). The measured heat capacity values of RE_6UO_{12}(s) are also given in this chapter. It gives measured Gibbs energy values of RE_6UO_{12}(s) and derived $\Delta_f H^o{}_m$(298.15K) and their variation with ionic radius of RE^{3+}. It identifies phase transitions in RE_6UO_{12}(s) and confirms them using thermal expansion and electrical conductivity measurements. The summary of studies on RE_6UO_{12}(s) system is given in this study.

Chapter -4

It describes the reported literature on thermo physical studies on Sr-Ce-O system and motivaton of the study. The synthesis and characterization of $SrCeO_3$(s) and Sr_2CeO_4(s) has been given. The thermal expansion study of these compounds using HT-XRD is given. The studies of heat capacity of these compounds are also given for these compounds. The identification of phase transition in Sr_2CeO_4(s) and conformation of it from thermal expansion is also given. The summary of studies on $SrCeO_3$(s) and Sr_2CeO_4(s) is given.

Chapter -5

It describes the literature survey on solid solutions of $BaMoO_4$(s) -$SrMoO_4$(s) system and their reported thermophysical properties. It gives the synthesis and characterization of solid solutions and measurements of their thermal expansion using HT-XRD. It gives the indexing of crystal structure of $Ba_{1-x}Sr_xMoO_4$(s) (x = 0, 0.18, 0.38, 0.60, 0.81, 1) from room temperature XRD data. The measured heat capacity data are given. The brief summary of the solid solutions are given.

Chapter -6

In this chapter, the literature of thermo-physical properties of $Ba_{1-x}Sr_x$ MoO_3(s) (x= 0, 0.2, 0.4, 0.5, 0.8, 1) solid solutions are given. The synthesis of this solid solution from the solid state reduction of $Ba_{1-x}Sr_x$ MoO_4(s) is described along with its characterizing methods. It gives the measurements of thermal expansion and heat capacity. The results are discussed and its summary is given.

Chapter -7

It gives literature on A-Te-O (A=Cr, Fe, Ni) system and their preparations and characterizations using XRD. The measurement method of Gibbs energy of formation is given. It gives method of calculation of chemical potential diagram. It also gives results, discussion and summary on tellurates of stainless components.

Chapter -8

It gives conclusions and highlights of the study and suggestions for further study related to this study.

References:

1. T. Yamashita, T. Fujino, J. Nucl. Mater. 132 (1985) 192.
2. K. Bakker, E.H.P. Cordfunke, R.J.M. Konings, R.P.C. Schram, J. Nucl. Mater. 250 (1997) 1.
3. H. Kleykamp, J. Nucl. Mater. 131 (1985) 221.
4. M.G. Adamson, E.A. Aitken, T.B. Lindemer, J. Nucl. Mater. 130 (1985) 375.
5. Y. Hinatsu, N. Masaki, T. Fujino, J. Solid State Chem. 73 (1988) 567.
6. E.A. Aitken, S.F. Bartram, E.F. Juenke, Inorg. Chem. 3 (1964) 949.
7. Y. Zheng, K. Kurosaki, K. Tokushima, Y. Ohishi, H. Muta, S, Yamanaka, J. Nucl. Mater. 419 (2011) 357.
8. H. Iwahara, T. Esaka, H. Uchida, N. Maeda, Solid State Ionics 3/4 (1981) 359.
9. H. Matsumoto, S. Hamajima, H. Iwahara, J. Electrochem. Soc. 148 (10) (2001) D121.

10. H. Iwahara, Solid State Ionics 77 (1995) 289.
11. E. Danielson, M. Devenney, D.M. Giaquinta, J.H. Golden, R.C. Haushalter, E.W. McFarland, D.M. Poojary, C.M. Reaves, W.H. Weinberg, X.D. Wu, J. Mol. Struct. 470 (1998) 229.
12. Y.M. Zhang, F.D. Yang, J. Yang, Y. Tang, P. Yuan, Solid State Commun. 133 (2005) 759.
13. Chang-Tai Xia, V.M. Fuenzalida, R.A. Zarate, J. Alloys Compd. 316 (2001) 250.
14. Y.Wang, S. Gai, C. Li, X. Zhang, N. Niu, F. He, M. Zhanga, P. Yang, RSC Adv. 3(2013) 5945.
15. PDF-2 Database, International Centre for Diffraction Data, Pennsylvania, 1997.
16. R. Dawar, R. Pankajavalli, J. Joseph, S. Anthonyswamy and V. Ganesan, J. Therm. Anal. Calorim. 112**(**2013) 95.
17. K.Krishnan, K.D.Singh Mudher, G.A. Rama Rao and V.Venugopal, J. Alloys Compd. 316**(**2001) 264.
18. K.Krishnan, G.A. Rama rao, K.D.Singh Mudher and V.Venugopal, J. Alloys Compd. 288**(**1999) 96.
19. M. Ali, R. Mishra, A.S. Kerkar, S.R. Bharadwaj and D. Das, J. Nucl. Mater. 301(2002)183.
20. C.Mallika and O.M. Sreedharan, Thermochim. Acta. 190**(**1991) 217.
21. M. Yamaguchi, M. Ishikawa, J. Phys. Soc. Jpn. 63 (1994) 1666.
22. T. Birchall, J. Solid State Chem. 27(1979) 293.
23. Y.N.Shyr and G.L. Price, Ind. Eng. Chem. Prod. Res. Dev. **23(**1984) 536.
24. V.K. Wadhawan, LATPAR, A least squares fitting program, Neutron Physics Division, Bhabha Atomic Research Centre, Mumbai, India, Private Communication.
25. M. Keskar, K. Krishnan, N.D. Dahale, J. Alloys Compd. 458 (2008) 104.
26. K.H. Kang, H.J. Ryu, K.C. Song, M.S. Yang, J. Nucl. Mater. 301(2-3) (2002) 242.
27. A.K. Tyagi, M.D. Mathews, B.R. Ambekar, R. Ramachandran, Thermochim. Acta. 421 (2004) 69.
28. M. Sahu, K. Krishnan, B.K. Nagar, M.K. Saxena, S. Dash, Thermochim. Acta 525 (2011) 167.
29. Z. Singh, S. Dash, R. Prasad and D.D. Sood, J. Alloys and Comp. 215 (1994) 303.
30. M. Sahu, D. Rawat, B. G. Vats, M.K. Saxena, S. Dash Thermochim. Acta, 585(2014) 50.

LIST OF FIGURES

Fig. Nos.	Figure Caption	Page No.
Fig.1.1.	The different stages of nuclear reactors	**4**
Fig.1.2.	The cross sectional view of nuclear fuel pellet, cladding and coolant flow.	**5**
Fig.1.3.	The fission yield curve of ^{233}U, ^{235}U and ^{239}Pu with thermal neutrons.	**7**
Fig.1.4.	The fission yield curve of ^{235}U with thermal and fast neutrons	**7**
Fig.1.5.	Ionic radii of lanthanides and actinides for +3 and +4 oxidation states	**12**
Fig.2.1.	The schematic of substitutional solid solutions.	**26**
Fig.2.2.	Schematic of Interstitial solid solutions	**27**
Fig. 2.3.	Schematics of powder X-ray diffractometer	**30**
Fig. 2.4.	Schematic of hexagonal unit cell incorporating rhombohedral structure	**33**
Fig.2.5.	Representation of Rayleigh scattering, Stokes scattering and anti-Stokes	**35**
Fig.2.6.	The experimental set up of Raman spectrometer	**36**
Fig.2.7.	Schematic of Scanning Electron Microscope	**37**
Fig.2.8.	The different signal obtained from the interaction of electron with samples	**38**
Fig.2.9.	Representation of Interaction volume	**39**
Fig.2.10.	A schematic of ICPMS.	**40**
Fig.2.11.	Schematic of simultaneous TG-DTA system(M/s Netzsch, Germany)	**41**
Fig.2.12.	A Jablonski diagram shows the possible relaxation processes in a molecule	**42**
Fig. 2.13.	The block diagram of spectrofluorometer	**43**
Fig.2.14.	a) The variation of the potential function with interatomic separation for a simple harmonic and an anharmonic oscillator (b) Representation of potential energy curve of a weakly and strongly bonded molecule	**44**
Fig.2.15.	X-ray diffraction geometry incorporating high temperature attachment	**48**

Fig.2.16. Schematic diagram of a heat flux DSC. **58**

Fig.2.17. A typical DSC signal showing measured heat flow rate as a function of temperature. **59**

Fig. 2.18. Schematic diagram of the DSC used in the present study (M/s. Mettler Toledo GmbH, Switzerland). **64**

Fig. 2.19. FRS-5 sensor of the DSC 823e/700(M/s. Mettler Toledo GmbH, Switzerland). **64**

Fig. 2.20. Three step procedure for measuring heat capacity **65**

Fig. 2.21. Typical DSC run for blank, sample and reference **65**

Fig.2.22. A typical measured temperature signal of TMDSC. **69**

Fig. 2.23. Schematic of the signal flow in a TMDSC. **70**

Fig. 2.24. (a)Fluorite structure(b) Generation of oxide vacancy with **75**

Fig.2.25 Phase Diagram for the Zirconia Yttria System. **76**

Fig. 2.26. Schematic representation of (a) conductivities of electrons, holes and ions, (b) transport number of ions in solid electrolyte, (c) effect of dopant concentration on conductivities of species. **80**

Fig. 2.27. Electrolytic domain boundary of calcia stabilized zirconia and yttria doped thoria. **81**

Fig. 2.28. Schematic diagram for solid oxide galvanic cell for emf measurements. **87**

Fig. 2.29. Schematic diagram of transpiration apparatus **91**

Fig.2.30. A typical flow rate Plateau in transpiration technique **92**

Fig.2.31. The representation of (a) and (b) first-order transitions, (c) and (d) second order transition. C is the specific heat. **102**

Fig.2.32. Equivalent electrical circuit of a ceramic electrolyte, consisting of a series combination of parallely connected resistors (R) and Capacitors (C) **104**

Fig.2.33. Impedance spectrum for a solid ionic conductor **104**

Fig.3.1. XRD pattern of RE_6UO_{12}(s) (RE = La, Pr, Nd, Sm, Eu, Gd, Tb, Dy, Ho, Tm, Yb, Lu). **108**

Fig 3.2. The X-ray Diffraction Patterns of Er_6UO_{12}(s) and Tm_6UO_{12}(s). **109**

Fig.3.3. The plot of room temperature lattice parameters (*a* &c) and unit cell volume (*V*) of RE_6UO_{12} (s) as a function of ionic raddi of rare earth ions (RE^{+3}). **112**

Fig.3.4. The high temperature XRD patterns of Sm_6UO_{12}(s). **113**

Fig.3.5. The lattice parameters along *a*- axis as a function of temperature for RE_6UO_{12}(s) (RE= La, Pr, Nd, Sm, Eu, Gd, Tb, Dy, Ho, Er, Tm, Yb, Lu). **114**

Fig.3.6. The lattice parameters along *c*- axis as a function of temperature for $RE_6UO_{12}(s)$(RE= La,Pr, Nd, Sm, Eu, Gd, Tb, Dy, Ho, Er, Tm, Yb, Lu). **114**

Fig.3.7. The unit cell volume as function of temperature for $RE_6UO_{12}(s)$ (RE= La,Pr, Nd, Sm, Eu, Gd, Tb, Dy, Ho, Er, Tm, Yb, Lu). **115**

Fig.3.8. The density as function of temperature for $RE_6UO_{12}(s)$(RE= La,Pr, Nd, Sm, Eu, Gd, Tb, Dy, Ho, Er, Tm, Yb, Lu). **115**

Fig.3.9. The percentage variation of lattice parameter along *a*- axis as a function of temperature for $RE_6UO_{12}(s)$(RE= La,Pr, Nd, Sm, Eu, Gd, Tb, Dy, Ho, Er, Tm, Yb, Lu) **121**

Fig.3.10. The percentage variation of lattice parameter along *c*- axis as a function of temperature for $RE_6UO_{12}(s)$(RE= La,Pr, Nd, Sm, Eu, Gd, Tb, Dy, Ho, Er, Tm, Yb, Lu). **121**

Fig.3.11. The percentage variation of unit cell volume as a function of temperature for $RE_6UO_{12}(s)$ (RE= La,Pr, Nd, Sm, Eu, Gd, Tb, Dy, Ho, Er, Tm, Yb, Lu). **122**

Fig.3.12. The heat capacity of $La_6UO_{12}(s)$ as function of temperature. **123**

Fig.3.13. The heat capacity of $Pr_6UO_{12}(s)$ as function of temperature. **123**

Fig.3.14. The heat capacity of $Nd_6UO_{12}(s)$ as a function of temperature. **124**

Fig.3.15. The heat capacity of $Sm_6UO_{12}(s)$ as a function of temperature. **124**

Fig.3.16. The heat capacity of $Eu_6UO_{12}(s)$ as a function of temperature. **125**

Fig.3.17. The heat capacity of $Gd_6UO_{12}(s)$ as a function of temperature. **125**

Fig.3.18. The heat capacity of $Tb_6UO_{12}(s)$ as a function of temperature **126**

Fig.3.19. The heat capacity of $Dy_6UO_{12}(s)$ as a function of temperature. **126**

Fig.3.20. The heat capacity of $Ho_6UO_{12}(s)$ as a function of temperature. **127**

Fig.3.21. The heat capacity of $Er_6UO_{12}(s)$ as a function of temperature. **127**

Fig.3.22. The heat capacity of $Tm_6UO_{12}(s)$ as a function of temperature. **128**

Fig.3.23. The heat capacity of $Yb_6UO_{12}(s)$ as a function of temperature. **128**

Fig.3.24. The heat capacity of $Lu_6UO_{12}(s)$ as a function of temperature. **129**

Fig.3.25. The variation of e.m.f as function of temperature for Cell-1 **133**

Fig.3.26. The plot of emfs against temperature for the cell (-)Pt, $\{La_6UO_{12}(s) + La_2O_3(s) + U_3O_8(s)\}$ //YSZ// air $\{(p_{O2} = 21.21 kPa)\}$, Pt (+) **135**

Fig.3.27. The plot of emfs against temperature for the cell (-)Pt, $\{Nd_6UO_{12}(s) + Nd_2O_3(s) + U_3O_8(s)\}$ //YSZ// air $\{(p_{O2} = 21.21 kPa)\}$,Pt (+) and (-)Pt, (Ni(s)+NiO(s)) //YSZ// $\{Nd_6UO_{12}(s) + Nd_2O_3(s) + U_3O_8(s)\}$ Pt (+) **135**

Fig.3.28. The plot of emfs against temperature for the cell (-)Pt, $\{Sm_6UO_{12}(s) + Sm_2O_3(s) + U_3O_8(s)\}$ //YSZ// air $\{(p_{O2} = 21.21 kPa)\}$, Pt (+) and (-)Pt, (Ni(s)+NiO(s)) //YSZ// $\{Sm_6UO_{12}(s) + Sm_2O_3(s) + U_3O_8(s)\}$ Pt (+) **136**

Fig.3.29. The plot of emfs against temperature for the cell (-)Pt, $\{Eu_6UO_{12}(s) + Eu_2O_3(s) + U_3O_8(s)\}$ //YSZ// air $\{(p_{O2} = 21.21 kPa)\}$, Pt (+) and (-)Pt, (Ni(s)+NiO(s)) //YSZ// $\{Eu_6UO_{12}(s) + Eu_2O_3(s) + U_3O_8(s)\}$ Pt (+). **136**

Fig.3.30. The plot of emfs against temperature for the cell (-)Pt, $\{Gd_6UO_{12}(s) + Gd_2O_3(s) + U_3O_8(s)\}$ //YSZ// air $\{(p_{O2} = 21.21 kPa)\}$, Pt (+) and (-)Pt, (Ni(s)+NiO(s)) //YSZ// $\{Gd_6UO_{12}(s) + Gd_2O_3(s) + U_3O_8(s)\}$ Pt (+). **137**

Fig.3.31. The plot of emfs against temperature for the cell (-)Pt, $\{Tb_6UO_{12}(s) + Tb_2O_3(s) + U_3O_8(s)\}$ //YSZ// air $\{(p_{O2} = 21.21 kPa)\}$, Pt (+) and (-)Pt, (Ni(s)+NiO(s))//YSZ//$\{Tb_6UO_{12}(s) + Tb_2O_3(s) + U_3O_8(s)\}$ Pt (+). **137**

Fig.3.32. The plot of emfs against temperature for the cell (-)Pt, $\{Dy_6UO_{12}(s) + Dy_2O_3(s) + U_3O_8(s)\}$ //YSZ// air $\{(p_{O2} = 21.21 kPa)\}$, Pt (+) and (-)Pt, (Ni(s)+NiO(s))//YSZ//$\{Dy_6UO_{12}(s) + Dy_2O_3(s) + U_3O_8(s)\}$ Pt (+). **138**

Fig.3.33. The plot of emfs against temperature for the cell (-)Pt, $\{Ho_6UO_{12}(s) + Ho_2O_3(s) + U_3O_8(s)\}$ //YSZ// air $\{(p_{O2} = 21.21 kPa)\}$, Pt (+) and (-)Pt, (Ni(s)+NiO(s))//YSZ//$\{Ho_6UO_{12}(s) + Ho_2O_3(s) + U_3O_8(s)\}$ Pt (+). **138**

Fig.3.34. The plot of emfs against temperature for the cell (-)Pt, $\{Tm_6UO_{12}(s) + Tm_2O_3(s) + U_3O_8(s)\}$ //YSZ// air $\{(p_{O2} = 21.21 kPa)\}$, Pt (+) and (-)Pt, (Ni(s)+NiO(s))//YSZ// $\{Tm_6UO_{12}(s) + Tm_2O_3(s) + U_3O_8(s)\}$ Pt (+) . **139**

Fig.3.35. The plot of emfs against temperature for the cell (-)Pt, $\{Yb_6UO_{12}(s) + Yb_2O_3(s) + U_3O_8(s)\}$ //YSZ// air $\{(p_{O2} = 21.21 kPa)\}$, Pt (+) and (-)Pt, (Ni(s)+NiO(s)) //YSZ// $\{Yb_6UO_{12}(s) + Yb_2O_3(s) + U_3O_8(s)\}$ Pt (+) . **139**

Fig.3.36. The plot of emfs against temperature for the cell (-)Pt, {Lu_6UO_{12}(s) + Lu_2O_3(s) + U_3O_8(s)} //YSZ// air {(p_{O2} = 21.21kPa)}, Pt (+) and (-)Pt, (Ni(s)+NiO(s))//YSZ// {Lu_6UO_{12}(s) + Lu_2O_3(s) + U_3O_8(s)} Pt (+). **140**

Fig. 3.37. XRD pattern of the sample {RE_6UO_{12}(s) + RE_2O_3(s) + U_3O_8(s)}(RE=La, Nd,Sm, Eu,Gd and Tb) before and after equilibration at various temperatures **145**

Fig. 3.38. XRD pattern of the sample {RE_6UO_{12}(s) + RE_2O_3(s) + U_3O_8(s)}(RE=Dy, Ho, Tm, Yb, Lu) before and after equilibration at various temperatures **146**

Fig.3.39. The Nyquist plot of Nd_6UO_{12}(s) **152**

Fig.3.40. The Nyquist plot of Gd_6UO_{12}(s) **153**

Fig.3.41. The Nyquist plot of Dy_6UO_{12}(s) **153**

Fig.3.42. The Nyquist plot of Tb_6UO_{12}(s) **154**

Fig.3.43. The high temperatures XRD patterns of Yb_6UO_{12}(s). **156**

Fig.3.44. The lattice parameters and unit cell volume of Dy_6UO_{12}(s) **157**

Fig.3.45. Lattice parameters and unit cell volume of Sm_6UO_{12}(s) **158**

Fig.3.46. The lattice parameters (*a* & *c*), unit cell volume (*V*), percentage expansion along *a* and *c* axis (%*a* &%c), percentage variation of unit cell volume (%*V*), the axial thermal expansion coefficients (α_a & α_c) and volume expansion coefficients (α_V) of Dy_6UO_{12}(s). **159**

Fig.3.47. The lattice parameters (*a* & *c*), unit cell volume (*V*), percentage expansion along *a* and *c* axis (%*a* &%c), percentage variation of unit cell volume (%*V*), the axial thermal expansion coefficients (α_a & α_c) and volume expansion coefficients (α_V) of Tb_6UO_{12}(s). **160**

Fig.3.48. The lattice parameters (*a* & *c*), unit cell volume (*V*), percentage expansion along *a* and *c* axis (%*a* &%c), percentage variation of unit cell volume (%*V*), the axial thermal expansion coefficients (α_a & α_c) and volume expansion coefficients (α_V) of Yb_6UO_{12}(s). **161**

Fig.3.49. The lattice parameters (*a* & *c*), unit cell volume (*V*), percentage expansion along *a* and *c* axis (%*a* &%c), percentage variation of unit cell volume (%*V*), the axial thermal expansion coefficients (α_a & α_c) and volume expansion coefficients (α_V) of Sm_6UO_{12}(s). **162**

Fig. 3.50. Comparison of the average linear thermal expansion coefficients (α_a and α_c) and volume thermal expansion coefficients (α_V) of RE_6UO_{12} (s) (RE = La, Pr, Nd, Sm, Eu, Gd, Tb, Dy, Ho, Er, Tm, Yb, Lu) as a function of radius of RE^{+3} in the temperature range 298-1273 K. **163**

Fig.3.51. The measured heat capcity of RE_6UO_{12}(s) (RE= Pr, Nd, Sm, Eu, Tb, Dy, Ho, Er, Tm, Yb). **165**

Fig.3.52. The computed heat capacity of RE_6UO_{12}(s)(RE= Pr, Nd, Sm, Eu, Tb, Dy, Ho, Er, Tm, Yb) using NK rule. **166**

Fig.3.53. A comparison of heat capacity of RE_6UO_{12}(s) and RE_2O_3(s). **166**

Fig.3.54. The volume expansion coefficients (α_V) of Nd_6UO_{12}(s) measured using push rod dilatometry **167**

Fig.3.55. Excess heat capacity of Nd_6UO_{12}(s) as a function of temperature. (a) Plot of $\Delta C^{o}_{p,m}$ (*T*) vs *T* (b) Plot of $\frac{\Delta C^{o}_{p,m}(T)}{T}$ vs *T* **168**

Fig.3.56. (a) Heat flow as a function of temperature for Tb_6UO_{12}(s) (b) Molar heat capacity data of Tb_6UO_{12}(s) in the temperature range of 300–870 K **169**

Fig.3.57. Excess heat capacity of Tb_6UO_{12} as a function of temperature. (a) Plot of $\Delta C^{o}_{p,m}$ vs T (b) Plot of $\frac{\Delta C^{o}_{p,m}}{T}$ vs T **170**

Fig.3.58. The plot of difference in ΔH_f^o(RE_6UO_{12},s,298.15K) calculated from cell 2 nd 3 from the sum of ΔH_f^o of ($3RE_2O_3$(s)+UO_3(s)) as function of atomic radii of rare earth ions. **172**

Fig.3.59. The plot of ΔH_f^o(RE_6UO_{12},s,298.15K) calculated from second law, ΔH_f^o(RE_2O_3,s,298.15K) from literature and the $\Delta_{OX}H_f^o$(RE_6UO_{12},s,298.15K) rom oxides as a function of atomic number of rare earth elements. **172**

Fig.3.60 ΔH_f^o(RE_6UO_{12},s,298.15K) calculated from second law and third law as a function of atomic number. **173**

Fig.3.61. The plot of S^o(RE_6UO_{12},s,298.15K) calculated from second law,S^o(RE_2O_3,s,298.15K) fom literature and $\Delta_{OX}S^o$(RE_6UO_{12},s,298.15K) as a function of atomic number of rare earth elements. **173**

Fig.3.62. Oxygen potential diagram for RE_6UO_{12}(s), U_3O_8(s) and UO_2(s) **174**

Fig.3.63. Conductivity of RE_6UO_{12}(s) (RE= Nd, Gd, Dy, Tb) in argon as a function of **175**

Fig.4.1 XRD pattern of $SrCeO_3$(s) and Sr_2CeO_4(s) **179**

Fig.4.2. The variation of lattice parameters and unit cell volume with temperature for $SrCeO_3$(s). **182**

Fig.4.3. The variation of percentage linear and volume expansion for $SrCeO_3$(s) and Sr_2CeO_4(s) as function of temperature **184**

Fig.4.4. The variation of lattice and volume expansion coefficients of $SrCeO_3$(s) and Sr_2CeO_4(s) as function of temperature **184**

Fig.4.5. The variation of lattice parameters and unit cell volume with temperature for Sr_2CeO_4(s). **185**

Fig.4.6. Heat capacity of CeO_2(s) as a function of temperature **187**

Fig.4.7. Heat capacity of $SrCeO_3$(s) as function of temperature **188**

Fig.4.8. Heat capacity of Sr_2CeO_4(s) as function of temperature. **189**

Fig 4.9. The Nyquist plot of Sr_2CeO_4(s) in argon ambient. **191**

Fig.4.10. The electrical conductivity of Sr_2CeO_4(s) as function of temperature **191**

Fig.4.11. Comparison of the XRD pattern of (a) pure $SrCeO_3$(s) synthesized in air, (b) $SrCeO_3$(s) heated in high pure argon and (c) $SrCeO_3$(s) heated in air after heating in high pure argon. **193**

Fig. 4.12. The emission spectra of $SrCeO_3$(s) heated in argon for 24 h at various temperatures. **195**

Fig.4.13. The comparison between the volume thermal expansion coefficients of $SrCeO_3$(s) and Sr_2CeO_4(s) as a function of temperature **196**

Fig.4.14. The comparison of percentage volume expansion and percentage reduction in density of $SrCeO_3$(s) and Sr_2CeO_4(s) as a function of temperature. **198**

Fig.5.1. TG-DTA of Precursors for the synthesis of $Ba_{1-x}Sr_xMoO_4$ (x = 0, 0.2, 0.4, 0.5, 0.8, 1) solid solution **201**

Fig.5.2. XRD pattern of $Ba_{1-x}Sr_x MoO_4$ (x = 0, 0.18, 0.38, 0.60, 0.81, 1) solid solutions. **202**

Fig.5.3. A plot of linear lattice parameters (a and c), unit cell volume (V) and density (ρ) as a function of mole fraction of $SrMoO_4$(s) for $Ba_{1-x}Sr_x MoO_4$ (x = 0, 0.18, 0.38, 0.60, 0.81, 1) solid solutions **203**

Fig.5.4. Unpolarised spontaneous Raman spectra of $Ba_{1-x}Sr_x MoO_4$ (x = 0, 0.18, 0.38, 0.60, 0.81, 1) solid solutions in the range of wave number 50-450 cm^{-1} **204**

Fig.5.5. Unpolarised spontaneous Raman spectra of Ba $_{1\text{-x}}$Sr$_\text{x}$ MoO$_4$ (x = 0, 0.18, 0.38, 0.60, 0.81, 1) solid solutions in the range of wave number 750-950 cm^{-1}. **205**

Fig.5.6. Variation of Raman peak widths with increasing Sr^{2+} concentration for Ba $_{1\text{-x}}$Sr$_\text{x}$ MoO$_4$ (x = 0, 0.18, 0.38, 0.60, 0.81, 1) solid solutions **208**

Fig.5.7. Scanning electron micrograph of SrMoO$_4$(s). **208**

Fig.5.8. Scanning electron micrograph of BaMoO$_4$(s). **209**

Fig.5.9. The percentage linear thermal expansion (% *l*) calculated from lattice parameter of Ba$_{1\text{-x}}$Sr$_\text{x}$ MoO$_4$ (x = 0, 0.6 and 1) solid solutions along *a* and *c* - axis. **213**

Fig.5.10. The percentage variation in volume (%*V*) and density ((%ρ) of Ba $_{1\text{-x}}$Sr$_\text{x}$MoO$_4$ (x = 0, 0.6 and 1) solid solutions calculated from unit cell volume and density at different temperatures. **213**

Fig.5.11. The plot of average linear thermal expansion coefficient (α_a and α_c) of Ba $_{1\text{- x}}$Sr$_\text{x}$ MoO$_4$(x = 0, 0.6 and 1) as a function of mole fraction of SrMoO$_4$(s) in the temperature range of 298-1273 K. **214**

Fig.5.12. A plot of average volume thermal expansion coefficient (α_V) of Ba $_{1\text{-x}}$Sr$_\text{x}$ MoO$_4$ (x = 0, 0.6 and 1) as a function of mole fraction of SrMoO$_4$(s) in the temperature range of 298- 1273 K **214**

Fig.5.13. Molar heat capacity data of BaMoO$_4$(s) in the temperature range of 300-87 K. **215**

Fig.5.14. Molar heat capacity data of SrMoO$_4$(s) in the temperature range of 300-870 K. **216**

Fig.5.15. Specific heat capacity of Ba $_{1\text{-x}}$Sr$_\text{x}$ MoO$_4$ (x = 0, 0.18, 0.38, 0.60, 0.81, 1) solid solutions as function of temperature in the temperature range of 300-870 K **220**

Fig.6.1. The XRD patterns of Ba$_{1\text{-x}}$Sr$_\text{x}$MoO$_3$ (s) (x = 0, 0.2, 0.4, 0.50, 0.8, 1) solid solution **226**

Fig.6.2. The plot of linear lattice parameters (*a)* and unit cell volume (*V*) as function of mole fraction of SrMoO$_3$(s) for Ba $_{1\text{-x}}$Sr$_\text{x}$ MoO$_3$(s)(x = 0, 0.2, 0.4, 0.5, 0.8, 1) solid solutions **227**

Fig.6.3. The scanning electron micrograph of SrMoO$_3$(s) **229**

Fig.6.4. The scanning electron micrograph of BaMoO$_3$(s). **229**

Fig.6.5. A plot of average linear and volume thermal expansion coefficient as a function of mole fraction of SrMoO$_3$(s) for Ba $_{1\text{-x}}$Sr$_\text{x}$ MoO$_3$ (s) (x = 0, 0.4, 0.8, 1) solid solutions **230**

Fig.6.6. The heat capacity of $BaMoO_3$(s) as a function of temperature. **233**

Fig.6.7. The heat capacity of $SrMoO_3$(s) as a function of temperature. **233**

Fig.6.8. A comparison of specific heat capacity of $Ba_{1-x}Sr_x MoO_3$ (s) (x=0, 0.4, 0.8, 1) solid solutions as a function of temperature **234**

Fig.7.1 XRD Patterns of Cr_2TeO_6(s), Fe_2TeO_6(s) and Ni_3TeO_6(s). **237**

Fig.7.2. Lattice parameters and unit cell volume of Cr_2TeO_6(s), Fe_2TeO_6(s) and Ni_3TeO_6(s) as function of temperature **241**

Fig.7.3. The measured molar heat capacity of Cr_2TeO_6(s), Fe_2TeO_6(s) and Ni_3TeO_6(s) as a function of temperature in the range 300-870 K. **243**

Fig.7.4. Heat capacity of TeO_3(s) derived from the tellurate containg Te(VI) using Newmann Kopp's rule **244**

Fig.7.5. The vapour pressures of TeO_2(g) over {Fe_2TeO_6(s) + Fe_2O_3(s)} and {Ni_3TeO_6(s) +NiO(s)} as a function of temperature. **245**

Fig.7.6. A comparison of Gibbs energy of formation of Cr_2TeO_6(s), Fe_2TeO_6(s) and Ni_3TeO_6(s) reported in the literature with that measured in this study. **248**

Fig.7.7. The plot of calculated enthalpy data for ternary tellurates (A_nTeO_6, s, 298.15K) against $\Delta_f H^\circ_m$(298.15K) of corresponding metal oxides(A_xO_y(s) normalized to 1.5 mole of oxygen. **252**

Fig.7.8. The chemical potential diagram of Cr-Te-O system at 900 K. The shaded region in the figure represent a typical $\Delta\mu(O_2)$ and $\Delta\mu$(Te) in the operating mixed oxide fuel. **262**

Fig.7.9. The chemical potential diagram of Fe-Te-O system at 900 K. The shaded region in the figure represent a typical $\Delta\mu(O_2)$ and $\Delta\mu$(Te) in the operating mixed oxide fuel. **262**

Fig.7.10. The chemical potential diagram of Ni-Te-O system at 900 K. The shaded region in the figure represent a typical $\Delta\mu(O_2)$ and $\Delta\mu$(Te) in the operating mixed oxide fuel. **263**

LIST OF TABLES

Table No.	Table Caption	Page No.
Table 1.1.	Chemical state of FPs in irradiated fuel	**7**
Table 1.2.	Electronic configurations of lanthanide and actinide elements	**11**
Table 1.3.	Fission yields of various rare earth fission products for the fission of different fissile isotopes in fast neutron spectrum	**13**
Table 2.1.	Seven crystal system: Relation between unit cell parameters and lattice symmetry	**32**
Table 3.1.	X-ray powder diffraction data of Er_6UO_{12}(s).	**110**
Table 3.2.	Crystal data for the RE_6UO_{12}(s) (RE=La, Pr, Nd, Sm, Eu, Gd, Tb, Dy, Ho, Er, Tm, Yb, Lu) measured by XRD.	**111**
Table 3.3.	The lattice parameters (a and c), volume (V), density (ρ), linear (α_a and α_c) and volume (α_V) thermal expansion coefficients of RE_6UO_{12}(s) (RE = Pr, Sm, Eu and Gd) at various temperature in the range 298-1273 K.	**116**
Table 3.4.	The lattice parameters (a and c), volume (V), density (ρ), linear (α_a and α_c) and volume (α_V) thermal expansion coefficients of RE_6UO_{12}(s) (RE = Tb, Dy, Ho and Er) at various temperature in the range 298–1,273 K.	**117**
Table 3.5.	Lattice parameters (a and c), volume (V), density (ρ), linear (α_a and α_c) and volume (α_V) thermal expansion coefficient of RE_6UO_{12}(s) (RE = Tm and Yb) at various temperature in the range 298–1,273 K.	**118**
Table 3.6.	Lattice parameters (a and c), volume (V), density (ρ), linear (α_a and α_c) and volume (α_V) thermal expansion coefficient of Lu_6UO_{12}(s) at various temperature in the range 298–1,273 K.	**119**
Table 3.7.	Polynomial Fitting parameters of lattice parameters (a, c) and the unit cell volume of RE_6UO_{12}(s) as function of temperature in the temperature range 298-1273 K.	**120**
Table. 3.8.	The coefficients of heat capacity, enthalpy increment, entropy and Gibbs energy function of RE_6UO_{12}(s) (RE=La, Pr, Nd, Sm, Eu, Gd).	**130**

Table. 3.9. The coefficients of heat capacity, enthalpy increment, entropy and Gibbs energy function of RE_6UO_{12}(s)(RE= Tb, Dy, Ho, Er, Tm, Yb, Lu). **131**

Table 3.10. The reversible emf of cell (1) **133**

Table 3.11. The reversible emfs of Cell (2) :(-)Pt, {RE_6UO_{12}(s) (RE=La, Nd, Sm) + RE_2O_3(s) + U_3O_8(s)} //YSZ// air {(p_{O2} = 21.21kPa)}, Pt (+) and Cell (3): (-)Pt, (Ni(s)+NiO(s)) //YSZ// {RE_6UO_{12}(s) + RE_2O_3(s) + U_3O_8(s)} Pt (+) **141**

Table 3.12. The reversible emfs of Cell (2):(-)Pt, {RE_6UO_{12}(s) (RE=Eu, Gd) + RE_2O_3(s) + U_3O_8(s)} //YSZ// air {(p_{O2} = 21.21kPa)}, Pt (+) and Cell(3):(-)Pt,(Ni(s)+NiO(s))//YSZ//{RE_6UO_{12}(s)+ RE_2O_3(s) + U_3O_8(s)}Pt (+) . **142**

Table 3.13. The reversible emfs of Cell (2):(-)Pt, {RE_6UO_{12}(s) (RE= Tb, Dy,Ho) + RE_2O_3(s) + U_3O_8(s)}//YSZ// air {(p_{O2} = 21.21kPa)},Pt(+) and Cell (3):(-)Pt, (Ni(s)+NiO(s))//YSZ// {RE_6UO_{12}(s) + RE_2O_3(s) + U_3O_8(s)} Pt (+). **143**

Table 3.14. The reversible emfs of Cell (2):(-)Pt, {RE_6UO_{12}(s) (RE= Tm, Yb, Lu) + RE_2O_3(s) + U_3O_8(s)} //YSZ// air {(p_{O2} = 21.21kPa)}, Pt (+) and Cell (3): (-)Pt, (Ni(s)+NiO(s)) //YSZ// {RE_6UO_{12}(s) + RE_2O_3(s) + U_3O_8(s)} Pt (+). **144**

Table 3.15. The e.m.f. data obtained for the electrochemical cells (2) and (3) with RE = La, Nd, Sm, Eu, Gd. **147**

Table 3.16. The e.m.f. data obtained for the electrochemical cells (2) and (3) with RE = Tb, Dy, Ho, Tm, Yb, Lu. **148**

Table 3.17. The ΔG_f^o (RE_6UO_{12},s), ΔH_f^o(RE_6UO_{12},s,298.15 K) derived from second and third law analysis and S^o(RE_6UO_{12},s,298.15K) derived from second law analysis from the e.m.f .data obtained for cell (2) & (3). **149**

Table 3.18. The ΔG_f^o (RE_6UO_{12},s), ΔH_f^o(RE_6UO_{12},s, 298.15 K) derived from second and third law analysis and S^o(RE_6UO_{12},s,298.15K) derived from second law analysis from the e.m.f data obtained for cell (2) & (3) **150**

Table 3.19. Conductivity values of RE_6UO_{12}(s) (RE= Nd, Gd, Dy, Tb) in air ambient **155**

Table 3.20. The average linear and volume thermal expansion coefficients of RE_6UO_{12} (s) (RE = La, Pr, Nd, Sm, Eu, Gd, Tb, Dy, Ho, Er, Tm, Yb, Lu). **164**

Table.4.1. Lattice parameters of $SrCeO_3$(s) and Sr_2CeO_4(s). **180**

Table.4.2. Impurity content analysed by Inductively Coupled Plasma Mass Spectrometry (ICPMS) in CeO_2(s), $SrCeO_3$(s) and Sr_2CeO_4(s). **181**

Table.4.3. The lattice parameters, volume, density, linear and volume expansion coefficients of $SrCeO_3$(s). **183**

Table.4.4. The lattice parameters, volume, density, linear and volume expansion coefficients of Sr_2CeO_4(s). **186**

Table 4.5. Thermodynamic functions of $SrCeO_3$(s). **188**

Table 4.6. Thermodynamic functions of Sr_2CeO_4(s) **190**

Table 4.7. Conductivity values of Sr_2CeO_4(s) in argon ambient **192**

Table.5.1. The stoichiometry of $Ba_{1-x}Sr_x MoO_4$ (x= 0.2, 0.4, 0.6, and 0.8) solid solutions determined by ICPMS. **200**

Table.5.2. Crystal system and lattice parameter of $BaMoO_4$(s) and $SrMoO_4$(s). **202**

Table 5.3. Raman mode frequencies of $Ba_{1-x}Sr_x MoO_4$ (x=0, 0.18, 0.38, 0.60, 0.81, 1) solid solutions at room temperature **207**

Table.5.4. X-Ray powder diffraction data of $Ba_{1-x} Sr_xMoO_4$ (s) solid solutions. **210**

Table.5.5. Lattice parameters (*a* and *c*), volume (*V*), density (ρ), linear (α_a and α_c) and volume (α_V) thermal expansion coefficients of $Ba_{1-x} Sr_xMoO_4$ (s) (x=0, 0.6 and 1) solid solutions in the temperature range 298-1273 K. **212**

Table.5.6. Heat capacities of $Ba_{1-x}Sr_x MoO_4$ solid-solution(x=0, 0.18, 0.38, 0.60, 0.81, 1) **217**

Table.5.7. The heat capacity coefficients of fitted polynomial for of $Ba_{1-x}Sr_x MoO_4$ (x=0, 0.18, 0.38, 0.60, 0.81, 1) solid-solutions in the temperature range of 140-450 K **218**

Table.5.8. The coefficients of heat capacity, enthalpy increment, entropy and Gibbs energy function of Ba $_{1-x}$Sr$_x$ MoO$_4$ (x=0, 0.18, 0.38, 0.60, 0.81, 1) solid-solutions **219**

Table.6.1. The stoichiometry of Ba$_{1-x}$Sr$_x$ MoO$_3$(s)(x = 0, 0.2, 0.4, 0.5, 0.8, 1) solid solutions determined from analysis of metallic content by ICPMS and non metallic oxygen by converting it to CO$_2$(g) **223**

Table.6.2. Crystal system and lattice parameter of BaMoO$_3$(s) and SrMoO$_3$(s) **225**

Table.6.3. X-Ray powder diffraction data of Ba $_{1-x}$ Sr $_x$MoO$_3$ (s) solid solutions **228**

Table.6.4. Lattice parameters(a), volume(V), linear(α_a) and volume(α_V) thermal expansion coefficients of Ba $_{1-x}$ Sr $_x$MoO$_3$(s) (x=0, 0.4 and 1) solid solutions in the temperature range 298-873 K **230**

Table.6.5. The coefficients of heat capacity, enthalpy increment, entropy and Gibbs energy function of Ba $_{1-x}$Sr$_x$ MoO3 (s) (x=0, 0.4, 0.8, 1). **232**

Table.7.1. Lattice parameters (a and c), volume (V), linear (α_a and α_c) and volume (α_V) thermal expansion coefficients of Fe$_2$TeO$_6$(s) in the temperature range 298-973 K and of Ni$_3$TeO$_6$(s) in the temperature range 298-923 K. **240**

Table.7.2. Experimentally determined molar heat capacity data for Cr$_2$TeO$_6$(s), Fe$_2$TeO$_6$(s) and Ni$_3$TeO$_6$(s) in the temperature range 298-870 K **242**

Table 7.3. Pressures of TeO$_2$(g) over {Fe$_2$TeO$_6$(s)+Fe$_2$O$_3$(s)} and $\Delta_f G^o{}_m$(Fe$_2$TeO$_6$,s,T) values as a function of temperature **246**

Table 7. 4. The $\Delta_f G^o{}_m(T)$ of binary oxides used for computation of Gibbs energy of formation of Fe$_2$TeO$_6$(s) and Ni$_3$TeO$_6$(s). **247**

Table 7.5. A comparison of $\Delta_f G^o{}_m$(Fe$_2$TeO$_6$,s,T) and $\Delta_f G^o{}_m$(Ni$_3$TeO$_6$,s,T) measured in this study and that reported in the literature. $\Delta_f G^o{}_m$(Cr$_2$TeO$_6$,s,T) reported in the literature has also been given. **249**

Table 7.6. Pressures of TeO$_2$(g) over {Ni$_3$TeO$_6$(s)+ NiO(s)} and $\Delta_f G^o{}_m$(Ni$_3$TeO$_6$,s,T) values as a function of temperature. **251**

Table 7.7. A comparison of $\Delta_f H^\circ_m$(A_nTeO_6,s, 298.15 K) values calculated in this study with that reported in the literature. **254**

Table 7.8. Thermodynamic functions for Cr_2TeO_6(s). **255**

Table 7.9. Thermodynamic functions for Fe_2TeO_6(s). **256**

Table 7.10. Thermodynamic functions for Ni_3TeO_6(s). **257**

Table 7.11. Constants of the fit equations of heat capacity and Gibbs energy of formation data of binary and ternary compounds in A-Te-O system. The enthalpy of formation and entropy at 298.15 K are also included. **261**

Table 7.12. The chemical potentials of Tellurium and oxygen at invariant points at 900K. **264**

CHAPTER-1

Introduction

Chapter-1

1.1. General Introduction

The per capita electrical energy consumption is an indicator of overall economic development of a country. The supply of electric energy at low cost with minimal adverse environmental effects is essential to civilized society. Nuclear energy is a clean, safe way to generate electricity. Nuclear energy is the energy (holds the nucleus together) that is stored in the nucleus of an atom. There are two ways to release the energy stored inside the atom. They are fusion (combining the atoms to make a new atom) and fission (splitting an atom into two smaller atoms). Fissile nuclides are those which are fissionable by neutrons of all energies and the known fissile nuclides are ^{235}U, ^{239}Pu and ^{233}U. The nuclear reactor used throughout the world for electric power generation obtains most of its energy from slow-neutron (0.025 eV) fission of ^{235}U, which occurs in natural uranium only to the extent of 1 part in 140. To obtain the full potential of nuclear energy it will be necessary to develop effective means for utilizing the abundant isotope, ^{238}U, which makes up the remaining 99.3% of natural uranium. The most promising type of reactor for this purpose is the fast-breeder reactor, in which ^{238}U is converted to plutonium, which then undergoes fission with fast neutrons (energy more than 1 MeV). The breeder reactor will provide the world with electric energy for thousands of years. The current nuclear power plants of the world are generating electricity at a cost as low as the cost of electricity from fossil fuels. However, breeder reactors, under development in many countries, are likely to generate electricity at an equally low cost.

The present contribution of nuclear energy in India is around 3% of its total electricity consumption. In order to provide quality of life to its growing population commensurate with other developed countries we need to increase the nuclear power to 9% of overall electricity generation capacity within 25 years and to increase the share of nuclear energy to 25% of the total power by 2052. The Indian nuclear power industry is expected to undergo a significant expansion in the coming years. India's domestic uranium reserves are small and the country is dependent on enriched uranium imports for light-water reactors that are currently under IAEA safeguards, but it has developed other aspects of the nuclear fuel cycle to support its reactors. Use of heavy water reactors has been particularly attractive for the nation because it allows uranium to be burnt with little to no enrichment capabilities. India has also done a great amount of work in the development of a thorium centered fuel cycle. While uranium deposits in the nation are limited there are much greater reserves of thorium and it could provide hundreds of times the energy with the same mass of fuel. A prototype fast breeder reactor (PFBR) of 500 MWe fuelled with Uranium-Plutonium oxide (from existing PHWRs) is under construction. This reactor has a flexibility to convert mixed oxide (MOX) to metallic fuelled ones to enable shorter doubling time. It has a blanket with uranium-thorium to breed fissile plutonium and U-233 respectively, taking the thorium program to stage two. India is engaged in designing an innovative reactor called Advanced Heavy Water Reactor (AHWR) using U-Th and Th-Pu MOX fuels. Theoretical studies on the use of thorium with plutonium or uranium have been completed for almost all types of reactors. To facilitate sustainable long term production of alternate fuel for transport sector, high temperature reactors options have been explored. India is designing prototype versions of two new reactors CHTR (compact High Temperature Reactor) and IHTR (Inovative High temperature Reactor) that will produce hydrogen to satisfy total energy needs of a region in the form of hydrogen, electricity and potable water. Work has also initiated towards a design of a molten salt reactor for hydrogen production. The R&D on future reactor ADSS (Accelerator Driven Subcritical System), where thorium based fuel in a sub-critical configuration will undergo fission with the spallation neutrons from a lead-Bi alloy to breed ^{233}U and power. India currently has six different configurations of power reactors in operation and under development, but these fall into a three-stage nuclear power program (Fig.1.1). Stage 1 reactors use natural uranium as fuel and produce plutonium which is recovered in reprocessing plants for initiating the second stage. The second stage—fast breeder reactors—use plutonium as fuel. The third stage of the program is thorium-based reactors. India has a vision of becoming a world leader in nuclear technology due to expertise in fast reactors and thorium fuel cycle. Electricity demand in India is increasing rapidly and the per capita electricity consumption figure is expected to double by 2020. Nuclear power for civil use is well established in India.

1.1. Challenges of reactor development

The major challenges for development and deployment of reactors are mainly related to fuel, coolant, structural materials and irradiation behavior of fuel etc. They have been briefly discussed.

1.2.1. Fuel: It contains heavy fissile elements that are capable of nuclear fission and has the highest energy density of all practical fuel sources. It is the heart of the reactor and is required to operate at high temperatures as well sustain high burn up.

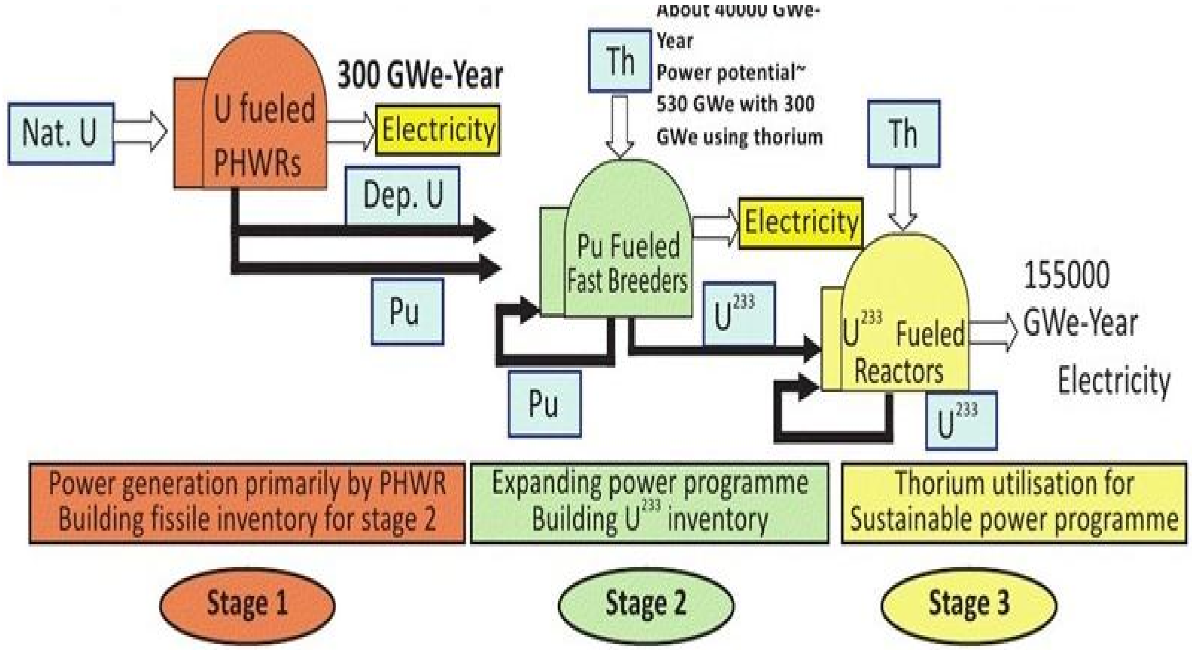

Fig.1.1.The different stages of nuclear reactors

Hence for a fissile material to be used as a nuclear fuel, a material has to satisfy many important criteria. It should be thermodynamically stable over a wide temperature range. There should be preferably no phase change in the operating temperature range of the reactor.

The fuel should have a high melting point, good thermal conductivity, compatibility with the coolant material, and be easy to fabricate and reprocess.

Diverse fuel configurations are proposed ranging from solid to liquid fuel e.g. TRISO coated particle fuel (ThC_2+UC_2), oxide fuel (UO_2, $(U,Pu)O_2$ (MOX)), carbide ($UC+UC_{1.5}$), nitride (UN), metallic fuel (U-Pu, U-Pu-Zr), metal actinide fuel (U+Zr+Pu+MA (minor actinide)) and molten salt based fuel ($ThF_4+UF_4+BeF_2+LiF+NaF$). These fuels need special technologies for fuel manufacture, their characterization and qualification for reactor application.

The metal oxides are used rather than the metals themselves because melting point of the oxide is much higher than that of the metal and because it cannot burn, being already in the oxidized state. MOX fuel is an alternative to low enriched uranium and are being used in the commercial reactor and a proven fuel for fast reactor. Metal fuels have the advantage of much higher heat conductivity than oxide fuels but cannot survive equally high temperatures. Metal fuels have a long history of use. Ceramic fuels other than oxides have the advantage of high heat conductivities and melting points, but they are more prone to swelling than oxide fuels and are not understood as well. The high thermal conductivity and high melting point makes uranium carbide an attractive advanced fuel for Generation IV reactors.

1.2.2. Coolant: A nuclear reactor coolant is used in the reactor to remove heat from the reactor core and transfer it to electrical generators and the environment. Frequently, a chain of two coolant loops are used because the primary coolant loop takes on short-term radioactivity from the reactor. Most commercial power reactors are using water as coolant and neutron moderator. However, fast reactors have a high power density and do not need neutron moderation and use liquid metal such as molten sodium, lead, lead-bismuth eutectic as coolant. Salts containing light elements like F, Li, and Be ($LiF+BeF_2$) can also be used as coolant and these can provide moderation. These coolants should be chemically compatible to clad materials.

1.2.3. Structural materials: It includes cladding, shielding, thermal insulation, moderator and reflector materials etc. Focus of this study is cladding material for fuel. The fission of fissile atoms produces radioactive materials, which emit neutrons, γ rays along with α and β particles. These particles can be lethal to humans, so the use of fuel cladding keeps the radioactive materials isolated from the coolant/moderator, which surrounds the cladding and maintains the fuel rods cooled (Fig.1.2).

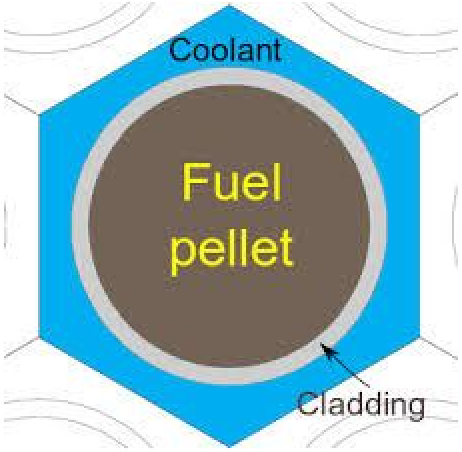

Fig.1.2. The cross sectional view of nuclear fuel pellet, cladding and coolant flow.

The material for fuel cladding is selected after other design aspects of the reactor's core have already been decided, such as the nuclear fuel and the moderator and coolant materials, defining, therefore, the multiple design constraints for the selection of the fuel cladding material. These constraints includes the cladding material should have an acceptable service temperature to increase the thermal efficiency of the reactor. Finally, the cladding material should be corrosion/oxidation resistant to the environment (coolant/moderator/fuel/fission products) and should have high thermal conductivity to increase the energy efficiency of the reactor; and low thermal expansion coefficient to minimize the thermal stresses in the cladding/pellet interface. Because of these strict constraints, fuel cladding and other structural components strictly dependent on reactor type. Several materials, such as Al and zircalloy for thermal and ferritic–martensitic stainless steel (F/M steel), oxide dispersion strengthened (ODS) alloy, nickel-based super alloys (Inconel and Incoloy), refractory metals and ceramic materials (SiC and ZrC) for advance reactors have been suggested as candidate fuel cladding materials.

1.3. Irradiation behavior of Fuel

During operation of reactor a number of fission products (FPs) are produced and the fuel composition undergoes continuous change in composition. The fission products along with the indirect products of decay chain of ^{235}U and ^{239}Pu consist of around 3% of the mass of fuel and are considered radioactive waste which might be further separated for various industrial and medical uses. A considerable number of medium to long-lived radioisotopes such as ^{90}Sr, ^{137}Cs, ^{99}Tc, ^{129}I and isotopes of neptunium, americium and curium are also present in the irradiated fuel. The amount formed depends greatly upon the nature of the fuel used and the conditions under which it was used. For instance, the use of MOX fuel (^{239}Pu in a ^{238}U matrix) is likely to lead to the production of more ^{241}Am and heavier nuclides than a uranium/thorium based fuel (^{233}U in a ^{232}Th matrix). The formation of FP can lead to new material properties of the fuel.

1.4. Chemical state of Fission products

The fission of ^{235}U and ^{239}Pu is asymmetric and gives rise to fission products which fall into two groups, a "light group", with mass numbers from 85 to 104 and a "heavy group", with mass numbers from 130 to149. The fission yield curve is almost symmetrical about minimum of the curve. A typical fission yield curve is shown in Fig. 1.3, which shows two humps which depicts the shifting of first peak towards higher atomic mass with higher atomic mass fissile nucleus. Fast neutron fission raises the valley between two peaks and at a particular energy of neutron, fission becomes symmetrical with single peak which is shown in Fig.1.4. Because of negligible reactivity of inert gas atoms, it forms bubbles or it comes out of the fuel to the plenum of the fuel pins. So dilution of cover gas helium takes place with reduction of thermal conductivity.

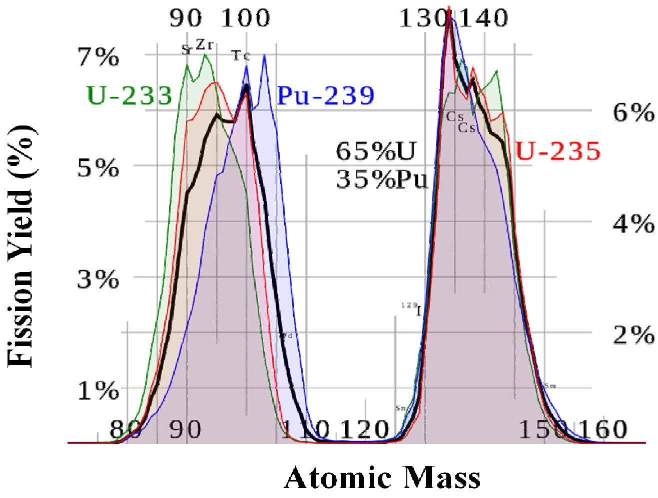

Fig.1.3.The fission yield curve of ^{233}U, ^{235}U and ^{239}Pu with thermal neutrons.

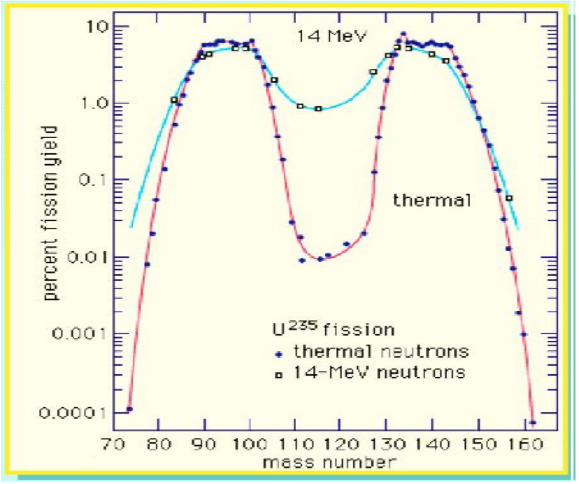

Fig.1.4. The fission yield curve of ^{235}U with thermal and fast neutrons.

The fission products (FPs) in nuclear fuel have been classified into four different categories [1-5] as presented in Table 1.1.

Table 1.1: Chemical state of FPs in irradiated fuel [1]

Classification	Elements
Gases and other volatile fission products	Kr, Xe, Br, I
Metallic precipitates	Mo, Tc, Ru, Rh, Pd, Ag, Cd, In, Sn, Sb, Te
Oxide precipitates	Rb, Cs, Ba, Zr, Nb, Mo, Te
Dissolved oxides	Sr, Zr, Nb, Y, La, Ce, Pr, Nd, Pm, Sm

The soluble fission products such as rare earths (REs) form solid solutions with fuel (U, Pu, Ln) O_2 and remain within the fuel matrix during normal operating conditions.

The group comprising of metallic element from molybdenum and platinum-family is called as "white inclusion" and is represented as Mo-Tc-Ru-Rh-Pd alloys, U-Me_3 (Me= Ru, Rh, Pd). Molybdenum prefers to exit in the alloys as well as oxide phase depending on the oxygen potential in the fuel. On the other hand, some FPs such as alkali, alkaline-earth elements form oxides of the form $(Ba,Sr)(U,Zr,Mo)O_3$, and $Ba(Mo,U)O_4$. The perovskite oxide phase is called as "Grey Phase" and is also observed in post irradiation study. This phase is represented as $(Ba,Cs,Sr)(U,Pu,Zr,RE,Mo)O_3(s)$. This phase compositions also keeps on changing with the oxidation potential and burn up of fuel. The rare earths are found in the perovskite oxide phase only at very high burn up. Further, the thermal gradient results in chemical potential gradients of U and Pu fuel materials, it might lead to various chemical interactions among the fuel materials and fission products and the transport of reacted fission products across the fuel. Thus the composition of the fuel changes as a function of time, the radial position and the oxygen potential.

This thesis compiles the various physico chemical data generated in this study for MOX fueled reactor materials which might have relevance for PFBR.

1.5. Thermophysico-chemical properties in support of prototype fast breeder reactor

PFBR is a sodium-cooled reactor of pool-type design. The fuel is (U, Pu) mixed oxide, with Pu/(U+Pu) ratio 0.21- 0.28. The UO_2-PuO_2 forms solid solution as they are iso-structural due to very close mass (238 and 239) and size. The swelling of the oxide fuel is very low compared to advanced fuels such as carbide or metallic. These properties help in compensating the lower breeding ratio and thermal conductivity. Further, extensive international experience on the behaviour of the oxide fuel under steady state as well as accident conditions has provided immense confidence in the choice of this fuel. Alloy D9 (titanium modified type 316 austenitic stainless steel (SS) with about 20% cold work) has been chosen as the reference material for the wrapper and clad tubes for PFBR. The core of the reactor consists of fuel subassemblies containing (U,Pu) mixed oxide fuel, which are immersed in a pool of liquid sodium. The heat transport system consists of a primary sodium circuit, secondary sodium circuit and steam–water system. The minimum sodium temperature in the primary pool of PFBR during normal operation (core inlet temperature) is about 670 K. The mean above-core temperature (core outlet temperature) is about 820 K during operation, and 923 K under plant transient conditions (arising due to failure of pumps).

The need for knowledge of the thermophysical and thermochemical properties investigations are required with regard to fuel and a host of other materials including fission product compounds likely to form in the fuel during irradiation, materials that could form matrices for immobilisation of the nuclear waste, materials for control rod applications, etc.

The chemical states of fission products are important as they influence many physicochemical properties of the fuel. The oxidation of the stainless steel clad (fast reactor), by the oxide fuel (MOX), is considerably influenced by the presence of the fission products, especially, cesium, iodine and tellurium, at the fuel-clad interface [6]. The thermodynamic properties as well as phase relations of the tellurium compounds of the clad components are required in detail. The extreme chemical environment can affect the mechanical as well as chemical properties of cladding and other structural components and result in interaction between, fuel-clad, fission product-clad, coolant-clad and finally fuel-coolant in the event of clad failure. Such interactions can become even more complex with increase in burn up. Burn up is the term used for the power extracted from the nuclear fuel during its residence inside the reactor. All the above interactions in turn decide the fuel performance. It is highly desirable to have a good understanding of the physicochemical processes involving the formation of various compounds and their thermophysical and thermo chemical properties.

To ensure that the fuel can be subjected to the desired linear heat ratings without the centerline temperature crossing the melting point of the fuel, a number of physico-chemical data are required for the design of reactor. The melting point and thermal conductivity of the fuel determines the power that can be extracted. The presence of solid FP in the fuel can change its melting point and thermal conductivity. Hence, the knowledge of thermal properties of nuclear material is important in predicting the integrity of fuel. The thermal expansion, which arises as a result of lattice anharmonicity, makes it a key quantity in fundamental studies on cohesive forces. If the expansion coefficient of FPs will be higher than fuel, it stresses the clad and leads to failure of fuel pin. Thus, thermal expansion data plays a key role in designing reactor code. The thermal conductivity of a material can be derived from heat capacity, density and diffusivity data, so heat capacity is also an important parameter for reactor designers and used in predicting fuel performance inside the reactor. In addition to the above mentioned thermal properties, the knowledge of one of the most fundamental property i.e. Gibbs energy of formation is imperative to predict the formation and stability of the compounds in various physico-chemical environments. This also helps in establishing phase diagrams of various systems. The thermodynamic data can also be used to develop suitable models, which can be used to derive thermodynamic parameters for the systems where the experiments is cumbersome or time consuming. Hence, a number of physicochemical, thermodynamic and mechanical data are required for the design of a nuclear reactor containing MOX fuel. Similar investigations are required for host of other materials including fission product compounds likely to form in the fuel during irradiation, materials that could form matrices for immobilizing the nuclear waste, materials for control of fission. Even with proven oxide fuel, there exist still many points that are doubtful and unclear with regards to the behaviour of FPs and actinides under irradiation. Hence, there is a requirement for R & D to bridge the gap existed in the literature.

The compounds formed in the nuclear reactors are also relevant in material science and technology. For the application of various compounds in different environment and temperature, it is essential to study the thermal stability of the compounds. The physico-chemical properties of compounds of f-block elements can provide an insight to the nature of chemical bonding between oxides of lanthanide and actinide. This study centered on the determination of thermo physical and thermodynamic properties of the mixed oxides in RE-U-O, Sr-Ce-O, Ba-Sr-Mo-O, Fe-Te-O, Cr-Te-O, and Ni-Te-O systems.

1.6. Importance of RE-U-O systems

The U-RE-O system is characterized with only ternary compound: RE_6UO_{12}(s) and solid solutions of UO_2(s) and RE_2O_3(s). RE_6UO_{12}(s) represents the chemical compound of oxides of rare earth and actinides.

1.6.1. Rare earths and actinides

The rare earths (lanthanides) and actinides are 3rd group elements of the periodic table. They are the elements that are often listed below the main section of the periodic table. There are thirty total elements in lanthanide and actinides series. The ground state neutral atom electronic configuration of lanthanide and actinide series is given in Table 1.2. The 4f- sub-shell is filled in lanthanide and 5f sub-shell is filled in actinides. The lanthanide series consists of elements from lanthanum (Z = 57) to lutetium (Z = 71) have electronic configuration $4f^{n+1}(5d^{0-1} 6s^2)$. These 15 elements (along with scandium and yttrium) are often called the rare earths because they exhibit similar chemical properties. All rare earths have single position in the periodic table because of great similarity in their electronic configurations and chemical properties. All of the lanthanides have at least one stable isotope except for promethium. All lanthanide elements form trivalent cations, RE^{3+}, whose chemistry is largely determined by the ionic radius, which decreases steadily from lanthanum to lutetium known as lanthanide contraction. All rare elements form RE_2O_3 with the exception of Ce, Pr and Tb, for which CeO_2, Pr_6O_{11} and Tb_4O_7 also exits as oxide phases.

Table 1.2. Electronic configurations of lanthanide and actinide elements

Lanthanides				**Actinides**			
Elements	A	E.C.	O.S.	Elements	A	E.C.	O.S.
La	57	$5d^1 6s^2$	3	Ac	89	$6d^1 7s^2$	3
Ce	58	$4f^1 5d^1 6s^2$	3,4	Th	90	$6d^2 7s^2$	3, 4
Pr	59	$4f^3 6s^2$	3	Pa	91	$5f^2 6d^1 7s^2$	3, 4, 5
Nd	60	$4f^4 6s^2$	3,4	U	92	$5f^3 6d^1 7s^2$	3,4,5,6
Pm	61	$4f^5 6s^2$	3	Np	93	$5f^4 6d^1 7s^2$	3,4,5,6,7
Sm	62	$4f^6 6s^2$	2,3	Pu	94	$5f^6 7s^2$	3,4,5,6,7
Eu	63	$4f^7 6s^2$	2,3	Am	95	$5f^7 7s^2$	2,3,4,5,6,7
Gd	64	$4f^7 5d^1 6s^2$	3	Cm	96	$5f^7 6d^1 7s^2$	3, 4
Tb	65	$4f^9 6s^2$	3,4	Bk	97	$5f^9 7s^2$	3, 4
Dy	66	$4f^{10} 6s^2$	3,4	Cf	98	$5f^{10} 7s^2$	2,3, 4
Ho	67	$4f^{11} 6s^2$	3	Es	99	$5f^{11} 7s^2$	2,3
Er	68	$4f^{12} 6s^2$	3	Fm	100	$5f^{12} 7s^2$	2,3
Tm	69	$4f^{13} 6s^2$	2,3	Md	101	$5f^{13} 7s^2$	2,3
Yb	70	$4f^{14} 6s^2$	2,3	No	102	$5f^{14} 7s^2$	2,3
Lu	71	$4f^{14} 5d^1 6s^2$	3	Lr	103	$5f^{14} 6d^1 7s^2$	3

A= Atomic number; E.C.= Electronic Configuration, O.S.= Oxidation State

Actinides are the 15 elements with electronic configuration $5f^{n+1}(6d^{0-1} 7s^2)$, with atomic numbers from actinium (Z = 89) to lawrencium (Z = 103). They are named after the first element in the series, actinium. All actinides are radioactive and release energy upon radioactive decay; naturally occurring uranium and thorium, and synthetically produced plutonium are the most abundant actinides on Earth. It is evident from the Table 1.2 that filling of electrons in f-shell in actinides preceding americium is not as systematic as observed in case of lanthanides which can be attributed to smaller energy difference between 5f, 6d and 7s orbitals. In case of all the actinide series, the relative energy of the orbital being occupied become lower as successive electrons are added and thus the energy of 5f orbital become lower than 6d orbital in the elements beyond thorium. Therefore, actinides, especially early members of the series, exhibit multiple oxidation states owing to the close proximity of 5f, 6d and 7s orbitals. On the contrary, in lanthanides the large energy differences between 4f and 5d orbitals do not favour the interchange of electrons among them and consequently all the lanthanides exhibit predominantly single valency. With increase in atomic number, f- orbital becomes more stabilized compared to 6d and 7s orbital and therefore actinides beyond americium exhibit +3 as the most stable oxidation state except nobelium for which +2 state is most stable owing to stability of full filled 5f shell. In contrast, +3 oxidation state is predominant in lanthanides series owing to the large difference in binding energy of 4f and 5d, 6s electrons. However, +2 (Eu and Yb) and +4 (Ce and Tb) oxidation states also exist which corresponds to vacant or enhanced stability of half-filled or full filled 4f configuration. Thus, later members of actinides series behave like lanthanides and exhibit +3 as the most stable oxidation state. Similar trend is observed in ionic radii of the elements of both the series. Fig. 1.5 shows similar trend in the ionic radius for +3 and+4 oxidation states of rare earth and actinides.

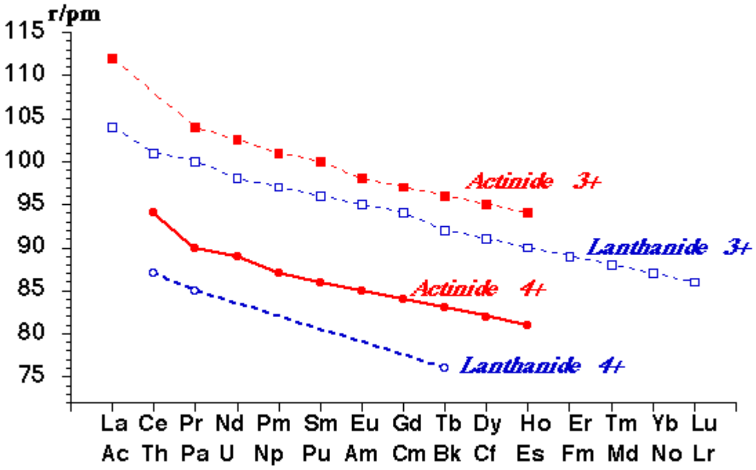

Figure 1.5. Ionic radii of lanthanides and actinides for +3 and +4 oxidation states

1.6.2. Nuclear perspective (Interaction between fuel and fission products)

Solid solutions of various rare earth oxides (Viz. $GdO_{1.5}$, $EuO_{1.5}$, $GdO_{1.5}$, $DyO_{1.5}$) with UO_2 or (U, Pu)O_2 are proposed as burnable poisons in thermal reactors to control the excess reactivity during the start up of the reactor. Burnable poisons are materials that have high neutron absorption cross section that are converted into materials of relatively low absorption cross section as the result of neutron absorption. Due to the burn-up of the poison material, the positive reactivity of the fuel in the initial period is controlled. UO_2–Gd_2O_3 fuel has already been used in BWR. Moreover, when pure uranium dioxide is exposed to elevated temperatures in an oxidizing atmosphere, gets transformed to U_3O_8 which has undesirable nuclear properties such as high vapour pressure, volumetric expansion, lower fission product retention capacity and irradiation stability. Prevention of U_3O_8 formation can be achieved by using rare earth oxide additive [7]. Hence, rare earth-urania solid solutions would be doubly beneficial in reactor core as they are efficient-burnable poison and also prevent oxidation of UO_2(s) matrix at high temperature.

The earlier rare earths have high fission yield among the fission products [8]. The fission yields of rare earths for the fission of various fissile isotopes are listed in **Table. 1.3.**

Table 1.3. Fission yields of various rare earth fission products for the fission of different fissile isotopes in fast neutron spectrum

Rare earth Fission products	Fast Fission yield (at. %)		
	^{235}U	^{238}U	^{239}Pu
La	6.65	6.04	5.83
Ce	11.69	10.93	10.16
Pr	5.93	6.76	5.62
Nd	20.127	20.22	16.41
Sm	4.121	5.821	4.973
Eu	0.156	0.439	0.515
Gd	0.0808	0.2312	0.5116
Total	42.105	50.441	44.0196

In order to predict the formation of RE_6UO_{12}(s) as a results of fuel fission product interactions in the reactor operating condition, Gibbs energy of formation of these compounds are required to know which are not reported in the literature. The thermodynamic properties of RE_6UO_{12}(s) are required to establish the ternary phase diagram of RE-U-O system. The specific heat and thermal expansion studies of these compounds are also required to know. Y_6AnO_{12} (s) and Yb_6AnO_{12} (s) have been studied as host matrix for immobilization of actinides [9]. Hence physico-chemical study of RE_6UO_{12}(s) will also be useful for storage of high level waste.

1.6.3. Non Nuclear applications

The rare earth compounds are the subject of great interest owing to their various non nuclear applications. The rare earths are the most important elements of the periodic table due to its photoluminescence property; the sole cause of the property is f-f transition. Many host matrices on doping with rare earths (Ce & Eu) are being used in modern solid state optical technology as phosphors. The rare earths magnets are being used in wind power generator for better reliability. Neodymium and samarium magnets are much more powerful than traditional ferric magnet. Rare earth element permanent magnets are installed in computer cathode ray tube (CRT) and plasma televisions as well as computer monitors are coated with phosphors which when subject to low pressure UV excitation generate the primary colours red, blue, and green. Rare earth element play a key role in wide range of health and medical applications, including drug treatments, diagnostic techniques and equipment. The behavior of RE_6UO_{12}(s) along the rare earth series is important to know. The thermochemical properties of RE_6UO_{12}(s) will give an insight into the nature of bonding between rare earth and actinide oxides which is important because fundamental studies on f-block compounds are scarce in the literature.

1.6.4. Literature survey

The literature [10-15] reports a compound RE_6UO_{12}(s) and solid solutions between RE_2O_3(s) and UO_2(s) in RE-U-O system. The crystal structure of RE_6UO_{12} (s) (RE=La, Pr-Lu) is reported to be rhombohedral [14, 15]. The thermal expansion of RE_6UO_{12}(s) (RE = La, Nd, Sm), heat capacity of RE_6UO_{12}(s) (RE = La, Sm, Eu) and thermal diffusivity of RE_6UO_{12} (s) (RE = La, Gd, Dy) were measured by Jena et al. [16], Venkata Krishnan et.al [17], and Krishnaiah et al. [18] respectively. Thermophysical properties and heat capacity of Dy_6UO_{12}(s) were studied by Venkata Krishnan et.al [19]. Heat capacity and thermal expansion coefficient of rare earth uranates RE_6UO_{12} (RE = Nd, Gd and Eu) is also studied by Venkata Krishnan et.al [20]. The systematic study of physico-chemical properties of RE_6UO_{12}(s) (RE= La, Pr, Nd, Sm, Eu, Gd, Tb, Dy, Ho, Er, Tm, Yb and Lu) have not been reported in the literature.

1.6.5. Properties studied

The heat capacity was measured for RE_6UO_{12}(s) (RE= La, Pr, Nd, Sm, Eu, Gd, Tb, Dy, Ho, Er, Tm, Yb and Lu) using differential scanning calorimeter (DSC) in the temperature range 300-870 K. Thermal expansion of RE_6UO_{12}(s) (RE= Pr, Sm, Eu, Gd, Tb, Dy, Ho, Er, Tm, Yb and Lu) was determined using high temperature X-Ray diffractometer (HT-XRD) and Gibbs energy of formation for RE_6UO_{12}(s) (RE= La, Nd, Sm, Eu, Gd, Tb, Dy, Ho, Tm, Yb and Lu) was measured using solid oxide galvanic cell with yttria stabilized zirconia as oxide ion conductor electrolyte. The $\Delta\mu(O_2)$ was calculated for $RE_6UO_{12}(s)$ to predict its formation under normal or off normal operating condition of the reactor. The thermodynamic functions were derived from the measured heat capacity and Gibbs energy of formation data.

1.7. Importance of Sr-Ce-O system

1.7.1. Nuclear perspective (Interaction between fuel and the fission product)

The fission product strontium may react with $PuO_2(s)$ to form compounds in Sr-Pu-O system. It is difficult to study the thermodynamic properties of plutonium containing compounds because of its handling in the radioactive glove box. Ceria is frequently being used as a surrogate material for plutonia [21].

The Ce also has appreciable fission yield during nuclear fissions of both ^{235}U and ^{239}Pu hence formation of compounds in Sr-Ce-O system is possible. Cerium exists both in +3 and +4 states. Depending on the oxidation states of cerium, different compounds are formed in SrO–Ce_2O_3 and SrO–CeO_2 systems. There exist two compounds: $SrCeO_3(s)$ and $Sr_2CeO_4(s)$ in SrO–CeO_2 system and $SrCe_4O_7(s)$ and $Sr_2Ce_2O_5(s)$ in SrO–Ce_2O_3 system. The formation of latter two compounds requires highly reducing atmosphere and temperature more than ~1800 K [22]. However, $SrCeO_3(s)$ and $Sr_2CeO_4(s)$ are stable in oxidizing medium. Sr-Pu-O system is characterized with two ternary oxides: $SrPuO_3(s)$ and $Sr_2PuO_4(s)$. Pu^{4+} and Ce^{4+} have $SrPuO_3(s)$ and $SrCeO_3(s)$ as stable compound, respectively. Hence, physic-chemical properties of $SrCeO_3(s)$ can be studied instead of $SrPuO_3(s)$. $SrCeO_3(s)$ is also important separately from the point of view of interactions amongst fission products SrO(s) and $CeO_2(s)$. The release of radioactivity from the fuel matrix can be predicted from the thermodynamic data of compounds containing the fission products.

1.7.2. Non Nuclear applications

$SrCeO_3(s)$ with perovskite structure is being used as the high temperature proton conducting electrolyte [23, 24] in hydrogen pumps [25] and solid oxide fuel cell (SOFC) [26]. Ideally, the electrolytes used for these applications should conduct only via proton in the temperature and the hydrogen pressure range of interest. Shimojo [27] suggested that the doping of trivalent rare earth element helps in introducing more oxide ion vacancy which in turn helps in increasing proton conductivity. As the activation energy for proton conduction is less than the oxide ion conduction, ceramic proton conducting electrolytes are preferred to oxide ion conducting electrolytes in solid oxide fuel cell (SOFC) in the temperature range of 773–1273 K. Therefore, the thermal behaviour of $SrCeO_3$(s) in this temperature range is important for its effective applications.

Sr_2CeO_4(s) emits a blue–white fluorescence by the excitation through the X-ray, cathode ray and ultraviolet ray. A blue phosphor has good potential applications in lamps and in field emission displays [28]. Sr_2CeO_4(s) exhibits efficient cathodoluminescence [29]. The cerium ions present in Sr_2CeO_4(s) is in +4 state and exhibit luminescence with an uncharacteristically long excited state lifetime (<51 ms) [30, 31]. The known cerium based phosphors show luminescence due to localized Ce^{3+} excited states and d–f transitions.

1.7.3. Literature survey

The thermodynamic stability of $SrCeO_3$(s) was determined by Gopalan and Virkar [32] using molten salt galvanic cells by Pankajavalli et al. [33] using fluoride cell technique and by Shirsat et al. [34] measuring equilibrium vapor pressure of CO_2(g). Yamanaka et al. [35, 36] have measured the thermal expansion coefficient, melting temperature, elastic moduli, Debye temperature, micro-hardness, heat capacity and thermal conductivity of $SrCeO_3$(s). Yamanaka et al. [36] have measured thermal expansion coefficients of $SrCeO_3$(s) using a dilatometer in the temperature range from room temperature to about 1000 K under reduction atmosphere. Authors [36] also measured the heat capacity by the differential scanning calorimeter in argon atmosphere. Enthalpy increment of $SrCeO_3$(s) has been measured by Saha et al. [37] using high temperature micro-calorimeter. Standard molar enthalpy of formation by solution calorimetry, low-temperature heat capacities by adiabatic calorimetry and high-temperature enthalpy increments by drop calorimetry was measured for $SrCeO_3$(s) by Cordfunke et al. [38]. The $\Delta_f H_m^o$ ($SrCeO_3$(s),298.15 K) have been determined by Goudikas et al. [39]. Thermodynamic stabilities of Sr_2CeO_4(s) were reported by Pankajavalli et al. [33] using E.M.F. technique employing fluoride electrolyte and that by Shirsat et al. [40] from the measurement of equilibrium pressure of CO_2(g). Recently Rakshit et al. [41] have measured the stability of $SrCeO_3$(s) and Sr_2CeO_4(s) with respect to their carbonates using Knudsen effusion mass spectrometry. The heat capacity data was reported on $SrCeO_3$(s) in high purity argon atmosphere which might be the heat capacity of sub-stoichiometric $SrCeO_{3-x}$(s). There is no heat capacity data reported on Sr_2CeO_4(s). Hence, it was concluded from the literature survey that, there is no heat capacity and linear thermal expansion data on phase pure CeO_2(s), $SrCeO_3$(s) and Sr_2CeO_4(s).

1.7.4. Properties studied

The stability of $SrCeO_3$(s) was studied in both reducing and oxidizing atmosphere. The oxidation state of Ce in $SrCeO_3$(s) has been studied in the reducing atmosphere. The thermal expansion and heat capacities of CeO_2(s), $SrCeO_3$(s) and Sr_2CeO_4(s) have been studied using HT-XRD and DSC, respectively.

1.8. Importance of Ba-Sr-Mo-O system

1.8.1. Nuclear perspective (Interaction amongst fission Products)

This system is important from the point of view of interactions amongst the fission products: Ba, Sr and Mo in BaO-SrO-MoO_2/MoO_3system. These fission product elements are having high fission yields in the nuclear reactors operating with (U,Pu)O_2(s) fuel. Under prevailing oxygen potential of nuclear fuel, formation of various compounds and solid solutions in BaO(s)–MoO_3(s), SrO(s)–MoO_3(s) and Ba–Sr–Mo–O systems are possible. The perovskite-type oxide phase:(Ba,Cs, Sr)(U,Pu,Zr,RE,Mo)O_3(s) has been observed in the fuel matrix [1]. Initially, barium forms $BaUO_3$(s) and $BaZrO_3$(s) phases in fuel which incorporates several radio-nuclides such as Sr, Cs, U, Pu, Mo and RE (rare earth) and precipitate in ABO_3(s) structure where A = Ba, Sr, Cs and B = U, Pu, Zr, Mo, RE. $BaMoO_4$(s) is predicted to be formed in very high burnt oxide fuels at temperature greater than 1650 K [42]. The $BaMO_3$(s) (M= U,Pu,Zr,RE,Mo) phase is stable under the low oxygen potentials (-500 and -400 kJ/mol) and the $BaMO_4$(s) (M= U,Pu,Zr,RE,Mo) phase is stable under the high oxygen potentials (-300 and -200 kJ/mol) [43]. The solid solutions of $SrMoO_4$(s)-$BaMoO_4$(s) and $SrMoO_3$(s)-$BaMoO_3$(s) are the phases incorporated in ABO_4 and ABO_3 phases are found in the irradiated nuclear reactor fuel.
The thermodynamic data of fission products present in ABO_3 and ABO_4 type oxides are required in predicting their behavior in both normal and off normal reactor operating conditions.

1.8.2. Non Nuclear applications

ABO_3(s) compounds have simple structure and can flexibly accommodate around 90 percent of the metallic elements of the periodic table. Due to compositional versatility of this structure, the properties of ABO_3(s) compounds can be tuned by substitution, creation of order or defect in its structures. Because of it, ABO_3(s) compounds exhibit important properties like ferro-electricity, ferromagnetism, superconductivity, thermal conductivity, ionic conductivity, piezoelectric, photo-catalytic and thermoelectricity. The perovskite-type oxides: $SrMoO_3$(s), $BaMoO_3$(s) and $Ba_{1-x}Sr_xMoO_3$(s) have a number of interesting properties. According to

Goodenough's classification [44], alkaline-earth molybdates containing Mo^{4+} ($4d^2$) in three fold t_{2g} orbital belong to the Pauli paramagnetic group, and have high electron-transfer energy [45]**.** Hence, these oxides show metallic conductivities.

Alkali earth metal molybdates and tungstates with a scheelite-type structure, such as AMO_4(s) (A = Ba, Sr, Ca and M = Mo, W) and their solid solutions, are also important materials in photoluminescence and have widely been used in optical fibers, solid-state-optical masers and electro-chromic materials [46]. The properties of these solid solutions are required for the safe application of these perovskites in various chemical environments.

1.8.3. Literature survey

$AMoO_4$(s) with a scheelite structure are used as scintillators [47] and laser host materials [48]. Rare earth doped $BaMoO_4$(s) and $SrMoO_4$(s) shows luminescent properties [49-51]. $SrMoO_4$(s) catalyzes the hydrogen evolution reaction in acidic electrolytes which has been demonstrated by Aruna et al [52]. $AMoO_3$(s) (where A = Sr, Ba) are choosen as anode material in SOFC due its metallic behavior with impressive electronic conductivities. Additionally, $AMoO_3$(s) have been reported to have high catalytic activity for the direct oxidation of alcohols [53].

$AMoO_4$(s)(A=Ba,Sr):

Singh et al. have studied enthalpy increment of $BaMoO_4$(s) and $SrMoO_4$(s) [54], Gibbs energy of formation of $BaMoO_4$(s) [55] and also $SrMoO_4$(s) [56]. But no thermodynamic properties of $Ba_{1-x}Sr_xMoO_4$ (s) solid solutions have been reported in the literature.

$AMoO_3$(s)(A=Ba,Sr):

Crystallographic, electrical and magnetic properties of $BaMoO_3$(s) and $SrMoO_3$(s) have been well studied [57-59]. The thermoelectric properties like electrical resistivity, Seebeck coefficient, and thermal conductivity of $BaMoO_3$(s) have been studied by Kurosaki et al. [60].Yamanaka et al. [61, 62] reported physical properties like thermal expansion coefficient, melting temperature, elastic moduli, Debye temperature, micro-hardness, heat capacity, and thermal conductivity of $SrMoO_3$(s) and also predicted the metallic behavior from the positive temperature dependency of electrical resistivity. A few research works on thermodynamic properties of $BaMoO_3$(s) and $SrMoO_3$(s) have been reported in the literature [63–71]. Agarwal et al. [63] measured enthalpy increment using drop calorimeter. Dash et al. [64–67] studied the standard molar Gibbs energy of formation of $BaMoO_3$(s) and $SrMoO_3$(s) and phase diagrams of Ba–Mo–O and Sr–Mo–O systems. Brixner [72] measured XRD of $Ba_{1-x}Sr_xMoO_3$(s) and observed complete range of solid solutions between $BaMoO_3$(s) and $SrMoO_3$(s) and also found metallic behavior of these solid solutions from the determination of electrical property. However, thermodynamic properties of $Ba_{1-x}Sr_xMoO_3$(s) solid solutions have not been reported in the literature.

1.8.4. **Properties studied**

The solid solutions between $BaMoO_4$(s) and $SrMoO_4$(s) were synthesized by complex polymerization method. The complete solid solutions were characterized using XRD and Raman spectroscopy. The exact stoichiometry of various solid solutions were found out by analyzing Sr, Ba and Mo content by Inductively coupled plasma mass spectrometry (ICPMS). The heat capacity of $Ba_{1-x}Sr_xMoO_4$(s) (x = 0, 0.18, 0.38, 0.60, 0.81, 1) solid solutions were measured using differential scanning calorimeter in the temperature range 140–870 K and thermal expansion measurements of $Ba_{1-x}Sr_xMoO_4$(s) (x = 0, 0.6, 1) solid solutions were carried out using high temperature X-ray diffractometer in the temperature range 298–1273 K. The thermodynamic functions were computed from the measured heat capacity data in the temperature range of 298.15–870 K.

$Ba_{1-x}Sr_xMoO_3$ (s) (x = 0, 0.2, 0.4, 0.5, 0.8, 1) was synthesized by optimizing the condition of reduction of corresponding $Ba_{1-x}Sr_xMoO_4$(s) (x = 0, 0.2, 0.4, 0.5, 0.8, 1). The heat capacity of $Ba_{1-x}Sr_xMoO_3$(s) (x = 0, 0.2, 0.4, 0.5, 0.8, 1) and thermal expansion were measured for $Ba_{1-x}Sr_xMoO_3$(s) (x = 0, 0.4, 0.8, 1) using DSC and HT-XRD, respectively. Thermodynamic functions of $Ba_{1-x}Sr_x MoO_3$(s) (x=0, 0.4, 0.8, 1) such as enthalpy increment, entropy and Gibbs energy functions were computed from the measured heat capacity.

1.9. Importance of A-Te-O (A= Cr, Fe, Ni) systems

1.9.1. **Nuclear perspective (Interaction of stainless steel clad with Te)**

The tellurium (Te) is one of the corrosive fission products with 1% fission yield, generated during the irradiation of MOX fuel. The presence of highly corrosive Te in the fuel-clad gap has been reported by many investigators [73-78]. D9 (Fe-15Cr-15Ni-Mo-Ti- Si alloy) steel has been used as cladding material [79] and $(U,Pu)O_2$ as fuel for PFBR. The tellurium bearing compounds which could be formed by all possible interactions between fuels, fission products, clad and coolant, during reactor operation is important in understanding the performance of MOX fuel of the PFBR [1]. Hence the thermodynamic stability of compounds in A-Te-O (A=Cr, Fe, Ni) system need to be investigated in detail.

1.9.2. Non Nuclear applications

A-Te-O (A=Cr, Fe, Ni) compounds have wide applications. Fe_2TeO_6(s) has industrial use as catalyst for the oxidation of 1-butene to butadiene and propylene to acrolein [80]. Fe_2TeO_6(s) and Cr_2TeO_6(s), members of isomorphous series of compounds, possess antiferromagnetic properties [81-83]. Similarly, Ni_3TeO_6(s) is a collinear antiferromagnet with ferromagnetic honeycomb planes [84].

1.9.3. Literature survey

The A-Te-O (A=Cr, Fe, Ni) system has been characterized with a number of compounds [85]. The metal rich phase boundaries of binary tellurides or ternary tellurates which exists in equilibrium with the respective metal are important while considering the chemical interaction of Te with the clad. There exist few literature reports on physico-chemical properties of ternary compounds in A-Te-O (A= Cr, Fe, Ni) system [86-90]. Chattopadhyay et al. [91] determined Gibbs energy of formation of various compounds which might be formed as the result of interaction of components of cladding material (Cr, Fe, Ni) with tellurium and oxygen. Although the Gibbs energy of formation has been determined for Fe_2TeO_6(s) and Ni_3TeO_6(s) by various authors, they are not consistent and hence are not conclusive. To the best of our knowledge, the heat capacity and coefficient of thermal expansion of Fe_2TeO_6(s) and Ni_3TeO_6(s) have not been reported in the literature. With this in view, tellurates of Fe-Te-O, Cr-Te-O and Ni-Te-O systems were chosen for the investigation.

1.9.4. Properties studied

In this study, thermal expansion coefficients of Fe_2TeO_6 (s) and Ni_3TeO_6 (s) were measured by high temperature X-ray diffraction (HT-XRD) in the temperature range 298-973 K and 298-923 K respectively. Heat capacity were measured for Cr_2TeO_6(s), Fe_2TeO_6(s) and Ni_3TeO_6(s) using temperature modulated differential scanning calorimeter (TMDSC) in the temperature range 300-870 K using TOPEM software. Gibbs energy of formation of Fe_2TeO_6(s) and Ni_3TeO_6(s) were measured using transpiration technique in the temperature range 940-1060 K. As self consistent thermodynamic functions for Cr_2TeO_6 (s), Fe_2TeO_6 (s) and Ni_3TeO_6 (s) were derived in the temperature range 298.15–1100 K using experimentally measured heat capacity data along with other relevant data from the literature.

The chemical potential diagram of Cr-Te-O, Fe-Te-O and Ni-Te-O systems was constructed using FactSage programme [92]. The thermodynamic information of the various binary alloys in

Cr-Te, Fe-Te, Ni-Te and binary oxide phases present in Cr-O, Fe-O, Ni-O, Te-O and ternary phases present in Cr-Te-O, Fe-Te-O and Ni-Te-O systems were given as input to the programme. These diagrams which are useful in illustrating the stability of various compounds formed between tellurium and the different stainless steel components under various tellurium and oxygen potentials. The oxygen and Te potentials calculated in this study were compared with that of the fuel to predict the chemical attack of cladding components by tellurium.

CHAPTER-2

Experimental methods and Techniques

Chapter-2

This chapter describes the experimental methods used in this thesis. It comprises of synthesis of ternary compounds employing various methods such as solid state, gel combustion and complex polymerization. Characterization of compounds was done byX-ray diffraction (XRD). Characterization of solid solution was done using XRD and Raman spectroscopy. Thermogravimetry and differential thermal analysis were employed for the characterization of organic precursors of quarternary molybedates. Inductively coupled plasma mass spectrometer (ICPMS) was used for impurity analysis as well as for determination of stoichiometry of solid solutions. A brief description of the working principles of the various techniques are discussed. The thermophysical properties like linear as well as volume thermal expansions and heat capacity were measured employing HT-XRD and DSC, respectively. The principles of these techniques are also elaborated. Solid electrolyte based galvanic cells and transpiration methods were used Gibbs energy of formation of various compounds. Details of the principle and experimental set up of these techniques are also described. Impedance spectroscopy was used as a complementary technique to confirm phase transition in various compounds. A brief description of its theory and measurements are also given.

2.1. Synthesis of compounds

In this study, both solid state reaction and soft chemistry route were used for synthesis of ternary oxides. Solid state method was used to synthesize Sr_2CeO_4(s), Cr_2TeO_6(s), Fe_2TeO_6(s) and Ni_3TeO_6(s). Citrate nitrate combustion synthesis was used for synthesis of most of the ternary oxides in RE-U-O system and $SrCeO_3$(s) in Sr-Ce-O system. Complex polymerization method was used for the synthesis of solid solutions in the Ba-Sr-Mo-O system. Detailed accounts of these syntheses are given in the following sub-sections.

2.1.1. Solid state reaction or ceramic route

This method is most widely used for the preparation of polycrystalline solids [93]. In this method, the constituent oxides were considered as reactants. These reactants were mixed to get a homogeneous mixture using mortar and pestle or by motorized ball mill. The overall reaction rate depends upon the particle size of the reactants, the degree of homogenization achieved on mixing and the intimate contact between the grains. The grinding and mixing process helps in increasing the surface area of the reactants which helps in reaction. These homogenized mixtures were later compacted into pellets and subjected to different temperature starting with lowest temperature to the maximum reaction temperature. The pellets were heated at each temperature for long duration. Before heating at each temperature, the process of grinding, mixing and pelletisation were repeated to break the diffusion barrier and to make intimate contact between the reactants. The reaction involves three processes viz: transport of the reactants to the interface, reaction at the interface, transfer of the products away from the interface. Products formation was governed by thermodynamic and kinetic factors. Thermodynamic considerations showed the feasibility of the reaction by taking into account of the change in Gibbs energy by the formation of the product from constituent reactants, whereas kinetic factor determines the rate of the reaction. Because of slow kinetics of such solid state reactions, it is mandatory to heat the reactants at high temperature, at least above T_M /2, where T_M is the melting point of lowest melting components among the reactants and the products. Moreover, if vaporizing reactant species like TeO_2(s) and MoO_3(s) involves, the reactions temperature should be increased very slowly and kept at respective temperatures for long durations.

2.1.2 Soft chemistry routes

2.1.2.1 Gel Combustion synthesis

Gel combustion synthesis has attracted attention as it is simple, fast, and versatile and a low temperature preparative technique, which forms nanoparticles with high surface area **[94]**. This technique involves preparation of a gel from a solution of metal nitrates (oxidant) and an organic additive (fuel) followed by the combustion of the gel. Citric acids, tartaric acids, EDTA, urea, glycine are the most used fuels. They easily form complexes with the metal cations which undergo polymerisation upon heating resulting in the formation of clear, transparent gel. Metal cations are distributed uniformly in the polymeric network and this inhibits their segregation and precipitation. In gel combustion an exothermic reaction between an oxidiser and fuel takes place. In combustion synthesis the ratio of oxidizer and fuel is fixed in such a way that the net oxidizing valency of the oxidizer becomes equal to the net reducing valency of the fuel. In the present work, citric acid, glycine was used as fuels. Metal oxides/ carbonates were dissolved in concentrated nitric acid. Deionised water was added to prepare the stock solution. The elemental composition was assayed using ICPMS. The required amounts of metal nitrate solutions were mixed with fuel using magnetic stirrer. The resultant solution was dehydrated on a hot plate at 353 K to end up with gel. The gel was heated at 773 K to initiate combustion process. This combustion reaction is a highly exothermic and self sustaining. During the combustion process, large amount of gaseous products were evolved. Fuel to oxidant ratio has a great role in determining the exothermicity of the reaction. The advantage of a combustion reaction is that final product is often formed in a single step and no calcination is required. However, precursor of the desired product may be formed in some cases. The released heat during the decomposition of metal-fuel complex is utilized for the phase formation.

2.1.2.2 Complex Polymerisation Method

Complex polymerization is also a wet chemical process like combustion method. The self sustaining gel combustion process is very fast and sometimes violent. The precursor sees very high temperature which leads to decomposition of final product and evaporation of highly volatile reactant phases. However, complex polymerization is a method where an intermediate is formed from the homogenous liquid mixture which undergoes a flame less combustion. The carbonaceous product obtained decomposes on heating and thermal reaction at moderate temperature gives the final product. The metal solutions were homogenously mixed to get a complex with complexing agent. Then, ethylene glycol was added for polyesterification. This method is also known as the Pechini process [95]. In this method, stoichiometric amounts of metal nitrates were taken in deionized water. Citric acid was added to the metal solution and P^H adjusted to 5-6 for complete complexation. Later, ethylene glycol was added. Then the resultant solution was heated with constant stirring on a hot-plate at 353 K. Further heating of the gel after total dehydration leads to fluffy charred mass. This amorphous polymeric precursor is calcined at desired temperature for phase formation. As the molecules are closely spaced, lower temperature is required for phase formation with better homogeneity compared to the conventional solid state route. This method is highly recommended to avoid loss of volatile reactants.

Formation of solid solutions changes the properties of material. In nuclear industry, MOX nuclear fuel is solid solutions of UO_2(s) and PuO_2(s). Some of the fission products also form solid solution with the fuel and among themselves. Hence, it is required to know the properties of various solid solutions and theory behind it.

2.2. Solid Solutions

The homogeneous solid mixtures of two or more kinds of atoms/molecules are known as solid solutions. The more abundant phase is solvent and the less abundant phase is solute. A solid solution is basically a crystalline phase that can have variable composition.

There are two types of solid solutions such as (a) Substitutional solid solutions and (b) Interstitial solid solutions.

2.2.1. Substitutional Solid Solutions

If the atoms of the solvent are replaced by atoms of the solute in the crystal lattice then the solid solution is known as substitutional solid solution.

e.g. Plutonium atoms from PuO_2(s) may substitute uranium atoms in UO_2(s) without disturbing the F.C.C. structure. **Fig. 2.1** shows schematic of substitutional solid solutions.

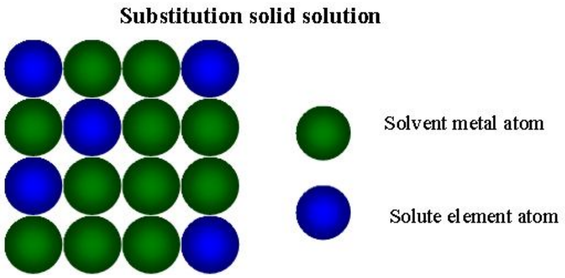

Fig.2.1 The schematic of substitutional solid solutions.

There are a set of basic rules describing the conditions under which an element or a compound could dissolve in another element or compound, forming a solid solution. They are known are Hume-Rothery rules [96-101], named after William Hume- Rothery.

2.2.1.1. Hume Rothery rules for the formation of substitutional solid solutions

Hume Rothery formulated certain rules by studying various metallic solid solutions systems, which govern the formation of substitutional solid solutions. These are:

(a) Crystal structure factor: For complete solid solubility, the two components (the solute and solvent) should have the same type of crystal structure.

(b) Relative size factor: As the size (atomic radii) difference between two elements increases, the solid solubility becomes more restricted. For extensive solid solubility the difference in atomic radii of two elements should be less than 15%. If the relative size factor is more than 15%, solid solubility is limited.

(c) Chemical affinity factor: The solute and solvent should have similar electronegativity. If the electronegativity difference is too great, the metals will tend to form compounds instead of solid solutions.

(d) Relative valence factor: Complete solubility occurs when the solvent and solute have the same valency. Metals with lower valency will tend to dissolve in metals with higher valency.

2.2.2. Interstitial Solid Solutions

In interstitial solid solutions, the solute atom does not displace a solvent atom, but enters one of the holes or interstices between the solvent atoms.

The **Fig.2.2** depicts interstitial solid solutions.

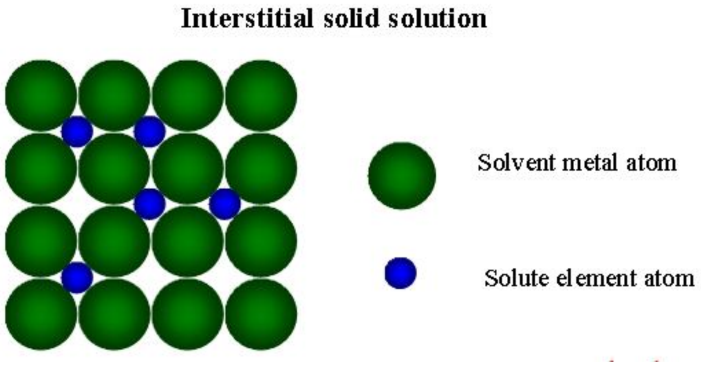

Fig.2.2.Schematic of Interstitial solid solutions

2.2.2.1. Hume Rothery rules for the formation of interstitial solid solutions

1. Solute atoms must be smaller than the interstitial sites in the solvent lattice.
2. The solute and solvent should have similar electronegativity.

In this study, the solid solutions of $BaMoO_4$(s)-$SrMoO_4$(s) and $BaMoO_3$(s)-$SrMoO_3$(s) were synthesized, characterized and its thermophysical properties were studied. Both the series of solid solutions forms substitutional solid solutions.

Satisfaction of Hume Rothery rule for $BaMoO_4$(s)-$SrMoO_4$(s) and $BaMoO_3$(s)-$SrMoO_3$(s) solid solutions

(1) Schellite crystal structure of both $BaMoO_4$(s) and $SrMoO_4$(s).

(2) Cubic crystal structure of both $BaMoO_3$(s) and $SrMoO_3$(s).

(3) size of Ba^{+2} is 1.35 Å and that of Sr^{+2} is 1.18 Å in six coordination, so the relative size difference is less than 15%.

(4) Electronegativity of Sr is 1.0 which is very close to that of Ba ~ 0.9.

(5) Ba^{+2} and Sr^{+2} has same valency.

In this study, these solid solutions were characterized by XRD and Raman spectroscopy.

2.3. Materials characterization techniques

This section describes the principles of different techniques employed in the present study to characterize the samples.

2.3.1 Powder X-ray Diffraction (XRD)

X-ray diffraction is one of the most important characterization tools used in solid state chemistry and materials science [**93, 102-103**]. It helps in elucidating the crystal structure and lattice parameters of crystalline solids. Diffraction of a characteristic X-ray beam from the planes of crystalline solid takes place when the wavelength of the X-ray beam (in Å scale) is in the same order as that of the inter planar spacing in crystals. Characteristic X-rays are produced when the energetic electrons strike the anode, made of a pure metal such as copper, molybdenum or chromium; it removes the inner (K) shell electrons. When this happens, other electrons from higher level shells drop into the vacant K-shell and in doing so emit a photon (X-ray) whose wavelength (energy) is characteristic of the metal target. In order to remove the inner shell electron, the incoming electron must have energy greater than the difference in energy between the inner (K) shell electron and a free electron in the conduction band of the target metal. The X-ray radiation most commonly used is that emitted by copper, whose characteristic wavelength for the K_α radiation is 1.54184 Å. Other metal targets commonly used in X-ray generating tubes include Cr (K_α-2.29 Å), Fe (K_α-1.94 Å), Co (K_α-1.79 Å), and Mo (K_α-0.71 Å).

2.3.1.1. Principle of X-ray diffraction

When an X-ray beam falls on a crystal comprised of atoms, the electrons around the atoms start oscillating with the same frequency as the incoming X-ray. Most of the waves coming out of the crystals end with destructive interference. But a very few waves remain in phase which results in constructive interference. This is due to the regular arrangement of atoms in a crystal. The constructive interference results in well defined X-ray beams leaving the sample at various directions. Hence, a diffracted beam may be described as a beam composed of a large number of scattered rays mutually reinforcing one another. Crystals are considered as a regular stacking of planes. These planes scattered the X-Ray beam if certain geometrical conditions are satisfied which is popularly known as Bragg's law:

$$n\lambda = 2d_{hkl} \sin \theta \qquad (2.1)$$

where, λ is wavelength of the X-ray used, d_{hkl} is inter planar spacing of the solid crystal and θ is angle of incidence of the X-rays and n is the order of reflection. The intensity of X-ray recorded at various (2θ) were recorded as function of 2θ, which is called as diffraction pattern.

2.3.1.2 Source of background radiation- fluorescence

The quality of the X-ray powder diffraction pattern is governed by the level of background radiation present. Background radiation is mainly because of fluorescence of the sample which occurs when the radiation from the primary beam (Cu K_{α}, when Cu is the source) knocks out inner shell electrons of the atoms of the sample. Electrons from the outer shell of the sample drop down to occupy the empty levels in the inner shell and hence they emit their excess energy as X- ray known as fluorescence. When the ionization energy of atoms/ions is less than the energy of primary X-ray, ionization occurs leading to fluorescence. For example, let us consider the analysis of a sample containing elemental Ni, Co and Fe with Cu Kα radiation. Energy of Cu Kα radiation (λ = 1.54184 Å) is higher than the ionization potential of 1s electron of Co (λ = 1.6081 Å) and Fe (λ = 1.7433 Å) but less than that of Ni (λ = 1.4880 Å). When Cu Kα radiation falls on the samples containing Co, Fe and Ni, it removes the 1s electron of Co and Fe but not of Ni. Hence a sample containing Co and Fe fluoresces strongly. The background radiation can be minimized by keeping monochromator between the sample and the detector. Alternatively, the primary source needs to be changed suitably.

X-ray diffraction technique requires an X-ray source, sample under investigation and a detector. X-ray diffraction methods employ single crystals as well as polycrystalline powder samples. The main use of single crystal method is to determine the space group and crystal structure, while the powder diffraction technique is widely used for phase identifications and crystallite size determinations. The diffraction pattern of an unknown mixture is usually compared with a powder diffraction file (PDF) collected and maintained by Joint Committee of Powder Diffraction Standards (JCPDS) for identification. From the powder diffraction patterns, various other useful informations like stress and strain on crystallites, thermal expansion of lattice, solid solution formation, phase transitions etc can also be derived. The high temperature XRD is useful to detect the phase changes occurring at elevated temperatures.

The schematic diagram of a powder X-ray diffractometer is shown in **Fig. 2.3.** A monochromatic beam of X-rays strikes a finely powdered sample, where the crystallites present themselves in random orientation.

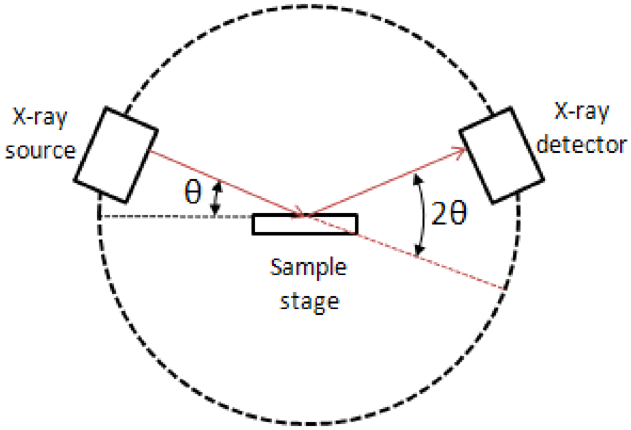

Fig. 2.3: Schematics of powder X-ray diffractometer

When the angle of incidence of X-rays is at the Bragg's angle θ of a crystalline phase of the sample, there would be some crystallites with the appropriate lattice planes oriented for diffraction. The diffracted beam is detected using a movable detector which is set to scan over a range of 2θ values at a constant angular velocity. Generally, a 2θ range of 10 to 80 degrees is sufficient to cover the most useful part of the powder pattern.

In the present work, the formation of compounds were confirmed using a Stoe theta–theta X-ray diffractometer employing monochromatic Cu K_{α} radiation (λ = 1.54184 Å) and graphite monochromator. NaI(Tl) detector was used. The powder sample was ground in mortar and pestle with 1-2 drops of 10% collodin-amyl acetate mixture and spread on a glass slide for room temperature identification of phase. The sample were scanned in the range 10 to 70^{o} with an interval of 0.02° and counting time of 2s.. The recorded "d" values were used for indexing.

2.3.1.3. Determination of lattice parameters

The crystals are built up of regular arrangement of atoms in three dimensions. This arrangement can be represented by a repeat unit called "unit cell". The unit cell is defined as the smallest repeating unit which shows the full symmetry of the crystal. The size and shape of unit cell describes in terms of three crystallographic axes (a, b, c) drawn from one corner of the cell and angles between them (α, β, γ). These lengths and angles are called as lattice parameters of the unit cell. On the basis of these lattice parameters all the crystals are classified in seven crystal system and 14 Bravais lattices. The crystal system and Bravais lattices are given in **Table 2.1.**

Crystal lattices are made up of a set of equidistance virtual planes which are known as lattice planes. A particular plane in a crystal is recognized by Miller indices (*h*, *k*, *l*). These planes cuts the *a*, b and c axis of the crystal with certain ratios. These ratios were reciprocated and converted to integer values to arrive at the miller indices (*h*, *k*, *l*). The different sets of planes have different values of interplannar spacing. The interplannnar spacing "d_{hkl}" are measured at right angle to the planes and it is a function of both miller indices (*h*, *k*, *l*) and lattice parameters (*a*, *b*, *c*, α, β, γ). These relations are also given in T**able 2.1**. Once the d_{hkl} value of the crystalline material is known from the diffraction experiment, they can be indexed with any of the crystal system given in **Table.2.1** and the lattice parameters are calculated by using different indexing procedure. The indexing of cubic system is easy as only one cell parameter is involved, however indexing the cell with lower symmetry from tetragonal to triclinic is more difficult as number of cell parameters increases.

In earlier days, indexing was being done manually by graphical and analytical techniques. Each crystal system has a particular relationship among $sin^2\theta$ values which is a signature of the crystal system to which the unknown pattern is matching.

Analytical method for indexing cubic system is given as an example. The relation used for cubic system is

$$sin^2\theta = A(h^2 + k^2 + l^2) \tag{2.2}$$

where $A=\lambda^2/4a^2$, λ is wavelength of X-ray and "*a*" is the lattice parameter. For a unknown compound, indexing is first tried with cubic system then proceeds to the lower symmetry systems gradually. In a simple cubic system, $sin^2\theta$ will be in multiple of 1, 2, 3, 4, 5, 6, 8, 9……………., in body centered it is 2, 4, 6, 8, 10…, in face centered it is 3, 4, 8, 11, 12, …………,whereas in base centered it is in ratios of 3, 8, 11, 16…….. From the differences of two successive $sin^2\theta$ values, "A" can be found out which gives the value of "*a*".

As these procedures are cumbersome for low symmetry systems, different computer programmes are being used for indexing. In this study, a computer programme written by Wadhawan **[104]** was used for indexing of various XRD patterns obtained for compounds and solid solutions. Once lattice parameters were known at different temperatures, volume at each temperature was calculated using the formula given in **Table 2.1.**

Table 2.1. Seven crystal system, 14 Bravais lattice, relation between unit cell parameters, unit cell volume, and relation between interplannar spacing and axial lattice parameters

Crystal system	Axial length	Axial angles	Bravais Lattice	Symbol	Unit cell volume	Relation between interplannar spacing and axial lattice parameters
Cubic	$a= b= c$	$\alpha=\beta=\gamma=90^o$	Simple	P	a^3	$\frac{1}{d^2}=\frac{h^2}{a^2}+\frac{k^2}{a^2}+\frac{l^2}{a^2}$
			Body centered	I		
			Face centered	F		
Tetragonal	$a= b\neq c$	$\alpha=\beta=\gamma=90^o$	Simple	P	a^2c	$\frac{1}{d^2}=\frac{h^2+k^2}{a^2}+\frac{l^2}{c^2}$
			Body centered	I		
Orthorhombic	$a\neq b\neq c$	$\alpha=\beta=\gamma=90^o$	Simple	P	$a\ b\ c$	$\frac{1}{d^2}=\frac{h^2}{a^2}+\frac{k^2}{b^2}+\frac{l^2}{c^2}$
			Body centered	I		
			Face centered	F		
			Base centered	C		
Rhombohedral	$a= b= c$	$\alpha=\beta=\gamma\neq 90^o$	Simple	P	$a^3\sqrt{1-3cos^2\alpha+2cos^3\alpha}$	$\frac{1}{d^2}=\frac{(h^2+k^2+l^2)sin^2\alpha+2(hk+kl+hl)(cos^2\alpha-cos\alpha)}{a^2(1-3cos^2\alpha+2cos^3\alpha}+\frac{l^2}{c^2}$
Hexagonal	$a= b\neq c$	$\alpha=\beta=90^o$, $\gamma=120^o$	Simple	P	$\frac{\sqrt{3}}{2}a^2$c	$\frac{1}{d^2}=\frac{4}{3}\left(\frac{h^2+hk+k^2}{a^2}\right)+\frac{l^2}{c^2}$
Monoclinic	$a\neq b\neq c$	$\alpha=\gamma=90^o\neq\beta$	Simple	P	abc sin(β)	$\frac{1}{d^2}=\frac{1}{sin^2\beta}\left(\frac{h^2}{a^2}+\frac{k^2sin^2\beta}{a^2}+\frac{l^2}{c^2}-\frac{2hl\cos\beta}{ac}\right)$
			Base centered	C		
Triclinic	$a\neq b\neq c$	$\alpha\neq\beta\neq\gamma\neq 90^o$	Simple	P	$abc\sqrt{\begin{matrix}1-cos^2\alpha-cos^2\beta-cos^2\gamma\\+2\ cos\alpha\cdot cos\beta\cdot cos\gamma\end{matrix}}$	$\frac{1}{d^2}=\frac{1}{V^2}(S_{11}h^2+S_{22}k^2+S_{33}l^2+2S_{12}hk+2S_{13}hl+2S_{23}\ kl)$

$\boldsymbol{S_{11}=b^2c^2sin^2\alpha}$, $\boldsymbol{S_{22}=a^2c^2sin^2\beta}$, $\boldsymbol{S_{33}=a^2b^2sin^2\gamma}$, $\boldsymbol{S_{12}=ab\ \ c^2(cos\alpha\ cos\beta-\cos\gamma)}$, $\boldsymbol{S_{23}=a^2bc(cos\beta cos\gamma\ -\cos\alpha)}$, $\boldsymbol{S_{13}=ab^2c(cos\gamma cos\alpha\ -\cos\beta)}$

Calculation of density

The density of unit cell was calculated at various temperatures. The density can be found out using the relation:

$$X - ray\ density = \frac{weight\ of\ the\ molecules\ in\ the\ unit\ cell}{Volume\ of\ the\ unit\ cell}$$

$$\rho = \frac{\sum Z \times M/N}{V} \tag{2.3}$$

Where, ρ is X-ray density in gcm^{-3}, Z is the no of molecular unit in the unit cell, M is the molecular weight in (g/mol), N is the Avogadro's number, V is the volume in the unit cell in cm^3. By inserting the value of Avogadro's number and converting the volume unit from cm^3 to Å^3, the density can be found out from the relation:

$$\text{X-ray density } (\rho) = 1.66042 \times Z \times (M/V) \tag{2.4}$$

In this study, RE_6UO_{12}(s) shows rhombohedral structure, but it was indexed with more symmetry hexagonal structure.

Relation between Rhombohedral and Hexagonal crystal structure

Rhombohedral unit cell has equal sides and angles as it is shown in Fig.2.4. The structure is incorporated inside the hexagonal structure. However, instead of choosing a primitive rhombohedral unit cell to represent the Bravais lattice, it is normal to choose an equivalent rhombohedrally-centred hexagonal cell as shown in Fig.2.4 .

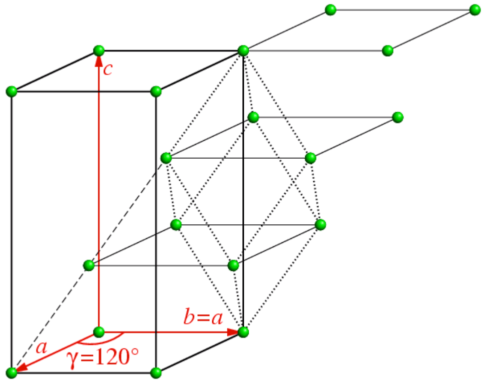

Fig2.4. Schematic of hexagonal unit cell incorporating rhombohedral structure

The relation between the unit cell parameters of rhombohedral and hexagonal system are:

$$a_r = \left(\frac{1}{3}\right)\sqrt{(3a_h^2 + c_h^2)} \tag{2.5}$$

$$\alpha = 2sin^{-1}\left(\frac{3}{2\sqrt{3+\left(\frac{c_h^2}{a_h^2}\right)}}\right) \tag{2.6}$$

$$a_h = 2a_r sin(\alpha/2) \tag{2.7}$$

$$c_h = a_{r\sqrt{(3+6cos\alpha)}} \tag{2.8}$$

From these relations rhombohedral parameters can be found out from the hexagonal lattice parameters and vice versa. The hexagonal cell has volume three times of rhombohedral cell.

2.3.2. Raman Spectroscopy

Raman spectroscopy is a spectroscopic technique used to observe vibrational, rotational, and other low-frequency modes in a system [105-107]. This technique involves photon-phonon interaction to study crystals. Raman Effect is an inelastic light scattering effect resulting from the excitation or de-excitation of vibrational modes.

When the energy of the incident photon is not large enough to excite the molecule from the ground state to the lowest excited electronic state, the molecule gets excited to a virtual state which exists between the ground and excited states. The electron in the excited molecule cannot stay long in the virtual state and immediately goes back to the ground state. If the electron goes back to its original state (ground state), the wavelength of the emitted photon is then same as that of the incident light photon. Such a scattering phenomenon is known as Rayleigh scattering. On the other hand, it is also possible for the electron to go to a virtual state that is different from where it is excited, giving rise to an energy difference between the emitted photon and the incident photon, and therefore a shift in wavelength (energy shift) for the emitted photon as compared to the incident photon. This is known as Raman scattering. If the emitted photon has energy smaller than that of the incident photon, this scattering process is known as Stokes scattering. However, when the incident photon has a lesser energy compared to the emitted photon, it is known as anti-Stokes scattering. The shift in energy gives information about the vibrational modes in the system.

Fig.2.5 illustrates the differences between Rayleigh scattering, Stokes scattering and anti-Stokes scattering.

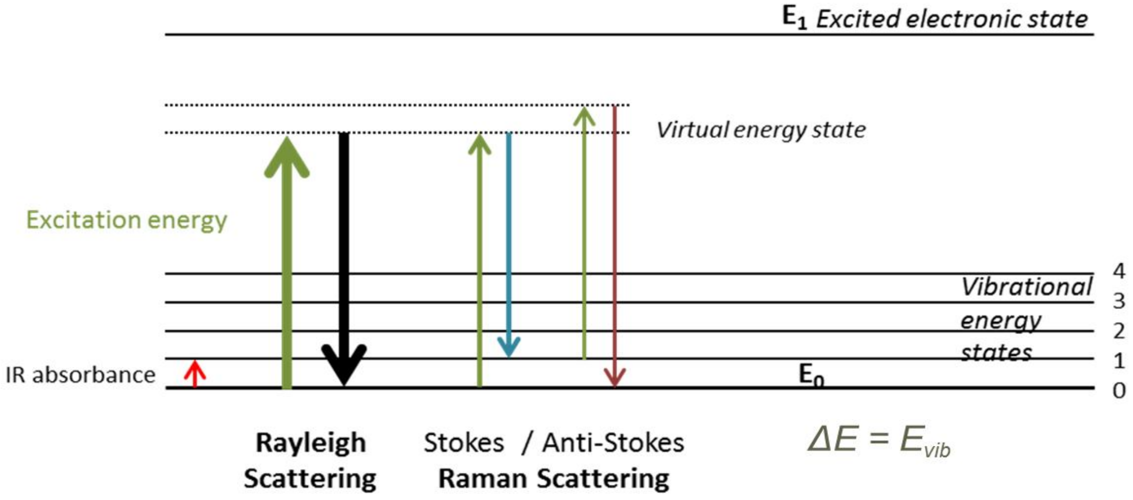

Fig.2.5. Representation of Rayleigh scattering, Stokes scattering and anti-Stokes scattering.

It is obvious from the figure that if the final state is above the initial state, then photon transfers energy to the sample and Stokes scattering occurs. But for anti-stokes scattering the system already has to be in excited state and the final state is below the initial state. In this case energy is transferred from the sample to photon. It is a complementary technique of Infrared spectroscopy.

Raman scattering is a phenomenon with a very low probability of occurrence. Only one in 10^6 of incident photons is inelastically scattered. Because the majority of incident light is Rayleigh scattered, Raman detector systems must remove this elastically scattered

light from the collected light, or else the Rayleigh scattered light can overwhelm the weaker Raman signal. The sample is illuminated with an intense laser beam. The scattered light from the illuminated spot is collected with a lens and sent through a monochromator. Wavelengths close to the incident laser line due to elastic Rayleigh scattering are filtered out while the rest of the collected light is dispersed onto a detector. It is difficult to separate the weak inelastically scattered light from the intense Rayleigh scattered laser light. The Raman spectrum is basically a recording of the shift in frequencies between incident and emitted light and intensities of the inelastically scattered photons. The intensity is given as photon counts per second per milliwatt of incoming light and frequency shift given as wave numbers. Since every atom and molecule has its own Raman spectrum, this can be used to figure out its atomic or molecular structure which can be used for identifying elements and/or compounds that are present in the sample being studied.

The experimental set up as shown in **Fig. 2.6** consists of a highly collimated and polarized laser source which focused on the sample. The backscattered light is collected with objective lens with large aperture and focused on spectrometer. After leaving the spectrometer the photons are counted by a highly sensitive CCD camera.

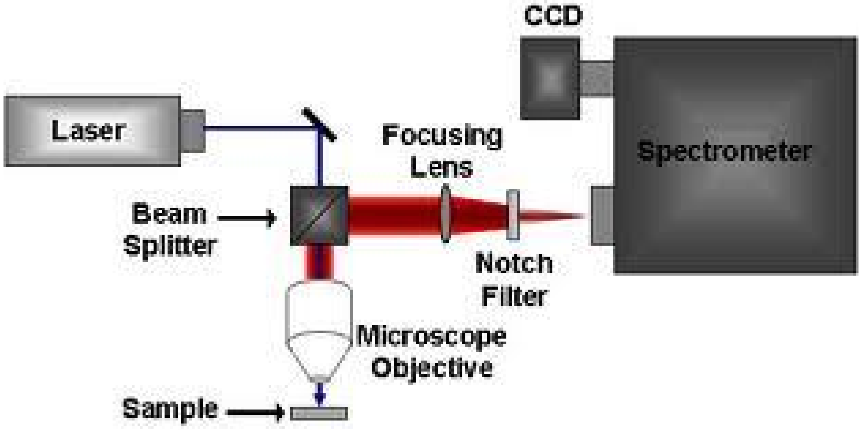

Fig. 2.6. The experimental set up of Raman spectrometer

In this study, the room temperature Raman spectra of all the synthesized compositions in the series $Ba_{1-x}Sr_xMoO_4$ (s) (x = 0, 0.2, 0.4, 0.6, 0.8, 1) were recorded on a micro/macro-Raman spectrometer (Model: LABRAM-1, France) using the 488 nm excitation line of an Ar^+ ion laser with 14mW power. The scattered Raman signals were collected in the back scattering geometry using a single monochromator spectrometer equipped with a Peltier-cooled CCD detector. Samples in the form of small pellets were used and the excitation laser line was focused on one of the flat surfaces of the sample using an optical microscope (Olympus BX-40, 50x, objective lens) connected to the spectrometer. The spectra were recorded with averaging 50 scans with a time interval of 2 s and a resolution of 2 cm^{-1}. Single crystal Silicon peak (~520 cm^{-1}) was used for the frequency calibration of the equipment prior to the sample measurements.

2.3.3. Scanning Electron Microscopy (SEM)

Scanning Electron Microscopy (SEM) is being widely used to characterize the properties like morphology (size and shape) and topography of various materials. The principle is based on the bombardment of electrons to the surface of a sample to generate signals which forms an image. Moreover, SEM has a large depth of field, which allows a large amount of the sample to be in focus. The combination of higher magnification, larger depth of field, greater resolution and compositional information makes SEM widely used equipment. The schematic diagram with the main parts of a scanning electron microscope is presented in **Fig. 2.7**.

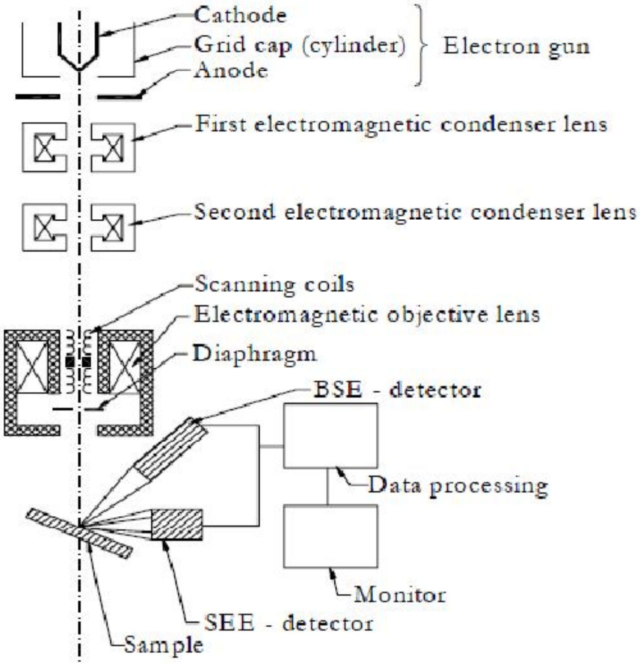

Fig.2.7. Schematic of Scanning Electron Microscope

SEM microscope can be divided into several sections with different vacuum levels. The highest vacuum is obtained at the electron gun section and then it reduces down the column up to the specimen chamber. An electron beam is generated in the very top of the microscope's column. There are two types of electron sources: tungsten thermionic gun and field emission gun. When a steady stream of electrons is generated, it passes through the condenser lenses (one or more) which adjust the beam current that impinges on the specimen, while the objective lens determines the final size of electron beam. The scan coils control the beam scanning across the specimen. The electrons are accelerated with a voltage in the range 0.1 – 30 keV towards the sample. Wavelength of the electron beam can be controlled by varying the velocity of electrons with the applied voltage. As the electron beam traces over the specimen, it interacts with the specimen and results in the generation of backscattered as well as secondary electrons [108].

Moreover some of the electrons can be absorbed or pass through the specimen. The signal (electron emitted) from the surface is registered by different detectors (e.g. backscattered and secondary electron). The detector counts the number of electrons given off from each point of the samples surface. The intensity of the emitted electron signal is displayed as brightness on a cathode ray tube (CRT). By synchronizing the CRT scan to that of the scan of the incident electron beam, the CRT display represents the morphology of the sample surface area scanned by the beam. The electron beam and CRT spot are scanned to a monitor [**108, 109**].

For a better understanding of the SEM, it is important to know the nature of the possible interactions between the primary electron (PE) beam and the atom. The negatively charged primary electrons interact strongly with the sample. The interaction between the electron and the sample atoms may be inelastic, elastic or electromagnetic which is shown in **Fig.2.8.**

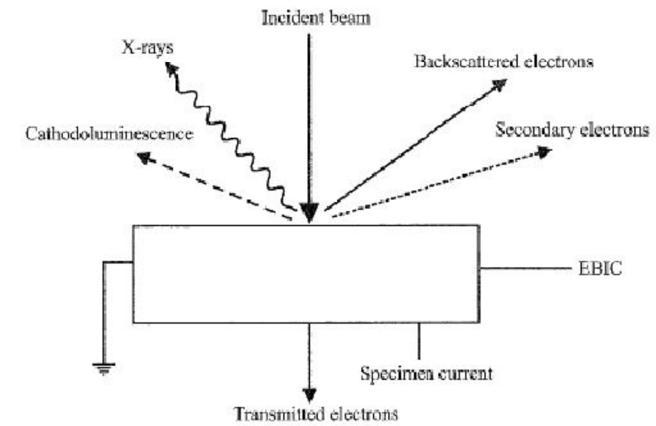

Fig.2.8.The different signal obtained from the interaction of electron with samples

The area where the elastic or inelastic interaction takes place is called the "interaction volume" as shown in **Fig. 2.9**. The size of the interaction volume depends on the electron's energy and the atomic number of the sample. Penetration depth of the primary electrons is higher in an element with lighter atomic number than that for a heavier atomic number. Emitted lower-energy electrons resulting from inelastic scattering are the secondary electrons (SE). They are collected on a SE detector (scintillator) which is positively charged to improve the signal to noise ratio (S/N). SE are abundant and they are used to give topological and morphological information of the sample. High-energy electrons resulted from an elastic collision of an incident electron, typically with a sample atom’s nucleus, are referred to as backscattered electrons (BSE). The energy of BSE will be comparable to that of the incident electrons. These high-energy electrons can escape from areas deeper than secondary electron, so surface topography is not as accurately resolved as for secondary electron imaging which gets generated from near surface area. BSE are highly influenced by atomic number of the sample, which is responsible for the phase contrast of the image.

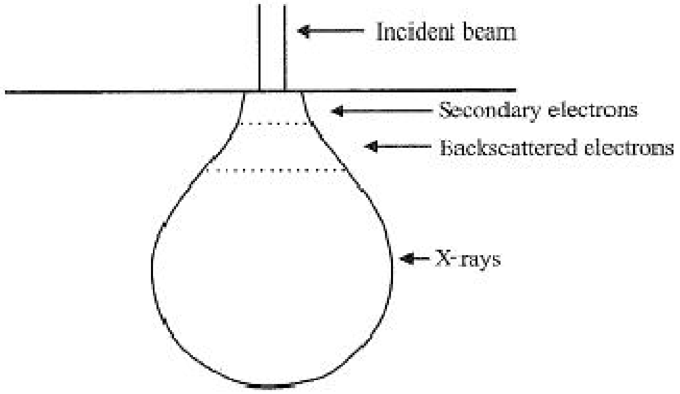

Fig. 2.9: Representation of Interaction volume

Microstructure of $BaMoO_4(s)$, $SrMoO_4(s)$, $BaMoO_3(s)$ and $SrMoO_3(s)$ was studied using scanning electron microscope. This was done on an instrument having both Everhart–Thornley secondary electron detector and solid state back scattered electron detector. The micrographs were taken at 20–30 kV acceleration voltages.

2.3.4. Inductively Coupled Plasma-Mass Spectrometry (ICPMS).

Inductively Coupled Plasma Mass Spectrometry (ICP-MS) is an analytical technique used for determinations of trace and ultra trace level of isotopes/ elements. The instrument comprised of three components (1) Argon plasma as ion source (2) Time of Flight (TOF) mass analyzer (3) Secondary Electron Multiplier (SEM) as detector. There are three concentric quartz tubes. Argon flowing through the innermost tube is initially seeded with free electrons from Tesla discharge coil. These electrons interact with the magnetic field, induced by rf field by a surrounding induction coil and gain sufficient energy to ionize other argon atoms by collisions. The cation and electrons thus generated collide with argon atoms to produce ionization and intense thermal energy. This is known as plasma which has temperature ranges from 6000 K to 10000 K. The plasma is maintained by flow of a stream of gas in the middle concentric quartz tube surrounding the primary plasma. The third outermost gas streams cool the quartz tube. The sample solution was introduced in the plasma through pneumatic nebulizer. The analyte in the sample solution gets atomized and ionized in the plasma. The ions were sampled inside the mass analyzer through differential pumping stages. Ions were sorted by mass to charge ratio in mass analyzer. The intensity of each mass peak (analyte) was then correlated with the concentration using calibration plot. A schematic of ICPMS is given in **Fig.2.10.**

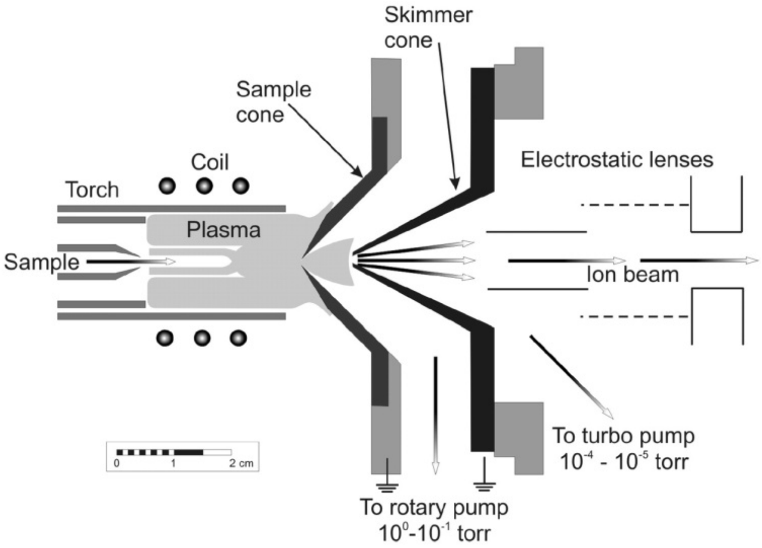

Fig.2.10. A schematic of ICPMS.

2.3.5. Thermo analytical Methods

Thermo analytical Methods involve the measurement of change in physical and chemical properties of materials especially enthalpy, heat capacity, coefficient of expansion and mass as a function of temperature. The three main thermal analytical techniques used to characterize the thermal properties of the materials are Thermo Gravimetric Analysis (TGA), Differential Thermal Analysis (DTA) and Differential scanning Calorimetry (DSC).

2.3.5.1. Simultaneous Thermogravimetry (TG) and Differential Thermal Analysis (DTA)

Thermo gravimetric analysis (TGA) is a technique, which measure the changes in the mass of a sample as a function of temperature/time, whereas DTA gives information on the associated thermal effects [93]. A sample of the test material is placed into an alumina crucible that is supported on, or suspended from an analytical balance located inside the furnace chamber. The sample crucible along with an inert reference is heated according to a predetermined thermal cycle. The balance sends the weight signal to the computer along with the sample temperature and the elapsed time. The TGA curve plots the TGA signal, converted to percent weight change on the Y-axis against the reference material temperature on the X-axis. Schematic of simultaneous TG-DTA instrument is given in **Fig. 2.11**.

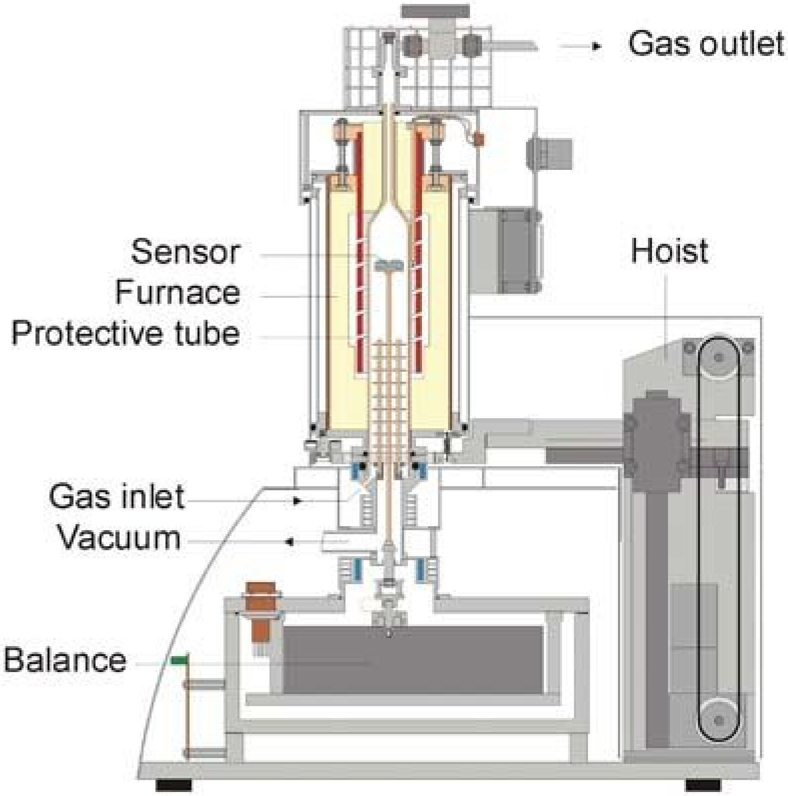

Fig.2.11. Scematic of simultaneous TG-DTA system (M/s Netzsch, Germany)

In DTA, the temperature difference between sample and inert reference is recorded when the sample and the reference are subjected to identical heating/cooling cycles. In the event of any thermal effect, the temperature difference between the sample and the reference results in the appearance of endothermic or exothermic peaks. The area under a DTA peak can be correlated to the enthalpy change in the process for the sample by proper calibration.

In this study, a TG/DTA system (M/s Netzsch, Germany) was employed for thermal characterization of organic precursors of $Ba_{1-x}Sr_xMoO_4$(s) solid solutions.

2.3.6. Photoluminescence spectroscopy (PL)

In this technique, a sample is excited by photons (generally in UV range) and the energy released as light by the sample during deexcitation is recorded. A spectrofluorometer is an instrument capable of recording both the excitation and emission spectra simultaneously. It takes advantage of fluorescent properties of compound to provide information on concentration and the chemical environment. In order to determine the **emission** spectrum of a particular compound, the wavelength of maximum absorption is determined and the compound is excited at that wavelength. A monochromator (a device that allows narrow bands of light wavelengths to pass) is then used to scan the fluorescence emission intensity over the entire series of emission wavelengths. The relative intensity of the fluorescence is measured at the various wavelengths to plot the emission spectrum. The **excitation** spectrum of a sample is determined in a similar manner by monitoring fluorescence emission at the wavelength of maximum intensity while the compound is excited through a group consecutive wavelength. The emission maximum is chosen and only emission light at that wavelength is allowed to pass to the detector. Excitation is induced (usually by means of a monochromator) at various excitation wavelengths and the intensity of the emitted fluorescence is measured as a function of wavelength. The result is a graph, which depicts the relative fluorescence intensity produced by excitation over the spectrum of excitation wavelengths.

The process of excitation and various ways of emission can be represented with the Jablonski diagram shown in **Figure 2.12**. The species is first excited (by absorbing a photon) from its ground electronic state to one of the vibrational states in the excited electronic state. The excited molecule loose vibrational energy on collisions with other molecules till it reaches the lowest vibrational state of the excited electronic state. The molecule then drops down to one of the vibrational levels of the ground electronic state, emitting a photon in the process. The molecule drops down into any of several vibrational levels in the ground state, and emits photons with different energies.

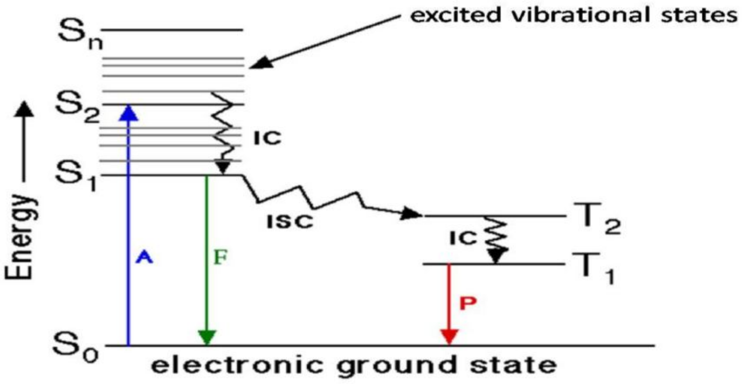

Fig. 2.12: A Jablonski diagram shows the possible relaxation processes in a molecule after the molecule has absorbed a photon (A): IC = internal conversion, ISC= intersystem conversion, F= fluorescence, P= phosphorescence

Spectrofluorometer consists of excitation source, monochromators for both excitation and emission light and detector. The source produces light photons. Various light sources like lasers, photodiodes and lamps are being used as excitation sources. Normally, xenon lamp is used as source, as it has high intensity at all wavelengths starting at 250 nm. Photons pass through monochromator, which selectively transmits light in a narrow specified excitation wavelength. Filters are used when laser is being used as excitation source, to produce monochromatic light. The transmitted light again passes through adjustable slits for further control of intensity and resolution. The filtered light falls on the sample. Similarly, the generated emitted light goes through a filter to prevent the excitation light entering the detector. The filtered light enters the emission monochromator, positioned at 90° from the excitation light to eliminate background signal and minimize noise. This emitted light is detected by a detector. The detector is a photomultiplier tube (PMT). Schematic diagram of a spectrofluorometer is shown in **Fig. 2.13.**

In this work, the stability of $SrCeO_3(s)$ is investigated using photoluminescence spectroscopy. The photoluminescence spectra of $SrCeO_3(s)$ heated in high purity argon atmosphere at different temperature were recorded. The experiments were conducted in an Edinburgh CD-920 unit equipped with a Xe Flash lamp as the excitation source. The data acquisition and analysis were done using F-900 software provided by Edinburgh Analytical Instruments, UK.

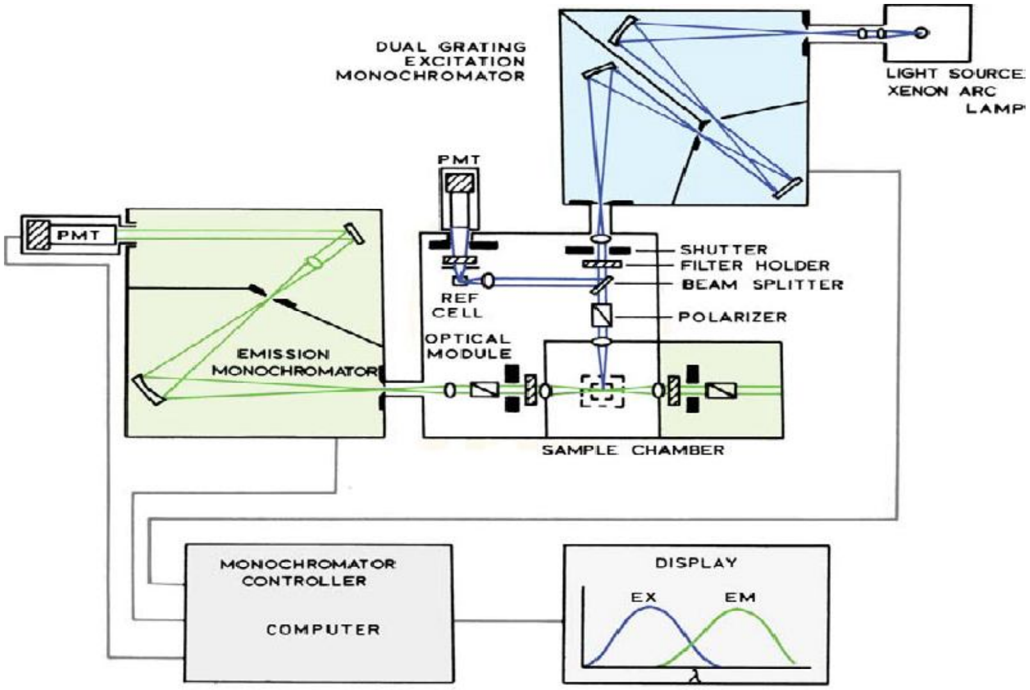

Fig. 2.13: The block diagram of spectrofluorometer.

2.4. Thermo-physical properties

In the present study, thermophysical properties like thermal expansion and heat capacity was measured. The theory, working principle and instrumentation of these two techniques are described in detail.

2.4.1. Thermal expansion

Thermal expansion of various constituents of irradiated fuel is essential to predict the induced stress between fuel and the clad. If expansion of fuel is very high compared to clad, then the fuel clad gap reduces and leads to intimate contact which in turn induce pressure on the clad and consequently failure of the fuel pin.

2.4.1.1. Theory

Thermal expansion of solids is a physical property that depends on the nature of the interatomic potential. As two atoms are brought together, attractive forces dominate the overall potential energy of the system. After the equilibrium distance of separation, the potential energy starts increasing due to the repulsive forces acting between the nuclei. The variation of the potential energy with interatomic separation for a simple harmonic and an anharmonic oscillator is represented in **Figure 2.14.**

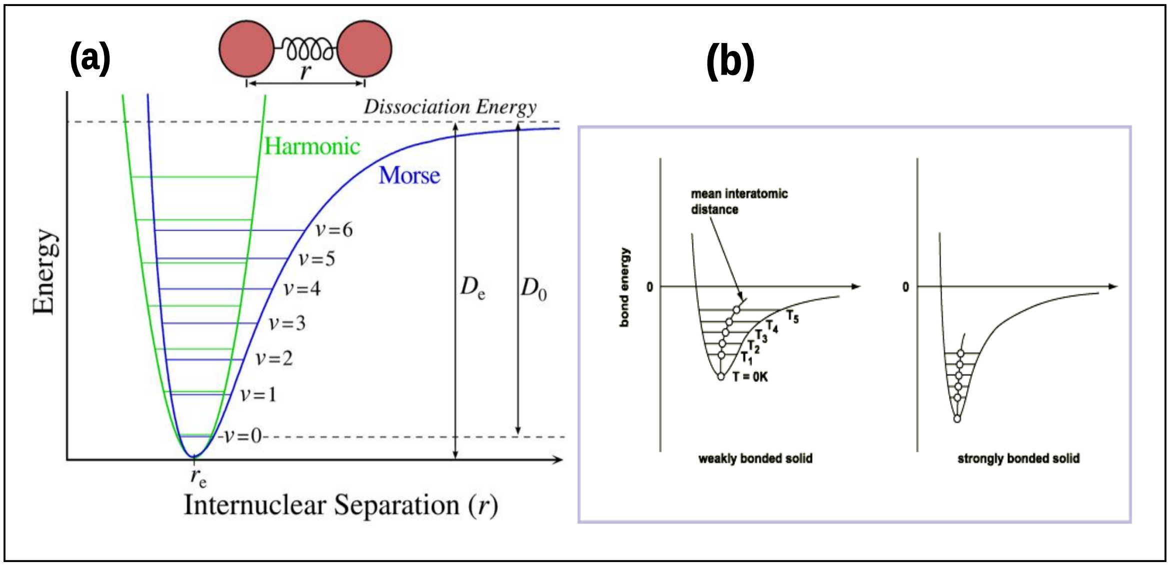

Fig.2.14. (a) The variation of the potential energy with interatomic separation for a simple harmonic and an anharmonic oscillator (b) Representation of potential energy curve of a weakly and strongly bonded molecule.

For a harmonic oscillator, as the temperature of the system increases from T_1 to T_2, there will not be change in the average bond distance so, no expansion will be observed. However, in reality atoms vibrate in an anharmonic fashion. This anharmonicity is due to an asymmetric potential energy well. This potential is also called as Morse potential. At one particular temperature T_1, the intersection of the horizontal line with the curve marks the extreme values of the inter-nuclear distance where oscillation energy is all potential energy. The midpoint of the line marks the average value. As the temperature increases to T_2, the average bond length shifts to larger distances due to the asymmetry of the potential well as shown in **Fig. 2.14(b).** This increase in the average bond length contributes to the thermal expansion. The extent of the asymmetry is dependent on the bond strength. A stronger bond results in a more symmetric potential well. This means a smaller bond expansion occurs in the material having stronger bond. In order to quantitatively measure and compare the extent of thermal expansion in solids, the thermal expansion coefficient is being calculated.

In the quasiharmonic approximation, thermal expansion is related to atomic vibrations. The contribution of each lattice vibration mode (phonon mode) of energy E to the thermal expansion is

$$\propto_v = \frac{\gamma C_v \beta}{V} \tag{2.9}$$

where β is the isothermal compressibility, V is the unit cell volume, γ is the mode Grüneisen parameter and C_v is the contribution of the phonon mode of energy E to the specific heat.

The Grüneisen parameter is defined as the volume dependence of mode frequencies according to:

$$\gamma = -\frac{\partial \ln \omega_i}{\partial \ln V} \tag{2.10}$$

where ω_i is the frequency of the i^{th} mode and V is the volume.

The molar specific heat at constant volume can be defined as the sum of the contributions of all the vibration modes:

$$c_v = \frac{1}{z} \sum p_i c_i \tag{2.11}$$

where p_i is the number of phonons of frequency ω_i and c_i is the specific heat contribution from a single mode of frequency ω_i.

The contribution of each phonon mode to the thermal expansion is proportional to the positive specific heat via the Grüneisen parameter. Each mode has an independent Grüneisen coefficient. As the compressibility and the volume will always have positive values, the signs and magnitude of the Grüneisen parameters and thus the contribution of the associated vibrational modes to the overall expansion will determine the actual nature (+ve/-ve) of thermal expansion displayed by the material.

Materials can be arbitrarily classified into three groups based on their thermal expansion coefficient (α):

High Expansion Group: $\alpha > 8 \times 10^{-6}\ K^{-1}$
Intermediate Group: $2 < \alpha < 8 \times 10^{-6} K^{-1}$
Low Expansion Group: $\alpha < 2 \times 10^{-6}\ K^{-1}$

2.4.1.2. Experimental determination of thermal expansion coefficients

Lattice thermal expansion is measured by high temperature X-ray and neutron diffraction methods whereas; bulk thermal expansion is measured by various optical and electrical methods such as dilatometry, interferometry, and thermomechanical analysis.

2.4.1.2.1. Lattice thermal expansion by high temperature XRD

The thermal expansion coefficients of solid materials were obtained from the calculated lattice parameters at different temperature as described in section 2.3.1.3. Once lattice parameters were known at different temperatures, volume at each temperature was calculated using the formula given in **Table 2.1.** The instantaneous (α_l), average (α_{ave}) linear and volume thermal expansion coefficients and percentage of thermal expansions were calculated from the lattice parameter at various temperatures. The density of crystal at different temperature was calculated using eqn.2.4.

Calculation of expansion coefficients and % expansion from lattice parameters

The calculated linear lattice parameters, volume and density were fitted to a second order polynomial equation of the form $p + qT + rT^2$, where p, q, and r are constants and T denotes the absolute temperature. The refined lattice parameters (l) can be represented by the following equation

$$l = p + qT + rT^2 \tag{2.12}$$

The instantaneous lattice and volume expansion coefficient can be expressed as:

$$\alpha_l = \frac{1}{l_o}\frac{dl}{dT} \tag{2.13}$$

where l_0 is the length/volume at initial temperature and dl/dT is the slope of the tangent of the plot of lattice parameter/unit cell volume vs. temperature (T), while the average coefficient is governed by the slope of the chord between two points on the curve of lattice parameters/unit cell volume as function of temperature.

$$\propto_{ave} = \frac{1}{l_{298}} \times \frac{l_T - l_{298}}{T - 298} \tag{2.14}$$

where l_{298} and l_T is the lattice parameter/volume at 298 K and T K. The percentage expansions can be calculated using the formula:

$$Expansion\ (\%) = \frac{l_T - l_{298}}{l_{298}} \times 100 \tag{2.15}$$

where l_T and l_{298} represents the linear lattice parameter/unit cell volume at any temperature T and 298.15 K, respectively. The most important advantage of X-ray diffraction technique is that the experiment requires small amount of powder sample and the presence of other phases does not affect the measurement. The data on thermal expansion are also not affected by porosity or thermally generated vacancies in the solid.

The high temperature attachment consists of a cylindrical brass chamber at the centre in which the sample is mounted. The cylinder is of double walled construction and is closed at one end. This end is fixed to a vertical goniometer. The body of the chamber is provided with long beryllium windows for the incidence and emergence of the X-ray beam in the 2θ angular range of 0˚ to 168˚. The powder sample is placed as a thin layer on a flat Pt-Rh alloy strip which is connected to two electrodes and is subjected to electrical resistance heating at programmed heating rate. The sample plate is spot welded at the bottom with a Pt/Pt–13% Rh thermocouple for temperature measurement. The thermocouple output is also used for temperature control. The temperature of the sample was controlled by a PID-type temperature controller within ±1 K during X-ray measurements. For minimizing thermal losses from the sample, the surroundings of the sample are maintained at a same temperature as that of the sample by means of a "U" shaped heater. Cooling water is circulated through the annular space between the chamber walls. The electrodes are also water-cooled. A schematic diagram showing the essential features of the high temperature attachment to XRD is given in **Fig. 2.15**.

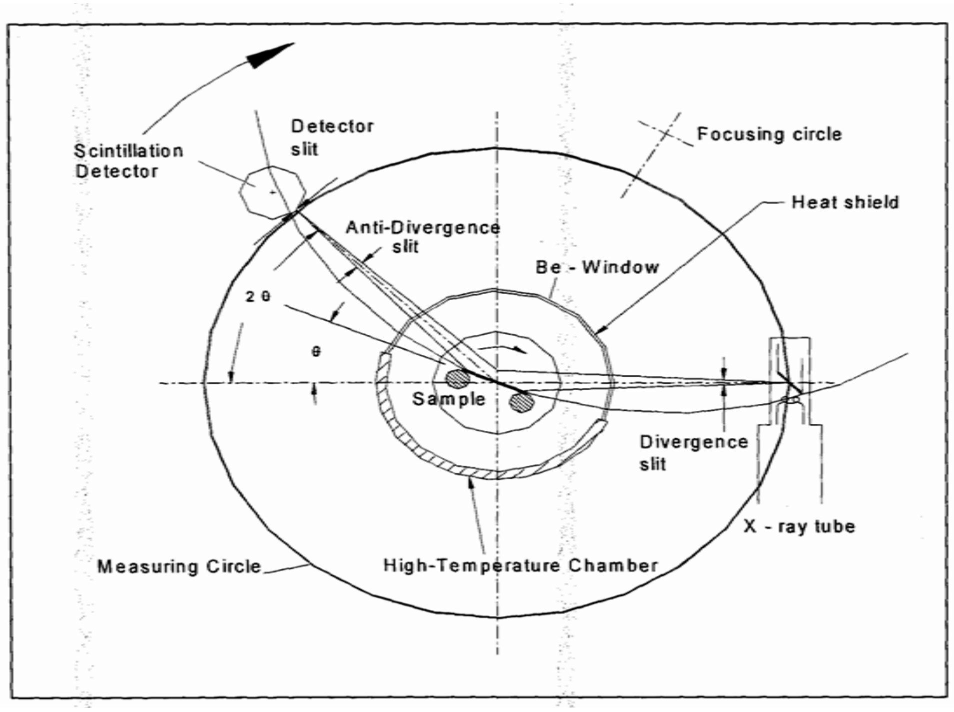

Fig.2.15. X-ray diffraction geometry incorporating high temperature attachment

In this present work, thermal expansion of RE_6UO_{12}(s) (RE=La, Pr,Sm, Gd, Tb, Dy, Ho, Er, Yb, Lu), $SrCeO_3$(s), Sr_2CeO_4(s), $Ba_{1-x}Sr_xMoO_4$(s), $Ba_{1-x}Sr_x$ MoO_3(s), Fe_2TeO_6(s) and Ni_3TeO_6(s) were measured by HT-XRD. X-ray powder diffraction (XRD) patterns of the heated samples were recorded using Stoe theta–theta diffractometer with HDK-2.4 Buhler high temperature attachment under vacuum (10^{-8} bar). The samples were heated at an interval of 100 K and equilibrated for 15 min at each temperature before the measurement. The refined lattice parameters, obtained within an accuracy of ±0.0001 nm, were calculated by the method of least squares using a computer program by Wadhawan [**104**]

2.4.1.2.1. 1. Calibration of HTXRD

Calibration for the temperature and diffraction angle is necessary for the precise measurement of lattice thermal expansion using HTXRD. For the calibration of diffraction angle at room temperature NBS standard Si powder was taken as standard. But MgO was taken for the calibration of diffraction angle at high temperatures. Any shift in the diffraction pattern of Si and MgO was used to calibrate the instrument. The diffraction patterns of Pt-Rh strip on which the sample is placed were also co-recorded, which is a additional confirmation of accuracy in diffraction angle.

2.4.1.2.2. Bulk thermal expansion using Dilatometry

The bulk expansion of the materials was studied by dilatometer (M/s Netszch, Germany) in Ar atmosphere. Pushrod type dilatometer (DIL 402) was used. The sample temperature was measured by a calibrated B-type thermocouple (Pt30%Rh–Pt6%Rh) placed directly below the sample. The temperature calibration of the dilatometer was carried out using the phase transition temperature of National Institute of Standards and Technology (NIST) reference materials (indium: T_{fus} = 429.748 K; tin T_{fus} = 505.078 K; zinc: T_{fus} = 692.750 K; gold T_{fus} = 1337.35 K). Selection of temperature program was controlled by a computer with data acquisition system. The sample supporter measuring unit and displaceable furnace of the dilatometer were mounted horizontally. The expansion was measured in the axial direction. The sample holder and push rod were made of recrystallized alumina. The expansion of the pellet under negligible load is measured as a function of temperature while subjected to the controlled temperature program. The change in length of the sample due to heating resulted in the movement in the pushrod which was detected by the linear variable displacement transducer (LVDT) giving rise to an electrical signal and transmitted to the analog to digital converter. The expansion signal and the e.m.f. of the thermocouple in the form of digitized experimental data are collected at periodic time intervals and are stored for the evaluation in the computer. The reference sample used was a single crystal of alumina of 25mmlength and 5mm in diameter.

In this study, the thermal expansion of Nd_6UO_{12}(s) was measured in the temperature range of 400 to 1100 K with a heating rate of 8 K min^{-1} to confirm the phase transition. The whole experiment was carried out in high purity argon flow with a flow rate of 6 l/h. The dimension was recorded at a temperature gap of 50 K.

2.4.2. Heat capacity

Specific heat capacity is defined as the quantity of heat required to raise the temperature of 1 gm of the substance by 1 K. Heat capacity is the heat required to raise the temperature of 1 mole of the substance by 1 K. The compounds with high heat capacity will not get heated very fast and power derived from the material will not be high. So for nuclear fuel the heat capacity should be low such that more power can be extracted. In addition the specific heat capacity should not be very low which leads to hot spots, the origin of melting down of fuel and clad.

2.4.2.1. Relevance of heat capacity in nuclear fuel

Heat capacity of any material is required to compute the thermal conductivity from the measured thermal diffusivity. Thermal conductivity is an important fuel design parameter, which determines the maximum linear power that can be extracted from the fuel element during its operation. The availability of reliable thermal conductivity data is essential to arrive at permissible linear power ratings. The linear power rating of the fuel is estimated from the following expression

$$\emptyset = 4\pi \int_{T_s}^{T_C} K \, dT \qquad (2.16)$$

where ' $\emptyset$ ' is the linear heat rating (LHR) and 'K' is the thermal conductivity of the fuel. It is interesting to note that the RHS of the equation does not contain any term involving the dimensions of the fuel element. Therefore, the centre line temperature (T_c) is independent of the fuel rod diameter for a given LHR and it is the property of the the fuel material only. T_s is the surface temperature of the fuel pin. Thermal conductivity is related to thermal diffusivity (λ) and heat capacity(C_p) by the following equation

$$K = \lambda \times \rho \times C_p \qquad (2.17)$$

where ' ρ ' is the density of the fuel. Generally, the thermal diffusivity rather than the thermal conductivity data are experimentally measured. Laser flash method is very often used for measurement of thermal diffusivity.

To define a system thermodynamically, many functions are required such as (1) The standard enthalpy of formation (2) Standard entropy, S^o $(298.15\,K)$. (4) Enthalpy of phase transformation, $\Delta_{tr}H(T)$ (5) Gibbs energy of formation $\Delta G\ _f^0(T)$. Heat capacity as a function of temperature is a key parameter to arrive at these functions.

In view of the importance, heat capacity measurements of various systems were taken up in the present work.

2.4.2.2. Theory of heat capacity

The heat capacity of most systems is not constant. Rather, it depends on the state variables of the thermodynamic system such as temperature, pressure and volume of the system. Measurements of heat capacity can therefore be performed, most commonly either at constant pressure (C_p) or at constant volume (C_v). Measurements under constant pressure produce larger values than those at constant volume because the constant pressure values also include heat energy that is used to do work to expand the substance against the constant pressure as its temperature increases. Maintaining constant volume is difficult for solids as thousand atmosphere pressures is required. Therefore C_v is being calculated theoretically and C_p being measured experimentally. The discussion about the heat capacity theories like Dulong and Petit, Einstein and Debye are discussed here.

2.4.2.2.1. Dulong and Petit theory of heat capacity

Dulong and Petit rule states that the molar heat capacity of solid metals and alloys with the same bonding in all three directions have the value of 3R (R= gas constant) at room temperature. Subsequently, Kopp introduced a rule which states that, at ambient temperatures, the molar heat capacity of a solid chemical compound is approximately equal to the sum of molar heat capacities of its constituent chemical elements. However, their theory fails to explain the experimental observations which show that heat capacity usually increases with increasing temperature and can have values significantly lower than 3R at low temperatures.

2.4.2.2.2. Einstein theory of heat capacity

Einstein theory is based on quantum mechanical approach. It assumes that individual atoms in a crystal behaves as harmonic oscillator and oscillate independently with a fixed single frequency about its lattice point.

The heat capacity expression at constant volume obtained by the theory is

$$C_v = 3R\left(\frac{\theta_E}{T}\right)^2\left(\frac{e^{\frac{\theta_E}{T}}}{\left(e^{\frac{\theta_E}{T}}-1\right)^2}\right) \tag{2.18}$$

Where θ_E is Einstein temperature = $h\nu_E / k$

ν_E = Einstein frequency

k = Boltzmann constant

T= Temperature in Kelvin

R= Gas constant

At high temperature $C_v \rightarrow 3R$ in agreement with Dulong and Petit's law and as $T \rightarrow 0$, $C_v \rightarrow 0$ which is in agreement with experimental observation. The limitation of Einstein's theory was observed in the temperature range 0.01 to $0.02\theta_E$ where the computed value approach to zero more rapidly than do the experimentally observed values. This discrepancy is caused by the assumption that each atoms are not independently vibrating.

2.4.2.2.3. Debye theory of heat capacity

Debye assumed that solids are continuous as elastic matrix and atoms are vibrating with a range of frequencies. The lower limit of these vibrations is determined by the interatomic distances in the solid. Theoretically, the shortest allowable wavelength is twice the interatomic distance, in which case neighboring atoms vibrate in opposition to one another. The heat capacity at constant volume obtained by the theory is as follows

$$C_v = 9R\left(\frac{T}{\theta_D}\right)^3 \int_0^{\frac{\theta_D}{T}} \frac{x^4 e^x}{(e^x-1)^2} \qquad (2.19)$$

Where $x = h\nu / kT$

θ_D = Debye temperature = $h\nu_D / k$

ν_D = Debye frequency

k = Boltzmann constant

T = Temperature in Kelvin

R= Gas constant

The above equation gives an excellent fit to the experimental data at lower temperature compared to that of Einstein equation. The value of the integral when $T \rightarrow 0$ is 25.98 and at low temperatures the above equation becomes

$$C_v = 9R \times 25.98\left(\frac{T}{\theta_D}\right)^3 \qquad (2.20)$$

Eqn. 2.20 is called the Debye T^3 law for low temperature heat capacities. Debye theory does not consider the contribution to the heat capacity by the uptake of energy by electrons or in other words electronic contribution to heat capacity. Also, the theoretical approach to the heat capacities does not consider the contribution made by the anharmonicity of the lattice vibration at elevated temperatures. As a consequence of the various uncertainties in the theoretical calculation of heat capacities, it is a normal practice to measure the variation of the constant pressure molar heat capacity with temperature and express the relationship analytically.

2.4.2.3. Various contributing factors to heat capacity

The heat capacity at constant pressure, C_p is the quantity generally needed in thermodynamic functions calculations. For the solids, C_p is related to C_v, by the relation

$$C_p = C_v + \frac{\alpha^2 TV}{\beta} \tag{2.21}$$

Where, α is the volume thermal expansivity at constant pressure and is expressed as $\frac{1}{V}\left(\frac{dV}{dT}\right)_P$

β is the isothermal compressibility $= -\frac{1}{V}\left(\frac{dV}{dP}\right)_T$

V is the molar volume

The term $\frac{\alpha^2 TV}{\beta}$ is known as the dilation term.

C_v is contributed by the following terms [**110-112**]

$$C_v = C_l + C_a + C_e + C_{sch} + C_m + C_d \tag{2.22}$$

Where, C_l is the term for harmonic lattice vibrations and constitutes the main part of the lattice heat capacity. C_a is the term for anharmonic lattice vibration, C_e for the electronic contribution to heat capacity. C_{sch} is schottky heat capacity, C_m for is magnetic and C_d for lattice defects contribution.

Debye model gives a fairly good description of the lattice heat capacity (C_l) [**113**], but in general does not give a quantitative fit when based on a constant Debye temperature (θ_D). This is because the vibrational frequency distribution in real materials does not follow the distribution assumed by Debye. Furthermore, the exact frequency distribution is very difficult to obtain either by theory or experiment. If θ_D values are calculated on point by point basis from experimental C_p versus T data, one finds usually that θ_D decreases to a minimum at around 20 – 40 K followed by a gradual increase to a new θ_D value at higher temperatures [**113**].

The anharmonic contribution (C_a) is relatively minor contribution that is difficult to predict either theoretically or experimentally. However, trend in the variation of heat capacity within the homologues series of elements or compounds can be explained using the experimental value of thermal expansion and heat capacity versus temperature. The contribution due to the anharmonicity varies as per the relation given below

$$C_a = \alpha T \tag{2.23}$$

Where α is a constant.

The electronic contribution or the conduction electron term for heat capacity (C_e) is given by the Sommerfeld formula:

$$C_e = (2/3)\pi^2 k^2 R(\varepsilon_F)\, T = \gamma_e T \tag{2.24}$$

Where, $R(\varepsilon_F)$ is the density of states at the Fermi level, ε_F and γ_e are the Fermi energy and electronic constant, k is Boltzmann constant and T is temperature in Kelvin. At temperature $T < T_F$, C_e is the major contributor to C_p, but as temperature increases the lattice heat capacity rises rapidly and dominates so that at room temperature the contribution of C_e is only in the order of 0.05% of C_p. At higher temperatures C_e again increases and C_l levels off [**110-117**]. The contributions from C_m are very important only in the case of certain 3d elements which give major lambda-type peaks that extend over considerable range. In the case of actinides there is uncertainty about the electronic ground state and multiplicity of the 5f electrons. Moreover, some 5f electrons often take part to the conduction (C_e) and the contributions of C_e and C_m cannot be distinguished [**117**] and therefore the contribution of C_m in case of actinides is considered to be negligible [**110**]. Lanthanides and actinides have f-electron transitions (C_{sch}) that give broad shallow heat capacity peaks [**110**] known as Schottky anomalies. This term comes from the excitation of electrons from low lying energy level to higher multiplets caused by the 4f electron coupling [**114**]. If the energy supplied kT is more or less same as the difference in the energy levels, then appreciable transitions occurs which is represented as hump in C_v. In case of rare earths the tail end of the hump extends to high temperature, so there is significant contribution of it at high temperature.

C_{sch} can be found out from the partition function as follows:

$$C_{sch} = T\frac{d^2(kTlnZ)}{dT^2} \tag{2.25}$$

where partition function $Z = \sum g_r \; e^{\frac{-\epsilon_r}{kT}}$ and ε_r is the energy of various levels.

Due to close spacing of energy levels in rare earths and actinides schottky heat capacity is one of the major contributions to the total heat capacity.

Lattice defect contribution to heat capacity (C_d) is significant and detectable at very high temperatures due to formation of various defects [**110-114**]. The temperature-dependence concentration of point defects in a crystal may by represented as:

$$n(T) = N \exp(S_d / k) \exp(-H_d / kT) \tag{2.26}$$

where S_d and H_d are the entropy and enthalpy of the defect formation process, N is the Avogadro number and k is Boltzmann constant. From **eqn 2.26**, excess heat capacity due to defect formation is

$$C_d = \frac{d}{dT}\lfloor H_d n(T) \rfloor = \left(\frac{A}{T^2}\right) e^{\frac{-H_d}{kT}} \tag{2.27}$$

Where $A = (NH_d / k) \exp(Sd / k)$.

C_d is detectable for most of the systems at temperatures more than 0.7 Tm (Tm – Temperature of melting) there are systems where it is detectable at intermediate temperatures (400 –1000 K).

The total heat capacity of a compound can be measured by calorimeter.

2.5. Calorimetry

Calorimetry involves measurement of thermal energy changes associated with the change in the state of the sample. The change of state may be brought in by change of temperature or pressure or a chemical reaction. It measures heat capacity as well as heat associated with the system. There are different types of calorimeters based on the nature of measurements to be made; heat content and heat capacity, enthalpy of fusion and transformation, and enthalpy of formation and reaction. However, a classification of calorimeters based on three main variables: the temperature of the calorimeter (T_c), the temperature of its surroundings (T_s), and the heat produced per unit time (Q), is more meaningful and is widely accepted. According to this classification there are four different types of calorimeters which are described below.

- **Isothermal calorimeter**: For this calorimeter $T_c = T_s$ = constant
- **Adiabatic Calorimeter**: For this calorimeter $T_c = T_s$ but is not constant. Such calorimeters have mainly been built for the determination of heat capacities, but also enthalpies of transformation and reaction can be found out.
- **Heat Flow calorimeter**: For this calorimeter, $T_s - T_c$ = constant. It is suitable for the direct determination of heat capacities and enthalpies of transformation, but not for the study of enthalpies of reaction because it cannot be stopped and held at constant temperature.
- **Isoperibol calorimeter**: For this calorimeter, the enclosure is held at constant temperature (T_s = constant) and T_c being measured before, during and after a reaction.

There are several modifications of the above mentioned calorimeters among which the Differential Scanning Calorimeter (DSC) is a versatile one widely used for the determination of heat capacity of the compound. In the present study a heat flux type DSC with normal software and temperature modulated software (TOPEM) is used for the determination of heat capacity of ternary solid oxides.

2.5.1. Differential Scanning Calorimeter (DSC)

Differential Scanning Calorimetry (DSC) is a thermoanalytical technique [**118-121**], where the difference in heat flow rate (power) to a sample and reference is monitored against time/ temperature while the temperature of the sample, in a specified atmosphere, is programmed. Determination of temperatures of first and second order phase transitions, enthalpies of phase transitions, study of polymorphism in food and pharmaceuticals, liquid crystalline transitions, phase diagrams, thermoplastic polymer phase changes, glass transition temperatures, purity measurements, phase diagram evaluation and kinetic studies can be mentioned as examples where DSC is highly efficient. DSC allows reaction heats and heats of transition to be quickly measured on small sample masses (milligram range), in wide temperature ranges and with high accuracy. DSC is very frequently used for measurement of heat capacities.

There are three types of Differential Scanning Calorimeters:

- The Power Compensated DSC
- The Heat Flux DSC
- The temperature modulated DSC

2.5.1.1. Power compensation DSC

This type of DSC contains two independent platforms for sample and reference [118, 122]. They are provided with separate heaters and thermocouples. At the time of identical temperature scanning, the electronic circuitry measures the temperature of the sample and reference and always maintains zero deferential temperature. The measurement signal here is the electrical energy supplied to the sample or reference to maintain the differential temperature zero.

2.5.1.2. Heat flux DSC

The heat flux DSC belongs to the class of heat-exchanging calorimeters. In this, a defined quantity of heat exchange takes place between the sample and its environment via a well defined heat conduction path with given thermal resistance. The main heat flow from the furnace to the sample passes symmetrically through a disk of medium thermal conductivity. The sample containers are positioned on this disk symmetrical to the center. The temperature sensors are integrated in the disk. Each temperature sensor covers more or less the area of support of the respective container so that calibration can be carried out independent of the position of the sample inside the container. To keep the uncertainties of measurement as small as possible, the arrangement of sample and reference sample containers and temperature sensor in relation to one another and to the support must always be the same. Metals, quartz glass or ceramics are used as disk materials. A schematic diagram of a heat flux type DSC is given in **Fig.2.16.**

When the furnace is heated (in general linearly in time), heat flows through the disk to the samples. In symmetrical arrangement (with samples of same kind and mass), the same amount of heat flows into sample and reference sample from the furnace. In this case, both the sample and reference see the same temperature and hence the differential temperature signal (ΔT) which is measured in the form of an electrical potential difference (ε) becomes zero. If this steady-state equilibrium is disturbed by a sample transition or reaction, a differential signal is generated which is proportional to the heat flow rates to the sample and to the reference.

$$\Delta T \ \alpha \ \varepsilon \ \alpha \ \Phi_{FS}-\Phi_{FR} \ , \text{ where } \Delta T = T_S - T_R. \tag{2.28}$$

Practically, it is difficult to maintain ideal thermal symmetry of the measuring system at all operating temperatures even outside the transition interval. Hence, there will always be a signal,

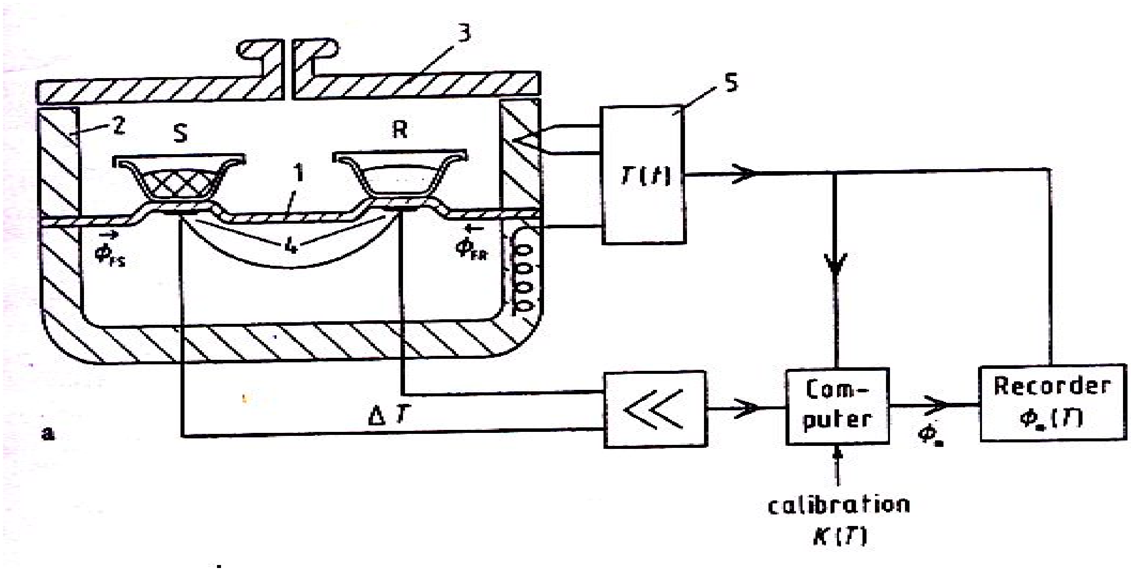

Fig.2.16. Schematic diagram of a heat flux DSC.

1: disk; 2: furnace; 3: lid; 4: differential thermocouples; 5: programmer and controller; S: crucible with sample substance; R: crucible with reference sample substance; Φ_{FS}: heat flow rate from furnace to sample crucible; Φ_{FR}: heat flow rate from furnace to reference sample crucible; Φ_m measured heat flow rate; K: calibration factor.

which depends on temperature and sample properties. The measurement signal ΔT is always obtained as electrical voltage. The measured heat flow rate Φ_m is internally assigned to this signal by calibration factor (K).

$$\Phi_m = K.\varepsilon \tag{2.29}$$

Hence, the measurement signal output accessible to the user is Φ_m (in µW or mW). A typical DSC signal is shown in **Fig.2.17**. Some characteristic terms are used to describe the measured curve.

Terms used in DSC curve

Zeroline: is the curve measured with both the sample and reference sample containers empty. It shows the thermal behavior of the measuring system itself and the degree and influence of unavoidable asymmetries. The smaller its range of variation with temperature or time, the better the instrument.

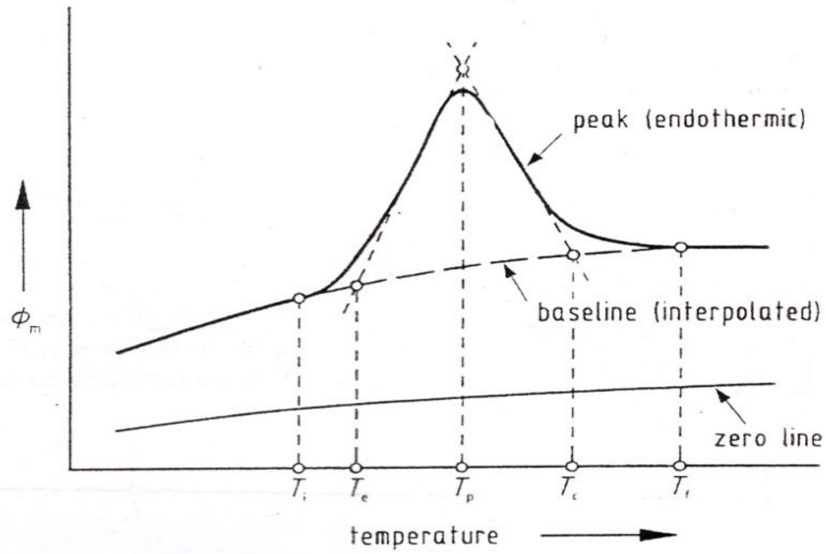

Fig.2.17. A typical DSC signal showing measured heat flow rate as a function of temperature

Baseline: is the part of the heat flow rate curve produced during steady state conditions (no reactions or transitions in the sample). The baseline is the sum of the zeroline and the heat flow rate caused by the difference of heat capacities of sample and reference sample during scanning mode.

Peak: in the measured curve appears when the steady state is disturbed by thermally activated heat production or consumption in the sample (e.g. from transition or reactions).

Initial peak temperature T_i*:** A peak begins at T_i (first deviation from the baseline). ***Extrapolated peak onset temperature T_e: Here the auxiliary line through the ascending peak slope intersects the baseline. The auxiliary line is drawn through the linear section of the ascending peak slope as inflectional tangent.

***Peak maximum temperature T_p*:** This temperature designates the maximum value of the difference between the curve of measured values and the baseline.

***Extrapolated peak offset temperature T_c*:** Here the auxiliary value through the descending peak slope intersects the baseline.

***Final peak temperature T_f*:** Here the curve of measured values reaches again the baseline, the peak is completed.

T_i and T_f cannot be determined with the required reliability because of the noise. T_p and T_c strongly depend on the thermal conductivity, mass and volume of the sample, heating rate and heat transfer from sample to sample container. While, the e*xtrapolated peak onset temperature* T_e alone is least dependent on heating rate and sample parameters so usually taken for representation and calibration.

2.5.1.2.1. Calibration of DSC

DSC is not an absolute heat and temperature measuring device hence, the relative data obtained must be correlated to absolute values by calibration. “Calibration means the establishment of relationship between a quantity measured by the instrument for a standard material to its true value.” The calibration factors for heat and heat flow rate are different and dependent on temperature, sample mass and heat flow rate. In addition, the result may depend on numerous boundary conditions e.g. parameter setting, emissivity and thermal resistance of the sample, sample geometry, etc. The International Confederation for Thermal Analysis and Calorimetry (ICTAC) describes procedures for temperature as well as caloric calibration [**123, 124**].

Four types of calibration procedures are followed before any measurement. These are:

- Temperature calibration
- Heat calibration
- Heat flow rate calibration
- τ- lag (thermal lag) calibration

2.5.1.2.1.1. Temperature calibration

The temperature recorded by DSC is not the true temperature due to the thermal resistance of the DSC disc, crucibles and the gas atmosphere. Therefore, temperature calibration is required which means the unambiguous assignment of the temperature indicated by the instrument to the true temperature [**122**]. Temperature calibration is performed using the transition points (usually melting points) of high purity metals [**125**]. Thermodynamically defined transition temperature is always the equilibrium temperature, whereas DSC measurements are dynamic. Therefore, DSC calibration results must be extrapolated to equilibrium conditions to ensure a temperature calibration, which is independent of the heating rate used. This is done by measuring the melting point of reference materials as a function of heating rate and extrapolated to zero heating rate. Only the extrapolated peak onset temperature (T_e) (**Fig 2.17**) is used for calibration as it is least dependent on heating rate and sample parameters to define temperature of DSC sensor:

***Characteristic of standard material used for temperature calibration* [118]**:

- Should represent fixed points of International Temperature Scale 1990 (ITS-90).
- Should have a transition point unequivocally defined from the viewpoint of thermodynamics
- Should display no measurable overheating
- Should possess a high rate of transition
- Should not show measurable influence of the grain size on the transition temperature
- Should be available in sufficiently high purity
- Should not react with the crucible material or purge gas
- Should not be hygroscopic
- Should be stable over a long period of time
- Should not undergo secondary reaction with gas and crucible.

For temperature calibration on heating mode, the general procedure followed was:

- ➢ Selection of at least three calibration substances which cover the desired temperature range as uniformly as possible. Three calibration substances are required to detect possible non-linear temperature dependence. The materials used for temperature calibration in the present work were In, Pb and Zn.
- ➢ The transition was measured with each calibration sample at a minimum of three different heating rates (2, 5, 10 K min^{-1}).
- ➢ The extrapolated peak onset temperature T_e for each melting was calculated.
- ➢ The T_e ($\beta \rightarrow 0$) was found from the intercept of the plot T_e vs. β for each calibration substance.
- ➢ The difference $\Delta T_{corr} = T_e (\beta = 0) - T_{fix}$ (or T_{lit}) was calculated for each sample.
- ➢ The temperature correction factor ΔT_{corr} was plotted vs. T_e.
- ➢ The temperature correction obtained in this way was applied to get correct temperature using:

$$T_{true} = T_e(\beta \rightarrow 0) + \Delta T_{corr}(\beta = 0) \tag{2.30}$$

2.5.1.2.1.2. Heat calibration

Heat calibration is basically a peak area calibration. Heat calibration means the unique assignment of the heat measured by the calorimeter to the true heat taken up or released by the sample as a result of a transition [126]. A known heat Q_{true} consumed or dissipated during melting of high purity NBS metal (In, Pb, Zn) was compared with the area of the resulting peak. Then the calibration factor was found out from the following relation

$$Q_{true} = K \cdot \int_{t_i}^{t_f} [\Phi_m - \Phi_{bl}]\, dt \qquad (2.31)$$

)

Where Φ_{bl} represents the heat flow rate corresponding to the base line as shown in **Fig.2.17.** The calibration factor K depends on temperature, systematic uncertainties due to shape of the DSC curve and uncertainties arising due to shape of the baseline. Hence the following procedures were generally followed to avoid such problems.

- Selection of calibration substance which cover the desired temperature range and whose thermophysical characteristic data are similar to those of the sample.
- The heat effect of standard and sample should match by taking required amount of standard.
- Calibration constants and measurement of the repeatability errors were found out at different heating rates.

At least three standards are chosen for accurate calibration. Let m_i be the mass and Q_i be the fusion heat content of the standard 'i' (in J/g). If S_i be the area of the fusion peak (in μV·s), then the calibration factor K_i is given by:

$$K_i = \frac{S_i}{Q_i} \cdot \frac{1}{m_i} \text{ (in μV/W)} \qquad (2.32)$$

Characteristic of standard material used for heat calibration [127]

- The material must exhibit a well-defined first-order phase transition
- The heat of transition should be known from at least two independent adiabatic calorimetric measurements
- The change of the heat capacity during phase transition should be small.

The heat calibration was carried out in the present work using enthalpy of melting of In, Pb and Zn.

2.5.1.2.1.3. Heat flow rate calibration

Heat flow rate calibration means the unique assignment of the heat flow rate taken up or released by the sample [126]. The materials used for heat flow rate calibration should not undergo any phase transition in the experimental temperature range. Sapphire (α-Al_2O_3) meets the above requirements and is generally used for heat flow rate calibration, as in the present study. The calibration factor *K* is found out by:

Measuring the steady-state heat flow rate into sapphire of known heat capacity C_p with a constant heating rate β = d*T*/dt.

$$C_p \cdot \beta = \Phi_{\mathrm{true}} = \mathrm{K} \cdot \Phi_{\mathrm{m}} \tag{2.33}$$

2.5.1.2.1.4. τ- lag calibration

The sample temperature, which is measured by the sensor, is not actually the temperature of the sample, but the temperature of the sample sensor as the sensor is located away from the sample. There is a definite amount of heat capacity existing between the sample sensor and the sample itself. Therefore, a definite period of time is required for the sample to attain the same temperature as that of the sample sensor. In other words, the sample temperature will be lagging behind the sample sensor by a definite period of time. This lag in the time can be calculated, by measuring the melting points of pure metals at different heating rates and plotting them versus the heating rate. The slope of this curve gives the τ- lag at that particular temperature.

2.5.1.2.2. DSC used in present investigation

DSC (model number DSC 823^e/700 of M/s. Mettler Toledo GmbH, Switzerland) was used in the present investigation was a disc type system. The discs are attached to FRS5 sensor and STAR^e software was used for control of the experimental conditions and for data analysis. The instrument is attached with liquid nitrogen cooling system for facilitating the measurement at low temperatures and also for rapid cooling to room temperature after the completion of experiment. The working temperature range of the instrument is from 133 K to 973 K. A schematic diagram of DSC and its sensor with 56 thermocouples are shown in **Fig. 2.18 and 2.19,** respectively.

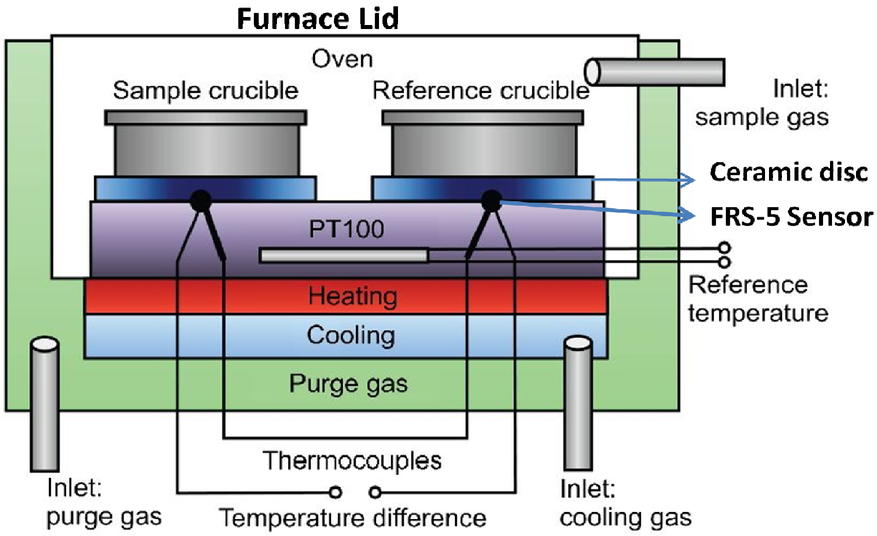

Fig.2.18. Schematic diagram of DSC used in present study(M/s. Mettler Toledo GmbH, Switzerland).

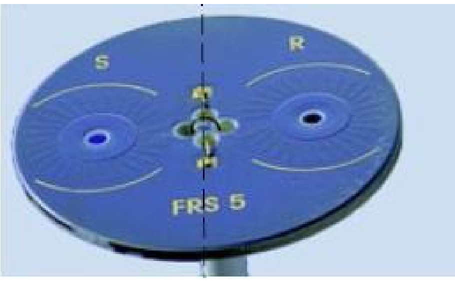

Fig. 2.19. FRS-5 sensor of the DSC 823e/700(M/s. Mettler Toledo GmbH, Switzerland)

2.5.1.3. Measurement of heat capacity using DSC

There are three methods to find the heat capacity such as (1) Enthalpy Method (2) Three Step Scanning method (3) Temperature Modulated (TOPEM) Method. In this study the last two methods was used and the procedures for scanning methods is given here and the TOPEM method is given in respective section.

2.5.1.3.1. Determination of heat capacity by three step scanning Method

Heat capacity was measured using classical three step procedure which is illustrated in **Fig. 2.20** and a typical plot is shown in **Fig. 2.21**. The three steps are (1) Blank run (2) sapphire run and (3) Sample run.

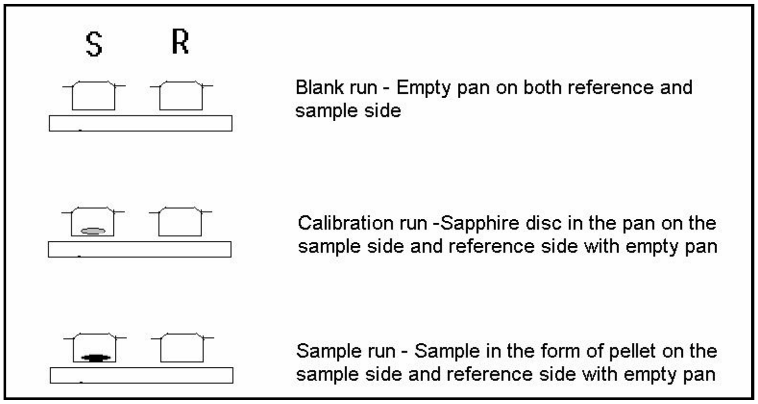

Blank run - Empty pan on both reference and sample side

Calibration run -Sapphire disc in the pan on the sample side and reference side with empty pan

Sample run - Sample in the form of pellet on the sample side and reference side with empty pan

Fig. 2.20: Three step procedure for measuring heat capacity

In each step, a typical three segment heating program used. The first segment is an isothermal one lasting typically for 10-15 minutes at the initial temperature; the second segment is a dynamic segment with a defined heating (normally 10K/min) rate and the final segment is again a isothermal segment for 10-15 minutes at the final temperature. At isothermal segments heat flow rate from furnace to the sample is nil whereas during the dynamic heating segment, an exponential endothermic effect is observed due to the flow of heat from the furnace to the sample and is proportional to the heat capacity of the sample. The slope of the line during the dynamic segment indicates the variation of the heat capacity of the material with temperature.

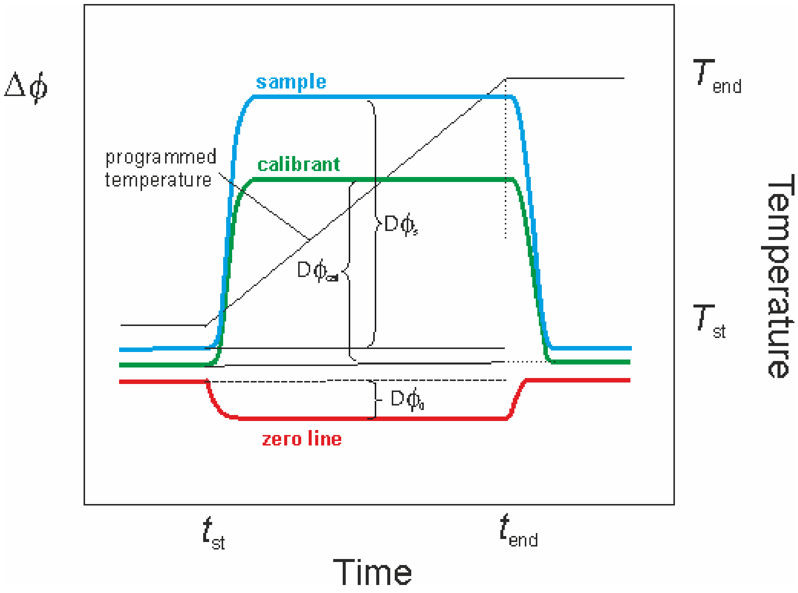

Fig. 2.21: Typical DSC run for blank, sample and reference.

Generally, aluminum pans are used for the sample and reference and are hermetically sealed with a pin hole on the lid. The measurements are done under constant pressure conditions and with the required gas atmosphere. It is better to divide the full temperature range of measurement to small segments where the segments should partially overlap to check the reproducibility of the data. The division to small segments in entire temperature range assures better thermal equilibrium thereby better accuracy in heat capacity. However, one run covering the entire temperature will give an idea of the presence of any phase transition.

Blank run: In this run, the heat flow rate of the zero line $\Phi_o(T)$ was determined using empty pans (of equal weight) in the sample and the reference sides. The temperature program was started, when the isothermal heat flow rate at the starting temperature T_{st} was constant for 10-15 minute. At the isothermal end temperature T_{end} the above computer check was repeated. For the evaluation procedure, all three regions of the curve are needed. The zero line reflects the (inevitable) asymmetry of the DSC.

Sapphire run: A calibration substance (Ref) of known heat capacity C_p (Ref) was placed into the sample pan (S), whereas the reference side (R) was unchanged. The heat flow rate was measured using the same experimental parameter as for the zero line. This difference in change in heat flow rate between the sapphire and zero line represent the heat capacity of sapphire. The heat capacity of reference was calculated from the following expression:

$$C_p\,(\text{Ref}).\, m_{Ref}.\, \beta = K_{\Phi}(T)\,(\Phi_{\text{Ref}} - \Phi_{o}) \qquad (2.34)$$

where C_p (Ref) = the specific heat capacity of the reference material (sapphire), β = heating rate, m_{Ref} = the mass of the reference material, Φ_{Ref} and Φ_o = the heat flow rates for the reference run and the blank run respectively and $K_{\Phi}(T)$ = temperature dependent calibration factor(sensitivity factor), which was obtained by comparing the measured specific heat capacity of sapphire with the literature reported true values.

Sample run: For the measurement of sample, the calibration substance (Ref) in pan was replaced by the sample (S). Similar equation for sample can be written.

$$C_p\,(\text{Sample}).\, m_{\text{Sample}}.\, \beta = K_{\Phi}(T)\,(\Phi_{\text{Sample}} - \Phi_{o}) \qquad (2.35)$$

where C_p (Sample) = the specific heat capacity of the sample, β = heating rate, m_{Sample} = the mass of the sample, Φ_{Sample} and Φ_o = the heat flow rate for the sample and the blank runs, respectively. The specific heat capacity C_p (Sample) (at a given temperature) was calculated by a simple comparison of the heat flow rates of the sample and reference substance which was calculated by dividing **Eq(2.35) by Eqn.(2.34) .** The final equation was represented as:

$$C_p(Sample) = \frac{C_p(Ref)\cdot(\emptyset_{Sample}-\emptyset_o)\cdot m_{Ref}}{(\emptyset_{Ref}-\emptyset_o)\cdot m_{Sample}} \tag{2.36}$$

In this method the calibration factor $K_\Phi(T)$, need not be known explicitly.

The samples for C_p measurements were taken as sintered a thin pellet (~0.1mm thick) which is very similar to the standard material used due to the following reasons:

(i) To get a good thermal contact between the pan and the sample (ii) To simulate the geometry of the calibration material and (iii) To eliminate temperature gradient within the sample.

Sources of error in the 'classical' three-step method:

- The quasi-steady-state conditions in the scanning and final isothermal regions are not reached immediately after changes in the scanning program but with a certain delay.
- The measured heat flow rate (with zeroline subtracted) may be smaller than the ideal (theoretical) one.
- The isothermal levels at t_{st} and t_{end} differ from each other and from run to run.

These discrepancies result from the finite thermal conductivity of the path between temperature sensor and sample and from the limited thermal conductivity of the sample itself. The above discrepancies are corrected by advanced software which takes into account of the smearing of the heat flow rate curve.

In the present study, the heat capacity of RE_6UO_{12}(s), $SrCeO_3$(s), Sr_2CeO_4(s), $Ba_{1-x}Sr_xMoO_4$(s) and $Ba_{1-x}Sr_xMoO_3$(s) were measured by three step scanning method. The accuracy and reproducibility of measurements were checked by measuring the heat capacity of ThO_2(s) (mass fraction 0.998).

2.5.1.4. Temperature Modulated DSC

The temperature modulated DSC is a new technique where a periodic temperature modulation of small amplitude is superimposed on the regular linear heating/cooling or isothermal segments of conventional DSC [128]. Several versions of the instrument exist in the market, including Modulated DSC (MDSC, M/s TA Instruments) and Alternating DSC (ADSC, M/s Mettler-Toledo), and they are usually referred as Temperature Modulated DSC techniques (TMDSC). These techniques fundamentally based upon the same principle, which involves a Fourier Transformation of the modulated heating rate and heat flow signals, from which one can obtain certain information additional to that available from conventional DSC. The total heat flow comprises of reversible and nonreversible component.

$$\Phi_{\text{Total}}\,(t,T) = \Phi_{\text{reversing}}\,(t,T) + \Phi_{\text{non-reversing}}\,(t,T) \qquad (2.37)$$

where heat flow = $\Phi(t,T)$

Reversing component: $\Phi_{\text{reversing}}\,(t,T) = mC_p^0(t,T)\,ß$ (2.38)

Non-reversing component: $\Phi_{\text{non-reversing}}\,(t,T)$

Mass: m

Specific heat capacity: $C_p^0\,(t,T)$

Heating rate: $ß$

From the total heat flow two different types of heat capacity can be obtained using TMDSC: (*i*) the 'thermal/quasi static' heat capacity from the underlying heating or cooling rate, which is identical to that available from conventional DSC at the same rate, and (*ii*) the 'dynamic/frequency dependent' heat capacity from the amplitudes of the heating rate and heat flow modulations, which is dependent on the frequency of the modulations.

2.5.1.4.1. Specialised TOPEM Software

TOPEM is specialized software developed by M/s Mettler Toledo Pvt Ltd, Switzerland which helps to run a heat flux DSC in TMDSC mode with multi-frequency temperature modulation. These modulations consist of temperature pulses, of fixed magnitude and alternating sign, with random durations within limits specified by the user. The lower time limit was given by the signal time constant of the instrument including the crucible whereas maximum time limit was related to the thermal behavior of the sample. The maximum pulse height (amplitude) is an important parameter of TOPEM software to fulfill linearity conditions [129]. The pulse height was determined by the behavior of the sample. A small pulse height is preferred over large pulse height as it allows thermal equilibrium of sample in less time. On the other hand, more information can be gained with higher pulse heights as the sample gives better signal for small thermal events. Therefore a compromise has to be made between higher and lower pulse heights. This multi-frequency perturbation introduces a broad frequency spectrum in the response. The actual input temperature signal at any time is given by underlying as well as the modulated heating rate as shown in **Fig.2.22**.

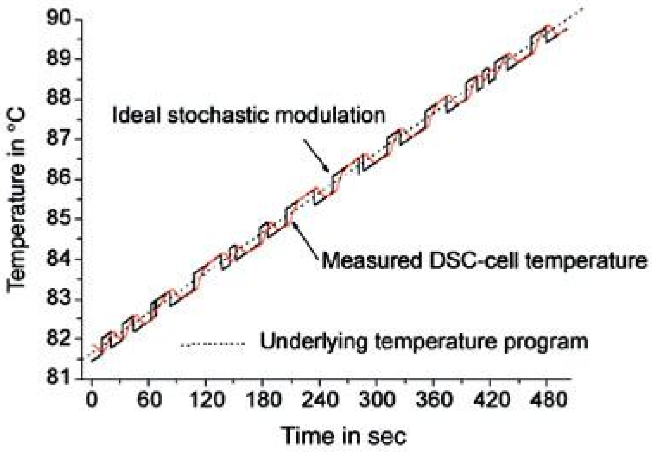

Fig.2.22. A typical measured temperature signal of TMDSC

The novel data analysis procedure, based upon a ‘parameter estimation method’ widely being used allows the evaluation of a so-called ‘quasi-static/thermal’ heat capacity (frequency independent) and the separation of reversible and non-reversible components of the heat flow with respect to the heating rate In particular, the broad frequency response implies that TOPEM is apparently able to determine the complex heat capacity $C_{p,0}{}^{*}$ over a range of frequencies in a single scan. In a single scan it is possible to distinguish frequency-dependent phenomena from frequency-independent phenomena. TOPEM software [129-133] has been used to study various thermal processes like glass transition, isothermal curing of thermosets and solid–solid transitions.

Parametric estimation method relates the input temperature and the reversible heat flow response and determines the quasi-static (frequency independent) heat capacity, $C_p^{o.}$ [130]. The influence of the heat transfer and the heat capacity of the sample on the reversible heat flow component is combined in the generalized impulse response function $G(t)$ which can be calculated by solving mathematical expressions [130]. The DSC instrument, crucibles and sample together is called as system and characterized with function $G(t)$. The processes involved in the system during mathematical analysis can be represented as in **Fig.2.23**. C_p^o and $G(t)$ are related as:

$$m \cdot C_p^o = \int_0^\infty G(t)dt \tag{2.39}$$

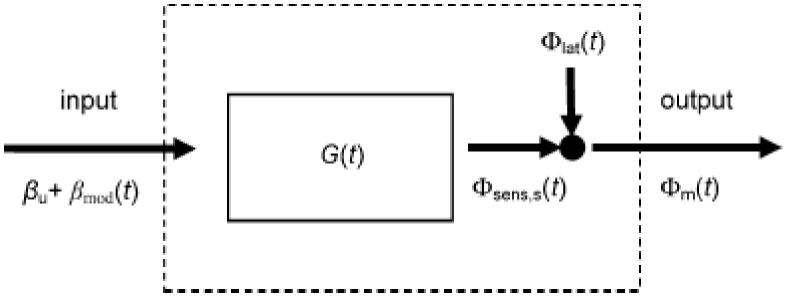

Fig. 2.23. Schematic of the signal flow in a TMDSC. β_u is the underlying heating rate and β_{mod} the additional heating rate due to the modulation function. Φ_{sens} is the smeared sensible/reversible heat flow, Φ_{lat} the latent heat flow/non reversible heat flow and Φ_m is the measured heat flow (total).

In the present study, quasi-statistic heat capacity $C_{p.m}^{o}(T)$ measurements were carried out with the same heat flux DSC (model number DSC 823^e/700) using TOPEM software for the first time. All the experimental runs were carried out with pulse width varying from 15-30 s and pulse height of ±1 K.

Advantages:

- Single measurement gives idea about the sample thermal behavior as a function of time and temperature over a large frequency range.
- It is possible to determine accurate quasi-static heat capacity.
- The measurement gives high sensitivity and high resolution which allows the measurement of low energy transitions and/or close-lying temperature-dependent effects.
- It is possible to separate reversing and non-reversing heat flow.

- Frequency-dependent effects (e.g. glass transitions) can be very easily distinguished from frequency independent effects (e.g. loss of moisture)
- It provides accurate frequency-dependent heat capacity values based on one single measurement

Disadvantage:

This technique is time consuming due to the very slow heating/cooling rate used.

2.5.1.4.2. Determination of heat capacity using TOPEM software

The heat capacity was determined from four experimental runs.

(1) **The first run (gives Zero line for standard run):** This was carried out by keeping empty crucibles in both sample and reference side of DSC.

(2) The second run (Standard run): This was carried out by keeping empty crucible in the reference cell and a crucible containing standard in the sample cell.

(3) **The third run (gives Zero line for sample run):** This was carried out with two empty crucibles as in case of first run.

(4) **The fourth run (Sample run):** This was carried out by keeping empty crucible in the reference cell and a crucible containing sample in the sample cell.

The experimental parameters for the first run (blank) and the second run (standard) were identical for precise determination of heat capacity of sapphire. Similarly, the experimental parameters for the third run (blank) and the fourth run (sample) were identical for precise determination of heat capacity of sample. The heat capacity of sapphire was proportional to the difference in the heat flow signals between second run (standard) and first run (blank). Similarly, the difference in the heat flow signals between the sample run and the corresponding blank run was proportional to the heat capacity of the sample. Heat capacity of sample was evaluated with respect to sapphire. Heat capacity calibration with sapphire was performed to correct the systematic experimental errors, which occurs as a result of dynamic asymmetry between sample and reference cell of DSC. The deviation between the measured value and the literature value of the calibration material (sapphire) was used to determine the contribution of this dynamic asymmetry. If this contribution is known, the measured C_p values of the unknown sample can be corrected with this data. This is the meaning of C_p calibration in TOPEM which was performed in this study.

In this study, heat capacity of A_nTeO_6 (A= Cr, Fe, n=2; A = Ni, n = 3) was measured by TOPEM software. The standard (sapphire) and the corresponding blank run were recorded using a single dynamic temperature segment from 300 K to 870 K with a heating rate 2 K min^{-1}. The temperature range of 300-870 K for the sample A_nTeO_6 (A= Cr, Fe, n=2; A = Ni, n = 3) as well as the corresponding blank run was divided into four segments and each segment comprised of a dynamic heating program with heating rate of 0.9 K min^{-1}. The slow heating rate was used for the sample to follow the programmed temperature closely by reducing thermal lag and temperature gradients and it also allows more time within any given temperature increment during which, the heat flow from any thermal events may be recorded. By using TOPEM, sample attains better thermal equilibrium than conventional heat flux DSC. For Two sapphire discs of 0.2 mm thickness (21.679 mg) were used as the standard for the heat capacity measurement. 50-60 mg of A_nTeO_6 (A= Cr, Fe, n=2; A = Ni, n = 3) was pelletised and taken for heat capacity measurement. All measurements were carried out in $2*10^{-5}$ dm^3 hermetically sealed aluminum pans with a hole at the centre and 0.05 dm^3 min^{-1} dynamic flow of high purity argon gas. The separation of total heat flow curve of A_nTeO_6(s) into reversible and latent heat flow components clearly showed absence of non reversible heat capacity.

Heat capacity of A_nTeO_6 (A= Cr, Fe, Ni) was calculated from the pulse response function of sample and sapphire, as given in **Eq. (2.40)**, employing TOPEM software.

$$C_{p(A_nTeO_6)}=\frac{\left(\int_0^\infty G(t)_{(A_nTeO_6)}\,dT\right)\cdot m_{sapphire}\cdot c_{p(sapphire)}}{\left(\int_0^\infty G(t)_{(sapphire)}\,dT\right)\cdot m_{(A_nTeO_6)}} \tag{2.40}$$

where $G(t)_{(A_nTeO_6)}$ and $G(t)_{(sapphire)}$ are the pulse response function of A_nTeO_6 (A= Cr, Fe, Ni) and sapphire, respectively. $m_{sapphire}$ and $m_{(A_nTeO_6)}$ are the mass of sapphire and sample respectively. $C_{p(sapphire)}$ and $C_{p(A_nTeO_6)}$ are the specific heat capacity of sapphire and sample, respectively. Prior to measurement of heat capacity of A_nTeO_6(s), heat capacity of ThO_2(s) was measured with TMDSC using TOPEM software.

2.5.1.5. Effect of Purge Gas

Purge gas should always be used during DSC experiments as it provides dry, inert atmosphere and ensures uniform heating. It also helps in sweeping away any evolved gases during heat treatment.

Commonly, inert gases like nitrogen, argon and helium with a typical flow rate of 50ml min^{-1} being used. Helium is being used at low temperature due to its inherent high thermal-conductivity and it helps in increasing the resolution. Air or oxygen is used to study oxidation reactions or to avoid the oxygen release from the oxide sample.

2.5.1.6. Treatment of heat capacity data

In this study, heat capacities of different solids were determined and were best fitted to the form of $C^{o}_{p,\,\mathrm{m}} = \mathrm{A} + \mathrm{B}T + \mathrm{C}/T^{2}$ or $C^{o}_{p,\,\mathrm{m}} = \mathrm{A} + \mathrm{B}T + \mathrm{C}/T^{2} + \mathrm{D}T^{2}$ as a function of temperature in various temperature ranges. For the solids having transitions, heat capacities were best fitted in the temperature ranges before and after transition peak. These polynomials were interpolated from 298 K and extrapolated to 1200 K for each solid, as these points were not derived experimentally. These fitted polynomials were used for further calculations of different thermodynamic functions.

2.6. Thermo-chemical Properties

Gibbs energy is a thermochemical property and it is defined as maximum portion of the energy that can be converted to mechanical work. It is also defined as the maximum non-expansion work that can be obtained from a process at constant pressure and temperature. It is used to study the physical and chemical equilibria and is driving force for any chemical change. This can be measured by two techniques such as (a) e.m.f. (b) vapour pressure measurement. In this study, both e.m.f. and transpiration methods (one of the vapour pressure techniques) were used, the details of which are described here.

2.6.1. Solid-state electrochemical technique using oxide ion conducting electrolyte

The solid-state electrochemical technique comprising of two electrodes (cathode and anode) and a solid electrolyte is widely used in determining the thermodynamic data at high temperatures for oxides, alloys and intermetallics [134]. The galvanic cell gives reliable and accurate values of standard Gibbs energy change associated with the net virtual cell reaction.

Solids with high ionic conductivity are termed as "solid electrolytes" where ions are the principal charge carriers. Ionic conductivity in solid electrolytes is due to high order lattice imperfections, i.e. defects and structural disorders. These defects are due to vacancies or the interstitials (of cations or anions) and conductivity arises due to the movement of these defects under a potential gradient. Solid electrolytes possess high band gap energy, larger than $T/300$eV, where T is the temperature in Kelvin. The electrical conductivity of pure ionic conductor is as high as 10^{-1} - 10^{-4} ohm^{-1} cm^{-1} at the chosen operating temperature and their electronic/hole conductivity is very small and their contribution to the total conductivity is negligible. Generally, t_e and t_h are less than 10^{-2} in these electrolytes where $t_e = \frac{\sigma_e}{\sigma_T}$ and $t_h = \frac{\sigma_h}{\sigma_T}$ are the transport number of the electrons and holes.

In this study, the Gibbs energies of formation of RE_6UO_{12}(s) have been determined using oxide ion conducting solid electrolyte in a concentration cell. In the galvanic cell, the open circuit e.m.f. is related to Gibbs energy by Nernst equation.

The choice of the solid electrolyte and the electrodes for a particular application depends on the physico-chemical properties of the investigated system. Several types of solid electrolytes are being used in thermodynamic measurements; they can be grouped as oxide ion conducting electrolytes, fluoride ion conducting electrolytes and metal ion conducting electrolytes. In the present context, only the basic principles of oxide ion conducting solid electrolytes have been discussed.

2.6.2. Conduction mechanism in solid oxide electrolyte

Solids with exceptionally high ionic conductivity due to rapid diffusion of one ionic species through an immobile lattice are termed as "solid electrolytes" [135]. The conductivity arises due to the movement of defects under a potential gradient. The electrical conductivity due to a charge species '*i*' can be defined as

$$\sigma_i = c_i q_i u_i \tag{2.41}$$

where, c_i is the concentration of the species (particles/cm^3), q_i is the charge (coulombs/particle) and u_i is the mobility (cm^2/sec.volt).

The total conductivity of an ionic solid, σ_T is given by,

$$\sigma_T = \sigma_i + \sigma_e + \sigma_h \tag{2.42}$$

where, σ_i is conductivity due to ions, σ_e due to electrons and σ_h due to holes.

Oxide ion conductors are most common anionic solid electrolytes. Oxide ion conduction is found mainly in ionic oxides with fluorite and fluorite related structures. The fluorite structure shown in **Fig. 2.24(a)** is a face centered cubic arrangement of cations with the anions occupying all the tetrahedral sites. In this structure, each metal cation is surrounded by 8 Oxygen anions and each oxygen anion are tetrahedrally coordinated by four metal cations and they possess large octahedral interstitial voids. This relatively open structure permits oxide ion movement from one lattice position to another with low activation energy (<1 eV). ThO_2 and the high temperature modification of ZrO_2 have the fluorite crystal structure are most commonly used oxide ion conductors.

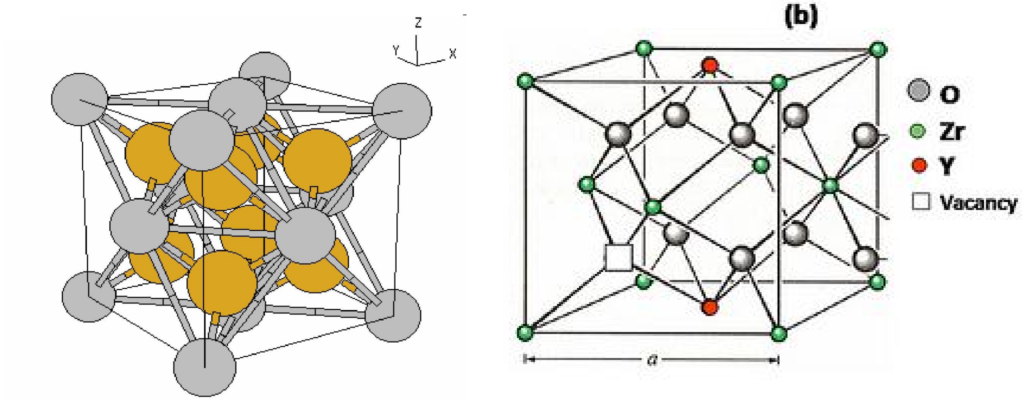

Fig. 2.24: (a) Fluorite structure (b) Generation of oxide vacancy with dopping of Y^{3+}

In this study, yttria doped zirconia was used as solid electrolyte. Pure zirconia can exist in three crystallographic forms, cubic, tetragonal and monoclinic as shown in **Fig.2.25.** The range of stability for each of these phases is shown below.

$$\text{Monoclinic} \overset{1173°C}{\Leftrightarrow} \text{Tetragonal} \overset{2370°C}{\Leftrightarrow} \text{Cubic}$$

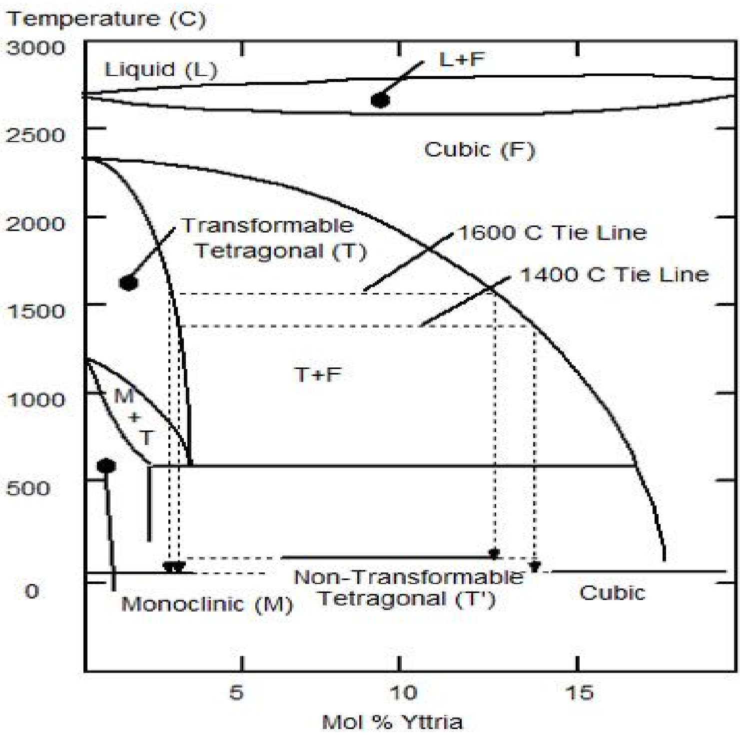

Fig. 2.25: Phase Diagram for the Zirconia Yttria System.

The addition of oxides soluble in zirconia (CaO, MgO, Y_2O_3) stabilizes the high temperature cubic phase at low temperature. The amount of alloying oxide required to produce stabilization is determined from the relevant phase diagram **Fig.2.25.**

Doping with aliovalent impurity is advantageous as (1) it increases the ionic conductivity by introduction of oxide ion vacancy as shown in **Fig.2.24(b)** and (2) stabilization of cubic phase at room temperature, which is required to maintain isotropic thermal expansion and to increase its thermal resistance during thermal cycling. Doping Zirconia with Yttria (Y_2O_3) replaces $2Zr^{4+}$ with $2Y^{3+}$and introduces one oxygen vacancy for charge neutralization as shown in **Fig.2.24(b)**.Zirconia based electrolytes have the advantage of possessing higher conductivity and are used in the high oxygen partial pressure range while ThO_2 based electrolytes are useful at very low oxygen partial pressures.

2.6.3. The relationship between defect equilibria and electrical conductivity

(a) Pure MO_2 based electrolyte

Considering an MO_2 type oxide with Frenkel defect in the anion sublattice, the electroneutrality requires

$$p + 2[V_o^{\cdot\cdot}] = n + 2[O_i^{''}] \tag{2.43}$$

where p: number of holes, $[V_o^{\cdot\cdot}]$: oxide ion vacancy, $[O_i^{''}]$: interstitial oxide ion and n: number of electrons.

By considering the fully ionized defect, formations of anionic Frenkel defect can be represented as,

$$O_o \quad \Leftrightarrow \quad V_o^{\cdot\cdot} + O_i^{\prime\prime} \tag{2.44}$$

The equilibrium constant for **eqn. 2.44** is:

$$K_1 = [V_o^{\cdot\cdot}][O_i^{\prime\prime}] \tag{2.45}$$

Since the formation of one anionic vacancy is accompanied by formation of an anionic interstitial (in case of anti-Frenkel defect),

$$[V_o^{\cdot\cdot}] = [O_i^{\prime\prime}] = K_1^{1/2} \tag{2.46}$$

At oxygen partial pressures higher than that required to maintain the stoichiometric MO_2, interstitial oxygen anions are introduced and oxide becomes metal deficient. Then, the defect equilibrium is,

$$\frac{1}{2}O_2(g) \quad \Leftrightarrow \quad O_i^{''} + 2h^{\bullet}$$

With $[O_i^{''}]$ >>$[V_o^{\cdot\cdot}]$, the equilibrium constant is

$$K_2 = [O_i^{\prime\prime}] \cdot h^2 \cdot p_{O_2}^{-1/2} \tag{2.47}$$

where p_{O_2} is the oxygen partial pressure.

By requirement of electro-neutrality,

$$[O_i^{\prime\prime}] = 2\,h$$

$h = \left[\frac{K_2}{2}\right]^{1/3} \cdot p_{O_2}^{1/6}$ (2.48)

which indicates a $p_{O_2}^{1/6}$ dependency of hole conductivity.

When oxygen partial pressures are lower than that required for stoichiometric MO_2, the defect equilibrium is represented as

$O_o \leftrightarrow \frac{1}{2}\, O_2(g) + V_o^{\cdot\cdot} + 2n'$ (2.49)

and $\left[V_O^{\bullet\bullet}\right] >> \left[O_i^{''}\right]$ and from the requirement of electro neutrality,

i.e. $\left[V_O^{\bullet\bullet}\right] = 2n'$

The equilibrium constant for the above reaction can be written as,

$$K_3 = P_{O_2}{}^{1/2} * \left[V_O^{\bullet\bullet}\right] * \left[n'\right]^2$$

$$\Rightarrow n = \left[\frac{K_3}{2}\right]^{1/3} * \left[p_{O_2}\right]^{-1/6} \quad (2.50)$$

which indicates a $\left[p_{O_2}\right]^{-1/6}$ dependency of electronic conductivity.

Thus, assuming that the electron and proton mobility are constant, The p-type conductivity is directly proportional to $p(O_2)^{1/6}$ in high oxygen pressure and n-type electronic conductivity is directly proportional to $p(O_2)^{-1/6}$ in the low oxygen pressure region.

(2) Doped MO_2

While adding a trivalent metal oxide impurity to form substitutional solid solution, addition of $2M^x$ ions creates one oxide ion vacancy. The overall electro neutrality condition will be,

$p + 2[V_o^{\cdot\cdot}] = n + 2[O_i''] + [Mx_M']$ (2.51)

If the added dopant concentration is large, then $[Mx_M']$ dominants on the right hand side of the above equation. The electroneutrality can be established either by electronic or ionic defects. Then,

$p = [Mx_M'] \;\; or \;\; 2[V_o^{\cdot\cdot}] = [Mx_M']$ (2.52)

In solid electrolytes, the ionic defects lead to enhancement of ionic conductivity. Ionic conductivity also varies as a function of prevailing oxygen partial pressures. There may be several limiting cases as discussed below.

(1) In the intermediate p_{O_2} region, $2[V_o^{\cdot\cdot}] = [Mx_M']$ '

At low pressures of oxygen within this region, the defect equilibrium would be given by **eqn 2.50**. Since $[V_o^{\cdot\cdot}]$ is almost constant for doped MO_2, the equilibrium constant,

$$K_4 = p_{O_2}^{\frac{1}{2}} \times [V_O^{\cdot\cdot}] \times [n']^2 = {}^1/_2\,[Mx_M'] \times p_{O_2}^{\frac{1}{2}} \times [n']^2$$

or

$$[n'] = (K_4 \times 2)^{\frac{1}{2}} \times [Mx_M']^{-\frac{1}{2}} \times p_{O_2}^{-\frac{1}{4}}$$

$$\sigma_e = n' q_e \mu_e = (K_4 \times 2)^{\frac{1}{2}} \times [Mx_M']^{-\frac{1}{2}} \times p_{O_2}^{-\frac{1}{4}} \times \mu_e \times q_e \tag{2.53}$$

At higher oxygen partial pressures within this region, the defect equilibrium that has to be considered is,

$$V_O^{\cdot\cdot} + \frac{1}{2}O_2 \leftrightarrow O_o + 2h^{\cdot}$$

$$K_5 = p^2 \times p_{O_2}^{-\frac{1}{2}} \times [V_O^{\cdot\cdot}]^{-1} = p^2 \times p_{O_2}^{-\frac{1}{2}} \times \left(\frac{1}{2}\right)^{-1} [Mx_M']^{-1}$$

or

$$p = \left({}^{K_5}/_2\right)^{\frac{1}{2}} \times p_{O_2}^{\frac{1}{4}} \times [Mx_M']^{\frac{1}{2}} \tag{2.54}$$

The conductivity due to the electron holes would be as given below:

$$\sigma_h = \left({}^{K_5}/_2\right)^{\frac{1}{2}} \times p_{O_2}^{\frac{1}{4}} \times [Mx_M']^{\frac{1}{2}} \times q_h \times \mu_h \tag{2.55}$$

In the middle of the region, $V_O^{\cdot\cdot}$ is always larger than *n* or *p* and therefore in the middle region, p_{O_2} independent ionic conduction predominates. At the boundaries conduction would be significant as given by **equations 2.53 and 2.55.**

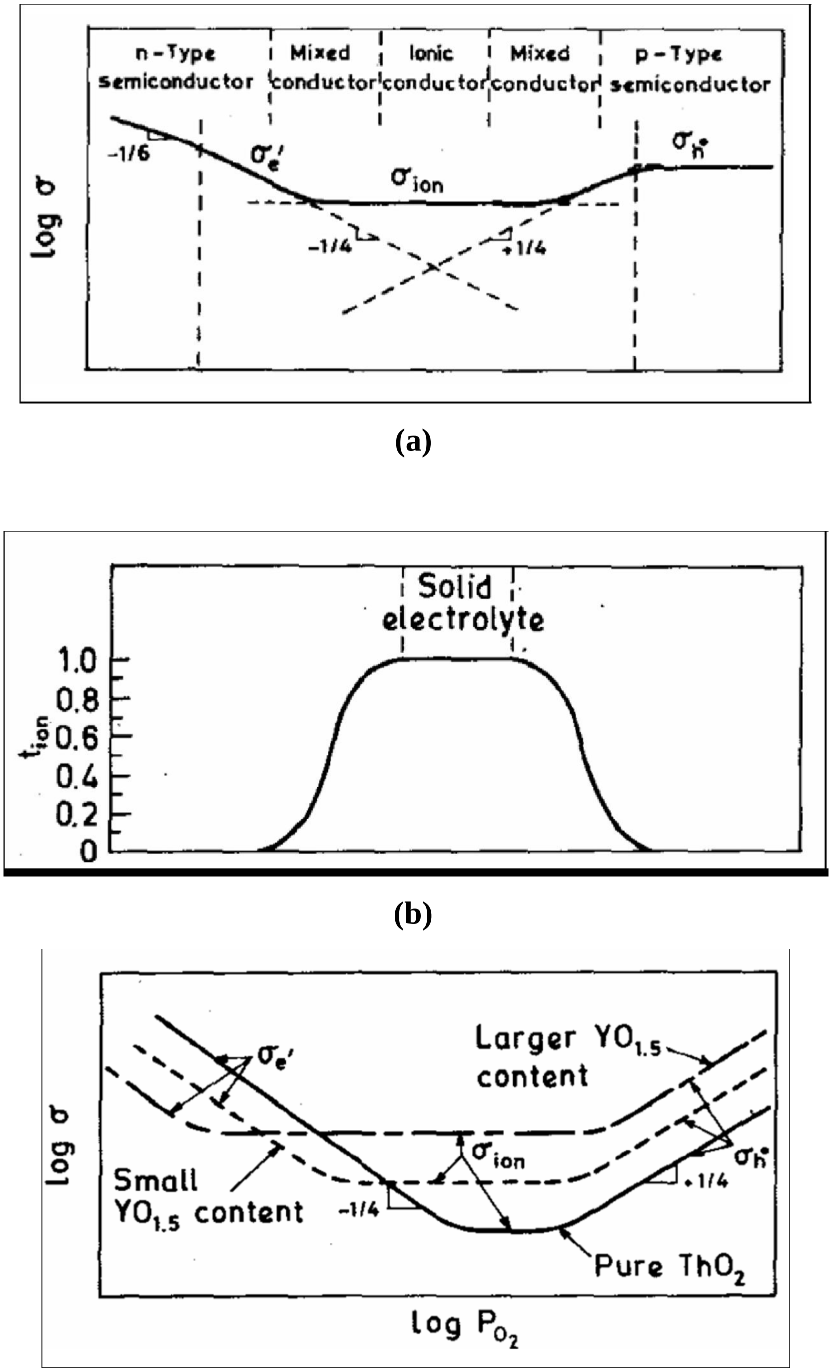

(a)

(b)

©

Fig. 2.26: Schematic representation of (a) conductivities of electrons, holes and ions, (b) transport number of ions in solid electrolyte, (c) effect of dopant concentration on conductivities of species [134]

(2) At very high p_{O_2} values, **eqn.2.52** transforms into $p = [Mx'_M]$. Electron holes will be the dominant defects and that would be independent of p_{O_2} . At still higher oxygen pressures, electron hole starts increasing as in the case of pure MO_2 given by **eqn.2.48**.

(3) At very low oxygen partial pressures, the effect of impurity becomes negligible and the solid electrolyte behaves like an intrinsic material (**eq. 2.50**). Both $[V_O^{\cdot\cdot}]$ and n dominates ineq. **2.51** and their concentration increases with decreasing p_{O_2} .

Fig. 2.26 represents (a) conductivities of electrons, holes and ions, (b) transport number of ions (c) effect of dopant concentration on conductivities of the species.

2.6.4. Electrolytic Domain

The temperature and oxygen pressure regions within which the electronic and hole contributions to total electrical conductivity of a material are less than 1% is called the electrolytic domains of the ionic solid. The electrolytic domain of ZrO_2 (15mol % CaO) and ThO_2 (15mol % $YO_{1.5}$) electrolytes are shown in **Fig. 2.27.**

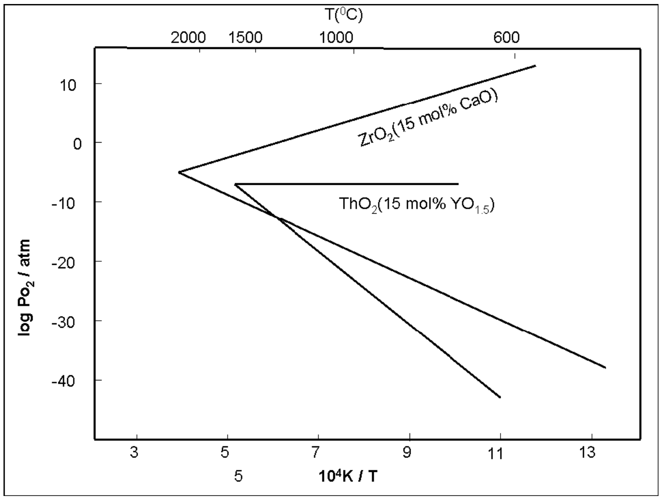

Fig. 2.27: Electrolytic domain boundary of calcia stabilized zirconia and yttria doped thoria.

The upper boundary line is known as upper electrolytic domain boundary (UEDB) and the lower boundary line is known as lower electrolytic domain boundary (LEDB). At all temperatures and oxygen pressures inside the boundary lines, the ionic fraction of the total conductivity is greater than 0.99. For example, the electrolytic domains of ThO_2 (15 mol%$YO_{1.5}$) is between ~10^{-6}

and 10^{-25} atm of p_{O_2} at 1273 K. At oxygen pressures above ~10^{-6} atm., hole conduction is greater than 1% while electron conductivity becomes greater than 1% at oxygen pressures below ~ 10^{-25} atm.

2.6.5. Transport properties of solid electrolytes

A useful electrolyte should have high electrical conductivity attributable primarily to ions (> 10^{-3} ohm^{-1} cm^{-1}). The temperature dependence of conductivity of these electrolytes can be represented by the general expression:

$$\sigma\,(x, T) = A\,(x, T)\,\exp(-E_a/RT) \qquad (2.56)$$

where σ (x, T) is the ionic conductivity which is a function of concentration x of the dopant and the temperature *T*. A (x, T) is pre-exponential factor and E_a is the activation energy for ionic transport. Both ionic conductivity and pre-exponential factor depend upon the oxide system under consideration.

2.6.6. Relation between Gibbs energy and e.m.f (*E*)

Consider an electrochemical cell made up of a solid compound, MO_2, as the electrolyte, in which oxygen ion (O^{2-}) as the major charge carriers with electrons (e′) or holes ($h^{\cdot}$) as minor carriers. Such a galvanic cell can be considered as oxygen concentration cell and can be represented formally as follows:

$$\text{Pt}, O_2\ (\mu_{O2}{'})\ /\text{Solid Oxide Electrolyte}/\ O_2\ (\mu_{O2}{''}), \text{Pt} \qquad (2.57)$$

The quantities $\mu_{O2}{'}$ and $\mu_{O2}{''}$ represent the chemical potentials of oxygen at the two electrodes, determined by appropriate electrode reactions. Under thermodynamic equilibrium at the electrode-electrolyte interfaces, the e.m.f., *E* of the cell is given by

$$E = \left(\frac{1}{4F}\right) \int_{\mu'_{O2}}^{\mu''_{O2}} t_{O^{2-}}\ d\mu_{O2} \qquad (2.58)$$

where 4 represents the number of electron involved in the transport of one oxygen molecule, *F* is the faraday constant (96486.4 C·mol^{-1})and $t_{O^{2-}}$ is the transport number of the oxygen ion and can be defined as $t_{O^{2-}} = \{\sigma_{O^{2-}}/\sigma_{total}\}$ in the solid electrolyte. Useful solid electrolytes have $t_{O^{2-}} >$

0.99. Quantities μ_{O2}' and μ_{O2}'' represent the chemical potentials of oxygen at the two electrodes compartments and where $\mu_{O2}' < \mu_{O2}''$ and $t_{O^{2-}} \sim 1$

$$E = \left(\frac{1}{4F}\right) \left[\mu_{O2}'' - \mu_{O2}'\right] \tag{2.59}$$

Thus, by measuring the e.m.f. of the galvanic cell and knowing the oxygen chemical potential of the reference electrode, the chemical potential of the test electrode can be determined by using Eq.(2.59).

In terms of partial pressures of oxygen at the two electrodes, **Eq.(2.59)** can be written as:

$$E = \left(\frac{1}{4F}\right) \int_{\mu_{O2}'}^{\mu_{O2}''} d\mu_{O2} = \frac{RT}{4F} \ln \frac{P_{O2}''}{P_{O2}'} \tag{2.60}$$

The oxygen partial pressures at one or both electrodes may be defined by a chemical reaction. If the condensed phases present at each electrode are at unit activity, the oxygen partial pressure can be related to the Gibbs energy change for the reaction. In such a case, the reversible e.m.f. of the galvanic cell is related to the Gibbs energy change of the virtual cell reaction by the following equation:

$$\Delta_r G^0 = -nFE \tag{2.61}$$

where, n is the number of electrons associated with electrochemical reactions at each electrode and F is the Faraday constant (96486.4 $\mathrm{C \cdot mol^{-1}}$). One of the most commonly used solid oxide electrolyte is made of 10-20 mol% - calcia (CaO) stabilized zirconia (ZrO_2) or yttria (Y_2O_3) doped thoria (ThO_2) or with other rare earth oxides. The choices of solid electrolyte for e.m.f. studies are:

(1) The oxygen partial pressure range of the system under study should fall within the electrolytic domain of the electrolyte used.

(2) It should be chemically compatible with the electrode materials at the temperature range of measurements.

(3) It should possesses high ionic conductivity and meet the criterion of $t_{ion} \geq 0.99$

In the galvanic cell, the open circuit e.m.f. is related to Gibbs energy of virtual cell reaction by Nernst equation provided the experiments are carried out keeping certain critical factors in mind.

2.6.7. Critical factors in e.m.f. measurements

a) Electrode polarization

Electrode polarization always results in lower value of e.m.f.. Polarization is caused by physical and electrochemical permeability of oxygen through the electrolyte. The oxygen flux can increase the oxygen potential at the interface of the solid electrolyte with the low oxygen potential electrode, and lower the oxygen potential at the interface of the solid electrolyte with the high oxygen potential electrode. Hence, the effective oxygen potential difference across the solid electrolyte is smaller than that in the bulk electrodes.

b) Physical permeability

Physical permeability arises because of pores and microcracks in the solid electrolyte. Porosity and microcracks in the electrolyte can provide paths for the migration of molecular oxygen from one electrode to the other, and thus change the oxygen chemical potentials at the two electrode-electrolyte interfaces. With proper preparation and sintering techniques, porosity in the electrolyte can be minimized. If a cell is heated or cooled too rapidly, thermal stresses cause microcracks formation in the electrolyte. This is particularly a severe problem while using electrolyte tubes. Leak testing at high temperature can reveal the presence of any microcracks.

c) Electrochemical permeability

The presence of trace electronic conduction in the solid electrolyte gives rise to a small electrochemical flux of oxygen from the electrode having higher oxygen chemical potential to the electrode having lower oxygen chemical potential. The flux is caused by coupled transport of oxygen ion and electrons (or holes) under the oxygen potential gradient. The electrochemical flux of oxygen would cause polarization of multiphase solid electrodes. The chemical potential of oxygen near the solid electrode/electrolyte interface would be altered because of the semi-permeability of the electrolyte to oxygen.

d) Influence of gas atmosphere

Difficulties in maintaining a fixed chemical potential at the electrode-electrolyte interface can be caused by the influence of gaseous phase and undesirable chemical reactions Electrochemical cell measurements can be made either in vacuum or in inert gas atmosphere. The inert gas atmosphere can be either static or dynamic. In most cases, a flowing inert gas (argon) atmosphere is maintained. The gas is first passed through purification systems to remove any residual hydrogen, moisture and then oxygen. Careful purification of inert gas is essential especially when working with low-oxygen-activity electrodes. It is also important to determine whether the inert gas flow rate has any effect on the measured e.m.f.. If there is flow rate effect, oxygen in the inert gas may be establishing a mixed potential at the electrode-electrolyte interface. In some electrochemical cells, the difference in the oxygen chemical potential between the two electrodes may be so large that the inert gas atmosphere will tend either to reduce one electrode or to oxidize the other. This can be avoided by choosing a reference electrode which establishes an oxygen pressure within one tenth of the estimated $p(O_2)$ of the measuring electrode or by using separate compartments for the two electrodes. Use of electrolyte tubes provides a convenient method for separating the gas phase over the two electrodes. With careful cell design, problems due to the gaseous atmosphere can be eliminated.

e) Electrode preparation

The equilibration of the electrodes' constituents is always of concern. Equilibration times are limited by diffusional processes and will vary with the particular electrode [136]. With two- and three-phase electrodes, compactly pressed electrode pellets of small particles can decrease diffusion distances and promote interphase contact and cathode and anode pellets are made from the required equilibrium phase mixtures. With solid electrodes, it is usually necessary to equilibrate the electrode mixtures at a temperature within the experimental range before assembling the electrochemical cell [137]. Cathode of e.m.f. cell should possess high electrical conductivity, high catalytic activity for oxygen reduction and compatibility with other cell compartments. The cathode performance depends on its surface area, porosity and microstructure. Therefore, the processing method used is very important in determination of cathode performance. Like cathode, anode must have catalytic activity for oxidation and electrical conductivity. Electronic conductivity is necessary to transport electrons resulting from the electrode reaction in the external circuit.

2.6.8. Criteria for selection of reference electrode

The reference electrode may consist of pure gas, an appropriate mixture of gases or a mixture of condensed phases that can establish the required equilibrium chemical potential of the active species at the electrode. It is essential to select the reference electrode having an equilibrium chemical potential of the active species close to that of the measuring electrode. This helps in reducing the gradient of chemical potential across the solid electrolyte. Consequently the semi-permeability of the active species and electrode polarization are also minimized. For an oxygen concentration cell, a biphasic mixture of metal and its oxide ($M + M_xO_y$) or two coexisting oxides in a M-O binary system such as {Cu(s) + Cu_2O(s)}, {Cu_2O(s) + CuO(s)}, {Ni(s) + NiO(s)}, {Cr(s) + Cr_2O_3(s)} and {Fe(s) + FeO(s)} can be used as the reference electrodes. The electrode material must be chemically inert towards the solid electrolyte and the measuring leads such as platinum.

2.6.9. Check of reversibility

To test the correct functioning of the cell, a number of tests should be performed.

- To get accurate e.m.f. data from the cell, it needs to check the cell with a thermodynamically well characterized system in the experimental temperature and pressure range.
- The unknown electrode system can be investigated using separate cells involving different reference electrodes. Each set of measurements should generate the same thermodynamic value for the unknown electrode.
- With the same chemical potentials of the active species at both the electrodes (identical electrodes), the open circuit e.m.f. should be zero. Departure from this condition is indicative of a thermal gradient across the electrolyte.
- Cell reversibility should be checked by micro-coulometric titration in both directions. A small quantity of current is passed (~100 μA for ~10 min) through the cell in either direction. After the removal of applied voltage, the cell e.m.f. should return to its original value recorded.

2.6.10. Description of experimental set up used in this study

As $\Delta_f G$ (RE_6UO_{12}(s)) was not reported in the literature, in this study it was decided to measure e.m.f. (RE_6UO_{12}(s) +U_3O_8(s) +RE_2O_3(s)) as working electrode and (Ni(s)+NiO(s)) mixture and air was separately used as reference electrode. The schematic of complete oxide cell set up used in this study is given in **Fig. 2.28.**

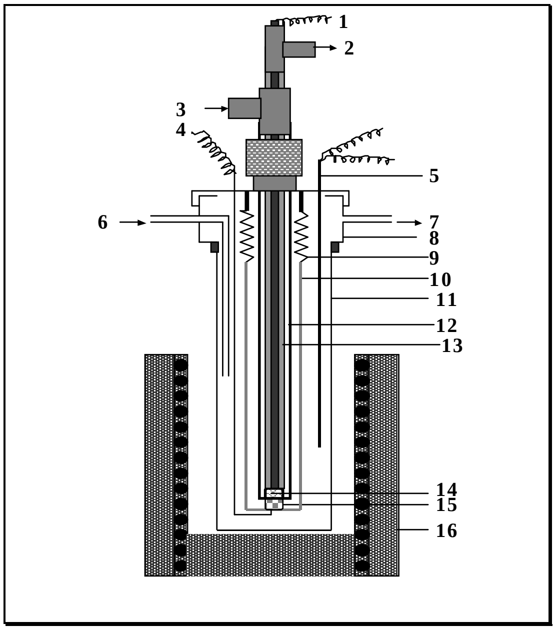

Fig. 2.28: Schematic diagram for solid oxide galvanic cell for e.m.f. measurements.1, 4: Pt-lead wire; 3, 6: gas inlet; 2, 7: gas outlet; 5: thermocouple; 8: stainless steel flange; 9: spring; 10: quartz/alumina holder; 11: quartz/alumina outer tube; 12: CSZ/YSZ electrolyte tube; 13: alumina pressing tube; 14: sample electrode; 15: reference electrode; 16: Kanthal wire wound resistance furnace.

It consisted of a double compartment cell, with 0.15 mole fraction Yttria-stabilized zirconia (YSZ) solid electrolyte tube. The one end closed flat bottom electrolyte tube supplied by Nikatto Corporation, Japan, was 380 mm long with 13 mm o.d. and 9 mm i.d. An inert environment was maintained throughout the experiment over each solid electrode by separate streams of purified argon gas. The argon gas was purified by passing it through different towers containing the reduced form of BASF catalyst, molecular sieves, magnesium perchlorate and hot uranium metal at 550 K. The cell temperature (±1 K) was measured by a calibrated chromel/alumel thermocouple (ITS-90). The e.m.f. (±0.1 mV) of the cell was measured by a Keithley 614 electrometer (impedance $\cong 10^{14}$ ohms).

In order to check the absence of any undesirable chemical reaction, the X-ray diffraction patterns of the equilibrium phase mixture used as electrodes were taken before and after the experiment.

2.6.11. E.m.f. data treatment

From the measured values of the e.m.f. (*E*) and the known oxygen potential of the reference electrode, the oxygen potential for the three-phase electrodes (RE_6UO_{12}(s) +U_3O_8(s)

+RE_2O_3(s) were calculated with the help of **Eq.(2.59).** In the present study the e.m.f. (E) was used to calculate Gibbs energy change for virtual cell reaction using **eqn. 2.61.**

By knowing Gibbs energy of the reaction, $\Delta_r G^0{}_m$ for the net virtual cell reaction and the values of standard molar Gibbs energy of formation ($\Delta_f G^0{}_m$) of known phases involved in the equilibrium reaction, the $\Delta_f G^0{}_m$ for the unknown phase is calculated.

Usually, for the case where the change in heat capacity of the reaction is zero, the e.m.f. varies linearly with the temperature. In such a case, the Gibbs energy change for the reaction ($\Delta_r G^0{}_m$) also shows the same linear relation with temperature. Thus, the e.m.f. values obtained at each experimental temperature were fitted to yield a linear relation:

$$E / \mathrm{V} = \mathrm{a} + \mathrm{b}\cdot(T/\mathrm{K}) \tag{2.62}$$

Then the $\Delta_f G^0{}_m$ for the compound is directly obtained as a linear relation in the experimental temperature range of measurements.

$$\Delta_f G^o{}_m = A + B\cdot(T/\mathrm{K}) \quad ` \tag{2.63}$$

The slope (B) and the intercept (A) of **Eq.(2.63)** represent the entropy of formation and enthalpy of formation of the compound at the experimental average temperature, respectively.

2.7. Measurement of Vapour Pressure

All the substances, both organic and inorganic in nature evaporate, but the degree of vaporization varies with the nature of the reaction and the type of bond formation or bond breakage in the condensed and in the vapor phase. The condensed phase may be a solid or a liquid substance or a compound or a mixture of them. Similarly, the vapor phase may contain one or more simple or complex species. Vaporization study gives thermodynamic information about condensed and gas phases if equilibrium exists during the measurements. The best way to understand the vaporization property of a material is to measure its vaporization under the required condition or evaluate it from the suitable thermodynamic quantities. Vaporization is a heterogeneous process involving equilibrium between the condensed and vapor phase. Hence, properties of both the phases determine the vaporization mode. The complexity of the vapor phase increases with temperature in the vaporization process unlike the homogeneous gas phase systems. These factors should be taken into consideration in any thermodynamic analysis of the materials at high temperatures and reduced pressure. The complexity will be reduced a lot when we do the experiment with permanent gaseous species such as O_2, N_2, CO, CO_2 etc. for this, we have to realize such a reaction which can produce these gaseous species in equilibrium condition. Meaningful vapour pressures can be obtained if the degree of freedom of the system is one. Thus by fixing temperature, pressure of the system is fixed automatically.

If a condensed phase is in thermal, mechanical and chemical equilibrium with the vapour phase, then the chemical potential of a species in the condensed and the vapour phase are equal and related by the following equation:

$$\mu(s,l) = \mu^o(g) + RT\ln a \qquad (2.64)$$

The activity "a" is the ratio between the unit free equilibrium constant over the system and over the pure substance. In case of ideal behavior the activity is unity and the excess thermodynamic quantity (non ideal term) is zero.

So, $\mu(g) = \mu^o(g)$

Which means the chemical potential is equal to the standard chemical potential.

Consider the equilibrium

$A(s) = A(g)$ with $K_p = \frac{p_{A(g)}}{a_{A(s)}}$ but $a_{A(s)} = 1$(if A(s) has no solubility)

Then $K_p = p_{A(g)}$

and it will be difficult to calculate logarithm $\ln K_p = \ln p_{A(g)}$ as the pressure unit(atm, bar, Pa or other) is not defined. To prevent this mathematical problem, the pressure $p_{A(g)}$ is divided by standard pressure p^o(1 atm, 1 bar and so on).This is the reason to write $p/_{p^o}$ and the value is unit free. To achieve unity the pressure p must be p^o , which is the standard pressure p^o at the boiling point. Hence, the ratio $p/_{p^o}$ does not define species under ideal condition.

Thus one can get partial, integral and excess thermodynamic quantities using standard calculations.

A wide variety of techniques is available for the vaporization studies at high temperatures and is categorized as follows:

a) Absolute methods like static manometry and boiling temperature method

b) Non absolute methods like Knudsen effusion, isopiestic and transpiration techniques.

Excellent monographs and reviews on different types of vapor pressure measurement techniques, the methodology and the problems encountered in each technique are available [**138-141**]. In this work, transpiration technique was used to determine the thermodynamic parameters of a reaction evolving $TeO_2(g)$, hence, only details of the transpiration technique is given below. Absolute method does not require prior knowledge of molecular weight of vapourising species. But the relative methods require prior knowledge of molar mass of the vapour species.

2.7.1. Transpiration Method

The transpiration method, also called the transport or the entrainment method is one of the oldest and most versatile ways of studying vapour pressure and heterogeneous equilibria involving gases [**142, 143**]. It is a relative method. It can be used in making measurements of vapour pressures in the range of 0.1 Pa to 100 kPa. It is one of the methods that can be used to measure the pressure of vapour in the presence of large concentrations of other gases.

In transpiration method the sample is kept in a boat in the constant temperature zone of the furnace. The carrier gas which may be pure or a mixture of gases, inert or reactive is introduced from one end of the reaction tube. It passes over the sample at a predetermined flow rate. Argon, nitrogen, hydrogen and oxygen are the most frequently used carrier gases. Since, hydrogen gives a reducing atmosphere it has often been used in measuring vapour pressure of metals and alloys. Reactive carrier gases are often used to form species or to prevent the dissociation of the species being studied. Under carefully optimized experimental conditions, the carrier gas gets saturated with sample vapour at the temperature of measurement. Then it enters the condensation region through a capillary. In the condensation region, the vapour gets condensed and the carrier gas escapes out. A schematic diagram of the apparatus is shown in the **Fig. 2.29**. The amount of vapour thus transported is dependent on the total volume of the carrier gas passed, the temperature of the sample, the flow rates of the carrier gas and the vapour pressure of the sample; hence, from the experimentally determined amount of condensate and the total volume of the carrier gas passed the vapour pressure at the experimental temperature can be computed as follows;

By the Dalton's law of partial pressures and assuming that the vapour behaves as an ideal gas under the conditions of low pressure and high temperature,

$$P_v = \frac{n_v}{n_v + n_g} P \qquad (2.65)$$

where P_v is the vapour pressure of the sample, n_v is the number of moles of sample vapours, n_g is number of moles of carrier gas passed and P is the total pressure ($P_v + P_g$) of the system, usually one atmosphere. A prior knowledge of molar mass of the vapour is essential for this technique.

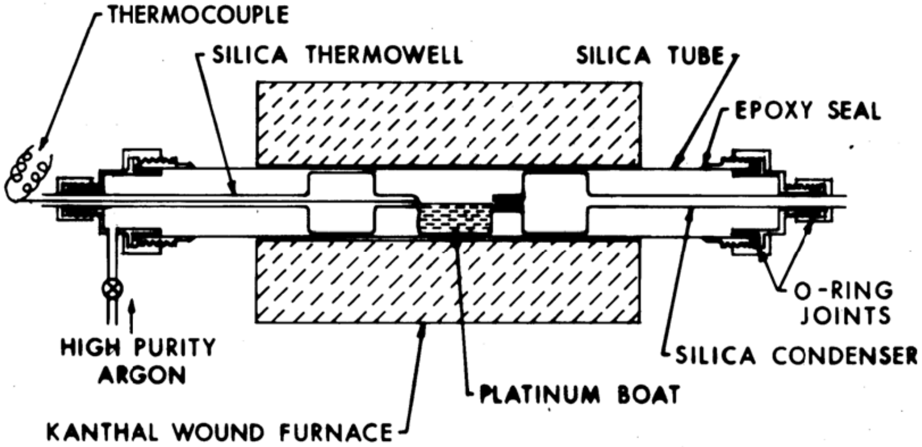

Fig. 2.29: Schematic diagram of transpiration apparatus

Transpiration measurements are basically dynamic in nature but are aimed at obtaining equilibrium data. It is therefore essential to control the experimental parameters in order to obtain meaningful vapour pressure data. Important parameters in this respect are:

a) Availability of a zone saturated with sample vapour,

b) The carrier gas flow rate and

c) Uniformity of temperature in the zone containing the sample, thermocouple and the condenser inlet.

2.7.1.1. Important parameters in transpiration measurements

2.7.1.1.1. Saturation zone

In order to ensure saturation of the carrier gas with sample vapour it is essential to have a wide enough zone in the vicinity of the sample which is saturated with the sample vapour. This is achieved by having a large surface area of the sample, small diameter of the reaction tube and by incorporating radiation shields on either side of the sample boat.

2.7.1.1.2. Effect of flow rate

This is one of the most important parameters in the transpiration technique. The gas flow rates are controlled within what is known as the ‘plateau region’. This is obtained by studying the variation of the mass of the condensate per unit volume of the carrier gas as a function of carrier gas flow rates. The result of a typical study is shown in **Fig. 2.30**.

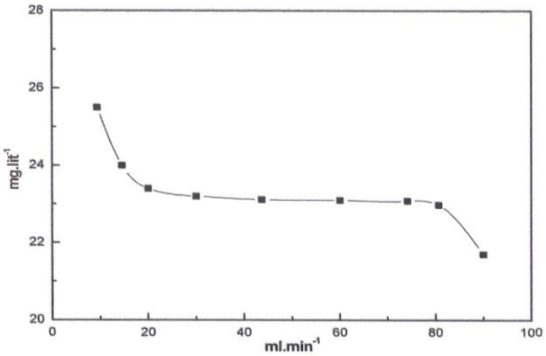

Fig.2.30. A typical flow rate Plateau in transpiration technique

There are three different regions in this plot, namely,

a) Low flow rate region or diffusion controlled region,

b) Plateau region where the mass of the condensate per unit volume of the carrier gas is independent of the carrier gas flow rates, and

c) High flow rate region or un-saturation region.

Low flow rate region

In this region the fraction n_v / (n_v + n_g) becomes larger compared to the equilibrium values since the vapour is transported to the condenser region not only by the carrier gas but also by self diffusion. In fact, the vapour diffuses in both directions of the sample chamber. Diffusion in the upstream direction may give a higher value of vapour pressure if mass loss of the sample is taken for the calculation of vapour pressure. Diffusion in the downstream condenser region complicates the vapour pressure measurements more seriously than does the upstream diffusion.

Plateau region

In this region the flow rates are high enough to nearly eliminate the problems related to the diffusion effect, but at the same time low enough so as not to cause any un-saturation effects due to the kinetics of the evaporation process. This region is insensitive to small variations in flow rate and represents the equilibrium values of vapour pressure. Since, the plateau region changes with the geometry of the experimental assembly and with the kinetics of the evaporation process, it is necessary to find out the plateau region with each experimental arrangement and with each sample whose vapour pressure is to be measured. To determine the region a series of experiments are carried out at a constant temperature using different flow rates. The temperature chosen for this purpose is normally the mean temperature of the range of interest.

High flow rate or un-saturation region

At high flow rates the saturation of carrier gas may be prevented by poor gas mixing or inadequate sample evaporation rate. These kinetics effects may be minimized by the proper experimental setup design to provide intimate contact between the sample and the carrier gas. A sample should provide an evaporating surface that is as large as possible.

In addition to the problem arising from diffusion and kinetics, vapour pressure data can also be affected by non-uniformity of temperature. Temperature gradient in the saturation chamber may result in redistribution of sample vapour to the coldest part of the chamber. If there is no condensation of the gaseous components on reaching the cold region, there may be a diffusive flow caused by temperature gradient in the exit portion of the apparatus. If a mixed carrier gas is employed, it may separate in the thermal gradient. While designing the apparatus, care must be taken to avoid any temperature gradient in the sample chamber and also the capillary end should not be the coldest portion of the system.

2.7.1.2. Vapour pressure data treatment

The standard Gibbs energy change for a gas-condensed phase equilibrium reaction at a particular temperature can be determined from the equilibrium constant at that temperature. The equilibrium constant depends on the activities and equilibrium pressure of the condensed and vapour phase, respectively.

Lets consider a typical reaction involving gaseous and condensed phase:

AB(s) = A(s) + B(g) (2.66)

Now, the equilibrium constant can be expressed as $K_p = \frac{a_A \times P_B}{a_{AB}}$ (2.67)

Where, P_B is the equilibrium vapour pressure of "B", a_A, a_{AB} are activities of A and AB respectively. a_A and a_{AB} are assumed to be unity for pure condensed phase A and AB, respectively.

Then equilibrium constant changes to the form $K_p = P_B$ (2.68)

where it depends solely on the equilibrium pressure of the vapourising species.

Various methods, like static (e.g.Manometric), dynamic (e.g boiling point) and method based on rate of evaporation (e.g. Knudsen effusion, Knudsen cell mass spectroscopic and transpiration method) are used to measure this quilibrium pressure of various vapour phases involved in the reaction.

The standard Gibbs energy change for the reaction at temperature T can be obtained as follow:

$$\Delta_r G^o(T) = -RT\, lnK_p = -RT \ln P_B \tag{2.69}$$

Now $\Delta_r G^o(T)$ can also be expressed as $\Delta_r G^o(T) = \Delta_r H^o(T) - T\Delta_r S^o(T)$ (2.70)

On equating eqn (**2.69**) and (**2.70**)

$$\Delta_r H^o(T) - T\Delta_r S^o(T) = -RTlnP_B$$

Implies:

$$\ln P_B = -\frac{\Delta_r H^o(T)}{RT} + \frac{\Delta_r S^o(T)}{R} \tag{2.71}$$

The logarithmic of equilibrium partial pressure measured by various techniques is plotted as a function of inverse temperature which leads to a straight line.

The value of the slope and the intercept of Eq**.(2.71)** represent the enthalpy and entropy of reaction at the experimental average temperature, respectively.

2.8. Calculation of thermodynamic functions

2.8.1. Derivation of thermodynamic functions from heat capacity data.

A knowledge of the heat capacity of a material as a function of temperature is the basis for determination of thermodynamic quantities like enthalpy increment $\left\{H^{\text{o}}_{\text{m}}(T) - H^{\text{o}}_{\text{m}}(298\text{ K})\right\}$, entropy $\left\{S^{\text{o}}_{\text{m}}(T) - S^{\text{o}}_{\text{m}}(0\text{ K})\right\}$ Gibbs energy functions $-\left\{\frac{G^{\text{o}}_{\text{m}}(T) - H^{\text{o}}_{\text{m}}(298.15\text{ K})}{T}\right\}$. These quantities help in construction of thermodynamic tables. The $\left\{S^{\text{o}}_{\text{m}}(T) - S^{\text{o}}_{\text{m}}(0\text{ K})\right\}$ and $\left\{H^{\text{o}}_{\text{m}}(T) - H^{\text{o}}_{\text{m}}(298.15\text{ K})\right\}$ functions are calculated by numerical integration of the $C^{\text{o}}_{p}(T)/T$ and $C^{\text{o}}_{p}(T)$ functions, respectively. These functions are constructed using polynomial fit of the $C^{\text{o}}_{p}(T)$ curve in small temperature ranges. The Gibbs energy function $-\left\{\frac{G_{\mathrm{m}}^{\mathrm{o}}(T)-H_{\mathrm{m}}^{\mathrm{o}}(298.15\ \mathrm{K})}{T}\right\}$ is calculated using the relation:

$$-\left(\frac{\left(G_{m}^{o}(T)-H_{m}^{o}(298.15)\right)}{T}\right)=S_{m}^{o}(T)-\frac{\left(H_{m}^{o}(T)-H_{m}^{o}(298.15)\right)}{T} \qquad (2.72)$$

where
$$H_{m}^{o}(T)-H_{m}^{o}(298.15)=\int_{298.15}^{T}(C_{p,m}^{o})dT \qquad (2.73)$$

and
$$S_{m}^{o}(T)=S_{m}^{o}(298.15)+\int_{298.15}^{T}\left(\frac{C_{p,m}^{o}(T)}{T}\right)dT \qquad (2.74)$$

In order to make full use of the thermodynamic data, $G_{\mathrm{m}}^{\mathrm{o}}(T)$ should be evaluated which requires a known value of $H_{\mathrm{m}}^{\mathrm{o}}(0\ \mathrm{K})$. However, absolute value of $H_{\mathrm{m}}^{\mathrm{o}}(0\ \mathrm{K})$ is difficult to determine or calculate. Therefore, first $H_{\mathrm{m}}^{\mathrm{o}}(T)$ is calculated using the relation:

$$H_{\mathrm{m}}^{\mathrm{o}}(T)=\Delta_{\mathrm{f}}H_{298.15K}^{\mathrm{o}}+\int_{298.15}^{T}C_{p,m}^{\mathrm{o}}(T)\mathrm{d}T \qquad (2.75)$$

The absolute value of $S_{\mathrm{m}}^{\mathrm{o}}(T)$ is calculated using the $S_{m}^{o}(298\ K)$ and the relation (**2.74**). $S_{\mathrm{m}}^{\mathrm{o}}(T)$ was calculated empirically using an additive rule similar to Newmann Kopp's rule used for calculation of $C_{p,m}^{o}(T)$.

Now $G_{\mathrm{m}}^{\mathrm{o}}(T)$ can be calculated using the relation:

$$G_{\mathrm{m}}^{\mathrm{o}}(T)=H_{\mathrm{m}}^{\mathrm{o}}(T)-TS_{\mathrm{m}}^{\mathrm{o}}(T) \qquad (2.76)$$

After calculation of all the thermodynamic functions, the values are tabulated at selected temperatures. The thermodynamic functions which are usually tabulated in tables are: $C_{p,m}^{\mathrm{o}}$, S_{m}^{o}, $\left\{H_{\mathrm{m}}^{\mathrm{o}}(T)-H_{\mathrm{m}}^{\mathrm{o}}(298.15\ \mathrm{K})\right\}$, H_{m}^{o}, $\Phi_{m}^{\mathrm{o}}(T)$, $\Delta_{\mathrm{f}}H_{m}^{\mathrm{o}}(T)$ and $\Delta_{\mathrm{f}}G_{m}^{\mathrm{o}}(T)$.

A knowledge of the heat capacity of a material as a function of temperature is the basis for determination of any thermodynamic quantity which helps in construction of thermodynamic tables.

2.8.2. Derivation of enthalpy and entropy from Gibbs energy data

The techniques for evaluation of thermodynamic quantities and their derivation from other quantities are described by M.W. Chase [144].

The standard molar enthalpy of formation of the unknown at 298.15 K is generally obtained by combining the C^o_p and $\Delta_r G^0_m$ data with the help of the second-law and the third-law methods, which are discussed below.

2.8.2.1. The Second-law method

From the measured $\Delta_r G^o(T)$, and known $\Delta_f G^o(T)$ of various compounds, $\Delta_f G^o(T)$ of the unknown compound can be found out and it is related to the entropy and enthalpy of formation by:

$$\Delta_f G^o_m = \Delta_f H^o_m - T\Delta_f S^o_m \tag{2.77}$$

The slope and the intercept represent the entropy of formation and enthalpy of formation of the compound at the experimental average temperature, respectively.

Then $\Delta_f H^o_m(298.15\,K)$ and $S^o_m(298.15\,K)$ can be obtained by knowing the heat capacity of various species involved in the formation reaction of compounds from its elements in their standard states using the relations:

$$\Delta_f H^o_m(298.15\,K) = \Delta_f H^o_m(T) - \int_{298.15\,K}^{T} \Delta\, C^o_{p,m}\; dT \tag{2.78}$$

$$S^o_m(298.15\,K) = S^o_m(T) - \int_{298.15\,K}^{T} \frac{\Delta C^o_{p,m}}{T}\, dT \tag{2.79}$$

This method of obtaining enthalpies and entropy from equilibrium measurements is known as a “second-law” calculation. For greatest accuracy the equilibrium measurements should extend over a wide range of temperature. It should be noted that the second law cannot be applied to a single observation, but the third-law method, which is described below, can be so used.

2.8.2.2. The third-law method

The “third-law” method is based on knowledge of the absolute entropy of the reactants and products. It allows the calculation of a reaction enthalpy from each data point when the change in the Gibbs energy function (*fef*) for the reaction is known. The Gibbs energy function used here is defined as:

$$\Phi^{\circ}_{\mathrm{m}}(T) = -\left[G^{\circ}_{\mathrm{m}}(T) - H^{\circ}_{\mathrm{m}}(298.15\ \mathrm{K})\right]/T \tag{2.80}$$

These functions are calculated for the gases from spectroscopic data and for condensed phase from the **eqn.2.72.**

The change in Gibbs energy function for e.m.f. cell and transpiration measurements can be written as:

$$\Delta_r G^o_m(T) = -T\Delta_r \Phi^o_m(T) + \Delta_r H^o_m(298.15\ K) = -nFE \tag{2.81}$$

and

$$\Delta_r G^o_m(T) = -T\Delta_r \Phi^o_m(T) + \Delta_r H^o_m(298.15\ K) = -RT \ln K_p \tag{2.82}$$

on rearrangement the $\Delta_r H^o_m(298.15\ K)$ can be obtained as follows:

$$\Delta_r H^o_m(298.15\ K) = -nFE + T\Delta_r \Phi^o_m(T) \tag{2.83}$$

$$\Delta_r H^o_m(298.15\ K) = -RT \ln K_p + T\Delta_r \Phi^o_m(T) \tag{2.84}$$

Gibbs energy functions are based on an enthalpy at reference temperature of 298.15 K and thus yield enthalpy changes at 298.15 K regardless of the temperature of the reaction. The analysis of data by the third-law method is generally considered to be superior to the second-law method if the Gibbs energy functions are accurately known. These values will often reveal trends that indicate non-equilibrium or erroneous values in the equilibrium constants of a set of data. If the data are good, the second-law value should agree with the third-law value. Values that are constant and that agree with the second-law enthalpy indicate that the Gibbs energy functions and the equilibrium data are mutually consistent. A drift with temperature of the third-law values indicates error in either the data or the functions.

2.9. Establishment of chemical potential diagram

The chemical potential diagram depicts the stability of various phases present in a system A-B-O (A, B =metallic elements) as a function of the chemical potentials of the components [**145,** 146] in which the area between the lines defines the stability domain of each stoichiometric phase (element, binary oxides and double oxides). Lines between two single phases and points represent two-phase equilibria and three-phase equilibria, respectively. The basic computational procedure for the construction of a chemical potential diagram is based on the minimization of Gibbs energy method. In this study chemical potential diagram of A-Te-O (A= Cr, Fe, Ni) system is evaluated using Factsage program. It is assumed that ternary or binary compounds are formed from the reaction of one mole of A(s) (A = Cr, Fe, Ni) hence it is not used as an axis variable, while tellurium and oxygen potential are taken as variable.

2.10. Phase transitions

The knowledge of phase transition is important for designing a material for different applications. A phase transition is the transformation of a thermodynamic system from one phase (state of matter) to another one by heat transfer. A phase of a thermodynamic system has uniform physical properties. During a phase transition certain properties of the phase change, often discontinuously, as a result of the change of some external condition, such as temperature, pressure, or others. Paul Ehrenfest’s classified phase transitions as first, second, or higher-order transitions depending on whether first, second or higher temperature derivative of the Gibbs energy become discontinuous at the transition point. The second order phase transition was explained by Landau using phenomenological theory.

Physics of phase transition

The different forces that hold molecules together in a phase are responsible for the phase transformation. These forces affect the behavior of different phase transitions. As particles undergo a phase change, the pressure and temperature affect the bonds between the molecules. These forces are called intermolecular forces or Van Der Waals Forces which can be further broken down into three sub-forces: Dispersion forces, Dipole-Dipole forces and Hydrogen Bond forces.

Dispersion forces are also known as London forces, which are caused by the movement of electrons in the molecules. This type of force is present in most molecules. The stronger the molecular mass, the stronger the force and London force also depends on the shape of the molecule. Dipole-Dipole forces are responsible for the movement of electrons in bonds, rather than in the molecule. The electro-negativity of the atoms in the molecule determines dipole-dipole forces. So it can increase by electronegativity difference between the atoms in the molecules. The higher is the electronegativity between the atoms in a molecule, the stronger is the Dipole-Dipole force. Hydrogen Bond forces occur when hydrogen atoms bond to highly electronegative atoms such as oxygen, nitrogen, and fluorine. This bond greatly affects the boiling and freezing points. If a phase is having all three of these forces, then the molecules in that phase are going to be held tightly together. This means that it will require more energy to break them apart, creating the phase transition point to be higher than that of molecules of phase having less of it.

Thermodynamics of phase transitions

Phase transition can be explained from thermodynamic principle that at a given T, P; a thermodynamic system will seek to minimize the Gibbs energy:

$$G = E + PV - TS. \qquad (2.85)$$

As pressure increases, this will clearly favor phases of lower volume (more compact packing of constituents). Or as one increases temperature, it will clearly favor phases of higher entropy (more disorder). The Clausius-Clapeyron relation can be used to calculate phase transition in a single component system which means a system that lacks compositional degrees of freedom.

$G = E + PV - TS \Rightarrow \mathrm{d}G = \mathrm{d}E + P\mathrm{d}V + V\mathrm{d}P - T\mathrm{d}S - S\,\mathrm{d}T$

But $\mathrm{d}E = -P\mathrm{d}V + T\mathrm{d}S$ [first law of thermodynamics]

$\Rightarrow \mathrm{d}G = V\mathrm{d}P - S\,\mathrm{d}T$; $(\partial \mathrm{G}/\partial \mathrm{P})_T = V$ and $(\partial \mathrm{G}/\partial T)_P = -S$.

If two phases (1 and 2) that are in equilibrium at P, T and still in equilibrium at $P + \mathrm{d}P$, $T+\mathrm{d}T$.

$G_1 = G_2$ and $G_1 + \mathrm{d}G_1 = G_2 + \mathrm{d}G_2 \Rightarrow \mathrm{d}G_1 = \mathrm{d}G_2$

$\Rightarrow V_1\,\mathrm{d}P - S_1\mathrm{d}T = V_2\,\mathrm{d}P - S_2\,\mathrm{d}T$

$\Rightarrow \mathrm{d}P/\mathrm{d}T = (S_2 - S_1)/(\mathrm{V}_2 - \mathrm{V}_1)$

$$(\mathrm{d}\,\ln P/\mathrm{d}\,\ln T) = T\Delta S/P\Delta V \qquad (2.86)$$

The RHS is a ratio of energies and the dimensionless derivative on the LHS will be large if the volume change is small and/or the entropy change is large; and small if the volume change is large and/or the entropy change is small. If volume changes substantial but a modest entropy change occur, it implies the transition pressure is only weakly T-dependent.

Systems that have compositional degrees of freedom include alloys, salt water etc. and do not satisfy the simplest form of Clausius -Clapeyron. When two multi-component phases are in contact and in equilibrium, they follow the Gibbs phase rule. The two phases need not have the same composition. The chemical potential of each species between two phases must be equal. The multi-component system do not have a single melting temperature, they have a solidus (a T at which melting begins) and a liquidus (at which the material is completely molten). Simple melting in multi component system is an exception rather than a rule. This study discusses two important types of phase transitions: first order and second order.

2.10.1. First Order Phase transition

The first order phase transitions involve a latent heat. During such a transition, a system either absorbs or releases a fixed large amount of energy. The Gibbs energy as a function of the state variables (*V*, *P*, *T*) is continuous whereas the first derivative of Gibbs energy with respect to given state variables is discontinuous. In a simplified way, G^o is continuous but the properties like internal energy, entropy, enthalpy, volume are discontinuous which can be given below.

$$\left(\frac{dG}{dT}\right)_p = -S = -H/T \tag{2.87}$$

$$\left(\frac{dG}{dP}\right)_T = V \tag{2.88}$$

$$\left(\frac{d(G/T)}{d(1/T)}\right)_p = H \tag{2.89}$$

In the first order phase transition, two different states (phase) of the same substance co-exists. One is stable at lower temperatures (low symmetry), another is stable at higher temperatures (high symmetry). However, in the first-order phase transitions a change in symmetry is not necessarily required. At the transition temperature, the Gibbs energy of both phases must be the same. This transition is accompanied by evolution or absorption of latent heat by sudden change in volume and the transition takes place in heterogeneous phases. The first order transitions can be found out as surfaces, lines and points from the diagrams of thermodynamic variables. Examples of first order transitions are fusion, melting, vaporization and structural transitions.

2.10.2. Second Order Phase transition

Second-order phase transitions are also called continuous phase transitions. In this phase transition thermodynamic quantities suffer no abrupt change and region of heterogeneous phase does not exist, so phenomena of super-cooling or a hysteresis are not possible. Landaue established that such transitions must always be associated with a change in symmetry property of the phase. It is of fundamental importance for the elucidation of the nature of the second order phase transition. The second order transition is possible only between phases of different symmetry. Thus, second-order phase transition is continuous structural transition and not an abrupt transition. Mathematically, Landau’s theory defines all possible symmetry groups of the phases involved. Every change of symmetry may not be associated with second order phase transitions. The symmetry theory imposes two restrictions on the possibility of a second-order transition. They are:

- If the low-symmetry phase is described by the symmetry group L, and the high-symmetry phase by the symmetry group H, L has to be a subgroup of H. This means the less symmetrical phase posses only such element of symmetry which is present in the more symmetry phase. But reverse transition {Less symmetry (second order axis) - High symmetry (fourth order axis)} is not second order.

- A second restriction states that a second-order transition can occur along a line in the p, T plane only if the components of the order parameter transform according to an irreducible representation of the group H. If this representation is one-dimensional, then the order of the symmetry group changes by a factor of 2 in the transition.

The order parameter is a quantity that characterizes the symmetry of the phases. It is a measure of the degree of order across the boundaries in a phase transition system; it normally ranges between zero in one phase (usually above the critical point) and nonzero in the other. The order parameter is zero in the high-symmetry phase, finite in the low-symmetry phase, and as the function of temperature turns to zero at the transition point, to account for the continuous nature of the transition. Since the order parameter is continuous at the transition and is zero above the transition, its derivative must be discontinuous. This discontinuity is responsible for the singularities in the thermodynamic properties.

In the second order phase transition the Gibbs energy and its first derivatives are continuous but the second derivatives are discontinuous. Therefore there will not be any discontinuity in G, S, V, H but discontinuity in heat capacity (C_p), the compressibility (β_T) and thermal expansion coefficients (α).The relations are given below:

$$\frac{d}{dT}\left(\frac{d(G/T)}{d(1/T)}\right)_p = \left(\frac{dH}{dT}\right)_P = C_p \qquad (2.90)$$

$$\left(\frac{d2G}{dP^2}\right)_T = \left(\frac{dV}{dP}\right)_T = -V\beta_T \qquad (2.91)$$

$$\left(\frac{d^2G}{dTdP}\right)_T = \frac{dV}{dT} = V\alpha \qquad (2.92)$$

Examples of second-order phase transitions are the ferromagnetic transition, superconducting transition (for a Type-I superconductor the phase transition is second-order at zero external field and for a Type-II superconductor the phase transition is second-order for both normal state-mixed state and mixed state-superconducting state transitions) and the super fluid transition.

Most phase transitions in crystals occur as first order transitions that are almost second-order. They are first-order transitions because of different physical reasons. Among these reasons, symmetry of phases is in a special position: if the change of symmetry is different than second order transition then the phase transition is certainly first- order. **Fig.2.31** represents the examples of first and second order phase transitions.

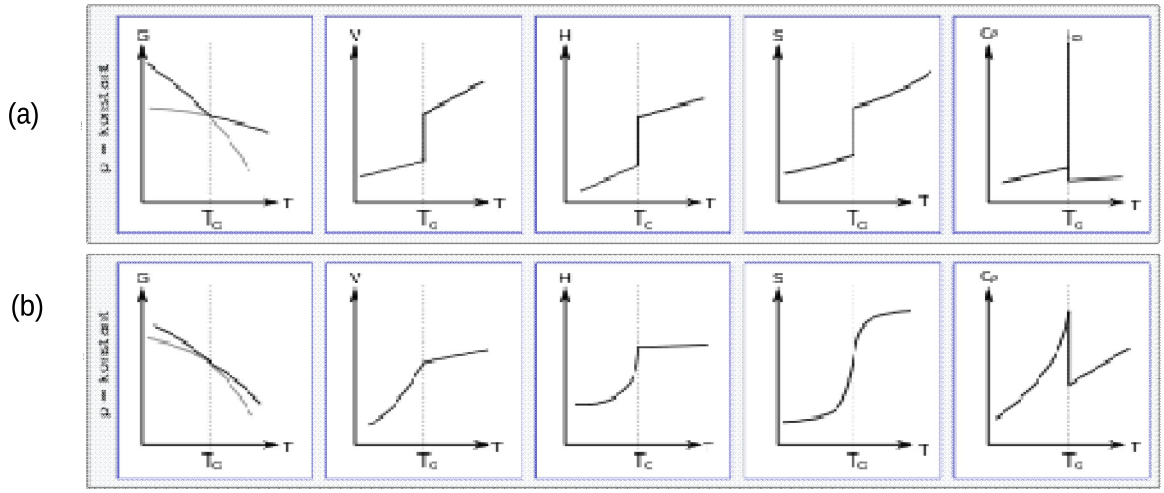

Fig.2.31. The representation of (a) first-order transitions, (b) second order transition.

In this present work, phase transitions were studied using HT-XRD, measurement of heat capacity. Impedance spectroscopy was also used as a complementary technique to confirm the phase transition, the theory of which is described here.

2.11. Impedance Spectroscopy

Impedance spectroscopy is a perturbation technique used for electrical characterization of materials. In this method an ac voltage of small magnitude is imposed across the material and the current response and the phase shift is measured. This measurement is carried out over a wide range of frequency [93, 147]. Impedance is the opposition to the flow of current, which is given by the ratio of applied voltage to the resulting current. The locus of impedance as a function of angular frequency is called impedance spectrum. In ac conductivity measurements, the substance is sandwiched between two electrodes and perturbed by a sinusoidal voltage of small amplitude and the resulting current across the sample is measured. The applied potential and resulting current are represented as

$$V=V_o \exp(j\omega t) \quad (2.93)$$

$$I=I_o \exp(j(\omega t+\Phi)) \quad (2.94)$$

This output current has the same angular frequency ω as that of input potential but differs in amplitude and phase which in turn depends on the impedance offered for charge transport processes.

The impedance in case of pure resistor, capacitor and inductor respectively are

$$Z = R \quad (2.95)$$

$$Z=1/ j\omega C \quad (2.96)$$

$$Z=j\omega L \quad (2.97)$$

where R is the resistance of the resistor, C the capacitance of the capacitor and L is the inductance of the inductor. The impedance of any real system is defined as Z = V/I and usually contains both resistive (R) and reactive (L and/or C) components. Unless the test system behaves as an ideal resistor, there will be a phase difference, (ϕ) between the applied voltage and the resultant flowing current. The phase shift is related to the reactive component of the system. In general, both the magnitude (resistive) and phase shift (reactive) of the impedance of a sample is frequency dependent. The current through a capacitor is referred imaginary and it leads the voltage by 90° i.e. a phase difference of 90° exists between the applied sinusoidal voltage and the resulting current. The impedance of the circuit $Z(\omega)$ at any frequency ω can be represented as:

$$Z=V/I = (V_o/I_o)\exp(-j\Phi) = Z_o \exp(-j\Phi) = Z_o \cos(\Phi)-j\, Z_o \sin(\Phi)$$

$$=Z'-JZ'' \quad (2.98)$$

where, $j = (-1)^{0.5}$ and Φ is phase angle (0 for simple resistor and 90 for simple capacitor). Z' and Z'' are real and imaginary parts of the impedance. The phase angle Φ is equal to

$\tan^{-1}(Z''/Z')$. The plot of real (in phase) and imaginary (out of phase) parts of impedance appears as semi circles and in some cases as straight line. When the centre of the semicircle is depressed below the Z' (real) axis, non-ideal response is indicated.

At an applied ac voltage, charge transfer across a sample consists of various processes at the electrode-sample interfaces and in the bulk of the sample. Processes at the electrode sample interface could involve adsorption, diffusion and dissociation of adsorbed species and charge transfer to or from the electrode. Charge transport across the bulk of a polycrystalline sample can be a combination of transport through grains and grain boundaries and could involve different ions also. The charge transport processes individually would have different time constants and hence during an ac measurement of conductivity, they would get separated in the frequency domain. Each arc can be identified with an elementary process. The measured impedance is correlated to the various elementary processes occurring in the material which can be understood by means of equivalent electrical circuits. The equivalent electrical circuit of a ceramic electrolyte, consisting of a series combination of parallely connected resistors (R) and Capacitors (C) is shown in **Fig. 2.32**. The corresponding impedance spectrum is shown in **Fig. 2.33**.

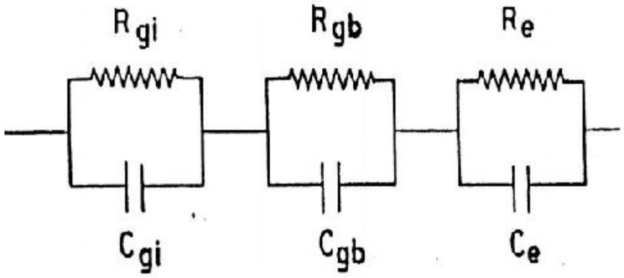

Fig. 2.32: Equivalent electrical circuit of a ceramic electrolyte, consisting of a series combination of parallely connected resistors (R) and Capacitors (C)

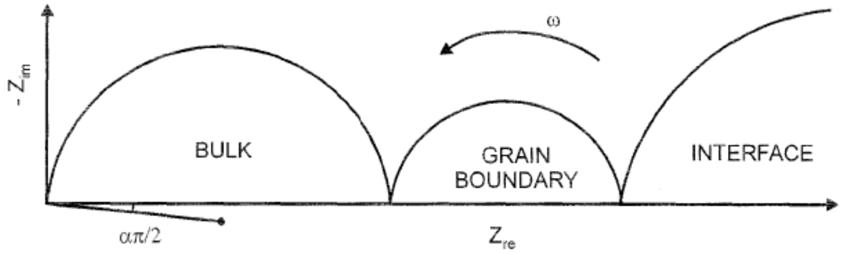

Fig. 2.33: Impedance spectrum for a solid ionic conductor

In the present study, electrical conductivity of Sr_2CeO_4(s), Tb_6UO_{12}(s) and Nd_6UO_{12}(s) was measured using a frequency response analyser (Model SI 1255, Solartron, Schlumberger, UK) coupled with an electrochemical interface (Model 1286, Solartron, Schlumberger, UK) in the frequency range of 10 Hz–1 MHz. Pellets of 10 mm diameter and 2–3 mm thickness were used. Platinum paste was applied on both sides of the pellet and sintered to ensure good electrical contacts. The pellet was mounted between two spring-loaded platinum foils of identical dimensions and placed inside a quartz chamber that in turn was heated in a furnace.

CHAPTER-3

RE-U-O System

CHAPTER-3

Rare earth elements are among the major fission products formed during irradiation of fuel in a nuclear reactor as mentioned in chapter-1. The thermo pysico-chemical properties of various phases in the system RE-U-O is necessary to predict the behavior of uranium bearing fuel during irradiation and off normal condition. It is also necessary to find out the oxygen potential required for the various species to predict its formation probability in the reactor operating conditions. The rare earths and actinides are also unique in their behavior in comparison to other group elements. Therefore, it is necessary to see the trend in the physico-chemical behavior of compounds containing f-block elements. Hence, in the present investigations, the compounds having formula RE_6UO_{12}(s) (RE= La, Pr, Nd, Sm, Eu, Gd, Tb, Dy, Ho,Er, Tm, Yb, Lu) were synthesized by citrate- nitrate combustion method and their physico-chemical properties were measured. Thermal expansion of RE_6UO_{12} (s) (RE= Pr, Sm, Eu, Gd, Tb, Dy, Ho, Er, Tm, Yb, Lu) were measured using HT-XRD, heat capacity of RE_6UO_{12} (s) (RE= La, Pr, Nd, Sm, Eu, Gd, Tb, Dy, Ho,Er, Tm, Yb, Lu) was measured using differential scanning calorimeter (DSC) and Gibbs energy of formation for RE_6UO_{12}(s) (RE= La, Nd, Sm, Eu, Gd, Tb, Dy, Ho, Tm, Yb and Lu) was measured using solid oxide galvanic cell.

3.1. Experimental

3.1.1. Synthesis of RE_6UO_{12} (s)

RE_6UO_{12}(s) (RE= La, Pr, Nd, Sm, Eu, Gd, Tb, Dy, Ho, Er, Tm, Yb, Lu) was synthesized by citrate – nitrate gel combustion method. This method uses the large exothermicity of the chemical reaction between the fuel (citric acid) and an oxidant to energize the synthesis [148-152]. U_3O_8(s) (nuclear grade purity supplied by Nuclear Fuel Complex, Hyderabad, India), RE_2O_3(s)(RE=La, Pr, Nd, Sm, Eu, Gd, Tb, Dy, Ho, Er, Tm, Yb, Lu) (99.99 % purity supplied by Rare Earth Development Section, BARC, Mumbai), Tb_4O_7, Pr_6O_{11}(s) (99.9 % purity supplied by Rare Earth Development Section, BARC, Mumbai), citric acid (99.7 %, M/s Chemco fine chemicals, Mumbai), selectipure HNO_3 (M/s Merck Ltd, Mumbai) and NH_3 solution (M/s Chemco fine chemicals, Mumbai) were used as reactants. As most of the rare earth oxides has a tendency to form carbonates and hydroxides when exposed to atmosphere. All the rare earth oxides were digested separately in minimum amount of concentrated HNO_3. The solutions were evaporated to dryness and finally solutions were made with 1 % HNO_3. The rare earth content in the solution was determined using inductively coupled plasma mass spectrometry (ICPMS). These quantified rare earth solutions were used for the synthesis of RE_6UO_{12}(s). Required amounts of U_3O_8(s) were also dissolved separately using concentrated HNO_3. Rare earth solution was mixed with required U_3O_8(s) solution to facilitate mixing of reactants at molecular level. These metallic solutions in nitric acid acted as oxidant in the self combustion process. Citric acid (fuel) was added to the final solutions. The fuel to oxidant ratio was 2. The resultant solution was evaporated at 353 K on a hot plate till the formation of gel. Then, the temperature of reaction was raised to 673 K. Combustion of the mixture took place with flame. The resultant carbonaceous powders were ground, calcined at 1,073 K in air for 4 h and compacted into pellets by applying uniaxial pressure of 500 MPa using hardened steel die and plunger. The pellets for the formation of Pr_6UO_{12} (s)and La_6UO_{12}(s) were heated in argon atmosphere at temperature 1525 K for 8 h but the pellets for the formation of RE_6UO_{12}(s)(RE= Nd, Sm, Eu, Gd, Tb, Dy, Ho,Er, Tm, Yb, Lu))were heated at 1,573 K in air for 8 h.

3.2. Results

3.2.1. Characterisation using XRD

The heat treated pellets of RE_6UO_{12}(s) (RE= La, Pr, Nd, Sm, Eu, Gd, Tb, Dy, Ho,Er, Tm, Yb, Lu) were ground and X-ray diffraction analysis was performed using Stoe theta–theta X-ray diffractometer employing monochromatic Cu Kα radiation (λ = 0.15406 nm) with curved graphite monochromator using NaI (Tl) scintillation detector. The scans were made in the range of $10^\circ \leq 2\theta \leq 60^\circ$. The X-ray diffraction patterns of RE_6UO_{12} (s) (RE = La, Pr, Nd, Sm, Eu, Gd, Tb, Dy, Ho, Tm, Yb, Lu) is shown in **Fig. 3.1** which are in good agreement with the respective reported literature patterns **[13, 14, 18, 153-163].** RE_6UO_{12}(s) (RE = La, Pr, Nd, Sm, Eu, Gd, Tb, Dy, Ho, Tm, Yb, Lu) has rhombohedral crystal structure. To the best of my knowledge, Er_6UO_{12} is not yet reported in the literature. The synthesis of Er_6UO_{12}(s) was also tried by combustion synthesis. The XRD pattern of Er_6UO_{12}(s) was found to similar to that of RE_6UO_{12}(s), which concludes the rhombohedral structure of Er_6UO_{12}.

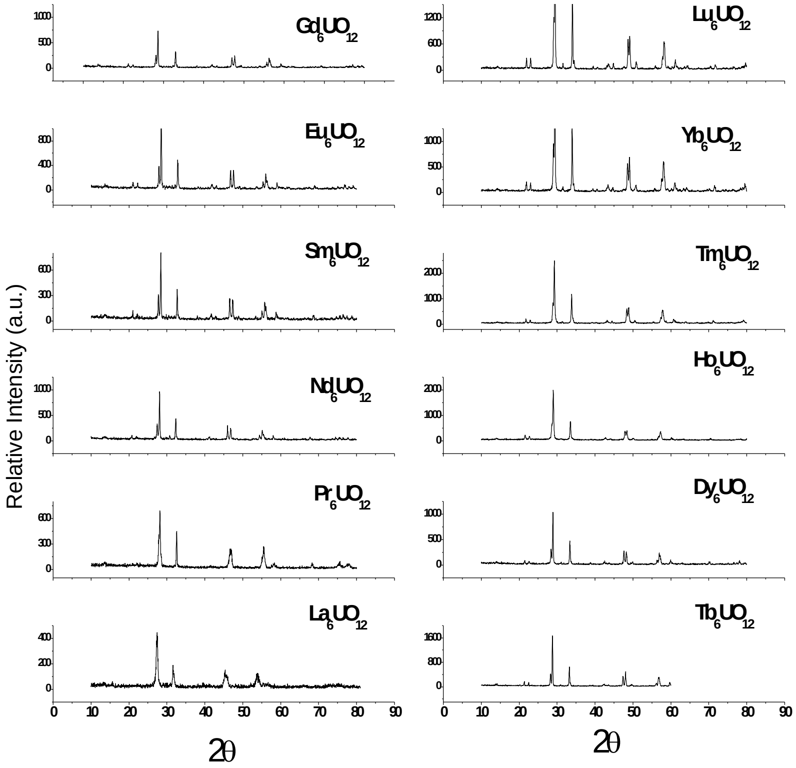

Fig.3.1. XRD pattern of RE_6UO_{12}(s) (RE = La, Pr, Nd, Sm, Eu, Gd, Tb, Dy, Ho, Tm, Yb, Lu)

The comparison between the XRD pattern of Er_6UO_{12}(s) with that of its nearest neighbor Tm_6UO_{12}(s) is shown in **Fig 3.2** .The patterns were found to be quite similar, hence Er_6UO_{12}(s) was indexed with rhombohedral structure. An asymmetric Rhombohedral structure can be indexed with symmetric hexagonal system, so hexagonal system is preferred for indexing rather the rhombohedral [**164**]. Hence Er_6UO_{12}(s) was indexed in the hexagonal system. The indexing parameters are given in **Table 3.1.** The lattice parameters computed using the programme by Wadhawan **[106]** for RE_6UO_{12}(s) are listed in **Table 3.2** are also in good agreement with the values reported in the literature [**13, 14, 18, 153-163**]. The lattice parameter values also suggest that the RE_6UO_{12}(s) compounds formed are stoichiometric.

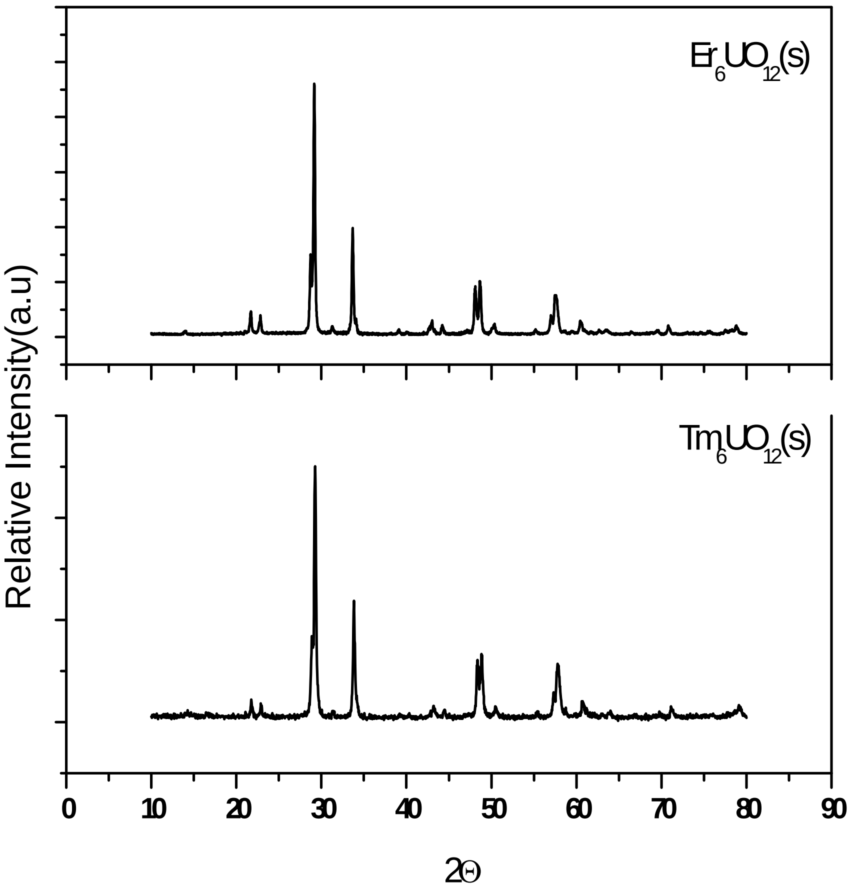

Fig 3.2.The X-ray Diffraction Patterns of $Er_6UO_{12}(s)$ and $Tm_6UO_{12}(s)$

Table 3.1. X-ray powder diffraction data of Er_6UO_{12}(s).

LINE	$2\theta_{obs}$	$2\theta_{cal}$	$\Delta 2\theta$	d_{obs}	d_{calc}	Δd	(*h k l*)	I/I_O
1	14.040	14.039	0.001	6.303	6.303	-0.001	(1 0 1)	2
2	21.720	21.722	-0.002	4.088	4.088	0.000	(1 0 2)	10
3	22.820	22.828	-0.008	3.894	3.892	0.001	(2 0 1)	9
4	28.760	28.769	-0.009	3.102	3.101	0.001	(0 0 3)	33
5	29.160	29.165	-0.005	3.060	3.059	0.001	(2 1 1)	100
6	31.260	31.281	-0.021	2.859	2.857	0.002	(3 0 0)	4
7	33.690	33.688	0.002	2.658	2.658	0.000	(2 1 2)	43
8	39.110	39.077	0.033	2.301	2.303	-0.002	(3 1 1)	3
9	43.020	43.013	0.007	2.101	2.101	0.000	(3 0 3)	7
10	44.240	44.279	-0.039	2.046	2.044	0.002	(2 0 4)	5
11	48.130	48.126	0.004	1.889	1.889	0.000	(2 1 4)	20
12	48.620	48.639	-0.019	1.871	1.870	0.001	(4 1 0)	22
13	50.350	50.339	0.011	1.811	1.811	0.000	(3 2 2)	5
14	55.180	55.209	-0.029	1.663	1.662	0.001	(3 1 4)	3
15	57.080	57.039	0.041	1.612	1.613	-0.001	(2 1 5)	9
16	57.540	57.495	0.045	1.600	1.602	-0.001	(4 1 3)	17
17	60.440	60.470	-0.030	1.530	1.530	0.001	(4 2 2)	7
18	70.810	70.835	-0.025	1.330	1.329	0.000	(4 2 4)	5
19	78.770	78.766	0.004	1.214	1.214	0.000	(5 3 1)	5

Table 3.2: Crystal data for the RE_6UO_{12}(s) (RE=La, Pr, Nd, Sm, Eu, Gd, Tb, Dy, Ho, Er, Tm, Yb, Lu) measured by XRD

Hexagonal Lattice parameters	**La_6UO_{12}**		**Pr_6UO_{12}**		**Nd_6UO_{12}**		**Sm_6UO_{12}**		**Eu_6UO_{12}**	
	Present study	**Literature [153]**	**Present study**	**Literature [154]**	**Present study**	**Literature [155]**	**Present study**	**Literature [156]**	**Present study**	**Literature [157]**
a /Å	10.4896(11)	10.46	10.2972(1)	10.30	10.2554(1)	10.25	10.1453(2)	10.14	10.1181(2)	10.128
c/Å	9.9976((12)	9.982	9.804(3)	9.8	9.7431(19)	9.748	9.6471(72)	9.63	9.5905(2)	9.60
V/Å^3	952.65	947.27	900.24	900.57	887.40	887.63	859.89	858.85	850.27	852.6
Z	3	3	3	3	3	3	3	3	3	3
ρ/g cm^{-3}	6.606	6.644	7.057	7.055	7.272	7.27	7.718	7.728	7.861	7.835
Hexagonal Lattice parameters	**Gd_6UO_{12}**		**Tb_6UO_{12}**		**Dy_6UO_{12}**		**Ho_6UO_{12}**		**Tm_6UO_{12}**	
	Present study	**Literature [158]**	**Present study**	**Literature [159]**	**Present study**	**Literature [157]**	**Present study**	**Literature [160]**	**Present study**	**Literature [161]**
a /Å	10.077	10.07	10.006(12)	10.01	9.9756(18)	9.9806(7)	9.9325(1)	9.935	9.856	9.853
c/Å	9.527	9.529	9.458 (3)	9.465	9.3994(5)	9.4403(8)	9.3668(2)	9.368	9.2798	9.283
V/Å^3	837.79	837.83	820.05 (33)	821.83	810.02(58)	814.4(1)	800.25	800.78	780.65	780.47
Z	3	3	3	3	3	3	3	3	3	3
ρ/g cm^{-3}	8.166	8.167	8.404	8.387	8.640	8.591	8.836	8.831	9.211	9.214
	Yb_6UO_{12}		**Lu_6UO_{12}**		**Er_6UO_{12}**					
Hexagonal Lattice parameters	**Present study**	**Literature [162]**	**Present study**	**Literature [163]**	**Present study**			**Literature**		
a /Å	9.8224	9.826	9.7976	9.797	9.8975(11)		**Not available in literature**			
c/Å	9.2288	9.248	9.1858	9.204	9.3021(2)					
V/Å^3	771.08	773.27	763.61	465.06	789.13					
Z	3	3	3	3	3					
ρ/g cm^{-3}	9.485	9.459	9.653	9.797	9.049					

The lattice parameters (*a* & c) and unit cell volume (*V*) at room temperature were plotted as function of ionic radii of rare earth ion (RE^{+3}) in hexa coordination taken from Shanon et al **[165]**. The data were best fitted to linear equation as shown in **Fig 3.3** and given in equations **3.1-3.3.**

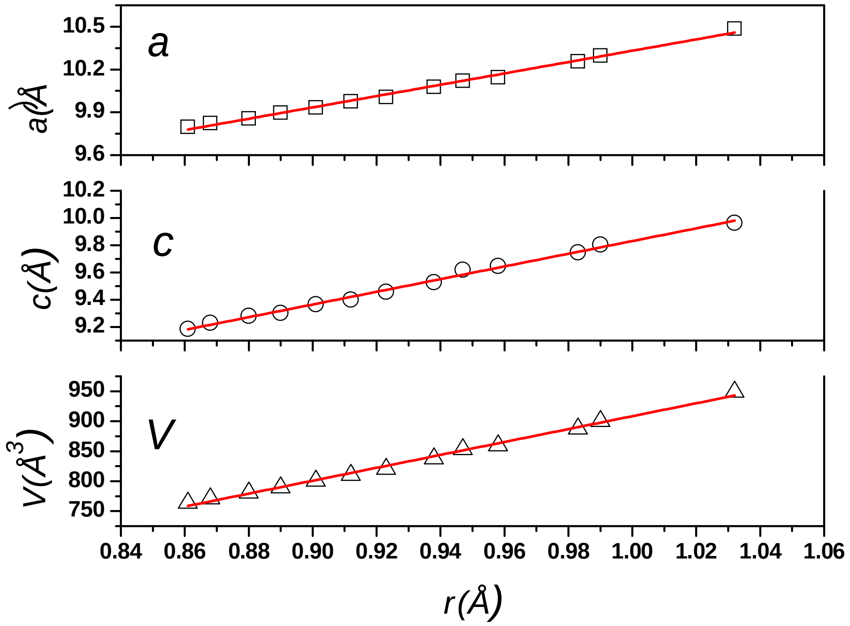

Fig.3.3. The plot of room temperature lattice parameters (*a* &c) and unit cell volume (*V*) of RE_6UO_{12} (s) as a function of ionic raddi of rare earth ions (RE^{+3}).

$$a(\text{Å}) = 6.3597 + 3.9717 \times r((\text{Å})) \qquad (3.1)$$

$$c(\text{Å}) = 5.1729 + 4.6579 \times r((\text{Å})) \qquad (3.2)$$

$$V\left(Å^3\right) = -168.1982 + 1076.595 \times r((Å)) \qquad (3.3)$$

3.2.2. Thermal expansion using HT-XRD

The axial thermal expansion measurements of RE_6UO_{12}(s) (RE = La, Pr, Sm, Eu, Gd, Tb, Dy, Ho, Er, Tm, Yb, Lu) was carried out using Stoe diffractometer under vacuum (10^{-8} Pa) using HDK-2.4 Buhler high temperature attachment. The XRD data were collected in the temperature range of 298–1,273 K. The detailed experimental procedure and about the instrument is described in section 2.4.1.2.1. The sample was heated at an interval of 100 K and equilibrated for 15 min at each temperature before XRD measurement. A typical XRD pattern of Sm_6UO_{12}(s) at various temperatures is given in **Fig.3.4.** The peaks at 40.25

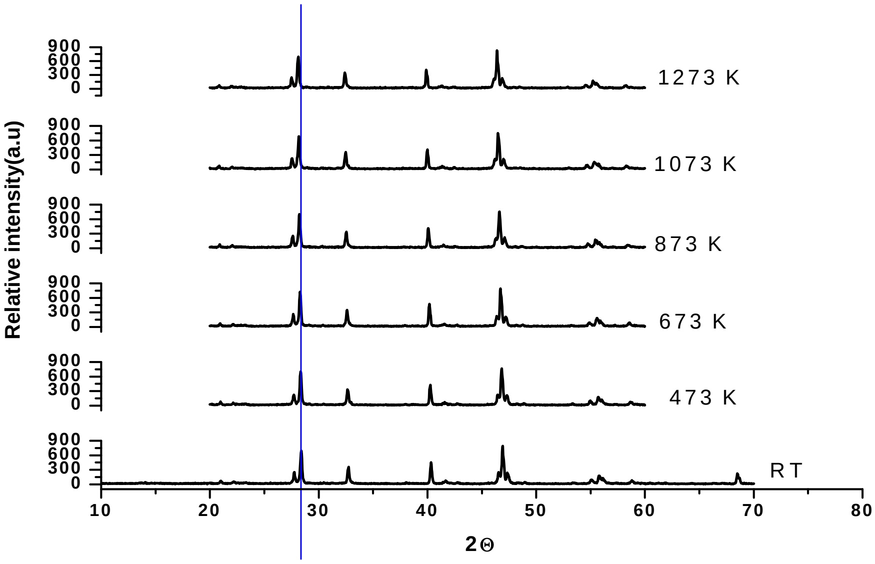

Fig.3.4. The high temperature XRD patterns of Sm_6UO_{12}(s).

and 46.86 were due to the Pt-Rh alloy heater used for the heating. The hexagonal lattice parameters of RE_6UO_{12}(s) were calculated from diffraction angles and the miller indices at different temperatures. The cell volume for this hexagonal system was computed by the expression $V = \sqrt{3}/2(a^2c)$. The density of RE_6UO_{12}(s) were calculated at different temperature using eqn. 2.4, taking the number of molecule in the unit cell as 3 from the unit cell data reported in the literature [**13, 14, 18, 153-163**]. The measured lattice parameters (*a* and *c*), unit cell volume (*V*) and density at different temperatures are given in **Table 3.3-3.6** and also shown in **Figs.3.5-3.8.** . The lattice parameters and unit cell volume, thus calculated were fitted against temperature (in Kelvin) to the polynomial expression: $l = x + yT + zT^2$. The coefficients of polynomial fitting for the axes (*a* and *c*) and volume (*V*) are given in **Table 3.7.** The axial expansion coefficient, average expansion coefficient, α_{ave}, and percentage expansion along axes and of unit cell volume were calculated using eqns. **2.13, 2.14** and **2.15**, respectively. The instantaneous thermal expansion coefficient along axes (*a* and *c*) and of unit cell volume are also given in **Table 3.3-3.6.**

The percentage variation in lattice parameters and unit cell volume were also computed and plotted against atomic number of rare earth element in **Figs 3.9-3.11.**

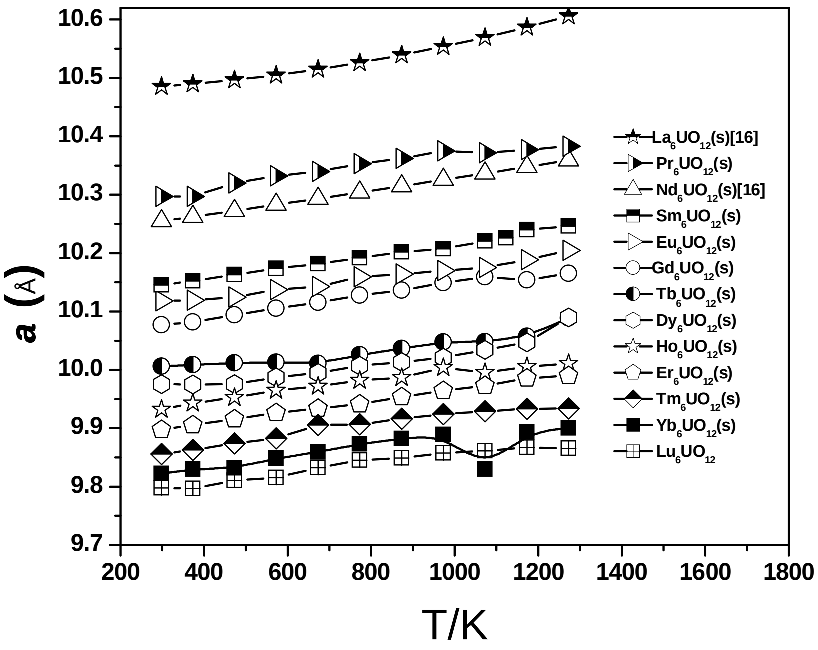

Fig.3.5. The lattice parameters along *a*- axis as a function of temperature for RE_6UO_{12}(s)(RE= La, Pr, Nd, Sm, Eu, Gd, Tb, Dy, Ho, Er, Tm, Yb, Lu).

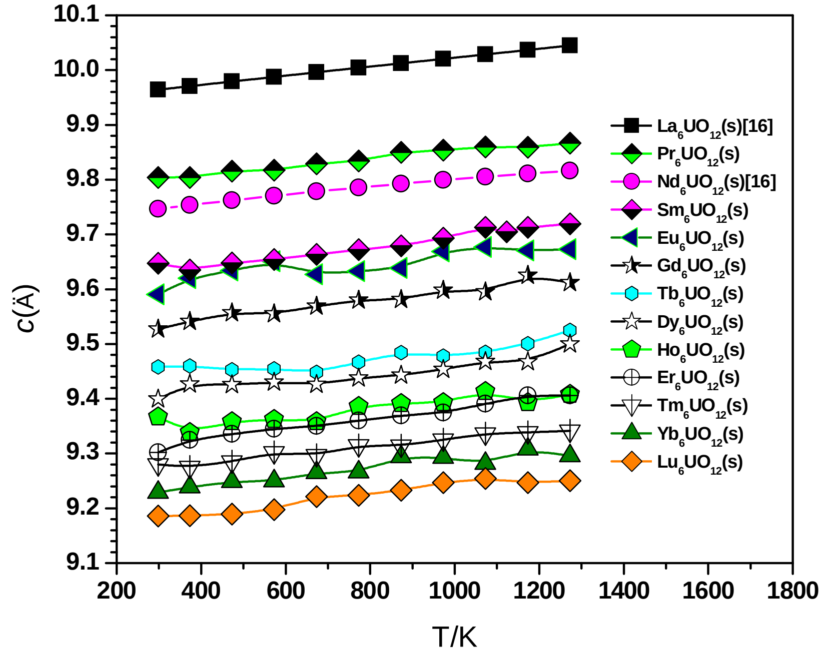

Fig.3.6. The lattice parameters along *c*- axis as a function of temperature for RE_6UO_{12}(s)(RE= La,Pr, Nd, Sm, Eu, Gd, Tb, Dy, Ho, Er, Tm, Yb, Lu).

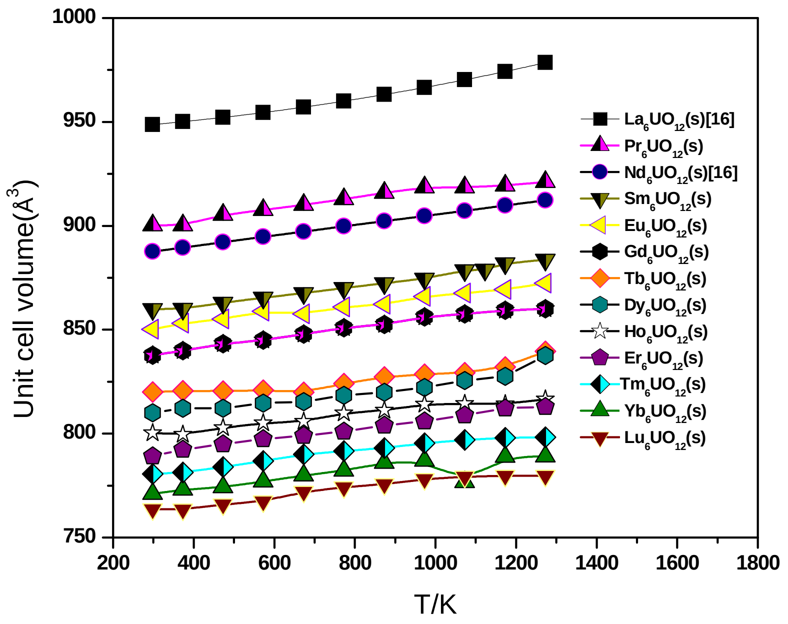

Fig.3.7. The unit cell volume as function of temperature for RE_6UO_{12}(s) (RE= La,Pr, Nd, Sm, Eu, Gd, Tb, Dy, Ho, Er, Tm, Yb, Lu).

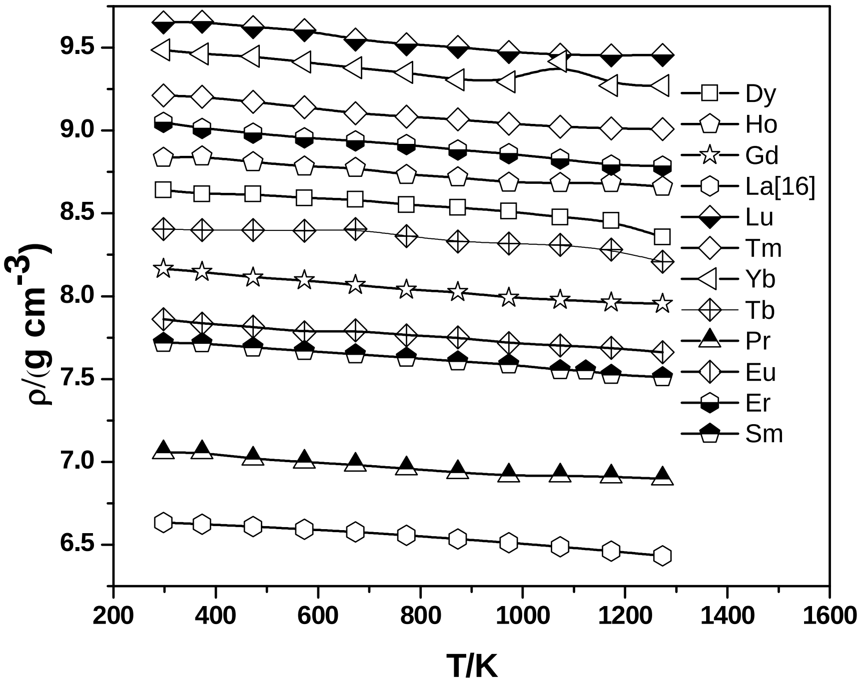

Fig.3.8. The density as function of temperature for RE_6UO_{12}(s)(RE= La,Pr, Nd, Sm, Eu, Gd, Tb, Dy, Ho, Er, Tm, Yb, Lu).

Table 3.3. The lattice parameters (a and c), volume (V), density (ρ), linear (α_a and α_c) and volume (α_V) thermal expansion coefficients of RE_6UO_{12}(s) (RE = Pr, Sm, Eu and Gd) at various temperature in the range 298-1273 K.

	Pr_6UO_{12}(s)							**Sm_6UO_{12}(s)**						
T/K	a /Å	c /Å	V /Å^3	ρ/ g cm^{-3}	α_a /10^{-6}K^{-1}	α_c / 10^{-6}K^{-1}	α_V /10^{-6}K^{-1}	a /Å	c /Å	V /Å^3	ρ /g cm^{-3}	α_a /10^{-6}K^{-1}	α_c / 10^{-6}K^{-1}	α_V / 10^{-6}K^{-1}
298	10.2972	9.8041	900.37	7.057	0.00	1.77	1.77	10.1453	9.6471	859.89	7.718	9.46	-16.70	2.18
373	10.3104	9.8054	905.31	7.056	11.12	6.03	28.32	10.1525	9.635	860.03	7.717	9.96	-1.68	18.20
473	10.3201	9.8155	907.59	7.018	16.99	6.02	40.11	10.1631	9.6479	862.98	7.691	10.50	10.10	31.20
573	10.3322	9.8172	910.03	7.000	9.61	6.83	26.20	10.1738	9.6545	865.39	7.669	9.22	8.19	26.70
673	10.3399	9.8289	912.86	6.982	10.20	8.67	29.27	10.1818	9.6637	867.58	7.650	8.87	9.23	27.10
773	10.3532	9.8342	915.92	6.960	10.88	10.70	32.71	10.1918	9.6723	870.06	7.628	9.86	8.09	28.00
873	10.3623	9.8498	918.56	6.937	10.59	10.10	31.62	10.2018	9.6793	872.40	7.608	7.59	10.90	26.30
973	10.3750	9.8540	918.49	6.917	4.47	5.15	14.26	10.2072	9.6933	874.59	7.589	9.31	17.40	36.40
1073	10.3715	9.8599	919.42	6.917	1.02	2.70	4.81	10.2207	9.7128	878.67	7.554	12.00	1.61	25.90
1173	10.3771	9.8593	921.15	6.910	5.54	3.52	14.80	10.2396	9.7126	881.90	7.552	18.60	-0.21	37.60
1273	10.3829	9.8668	900.37	6.897	5.63	7.65	19.19	10.2464	9.7194	883.69	7.526	16.70	11.80	45.90
	Eu_6UO_{12}(s)							**Gd_6UO_{12}(s)**						
298	10.1181	9.5905	850.27	7.861	1.45	41.30	44.20	10.077	9.527	837.79	8.17	6.62	19.60	32.80
373	10.1192	9.6202	853.09	7.835	3.29	27.80	34.40	10.082	9.541	839.86	8.15	9.26	18.20	36.80
473	10.1244	9.6339	855.18	7.816	8.99	15.90	34.00	10.094	9.557	843.27	8.11	11.50	7.35	30.50
573	10.1374	9.6507	858.87	7.782	8.94	-3.70	14.30	10.105	9.555	844.96	8.10	10.70	6.30	28.00
673	10.1425	9.6268	857.61	7.793	10.80	-9.38	12.30	10.116	9.569	847.95	8.07	11.10	13.10	35.70
773	10.1592	9.6327	860.96	7.763	10.50	6.10	27.40	10.128	9.580	850.94	8.04	10.20	6.30	26.90
873	10.1638	9.6385	862.26	7.751	5.34	18.90	29.80	10.136	9.581	852.47	8.03	10.70	9.45	31.20
973	10.17	9.6689	866.04	7.718	5.68	20.00	31.70	10.149	9.598	856.16	7.99	11.30	7.35	30.40
1073	10.1753	9.6769	867.66	7.703	9.24	0.94	19.70	10.159	9.595	857.56	7.98	2.25	14.20	18.90
1173	10.1887	9.6707	869.39	7.688	14.60	-2.03	27.60	10.154	9.625	859.33	7.96	2.98	8.92	15.10
1273	10.2048	9.673	872.34	7.662	15.90	2.40	34.80	10.165	9.612	860.09	7.95	11.30	-13.60	9.08

Table 3.4. The lattice parameters (*a* and *c*), volume (*V*), density (ρ), linear (α_a and α_c) and volume (α_V) thermal expansion coefficients of $RE_6UO_{12}(s)$ (RE = Tb,Dy, Ho, Er) at various temperature in the range 298-1273 K.

	$Tb_6UO_{12}(s)$							**$Dy_6UO_{12}(s)$**						
T/K	*a* /Å	*c* /Å	*V* /$Å^3$	*ρ* /g cm^{-3}	α_a /$10^{-6}K^{-1}$	α_c / $10^{-6}K^{-1}$	α_V /$10^{-6}K^{-1}$	*a* /Å	*c* /Å	*V* /$Å^3$	*ρ* /g cm^{-3}	α_a /$10^{-6}K^{-1}$	α_c / $10^{-6}K^{-1}$	α_V / $10^{-6}K^{-1}$
298	10.006	9.458	820.05	8.404	3.47	2.40	-52.14	9.9756	9.3994	810.02	8.640	-0.94	38.73	36.85
373	10.0086	9.4597	820.62	8.398	3.28	-2.45	-26.62	9.9749	9.4267	812.26	8.616	-0.12	18.72	18.49
473	10.0117	9.4528	820.53	8.399	2.20	-2.80	1.59	9.9756	9.4255	812.27	8.616	6.32	2.02	14.70
573	10.013	9.4544	820.88	8.396	-0.60	-2.54	-3.74	9.9875	9.4305	814.64	8.591	9.47	0.32	19.34
673	10.0105	9.448	819.92	8.406	6.35	6.66	19.39	9.9945	9.4261	815.40	8.583	9.82	3.83	23.61
773	10.0257	9.467	824.06	8.363	13.04	19.08	45.30	10.0071	9.4377	818.47	8.551	9.47	8.99	28.11
873	10.0366	9.4841	827.35	8.330	10.84	5.82	27.64	10.0134	9.443	819.96	8.536	7.02	8.51	22.73
973	10.0474	9.478	828.59	8.318	5.75	0.42	11.99	10.0211	9.4537	822.15	8.513	10.53	13.41	34.82
1073	10.0481	9.4849	829.31	8.310	4.85	11.79	21.67	10.0344	9.4682	825.60	8.477	13.08	7.29	33.86
1173	10.0571	9.5003	832.15	8.282	20.29	21.20	62.50	10.0472	9.4674	827.63	8.456	27.77	16.97	73.79
1273	10.0887	9.525	839.56	8.209	31.58	26.12	90.42	10.0898	9.5001	837.55	8.356	42.70	34.79	122.40
	$Ho_6UO_{12}(s)$							**$Er_6UO_{12}(s)$**						
298	9.9325	9.3668	800.25	8.836	14.20	-40.30	-11.90	9.8975	9.3021	789.13	9.013	10.60	32.40	53.70
373	9.9431	9.3385	799.54	8.844	11.80	-9.63	14.00	9.9054	9.3247	792.31	8.984	10.60	21.90	43.30
473	9.9524	9.3582	802.72	8.809	11.00	12.60	34.60	9.9159	9.3354	794.90	8.955	10.60	11.00	32.30
573	9.9649	9.3621	805.08	8.784	9.77	0.00	19.60	9.9264	9.3451	797.42	8.937	9.04	7.79	26.10
673	9.9718	9.3582	805.86	8.775	8.51	12.80	30.00	9.9338	9.3499	799.02	8.914	7.53	7.90	23.20
773	9.9818	9.3860	809.87	8.732	7.60	17.60	33.10	9.9413	9.3598	801.07	8.883	10.10	10.50	31.00
873	9.9869	9.3912	811.15	8.718	11.10	3.79	26.30	9.9537	9.3695	803.90	8.859	11.60	7.90	31.50
973	10.0039	9.3931	814.08	8.686	4.13	11.80	20.30	9.9643	9.3745	806.05	8.828	9.80	11.60	31.60
1073	9.9951	9.4133	814.39	8.683	0.65	-0.11	1.21	9.9731	9.3910	808.89	8.792	10.70	17.00	39.00
1173	10.0052	9.3929	814.27	8.684	7.95	-2.72	13.30	9.9855	9.4061	812.21	8.785	8.59	7.85	25.50
1273	10.0109	9.4082	816.53	8.660	5.74	16.30	28.20	9.9901	9.4056	812.91	9.013	4.65	-0.54	8.94

Table 3.5. The lattice parameters (*a* and *c*), volume (*V*), density (ρ), linear (α_a and α_c) and volume (α_V) thermal expansion coefficients of RE_6UO_{12}(s) (RE = Tm & Yb) at various temperature in the range 298-1273 K.

	Tm_6UO_{12}(s)							**Yb_6UO_{12}(s)**						
***T*/K**	***a*** **/Å**	***c*** **/Å**	***V*** **/$Å^3$**	***ρ*** **/g cm^{-3}**	**α_a /$10^{-6}K^{-1}$**	**α_c / $10^{-6}K^{-1}$**	**α_V /$10^{-6}K^{-1}$**	***a*** **/Å**	***c*** **/Å**	***V*** **/$Å^3$**	***ρ*** **/g cm^{-3}**	**α_a /$10^{-6}K^{-1}$**	**α_c / $10^{-6}K^{-1}$**	**α_V / $10^{-6}K^{-1}$**
298	9.856	9.279	780.6	9.206	9.06	-6.32	11.80	9.822	9.228	771.0	9.485	9.77	14.3	33.87
373	9.862	9.275	781.3	9.203	10.40	2.01	22.80	9.829	9.238	773.0	9.461	6.11	12.52	24.76
473	9.874	9.285	783.9	9.173	10.20	14.30	34.80	9.832	9.248	774.2	9.446	9.52	6.12	25.25
573	9.882	9.302	786.7	9.140	15.80	6.47	38.30	9.848	9.25	776.9	9.414	13.79	8.67	36.44
673	9.905	9.297	789.9	9.103	12.10	6.95	31.30	9.859	9.264	779.8	9.378	12.62	8.61	34.11
773	9.906	9.314	791.6	9.083	5.38	9.16	20.10	9.873	9.265	782.1	9.350	11.76	15.82	39.74
873	9.916	9.314	793.1	9.067	8.83	5.50	23.40	9.882	9.293	785.9	9.305	8.09	14.52	31.07
973	9.924	9.325	795.3	9.042	6.49	11.90	25.20	9.889	9.292	786.9	9.293	-26.78	-6.66	-60.78
107	9.928	9.336	797.0	9.022	4.67	7.11	16.70	9.829	9.281	776.6	9.417	2.14	8.18	12.63
117	9.933	9.338	797.9	9.012	2.54	3.02	8.21	9.893	9.307	788.9	9.271	35.84	7.69	80.21
127	9.933	9.341	798.3	9.008	0.61	3.56	4.85	9.9	9.295	788.9	9.270	6.92	-13.11	0.75

Table 3.6. Lattice parameters (*a* and *c*), volume (*V*), density (ρ), linear (α_a and α_c) and volume (α_V) thermal expansion coefficient of $Lu_6UO_{12}(s)$ at various temperature in the range 298–1,273 K.

	$Lu_6UO_{12}(s)$						
T/K	*a* /Å	*c* /Å	*V* /Å^3	*ρ* /g cm^{-3}	α_a /10^{-6}K^{-1}	α_c / 10^{-6}K^{-1}	α_V /10^{-6}K^{-1}
298	9.7976	9.1858	763.61	9.606	-1.63	0.58	-2.68
373	9.7964	9.1862	763.46	9.548	6.48	1.87	14.85
473	9.8107	9.1891	765.93	9.520	9.75	6.04	25.58
573	9.8155	9.1973	767.37	9.504	11.02	17.53	39.76
673	9.8323	9.2213	772.01	9.473	15.31	14.32	45.22
773	9.8455	9.2236	774.27	9.458	8.57	6.32	23.67
873	9.8491	9.2329	775.62	9.454	6.18	12.52	25.10
973	9.8576	9.2466	778.11	9.454	6.18	11.76	24.40
1073	9.8612	9.2545	779.35	9.606	4.95	0.22	10.25
1173	9.8673	9.2470	779.68	9.548	2.19	-2.29	2.13
1273	9.8655	9.2503	779.67	9.520	-1.84	3.59	-0.08

Table 3.7. Polynomial Fitting parameters of lattice parameters (*a*, c) and the unit cell volume of RE_6UO_{12}(s) as function of temperature in the temperature range 298-1273 K.

	***a*(Å)**			***c* (Å)**			**Unit cell volume(Å^3)**		
Compound	**A**	**B $\times 10^5$**	**C $\times 10^8$**	**A**	**B $\times 10^5$**	**C $\times 10^8$**	**A**	**B $\times 10^3$**	**C $\times 10^6$**
La_6UO_{12}(s) [16]	10.477	0.567	7.506	9.938	8.832	-0.338	944.776	9.040	13.698
Pr_6UO_{12}(s)	10.238	20.417	-7.138	9.772	9.775	-1.771	886.918	44.77	-14.054
Nd_6UO_{12} (s) [16]	10.226	9.495	0.757	9.717	10.590	-2.207	879.952	25.960	-0.476
Sm_6UO_{12}(s) [This study]	10.123	7.351	1.802	9.624	3.721	3.239	854.192	15.54	6.234
Sm_6UO_{12}(s) [16]	10.126	12.85	-1.471	9.61	11.03	-2.17	853.298	31.61	-4.246
Eu_6UO_{12}(s)	10.097	5.724	1.942	9.573	11.718	-2.872	845.190	19.880	0.918
Gd_6UO_{12}(s)	10.031	15.581	-3.919	9.497	12.022	-1.980	827.418	36.510	-8.134
Tb_6UO_{12}(s)	10.017	-5.585	8.377	9.480	-10.697	10.866	823.888	-18.73	23.416
Dy_6UO_{12}(s) [This study]	9.985	-6.214	10.620	9.411	-0.951	5.655	812.709	-11.450	22.613
Dy_6UO_{12}(s) [19]	9.975	1.909	3.059	9.440	1.39	1.89	813.411	4.21	6.746
Ho_6UO_{12}(s)	9.891	15.403	-4.805	9.332	5.583	0.485	790.644	29.600	-7.261
Er_6UO_{12}(s)	9.869	9.836	-0.113	9.275	12.516	-1.623	782.242	26.190	-1.321
Tm_6UO_{12}(s)	9.804	18.391	-6.327	9.250	8.439	-0.825	769.863	36.290	-10.656
Yb_6UO_{12}(s) (298-973 K)	9.793	9.051	1.155	9.212	5.264	3.427	765.068	18.4	4.968
Lu_6UO_{12}(s)	9.748	15.952	-5.064	9.138	14.499	-4.149	751.855	37.010	-11.313

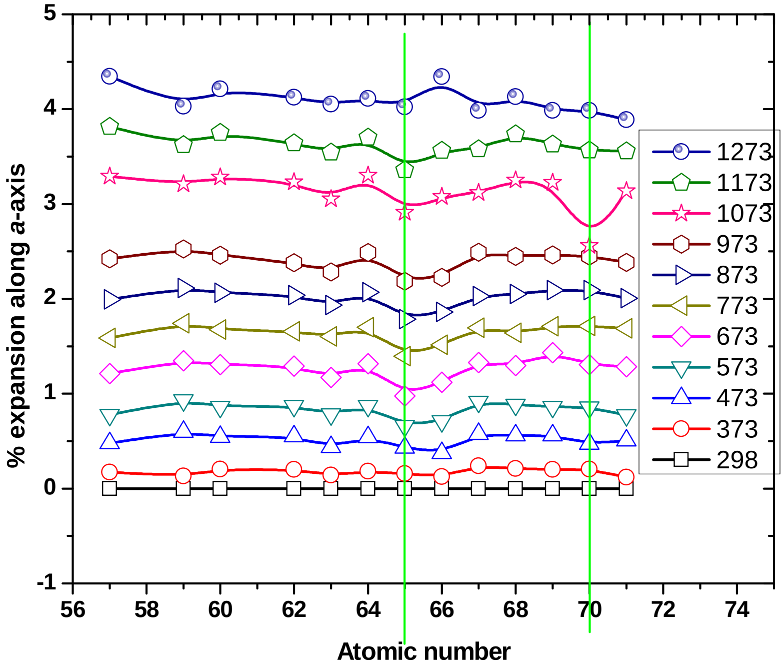

Fig.3.9. The percentage variation of lattice parameter along *a*- axis as a function of temperature for RE_6UO_{12}(s)(RE= La,Pr, Nd, Sm, Eu, Gd, Tb, Dy, Ho, Er, Tm, Yb, Lu).

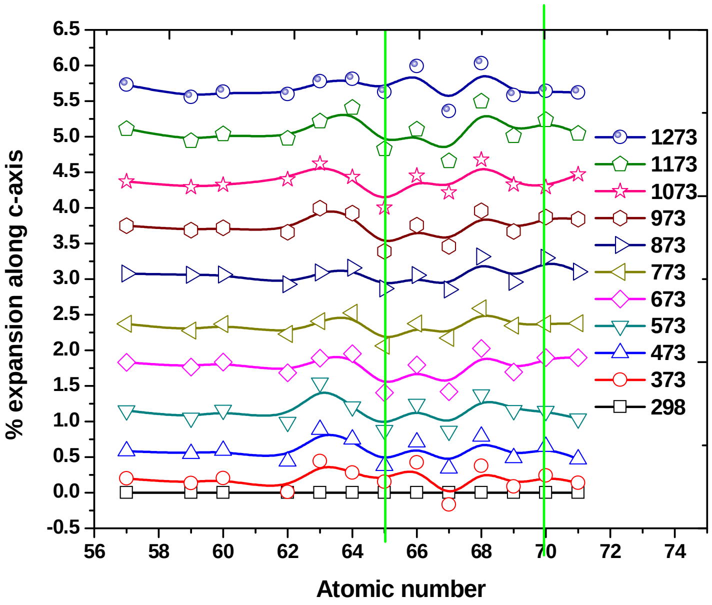

Fig.3.10. The percentage variation of lattice parameter along *c*- axis as a function of temperature for RE_6UO_{12}(s)(RE= La, Pr, Nd, Sm, Eu, Gd, Tb, Dy, Ho, Er, Tm, Yb, Lu).

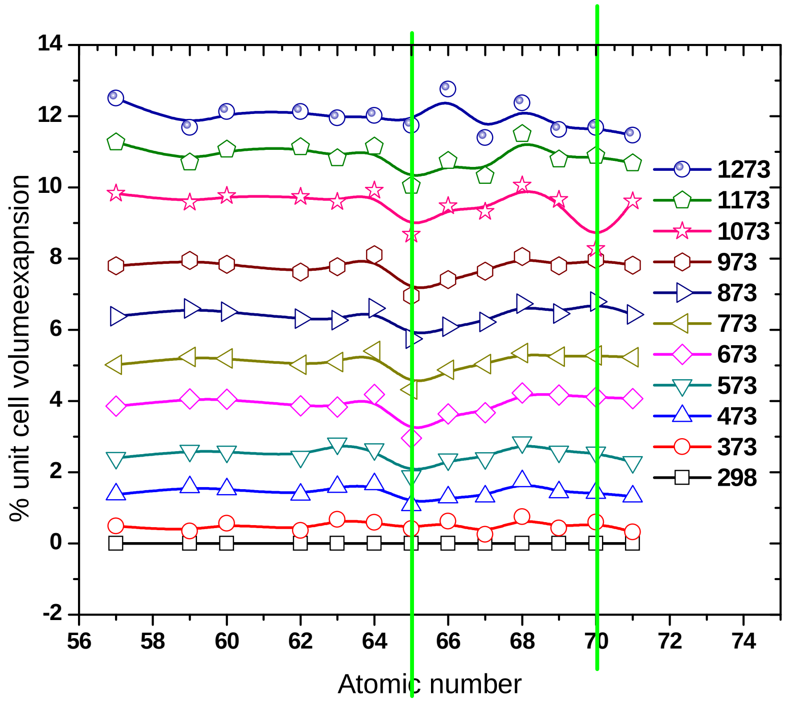

Fig.3.11. The percentage variation of unit cell volume as a function of temperature for RE_6UO_{12}(s) (RE= La,Pr, Nd, Sm, Eu, Gd, Tb, Dy, Ho, Er, Tm, Yb, Lu).

3.2.3. Heat capacity measurements using DSC

Heat capacity of RE_6UO_{12}(s) (RE= La, Pr, Nd, Sm, Eu, Gd, Tb, Dy, Ho, Er, Tm, Yb, Lu) was measured using DSC. For DSC measurements, the powders of the samples were compacted into pellets of 5 mm diameter and sintered by heating at 1673 K in air for 8 h. The pellet of Pr_6UO_{12}(s) and La_6UO_{12}(s) was sintered in argon atmosphere at 1550 K for 12 h. A heat flux type differential scanning calorimeter (model number DSC823e/700 of M/s. Mettler Toledo GmbH, Switzerland) was used in this study. Pellets were hermetically sealed in 40 µl Al-pans with pin hole on the lid. A thin disc of sapphire was used as the heat capacity standard. A three segment-heating programme was used for heat capacity measurements in the temperature range 298-870 K as discussed in chapter 2. The samples were run in argon atmosphere. The heat capacities of various RE_6UO_{12}(s) along with the additive values calculated using Newmann Kopp's rule and the literature values wherever available are plotted in **Figs.3.12-3.24.** The values taken were the average of 5-6 runs. The percentage deviations from the additive values are also plotted in right Y-axis. The deviations from NK rule move from –ve to +ve in the temperature range 298 to 870 K.

But for RE_6UO_{12}(s) (RE=La, Gd, and Lu), the deviations remain –ve throughout the experimental temperature range.

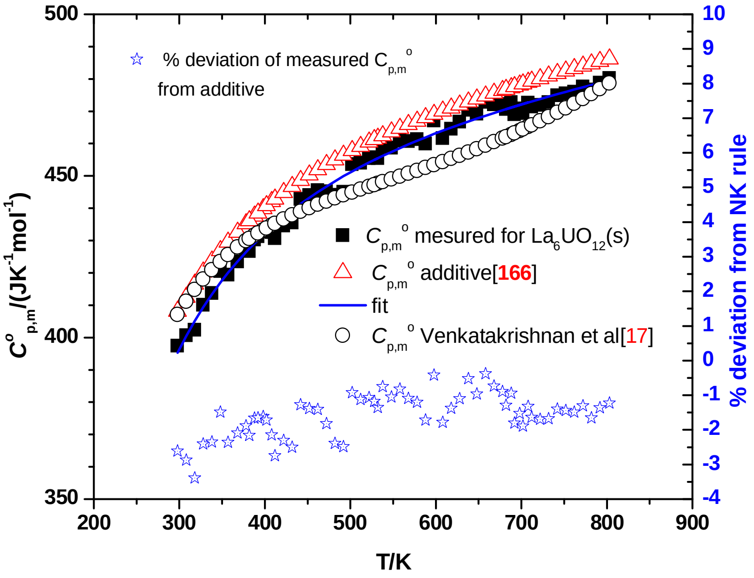

Fig.3.12. The heat capacity of La_6UO_{12}(s) as function of temperature.

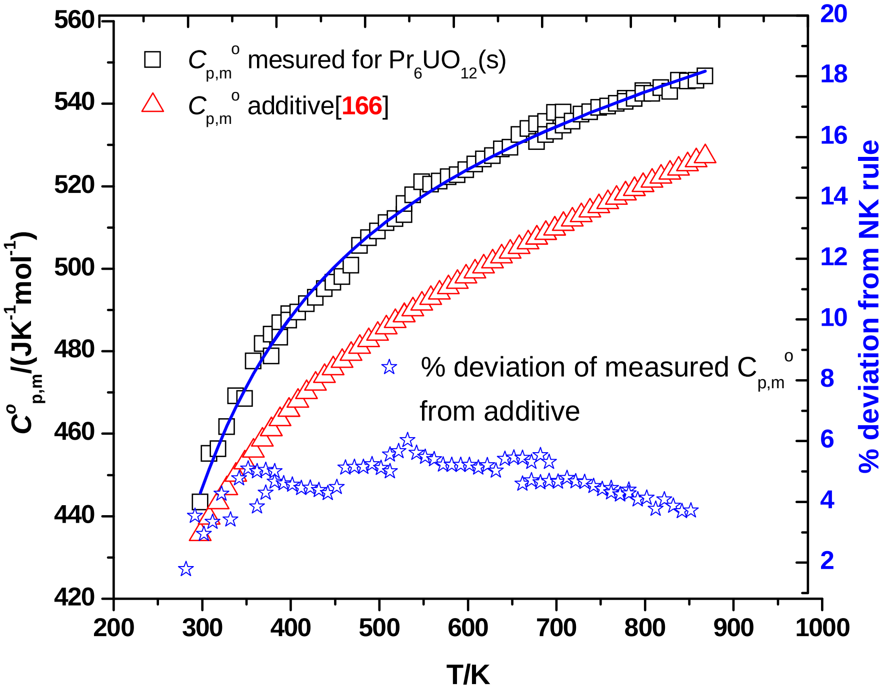

Fig.3.13. The heat capacity of Pr_6UO_{12}(s) as function of temperature.

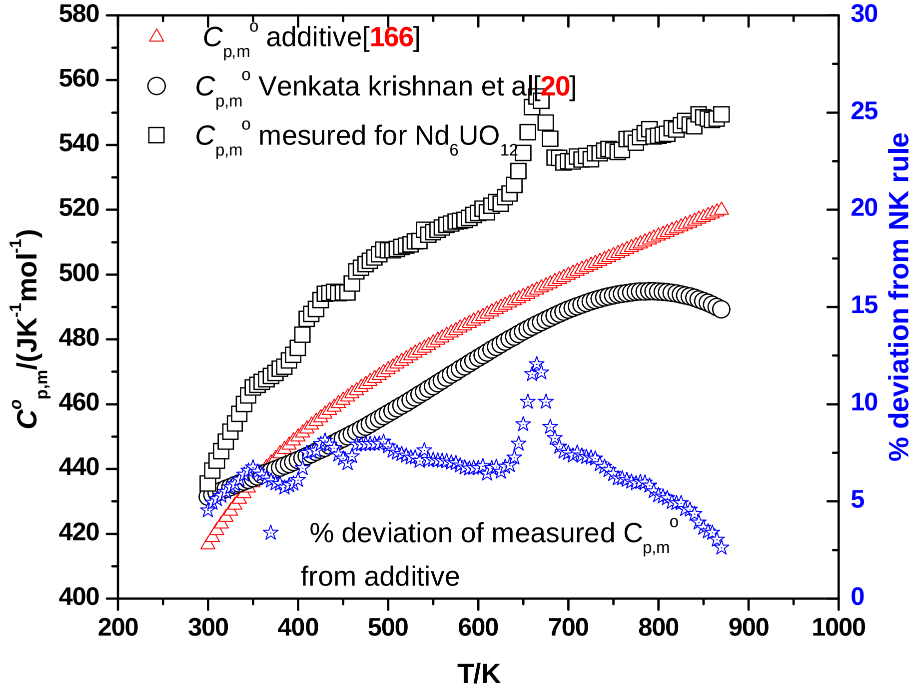

Fig.3.14. The heat capacity of Nd_6UO_{12}(s) as a function of temperature.

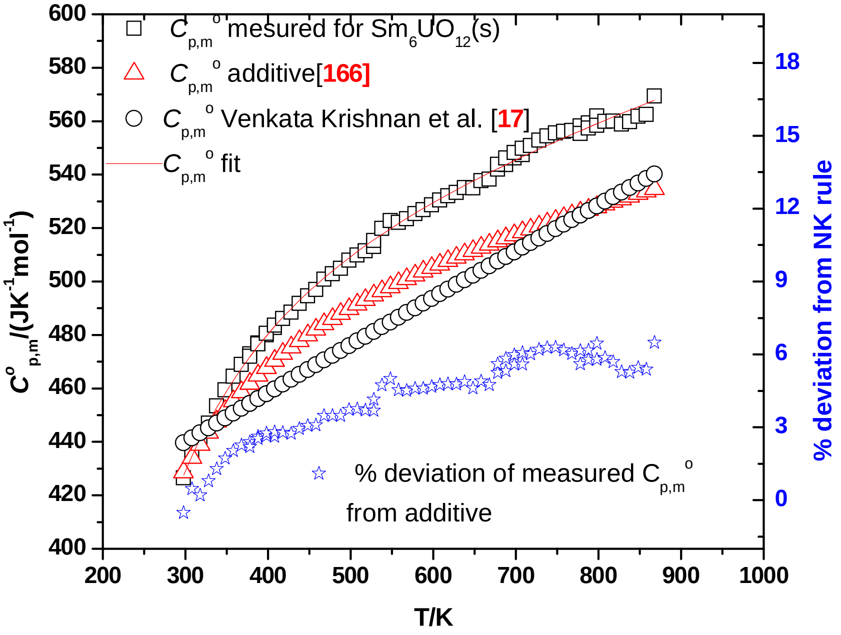

Fig.3.15. The heat capacity of Sm_6UO_{12}(s) as a function of temperature.

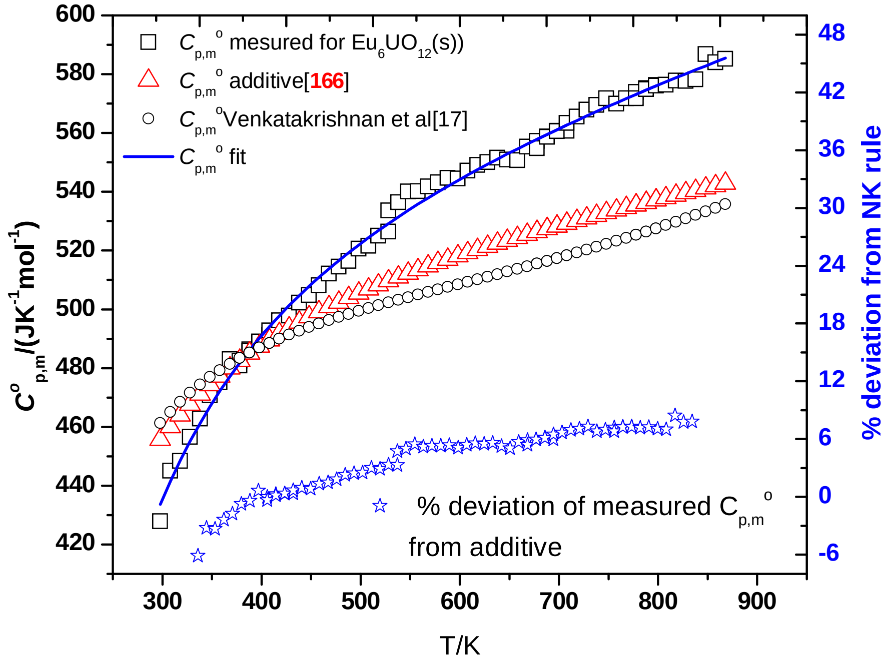

Fig.3.16. The heat capacity of Eu_6UO_{12}(s) as a function of temperature.

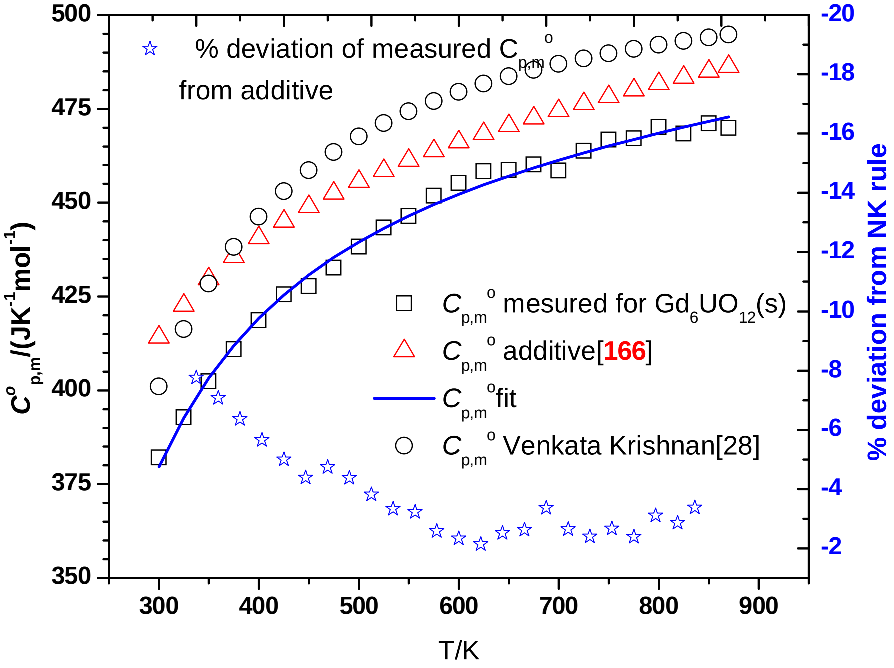

Fig.3.17. The heat capacity of Gd_6UO_{12}(s) as a function of temperature.

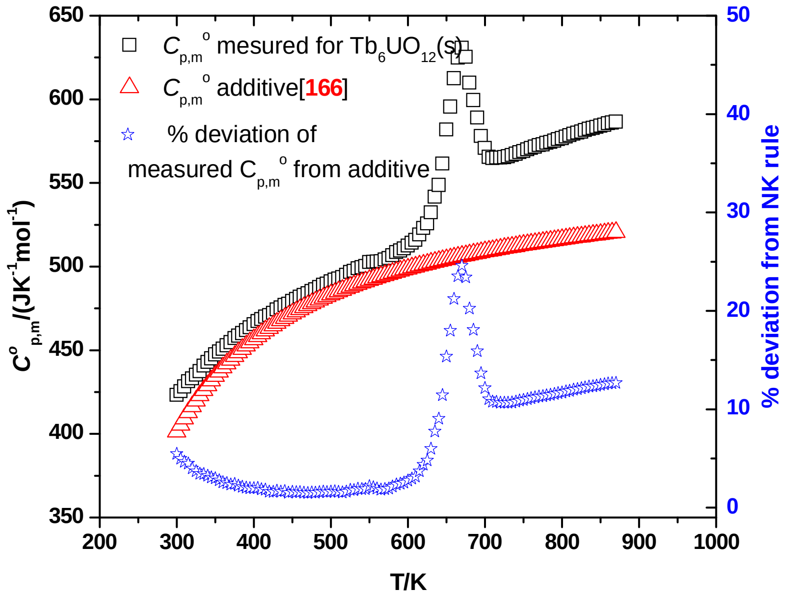

Fig.3.18. The heat capacity of Tb_6UO_{12}(s) as a function of temperature.

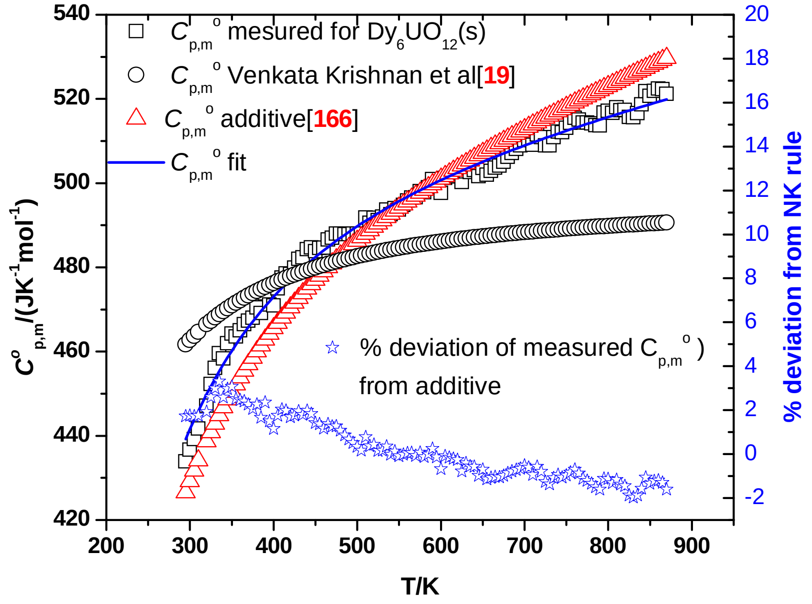

Fig.3.19. The heat capacity of Dy_6UO_{12}(s) as a function of temperature.

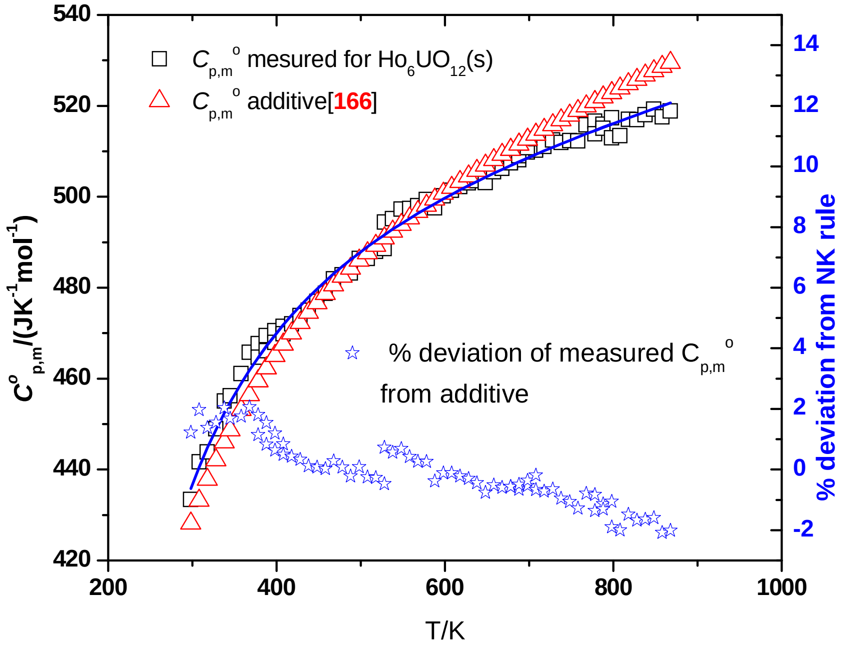

Fig.3.20. The heat capacity of Ho_6UO_{12}(s) as a function of temperature.

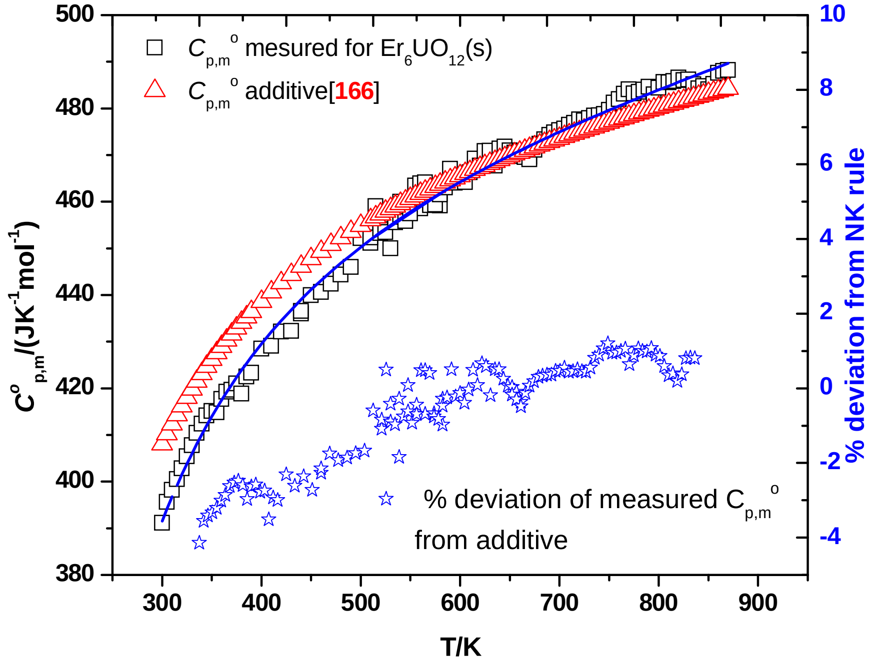

Fig.3.21. The heat capacity of Er_6UO_{12}(s) as a function of temperature.

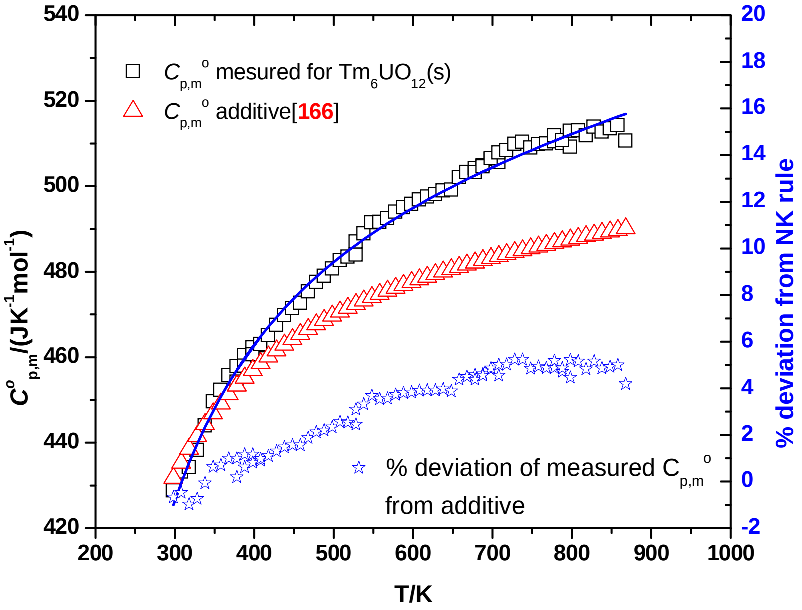

Fig.3.22. The heat capacity of Tm_6UO_{12}(s) as a function of temperature.

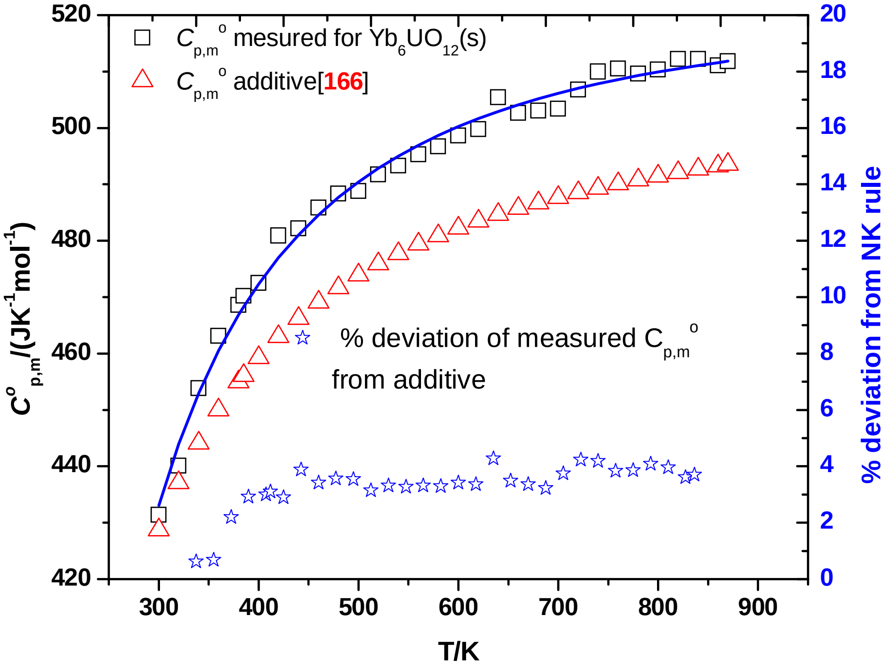

Fig.3.23. The heat capacity of Yb_6UO_{12}(s) as a function of temperature.

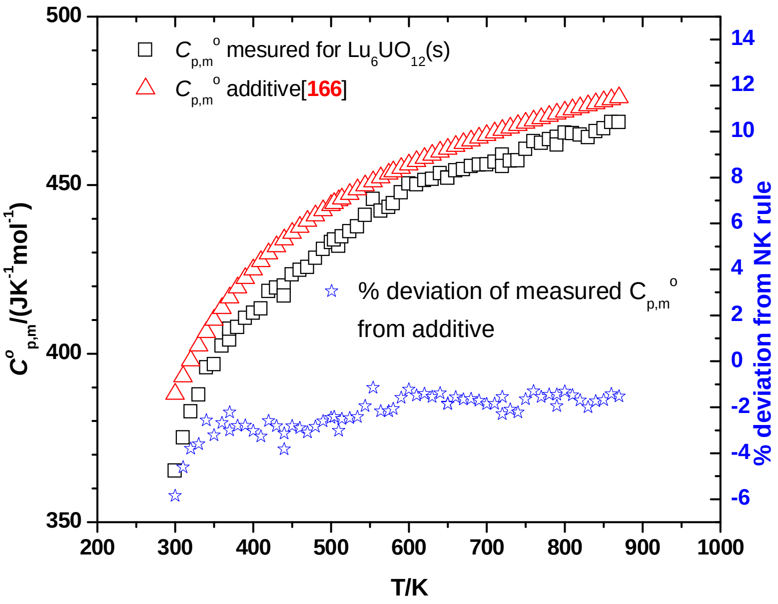

Fig.3.24. The heat capacity of $Lu_6UO_{12}(s)$ as a function of temperature.

The values reported by Venkata Krishnan et al [**17**] also show –ve deviation from additive values for $La_6UO_{12}(s)$ as shown in **Fig.3.12.** The values reported by Venkata Krishnan et al **[20]** for $Gd_6UO_{12}(s)$ also shows –ve deviation up to temperature ~400K and latter it shows slight positive deviation of ~ 2.8% which is shown in **Fig.3.17**. The heat capacity values for $RE_6UO_{12}(s)$ were fitted to equation $A+BT+CT^{-2}$. **Fig.3.14 and 3.18** show the plot of heat capacity as a function of temperature for $Nd_6UO_{12}(s)$ and $Tb_6UO_{12}(s)$ which show anomaly at 665 K and 670 K, respectively. The anomaly in heat capacity for $Nd_6UO_{12}(s)$ and $Tb_6UO_{12}(s)$ covers the temperature range of 615-700 K and 600–720 K, respectively. Therefore, the heat capacity data for $Nd_6UO_{12}(s)$ were least square fitted to the polynomials in the temperature range 300-600 K and 700-870 K. Similarly, heat capacity of $Tb_6UO_{12}(s)$ were fitted in the temperature ranges 300-550 K and 730-870 K. Thermodynamic functions such as enthalpy, entropy and Gibbs energy functions of RE_6UO_{12} were derived using the measured heat capacity data and $S_m^o(298.15\,K)$. The values of $S_m^o(\mathrm{RE_6UO_{12}(s)}, 298.15\,K)$ was estimated by assuming $\Delta S_m^o(298.15\,K) = 0$, for the reaction $3RE_2O_3(s) + UO_3(s) = RE_6UO_{12}(s)$. The standard entropy values for $RE_2O_3(s)$ and $UO_3(s)$ were taken from the literature [**166**]. The coefficient of heat capacity values and calculated thermodynamic functions for $RE_6UO_{12}(s)$ in various experimental temperature ranges are given in **Table 3.8 and 3.9.**

Table. 3.8. The coefficients of heat capacity, enthalpy increment, entropy and Gibbs energy function of RE_6UO_{12}(s) (RE=La, Pr, Nd, Sm, Eu, Gd).

RE_6UO_{12}(s)	**Temp range**	$C^o_{p,m}(T)$ $A+BT+CT^{-2}$ **(Jmol^{-1}K^{-1})**			$H^o_m(T)-H^o_m(298.15)$ $=DT+ET^2+FT^{-1}+G$ **(kJ mole^{-1})**				$S^o_m(T)=$ $=H\log(T)+IT+JT^{-2}+K$ **(J mole^{-1}K^{-1})**				$-\left(\frac{G^o_m(T)-H^o_m(298.15)}{T}\right)$ $=L\log(T)+MT+NT^{-2}+O$ **(J mole^{-1}K^{-1})**			
RE		***A***	***B***	***C*** × **10** $^{-6}$	***D***	***E***× **10**^{5}	***F***	***G***	***H***	***I***	***J***× **10**$^{-6}$	***K***	***L***	***M***	***N***× **10**$^{-6}$	***O***
La	298.15-870K	456.69	0.041	-6.54	0.457	2.0	6532	-159.82	1051.8	0.041	3.27	-2174	321.3	0.220	9.51	-489.65
Pr	298.15-870K	516.36	0.048	-7.55	0.516	2.0	7537	-181.27	1189.3	0.048	3.78	-2436	360.6	0.251	10.73	-524.54
Nd	298.15-600K	522.49	0.037	-8.86	0.522	2.0	8852	-187.01	1202.9	0.037	4.43	-2465	348.6	0.252	10.53	-484.16
Sm	298.15-870K	495.13	0.097	-8.56	0.495	5.0	8566	-180.60	1140.0	0.097	4.28	-2367	315.2	0.274	10.16	-445.43
Eu	298.15-87K	507.75	0.104	-9.33	0.508	5.0	9318	-187.15	1169.3	0.104	4.67	-2460	313.9	0.286	10.31	-461.19
Gd	298.15-870K	450.84	0.037	-7.39	0.451	2.0	7423	-160.99	1038.5	0.037	3.7	-2074	303.6	0.219	9.16	-371.71

Table. 3.9. The coefficients of heat capacity, enthalpy increment, entropy and Gibbs energy function of RE_6UO_{12}(s)(RE= Tb, Dy, Ho, Er, Tm, Yb, Lu).

RE_6UO_{12}(s)	**Temp range**	$C^o_{p,m}(T)$ $A+BT+CT^{-2}$ **(Jmol^{-1}K^{-1})**			$H^o_m(T)-H^o_m(298.15)$ $=DT+ET^2+FT^{-1}+G$ **(kJ mole^{-1})**				$S^o_m(T)=$ $=H\log(T)+IT+JT^{-2}+K$ **(J mole^{-1}K^{-1})**				$-\left(\frac{G^o_m(T)-H^o_m(298.15)}{T}\right)$ $=L\log(T)+MT+NT^{-2}+O$ **(J mole^{-1}K^{-1})**			
RE		***A***	***B***	***C* × 10 $^{-6}$**	***D***	***E*× 10^5**	***F***	**G**	***H***	***I***	***J*× 10^{-6}**	***K***	***L***	***M***	***N*× 10^{-6}**	***O***
Tb	298.15-550 K	450.74	0.129	-5.97	0.451	6.0	5978	-160.12	1037.7	0.129	2.98	-2073	306.7	0.265	9.82	-381.15
Dy	298.15-870 K	492.00	0.041	-5.64	0.492	2.0	5650	-167.43	1132.9	0.041	2.82	-2302	368.4	0.230	10.56	-553.23
Ho	298.15-870 K	488.34	0.046	-5.89	0.488	2.0	5881	-167.32	1124.4	0.046	2.94	-2258	360.2	0.232	10.44	-507.16
Er	298.15-870 K	447.34	0.059	-6.61	0.447	3.0	6615	-158.15	1029.8	0.059	3.30	-2040	307.8	0.227	9.34	-371.31
Tm	298.15-870 K	484.93	0.047	-6.52	0.485	2.0	6515	-168.44	1116.6	0.047	3.26	-2298	347.0	0.234	10.21	-527.89
Yb	298.15-870 K	523.13	-0.0007	-8.09	0.523	-2.67	8078	-182.93	1204.4	-0.0006	4.04	-2530	368.6	0.228	10.59	-603.75
Lu	298.15-870 K	445.98	0.038	-7.81	0.446	2.0	7816	-160.84	1027	0.038	3.90	-2170	292.4	0.220	8.95	-463.76

The Standard Gibbs energy of formation measurements

3.2.4. E.m.f. measurements on solid-state electrochemical cells

The elaborate description of experimental set up used for e.m.f. measurement is given in section 2.6.12.

3.2.4.1. Standardization of oxide cell setup

Prior to the actual experiments, the experimental cell assembly was standardized with one end closed flat bottom YSZ tube as solid electrolyte, phase mixtures of {Ni(s) + NiO(s)} as anode and air $\{p(O_2) = 21.21$ kPa$\}$ as cathode. This cell is represented as:

Cell (**1**): (–) Pt / {Ni(s) + NiO(s)}// CSZ // air $\{ p(O_2) = 21.21$ kPa $\}$ / Pt(+).

The reversible e.m.f. values obtained at different experimental temperatures for **cell (1)** are listed in Table **3.10** and the variation of e.m.f.s with temperature is shown in F**ig. 3.25**. The e.m.f. data were least squares fitted to yield the following linear expression:

$$E / \mathrm{V}\ (\pm 0.002) = 1.2322 - 4.9427\times10^{-4}\cdot(T/\mathrm{K}). \qquad (3.4)$$

The half-cell reactions at each electrode can be represented as:

$$\tfrac{1}{2}\,O_2(g) + 2e^- = O^{2-} \qquad \text{(at +ve electrode)}, \qquad (3.5)$$

and,

$$Ni(s) + O^{2-} = NiO(s) + 2e^- \qquad \text{(at –ve electrode)}. \qquad (3.6)$$

The net virtual cell reaction for one mole of $O_2(g)$ can be represented as:

$$2\,Ni(s) + O_2(g) = 2\,NiO(s). \qquad (3.7)$$

The values of $\Delta_rG^0(T)$ for reaction (3.7) as a function of temperature can be calculated using Eq. (3.4) and is represented by the following expression:

$$\Delta_rG^o(T)\ /\ \mathrm{kJ\cdot mol^{-1}}\ (\pm 0.8) = -475.57 + 0.191\cdot(T/\mathrm{K}). \qquad (3.8)$$

The values of $\Delta_rG^0(T)$ for reaction (3.8) obtained in this study are in good agreement (within ±2.0 kJ·mol^{-1}) with those calculated using the values of $\Delta_fG^o_m(T)$ for NiO(s) from the literature [**166**]

.

Table 3.10: The reversible e.m.f. of cell (1)

Cell (1)			
***T* / K**	***E* / V**	***T* / K**	***E* / V**
866.65	0.8092	1041.15	0.7175
920.65	0.7731	1080.65	0.699
967.65	0.7513	1122.65	0.6793
1005.15	0.734		

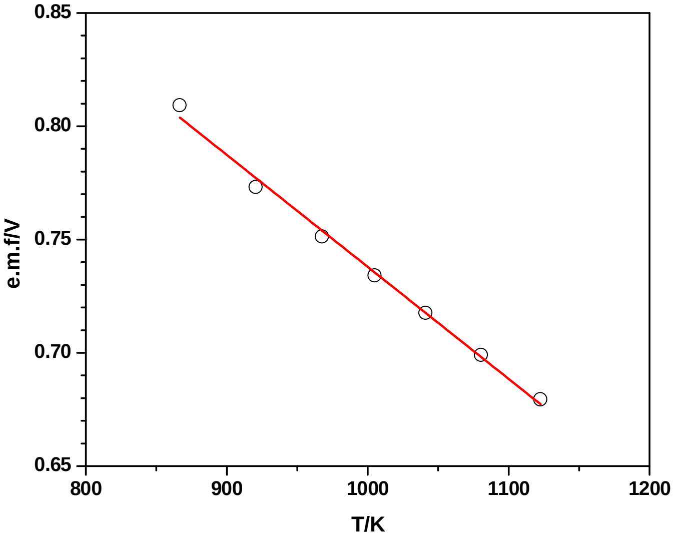

Fig.3.25.The variation of e.m.f as function of temperature for Cell-1

3.2.4.2. Standard molar Gibbs energies of formation of RE_6UO_{12}(s) (RE=La, Nd, Sm, Eu, Gd, Tb, Dy, Ho, Tm, Yb, Lu)

For the determination of Gibbs energy of formation of RE_6UO_{12} (RE=La, Nd, Sm, Eu, Gd, Tb, Dy, Ho, Tm, Yb, Lu), (Ni+NiO) mixture and air was taken separately as reference electrode as there was no data on oxygen potential of RE_6UO_{12}. For each system, the galvanic cell used can be represented as follows:

Cell (**2**) :(-) Pt, {RE_6UO_{12}(s) + RE_2O_3(s) + U_3O_8(s)} //YSZ// air {(p_{O2} = 21.21kPa)}, Pt (+)
Cell (**3**) :(-) Pt, (Ni(s)+NiO(s)) //YSZ// {RE_6UO_{12}(s) + RE_2O_3(s) + U_3O_8(s)} Pt (+)

The sample electrode was made of platinum sheet attached to a pelletized mixture of {RE_6UO_{12}(s) + RE_2O_3(s) + U_3O_8(s)} in the ratio of 3:9:1 sintered at 1073 K in ultra pure argon gas for 24 h. For the preparation of equilibrium phase mixture for the determination of Gibbs energy of formation of Tb_6UO_{12}(s), Tb_4O_7(s) was converted to Tb_2O_3(s) by heating at 1273 K for 10 h in high purity Ar atmosphere and the complete conversion was confirmed by XRD analysis.

The X-ray diffraction patterns of the pellets before and after the experiment were taken to confirm the existence of initial equilibrium phase mixture during/after the experiment.

3.2.4.2.1. Standard molar Gibbs energies of formation of RE_6UO_{12}(s) (RE=La, Nd, Sm, Eu, Gd, Tb, Dy, Ho, Tm, Yb, Lu) using air as reference electrode

The reversible e.m.f. of the solid-state galvanic cell (2) was measured as a function of temperature.

The half cell reactions can be represented as:

At cathode $O_2 + 4e^- = 2O^{2-}$ (3.9)

At anode $18RE_2O_3(s) + 2U_3O_8(s) + 2O^{2-} = 6RE_6UO_{12}(s) + 4e^-$ (3.10)

The overall virtual reaction for the electrochemical cell is given as:

$$18RE_2O_3(s) + 2\,U_3O_8(s) + O_2 = 6\,RE_6UO_{12}(s) \quad (3.11)$$

The e.m.f. data obtained from the electrochemical cells for RE_6UO_{12}(s) are given in Table **3.11-3.14** and are plotted in Figs. **3.26-3.36** as a function of temperature.

These data were least squares analyzed and were best fitted to linear equations whose coefficients are also given in **Table 3.15 & 3.16** along with the experimental temperature range. The error given is the standard deviation of the least squares fitted e.m.f. data. The $\Delta_f G^o_m(RE_6UO_{12}, s, T)$ can be calculated using the respective e.m.f. values from the **Table 3.15 and 3.16** and $\Delta_f G^o_m(T)$ values of the corresponding RE_2O_3(s),U_3O_8(s) and NiO(s) from the literature [166].The $\Delta_f G^o_m(RE_6UO_{12}, s, T)$ values were found to fit to the linear equations as function of temperature, whose intercept and slope values are also given in the **Table 3.15 and 3.16.** The existence of equilibrium phases during the experiments were checked by taking X-ray diffraction patterns of the mixture before and after the e.m.f. measurements. The patterns were found to match with the presence of peaks due to RE_6UO_{12}(s), RE_2O_3(s) and U_3O_8(s). These patterns are shown in **Figs.3.37 & 3.38.** The ΔG_f^o (RE_6UO_{12},s) ΔH_f^o(RE_6UO_{12},s,298.15 K) derived from second and third law analysis and S^o(RE_6UO_{12},s,298.15K) derived from second law analysis are given in **Table 3.17 and 3.18.**

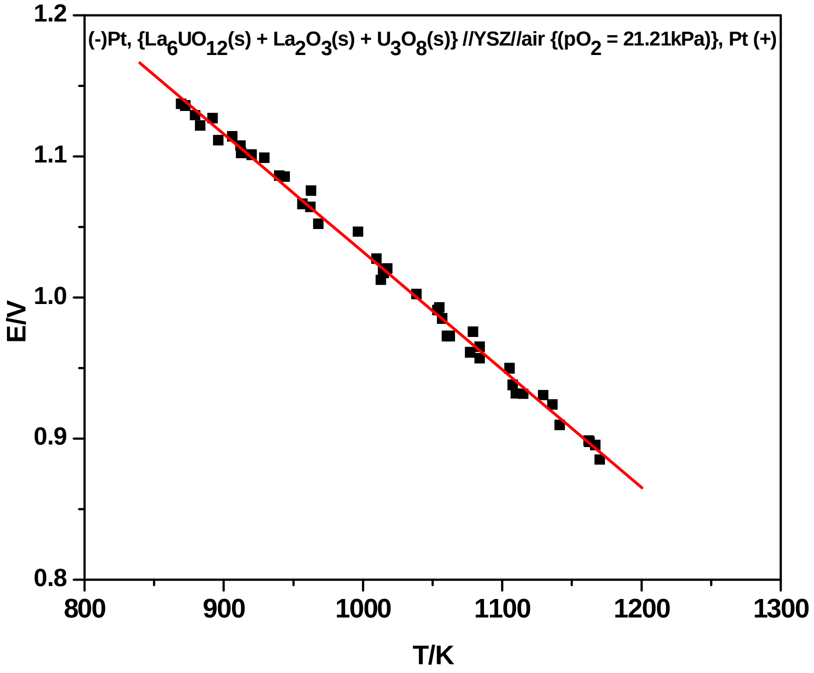

Fig.3.26. The plot of e.m.f.s against temperature for the cell (-)Pt, {La_6UO_{12}(s) + La_2O_3(s) + U_3O_8(s)} //YSZ// air {(p_{O2} = 21.21kPa)}, Pt (+)

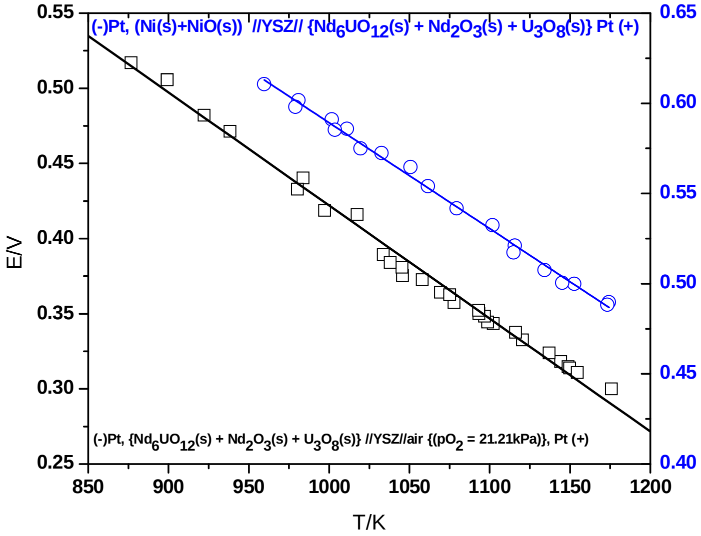

Fig.3.27. The plot of e.m.f.s against temperature for the cell (-)Pt, {Nd_6UO_{12}(s) + Nd_2O_3(s) + U_3O_8(s)} //YSZ// air {(p_{O2} = 21.21kPa)},Pt (+) and (-)Pt, (Ni(s)+NiO(s)) //YSZ// {Nd_6UO_{12}(s) + Nd_2O_3(s) + U_3O_8(s)} Pt (+)

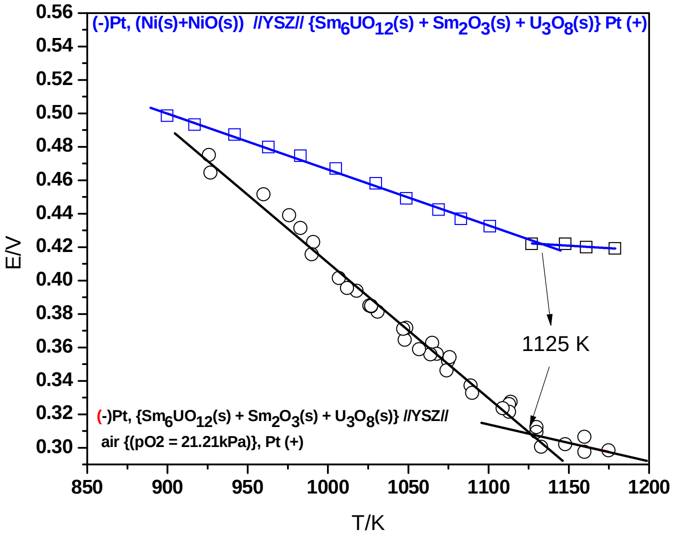

Fig.3.28. The plot of e.m.f.s against temperature for the cell (-)Pt, {Sm_6UO_{12}(s) + Sm_2O_3(s) + U_3O_8(s)} //YSZ// air {(p_{O2} = 21.21kPa)}, Pt (+) and (-)Pt, (Ni(s)+NiO(s)) //YSZ// {Sm_6UO_{12}(s) + Sm_2O_3(s) + U_3O_8(s)} Pt (+)

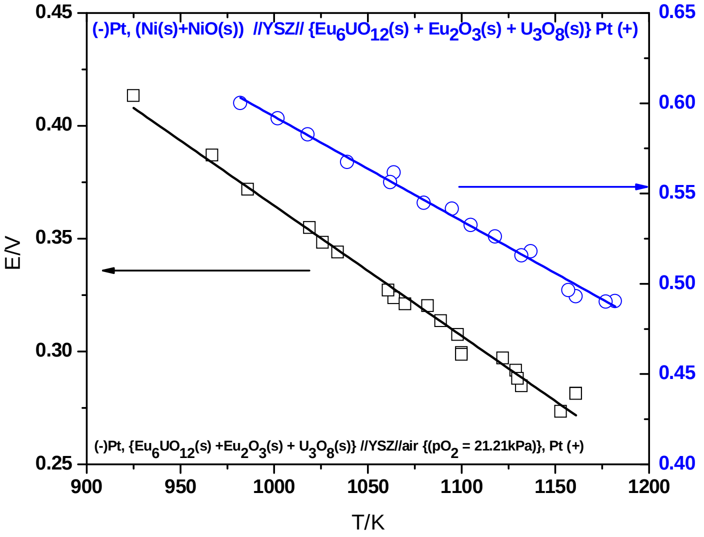

Fig.3.29. The plot of e.m.f.s against temperature for the cell (-)Pt, {Eu_6UO_{12}(s) + Eu_2O_3(s) + U_3O_8(s)} //YSZ// air {(p_{O2} = 21.21kPa)}, Pt (+) and (-)Pt, (Ni(s)+NiO(s)) //YSZ// {Eu_6UO_{12}(s) + Eu_2O_3(s) + U_3O_8(s)} Pt (+).

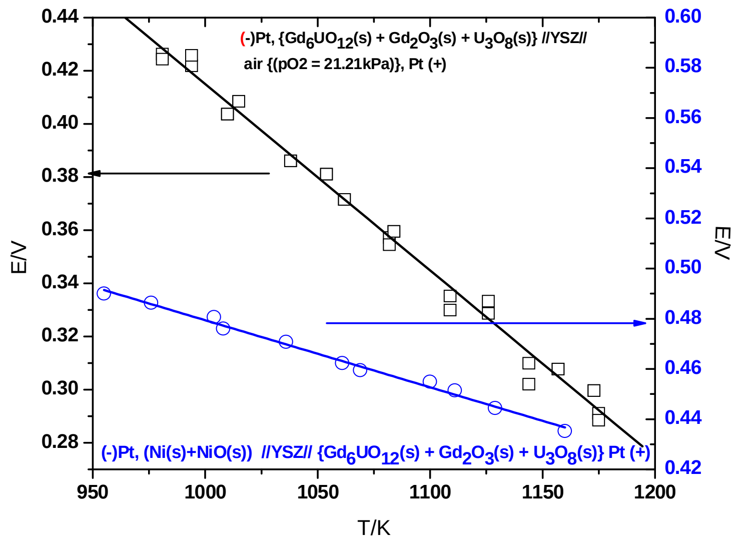

Fig.3.30. The plot of e.m.f.s against temperature for the cell (-)Pt, $\{Gd_6UO_{12}(s) + Gd_2O_3(s) + U_3O_8(s)\}$ //YSZ// air $\{(p_{O2} = 21.21kPa)\}$, Pt (+) and (-)Pt, (Ni(s)+NiO(s)) //YSZ// $\{Gd_6UO_{12}(s) + Gd_2O_3(s) + U_3O_8(s)\}$ Pt (+).

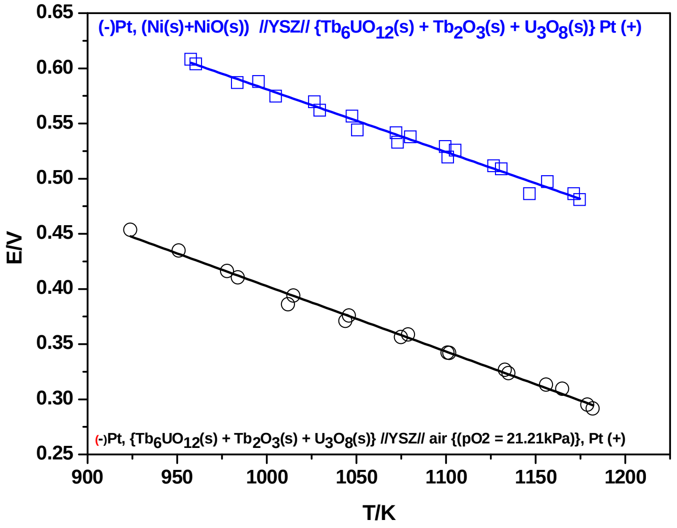

Fig.3.31. The plot of e.m.f.s against temperature for the cell (-)Pt, $\{Tb_6UO_{12}(s) + Tb_2O_3(s) + U_3O_8(s)\}$ //YSZ// air $\{(p_{O2} = 21.21kPa)\}$, Pt (+) and (-)Pt, (Ni(s)+NiO(s)) //YSZ// $\{Tb_6UO_{12}(s) + Tb_2O_3(s) + U_3O_8(s)\}$ Pt (+).

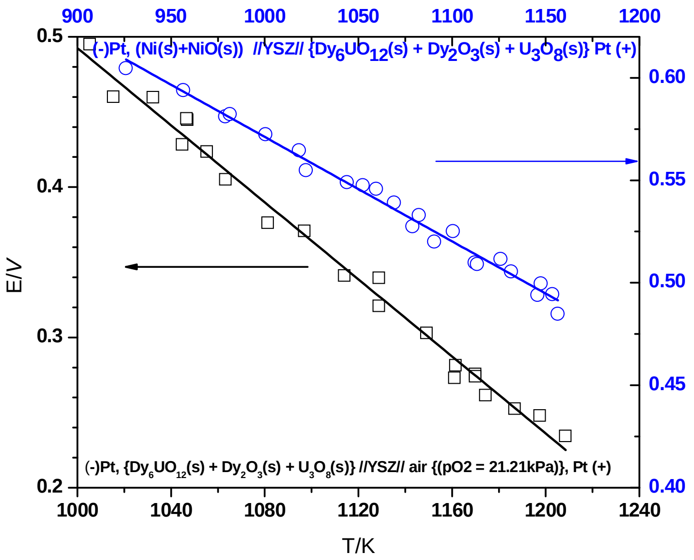

Fig.3.32. The plot of e.m.f.s against temperature for the cell (-)Pt, {Dy_6UO_{12}(s) + Dy_2O_3(s) + U_3O_8(s)} //YSZ// air {(p_{O2} = 21.21kPa)}, Pt (+) and (-)Pt, (Ni(s)+NiO(s)) //YSZ// {Dy_6UO_{12}(s) + Dy_2O_3(s) + U_3O_8(s)} Pt (+).

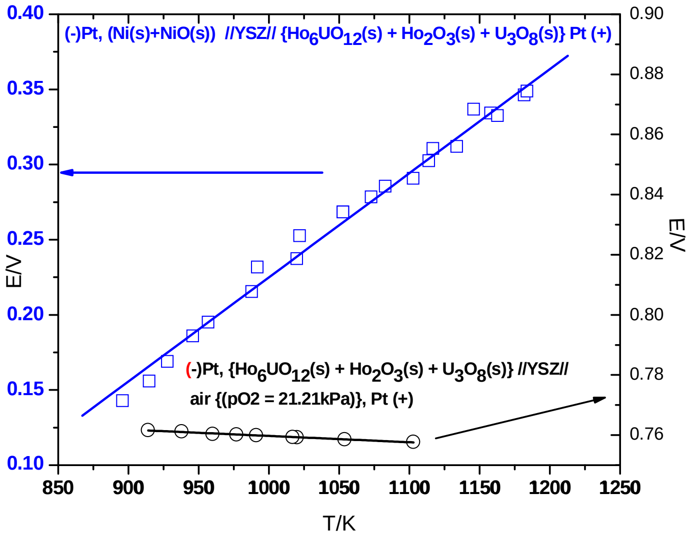

Fig.3.33. The plot of e.m.f.s against temperature for the cell (-)Pt, {Ho_6UO_{12}(s) + Ho_2O_3(s) + U_3O_8(s)} //YSZ// air {(p_{O2} = 21.21kPa)}, Pt (+) and (-)Pt, (Ni(s)+NiO(s)) //YSZ// {Ho_6UO_{12}(s) + Ho_2O_3(s) + U_3O_8(s)} Pt (+).

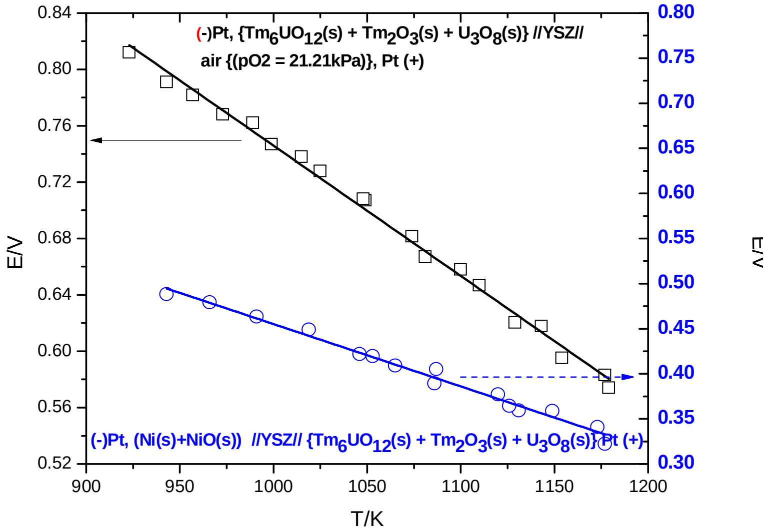

Fig.3.34. The plot of e.m.f.s against temperature for the cell (-)Pt, $\{Tm_6UO_{12}(s) + Tm_2O_3(s) + U_3O_8(s)\}$ //YSZ// air $\{(p_{O2} = 21.21kPa)\}$, Pt (+) and (-)Pt, (Ni(s)+NiO(s))//YSZ// $\{Tm_6UO_{12}(s) + Tm_2O_3(s) + U_3O_8(s)\}$ Pt (+) .

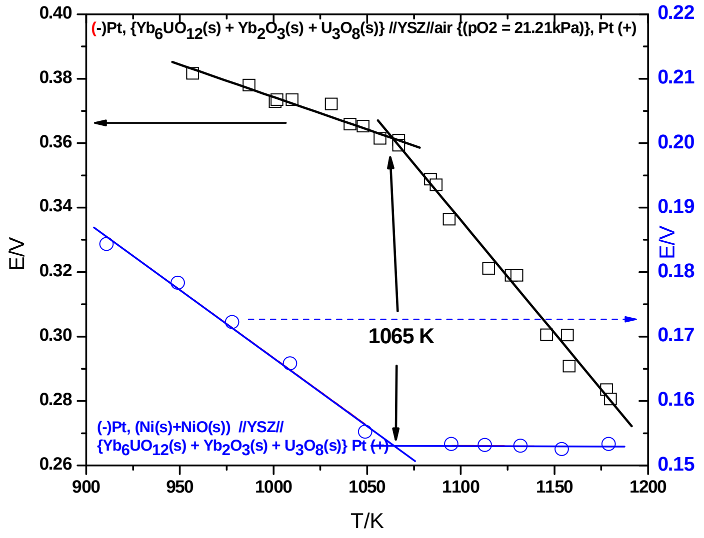

Fig.3.35. The plot of e.m.f.s against temperature for the cell (-)Pt, $\{Yb_6UO_{12}(s) + Yb_2O_3(s) + U_3O_8(s)\}$ //YSZ// air $\{(p_{O2} = 21.21kPa)\}$, Pt (+) and (-)Pt, (Ni(s)+NiO(s)) //YSZ// $\{Yb_6UO_{12}(s) + Yb_2O_3(s) + U_3O_8(s)\}$ Pt (+) .

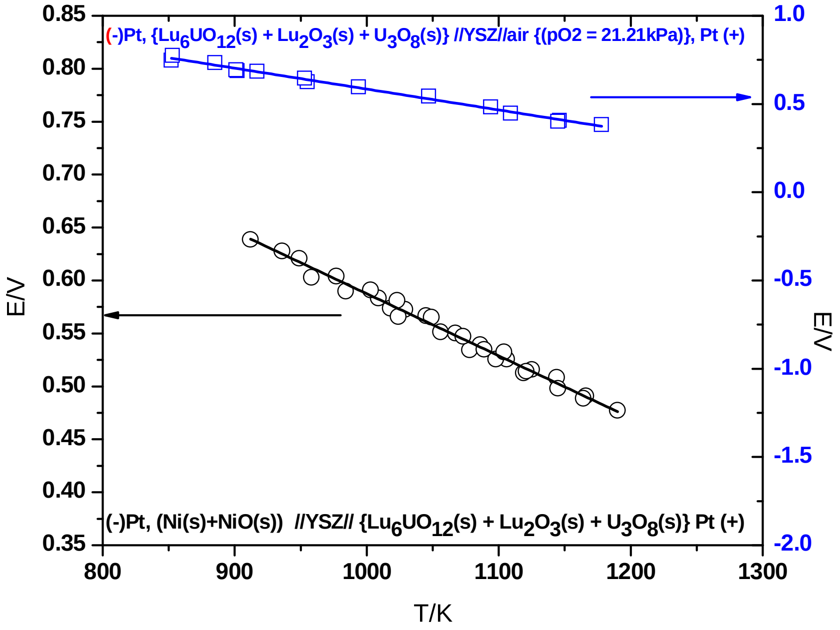

Fig.3.36. The plot of e.m.f.s against temperature for the cell (-)Pt, {Lu_6UO_{12}(s) + Lu_2O_3(s) + U_3O_8(s)} //YSZ// air {(p_{O2} = 21.21kPa)}, Pt (+) and (-)Pt, (Ni(s)+NiO(s))//YSZ// {Lu_6UO_{12}(s) + Lu_2O_3(s) + U_3O_8(s)} Pt (+).

Table 3.11: The reversible e.m.f.s of Cell (2) :(-)Pt, {RE_6UO_{12}(s) (RE=La, Nd, Sm) + RE_2O_3(s) + U_3O_8(s)} //YSZ// air {(p_{O2} = 21.21kPa)}, Pt (+) and Cell (3): (-)Pt, (Ni(s)+NiO(s)) //YSZ// {RE_6UO_{12}(s) + RE_2O_3(s) + U_3O_8(s)} Pt (+)

RE	La		Nd				Sm			
Cell	2		2		3		2		3	
	T/K	e.m.f/V	T/K	e.m.f/V	T/K	e.m.f/V	T/K	e.m.f/V	T/K	e.m.f/V
	873	1.1360	1176	0.2999	981	0.6017	927	0.4643	900	0.4984
	944	1.0855	1144	0.3180	1002	0.5911	976	0.4389	917	0.4931
	968	1.0519	1102	0.3434	1011	0.5858	1026	0.3849	942	0.4871
	1013	1.0123	1078	0.3574	1033	0.5724	1075	0.3519	963	0.4797
	1060	0.9725	1034	0.3892	1051	0.5646	1114	0.3273	983	0.4745
	880	1.1293	1099	0.3444	1062	0.554	1113	0.3259	1005	0.4669
	913	1.1022	1046	0.3752	1080	0.5417	1074	0.3461	1030	0.458
	957	1.0663	1149	0.3146	1102	0.5323	1048	0.3644	1069	0.4423
	1015	1.0171	984	0.4403	1116	0.521	1018	0.3937	1101	0.4323
	1063	0.9725	1097	0.3483	1134	0.5075	991	0.4228	1049	0.4489
	1108	0.9380	1150	0.3137	1153	0.4999	926	0.4749	1083	0.4368
	870	1.1371	1045	0.3809	1174	0.4896	960	0.4514	1127	0.4218
	1170	0.8851	1069	0.3642	1115	0.5172	990	0.4156	1161	0.4198
	1141	0.9094	1093	0.3499	1145	0.5004	1012	0.3954	1179	0.4191
	1110	0.9320	1120	0.3324	1173	0.4882	1031	0.3811	1148	0.4218
	1077	0.9610	877	0.5170	1020	0.5749	1049	0.3715		
	896	1.1113	899	0.5057	1004	0.5853	1065	0.3626		
	940	1.0863	899	0.5056	979	0.598	1076	0.3540		
	963	1.0755	922	0.4819	960	0.6105	1089	0.3370		
	997	1.0467	938	0.4713			1113	0.3213		
	1039	1.0023	980	0.4327			983	0.4312		
	883	1.1216	997	0.4187			1007	0.4014		
	929	1.0989	1018	0.4160			1027	0.3844		
	962	1.0640	1038	0.3841			1047	0.371		
	1010	1.0273	1058	0.3725			1068	0.356		
	1057	0.9851	1075	0.3625			1064	0.3557		
	912	1.1074	1093	0.3522			1109	0.3235		
	1079	0.9756	1116	0.3375			1090	0.3326		
	1105	0.9497	1137	0.3238			1057	0.3587		
	1162	0.8979	1155	0.3108			1027	0.3848		
	1163	0.8976					1160	0.2974		
	892	1.1270					1130	0.3121		
	1054	0.9911					1160	0.3063		
	1055	0.9929					1130	0.3092		
	1015	1.0199					1148	0.3020		
	1115	0.9316					1175	0.2983		
	906	1.1139					1133	0.3003		
	1167	0.8954					1160	0.3063		
	1136	0.9240					1130	0.3092		
	1084	0.9648					1148	0.3020		
	1084	0.9568					1175	0.2983		
	1162	0.8984								

Table 3.12: The reversible e.m.f.s of Cell (2):(-)Pt, {RE_6UO_{12}(s) (RE=Eu, Gd) + RE_2O_3(s) + U_3O_8(s)} //YSZ// air {(p_{O2} = 21.21kPa)}, Pt (+) and Cell (3): (-)Pt, (Ni(s)+NiO(s)) //YSZ// {RE_6UO_{12}(s) + RE_2O_3(s) + U_3O_8(s)} Pt (+) .

RE	**Eu**				**Gd**			
Cell	**2**		**3**		**2**		**3**	
	T/K	**e.m.f/V**	**T/K**	**e.m.f/V**	**T/K**	**e.m.f/V**	**T/K**	**e.m.f/V**
	925	0.4134	1064	0.5616	994	0.4217	976	0.4863
	967	0.3870	1095	0.54147	1015	0.4084	1004	0.4806
	1019	0.3549	1118	0.5262	1054	0.3810	1036	0.4707
	1082	0.3203	1137	0.518	1084	0.3594	1069	0.4594
	1129	0.2917	1161	0.493	1126	0.3286	1100	0.4548
	1161	0.2814	1182	0.4904	1157	0.3076	1129	0.4443
	1098	0.3075	982	0.6001	1173	0.2995	1160	0.4352
	1132	0.2847	1002	0.5916	981	0.4262	1111	0.4514
	1100	0.2994	1018	0.5827	1010	0.4036	1061	0.4623
	1064	0.3237	1039	0.5674	1038	0.3860	1008	0.4760
	1026	0.3483	1062	0.5563	1062	0.3714	955	0.4899
	986	0.3718	1080	0.5448	1082	0.3571		
	1153	0.2735	1105	0.5325	1109	0.3351		
	1130	0.2880	1132	0.5156	1144	0.3098		
	1100	0.2987	1157	0.4965	1175	0.2910		
	1070	0.3210	1177	0.4901	981	0.4242		
	1034	0.3440			1010	0.4036		
	1061	0.3271			1038	0.3860		
	1089	0.3136			1062	0.3714		
	1122	0.2971			1082	0.3544		
	1161	0.2813			1109	0.3298		
					1144	0.3019		
					1175	0.2884		
					994	0.4257		
					1015	0.4084		
					1054	0.3810		
					1084	0.3594		
					1126	0.3332		
					1157	0.3076		

Table 3.13: The reversible e.m.f.s of Cell (2):(-)Pt, {RE$_6$UO$_{12}$(s) (RE= Tb, Dy,Ho) + RE$_2$O$_3$(s) U$_3$O$_8$(s)}//YSZ// air {(p$_{O2}$ = 21.21kPa)},Pt (+) and Cell (3): (-)Pt, (Ni(s)+NiO(s))//YSZ//+ {RE$_6$UO$_{12}$(s) + RE$_2$O$_3$(s) + U$_3$O$_8$(s)} Pt (+).

RE	**Tb**				**Dy**				**Ho**			
Cell	**2**		**3**		**2**		**3**		**2**		**3**	
	T/K	**e.m.f/V**	**T/K**	**e.m.f/V**	**T/K**	**e.m.f/V**	**T/K**	**e.m.f/V**	**T/K**	**e.m.f/V**	**T/K**	**e.m.f/V**
	924	0.4535	961	0.6039	1170	0.2755	926	0.6046	1020	0.7592	1114	0.3025
	951	0.4346	996	0.5878	1161	0.273	957	0.5939	991	0.7599	1158	0.3342
	984	0.4103	1027	0.5696	1170	0.274	979	0.5810	960	0.7603	1182	0.3462
	1015	0.3938	1048	0.5566	1047	0.4447	1001	0.5723	914	0.7617	1146	0.3367
	1046	0.3758	1080	0.5377	1047	0.4455	1022	0.5548	938	0.7612	1117	0.3106
	1079	0.3587	1105	0.5257	1209	0.2342	1044	0.5489	977	0.7602	1083	0.2854
	1102	0.3418	1131	0.5087	1198	0.2479	1060	0.5457	1017	0.7593	1053	0.2683
	1135	0.3236	1171	0.4863	1162	0.2813	1079	0.5274	1054	0.7586	1022	0.2525
	1165	0.3094	1072	0.5413	1114	0.341	1101	0.5251	1103	0.7577	992	0.2317
	1182	0.2915	1100	0.5289	1045	0.4283	1126	0.5115			957	0.1950
	978	0.4162	1127	0.5114	1032	0.4596	1146	0.4939			928	0.1689
	1012	0.386	1157	0.4972	1063	0.405	1069	0.5390			896	0.1428
	1044	0.3709	1175	0.4809	1055	0.4235	1091	0.5200			915	0.1559
	1075	0.3563	1147	0.4861	1015	0.4599	1112	0.5097			946	0.1859
	1101	0.342	1101	0.5193	1005	0.4949	1132	0.5054			988	0.2154
	1133	0.3265	1073	0.5328	973	0.5216	1154	0.4943			1020	0.2372
	1156	0.313	1051	0.544	1081	0.3762	1157	0.4848			1053	0.2683
	1179	0.2949	1030	0.5618	1129	0.3208	981	0.5822			1073	0.2784
			1005	0.5746	1129	0.3396	1018	0.5645			1103	0.2907
			984	0.5869	1187	0.2525	1052	0.5475			1134	0.3119
			958	0.6081	1174	0.2614	1082	0.5329			1163	0.3325
					1149	0.3028	1113	0.5090			1184	0.3488
					1097	0.3707	1147	0.4996				

Table 3.14: The reversible e.m.f.s of Cell (2):(-)Pt, {RE_6UO_{12}(s) (RE= Tm, Yb, Lu) + RE_2O_3(s) + U_3O_8(s)} //YSZ// air {(p_{O2} = 21.21kPa)}, Pt (+) and Cell (3): (-)Pt, (Ni(s)+NiO(s)) //YSZ// {RE_6UO_{12}(s) + RE_2O_3(s) + U_3O_8(s)} Pt (+).

RE	**Tm**				**Yb**				**Lu**			
Cell	**2**		**3**		**2**		**3**		**2**		**3**	
	T/K	**e.m.f/V**	**T/K**	**e.m.f/V**	**T/K**	**e.m.f/V**	**T/K**	**e.m.f/V**	**T/K**	**e.m.f/V**	**T/K**	**e.m.f/V**
	923	0.8120	1177	0.3221	957	0.3816	911	0.1843	1146	0.406	1009	0.5832
	943	0.7909	1131	0.3591	987	0.3780	949	0.1783	1178	0.383	1029	0.5725
	973	0.7679	1086	0.3891	1001	0.3728	978	0.1722	1145	0.4002	1045	0.5666
	999	0.7468	1046	0.4215	1002	0.3734	1009	0.1658	1109	0.447	1067	0.5501
	1025	0.7277	1126	0.3642	1010	0.3734	1049	0.1552	955	0.6255	1086	0.5392
	1049	0.7069	1065	0.4088	1031	0.3721	1095	0.1533	902	0.6876	1106	0.5257
	1074	0.6815	943	0.4880	1041	0.3658	1113	0.15311	901	0.6929	1125	0.5161
	1100	0.6579	966	0.4790	1048	0.3651	1132	0.15299	852	0.7464	1144	0.5085
	1129	0.6204	991	0.4633	1057	0.3614	1154	0.1525	853	0.7751	1166	0.4907
	1154	0.5951	1019	0.4488	1067	0.3593	1179	0.1533	885	0.7342	1190	0.4773
	1179	0.5740	1053	0.4194	1067	0.3608			917	0.6837	1164	0.4887
	957	0.7818	1087	0.4049	1084	0.3487			953	0.6454	1145	0.4982
	989	0.7620	1120	0.3770	1087	0.3469			994	0.597	1119	0.5127
	1015	0.7379	1149	0.3585	1094	0.3363			1047	0.5438	1098	0.5257
	1048	0.7081	1173	0.3408	1115	0.3210			1094	0.4826	1078	0.5344
	1081	0.6669			1127	0.3189			1146	0.406	1018	0.5737
	1110	0.6467			1130	0.3189			1178	0.383	984	0.5898
	1143	0.6178			1146	0.3005			1145	0.4002	958	0.6028
	1177	0.5830			1157	0.3003			1109	0.447	912	0.6387
					1158	0.2907			955	0.6255	936	0.6276
					1178	0.2834			902	0.6876	949	0.6208
					1180	0.2805			901	0.6929	977	0.6041
					1067	0.3608			852	0.7464	1003	0.5909
					1084	0.3487			853	0.7751	1023	0.5811
					1087	0.3469			885	0.7342	1049	0.5652
					1094	0.3363			917	0.6837	1073	0.5472
					1115	0.3210			953	0.6454	1104	0.5323
					1127	0.3189			994	0.597	1121	0.5143
									1047	0.5438	1089	0.5349
											1056	0.5513

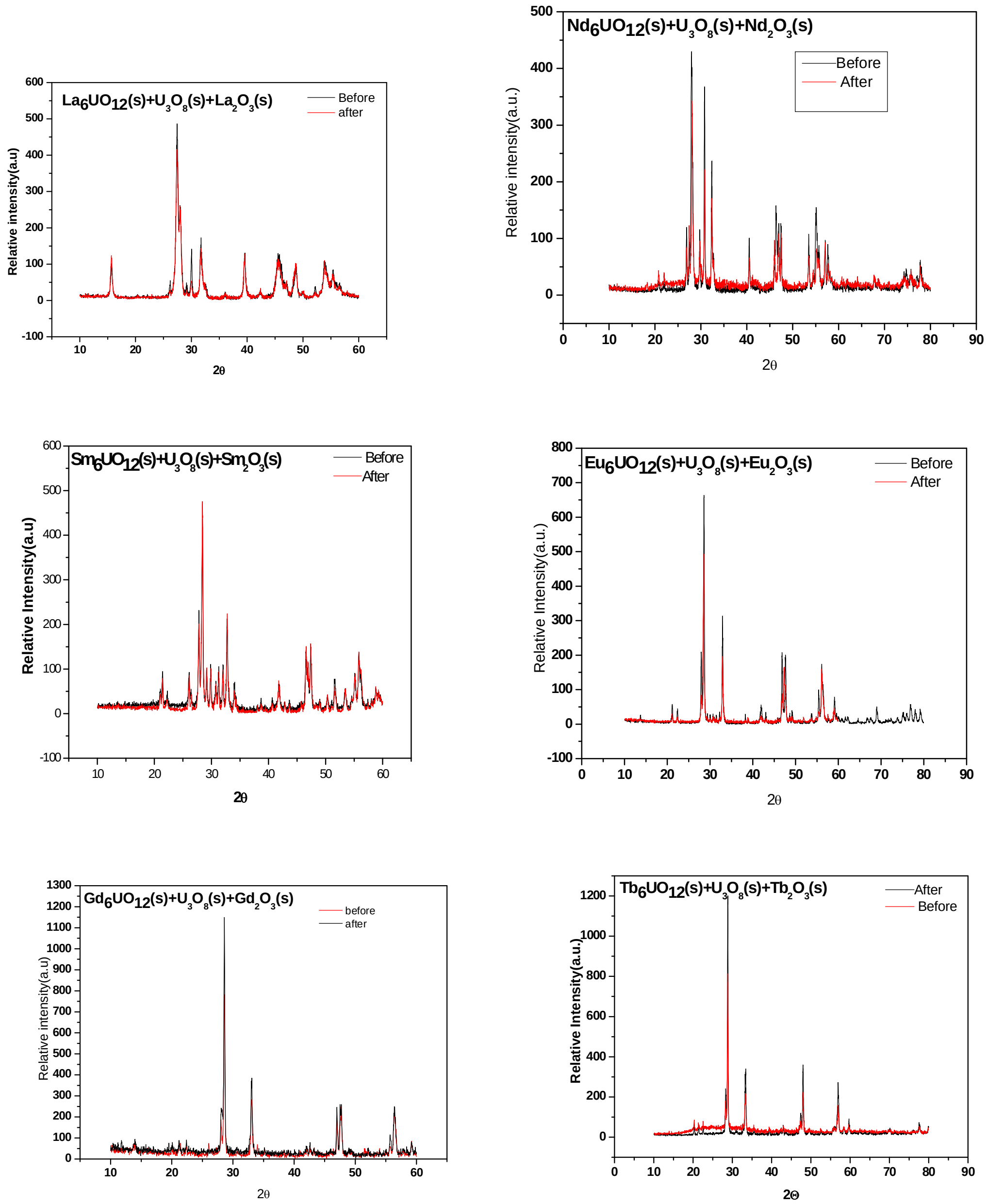

3.37. XRD pattern of the sample {$RE_6UO_{12}(s) + RE_2O_3(s) + U_3O_8(s)$}(RE=La, Nd,Sm, Eu,Gd and Tb) before and after equilibration at various temperatures.

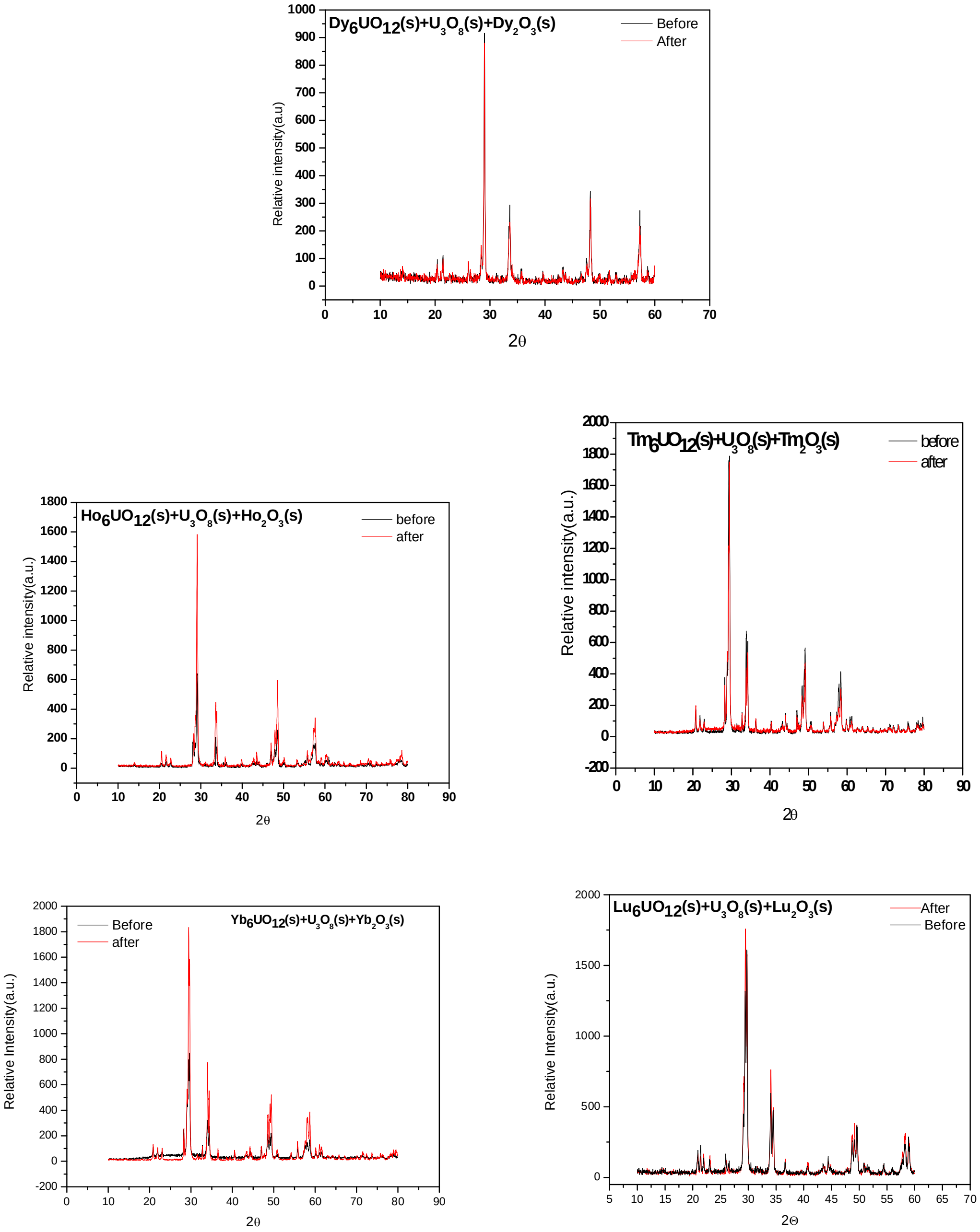

3.38. XRD pattern of the sample {$RE_6UO_{12}(s) + RE_2O_3(s) + U_3O_8(s)$}(RE=Dy, Ho, Tm, Yb, Lu) before and after equilibration at various temperatures.

Table 3.15.The e.m.f. data obtained for the electrochemical cells (2) and (3) with RE = La, Nd, Sm, Eu, Gd.

compound	**Sample**	**Reference**	**e.m.f (*V*) =A+B·(*T*/K)**		**Error in e.m.f.**	**ΔG_r(kJ mol^{-1})= A+ B·(*T*/K)**		**Error inΔG_r(kJ mol^{-1})**	**Temp Range (K)**
			A	**B × 10^4**		**A**	**B**		
La_6UO_{12}(s)	**La_6UO_{12}(s)+U_3O_8(s)+La_2O_3(s)**	**Air(O_2=0.21kPa)**	**1.8670**	**-8.346**	**±0.005**	**-720.55**	**0.3221**	±1.93	**870-1170**
Pr_6UO_{12}(s)	***Investigation of coexisting phase field is required***								
Nd_6UO_{12}(s)	**Nd_6UO_{12}(s)+U_3O_8(s)+Nd_2O_3(s)**	Air(O_2=0.21kPa)	1.1742	-7.5213	±0.005	-453.17	0.2903	±1.93	876-1176
		Ni(s)+NiO(s)	**1.177**	**-5.876**	**±0.003**	**-454.25**	**0.2268**	±1.16	**960-1174**
Sm_6UO_{12}(s)	**Sm_6UO_{12}(s)+U_3O_8(s)+Sm_2O_3(s)**	Air(O_2=0.21kPa)	1.2207	-8.101	±0.004	-471.12	0.3127	±1.54	926-1114
			0.5419	-2.075	±0.005	-209.14	0.08	±1.93	1129-
		Ni(s)+NiO(s)	**0.8048**	**-3.382**	**±0.001**	**-310.61**	**0.131**	±0.39	**900-1101**
			0.4887	**-0.5897**	**±0.003**	**-188.61**	**0.0228**	±1.16	**1127-**
Eu_6UO_{12}(s)	**Eu_6UO_{12}(s)+U_3O_8(s)+Eu_2O_3(s)**	Air(O_2=0.21kPa)	0.9417	-5.7718	±0.005	-363.44	0.2228	±1.93	924-1161
		Ni(s)+NiO(s)	**1.1711**	**-5.7848**	**±0.004**	**-451.97**	**0.2233**	±1.54	**980-1185**
Gd_6UO_{12}(s)	**Gd_6UO_{12}(s)+U_3O_8(s)+Gd_2O_3(s)**	Air(O_2=0.21kPa)	1.1166	-7.0154	±0.006	-430.94	0.2708	±2.32	981-1175
		Ni(s)+NiO(s)	**0.7466**	**-2.6722**	**±0.005**	**-288.14**	**0.1031**	±1.93	**955-1160**

Table 3.16. The e.m.f. data obtained for the electrochemical cells (2) and (3) with RE = Tb, Dy, Ho, Tm, Yb, Lu.

compound	**Sample**	**Reference**	**e.m.f (*V*) =A+B·(*T*/K)**		**Error in e.m.f.**	**ΔG_r(kJ mol^{-1})= A+ B·(*T*/K)**		**Error inΔG_r (kJ mol^{-1})**	**Temp Range (K)**
			A	**B × 10^4**		**A**	**B**		
Tb_6UO_{12}(s)	**Tb_6UO_{12}(s)+U_3O_8(s)+Tb_2O_3(s)**	Air(O_2=0.21kPa)	0.9958	-5.9322	±0.005	-384.32	0.2289	±1.54	924-1182
		Ni(s)+NiO(s)	**1.1487**	**-5.6782**	±0.002	**-443.33**	**0.2191**	±0.77	**957-1175**
Dy_6UO_{12}(s)	**Dy_6UO_{12}(s)+U_3O_8(s)+Dy_2O_3(s)**	Air(O_2=0.21kPa)	0.4368	-1.4465	±0.001	-168.58	0.0558	±0.39	915-1076
		Ni(s)+NiO(s)	**1.0806**	**-5.094**	**±0.004**	**-417.05**	**0.1966**	±1.54	**925-1157**
Ho_6UO_{12}(s)	**Ho_6UO_{12}(s)+U_3O_8(s)+Ho_2O_3(s)**	**Air(O_2=0.21kPa)**	**0.7808**	**-0.2103**	**±0.003**	**-301.34**	**0.0081**	±1.16	**914-1103**
		Ni(s)+NiO(s)	-0.4789	7.033	±0.004	184.83	-0.2714	±1.54	896-1184
Er_6UO_{12}(s)									
Tm_6UO_{12}(s)	**Tm_6UO_{12}(s)+U_3O_8(s)+Tm_2O_3(s)**	**Air(O_2=0.21kPa)**	**1.6708**	**-9.2486**	**±0.003**	**-644.83**	**0.3569**	±1.16	**923-1179**
		Ni(s)+NiO(s)	1.1467	-6.9155	±0.005	-442.56	0.2669	±1.93	943-1177
Yb_6UO_{12}(s)	**Yb_6UO_{12}(s)+U_3O_8(s)+Yb_2O_3(s)**	**Air(O_2=0.21kPa)**	**0.5755**	**-2.0116**	**±0.004**	**-222.10**	**0.0776**	±1.54	**957-1067**
		Air(O_2=0.21kPa)	**1.1061**	**-6.9998**	**±0.005**	**-426.89**	**0.2702**	±1.93	**1067-1180**
		Ni(s)+NiO(s)	0.3775	-2.1076	±0.003	-145.69	0.0813	±1.16	911-1049
		Ni(s)+NiO(s)	0.1558	-0.0242	±0.004	-60.122	0.0009	±1.54	1095-1178
Lu_6UO_{12}(s)	**Lu_6UO_{12}(s)+U_3O_8(s)+Lu_2O_3(s)**	**Air(O_2=0.21kPa)**	**1.7687**	**12.0**	**±0.004**	**-682.61**	**0.4631**	±1.54	**852-1178**
		Ni(s)+NiO(s)	1.1740	5.8645	±0.005	-453.09	0.2263	±1.93	912-1190

Table 3.17.The ΔG_f^o (RE_6UO_{12},s), ΔH_f^o(RE_6UO_{12},s,298.15 K) derived from second and third law analysis and S^o(RE_6UO_{12},s,298.15K) derived from second law analysis from the e.m.f .data obtained for cell (2) & (3).

Compound	**Sample**	**Reference**	**ΔG_f^o (kJ mol^{-1})= A+ B·(*T*/K)**		**ΔH_f^o(298K) (kJ mol^{-1}) Second law**	**ΔH_f^o(298K) (kJ mol^{-1}) Third law**	**S^o(298K) (J mol^{-1} K^{-1}) Second law**
			A	**B**			
La_6UO_{12}(s)	**La_6UO_{12}(s)+U_3O_8(s)+La_2O_3(s)**	**Air(O_2=0.21kPa)**	**-6662**	**1.102**	**-6699.3**	**-6682.4**	**454.8**
Pr_6UO_{12}(s)							
Nd_6UO_{12}(s)	**Nd_6UO_{12}(s)+U_3O_8(s)+Nd_2O_3(s)**	Air(O_2=0.21kPa)	-6660	1.086	-6726.0	-6678.4	506.1
		Ni(s)+NiO(s)	**-6588**	**1.031**	**-6652.0**	**-6638.2**	**563.0**
Sm_6UO_{12}(s)	**Sm_6UO_{12}(s)+U_3O_8(s)+Sm_2O_3(s)**	Air(O_2=0.21kPa)	-6733	1.142	-6770.3	-6739.9	489.4
			-6689	1.103	-6728.9	-6718.1	526.2
		Ni(s)+NiO(s)	**-6682**	**1.099**	**-6718.3**	**-6713.8**	**533.4**
			-6702	**1.117**	**-6741.9**	**-6724.0**	**512.1**
Eu_6UO_{12}(s)	**Eu_6UO_{12}(s)+U_3O_8(s)+Eu_2O_3(s)**	Air(O_2=0.21kPa)	-6190	1.13	-6283.8	-6737.6	465.5
		Ni(s)+NiO(s)	**-6133**	**1.087**	**-6227.4**	-6206.0	**508.0**
Gd_6UO_{12}(s)	**Gd_6UO_{12}(s)+U_3O_8(s)+Gd_2O_3(s)**	Air(O_2=0.21kPa)	-6713	1.096	-6737.3	**-6739.4**	549.1
		Ni(s)+NiO(s)	**-6672**	**1.065**	**-6695.6**	**-6717.1**	**584.7**

Table 3.18.The ΔG_f^o (RE_6UO_{12},s), ΔH_f^o(RE_6UO_{12},s, 298.15 K) derived from second and third law analysis and S^o(RE_6UO_{12},s,298.15K) derived from second law analysis from the e.m.f data obtained for cell (2) & (3)

compound	**Sample**	**Reference**	**ΔG_f^o(kJ mol^{-1})= A+ B·(*T*/K)**		**ΔH_f^o(298K) (kJ mol^{-1}) Second law**	**ΔH_f^o (298K) (kJ mol^{-1}) Third law**	**S^o(298K) (J mol^{-1} K^{-1}) Second law**
			A	**B**			
Tb_6UO_{12}(s)	**Tb_6UO_{12}(s)+U_3O_8(s)+Tb_2O_3(s)**	Air(O_2=0.21kPa)	-6805	1.072	-6888.3	-6847.5	517.9
		Ni(s)+NiO(s)	**-6746**	**1.028**	**-6830.6**	**-6814.1**	**560.2**
Dy_6UO_{12}(s)	**Dy_6UO_{12}(s)+U_3O_8(s)+Dy_2O_3(s)**	Air(O_2=0.21kPa)	-6773	1.073	-6828.6	-6821.6	556.4
		Ni(s)+NiO(s)	**-6755**	**1.062**	**-6820.8**	**-6810.2**	**557.1**
Ho_6UO_{12}(s)	**Ho_6UO_{12}(s)+U_3O_8(s)+Ho_2O_3(s)**	**Air(O_2=0.21kPa)**	**-6835**	**1.040**	**-6928.4**	**-6899.7**	**538.0**
		Ni(s)+NiO(s)	-6895	1.115	-6991.1	-6918.2	460.0
Er_6UO_{12}(s)							
Tm_6UO_{12}(s)	**Tm_6UO_{12}(s)+U_3O_8(s)+Tm_2O_3(s)**	**Air(O_2=0.21kPa)**	**-6915**	**1.143**	**-6929.3**	**-6949.2**	**545.8**
		Ni(s)+NiO(s)	-6813	1.07	-6826.3	-6889.0	621.5
Yb_6UO_{12}(s)	**Yb_6UO_{12}(s)+U_3O_8(s)+Yb_2O_3(s)**	**Air(O_2=0.21kPa)**	**-6723**	**1.055**	**-6781.3**	**-6706.0**	**482.2**
		Air(O_2=0.21kPa)	**-6757**	**1.087**	**-6816.2**	**-6698.1**	**458.0**
		Ni(s)+NiO(s)	-6741	1.059	-6796.9	-6698.1	480.5
		Ni(s)+NiO(s)	-6755	1.072	-6810.5	-6704.9	476.7
Lu_6UO_{12}(s)	**Lu_6UO_{12}(s)+U_3O_8(s)+Lu_2O_3(s)**	**Air(O_2=0.21kPa)**	**-6903**	**1.138**	**-6933.7**	**-6916.9**	**397.6**
		Ni(s)+NiO(s)	-6793	1.055	-6820.5	-6854.8	483.6

3.2.4.2.2. Standard molar Gibbs energies of formation of RE_6UO_{12} (s) (RE= Nd, Sm, Eu, Gd, Tb, Dy, Ho, Tm, Yb, Lu) using Ni (s) + NiO(s) as reference electrode

The reversible e.m.f. of the solid-state galvanic cell (3) was measured as a function of temperature: The e.m.f generated due to half cell reactions can be given as:

At cathode:

$$6RE_6UO_{12}(s) + 4e = 18RE_2O_3(s) + 2U_3O_8(s) + 2O^{2-} \qquad (3.12)$$

At anode:

$$2Ni\ (s) + 2O^{2-} = 2NiO(s) + 4e^- \qquad (3.13)$$

The overall virtual cell reaction is:

$$6RE_6UO_{12}(s)+2Ni=18RE_2O_3(s)+2U_3O_8(s)+2NiO(s) \qquad (3.14)$$

The e.m.fs. data obtained from the electrochemical cell (3) for various $RE_6UO_{12}(s)$ are also given in Table **3.11-3.14** and are plotted in Figs. **3.27-3.36** as a function of temperature.

These data were least squares analyzed and were best fitted to linear equations whose coefficients are also given in **Table 3.15 & 3.16** along with their experimental temperature range. The error given is the standard deviation of the least squares fitted line. The $\Delta_f G^o{}_m(RE_6UO_{12}, s, T)$ can be calculated using the respective e.m.f. values from the **Table 3.15 and 3.16** and $\Delta_f G^o{}_m(T)$ values of the corresponding RE_2O_3(s),U_3O_8(s) and NiO(s) from the literature [**166**].The intercept and slope of $\Delta_f G^o{}_m(RE_6UO_{12}, s, T)$ are also given in the **Tables 3.17 and 3.18.** The existence of equilibrium phases during the experiments were checked by taking X-ray diffraction patterns of the mixture before and after the e.m.f. measurements. The ΔG_f^o (RE_6UO_{12},s) $\Delta H_f^o(RE_6UO_{12}$,s,298.15 K) derived from second and third law analysis and $S^o(RE_6UO_{12}$,s,298.15K) derived from second law analysis are given in **Tables 3.17 and 3.18.**

The e.m.f. data obtained from the electrochemical cell (2 & 3) for finding ΔG_f^o (T) of Sm_6UO_{12}(s) and Yb_6UO_{12}(s) showed change in slope as a function of temperature as shown in **Figs 3.28 and 3.35**, respectively. The change in slope appears at 1125 K and 1065 K for Sm_6UO_{12}(s) and Yb_6UO_{12}(s), respectively. This observation implies phase transition at these temperatures. These data were least squares fitted in two temperature ranges. $\Delta_f G^o{}_m(Sm_6UO_{12}, s, T)$ and $\Delta_f G^o{}_m(Yb_6UO_{12}, s, T)$ were calculated using e.m.f.s of both the temperature ranges and the $\Delta_f G^o{}_m(T)$ values of RE_2O_3(s), NiO(s) and U_3O_8(s) from the literature[**166**] and these calculated values are also given in Tables **3.17 and 3.18** for cell (2) and (3), respectively.

3.2.5. Study of phase transition using electrical conductivity measurement

Electrical conductivity of Nd_6UO_{12}(s) Gd_6UO_{12}(s) Dy_6UO_{12}(s) and Tb_6UO_{12}(s) was measured using a frequency response analyser as described in section 2.11 to further confirm the phase transitions. Pellets of 10 mm diameter and 2–3 mm thickness were used. Platinum paste was applied on both side of the pellet and sintered at 873 K for 6 h to ensure good electrical contacts. The sample pellet was mounted between two spring-loaded platinum foils of identical dimensions and placed inside a quartz chamber that in turn was heated in a furnace. Measurements were carried out in the temperature range of 523-973 K, 498-998 K, 598-998 K and 298-798 K for Nd_6UO_{12}(s) Gd_6UO_{12}(s) Dy_6UO_{12}(s) and Tb_6UO_{12}(s), respectively. Nyquist plots of RE_6UO_{12}(s)(RE= Nd, Gd, Dy, Tb) in air are shown in **Figs.3.39-3.42** and the conductivity values are shown in **Table 3.19.**

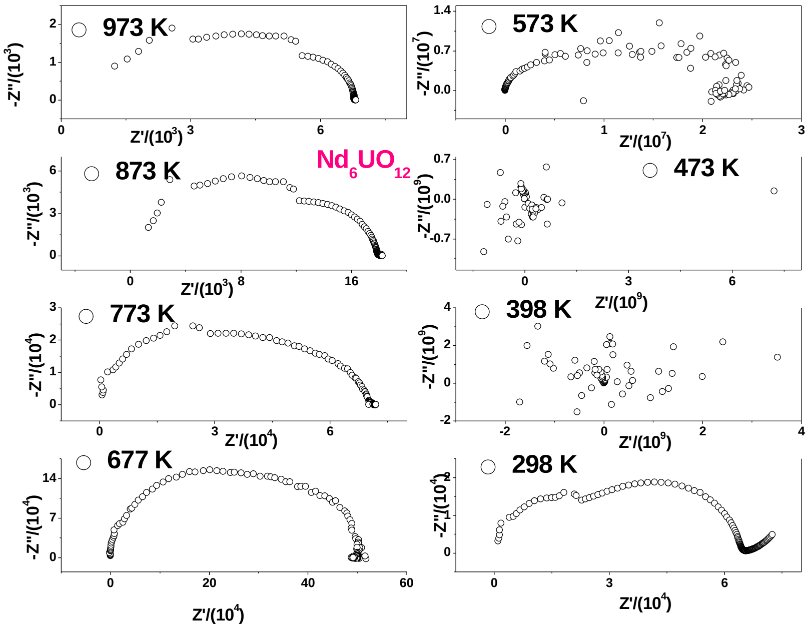

Fig.3.39. The Nyquist plot of Nd_6UO_{12}(s)

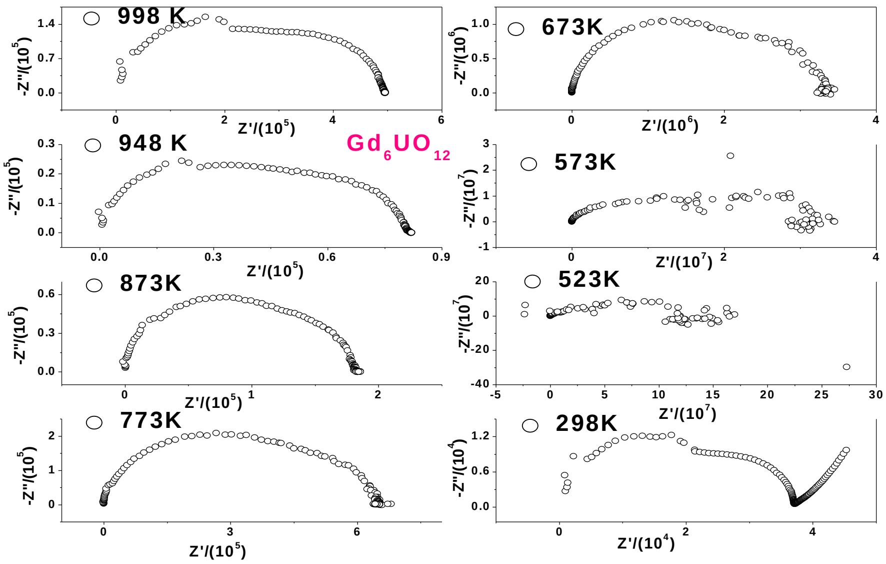

Fig.3.40. The Nyquist plot of Gd_6UO_{12}(s)

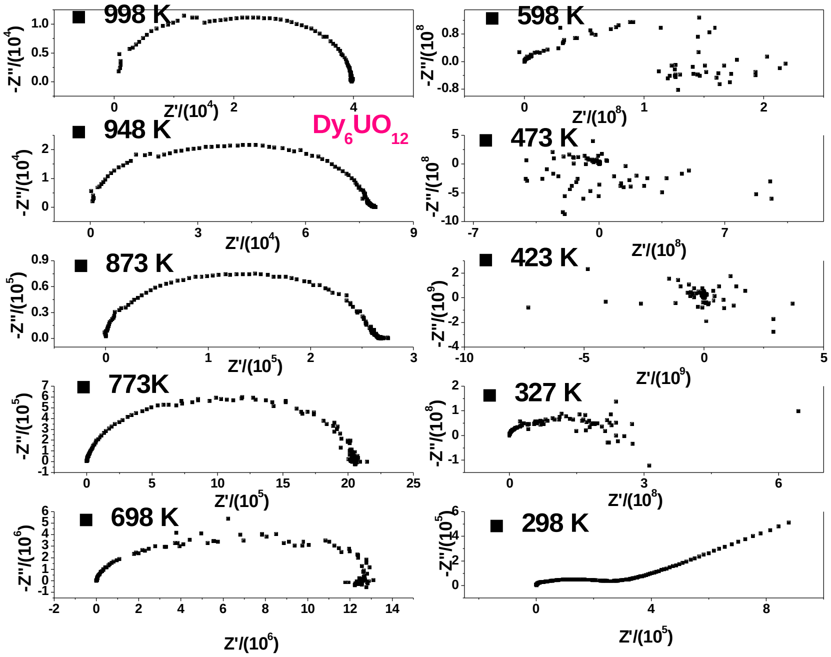

Fig.3.41.

The Nyquist plot of Dy_6UO_{12}(s)

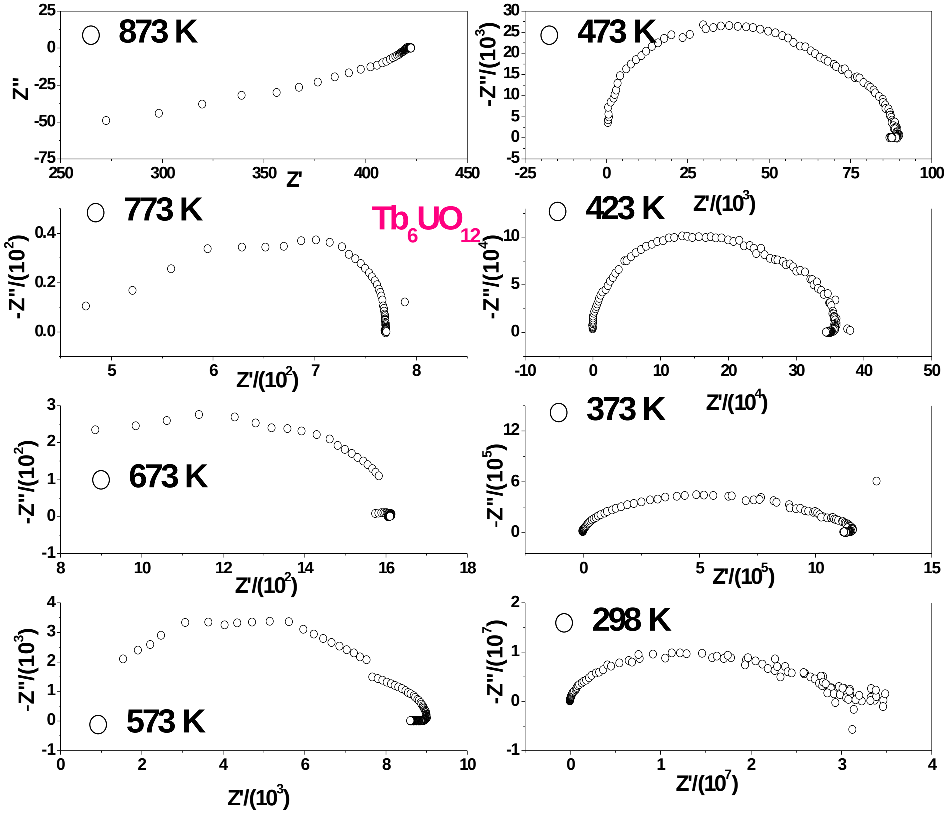

Fig.3.42. The Nyquist plot of Tb$_6$UO$_{12}$(s)

The scatter in impedance plots is factor which decides the lowest temperature of measurement and the highest temperature is limited by the heating element of the furnace. In this experiment, nichrome heating element was used.

Table 3.19: Conductivity values of RE$_6$UO$_{12}$(s) (RE= Nd, Gd, Dy, Tb) in air ambient

Nd$_6$UO$_{12}$(s)		**Gd$_6$UO$_{12}$(s)**		**Tb$_6$UO$_{12}$(s)**		**Dy$_6$UO$_{12}$(s)**	
T / K	**ln (σ) / ohm $^{-1}$ cm $^{-1}$**	**T / K**	**ln (σ) / ohm $^{-1}$ cm $^{-1}$**	**T / K**	**ln (σ) / ohm $^{-1}$ cm $^{-1}$**	**T / K**	**ln (σ) / ohm $^{-1}$ cm $^{-1}$**
523	-19.1658	498	-19.7342	298	-17.1958	598	-19.5154
548	-18.0429	523	-19.0401	323	-16.4852	623	-18.9198
573	-17.0870	548	-18.3426	333	-15.8855	648	-18.1653
598	-15.6642	573	-17.4546	361	-14.796	673	-17.5838
623	-14.6287	598	-16.9046	373	-14.3077	698	-16.8952
677	-13.2400	623	-16.2669	398	-13.9167	723	-16.2355
688	-12.9911	648	-15.723	423	-13.1386	748	-15.6394
703	-12.6778	673	-15.2031	449	-12.3272	773	-15.0727
723	-12.2622	698	-14.73	473	-11.7486	798	-14.506
738	-11.9767	723	-14.3133	498	-11.0043	823	-13.9897
758	-11.6022	748	-13.9143	523	-10.3901	848	-13.4764
773	-11.2788	773	-13.5629	548	-9.91082	873	-12.9995
793	-10.9841	798	-13.216	573	-9.45144	898	-12.5683
813	-10.6823	823	-12.8805	598	-8.6652	923	-12.2032
833	-10.4033	848	-12.5649	623	-8.3182	948	-11.7892
853	-10.1264	873	-12.2828	648	-7.98148	973	-11.4337
873	-9.9090	898	-12.0149	673	-7.73617	998	-11.1132
893	-9.6776	923	-11.747	773	-6.99078		
913	-9.4888	948	-11.4753	798	-6.8401		
933	-9.2753	973	-11.2222				
953	-9.1069	998	-10.9788				
973	-8.9387						

3.3. Discussion

3.3.1. Thermal expansion using HT-XRD

The lattice parameters (*a* and *c*) and unit cell volume (*V*) were found to increase with temperature for RE$_6$UO$_{12}$(s)(RE= La,Pr, Nd, Sm, Eu, Gd, Tb, Dy, Ho, Er, Tm, Yb, Lu), which are shown in **Figs. 3.5-3.7.** The expansion data from literature **[16]** for RE_6UO_{12}(s) (RE= La, and Nd) are also included. However, the density of RE_6UO_{12}(s) is found to decrease with temperature as shown in **Fig. 3.8.** Figures **3.5-3.7** show that the lattice parameters (*a* and *c*) and unit cell volume of RE_6UO_{12}(s)(RE= La,Pr, Nd, Sm, Eu, Gd, Tb, Dy, Ho, Er, Tm, Lu) are continuous, but, Yb_6UO_{12}(s) shows deviation in the lattice parameters along *a* axis and unit cell volume which peaks up at 1073 K. The lattice parameters (*a*, c), the unit cell volume (*V*) were found to decrease with reduction in ionic radii of rare earth ions along the series. **Fig.3.9** represents the percentage deviation of lattice parameter along *a*-axis for RE_6UO_{12}(s) (RE= La,Pr, Nd, Sm, Eu, Gd, Tb, Dy, Ho, Er, Tm, Yb, Lu), where the anomaly for Tb_6UO_{12}(s) was observed 573 K onwards. **Fig.3.10 and Fig. 3.11** represents the percentage deviation of lattice parameter along *c*-axis and of unit cell volume for RE_6UO_{12}(s) (RE= La, Pr, Nd, Sm, Eu, Gd, Tb, Dy, Ho, Er, Tm, Yb, Lu), which shows anomaly at 473 K for Tb_6UO_{12}(s). Similarly, anomally was observed for Yb_6UO_{12}(s) in percentage variation along *a*-axis and of unit cell volume at ~ 1073 K. These anomally predicts displacive phase transition in RE_6UO_{12}(s) (RE= Tb and Yb). The XRD patterns of these compounds don't show any extra peak near the temperature of anomally as it is shown for Yb_6UO_{12}(s) as an example in **Fig 3.43.**

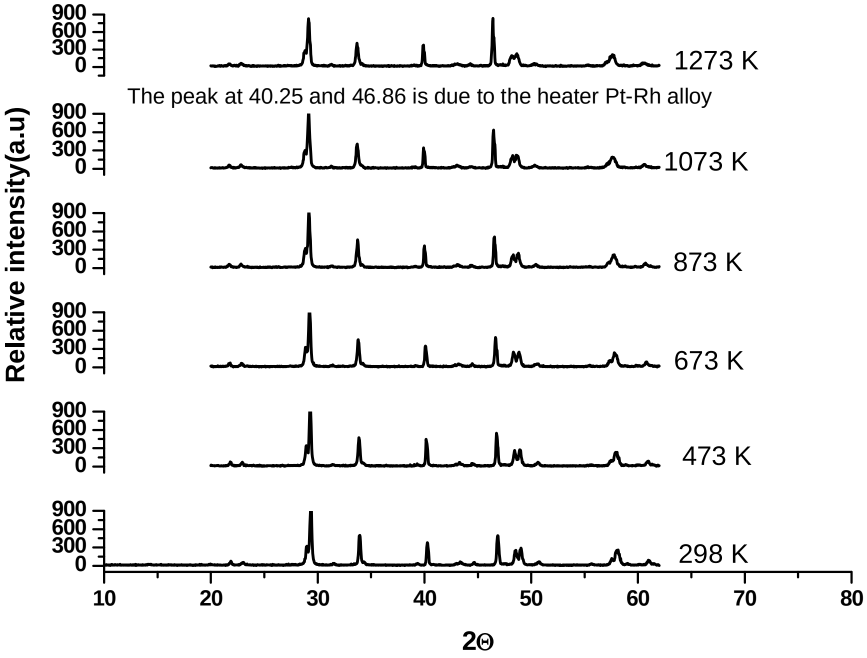

Fig.3.43. The high temperatures XRD patterns of Yb_6UO_{12}(s).

The unit cell parameters and the unit cell volume of Dy_6UO_{12}(s) as a function of temperature is reported by Venkata Krishnan et al. [19], which is also plotted against the values obtained in this study in Fig. 3.44 and these parameters were found to match with that of the present investigation within the error limit. The unit cell parameters and the unit cell volume of Sm_6UO_{12}(s) as a function of temperature is reported by Jena et al. [24], which is also plotted against the data obtained in this study in **Fig. 3.45** and these parameters also were found to match with that of the present investigation.

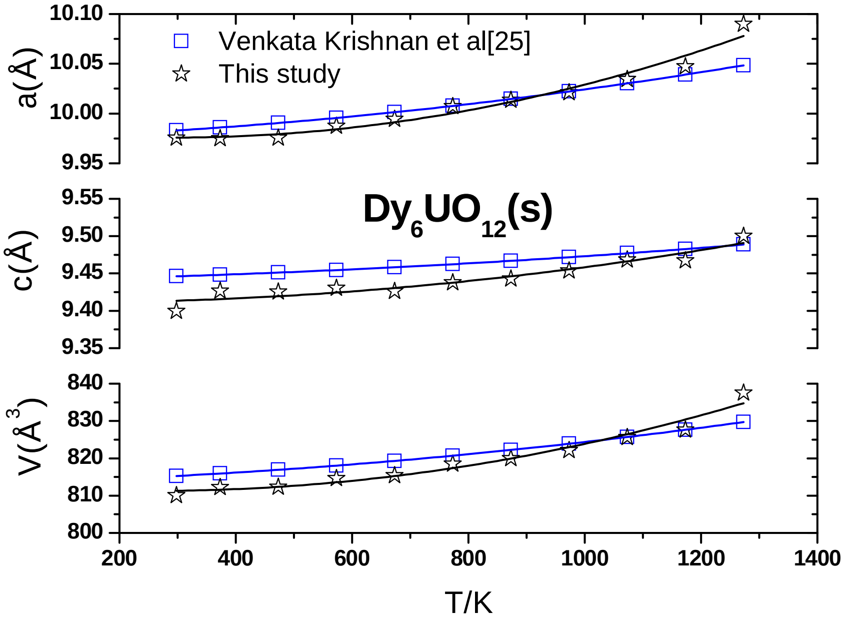

Fig. 3.44. The lattice parameters and unit cell volume of Dy_6UO_{12}(s)

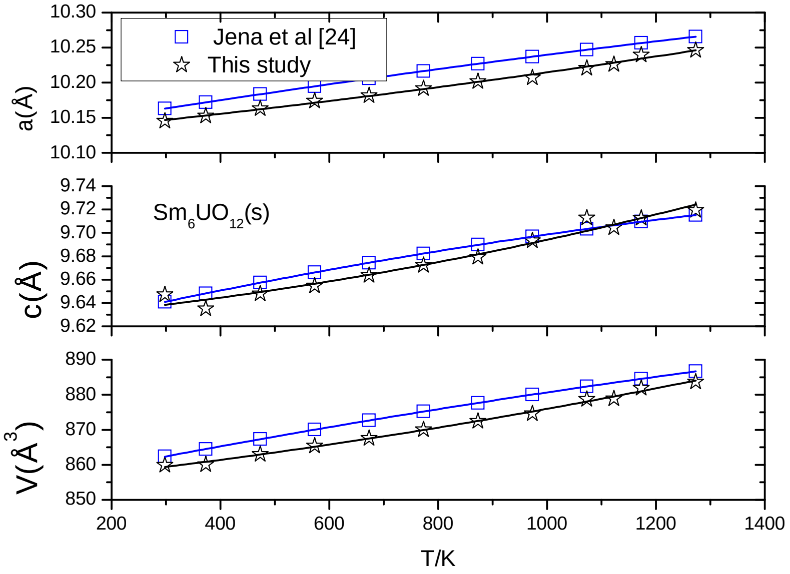

Fig. 3.45. Lattice parameters and unit cell volume of Sm_6UO_{12}(s)

Then the lattice parameters (*a* & *c*) , unit cell volume, percentage expansion along *a* and *c* axis , percentage variation of unit cell volume, the axial thermal expansion coefficients and volume expansion coefficients of Dy_6UO_{12}(s), Tb_6UO_{12}(s) and Yb_6UO_{12}(s) were plotted separately for comparision. Among the three compounds, Dy_6UO_{12}(s) did not show any anomaly, but Tb_6UO_{12}(s) and Yb_6UO_{12}(s) showed anomaly in thermal expansion measurement as described in earlier paragraph.

Fig. 3.46 shows smooth and continuous variation of lattice parameters (*a* & *c)*, unit cell volume (*V*), percentage expansion along *a* and *c* axis (%*a* &%c), percentage variation of unit cell volume(%*V*). The axial thermal expansion coefficients (α_a & α_c) and volume expansion coefficients (α_V) of Dy_6UO_{12}(s) also don't show any prominent peak, though there is no regular trend in axial thermal expansion coefficients along *c*-axis (α_c). These observations confirm the absence of any kind of phase transition in Dy_6UO_{12}(s).

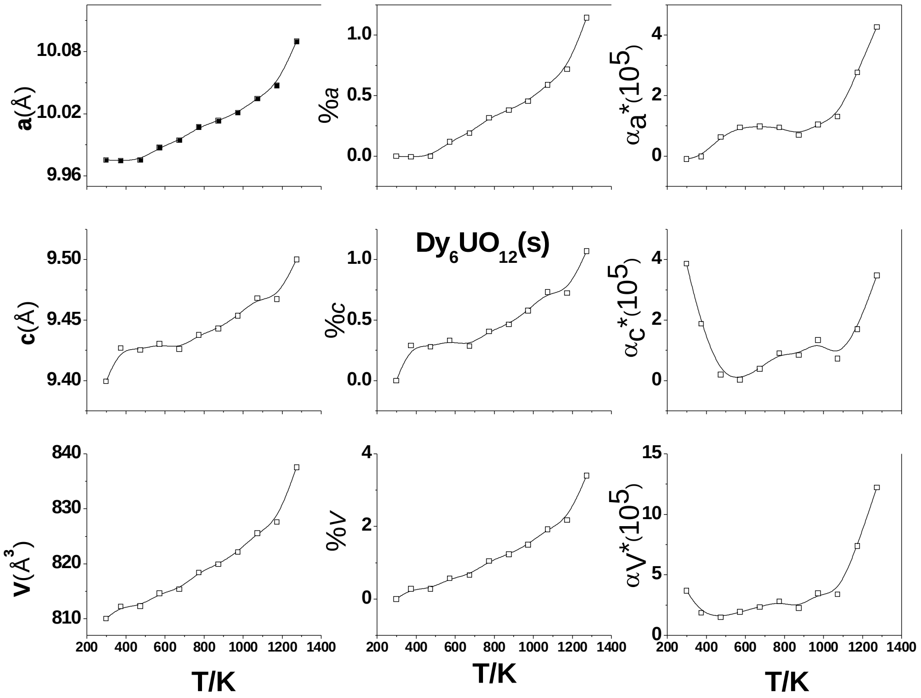

Fig.3.46. The lattice parameters (*a* & *c*), unit cell volume (*V*), percentage expansion along *a* and *c* axis (%*a* &%c), percentage variation of unit cell volume(%*V*), the axial thermal expansion coefficients (α_a & α_c) and volume expansion coefficients (α_V) of Dy_6UO_{12}(s).

Fig. 3.47 shows the lattice parameters (*a* & *c*), unit cell volume (*V*), percentage expansion along *a* and *c* axis (%*a* &%c), percentage variation of unit cell volume (%*V*), the axial thermal expansion coefficients (α_a & α_c) and volume expansion coefficients (α_V) of Tb_6UO_{12}(s). It shows change in slope of lattice parameters along *a* axis at 673 K and 973 K and change in slope of lattice parameters along *c*- axis at 673 K and 873 K. The change in slope was also observed for unit cell volume (*V)* at 673 K and 1073 K. The first slope change occurred at invariant temperature of 673 K for lattice parameters, unit cell volume and % thermal expansions. But the second change in slope observed at 973 K, 873 K and 1073 K for % *a*, % c, and % V respectively. Moreover, the magnitude of second slope change is quite small and not well defined. The plot of axial thermal expansion coefficients (α_a & α_c) and volume expansion coefficients (α_V) of Tb_6UO_{12}(s) show a prominent peak starting at 573 K which extend up to 973 K and the peak temperature was found to be 775 K. These observations confirm the presence of a phase transition at around 673 K. This transition is not due to any structural transition which is confirmed from the identical XRD pattern obtained in the complete experimental temperature range by HT-XR

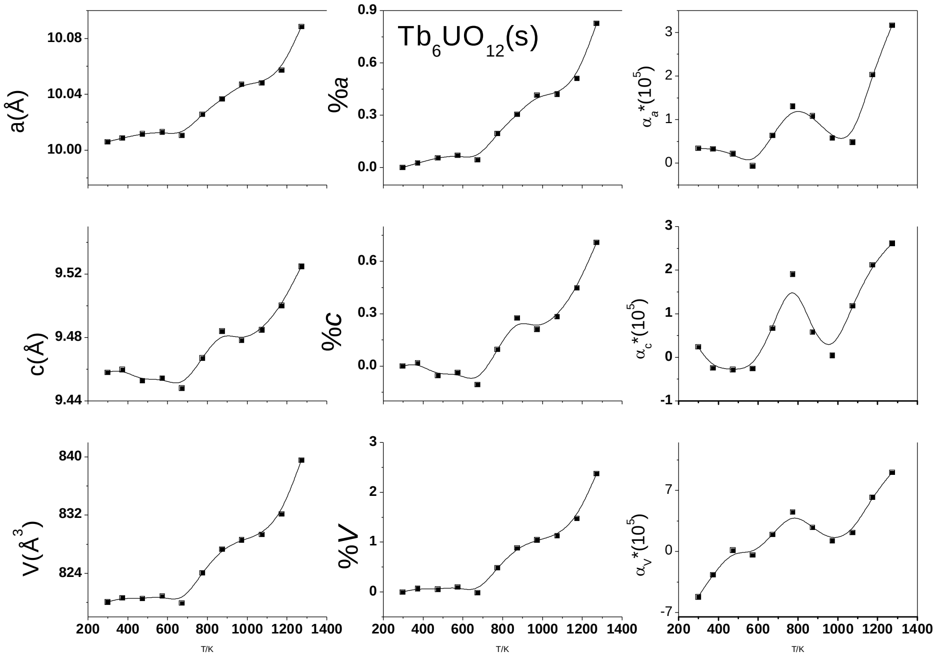

Fig.3.47.

The lattice parameters (*a* & *c*), unit cell volume (*V*), percentage expansion along *a* and *c* axis (%*a* &%c), percentage variation of unit cell volume(%*V*), the axial thermal expansion coefficients (α_a & α_c) and volume expansion coefficients (α_V) of Tb_6UO_{12}(s).

Fig.**3.48** shows lattice parameters (*a* & *c*), unit cell volume (*V*), percentage expansion along *a* and *c* axis (%*a* &%c), percentage variation of unit cell volume (%*V*), the axial thermal expansion coefficients (α_a & α_c) and volume expansion coefficients (α_V) as a function of temperature for Yb_6UO_{12}(s). In all the plots a well defined peak was observed at 1073 K. Moreover the magnitudes of change in various parameters along *c*-axis are comparatively smaller than along a-axis, which is reflected in the dependent unit cell volume. These observations predict a phase transition at around 1073 K. This transition is not due to any structural transition which is confirmed from the identical XRD pattern obtained through the experimental temperature range as shown in **Fig.3.43.**

The transition in Tb_6UO_{12}(s) and Yb_6UO_{12}(s) could be second-order phase transitions at the temperature 673K and 1073 K respectively. This result for Yb_6UO_{12}(s) corroborates the e.m.f. measurement where a slope change was observed for Yb_6UO_{12}(s) at 1065 K as shown in **Fig.3.35**. The difference in temperature of 10 K is acceptable as the thermal expansion measurements were being carried out at a temperature interval of 100K which is very large. These types of predictions were also made in the literature [**167-169**] for the phase transition in different compounds using HT-XRD.

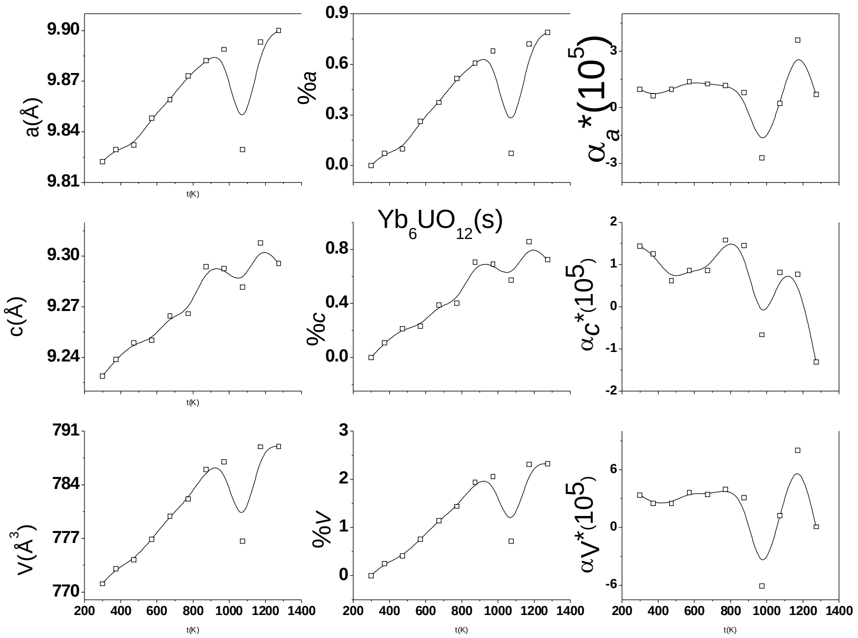

Fig.3.48. The lattice parameters (*a* & *c*), unit cell volume (*V*), percentage expansion along *a* and *c* axis (%*a* &%c), percentage variation of unit cell volume (%*V*), the axial thermal expansion coefficients (α_a & α_c) and volume expansion coefficients (α_V) of Yb_6UO_{12}(s).

Sm_6UO_{12}(s) also showed a slope change in the e.m.f. measurement on the preliminary study at 1125 K. This was confirmed from the thermal expansion data representation in **Fig.3.49.** Similar explanations as that for Yb_6UO_{12}(s) can assist in confirming the phase transition to be second order type.

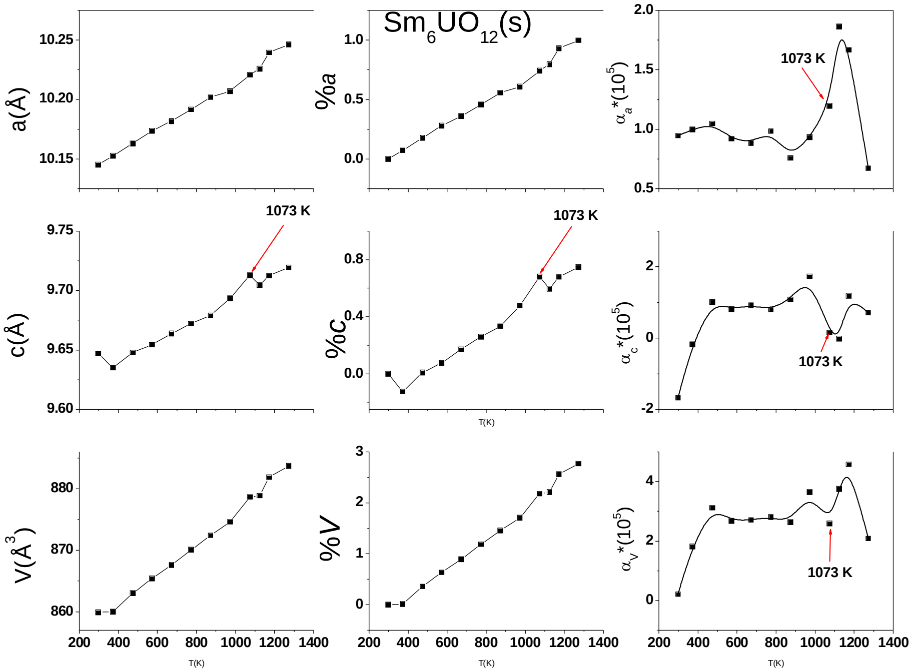

Fig.3.49. The lattice parameters (*a* & *c*), unit cell volume (*V*), percentage expansion along *a* and *c* axis (%*a* &%c), percentage variation of unit cell volume (%*V*), the axial thermal expansion coefficients (α_a & α_c) and volume expansion coefficients (α_V) of Sm_6UO_{12}(s).

Figure 3.50 compares the average linear thermal expansion coefficients (α_a and α_c) and volume thermal expansion coefficients (α_V) of RE_6UO_{12} (s) (RE = La, Pr, Nd, Sm, Eu, Gd, Tb, Dy, Ho, Er, Tm, Yb, Lu) as a function of radius of RE^{+3}. This figure shows a linear behaviour for RE_6UO_{12} (s) (RE = La, Gd, Lu), which might be due to the empty, half filled and full filled 4f orbital in La^{+3}, Gd^{+3} and Lu^{+3}, respectively. The data for RE_6UO_{12} (s) (RE = La, Nd) were taken from literature **[16]**. The reported data for RE_6UO_{12}(s) (RE =Eu, Gd, Sm) [**16 &20**] were also compared in **Table.3.20.**

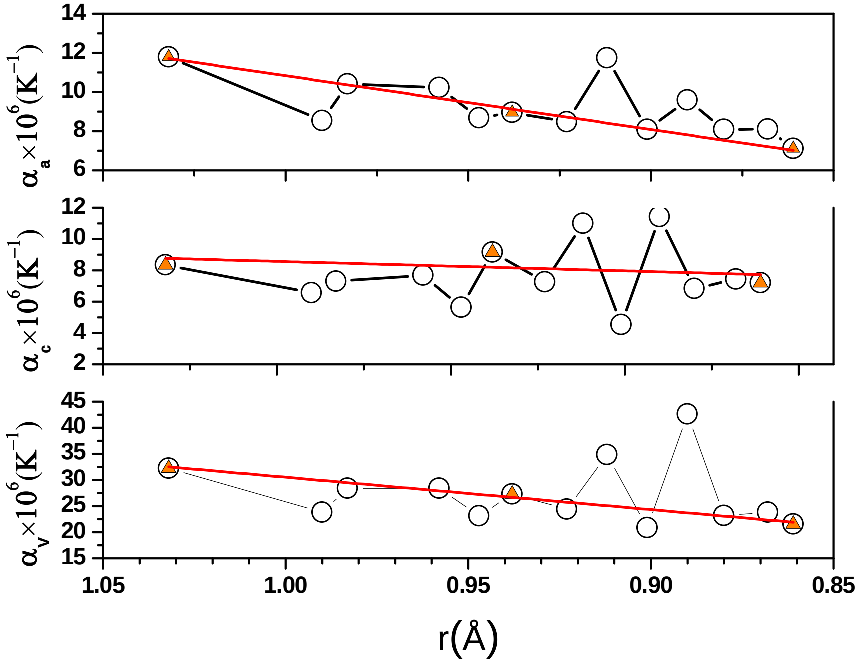

Fig.3.50. Comparison of the average linear thermal expansion coefficients (α_a and α_c) and volume thermal expansion coefficients (α_V) of RE_6UO_{12} (s) (RE = La, Pr, Nd, Sm, Eu, Gd, Tb, Dy, Ho, Er, Tm, Yb, Lu). as a function of radius of RE^{+3} in the temperature range 298-1273 K.

The thermal expansion in RE_6UO_{12}(s) (RE = La, Gd, Lu) are significantly contributed by lattice phonon and there is no excess electronic contribution due to empty, half filled and full filled 4 f orbitals, respectively. Therefore, it could be interpreted that the thermal expansion coefficients are due to the strength of the bonds involved in the compound as the lattice structure are same. The bond strength depends on the mass of the ions involved and in this case only rare earth ions changes on proceeding through the series. Therefore, the bond strength increases with reduction in size of trivalent rare earths ions (RE^{+3}). Hence, it was observed that the expansion coefficient reduces with reduction in RE^{+3} size and there exist a linear relation between expansion coefficients contributed by lattice phonon and the size of the rare earth ions as shown in **Fig 3.50** and the linear relation can be represented as:

$$\alpha_a(\text{Å}) = 10^{-5}\left(-1.6631 + 2.7462 \times r((\text{Å})\right) \tag{3.15}$$

$$\alpha_c(\text{Å}) = 10^{-6}\left(2.4869 + 6.0862 \times r((\text{Å})\right) \tag{3.16}$$

$$\alpha_V(\text{Å}^3) = 10^{-5}\left(-3.1455 + 6.198 \times r((\text{Å})\right) \tag{3.17}$$

Table 3.20. The average linear and volume thermal expansion coefficients of RE_6UO_{12} (s) (RE = La, Pr, Nd, Sm, Eu, Gd, Tb, Dy, Ho, Er, Tm, Yb, Lu).

Compound	**Ionic radius of RE^{3+}**	**$\alpha_a \times 10^6$ (K^{-1})**	**$\alpha_c \times 10^6$ (K^{-1})**	**$\alpha_V \times 10^5$ (K^{-1})**	**Temperature range(K)**
La_6UO_{12}(s)[16]	1.032	11.787	8.338	3.223	298-1173
Pr_6UO_{12}(s)	0.99	8.536	6.559	2.381	298-1273
Nd_6UO12(s) [16]	0.983	10.411	7.303	2.839	298-1173
Sm_6UO_{12}(s)	0.958	10.221	7.687	2.839	298-1273
Sm_6UO_{12}(s)[16]	0.958	10.36	7.904	2.891	298-1173
Eu_6UO_{12}(s)	0.947	8.676	5.629	2.314	298-1273
Eu_6UO_{12}(s)[20]	0.947	10.5	7.3	2.83	298-873
Gd_6UO_{12}	0.938	8.957	9.151	2.730	298-1273
Gd_6UO_{12}[20]	0.938	10.0	9.7	2.97	298-873
Tb_6UO_{12}(s)	0.923	8.477	7.266	2.440	298-1273
Dy_6UO_{12}(s)	0.912	11.742	10.988	3.486	298-1273
Dy_6UO_{12}(s)[19]	0.912	6.726	4.615	1.817	298-1973
Ho_6UO_{12}(s)	0.901	8.096	4.533	2.087	298-1273
Er_6UO_{12}(s)	0.89	9.596	11.412	4.260	298-1273
Tm_6UO_{12}(s)	0.88	8.096	6.830	2.320	298-1273
Yb_6UO_{12}(s)	0.868	8.103	7.435	2.382	298-1273
Lu_6UO_{12}(s)	0.861	7.108	7.202	2.157	298-1273

3.3.2. Heat capacity measurement using DSC

As RE_6UO_{12}(s)(RE= Pr, Nd, Sm, Eu, Tb, Dy, Ho, Er, Tm, Yb) has the same crystal structure, the heat capacity measurement of all the compounds will give an idea about the trend along the series. The heat capacity of RE_6UO_{12}(s)(RE= Pr, Nd, Sm, Eu, Tb, Dy, Ho, Er, Tm, Yb) show positive deviation from additive oxide values in all the cases. But for RE_6UO_{12}(s)(RE= La Gd and Lu) with f^0, f^7 and f^{14} show slight –ve deviation for additive values this could be due to the difference in the bond strength in RE_6UO_{12}(s) and in the binary oxides. In RE_2O_3(s), RE is seven coordinated and in RE_6UO_{12}(s), it is six coordinated. For RE_6UO_{12}(s)(RE= La Gd and Lu) due to the f^0, f^7 and f^{14} electronic configuration, the electronic and schottky contributions is negligible and the heat capacity is primarily contributed due to the lattice phonon vibrations. Decrease in heat capacity was observed with increase in atomic number for RE_6UO_{12}(s) (RE= La Gd and Lu).The increase in mass results in decrease in vibrational frequencies of unit cells and therefore correspondingly increases the lattice contributions to heat capacity. The interpolated heat capacity of RE_6UO_{12}(s)(RE= La Gd and Lu) will give an account of lattice heat capcity of other RE_6UO_{12}(s).The lattice heat capacity contribution is interpolated linearly in terms of atomic numbers of rare earth elements. The heat capacity of RE_6UO_{12}(s)(RE= Pr, Nd, Sm, Eu, Tb, Dy, Ho, Er, Tm, Yb) follows the trend of the computed heat capacity values using Newmann Kopp's rule as shown in **Figs.3.51 and 3.52.**

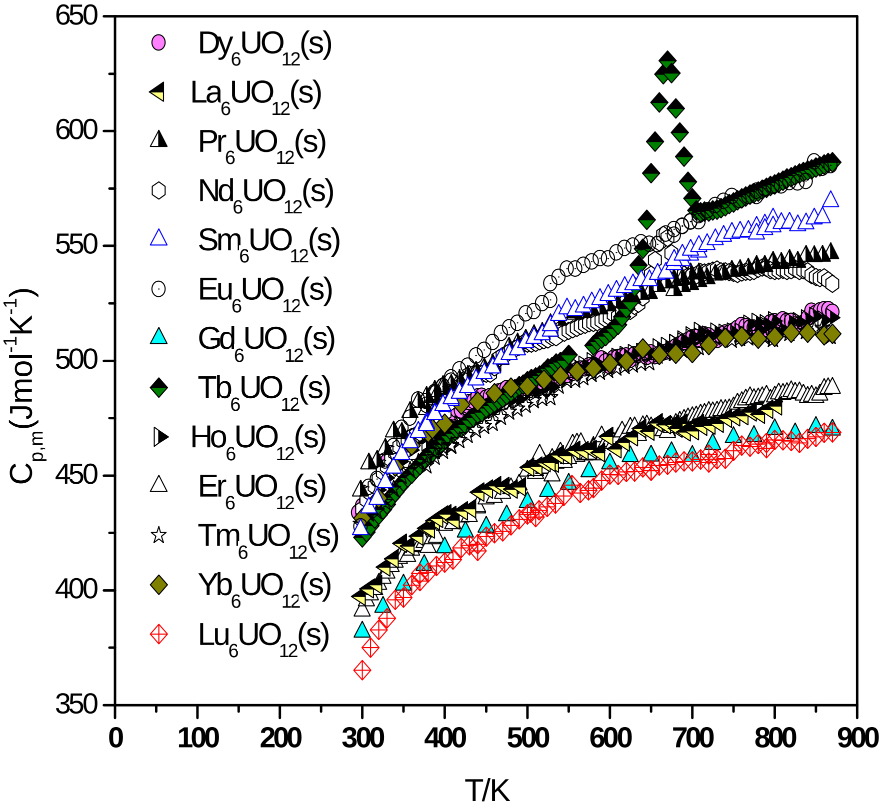

Fig.3.51. The measured heat capcity of RE_6UO_{12}(s)(RE= Pr, Nd, Sm, Eu, Tb, Dy, Ho, Er, Tm, Yb).

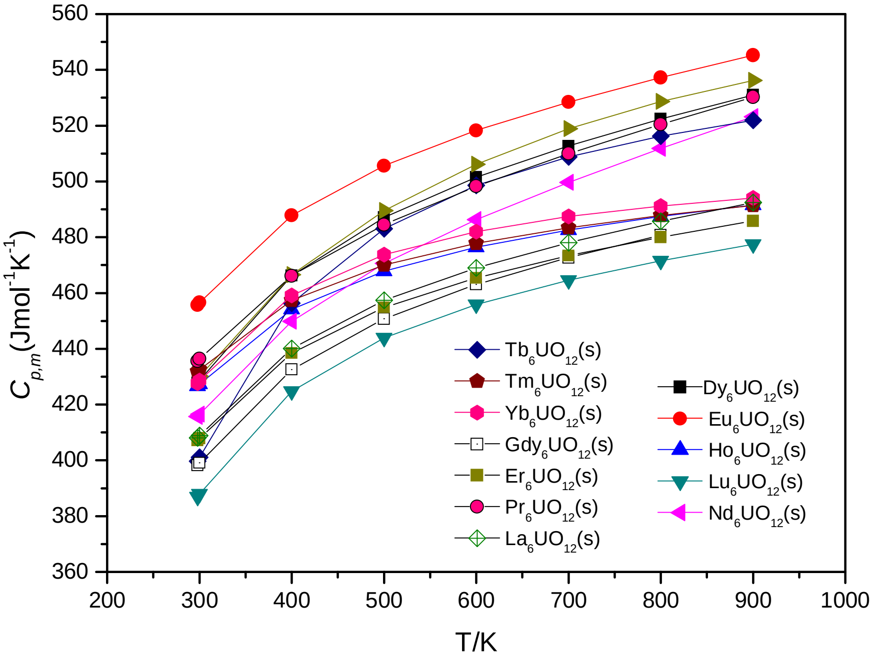

Fig.3.52. The computed heat capacity of RE_6UO_{12}(s)(RE= Pr, Nd, Sm, Eu, Tb, Dy, Ho, Er, Tm, Yb) using NK rule.

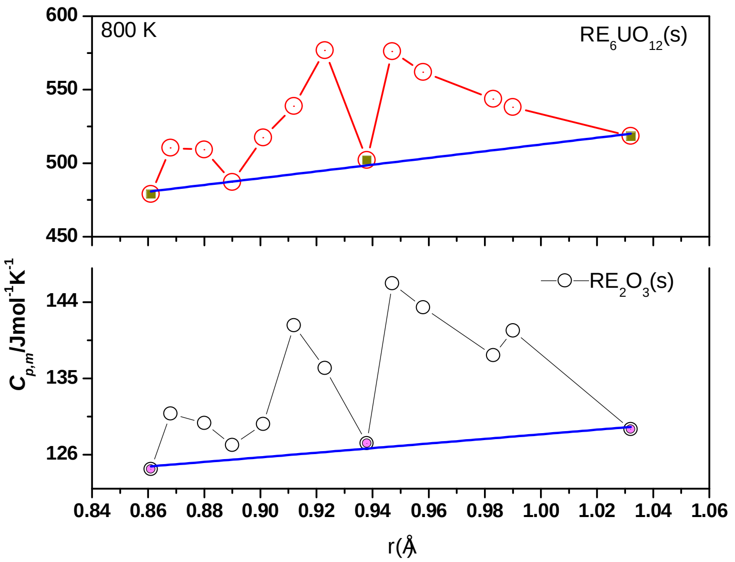

Fig.3.53. A comparison of heat capacity of RE_6UO_{12}(s) and RE_2O_3(s)

The heat capacity values of RE_6UO_{12}(s)(RE= Pr, Nd, Sm, Eu, Tb, Dy, Ho, Er, Tm, Yb) at 800 K as a function of ionic radii of rare earth ions in hexa coordination was compared with that of RE_2O_3(s)(RE= Pr, Nd, Sm, Eu, Tb, Dy, Ho, Er, Tm, Yb) in **fig.3.53**. There was a regular trend observed for both the ternary and binary compounds containing rare earth elements. Therefore it can be concluded that the rare earth ions are playing the major role.

The heat capacity plot of Nd_6UO_{12}(s) and Tb_6UO_{12}(s) shows anomaly at 665 and 670 K, respectively. The transition in Nd_6UO_{12}(s) was confirmed from the measurement of expansion coefficients using dilatometry as given in Fig.**3.54.** Similarly, the phase transition in Tb_6UO_{12}(s) was also observed in thermal expansion measurement as explained earlier and now it was confirmed by DSC. **Fig 3.54** shows the plot of thermal expansion coefficient as a function of temperature using dilatometry. The experimental procedure followed is described in section 2.4.1.2.2.

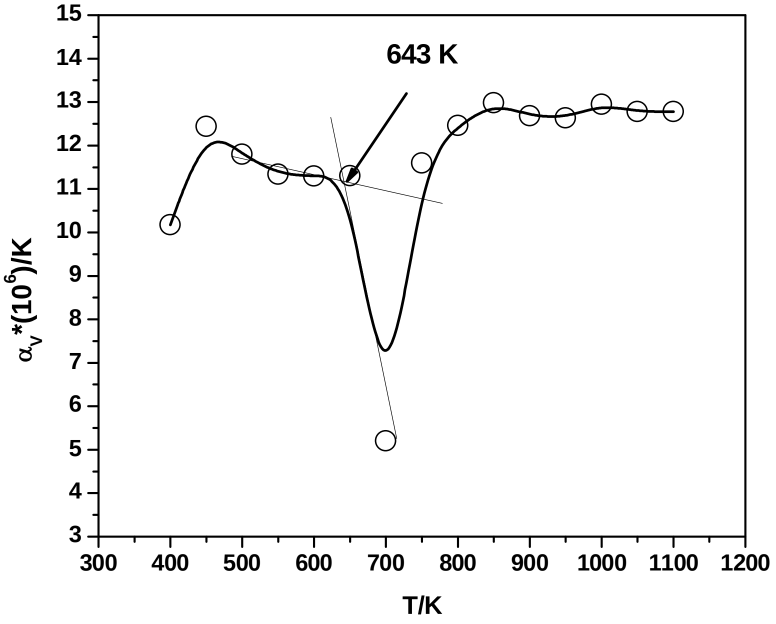

Fig.3.54. The volume expansion coefficients (α_V) of Nd_6UO_{12}(s) measured using push rod dilatometry.

The plot shows a peak at ~700 K. The difference in temperature of transition between dilatometry and DSC was 35 K, which could be due to the thermal expansions measurement was carried out in a gap of 50 K. Therefore, it concludes that the temperature of transition at 665 K for Nd_6UO_{12}(s) is a second order transition. The baseline of heat capacity curve was determined by interpolating the heat capacities in both higher and lower temperature ranges excluding the C_p of phase transition temperatures. The excess heat capacities of Nd_6UO_{12} (s) was obtained by subtracting the baseline and are shown in **Fig. 3.55.**

The transition enthalpy and entropy was obtained from the following integrations (i.e. area under the curve represented in Fig.3.55(a) and 3.55(b).

$$\Delta H_{Trs} = \int \Delta C^{o}_{p,m} \; dT \qquad (3.18)$$

$$\Delta S_{Trs} = \int \frac{\Delta C^{o}_{p,m}}{T} \; dT \qquad (3.19)$$

The transition enthalpy and entropy of Nd_6UO_{12} was calculated to be 3.21 kJ/mole and 4.75 J $mol^{-1}K^{-1}$, respectively.

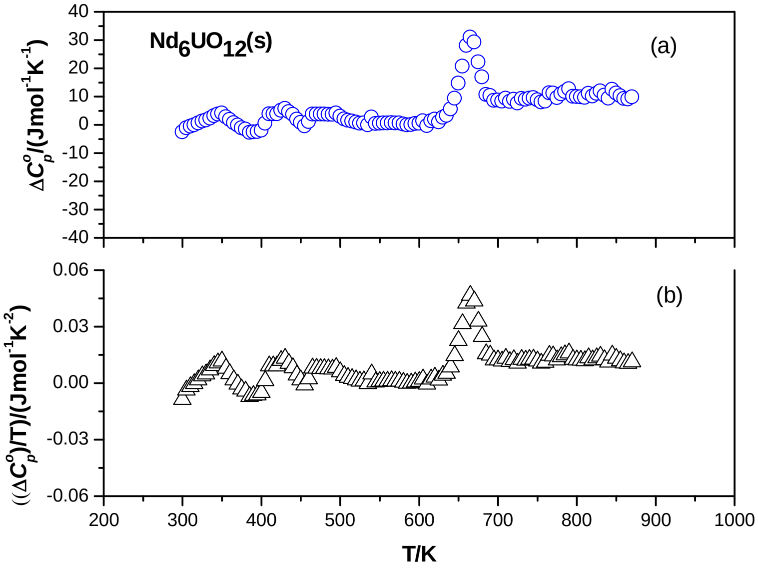

Fig.3.55. Excess heat capacity of Nd_6UO_{12}(s) as a function of temperature. (a) Plot of $\Delta C^{o}_{p,m}$ (T) vs T (b) Plot of $\frac{\Delta C^{o}_{p,m}(T)}{T}$ vs T

The heat flow curve obtained for both heating and cooling runs of Tb_6UO_{12}(s) are shown in the **Fig. 3.56(a).** A prominent baseline shift was observed in the heat flow curve at temperature of 646 K which ends at 673 K. Shift in baseline was due to change in heat capacity of Tb_6UO_{12}(s). The effect of baseline shift was observed as a prominent peak in heat capacity curve which gave confirmation about the second-order phase transition as suggested in the literature [**167-169**]. But no prominent shift in baseline was observed in the cooling curve, which could be either due to slow kinetics of transition/ super cooling effect. This peak in heat capacity curve had a shape similar to λ, which is the shape of second-order transition. The excess heat capacities of Tb_6UO_{12} (s) were obtained following the same procedure as in Nd_6UO_{12}(s) by subtracting the baseline and are shown **in Fig. 3.57.** The transition enthalpy and entropy of Tb_6UO_{12}(s) was calculated to be 4.24 kJ mol^{-1} and 6.4 J $mol^{-1}K^{-1}$, respectively.

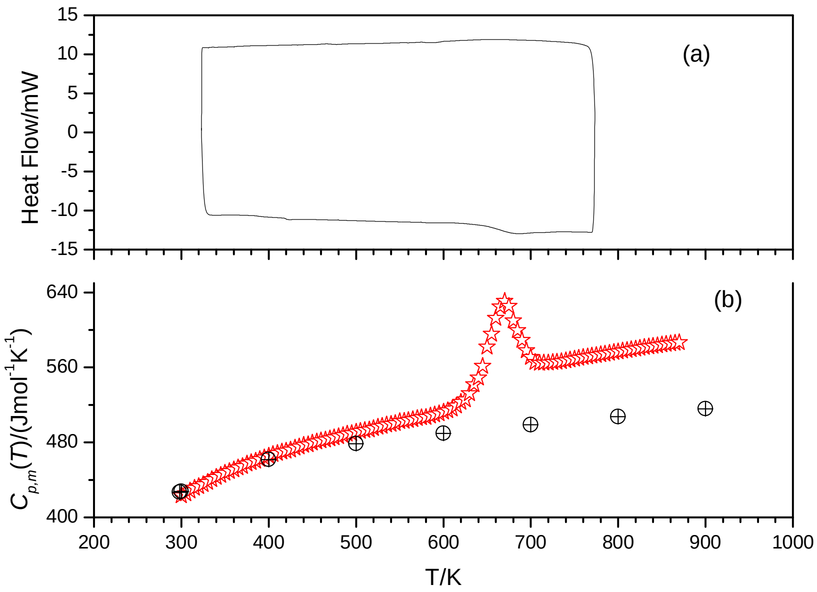

Fig.3.56. (a) Heat flow as a function of temperature for Tb_6UO_{12}(s) (b) Molar heat capacity data of Tb_6UO_{12}(s) in the temperature range of 300–870 K

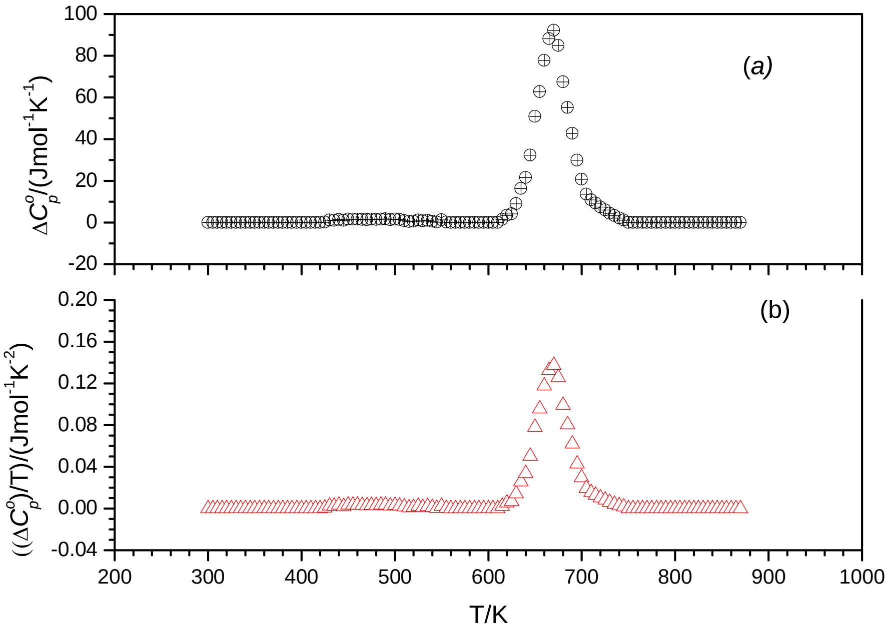

Fig.3.57. Excess heat capacity of Tb_6UO_{12} as a function of temperature. (a) Plot of $\Delta C^o_{p,m}$ vs T (b) Plot of $\frac{\Delta C^o_{p,m}}{T}$ vs T

3.3.3. E.m.f. measurements

As the oxygen potential of system RE_6UO_{12}(s) is not reported in the literature, the e.m.f was measured with low oxygen potential (Ni(s) + NiO(s)) as well as high oxygen potential (air) reference electrodes. ΔH_f^o(RE_6UO_{12},s,298.15K) was calculated by both second and third analysis for cell (2) and (3) and is given in Table 3.17 and 3.18. The difference in values of ΔH_f^o(RE_6UO_{12},s,298.15K) calculated from cell 2 and 3 from 3×(ΔH_f^o RE_2O_3(s), s, 298.15 K) + ΔH_f^o UO_3(s),s, 298.15 K) as function of atomic number of rare earth elements were plotted in **Fig.3.58**. The values calculated for earlier rare earth uranates RE_6UO_{12}(s) (RE= La to Dy) shows difference of ± 40 kJ mol^{-1} in the case of Ni(s)+NiO(s) reference while the difference is more in case of air reference (- 60 kJ mol^{-1}- 20 kJ mol^{-1}). This concludes the low oxygen potential of the phase mixture (RE_6UO_{12}(s) +U_3O_8(s) +RE_2O_3(s)) where RE= La -Dy. The difference is still higher for higher rare earths uranates RE_6UO_{12}(s) (RE= Dy to Lu). Moreover, the difference in case of air reference was found to be - 80 kJ mol^{-1} to 40 kJ mol^{-1} for RE_6UO_{12}(s) (RE= Dy to Lu) as compared to the (Ni(s) +NiO(s)) reference which is -100 kJ mol^{-1} to 80 kJ mol^{-1} . From this observation it can be concluded that the phase mixture RE_6UO_{12}(s) +U_3O_8(s) +RE_2O_3(s) has higher oxygen potential with RE = Dy-Lu. Therefore, it was concluded that, the data of ΔH_f^o(RE_6UO_{12},s,298.15K) for RE=La-Dy with respect to reference Ni(s)+NiO(s) and the data of ΔH_f^o(RE_6UO_{12},s,298.15K) for RE= Ho-Lu with respect to air was found to be correct and taken for further representation. The correct data were highlighted with bold letter in the table 3.17 and 3.18. In addition ΔH_f^o(RE_6UO_{12},s,298.15K) was calculated for RE=Sm and Yb for two temperature ranges due to the presence of phase transition. The ΔH_f^o(RE_6UO_{12},s,298.15K) calculated from the two linear fit e.m.f. for RE=Sm and Yb were found to be matching with each other within ± 10 kJ mol^{-1} . The ΔH_f^o(RE_6UO_{12},s,298.15K) calculated from second law , ΔH_f^o(RE_2O_3,s,298.15K) from literature [**166**] and the $\Delta_{OX}H_f^o$(RE_6UO_{12},s,298.15K) from oxides were plotted as function of atomic number of rare earth elements in **fig.3.59**.The figure shows similar trend for RE_6UO_{12}(s) and RE_2O_3(s) which is an additional evidence of the correctness of the data measured in this study. Moreover, $\Delta_{OX}H_f^o$(RE_6UO_{12},s,298.15K) was found to be within -114 to 8 kJ mol^{-1}. S^o(RE_6UO_{12},s,298.15K) was calculated from second law analysis and given in table table 3.17 and 3.18. ΔH_f^o(RE_6UO_{12},s,298.15K) calculated from second law and third law as a function of atomic number were also compared in **Fig.3.60** and found to be in agreement. S^o(RE_6UO_{12},s,298.15K), S^o(RE_2O_3,s,298.15K) and $\Delta_{OX}S^o$(RE_6UO_{12},s,298.15K) were plotted as function of atomic number of rare earth elements in **Fig.3.61.** S^o(RE_6UO_{12},s,298.15K) and S^o(RE_2O_3,s,298.15K) shows more or less similar trend and the values of $\Delta_{OX}S^o$(RE_6UO_{12},s,298.15K) were within ± 36 $Jmol^{-1}K^{-1}$. S^o(RE_6UO_{12},s,298.15K) values for RE=La-Dy calculated from the cell with reference electrode (Ni(s)+NiO(s)) and for RE=Ho-Lu with reference electrode as air are considered to be correct and highlighted with bold font in Table 3.17 and 3.18.

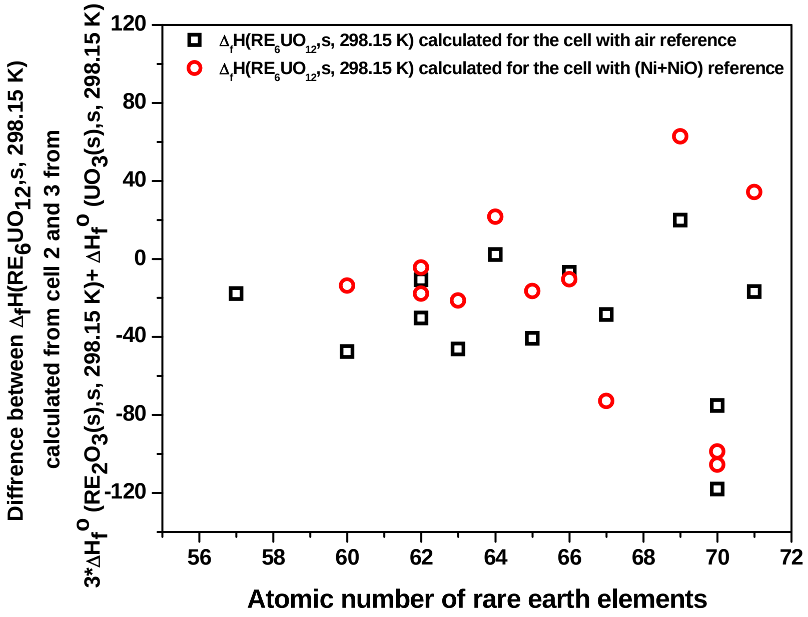

Fig.3.58. The plot of difference in $\Delta H_f^o(RE_6UO_{12}$,s,298.15K) calculated from cell 2 and 3 from the sum of ΔH_f^o of $(3RE_2O_3(s)+UO_3(s))$ as function of atomic radii of rare earth ions.

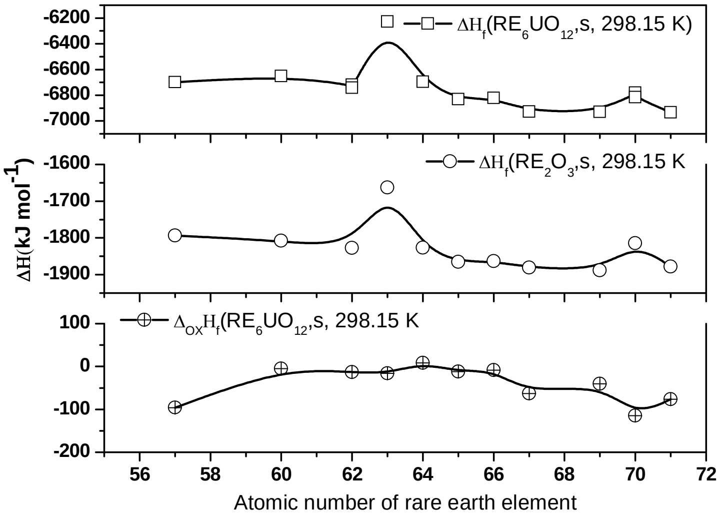

Fig.3.59.The plot of $\Delta H_f^o(RE_6UO_{12}$,s,298.15K) calculated from second law, $\Delta H_f^o(RE_2O_3$,s,298.15K) from literature [26] and the $\Delta_{OX}H_f^o(RE_6UO_{12}$,s,298.15K) from oxides as a function of atomic number of rare earth elements.

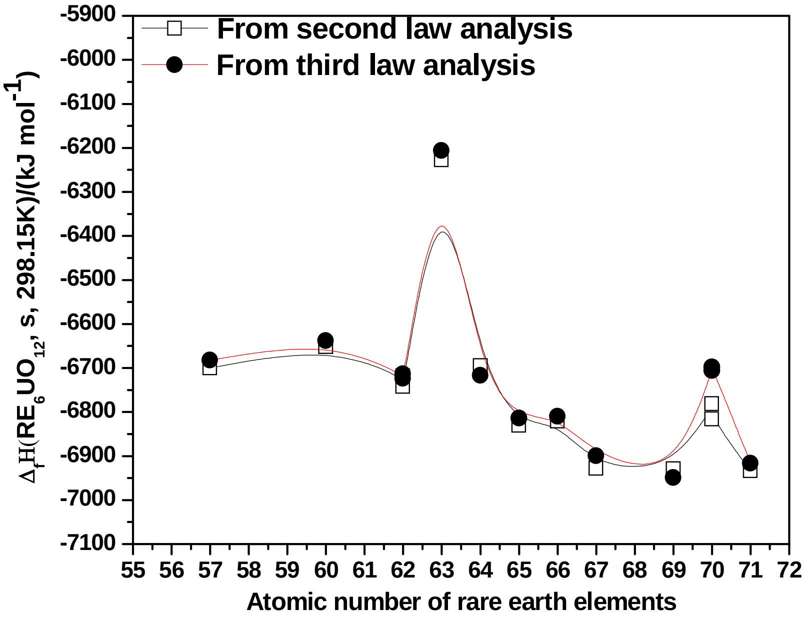

Fig.3.60.$\Delta H_f^o(RE_6UO_{12}$,s,298.15K) calculated from second law and third law as a function of atomic number.

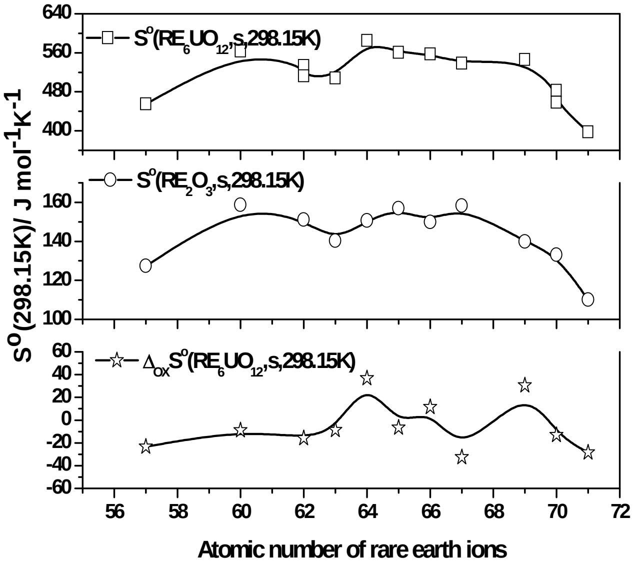

Fig.3.61.The plot of $S^o(RE_6UO_{12}$,s,298.15K) calculated from second law, $S^o(RE_2O_3$,s,298.15K) from literature [166] and $\Delta_{OX}S^o(RE_6UO_{12}$,s,298.15K) as a function of atomic number of rare earth elements.

The oxygen potential required for the formation of these compounds was essential to know its formation probability in nuclear reactor with oxide fuel. Therefore the oxygen potential was calculated for various rare earth uranates and compared with that of pure UO_2(s) and U_3O_8(s) in **fig.3.62.** Figure shows highest stability of La_6UO_{12}(s) whose oxygen potential lies between UO_2(s) and U_3O_8(s). It is also well known that the earlier rare earths like La have highest fission yeild in the reactor which again accelerates the formation probability of lanthanum uranates. From the figure it is clear that the stability order is UO_2(s) > La_6UO_{12}(s) >Tm_6UO_{12}(s) ~Ho_6UO_{12}(s)> >Lu_6UO_{12}(s) > U_3O_8(s) and other RE_6UO_{12}(s) fall above U_3O_8(s) with very small variation in oxygen potential.

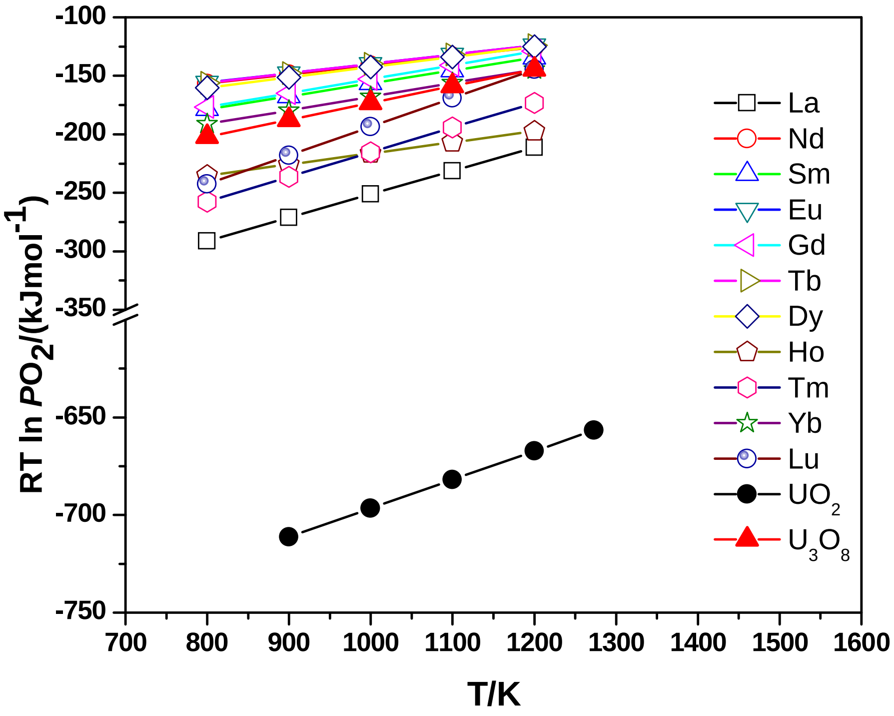

Fig.3.62. Oxygen potential diagram for RE_6UO_{12}(s), U_3O_8(s) and UO_2(s)

3.3.4. Electrical conductivity measurements of RE_6UO_{12}(s) (RE= Nd, Gd, Dy, Tb)

Fig.3.63 shows the electrical conductivity of RE_6UO_{12}(s)(RE= Nd, Gd, Dy, Tb) as a function of temperature. The observed variation of conductivity with temperature could be represented as log $\sigma = A - E/kT$, where A is Arrhenius constant, E is activation energy for the conduction process, *k* is the Boltzmann constant and *T* is temperature in Kelvin. From the conductivity measurement of Nd_6UO_{12}(s), a clear distinct break at 662 K was observed indicating a phase transition, which was strongly supported by the heat capacity data where the second order phase transition was observed at 665 K.

Similarly, the conductivity plot of Tb_6UO_{12}(s) showed two distinct breaks at 435 and 660 K. The second break at 660 K was corroborates the heat capacity data which showed a second order transition at 670 K. The first break at 435 K is supported by the percentage thermal expansion data where Tb_6UO_{12}(s) showed deviation in comparison to other rare earth uranates and it continues up to 1173 K as shown in **Fig.3.9-3.11**. There is a well defined slope change in thermal expansion coefficient at 473 K in Fig.3.43 which supports the presence of second order transition. But the evidence was not seen in heat capacity measurement which could be due to kinetic reason where the scan rate was kept to be 10 $Kmin^{-1}$.

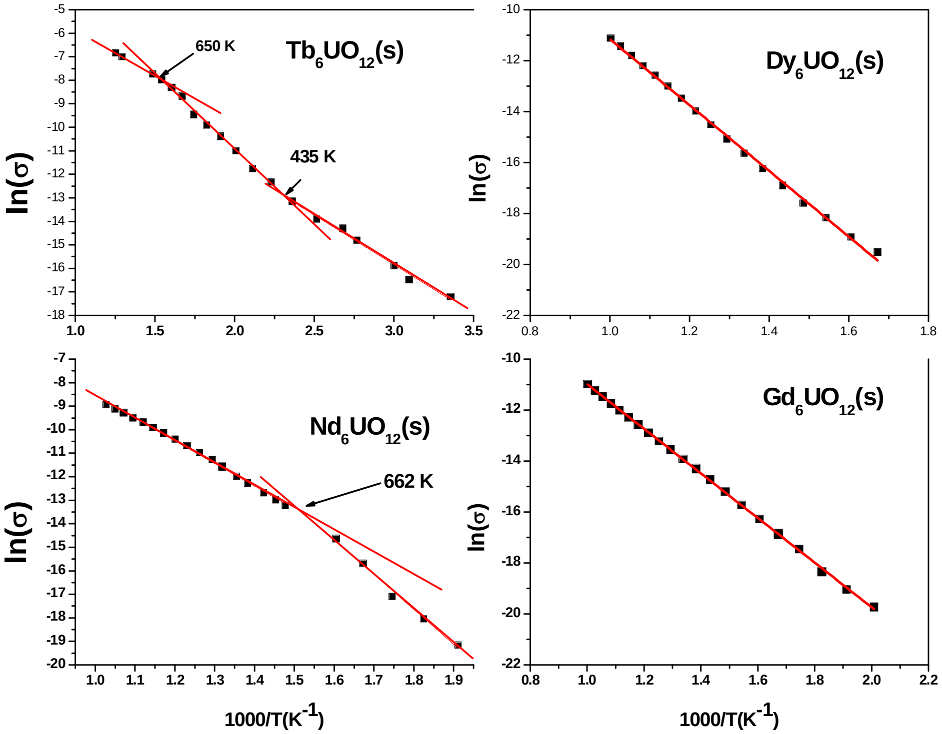

Fig.3.63: Conductivity of RE_6UO_{12}(s) (RE= Nd, Gd, Dy, Tb) in argon as a function of temperature

3.4 Summary

1. Synthesis conditions for RE_6UO_{12}(s) (RE= La, Pr, Nd, Sm, Eu, Gd, Tb, Dy, Ho, Er, Tm, Yb, Lu) using citrate – nitrate gel combustion method were optimised. Pr_6UO_{12}(s) and La_6UO_{12}(s) were synthesized in argon atmosphere but all other RE_6UO_{12}(s) were synthesized in air.
2. Er_6UO_{12}(s) was synthesized for the first time and its XRD pattern was indexed with hexagonal unit cell.Theoretical density was also calculated.
3. The lattice parameters of RE_6UO_{12}(s) was found to vary linearly with ionic radii of RE^{+3} in hexa coordination.
4. The thermal expansion of RE_6UO_{12} (s) (RE = La, Pr, Sm, Eu, Gd, Tb, Dy, Ho, Er, Tm, Yb, Lu) was measured using high temperature XRD and the axial and volume thermal expansion coefficients were calculated for these compounds.
5. Thermal expansion data revealed the phase transition in RE_6UO_{12} (RE=Sm, Tb and Yb). The transition temperatures are at 1173K, 673 K and 1073K, respectively.
6. The average linear (α_a and α_c) and volume thermal expansion coefficients (α_V) of RE_6UO_{12}(s) (RE = La, Pr, Nd, Sm, Eu, Gd, Tb, Dy, Ho, Er, Tm, Yb, Lu) as a function of radius of RE^{+3} were compared. The plot showed a linear behaviour for RE_6UO_{12}(s) (RE = La, Gd, Lu), which might be due to the empty, half filled and full filled 4 f orbital in La^{+3}, Gd^{+3} and Lu^{+3}, respectively.However other RE_6UO_{12}(s) showed irregularity.
7. The expansion coefficient found to reduce with reduction in size and there exist a linear relation between expansion coefficients contributed by lattice phonon and the size of the rare earth ions.
8. Heat capacity of RE_6UO_{12}(s) (RE= La, Pr, Nd, Sm, Eu, Gd, Tb, Dy, Ho, Er, Tm, Yb, Lu) was measured using DSC.
9. The heat capacity of RE_6UO_{12}(s) (RE= Pr, Nd, Sm, Eu, Tb, Dy, Ho, Er, Tm, Yb,) were found to be higher than the additive values computed by NK rule.
10. Heat capacity plot of Nd_6UO_{12}(s) and Tb_6UO_{12}(s) as a function of temperature showed presence of second order phase transition at 665 and 670 K, respectively.
11. The phase transition in Nd_6UO_{12}(s) was supported by thermal expansion measurement by dilatometry.

12. The electrical conductivity measurement of Nd_6UO_{12}(s) and Tb_6UO_{12}(s) as a function temperature also showed change in slope at 662 and 660K which support the presence of phase transition in heat capacity.

13. Thermodynamic functions like enthalpy increment, entropy and Gibbs energy function were generated from the measured heat capacity data.

14. Standard molar Gibbs energies of formation of RE_6UO_{12}(s) (RE=La, Nd, Sm, Eu, Gd, Tb, Dy, Ho, Tm, Yb, Lu) were measured using solid oxide galvanic cell.

15. The e.m.f.s as function of temperature plots of Sm_6UO_{12}(s) and Yb_6UO_{12}(s) showed change in slope at 1125 and 1065 K, respectively.

16. Second law as well as third law methods were used for finding $\Delta H_f^o(RE_6UO_{12}$, s, 298.15 K). $S^o(RE_6UO_{12}$,s,298.15K) was calculated from second law data analysis.

17. The plot of ΔH_f^o (298.15K) for the ternary oxides RE_6UO_{12}(s) and that for the binary oxides RE_2O_3 as a function of atomic number of rare earth elements followed the same trend as the moiety of rare earth element only changes though moiety of uranium remains the same.

18. $\Delta_{OX}H_f^o(RE_6UO_{12}$,s,298.15K) was found to be within -114 to 8 kJ mol^{-1} and it is maximum for Yb_6UO_{12}(s) and minimum for G_6UO_{12} (s).

19. The $S^o(RE_6UO_{12}$,s,298.15K) and $S^o(RE_2O_3$,s,298.15K) showed approximately similar trend and the values of $\Delta_{OX}S^o(RE_6UO_{12}$,s,298.15K) were found to be within ± 36 $Jmol^{-1}K^{-1}$.

20. The oxygen potential was calculated for various rare earth uranates and compared with that of pure UO_2(s) and U_3O_8(s). La_6UO_{12}(s) was found to have maximum stability whose oxygen potential situated between UO_2(s) and U_3O_8(s). The stability order of rare earth actinide oxides was found to be UO_2(s) > La_6UO_{12}(s) > Tm_6UO_{12}(s) ~ Ho_6UO_{12}(s) > Lu_6UO_{12}(s) > U_3O_8(s). The $\Delta\mu(O_2)$ of RE_6UO_{12}(s) (RE= Nd, Sm, Eu, Gd, Tb, Dy, Yb) was calculated to be higher than that of U_3O_8(s).

CHAPTER-4

Sr-Ce-O system

Chapter-4

The thermopysico chemical properties of various phases in the Sr-Ce-O system can be used to predict the behavior of plutonium bearing fuel as Ce is a surrogate of Pu. Sr-Ce-O system is characterized with $SrCeO_3$(s) and Sr_2CeO_4(s) and there are limited studies on these compounds. Hence, in the present investigations, thermal exapansion of $SrCeO_3$(s) and Sr_2CeO_4(s) were measured using HT-XRD and heat capacity of CeO_2(s), $SrCeO_3$(s) and Sr_2CeO_4(s) were measured using DSC.

4.1. Synthesis of Ternary compounds

CeO_2(s) (99.9% purity supplied by Rare Earth Development Section, BARC, Mumbai) and $SrCO_3$(s) (99.99% purity supplied by M/s Alfa Aesar, USA), $Ce(NO_3)_3{\cdot}5.6\ H_2O$ (99.5% purity supplied by M/s Across Organics, Mumbai) and Glycine (99.5% purity supplied by M/s Sisco Lab Pvt. Ltd., India) were used as precursor for the synthesis of $SrCeO_3$(s) and Sr_2CeO_4(s).

4.1.1. $SrCeO_3$(s)

The glycine–nitrate gel combustion method was adopted for the synthesis of $SrCeO_3$(s). Required amount of $SrCO_3$(s) was dissolved in dilute suprapure HNO_3 (aq). $Ce(NO_3)_3{\cdot}5.6\ H_2O$ was separately dissolved in 1 M HNO_3(aq) and 1 M H_2SO_4 (aq). Cerium content in the solution was determined using potentiometric method developed for plutonium by Drummond et al. [170]. The analysed cerium solution was used for the synthesis of $SrCeO_3$(s). The required quantity of cerium and strontium solutions was mixed thoroughly for mixing reactants at molecular level. Excess amount of glycine was added to the mixed solution. The pH of the solution was adjusted to 5.7 using ammonia to stabilize the metal–glycine complex. The resultant solution was evaporated at 353 K on a hot plate till gel formation. The temperature of reaction vessel was raised to 673 K upon which combustion of the mixture occured with flame. The resultant carbonaceous powder was ground, calcined at 1073 K in air for 4 h and compacted into pellets by applying uniaxial pressure of 500 MPa using hardened steel die and plunger. These pellets were heated at 1573 K in oxygen for 16 h.

4.1.2. Sr_2CeO_4(s)

Solid state synthesis route was adopted for the preparation of Sr_2CeO_4(s). In this case the required amount of $SrCO_3$(s) and CeO_2(s) were ground and mixed thoroughly using an agate and mortar pestle. The mixture was pelletized to a pellet of 12 mm dia applying a pressure of 500 MPa and subsequently heated progressively at 1073 K, 1173 K and 1273 K for duration of 12 h at each temperature with thorough grinding, mixing and palletization before shifting to next higher temperature.

4.2. Characterisation of $SrCeO_3$(s) and Sr_2CeO_4(s)

4.2.1. XRD

The formation of these compounds were confirmed by X-ray diffraction analysis using a STOE theta–theta X-ray diffractometer employing monochromatic Cu K∝radiation (λ = 0.15406 nm) and scanning for 2θ in the range of 10–60◦.The X-ray diffraction pattern of $SrCeO_3$(s) and Sr_2CeO_4(s) are shown in **Fig. 4.1** and these patterns are in good agreement with that in the literature [**171, 172**].

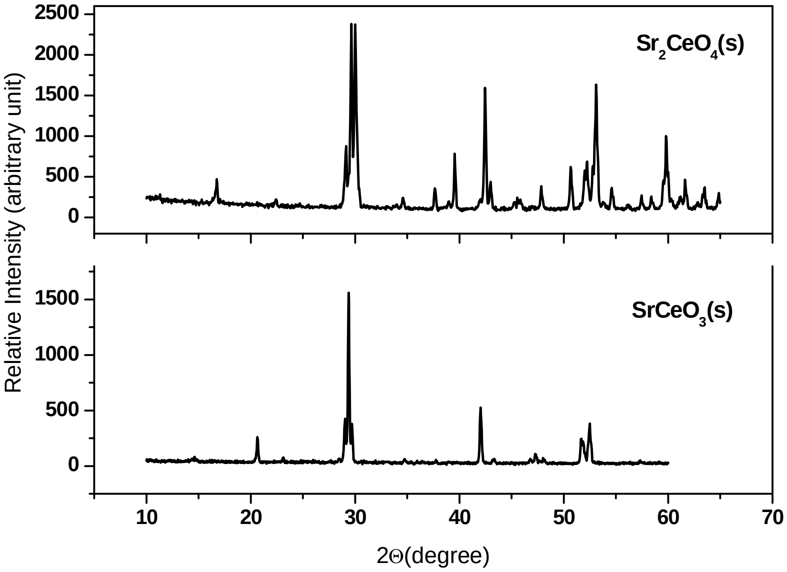

Fig.4.1.XRD pattern of $SrCeO_3$(s) and Sr_2CeO_4(s)

The computed crystallographic parameter values listed in **Table 4.1** are in good agreement with that reported in the literature [**30, 173**]. The unit cell volumes (*V*) of $SrCeO_3$(s) and Sr_2CeO_4(s) were calculated from the lattice parameters of the orthorhombic crystal.

Table.4.1: Lattice parameters of $SrCeO_3$(s) and Sr_2CeO_4(s).

Lattice parameter	Orthorhombic Sr_2CeO_4(s)		Orthorhombic $SrCeO_3$(s)	
	Present study	Literature [30]	Present study	Literature[173]
a (*Å*)	6.1207(24),	6.11897(9)	6.0131(12),	6.1530(4)
b(*Å*)	10.3551(44)	10.3495(2)	6.1489(11)	6.0118(5)
c (*Å*)	3.5991(16)	3.5970(1)	8.5929(23)	8.5891(9)
V($Å^3$)	228.11	227.79	317.70	317.72
Z	2	2	4	4
ρ (g cm^{-3})	5.523	5.524	5.764	5.795

4.2.2. Impurity analysis using ICPMS

Impurity present in $SrCeO_3$(s) and Sr_2CeO_4(s) were analysed using inductively coupled plasma mass spectrometry (ICPMS) and the major impurities present in these compounds are given in **Table 4.2.**

4.2.3. Thermal Expansion measurements using HT-XRD.

The axial thermal expansion measurements of $SrCeO_3$(s) and Sr_2CeO_4(s) were carried out using STOE diffractometer under vacuum (10^{-8} bar) using HDK-2.4 Buhler high temperature attachment in the temperature range of 298-1273 K using experimental procedure described in section 2.4.1.2.

4.2.4. Heat capacity measurement using DSC

A heat flux type differential scanning calorimeter as described in section-2.5.1.2.2. was used for the measurement of heat capacity. Pellets of 5.0 mm dia were made employing pressure of 500 MPa. The pellets of ~80–90 mg were loaded in $7*10^{-5}$ dm^3 platinum pan. High pure oxygen was passed at a flow rate of 0.05 dm^3 min^{-1}. The DSC furnace was heated at a rate of 10 K min^{-1}. Heat capacity measurements were carried out in the temperature range of 300–870 K. A thin disc of sapphire (~47 mg) was used as the heat capacity standard. For $C_{p,m}^{O}(T)$ measurement, three step scanning method was used. The first segment was an isothermal one for fifteen minutes at 300 K; the second segment was a dynamic one with a heating rate of 10 K min^{-1} and the final segment was another isothermal for fifteen minutes at 870 K. Prior to measurement of heat capacity the temperature and the heat flow calibration of DSC were performed.

Table.4.2: Impurity content analysed by Inductively Coupled Plasma Mass Spectrometry (ICPMS) in CeO_2(s), $SrCeO_3$(s) and Sr_2CeO_4(s).

Name of Impurity	CeO_2(s) (ppm)	$SrCeO_3$(s) (ppm)	Sr_2CeO_4(s) (ppm)	Name of Impurity	CeO_2(s) (ppm)	$SrCeO_3$(s) (ppm)	Sr_2CeO_4(s) (ppm)
Mg	7.48	0.54	5.11	Ba	25.3	12608.7	3977.1
Al	92.9	218.1	365.2	La	358.0	160.4	134.4
Sc	BDL[a]	0.96	BDL[a]	Pr	171.1	111.0	71.2
Ti	28.1	7.36	60.2	Nd	221.1	167.2	110.8
Cr	19.2	BDL[a]	BDL[a]	Eu	11.8	42.4	10.37
Mn	10.3	1.31	1.05	Tb	82.1	54.8	39.3
Co	1.4	BDL[a]	BDL[a]	Gd	21.7	54.3	18.2
Ni	4.7	0.91	BDL[a]	Dy	BDL[a]	14.3	1.23
Cu	6.1	25.8	BDL[a]	Ho	9.7	26.0	0.79
Zn	11.1	BDL[a]	BDL[a]	Er	184.2	130.7	21.5
Ge	7.5	1.38	0.46	Tm	5.4	BDL[a]	BDL[a]
As	3.3	BDL[a]	BDL[a]	Yb	18.9	17.4	14.9
Rb	0.4	102.9	159.8	Hf	12.7	BDL[a]	BDL[a]
Y	11.5	61.6	70.9	Ta	52.9	12.4	20.5
Zr	14.1	0.83	6.47	Re	9.3	62.3	63.3
Nb	37.1	3.99	23.2	Os	2.6	2.37	BDL[a]
Mo	12.8	35.9	41.1	Ir	1.9	BDL[a]	BDL[a]
Ru	3.7	272.8	409.4	Pt	2.1	BDL[a]	BDL[a]
Rh	BDL[a]	91.8	133.7	Tl	1.0	BDL[a]	BDL[a]
Pd	0.1	14.5	19.9	Pb	BDL[a]	0.01	0.46
Ag	10.7	13.9	57.5	U	9.4	44.9	27.2
In	3.2	BDL[a]	BDL[a]	Total impurity	1499	14406	6279
Th	12.3	42.0	413.9	**Purity of the compds**	**99.85 %**	**98.56%**	**99.37%**

[a] Below detection limit

4.2.5. Luminescence study of $SrCeO_3$(s)

The pure compound $SrCeO_3$(s) was heated in the temperature 1273-1473 K with an interval of 100 K in high purity argon atmosphere for 24 hrs at each temperature. Photoluminescence data were recorded for all the heated samples as described in section 2.3.6.

4.2.6. Electrical conductivity measurement of Sr_2CeO_4(s)

Electrical conductivity of Sr_2CeO_4(s) was measured using a frequency response analyser as described in section. 2.11.

4.3.Results

4.3.1. Thermal expansion by HT-XRD

$SrCeO_3$(s) and Sr_2CeO_4(s) were indexed using orthorhombic crystal structure. The orthorhombic lattice parameters of $SrCeO_3$(s) and Sr_2CeO_4(s) were calculated from diffraction angles at different temperatures. The density of unit cell of $SrCeO_3$(s) and Sr_2CeO_4(s) given in **Table 4.3** were calculated using expression 2.4.

The calculated lattice parameter *l* (*a*, *b*, and *c*) can be represented using polynomial expression 2.12. The coefficient of linear expansion (α_l), at various temperatures and average expansion coefficients (α_{ave}) were calculated using eqns. 2.13 and 2.14. The percentage expansions of $SrCeO_3$(s) andSr_2CeO_4(s) were calculated using the formula 2.15.

4.3.1.1. $SrCeO_3$(s)

The lattice parameters (*a*, *b*, *c*) and unit cell volume (*V*) were found to increase with temperature which is shown in **Fig. 4.2.**

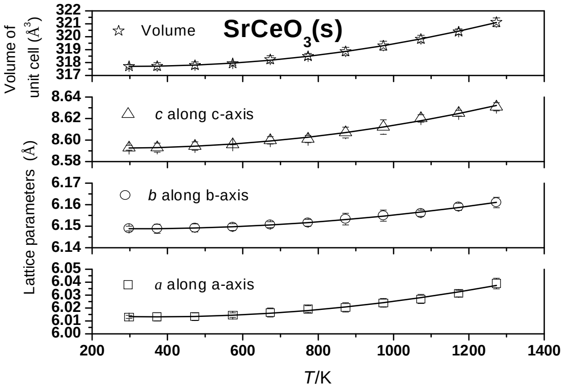

Fig.4.2 The variation of lattice parameters and unit cell volume with temperature for $SrCeO_3$(s).

The measured lattice parameters ($l = a, b, c$), unit cell volume (V) are given in **Table 4.3.** The density (ρ), coefficients of linear expansion (α_a, α_b and α_c) and coefficient of volume expansion (α_V) of $SrCeO_3$(s) at different temperatures was calculated and are also given in **Table 4.3.**

Table.4.3: The lattice parameters, volume, density, linear and volume expansion coefficients of $SrCeO_3$(s).

***T*/K**	***a*** **(Å)**	***b*** **(Å)**	***c*** **(Å)**	***V*** **($Å^3$)**	**ρ (gm/cc)**	**$\alpha_a \cdot 10^6$ (K^{-1})**	**$\alpha_b \cdot 10^6$ (K^{-1})**	**$\alpha_c \cdot 10^6$ (K^{-1})**	**$\alpha_v \cdot 10^6$ (K^{-1})**
298.15	6.0131	6.1489	8.5929	317.71	5.764	0	0	0	0
373	6.0132	6.1488	8.5930	317.72	5.764	0.19	0.22	0.89	1.31
473	6.0133	6.1492	8.5944	317.79	5.763	1.08	0.651	1.69	3.31
573	6.0145	6.1496	8.5959	317.93	5.76	2.66	1.22	3.08	7.08
673	6.0165	6.1507	8.5997	318.24	5.755	3.91	1.63	2.97	8.66
773	6.0192	6.1516	8.6010	318.48	5.75	3.41	2.11	4.25	9.76
873	6.0206	6.1533	8.6070	318.86	5.744	3.99	2.68	6.46	13.06
973	6.0240	6.1549	8.6121	319.31	5.735	5.32	2.20	7.62	15.11
1073	6.0270	6.1560	8.6201	319.82	5.726	5.99	3.33	7.51	17.00
1173	6.0312	6.1590	8.6250	320.39	5.716	9.98	4.07	6.28	20.46
1273	6.0390	6.1610	8.6309	321.12	5.703	12.97	3.25	6.87	22.98

The lattice parameters (a, b, and c), unit cell volume (V) and density (ρ) as a function of temperature have been fitted separately into the following polynomial expressions:

$$a\ (\text{Å}) = 6.017 - 2.00 \times 10^{-5}\ (T/K) + 2.949 \times 10^{-8}\ (T/K)^2 \qquad (4.1)$$

$$b(\text{Å}) = 6.150 - 7.737 \times 10^{-6}\ (T/K) + 1.294 \times 10^{-8}\ (T/K)^2 \qquad (4.2)$$

$$c\ (\text{Å}) = 8.595 - 2.00 \times 10^{-5}\ (T/K) + 3.854 \times 10^{-8}\ (T/K)^2 \qquad (4.3)$$

$$V(\text{Å}^3) = 318.062 - 2.28 \times 10^{-3}\ (T/K) + 3.663 \times 10^{-6}\ (T/K)^2 \qquad (4.4)$$

$$\rho\ (g/cm^3) = 5.758 + 4.0 \times 10^{-5}\ (T/K) - 6.594 \times 10^{-8}\ (T/K)^2 \qquad (4.5)$$

The percentage expansion of lattice parameters and volume of $SrCeO_3$(s) is shown in **Fig. 4.3.** The lattice and volume expansion coefficients as a function of temperature are shown in **Fig. 4.4.** The average value of α_a, α_b and α_c in the temperature range of 298.15–1273 K are $(4.5 \pm 1.21) \times 10^{-6}$, (1.94 ± 0.40) ×10−6 and $(4.33 \pm 0.83) \times 10^{-6}\ K^{-1}$, respectively. Similarly, the average value of coefficient of volume expansion (α_V) was calculated in the temperature range of 298–1273 K to be (10.79 ±2.31) $\times 10^{-6}$ K^{-1}, which is very close to 11.1×10^{-6} K^{-1}, reported by Yamanaka et al. [**36**].

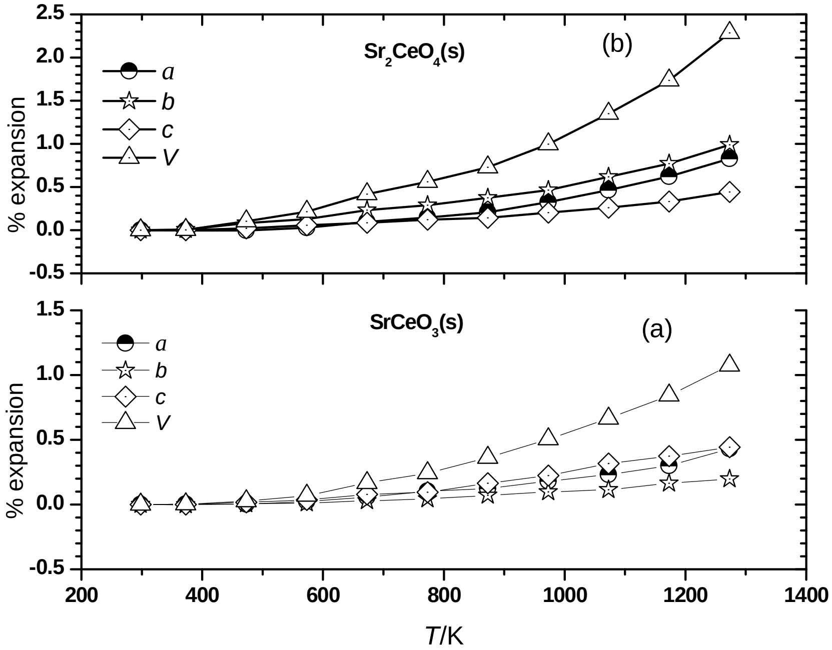

Fig.4.3. The variation of percentage linear and volume expansion for $SrCeO_3$(s) and Sr_2CeO_4(s) as function of temperature.

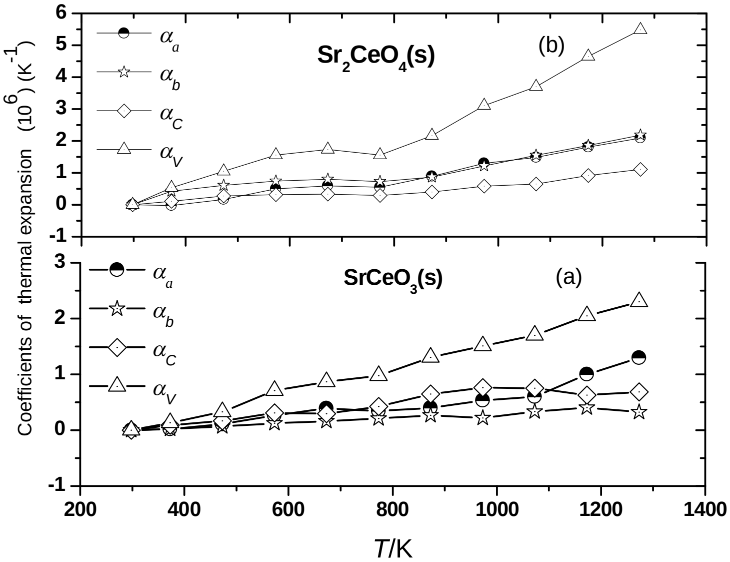

Fig.4.4. The variation of lattice and volume expansion coefficients of $SrCeO_3$(s) and Sr_2CeO_4(s) as function of temperature.

4.3.1.2. Sr_2CeO_4(s)

The lattice parameters (*a*, *b*, *c*) and unit cell volume (*V*) were found to increase with temperature in the temperature range of 298–1273 K as shown in **Fig. 4.5.** However, the density Sr_2CeO_4(s) decreases with temperature. The density and the coefficient of linear and volume expansions were calculated and are given in **Table 4.4.** The polynomial expression for lattice parameters (*a*, *b*, and *c*), unit cell volume (*V*) and density (ρ) are given as:

$$a(\text{Å}) = 6.132 - 6.00 \times 10^{-5}\,(\text{T/K}) + 6.783 \times 10^{-8}\,(\text{T/K})^2 \quad (4.6)$$

$$b(\text{Å}) = 10.358 - 3.00 \times 10^{-5}\,(\text{T/K}) + 8.323 \times 10^{-8}\,(\text{T/K})^2 \quad (4.7)$$

$$c(\text{A}) = 3.600 - 7.816 \times 10^{-6}\,(\text{T/K}) + 1.485 \times 10^{-8}\,(\text{T/K})^2 \quad (4.8)$$

$$V(\text{Å}^3) = 228.685 - 3.33 \times 10^{-3}\,(\text{T/K}) + 5.366 \times 10^{-6}\,(\text{T/K})^2 \quad (4.9)$$

$$\rho(\text{g/cm}^3) = 5.511 + 7.00 \times 10^{-5}\,(\text{T/K}) - 1.246 \times 10^{-7}\,(\text{T/K})^2 \quad (4.10)$$

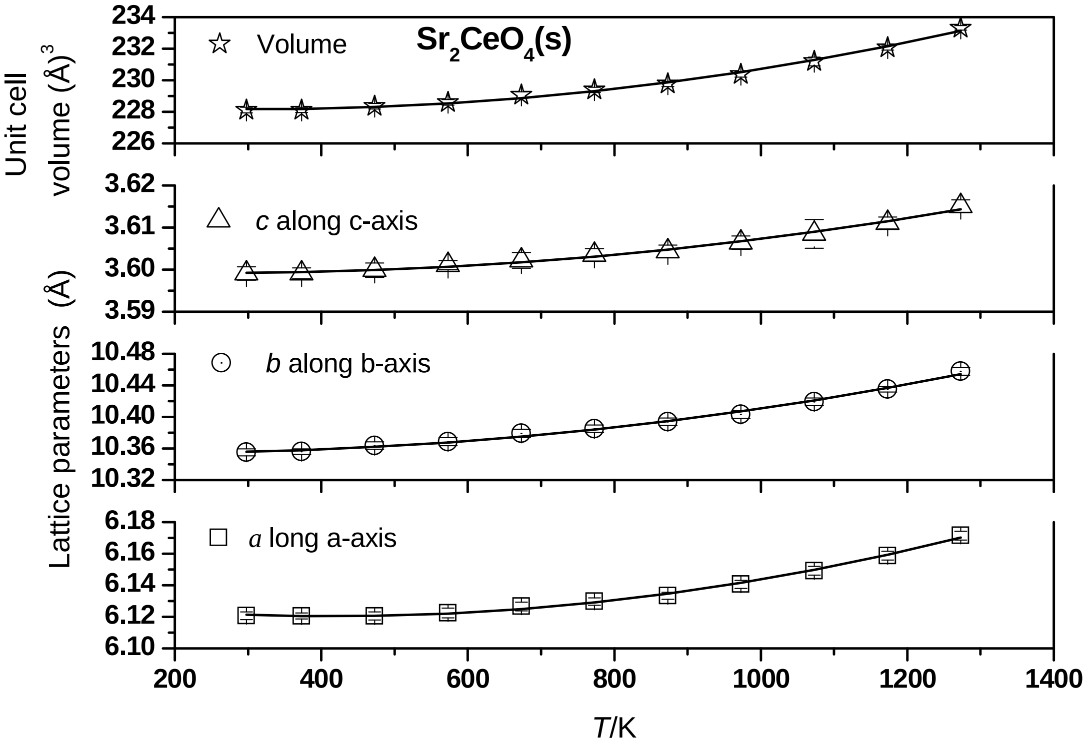

Fig.4.5. The variation of lattice parameters and unit cell volume with temperature for Sr_2CeO_4(s).

Table.4.4: The lattice parameters, volume, density, linear and volume expansion coefficients of Sr_2CeO_4(s).

***T*/K**	***a*** **(Å)**	***b*** **(Å)**	***c*** **(Å)**	***V*** **($Å^3$)**	**ρ (gm/cc)**	**$\alpha_a\cdot10^6$ (K^{-1})**	**$\alpha_b\cdot10^6$ (K^{-1})**	**$\alpha_c\cdot10^6$ (K^{-1})**	**$\alpha_v\cdot10^6$ (K^{-1})**
298.15	6.1207	10.3551	3.5991	228.11	5.523	0	0	0	0
373	6.1205	10.3559	3.5991	228.12	5.523	-0.23	4.28	1.11	5.35
473	6.1205	10.3637	3.5999	228.35	5.517	1.63	6.08	2.78	10.52
573	6.1225	10.3685	3.6011	228.60	5.511	4.98	7.39	3.20	15.56
673	6.1266	10.3790	3.6022	229.06	5.5	5.88	8.02	3.33	17.32
773	6.1297	10.3851	3.6035	229.39	5.492	5.47	7.24	2.92	15.56
873	6.1333	10.3940	3.6043	229.77	5.483	8.90	8.64	4.03	21.70
973	6.1406	10.4030	3.6064	230.38	5.468	13.00	12.17	5.83	31.13
1073	6.1492	10.4191	3.6085	231.19	5.449	14.79	15.45	6.52	37.04
1173	6.1587	10.4351	3.6111	232.07	5.429	18.14	18.64	9.17	46.47
1273	6.1715	10.4577	3.6151	233.32	5.399	20.91	21.82	11.11	54.80

The percentage lattice parameters and unit cell volume expansion of Sr_2CeO_4(s) are shown in **Fig. 4.3.** The lattice and volume expansion coefficients as a function of temperature are shown in **Fig. 4.4.** The average value of expansion coefficients along *a*-axis, *b*-axis and *c*-axis in the temperature range of 298–1273 K are $(8.50 \pm 2.19) \times 10^{-6}$, $(9.98 \pm 1.95) \times 10^{-6}$, and $(4.55 \pm 1.00) \times 10^{-6}$ K^{-1}, respectively. Similarly, the average coefficient of volume expansion was calculated to be $(23.22 \pm 5.19) \times 10^{-6}$ K^{-1} in the temperature range 298–1273 K.

4.3.2. Heat capacity measurement by DSC

4.3.2.1. CeO_2(s)

The accuracy in the $C^o_{p,m}(T)$ measurements was checked by measuring the heat capacity of CeO_2(s). In the low oxygen potential atmosphere, Ce^{+4} can get converted to Ce^{+3} as reported by Riess et al. [174]. In order to avoid the formation Ce^{+3} in CeO_2(s), experiments were carried out in ultra pure O_2(g) atmosphere. The measured $C^o_{p,m}(T)$ of CeO_2(s) along with the fit values of CeO_2(s) and the data reported by Riess et al. [174] are shown in **Fig. 4.6.**

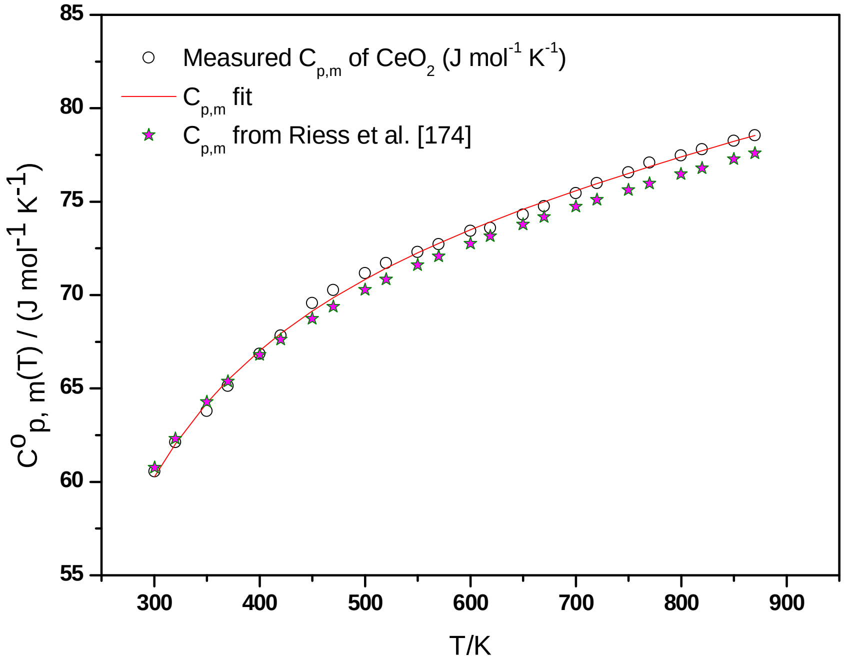

Fig.4.6.Heat capacity of CeO_2(s) as a function of temperature

The heat capacity values as a function of temperature has been least square fitted to the following equation:

$$C^o_{p,m}(CeO_2,s,T)(J\ mol^{-1}\ K^{-1}) = 69.0608 + 0.0126 \times T/(K) - 1.1332 \times 10^6 (T/(K))^{-2}$$

[300≤T/K≤870] (4.11)

The heat capacity values, for CeO_2(s) given in **Fig. 4.6** are the average of 4 to 5 measurements. The relative standard deviations among the measurements are in the range of 0–2.0%. The present data deviate from the Riess et al. by −1.47 to 0.7% in the temperature range of 300–870 K.

4.3.2.2. $SrCeO_3$(s)

The heat capacities of $SrCeO_3$(s) were measured in high purity oxygen atmosphere and is shown in **Fig. 4.7** and given in **Table 4.5.** The heat capacity values as a function of temperature has been least square fitted to the following polynomial equation

$$C^o_{p,m}(SrCeO_3, s, T)(J\ mol^{-1} K^{-1}) = 125.4217 + 0.0123 \times T/(K) - 1.8233 \times 10^6 (T/K)^{-2}$$

[300 ≤ T/K ≤870] (4.12)

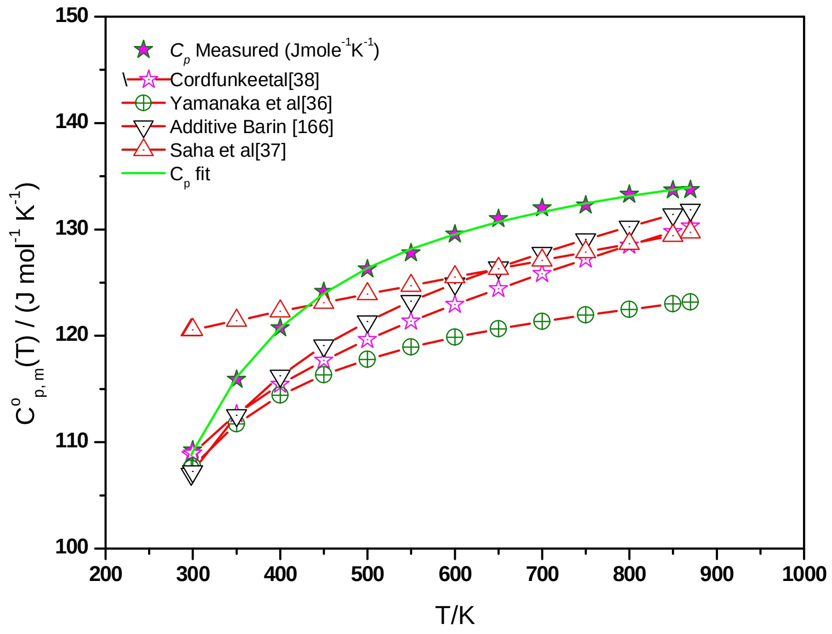

Fig.4.7.Heat capacity of $SrCeO_3$(s) as function of temperature

Table 4.5: Thermodynamic functions of $SrCeO_3$(s)

T/K	$C^o_{p,m}$ measured	$C^o_{p,m}$ fit (J mol^{-1} K^{-1})	$C^o_{p,m}$ additive [166] (J mol^{-1} K^{-1})	$H^o_T - H^o_{298.1}$ (kJ mol^{-1})	S^o_T (J mol^{-1} K^{-1})	$-(G^o_T - H^o_{298.15})/T$ (J mol^{-1} K^{-1})
298	--	108.56	107.00	0.0	117.8	117.8
300	109.25	108.84	107.26	0.2	118.5	117.8
350	114.44	114.82	112.52	5.8	135.8	119.2
400	118.48	118.93	116.24	11.7	151.4	122.2
450	121.85	121.93	119.07	17.7	165.6	126.3
500	124.32	124.25	121.35	23.8	178.5	130.9
550	126.23	126.13	123.26	30.1	190.5	135.8
600	127.80	127.71	124.93	36.4	201.5	140.8
650	129.38	129.07	126.42	42.9	211.8	145.8
700	130.50	130.28	127.78	49.3	221.4	151.0
750	131.51	131.37	129.05	55.9	230.4	155.9
800	132.41	132.37	130.26	62.5	238.9	160.8
850	133.19	133.31	131.40	69.1	247.0	165.7
870	133.30	133.67	131.85	71.8	250.1	167.6

Thermodynamic functions such as enthalpy, entropy and Gibbs energy functions of $SrCeO_3$(s) were derived using the measured heat capacity data and $S^o_m(298.15\text{ K})$. $S^o_m(298.15\text{ K})$ for $SrCeO_3$(s) was taken from Cordfunke et al. [38]. The calculated thermodynamic functions for $SrCeO_3$(s) are given in **Table 4.5**.

4.3.2.3. Sr_2CeO_4(s)

The heat capacity of Sr_2CeO_4(s) was measured in high purity oxygen atmosphere and is plotted as a function of temperature in **Fig. 4.8** along with that calculated from Neumann–Kopps (NK) rule. It shows a phase transition peak at 750 K**. Fig. 4.8** showed reversible peaks in the heat flow flow curve for both cooling and heating.

Heat capacity data up to temperatures 600 K (given in **Table 4.6**) were least square fitted to the polynomial:

$$C^o_{p,m}(Sr_2CeO_4, s, T)(J\,mol^{-1}K^{-1}) = 171.992 + 0.0656 \times T/(K) - 2.0154 \times 10^6 (T/K)^{-2}$$

$$[300 \leq \text{T/K} \leq 600] \qquad (4.13)$$

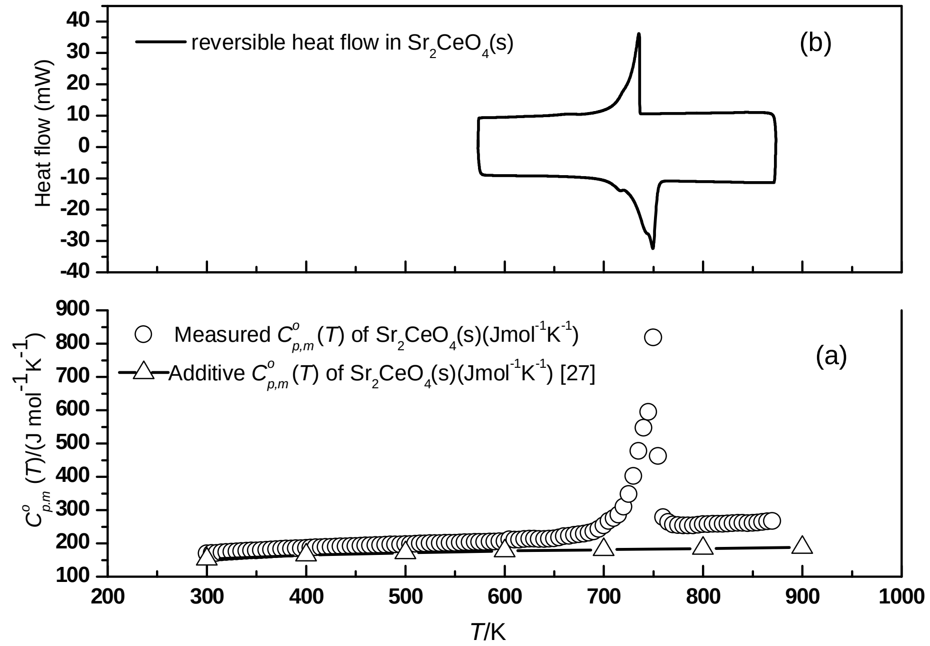

Fig.4.8. Heat capacity of Sr_2CeO_4(s) as function of temperature.

Thermodynamic functions such as enthalpy, entropy and Gibbs energy functions of Sr_2CeO_4(s) were derived using the measured heat capacity data and S^o_m(298.15 K). S^o_m(298.15 K) for Sr_2CeO_4 was estimated by assuming $\Delta_f S^o(ox) = 0$, and taking the entropy of component oxides at 298.15 K from the literature[166]. The calculated thermodynamic functions up to temperature of 873 K for Sr_2CeO_4(s) are given in **Table 4.6**.

Table 4.6: Thermodynamic functions of Sr_2CeO_4(s)

T/K	$C^o_{p,m}$ measured	$C^o_{p,m}$ fit (Jmol^{-1}K^{-1})	$C^o_{p,m}$ additive[166] (Jmol^{-1}K^{-1})	$H^o_T - H^o_{298.15}$ (kJ mol^{-1})	S^o_T (J mol^{-1} K^{-1})	$-(G^o_T - H^o_{298.15})/T$ (J mol^{-1} K^{-1})
298	--	168.89	152.39	0	173.3	173.3
300	169.29	169.29	152.71	0.3	174.4	173.4
350	178.52	178.51	159.82	9.0	201.2	175.5
400	185.57	185.65	164.89	18.1	225.5	180.3
450	191.73	191.57	168.77	27.6	247.7	186.4
500	196.88	196.74	171.91	37.3	268.2	193.6
550	200.99	201.42	174.58	47.2	287.2	201.4
600	205.98	205.77	176.91	57.4	304.9	209.2

4.3.3. Electrical conductivity measurement of Sr_2CeO_4(s)

Electrical conductivity measurements were carried out in the temperature range of 298-998 K to further confirm the phase transition. A typical Nyquist plot of Sr_2CeO_4(s) in argon ambient is shown in **Fig 4.9** and the conductivity values are shown in **Table 4.7.** **Fig.4.10** shows the electrical conductivity of Sr_2CeO_4(s) as a function of temperature. The observed variation of conductivity with temperature could be represented as log (σT) = A – E/kT, where A is Arrhenius constant, E is activation energy for the conduction process, k is the Boltzmann constant and *T* is temperature in Kelvin.

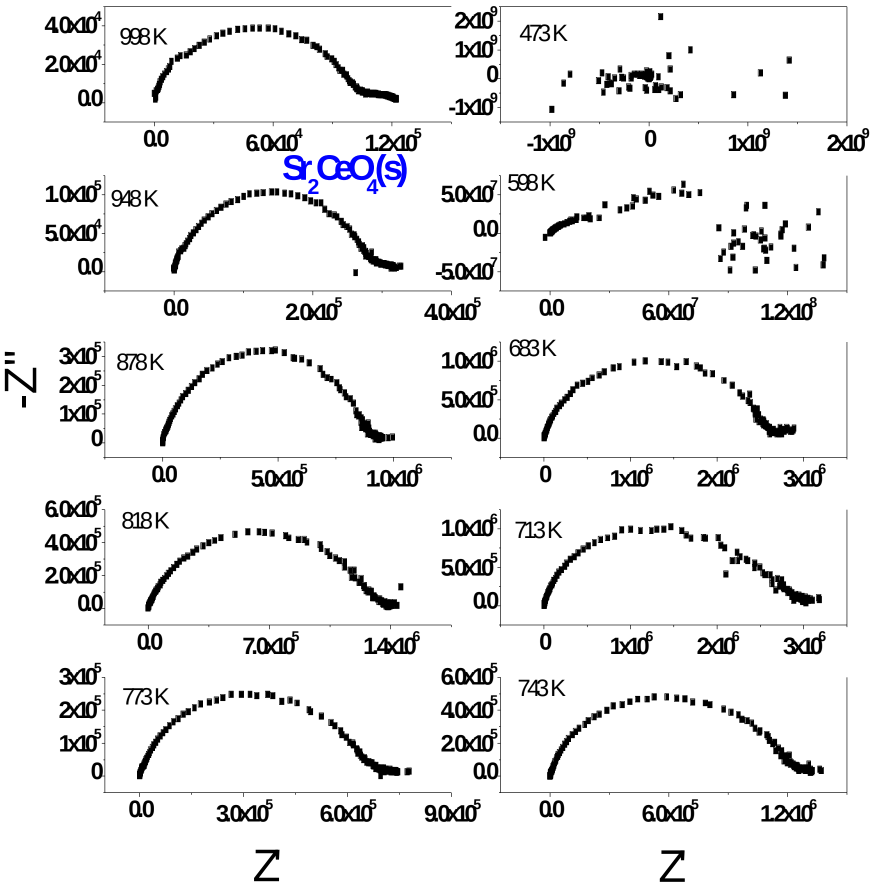

Fig 4.9. The Nyquist plot of Sr_2CeO_4(s) in argon ambient

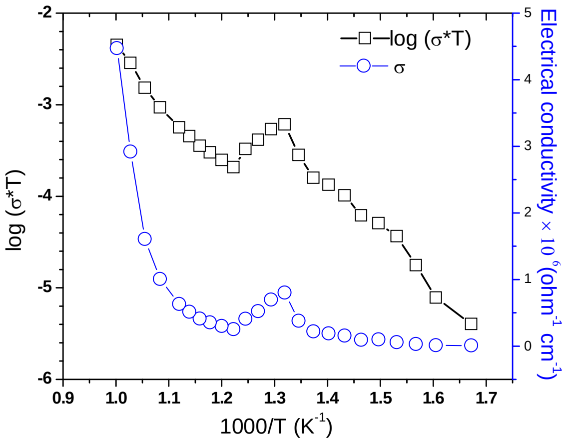

Fig.4.10. The electrical conductivity of Sr_2CeO_4(s) as function of temperature

Table 4.7: Conductivity values of Sr_2CeO_4(s) in argon ambient

T/K	**Conductivity × (10^7) /$Ohm^{-1}cm^{-1}$**	**T/K**	**Conductivity × (10^7) /$Ohm^{-1}cm^{-1}$**
598	0.067	788	5.220
623	0.114	803	4.075
638	0.276	818	2.524
653	0.559	833	2.979
668	0.966	849	3.539
683	0.903	863	4.115
698	1.549	878	5.129
713	1.865	893	6.293
728	2.171	923	10.06
743	3.778	948	16.05
758	8.010	973	29.20
773	6.952	998	44.71

4.4. Discussion

4.4.1. Heat capacity of $SrCeO_3$(s).

The measured heat capacity of $SrCeO_3$(s) is higher than that reported in the literature [**1, 35, 36, 38**]. **Fig. 4.7** shows the measured heat capacity of $SrCeO_3$(s) along with the fit values, the heat capacities already reported in the literature and that computed by Neumann–Kopp's (NK) rule. The experimental $C^o_{p,m}(T)$ values for $SrCeO_3$(s) obtained in the present study are agreeing with that of Cordfunke et al. [**38**] near room temperature, while at higher temperatures, all the measured values of present study are higher than that of literature values [**1, 35, 36, 38**]. The variation in the results between the present and the reported measurements could be due to the use of O_2(g) as carrier gas in the present study. Hence, it was required to study the stability of $SrCeO_3$(s) in oxygen and inert atmosphere. No phase transition was observed in $SrCeO_3$(s) in the temperature range of 300–870 K.

4.4.2. Confirmation of instability of $SrCeO_3$(s) by:

4.4.2.1. XRD

In order to find out the influence of Ar and oxygen atmosphere on stability of $SrCeO_3$(s), the compound was heated in high pure Ar at 1123 K for 48 h and latter it was heated in air at 1123 K for 2 h. These XRD patterns of $SrCeO_3$(s) heated in Ar(g) and air are compared in **Fig. 4.11.** The XRD pattern of the $SrCeO_3$(s) (heated in Ar) shows a few extra peaks due to $SrCO_3$(s) and CeO_2(s). $SrCO_3$(s) peaks were observed due to the reaction between SrO(s) and CO_2(g) present in air. In addition it was also observed that intensity of peaks of $SrCeO_3$(s) were reduced in Ar. The XRD pattern of $SrCeO_3$(s) (heated in air) shows reduction in the peak intensity of $SrCO_3$(s) and CeO_2(s) and increase in the peak intensity of $SrCeO_3$(s). These observations infer that $SrCeO_3$(s) is not stable as a pure phase in reducing atmosphere.

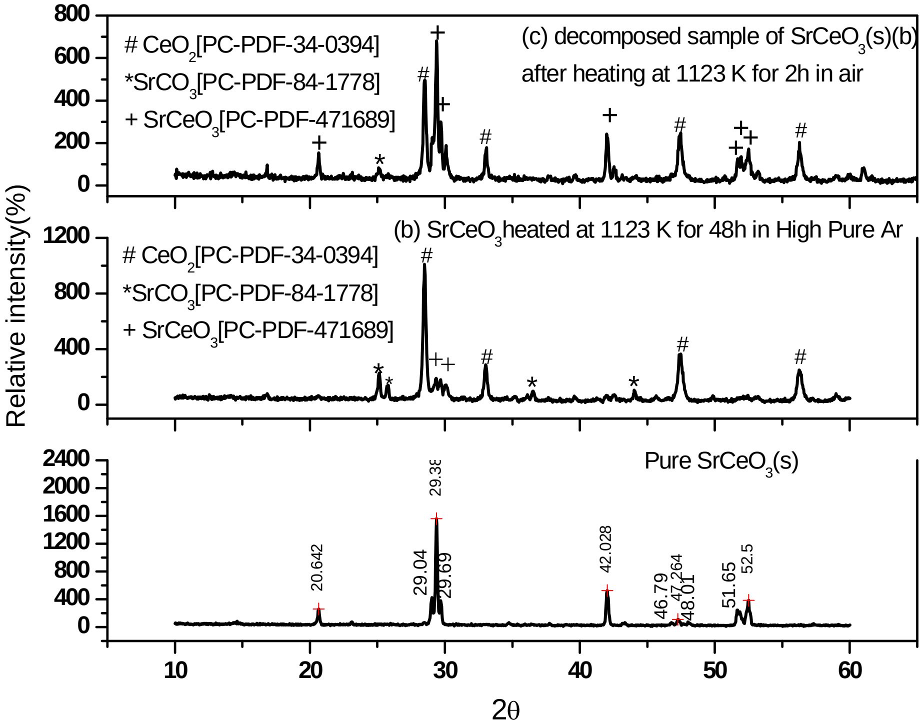

Fig.4.11. Comparison of the XRD pattern of (a) pure $SrCeO_3$(s) synthesized in air, (b) $SrCeO_3$(s) heated in high pure argon and (c) $SrCeO_3$(s) heated in air after heating in high pure argon.

4.4.2.3. Luminescence Study

The emission spectrum for $SrCeO_3$(s) heated at temperature 1173 K, 1273 K, 1373 K and 1473 K with λ_{ex} = 240nm is shown in **Fig. 4.12.** The broad emission band observed in this case at 400-470 nm is the characteristic of Ce^{3+}. On excitation of Ce^{3+} by VUV/UV light, the lone electron goes to one of the excited 5d levels. In most cases, upon de-excitation to the ground level two prominent bands are observed separated by few thousand cm^{-1} which is due to the deexcitation from 5d to spin orbit splitted($^2F_{5/2}$ and $^2F_{7/2}$) ground state of $4f^1$. In the present case, these two transitions are merged with each other to give the broad hump in the spectrum. This confirms the presence of Ce^{3+} in the heated $SrCeO_3$(s).

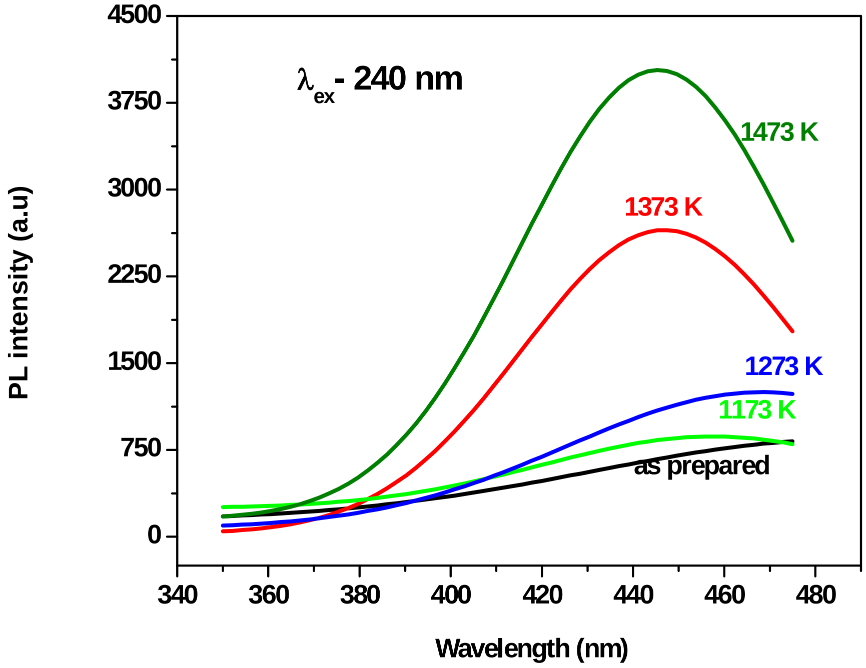

Fig. 4.12. The emission spectra of $SrCeO_3$(s) heated in argon for 24 h at various temperature

4.4.3. Heat capacity of Sr_2CeO_4(s).

Heat capacities of Sr_2CeO_4(s) are not reported in the literature to compare. All $C^o_{p,m}(T)$ values (given in **Table 4.6**) show positive deviations (more than 10%) from NK rule. In order to find out the reason of higher heat capacities of compounds in SrO–CeO_2 system, the experimental heat capacity values of $SrTiO_3$(s), $BaCeO_3$(s), Sr_2TiO_4(s), $SrWO_4$(s) and $SrAl_2O_4$ (s) and those calculated from NK rule were compared. It was observed that the heat capacity of $SrTiO_3$(s), $BaCeO_3$(s) and Sr_2TiO_4(s) showed +ve deviation from NK rule, $SrWO_4$(s) showed −ve deviation from the NK rule and that of $SrAl_2O_4$ followed NK rule. This observation shows that NK rule is not universally followed by all compounds but it depends on the constituent oxides making the compounds.

4.4.4. Detection of second order transition in Sr_2CeO_4(s).

Fig.4.8 shows continuous variation in the enthalpy change and discontinuity in the heat capacity values as a function of temperature which is a behavior shown by second order phase transition. The peak transition temperature is 750 K. The shape o transition peak is similar to lambda.

4.4.5. Confirmation of second order phase transition in Sr_2CeO_4(s) from the comparison of thermal expansion of Sr_2CeO_4(s) with $SrCeO_3$(s)

Figs. 4.2 and 4.5 shows that the lattice parameters (*a*, *b*, *c*) and unit cell volume of $SrCeO_3$(s) and Sr_2CeO_4(s) are continuous. Fig. 4.3 shows that the percentage expansion of volume of $SrCeO_3$(s) is the highest and percentage linear expansion is lowest along the *b*-axis. The percentage linear expansions along *a*- and *c*-axis are almost similar up to 773 K and beyond it linear expansion is higher along *c*-axis. Hence, the thermal expansion in $SrCeO_3$(s) is not isotropic. The percentage expansion of *a*, *b* and *c* are within 0.5 % in the temperature range of 298–1273 K. **Fig. 4.5** also shows similar trend in *a*, *b*, *c* and *V* values. Both the DSC and the HTXRD results show no phase transition in the temperature range of 298–1273 K for $SrCeO_3$(s). **Fig. 4.3** shows that the percentage expansion of volume of Sr_2CeO_4(s) is highest (2.3%) at 1273 K. The percentage linear expansion along *b*-axis is the highest among different axis and it is almost same along *a*- and *c*-axis up to 773 K and there after the expansion along *a*-axis is higher than that of *c*-axis. The percentage expansion of *a*, *b* and *c* of Sr_2CeO_4(s) are within 1% in the temperature range of 298–1273 K. **Fig. 4.13** compares the coefficient of volume expansion of $SrCeO_3$(s) and Sr_2CeO_4(s).

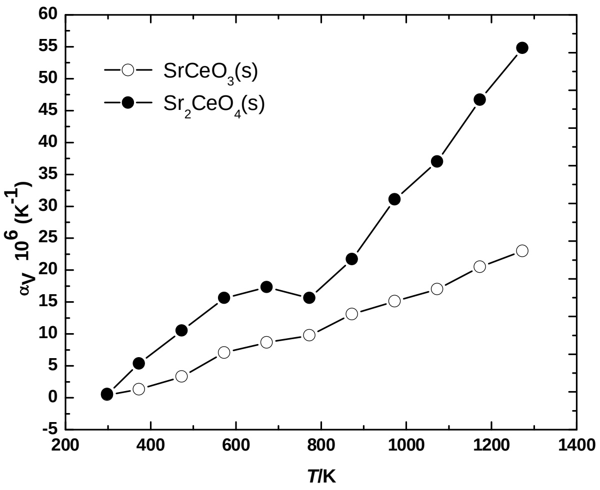

Fig.4.13. The comparison between the volume thermal expansion coefficients of $SrCeO_3$(s) and Sr_2CeO_4(s) as a function of temperature

It shows no change in slope of α_V of $SrCeO_3$(s), but α_V of Sr_2CeO_4(s) curve shows a slope change in the temperature range of 673–773 K. There is no change in slope in volume (**Fig. 4.5**), but α_V (**Fig. 4.4**) shows a slope change. Hence, the phase transition type is second order. This observation corroborates the results of $C^{o}_{p,m}(T)$ which also showed a peak at 750 K (**Fig. 4.8**). This confirms the presence of a second order phase transition in Sr_2CeO_4(s). **Fig. 4.14** gives the comparison of percentage volume expansion and percentage reduction in density of $SrCeO_3$(s) and Sr_2CeO_4(s). It shows the percentage volume expansion and percentage density reduction in Sr_2CeO_4(s) are more than that of $SrCeO_3$(s).

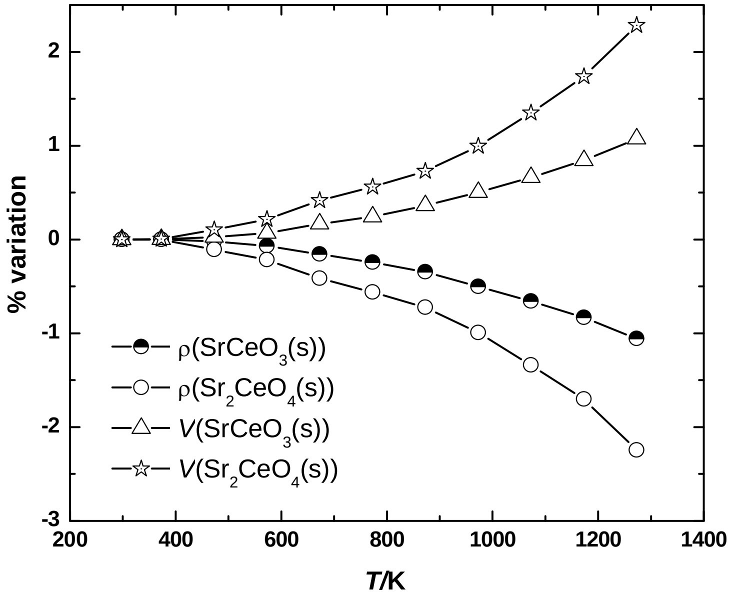

Fig.4.14. The comparison of percentage volume expansion and percentage reduction in density of $SrCeO_3$(s) and Sr_2CeO_4(s) as a function of temperature.

4.4.6. Electrical conductivity measurement of Sr_2CeO_4(s)

Fig.4.10 shows the plot of electrical conductivity as a function of temperature where a clear distinct peak at 758 K was observed indicating a phase transition in Sr_2CeO_4(s), which was supported by the peak observed in the heat capacity measurements.

4.5. Summary

1. The thermal expansion coefficients and heat capacity of $SrCeO_3$(s) and Sr_2CeO_4(s) was measured using HTXRD and DSC techniques.
2. Average linear and volume thermal expansion coefficient of $SrCeO_3$(s) were calculated.

3. The average volume expansion coefficient (αV) of $SrCeO_3$(s) and $S_{r2}CeO_4$(s) was found to be (10.79 ±2.31) $\times 10^{-6}$ K^{-1} and (23.22 ± 5.19) $\times 10^{-6}$ $K^{-1,}$ respectively.
4. Both the heat capacity measurement and the HTXRD results of $SrCeO_3$(s) did not show any phase transition up to 1273 K.
5. The average coefficient of volume expansion of Sr_2CeO_4(s) showed a break in the expansion coefficient versus temperature in the region of 673-773 K. The electrical conductivity as well as heat capacity as a function of temperature showed peak at 757 K and 750 K, respectively. There might be a second order phase transition in Sr_2CeO_4(s) at 750 K.
6. The volume expansion coefficient of Sr_2CeO_4(s) was found to be higher than that of $SrCeO_3$(s) in the entire temperature range 298-1273 K.
7. Heat capacity of Sr_2CeO_4(s) was measured in the temperature range 330-870 K for the first time.
8. Thermodynamic functions like $S_T^o, C_p^o, \{H^o(T) - H^o(298.15)\}$, Gibbs energy functions were also calculated for $SrCeO_3$(s) in the temperature range 298 - 870 K and for Sr_2CeO_4(s) in the temperature range 298 - 600 K. The thermodynamic functions generated in this study along with required literature data will help in establishing the phase relations in the Sr- Ce-O system.

CHAPTER-5

$Ba_{1-x}Sr_xMoO_4$ solid-solutions

CHAPTER-5

The molybdenum, barium and strontium are among the fission product elements having high fission yields in nuclear reactors operating with mixed oxide (MOX) fuel. The thermopysico chemical properties of various phases in the system Ba-Sr-Mo-O is necessary to predict the behavior of MOX fuel. The formation of $SrMoO_4$(s) and $BaMoO_4$(s) solid solutions could be expected in the reactor fuel at high burn up.

Alkali earth metal molybdates and tungstates AMO_4(s) (A = Ba, Sr, Ca and M = Mo, W) and their solid solutions, are important materials in photoluminescence and have widely been used in optical fibers, solid-state-optical masers and electrochromic materials. In this study, the solid solution of $Ba_{1-x}Sr_xMoO_4$(s) was synthesized by complex polymerization method, thermal expansion of $Ba_{1-x}Sr_xMoO_4$(s)(x = 0, 0.6, 1) solid solutions was measured using HT-XRD in the temperature range 298–1273 K and heat capacity of $Ba_{1-x}Sr_xMoO_4$(s) (x = 0, 0.18, 0.38, 0.60, 0.81, 1) solid solutions was measured using heat flux DSC in the temperature range 140–870 K. The thermodynamic functions were computed from the measured heat capacity data.

5.1. Experimental.

5.1.1. Synthesis of solid solutions

$Ba_{1-x}Sr_xMoO_4$(s) (x = 0, 0.2, 0.4, 0.6, 0.8, 1) solid solutions were synthesized by complex polymerization method [175]. The starting materials used were $BaCO_3$(s) (99.999%, M/s Across Organics, Belgium), $SrCO_3$(s) (99.99%, M/s Alfa Aesar, Lancaster), MoO_3(s) (99.5%, Mallinck-rodt chemical works, New York), citric acid (99.7%, M/s Chemco fine chemicals, Mumbai), ethylene glycol (99.0%, M/s Thomas Baker, Mumbai), selectipure HNO_3 (M/s Merck Ltd, Mumbai) and NH_3 solution (M/s Chemco fine chemicals, Mumbai). $SrCO_3$(s) and $BaCO_3$(s) were preheated at 1123 K for 8 h and MoO_3(s) was preheated at 573 K for 4 h before weighing for the synthesis of $Ba_{1-x}Sr_xMoO_4$(s) (x = 0, 0.2, 0.4, 0.6, 0.8, 1) solid solutions. For preparation of $BaMoO_4$(s), the required amount of MoO_3(s) was added to the aqueous solution of citric acid which resulted in turbid solution and was stirred at 333–353 K for 2–3 h. Then the proper stoichiometric amount of $BaCO_3$(s) was added to molybdenum citrate solution and the solution was well stirred for 1 h. The pH of the solution was adjusted to 6.5 using ammonia solution to produce a homogeneous and transparent solution, which ensures mixing of reactants at molecular level and complexation of citric acid with metal ions. After homogenization ethylene glycol was added upon constant stirring for polyesterification in the temperature range 333–353 K. No visible phase separation was observed. The citric acid and ethylene glycol were added in the mass ratio of 6:4. For synthesis of $SrMoO_4$(s) and solid solutions $Ba_{1-x}Sr_xMoO_4$(s) (x = 0.2, 0.4, 0.6, and 0.8), minimum amount of dilute HNO_3(aq) was added to dissolve $SrCO_3$(s), $BaCO_3$(s) and MoO_3(s) till the formation of a clear solution. After mixing and dissolving citric acid, pH of the solution was adjusted to 6.5. Ethylene glycol was added to this solution with constant stirring for an hour. The solution was evaporated at 353 K on a hot plate till the formation of a transparent gel. Then the temperature of reaction vessels was raised to 673 K. Combustion of the mixtures took place which resulted in the formations of porous carbonaceous powder. These intermediates for each composition were ground and calcined separately at 873 K for 4 h and at 1173 K for 6 h in air.

5.1.2. Characterisation of $Ba_{1-x}Sr_x MoO_4$) (x=0, 0.2, 0.4, 0.5, 0.8, 1) solid solutions

5.1.2.1. Determination of reaction temperature for using TG-DTA

In order to identify the reaction temperatures for the formation of $Ba_{1-x}Sr_xMoO_4$ (s) (x = 0, 0.2, 0.4, 0.6, 0.8, 1) solid solutions, respective precursor was analyzed with a thermo analyzer (Mettler Thermoanalyzer, TA-1, Switzerland). The sample was heated, under air flow rate of 0.05 dm^3 min^{-1}, at a heating rate of 10 K min^{-1} up to 1373 K.

5.1.2.3. Characterisation by XRD

The calcined samples were identified by X-ray diffractometry (XRD) using a STOE theta–theta X-ray diffractometer employing graphite monochromatic Cu Kα radiation (λ = 0.15406 nm). The scans were made in the range of $10^o \leq 2\theta \leq 70^o$.

5.1.2.3. Accurate composition analysis by ICPMS

The compositions of $Ba_{1-x}Sr_xMoO_4$ (s) (x = 0.2, 0.4, 0.6, 0.8) solid solutions were found out using inductively coupled mass spectrometry (ICPMS). For this study, accurately weighed amounts of solid solutions were digested in concentrated nitric acid and dried. The final analyte solution was made with 1% nitric acid. The solutions were fed into ICPMS and elemental compositions were measured, which were used to find out the stoichiometry of the solid solutions. The actual stoichiometry determined by ICPMS is given in **Table 5.1** and was taken for further representation and calculations.

Table.5.1: The stoichiometry of $Ba_{1-x}Sr_x MoO_4$ (x= 0.2, 0.4, 0.6, and 0.8) solid solutions determined by ICPMS

Sl No.	**Approximate stoichiometry synthesized**	**Actual Stoichiometry determined by ICPMS**
1	$Ba_{0.8}Sr_{0.2}MoO_4$	$Ba_{0.821 \pm 0.019}Sr_{0.179 \pm 0.028}MoO_4$
2	$Ba_{0.6}Sr_{0.4}MoO_4$	$Ba_{0.625 \pm 0.068}Sr_{0.375 \pm 0.045}MoO_4$
3	$Ba_{0.4}Sr_{0.6}MoO_4$	$Ba_{0.399 \pm 0.007}Sr_{0.601 \pm 0.006}MoO_4$
4	$Ba_{0.2}Sr_{0.8}MoO_4$	$Ba_{0.190 \pm 0.117}Sr_{0.810 \pm 0.034}MoO_4$

5.1.2.4. Characterisation using Raman spectroscopy

The room temperature Raman spectra of all the synthesized compositions in the series $Ba_{1-x}Sr_xMoO_4$ (s) (x = 0, 0.2, 0.4, 0.6, 0.8, 1) were recorded as described in section 2.3.2.

5.1.2.5. Morphology using Scanning Electron microscopy

The morphological investigations of the powder samples of $SrMoO_4$ and $BaMoO_4$ were carried out using a scanning electron microscope (SEM) as described in section 2.3.3.

5.1.2.6. Thermal expansion studies using HT-XRD

The axial and volume thermal expansion measurements of $Ba_{1-x}Sr_x MoO_4$(s) (x=0, 0.6 and 1) were carried out using STOE diffractometer in the temperature range of 298-1273 K following the procedure described in section 2.4.1.2.1.

5.1.2.7. Heat capacity measurements using DSC

Heat capacity $C^{o}_{p,m}(T)$ measurements of $Ba_{1-x}Sr_xMoO_4$ (x = 0, 0.18, 0.38, 0.60, 0.81, 1) solid-solutions were carried out using the heat flux-type differential scanning calorimeter with three step scanning method and the procedure followed is same as described in section 2.5.1.3. Measurements were carried out in the temperature range of 140-450 K and 300-870 K. High purity helium or high purity argon gas was passed at a flow rate of 0.05 dm^3 min^{-1} for low or high temperature runs respectively. Powder samples (70-80 mg) were kept on $4{\cdot}10^{-5}$ dm^3 Al pan for heat capacity measurements. The values of specific heat capacity for $Ba_{1-x}Sr_xMoO_4$ (x = 0, 0.18, 0.38, 0.60, 0.81, 1) solid-solutions were calculated.

5.2. Results and Discussion

5.2.1. Characterisation of $Ba_{1-x}Sr_x MoO_4$) (x=0, 0.2, 0.4, 0.5, 0.8, 1) solid solutions

5.2.1.1. TG-DTA of Precursors

The thermograms of the decomposition of precursors for the formation of $Ba_{1-x}Sr_xMoO_4$ (s) (x=0, 0.2, 0.4, 0.5, 0.8, 1) solid solutions are shown in the **Fig 5.1.** It shows that the complete decomposition of all the precursors was taken place at around 1073 K. The peaks of DTA curves are due to exothermicity of the combustion reaction of precursors. TG plot shows single and continuous step of decomposition. The precursor for composition $Ba_{0.2}Sr_{0.8}MoO_4$ (s) showed some peculiar behavior both in TG and DTA plot which could be due to the different types of complexation behavior of metallic element in this composition. The precursors were calcined at 1273 K for 6 h and the resulting white powders were stored for the characterization.

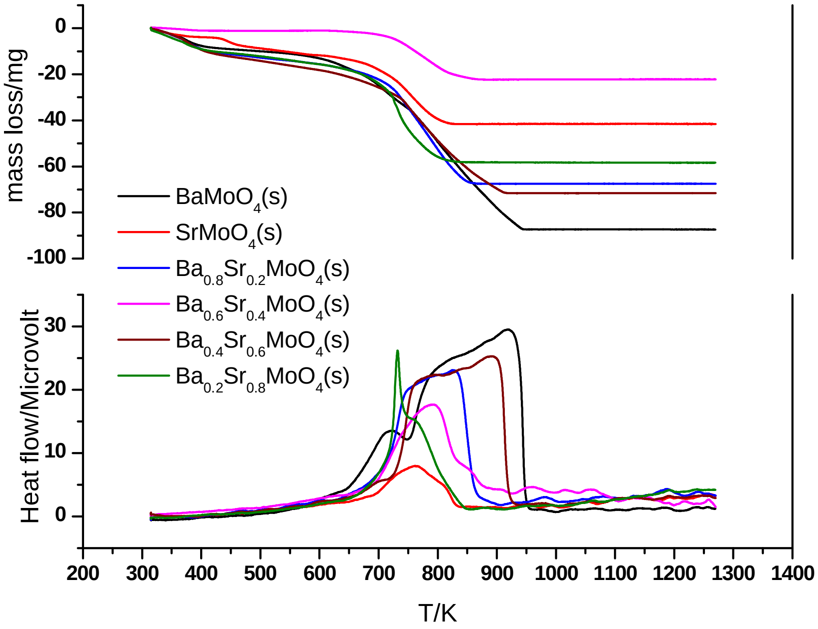

Fig.5.1.TG-DTA of Precursors for the synthesis of $Ba_{1-x}Sr_xMoO_4$ (x = 0, 0.2, 0.4, 0.5, 0.8, 1) solid solution.

5.2.1.2. Characterisation by XRD

X-ray diffraction patterns of $Ba_{1-x}Sr_x MoO_4$ (x=0, 0.18, 0.38, 0.60, 0.81, 1) prepared by complex polymerization method are shown in **Fig.5.2.** All the samples showed well crystalline structure and could be indexed in the tetragonal system. No phase impurity was found. The diffraction peak positions for the end members $SrMoO_4$(s) and $BaMoO_4$(s) are in agreement with the literature [**176, 177**]. The average crystalline size of $Ba_{1-x}Sr_x MoO_4$ (s) (x=0, 0.18, 0.38, 0.60, 0.81, 1) was estimated to be in the range of 52-67 nm from X-ray diffraction peaks using Scherrer's formula [**178**]. The computed room temperature lattice parameters, unit cell volume and density values of tetragonal $SrMoO_4$(s) and $BaMoO_4$(s) are listed in **Table 5.2** and these values are in good agreement with that reported in the literature [**176, 177**]. Similarly the lattice parameters for $Ba_{1-x}Sr_x MoO_4$ (s) (x= 0.18, 0.38, 0.60, 0.81) were refined by least square method and compared with that of Ba $_{0.5}$Sr$_{0.5}$ MoO$_4$ (s) and Ba $_{0.25}$Sr$_{0.75}$ MoO$_4$ (s) reported in the literature [**179, 180**]**.** The complete range of compositions was found to obey Vegard's law as represented in **Fig.5.3**.

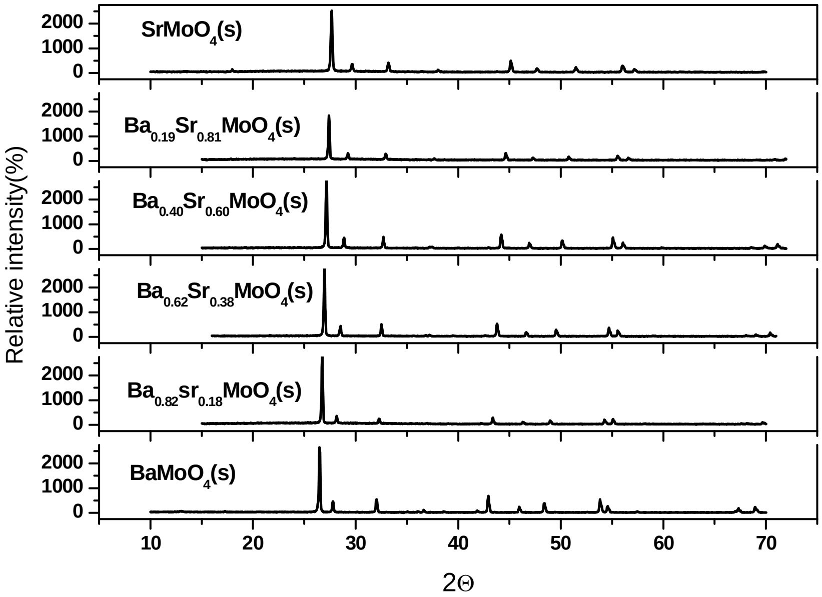

Fig.5.2. XRD pattern of Ba $_{1-x}$Sr$_x$ MoO$_4$ (x = 0, 0.18, 0.38, 0.60, 0.81, 1) solid solutions.

Table.5.2: Crystal system and lattice parameter of BaMoO$_4$(s) and SrMoO$_4$(s)

Lattice parameters	**Tetragonal**			
	SrMoO$_4$(s)		**BaMoO$_4$(s)**	
	Present study	**Literature [176]**	**Present study**	**Literature [177]**
a /Å	5.3909(1)	5.3944	5.5800(1)	5.5802
c/Å	12.0300(39)	12.020	12.8212(1)	12.821
V/Å^3	349.6135(1137)	349.78	399.2060(106)	399.23
Z	4	4	4	4
ρ/g cm^{-3}	4.70	4.70	4.95	4.95

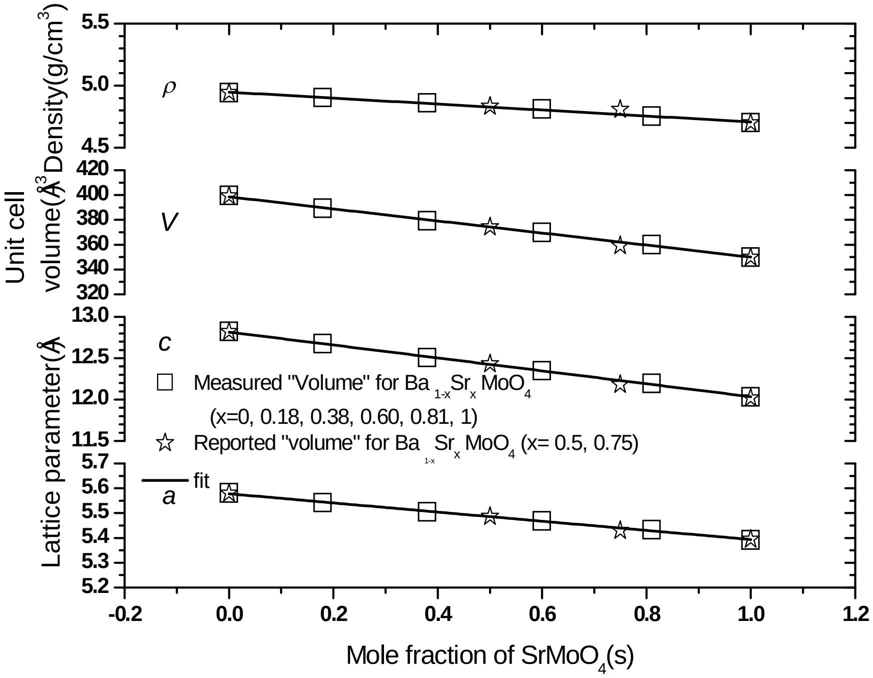

Fig.5.3. A plot of linear lattice parameters (*a* and *c*), unit cell volume (*V*) and density (*ρ*) as a function of mole fraction of SrMoO$_4$(s) for Ba $_{1-x}$Sr$_x$ MoO$_4$ (x = 0, 0.18, 0.38, 0.60, 0.81, 1) solid solutions

The measured lattice parameters, unit cell volume and density of Ba $_{1-x}$Sr$_x$ MoO$_4$ (s) (x=0, 0.18, 0.38, 0.60, 0.81 and 1) were fitted as a function of mole fraction of SrMoO$_4$(s) and the resulting equations are given as:

$$a\ (\text{Å}) = 5.5799 - 0.1871 \cdot x \qquad (5.1)$$

$$c\ (\text{Å}) = 12.8259 - 0.7941 \cdot x \qquad (5.2)$$

$$V\ (\text{Å})^3 = 399.277 - 52.391 \cdot x + 6.235 \cdot x^2 - 3.429 \cdot x^3 \qquad (5.3)$$

$$\rho\ (\text{gm cm}^{-3}) = 4.945 - 0.177 \cdot x - 0.107 \cdot x^2 + 0.0403 \cdot x^3 \qquad (5.4)$$

Where ” *x*” is the mole fraction of SrMoO$_4$(s) in the solid solutions. The reported lattice parameters, unit cell volumes and densities of Ba $_{1-x}$Sr$_x$ MoO$_4$(s) (x= 0.5, 0.75) are found to obey the linear relations as shown in **Fig.5.3**.

5.2.1.3. Characterisation by Raman Spectroscopy

The Raman spectra measured on compositions Ba $_{1-x}$Sr$_x$ MoO$_4$ (x=0, 0.18, 0.38, 0.60, 0.81,1) are presented in **Figs. 5.4 and 5.5** in the wave number region 50-450 cm^{-1} and 750-950 cm^{-1}, respectively. All the wave numbers obtained in this study along with the reported wave numbers for BaMoO$_4$(s) [**175**] and SrMoO$_4$(s) [**181**] and the variation in wave numbers with increasing Sr concentration (i.e., x) are given in detail in table 5.3. According to Basiev [**181**], these molybdates MMoO$_4$(s) (M = Ba, Sr) crystallize into scheelite structure with tetragonal symmetry 'C^6_{4h}' at room temperature. The primitive cell of MMoO$_4$(s) has two formula units. These scheelite MMoO$_4$(s) structured compounds have the molecular ionic group [MoO$_4$]$^{2-}$, which has four strong covalent Mo–O bonds. However, there is weak coupling between [MoO$_4$]$^{2-}$ ionic group and M^{2+} cations in the crystal lattice. The vibrational modes observed in the spontaneous Raman spectra of these MMoO$_4$(s) scheelite crystals, can therefore be divided into two groups; internal and external modes. The internal modes correspond to the vibrations within [MoO$_4$]$^{2-}$ molecular group, with an immovable centre of mass. The external or lattice phonons correspond to the relative motion of the M^{2+} cations and the rigid molecular unit. The [MoO$_4$]$^{2-}$ moiety is arranged in a tetrahedral geometry in free space having T$_d$-symmetry. However, upon placing this [MoO$_4$]$^{2-}$ molecular unit into a scheelite type lattice, its point symmetry is reduced to S$_4$. Factor group analysis

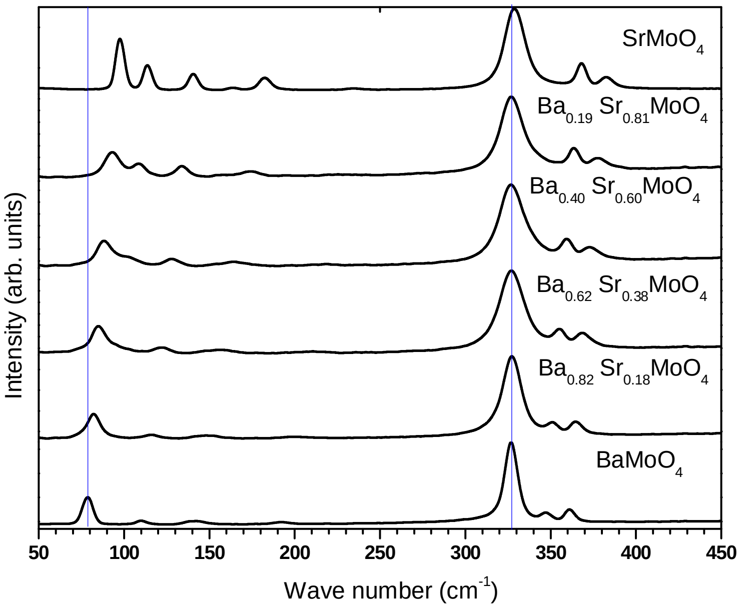

.

Fig.5.4. Unpolarised spontaneous Raman spectra of Ba $_{1-x}$Sr$_x$ MoO$_4$ (x = 0, 0.18, 0.38, 0.60, 0.81, 1) solid solutions in the range of wave number 50-450 cm^{-1}.

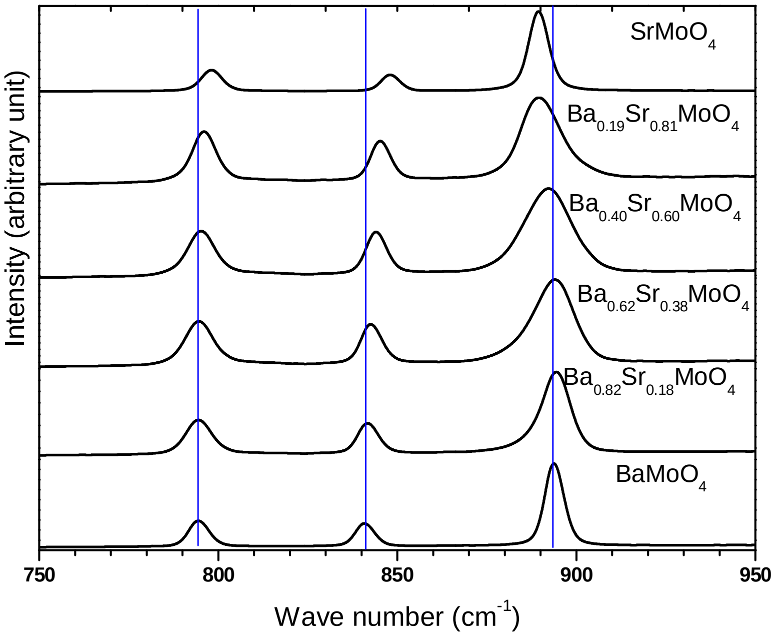

Fig.5.5. Unpolarised spontaneous Raman spectra of Ba $_{1-x}$Sr$_x$ MoO$_4$ (x = 0, 0.18, 0.38, 0.60, 0.81, 1) solid solutions in the range of wave number 750-950 cm^{-1}.

of the above system finally shows a total of 26 different vibration modes for the scheelite primitive cell for K = 0 wave vector and are presented as:

$$\Gamma = 3A_g + 5A_u + 5B_g + 3\ B_u + 5E_g + 5E_u$$

Here, the even vibrational modes (A_g, B_g and E_g) are Raman-active, while the odd modes ($4A_u$ and $4E_u$) can be observed only in the infrared spectra. The three B_u vibrations are silent modes. The remaining ($1A_u$ and $1E_u$) modes are acoustic vibrations. The Raman spectra of Ba $_{1-x}$Sr$_x$ MoO$_4$ (x=0, 0.18, 0.38, 0.60, 0.81,1) solid solutions in **Figs. 5.4 & 5.5** show well-resolved sharp peaks indicating that the samples are highly crystalline in nature. In the present work, 11 and 12 Raman mode vibrations were observed for BaMoO$_4$(s) and SrMoO$_4$(s), respectively. The corresponding theoretical modes are also assigned for each wave numbers for these molybdates and given in **Table 5.3.** In the present study, the internal modes, free rotation mode and the external modes were localized within the range of 329-889 cm^{-1}, 183 cm^{-1} and 97-164cm^{-1}, respectively for SrMoO$_4$(s). The external modes shift to larger wave numbers as the doping level of Sr increases. This could be due to the smaller size of Sr^{2+} ions 1.26 Å) compared to Ba^{2+} ions (1.42 Å) in an eight coordinated geometry, which leads to stronger interaction between Sr^{2+} and $[MoO_4]^{2-}$ ionic groups and thereby resulting in higher force constants for the corresponding vibration modes. The crystal field effect due to presence of the $[MoO_4]^{2-}$ group into a scheelite crystal structure causes splitting of its degenerate vibrational levels and therefore results in four peaks in case of $SrMoO_4$(s) in the range of 97-164 cm^{-1}. The results of this study indicated a notable increase in the frequency of all the modes with increasing Sr^{2+} concentration except two modes, namely B_g (~327 cm^{-1}) and A_g (889-894 cm^{-1}) for which, a near invariant and reducing frequency variation was observed with increasing Sr^{2+} concentration, respectively. The increasing trend of frequencies for most of the modes while increasing the Sr^{2+} concentration in a pure $BaMoO_4$ lattice can be explained due to combined effect of size, mass and electro negativity of Sr^{2+} and Ba^{2+} ions as all these factors affect the force constants and thereby alters the vibronic frequencies.

The near invariant trend of internal mode B_g (~327 cm^{-1}) is similar to the observation made by Basiev et al. **[181]** whereas the opposite variation of frequency reduction of the A_g mode (~889-894 cm^{-1}) corresponding to the totally symmetric stretching vibronic mode of $[MoO_4]^{2-}$ group can be explained as due to Davydov Splitting (also known as DS splitting) effect arising due to strong coupling of two $[MoO_4]^{2-}$ groups within the primitive unit cell of the scheelite lattice [**182**].

Fig. 5.6 shows the variation of peak widths of few representative Raman modes with increasing Sr^{2+} concentration. As evident from the trend, the Raman peaks get broadened with initial doping of Sr^{2+} in $BaMoO_4$ lattices, reaches a maxima between 40 to 60 at.% of Sr content and then reduces further while approaching pure $SrMoO_4$. The parabolic trend of this broadening can be attributed to the extent of disorder created in the lattice upon Ba/Sr lattice site mixing in these solid solutions which is increasing in initial levels of doping at either end (Sr^{2+} incorporation in $BaMoO_4$ or Ba^{2+} incorporation in $SrMoO_4$) and reaches to a maximum near equal concentration of both the metal cations (x = 0.50).

Table 5.3.Raman mode frequencies of Ba $_{1-x}$Sr$_x$ MoO$_4$ (x=0, 0.18, 0.38, 0.60, 0.81, 1) solid solutions at room temperature

Sl No	**Lattice Mode symmetry C_{4h}^{6}**	**BaMoO$_4$ [present study]**	**BaMoO$_4$ [175]**	**Ba$_{0.82}$Sr$_{0.18}$MoO$_4$**	**Ba$_{0.62}$Sr$_{0.38}$MoO$_4$**	**Ba$_{0.40}$Sr$_{0.60}$MoO$_4$**	**Ba$_{0.19}$Sr$_{0.81}$MoO$_4$**	**SrMoO$_4$ [present study]**	**SrMoO$_4$ [181]**
1	E_g		76						
2	B_g	79	78	82	85	88	93	98	
3	A_g	------	------	------	95	102	109	114	
4	E_g	110	107	116	122	128	134	140	
5	A_g	139	------	142	149	154	158	164	
6	B_g	142	141	147	155	165	174	182	180
7	E_g	192	190	199	211	219	226	235	
8	B_g	327	325	327	327	327	327	329	327
9	B_g	347	346	351	355	359	364	368	369
10	E_g	361	359	365	368	373	378	382	
11	E_g	794	791	794	794	795	796	798	797
12	B_g	841	838	842	842	844	845	848	846
13	A_g	894	891	894	894	892	889	889	888

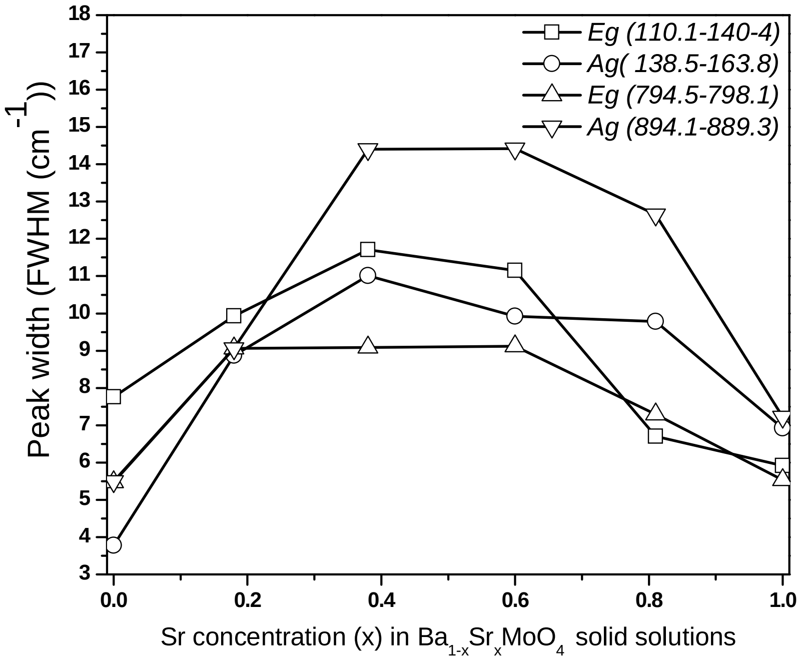

Fig.5.6. Variation of Raman peak widths with increasing Sr^{2+} concentration for $Ba_{1-x}Sr_x MoO_4$ (x = 0, 0.18, 0.38, 0.60, 0.81, 1) solid solutions.

5.2.1.4. Characterisation of $SrMoO_4$(s) but $BaMoO_4$(s) by SEM

The scanning electron micrographs are shown in **Fig.5.7 and 5.8.** The nonuniformity in the particle size is seen in $SrMoO_4$ but $BaMoO_4$ showed the uniformity and porous structure. The particle sizes of both the samples are in micrometer range which could be due to the long annealing time.

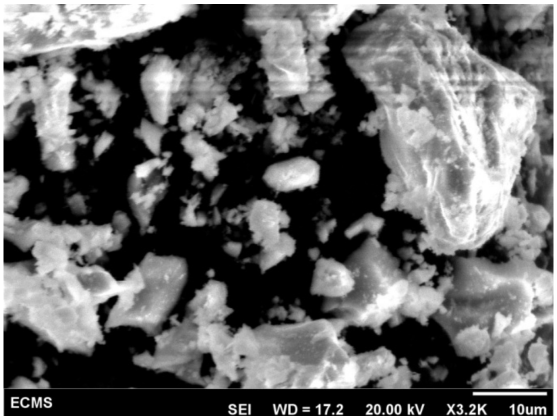

Fig.5.7. Scanning electron micrograph of $SrMoO_4$(s)

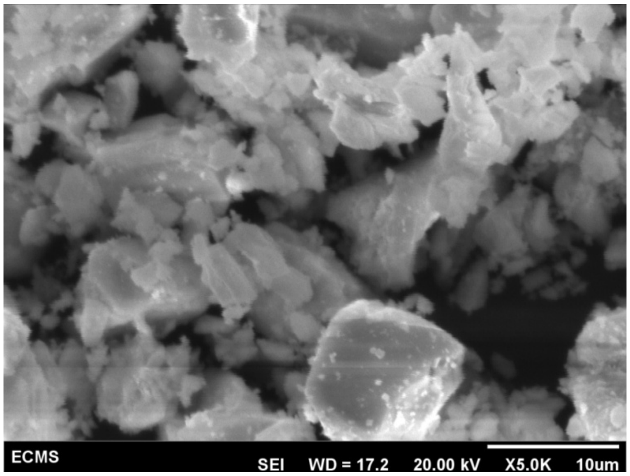

Fig.5.8. Scanning electron micrograph of $BaMoO_4(s)$

5.2.1.5. Crystal Structure indexing of $Ba_{1-x}Sr_x MoO_4(s)$ (x= 0.18, 0.38, 0.60, 0.81)

$Ba_{1-x}Sr_x MoO_4(s)$ (x= 0, 0.18, 0.38, 0.60, 0.81, 1) can be indexed using tetragonal crystal structure, described in the literature [**176, 177, 179, 180**]. All these compositions belong to the space group $14_1/a$. The tetragonal unit cell parameters were refined using the program written by Wadhawan **[104]**. The observed and calculated reflection for $Ba_{1-x}Sr_x MoO_4(s)$ (x= 0.18, 0.38, 0.60, 0.81) along with their indices, which are not reported in the literature, are given in **Table 5.4.**

Thermophysical Properties of $Ba_{1-x}Sr_x MoO_4(s)$ solid solutions

5.2.1.6. *Thermal expansion of $Ba_{1-x}Sr_x MoO_4(s)$ (x = 0, 0.6 and 1)*

The lattice parameters of $Ba_{1-x}Sr_x MoO_4(s)$ (x = 0, 0.6 and 1) were calculated from diffraction angles and the miller indices at different temperatures. Densities of $Ba_{1-x}Sr_x MoO_4(s)$ (x=0, 0.6 and 1) were also calculated at different temperatures using formula given in **section 2.4** by taking Z = 4. The calculated linear lattice parameters, volume and density were fitted to a second order polynomial equation of the form $p + qT + rT^2$, where p, q, and r are constants and T denotes the absolute temperature.

Percentage expansions (% l) of lattice parameters of $Ba_{1-x}Sr_x MoO_4(s)$ (x=0, 0.6 and 1) was calculated. Similarly percentage expansions in volume and percentage reduction in density were calculated at different temperatures. The instantaneous and average thermal expansion coefficient (α) at any temperature T was also calculated

Table.5.4. X-Ray powder diffraction data of $Ba_{1-x}Sr_xMoO_4$ (s) solid solutions

$Ba_{0.82}Sr_{0.18}MoO_4$(s)						**$Ba_{0.62}Sr_{0.38}MoO_4$ (s)**						**$Ba_{0.40}Sr_{0.60}MoO_4$ (s)**						**$Ba_{0.19}Sr_{0.81}MoO_4$ (s)**					
d_{obs}	d_{cal}	I/I_o	h	k	l	d_{obs}	d_{cal}	I/I_o	h	k	l	d_{obs}	d_{cal}	I/I_o	h	k	l	d_{obs}	d_{cal}	I/I_o	h	k	l
3.334	3.333	100	1	1	2	3.303	3.305	100	1	1	2	3.279	3.278	100	1	1	2	3.251	3.250	100	1	1	2
3.169	3.169	16	0	0	4	3.126	3.127	20	0	0	4	3.090	3.089	24	0	0	4	3.050	3.048	25	0	0	4
2.771	2.771	20	2	0	0	2.751	2.752	22	2	0	0	2.736	2.735	25	2	0	0	2.716	2.716	24	2	0	0
2.538	2.539	2	2	0	2	2.438	2.438	7	1	1	4	2.401	2.400	11	1	2	1	2.385	2.388	14	1	1	4
2.465	2.464	3	1	1	4	2.418	2.416	8	2	1	1	2.105	2.103	10	2	1	3	2.028	2.028	25	2	0	4
2.432	2.432	4	2	1	1	2.279	2.277	6	1	0	5	2.047	2.048	27	2	0	4	1.921	1.921	14	2	2	0
2.305	2.305	3	1	0	5	2.066	2.066	22	2	0	4	1.934	1.934	17	2	2	0	1.797	1.796	18	1	1	6
2.136	2.138	2	2	1	3	1.946	1.946	10	2	2	0	1.818	1.818	20	1	1	6	1.653	1.654	19	3	1	2
2.086	2.086	24	2	0	4	1.838	1.838	14	1	1	6	1.666	1.666	24	3	1	2	1.625	1.625	15	2	2	4
1.959	1.959	9	2	2	0	1.677	1.677	17	3	1	2	1.639	1.639	17	2	2	4	1.329	1.329	12	0	2	8
1.859	1.859	13	1	1	6	1.652	1.652	13	2	2	4	1.544	1.544	10	0	0	8						
1.689	1.689	18	3	1	2	1.376	1.376	7	4	0	0	1.367	1.367	11	4	0	0						
1.666	1.666	10	2	2	4	1.359	1.359	8	2	0	8	1.345	1.345	12	2	0	8						
1.584	1.584	2	0	0	8	1.336	1.336	10	3	1	6	1.324	1.324	15	3	1	6						
1.386	1.385	3	4	0	0																		
1.376	1.375	5	2	0	8																		
1.349	1.349	8	3	1	6																		
Sys: Tetragonal, Space Group: $14_1/a$ (88) , Cu K_α (λ=1.5406 Å), Filter:Ni																							
a = 5.5417 Å, c =12.6741 Å, Z=4, Mwt: 287.328, Volume: 389.23 $Å^3$, ρ = 4.903g cm^{-3}						a =5.5049 Å, c =12.5062 Å, Z=4, Mwt: 277.386,Volume: 378.99 $Å^3$, ρ =4.861 g cm^{-3}						a =5.4675 Å, c =12.3491 Å, Z=4, Mwt: 267.444, Volume: 369.16, ρ =4.812 g cm^{-3}						a =5.4327 Å, c =12.1922 Å, Z=4, Mwt: 257.502, Volume: 359.84 $Å^3$, ρ =4.753 g cm^{-3}					

The lattice parameters were best fitted to the second order polynomial expressions as given below:

For Ba MoO_4(s)

a (Å) = $5.583 - 2.0 \times 10^{-5}$ (T/K) + 3.314×10^{-8} $(T/K)^2$ (5.5)

c (Å) = $12.823 - 7.0\times 10^{-5}$ (T/K) + 2.387×10^{-7} $(T/K)^2$ (5.6)

For Ba $_{0.4}Sr_{0.6}$ MoO_4(s)

a (Å) = $5.468 - 1.0 \times 10^{-5}$ (T/K) + 3.254×10^{-8} $(T/K)^2$ (5.7)

c (Å) = $12.327 + 4.0 \times 10^{-5}$ (T/K) + 1.332×10^{-7} $(T/K)^2$ (5.8)

For Sr MoO_4(s)

a (Å) = $5.387 + 3.8\times 10^{-6}$ (T/K) + 2.820×10^{-8} $(T/K)^2$ (5.9)

c (Å) = $12.011 + 3.0 \times 10^{-5}$ (T/K) + 1.060×10^{-7} $(T/K)^2$ (5.10)

The variation of lattice parameters, unit cell volume and the density as a function of temperature for Ba $_{1-x}Sr_x$ MoO_4(s) (x=0, 0.6 and 1) are given in **Table 5.5.** The percentage linear expansion (along a and c) as a function of temperature is shown in **Fig.5.9.** It shows that the percentage expansion of Ba MoO_4(s) is found to be lowest along a -axis and highest along c -axis, however, the percentage expansion of Sr MoO_4(s) is found to be highest along a -axis and lowest along c -axis. The expansion for Ba $_{0.4}Sr_{0.6}$ MoO_4(s) falls in between $BaMoO_4$(s) and $SrMoO_4$(s). Similarly, the variation of volume and density in percentage as a function of temperature is shown in **Fig.5.10.** The values of the linear (α_a and α_c) and volume (α_V) thermal expansion coefficients at different temperatures were calculated and given in **Table 5.5.**

Table.5.5. Lattice parameters (*a* and *c*), volume (*V*), density (*ρ*), linear (α_a and α_c) and volume (α_V) thermal expansion coefficients of Ba $_{1-x}$ Sr $_x$MoO$_4$ (s) (x=0, 0.6 and 1) solid solutions in the temperature range 298-1273 K.

SrMoO$_4$(s)							
***T*/K**	***a* (Å)**	***c* (Å)**	***V* (Å^3)**	***ρ*(g/cm^3)**	α_a	α_c	α_V
298.15	5.3909	12.0300	349.61	4.703	3.83	7.74	15.43
373	5.3929	12.0378	350.10	4.696	4.61	9.06	18.4
473	5.3956	12.0501	350.81	4.687	5.66	10.82	22.37
573	5.3989	12.0644	351.65	4.676	6.71	12.59	26.34
673	5.4028	12.0809	352.64	4.663	7.75	14.35	30.31
773	5.4072	12.0995	353.76	4.648	8.80	16.11	34.28
873	5.4122	12.1202	355.02	4.631	9.85	17.87	38.24
973	5.4178	12.1431	356.43	4.613	10.89	19.63	42.21
1073	5.424	12.1680	357.98	4.593	11.94	21.39	46.18
1173	5.4307	12.1951	359.66	4.572	12.98	23.15	50.15
1273	5.4381	12.2243	361.50	4.548	14.03	24.91	54.11
Ba$_{0.4}$Sr$_{0.6}$MoO$_4$(s)							
298.15	5.4675	12.3491	369.16	4.812	1.72	9.67	11.70
373	5.4682	12.3585	369.53	4.807	2.61	11.30	15.20
473	5.4697	12.3733	370.18	4.798	3.80	13.40	19.80
573	5.4719	12.3908	371.00	4.788	4.99	15.60	24.50
673	5.4747	12.4110	371.99	4.775	6.18	17.80	29.10
773	5.4782	12.4338	373.15	4.760	7.37	19.90	33.80
873	5.4823	12.4593	374.47	4.743	8.56	22.10	38.40
973	5.4871	12.4875	375.98	4.724	9.75	24.20	43.00
1073	5.4925	12.5183	377.65	4.703	10.94	26.40	47.70
1173	5.4986	12.5518	379.50	4.681	12.14	28.50	52.30
1273	5.5053	12.5879	381.52	4.656	13.33	30.70	57.00
BaMoO$_4$(s)							
298.15	5.5800	12.8212	399.21	4.946	-0.04	5.63	1.68
373	5.5804	12.8277	399.47	4.943	0.85	8.43	5.44
473	5.5822	12.8443	400.24	4.933	2.03	12.20	10.40
573	5.5829	12.8581	400.77	4.926	3.22	15.90	15.50
673	5.5851	12.8805	401.79	4.914	4.41	19.60	20.50
773	5.5880	12.9077	403.05	4.899	5.60	23.30	25.50
873	5.5916	12.9396	404.57	4.880	6.79	27.00	30.50
973	5.5959	12.9763	406.33	4.859	7.97	30.80	35.50
1073	5.6008	13.0178	408.35	4.835	9.16	34.50	40.50
1173	5.6064	13.0641	410.63	4.808	10.40	38.20	45.50
1273	5.6126	13.1151	413.14	4.779	11.50	41.90	50.50

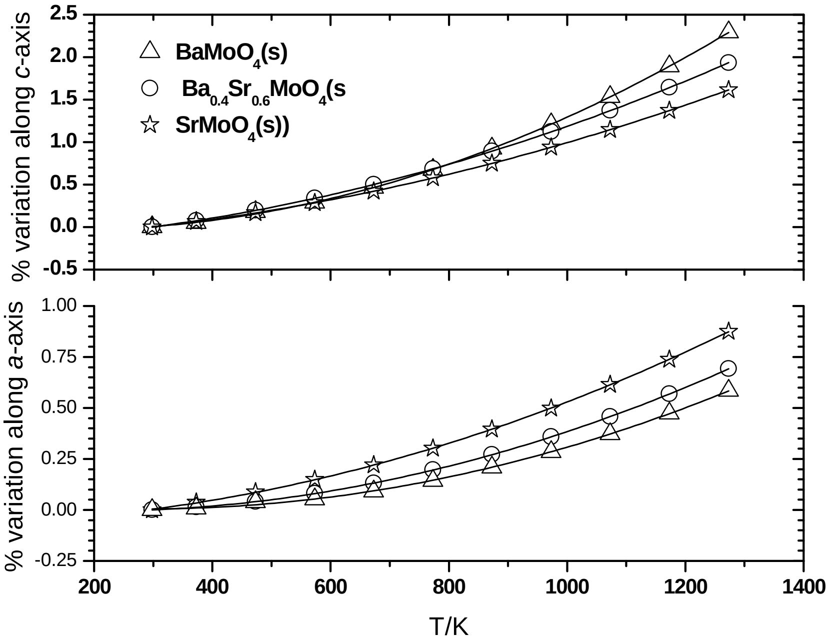

Fig.5.9. The percentage linear thermal expansion (% *l*) calculated from lattice parameter of Ba$_{1-x}$Sr$_x$ MoO$_4$ (x = 0, 0.6 and 1) solid solutions along *a* and *c* -axis.

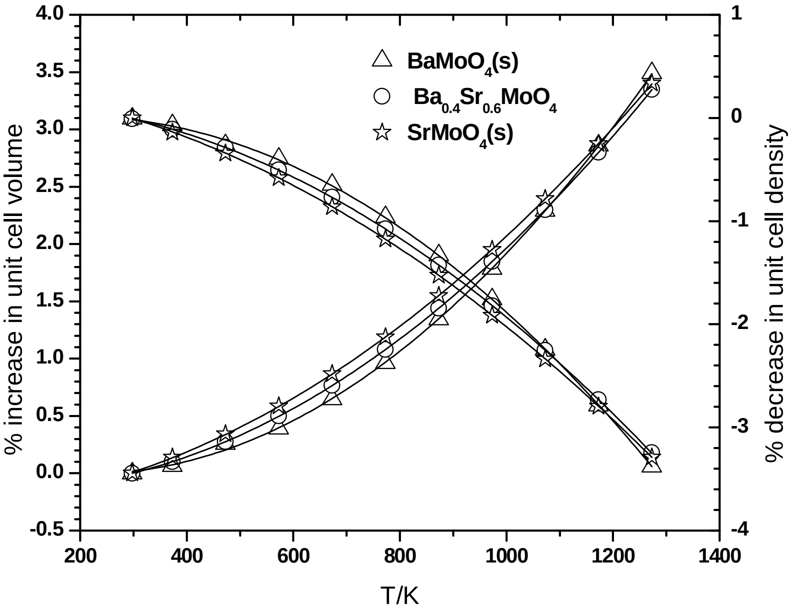

Fig.5.10. The percentage variation in volume (%*V*) and density ((%ρ) of Ba $_{1-x}$Sr$_x$ MoO$_4$ (x = 0, 0.6 and 1) solid solutions calculated from unit cell volume and density at 0different temperatures.

The average of linear (α_a and α_c) and volume (α_V) thermal expansion coefficients were linearly fitted as a function of the mole fraction of $SrMoO_4$(s) and are represented in **Fig.5.11 and 5.12**, respectively.

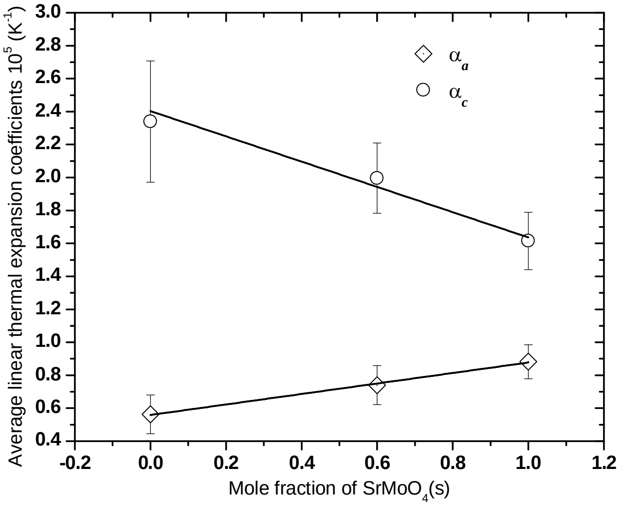

Fig.5.11. The plot of average linear thermal expansion coefficient (α_a and α_c) of $Ba_{1-x}Sr_x MoO_4$(x = 0, 0.6 and 1) as a function of mole fraction of $SrMoO_4$(s) in the temperature range of 298-1273 K.

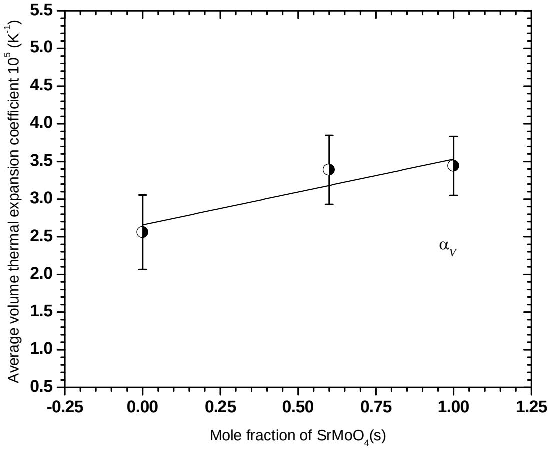

Fig.5.12. A plot of average volume thermal expansion coefficient (α_V) of $Ba_{1-x}Sr_x MoO_4$ (x = 0, 0.6 and 1) as a function of mole fraction of $SrMoO_4$(s) in the temperature range of 298- 1273 K.

Expressions for the average of linear (α_a and α_c) and volume (α_V) thermal expansion coefficients are given below:

$$\alpha_a = 5.5901 \times 10^{-6} + 3.1835 \times 10^{-6} \cdot x \tag{5.11}$$

$$\alpha_c = 2.4032 \times 10^{-5} - 7.6696 \times 10^{-6} \cdot x \tag{5.12}$$

$$\alpha_V = 2.6571 \times 10^{-5} + 8.7427 \times 10^{-6} \cdot x \tag{5.13}$$

Where "x" is the mole fraction of $SrMoO_4$ (s) in the solid solutions. The average of the linear thermal expansion coefficients along *a* –axis is found to increase with increase in concentration of Sr but the average of linear thermal expansion coefficients along *c* –axis is found to decrease with increase in concentration of Sr. But the most useful volume thermal expansion coefficients are found to increase with increase in concentration of Sr. The values of average volume thermal expansion coefficient in the present study are close to the ceramic nuclear fuels [**183-184**].

5.2.1.7. Heat capacity

The measured heat capacities of $BaMoO_4$(s) and $SrMoO_4$(s) along with that reported in the literature, estimated and fit values in the temperature range of 300-870 K are shown in **Figs. 5.13 and 5.14,** respectively.

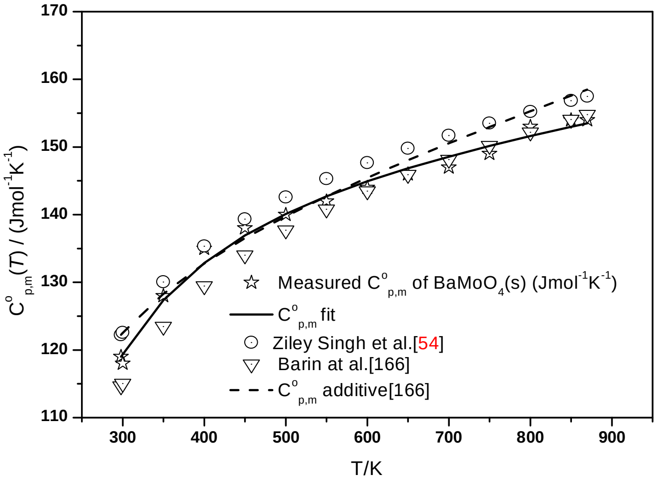

Fig.5.13. Molar heat capacity data of $BaMoO_4$(s) in the temperature range of 300-870 K

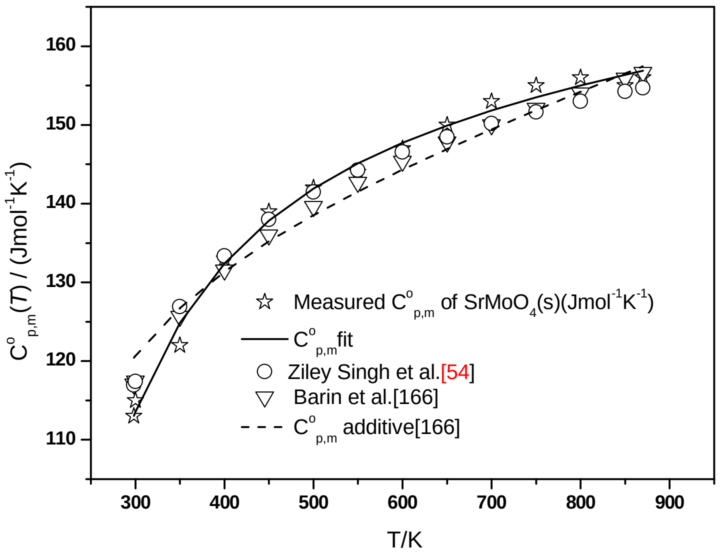

Fig.5.14. Molar heat capacity data of $SrMoO_4$(s) in the temperature range of 300-870 K.

The heat capacity of $BaMoO_4$(s) and $SrMoO_4$(s) are the mean values of eight measurements. The error derived from the mean standard deviation for $BaMoO_4$(s) and $SrMoO_4$(s) are 0.5–4.4 % and 1-2.7 %, respectively. The experimentally measured heat capacity values for $BaMoO_4$(s) and $SrMoO_4$(s) are given in **Table 5.6** in the two temperature ranges 140-450K and 300-870 K, respectively.

For each composition, the experimental molar heat capacity values in the complete temperature range: 140 to 870 K were best fitted to a single polynomial equation and heat capacity at 298.15 K was calculated. $C_{p,m}$(298.15 K) of $Ba_{1-x}Sr_x MoO_4$(s) (x= 0,0.18, 0.38, 0.60, 0.81 and 1) were calculated to be 119,117,115,112,117 and 113 respectively. This $C_{p,m}$(298.15 K) value was introduced for fitting molar heat capacity data given in **Table 5.6** for two separate temperature range 140-450K and 298.15-870 K, respectively. The heat capacities of $BaMoO_4$(s) and $SrMoO_4$(s) were fitted to the polynomial $a + bT + cT^{-2} + dT^2$ in the temperature range 140-450 K and to $A + BT + CT^{-2}$ in the temperature range 298.15-870 K. Where *a, b, c, d, A, B, and C* are constants and *T* is absolute temperature. The values of coefficients *a*, *b*, *c* and *d* in the temperature range 140-450 K are given in **Table 5.7.** Similarly the values of coefficients *A*, *B*, and *C* in the temperature range 298.15-870 K are given in **Table 5.8.**

Table.5.6. Heat capacities of Ba $_{1-x}$Sr$_x$ MoO$_4$ solid-solution(x=0, 0.18, 0.38, 0.60, 0.81, 1)

T/K	$C^o_{p,m}(T)$ (J mol^{-1} K^{-1}) in the Temperature range of 140-450 K					
	BaMoO$_4$(s)	(Ba$_{0.82}$Sr$_{0.18}$)MoO$_4$(s)	(Ba$_{0.62}$Sr$_{0.38}$)MoO$_4$(s)	(Ba$_{0.40}$Sr$_{0.60}$)MoO$_4$(s)	(Ba$_{0.19}$Sr$_{0.81}$)MoO$_4$(s)	SrMoO$_4$(s)
140	89	91	84	86	85	85
150	91	92	87	87	90	88
200	98	100	96	95	97	93
250	108	109	105	104	107	101
300	118	118	115	113	116	111
350	127	127	126	121	128	121
400	134	132	133	127	134	130
450	139	137	139	131	139	136
	$C^o_{p,m}(T)$ (J mol^{-1} K^{-1}) in the Temperature range of 300-870 K					
300	118	117	113	110	117	115
350	128	124	122	123	125	122
400	135	133	130	132	131	133
450	138	137	135	135	135	139
500	140	140	140	140	139	142
550	142	145	143	146	142	144
600	144	147	146	148	145	147
650	146	149	148	151	148	150
700	147	150	150	154	150	153
750	149	150	152	155	153	155
800	153	152	154	155	155	156
850	154	153	155	156	157	155
870	154	154	156	157	158	156

Table.5.7.The heat capacity coefficients of fitted polynomial for of Ba $_{1-x}$Sr$_x$ MoO$_4$ (x=0, 0.18, 0.38, 0.60, 0.81, 1) solid-solutions in the temperature range of 140-450 K

Solid Solutions **(Ba $_{1-x}$Sr$_x$ MoO$_4$)**	$C^{o}_{p,m}(T) = a + bT + cT^{-2} + dT^{2}$ **(Jmol^{-1}K$^{-1)}$**			
x	a	b	$c\times 10^{-5}$	$d\times 10^{4}$
1.0	15.60	0.389	4.25	-2.8
0.81	19.20	0.421	3.01	-3.5
0.60	18.40	0.410	3.32	-3.7
0.38	26.26	0.371	2.34	-2.7
0.18	23.32	0.412	3.36	-3.6
0.0	8.154	0.481	4.41	-4.4

The heat capacity data of BaMoO$_4$(s) measured in this study along with the reported values by Singh et al. **[54]** and Barin et al. **[166]** are shown in **Fig.5.13.** The standard errors of the polynomial fit for the heat capacity of BaMoO$_4$(s) are 0.2 and 1.56J K^{-1} mol^{-1} in the temperature range 140-450 K and 300-870 K, respectively. It can be seen from **Fig. 5.13** that present heat capacity data for BaMoO$_4$(s) are in good agreement (within ± 3.0 %) with those computed using Neumann–Kopp rule and also present $C_{p,m}(T)$ data of BaMoO$_4$(s) match with that reported by Barin et al. **[166]** in the high temperature range and that reported by Singh et al. **[54]** around room temperature.

The heat capacity data of SrMoO$_4$(s) measured in this study along with the reported values by Singh et al. **[54]** and Barin et al. **[166]** are shown in **Fig.5.14.** The standard errors of the polynomial fit for heat capacity of SrMoO$_4$(s) are 1.53 and 1.91 J K^{-1} mol^{-1} in the temperature range of 140-450 K and 300-870 K respectively. The present data for SrMoO$_4$(s) are in good agreement (within ± 6 %) with those computed using Neumann–Kopp rule. It is evident from **Fig. 5.14** that the present data are in good agreement with the data reported in the literature.

Heat capacity data of Ba $_{1-x}$Sr$_x$ MoO$_4$(s) (x= 0.18, 0.38, 0.60 and 0.81) solid solutions at selected temperatures are the mean values of 3-4 measurements. The error derived from the mean standard deviation for the measurements of each sample is less than 3.5 %.

Table.5.8.The coefficients of heat capacity, enthalpy increment, entropy and Gibbs energy function of Ba $_{1-x}$Sr$_x$ MoO$_4$ (x=0, 0.18, 0.38, 0.60, 0.81, 1) solid-solutions

Solid Solutions (Ba $_{1-x}$Sr$_x$ MoO$_4$)	$C^o_{p,m}(T)$ $A + BT + CT^{-2}$ (Jmol^{-1}K^{-1}) [300-870 K]			$H^o_m(T) - H^o_m(298.15)$ $= DT + ET^2 + FT^{-1} + G$ (kJ mole^{-1}) [298.15-870 K]				$S^o_m(T) =$ $= H\log(T) + IT + JT^{-2} + K$ (J mole^{-1}K^{-1}) [298.15-870 K]				$-\left(\frac{G^o_m(T) - H^o_m(298.15)}{T}\right)$ $= L\log(T) + MT + NT^{-2} + O$ (J mole^{-1}K^{-1}) [298.15-870 K]			
x	*A*	*B*	*C* × 10 $^{-6}$	*D*	*E* × 10^6	*F*	*G*	*H*	*I*	*J* × 10^{-6}	*K*	*L*	*M*	***N*** × 10^{-6}	*O*
1	148.85	0.015	-3.57	0.148	7.65	3477	-56.38	340.56	0.015	1.76	-738.15	85.67	0.076	2.82	-137.58
0.81	128.55	0.037	-2.02	0.129	20.0	2085	-47.15	296.12	0.037	1.01	-620.50	78.74	0.080	2.66	-113.79
0.60	148.96	0.016	-3.84	0.147	9.27	3641	-56.79	344.69	0.015	1.94	-741.12	77.31	0.081	2.71	-107.74
0.38	139.01	0.024	-2.93	0.139	10.0	2893	-52.10	321.28	0.023	1.48	-678.57	81.07	0.077	2.72	-114.13
0.18	147.03	0.013	-3.09	0.144	7.85	2813	-53.03	339.50	0.012	1.55	-720.94	90.64	0.074	2.86	-138.44
0.0	140.16	0.019	-2.38	0.142	8.04	2515	-51.61	322.60	0.019	1.19	-679.32	91.48	0.073	2.86	-142.15

The values of measured heat capacities of Ba $_{1-x}$Sr$_x$ MoO$_4$(s) (x= 0.18, 0.38, 0.60 and 0.81) solid solutions were fitted to polynomial in two temperature segments by the least squares method similar to BaMoO$_4$(s) and SrMoO$_4$(s). The coefficients of the fitted polynomial for Ba $_{1-x}$Sr$_x$ MoO$_4$(s) (x= 0.18, 0.38, 0.60 and 0.81) are also given in **tables 5.7 & 5.8** in the temperature range of 140-450K and 300-870 K, respectively.

From fitted equations, other thermodynamic functions such as enthalpy increment$H_m^o(T) - H_m^o(298.15K)$, entropy $S_m^o(T)$ and Gibbs energy function $-\left(G_m^o(T) - H_m^o(298.15)\right)/T$ were calculated in the temperature range of 298.15-870 K. Entropies of Ba $_{1-x}$Sr$_x$ MoO$_4$(s) (x=0,0.18, 0.38, 0.60, 0.81,1) solid solutions were computed assuming ideal solution model.

$S_m^o(Ba_{1-x}Sr_xMoO_{4,}s, 298.15)$ was estimated by taking $S_m^o(298.15)$ for SrMoO$_4$(s) and BaMoO$_4$(s) from Barin et al. **[166]** in the stoichiometric ratio and using ideal entropy of mixing ($\Delta S^{mix,id}$).

The relations used for calculations of thermodynamic functions from heat capacity and entropy values are given in **section 2.8.1.** The computed thermodynamic functions in the form of polynomial expression of temperature are given in **Table 5.8.**

The specific heat capacity of Ba $_{1-x}$Sr$_x$ MoO$_4$(s) (x= 0, 0.18, 0.38, 0.60, 0.81, 1) solid solutions were plotted in **Fig.5.15**. It was observed that specific heat of these solid solutions increase with increase in the concentration of strontium from *x* = 0 to 1. This is attributed to the higher heat capacity of SrMoO$_4$(s) than that of BaMoO$_4$(s).

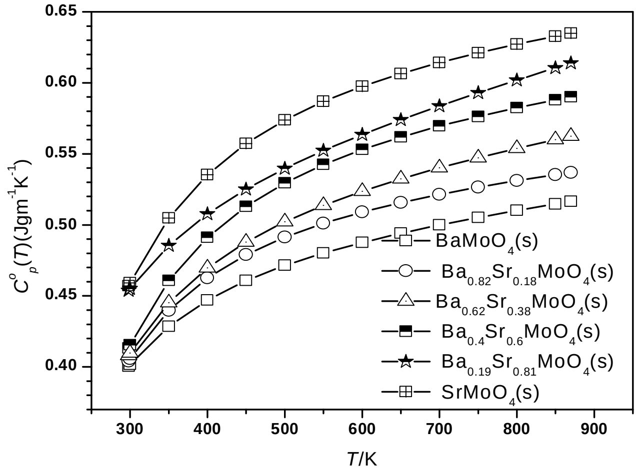

Fig.5.15. Specific heat capacity of Ba $_{1-x}$Sr$_x$ MoO$_4$ (x = 0, 0.18, 0.38, 0.60, 0.81, 1) solid solutions as function of temperature in the temperature range of 300-870 K.

5.3. Summary

1. Ba $_{1-x}$Sr$_x$ MoO$_4$ (x=0, 0.18, 0.38, 0.60, 0.81, 1) solid-solutions were synthesized by complex polymerization method. Chemical compositions were determined by ICPMS and solid solutions were characterized using XRD and Raman spectroscopy.

2. Single tetragonal phase was observed for Ba $_{1-x}$Sr$_x$ MoO$_4$(s) (x = 0 - 1) which was found to obey Vegard's law.

5. The thermal expansion coefficient of Ba $_{1-x}$Sr$_x$ MoO$_4$(s) (x=0, 0.6 and 1) solid solution was measured by HT-XRD in the temperature range of 298-1273 K for the first time.

6. The average volume thermal expansion coefficient was found to increase with increase in concentration of Sr.

7. The average volume thermal expansion coefficient of Ba $_{1-x}$Sr$_x$ MoO$_4$(s) (x=0, 0.6 and 1) was found to be 25.59×10^{-6} K^{-1}, 33.86×10^{-6} K^{-1} and 34.37×10^{-6} K^{-1} respectively.

3. Heat capacity of solid solutions was measured by a heat flux-type differential scanning calorimeter in the temperature range of 140-870 K for the first time.

4. The specific heat capacity data of Ba$_{1-x}$Sr$_x$MoO$_4$(s) (x=0, 0.18, 0.38, 0.60, 0.81,1) solid solutions were found to increase with increasing concentration of SrMoO$_4$ similar to the observation found in case of thermal expansion. Enthalpy increment, entropy and Gibbs energy functions were computed from the measured heat capacity.

These data could be useful for the assessment of performance of nuclear reactors operating with high burn up oxide fuels.

CHAPTER-6

$Ba_{1-x}Sr_xMoO_3(s)$ solid-solutions

CHAPTER-6

The perovskite-type oxide (Ba, Cs, Sr)(U,Pu,Zr,RE,Mo)O_3(s) phase has been observed in the irradiated fuel matrix. The composition of these phases changes with mixed oxide fuel composition and burn-up. ABO_3 compounds also exhibits ferro-electricity, ferromagnetism, superconductivity, thermal conductivity, ionic conductivity, piezoelectric, photo-catalytic and thermoelectricity. Moreover, thermodynamic properties of $Ba_{1-x}Sr_xMoO_3$(s) solid solutions have not been reported in the literature which will help in predicting the performance of the nuclear fuel under irradiation and the safe application of these perovskites in various physico chemical environments. The present study is focused on the synthesis of $Ba_{1-x}Sr_xMoO_3$(s) (x = 0, 0.2, 0.4, 0.5, 0.8, 1) and measurements of their thermal expansion and heat capacity using HTXRD and DSC, respectively.

6.1. Experimental

6.1.1. Synthesis of $Ba_{1-x}Sr_xMoO_3$ (s) (x=0, 0.2, 0.4, 0.5, 0.8, 1) solid solutions

Perovskite-type oxides of $Ba_{1-x}Sr_xMoO_3$(s) (x = 0, 0.2, 0.4, 0.5, 0.8, 1) were prepared by reduction of corresponding $Ba_{1-x}Sr_xMoO_4$(s) (x = 0, 0.2, 0.4, 0.5, 0.8, 1) oxides having scheelite-type structure. $Ba_{1-x}Sr_xMoO_4$(s) (x = 0, 0.2, 0.4, 0.5, 0.8, 1) oxides was synthesized using complex polymerization method as described in section 5.1.1. In order to optimize the condition for reduction of $SrMoO_4$(s) and $BaMoO_4$(s) to $SrMoO_3$(s) and $BaMoO_3$(s), the reduction was tried separately in 8% H_2(g) + Ar (g) mixture, pure H_2(g) and by carbothermic reduction in Ar (g) ambient by varying the temperature. The reduction in 8% H_2(g) + Ar(g) and carbothermic reduction was tried in the temperature range 1173 K- 1573 K by keeping for 10 h at each temperature with a interval of 50 K. But the reduction in pure H_2 was carried out at 1293 K for 20 h.

6.1.2. Characterisation by X-Ray Diffractometry

Perovskite-type oxides $Ba_{1-x}Sr_xMoO_3$(s) (x = 0, 0.2, 0.4, 0.5, 0.8, 1) was characterized using a STOE theta–theta X-ray diffractometer employing graphite monochromatic Cu Kα (λ = 0.15406 nm) radiation. The scans of 2θ were made in the range of 10^o to 70^o.

6.1.3. Characterisation by SEM

The morphological investigations of the powder samples of $SrMoO_4$(s) and $BaMoO_4$(s) were carried out using a scanning electron microscope (SEM) as described in section 2.3.3.

6.1.4. Analysis of metalic elements by ICPMS

An inductively coupled plasma time of flight mass spectrometer (ICP-TOF-MS), model: 8000R (GBC, Australia) was used for the determination of metallic elements in $Ba_{1-x}Sr_xMoO_3$(s) (x = 0, 0.2, 0.4, 0.5, 0.8, 1) solid solutions. For this study, quantitative amounts of solid solutions were digested in concentrated nitric acid and dried. The final analyte solutions for ICPMS were made with 1% nitric acid. The solutions were fed into ICPMS and the measured elemental compositions were used to find out the stoichiometry of Ba and Sr which is given in **Table 6.1.**

Table.6.1: The stoichiometry of $Ba_{1-x}Sr_x\ MoO_3$(s)(x = 0, 0.2, 0.4, 0.5, 0.8, 1) solid solutions determined from analysis of metallic content by ICPMS and non metallic oxygen by converting it to CO_2(g)

Sl No.	**Approximate stoichiometry synthesized**	**Actual Stoichiometry determined by ICPMS**
1	$BaMoO_3$(s)	$Ba_{1.048\pm 0.053}MoO_{3.17\pm0.1}$(s)
2	$Ba_{0.8}Sr_{0.2}MoO_3$(s)	$Ba_{0.779 \pm 0.068}Sr_{0.198 \pm 0.045}MoO_{3.1\pm0.09}$(s)
3	$Ba_{0.6}Sr_{0.4}MoO_3$(s)	$Ba_{0.568 \pm 0.026}Sr_{0.456 \pm 0.015}MoO_{3.32\pm0.1}$(s)
4	$Ba_{0.5}Sr_{0.5}MoO_3$(s)	$Ba_{0.473 \pm 0.04}Sr_{0.49 \pm 0.057}MoO_{3.07\pm0.09}$(s)
5	$Ba_{0.2}Sr_{0.8}MoO_3$(s)	$Ba_{0.194 \pm 0.013}Sr_{0.811 \pm 0.012}MoO_{3.09\pm0.07}$(s)
6	$SrMoO_3$(s)	$Sr_{0.961 \pm 0.02}MoO_{3.02\pm0.09}$(s)

6.1.5. Oxygen analysis

$Ba_{1-x}Sr_xMoO_3$(s) (x = 0, 0.2, 0.4, 0.5, 0.8, 1) was synthesized by reduction of $Ba_{1-x}Sr_xMoO_4$(s) (x = 0, 0.2, 0.4, 0.5, 0.8, 1). In order to know the percentage conversion of reactant to product, the O/M ratio of $Ba_{1-x}Sr_xMoO_3$(s) (x = 0, 0.2, 0.4, 0.5, 0.8, 1) is required. Moreover the O/M ratio has significant impact on the thermophysical properties of barium strontium molybedites. In this study, the oxygen content of $Ba_{1-x}Sr_xMoO_3$(s) (x = 0, 0.2, 0.4, 0.5, 0.8, 1) solid solutions were determined using determinator supplied by M/s Chromatography and Instruments Company (CIC), Vadodara, India. Stainless steels with different content of oxygen supplied by M/s LECO Corporation (St. Joseph, MI, USA) were used as standards in this study. In this technique, the sample was fused in a graphite crucible in the presence of nickel as flux at high temperature (~3000 K) in flowing inert (helium) gas. Under these conditions, major amount of oxygen gets released as CO(g) and trace amounts as CO_2(s) depending on the oxygen content in the sample. These released gases are carried away along with flowing helium and allowed to pass through hot copper oxide (CuO at 773 K) catalyst column, where CO (g) also gets converted to CO_2(g) . The total CO_2(g) released was determined by IR detector. The elaborate procedure and description of instrument used is given by Ramanjaneyulu et al [**185**]. The oxygen stoichiometry for $Ba_{1-x}Sr_xMoO_3$(s) (x = 0, 0.2, 0.4, 0.5, 0.8, 1) were calculated from the determined oxygen amount and are also given in **Table 6.1.**

Thermophysical Properties Measurements

6.1.6. Thermal expansion Measurements using HT-XRD

The axial and volume thermal expansion measurements of $Ba_{1-x}Sr_xMoO_3$(s) (x = 0, 0.4, 0.8 and 1) were carried out using STOE diffractometer following the procedure described in section 2.4.1.2.1. The high temperature XRD patterns were recorded in the temperature range of 298–873 K.

6.1.7. Measurement of heat capacity

Heat capacity $C^o_{p,m}(T)$ measurements of $Ba_{1-x}Sr_xMoO_3$(s) (x = 0, 0.4, 0.8 and 1) were carried out using a heat flux-type DSC in the temperature range 290-870 K and the procedure followed is same as described in section 2.5.1.3.1. The entire temperature range was divided into three segments (283-473K, 453-673K and 653-873K) to ensure good thermal equilibrium. High purity gas mixture 4%H_2-Ar was passed at a flow rate of 0.05 $dm^3\ min^{-1}$ over the sample. 70-80 mg of powder samples of $Ba_{1-x}Sr_xMoO_3$(s) (x = 0, 0.4, 0.8 and 1) were pelletised and loaded in $4\cdot10^{-5}$ dm^3 Al pan and used for heat capacity measurements. The values of specific heat capacity were calculated using equation 2.36.

6.2. Results and Discussion

6.2.1. Reduction condition of $Ba_{1-x}Sr_xMoO_4$(s)(x = 0, 0.2, 0.4, 0.5, 0.8, 1) solid solution

It was observed that $SrMoO_3$(s) could be prepared using all the three reduction conditions mentioned in the experimental section. However, pure $BaMoO_3$(s) phase could not be prepared either by reduction in 8% H_2(g)+Ar (g) atmosphere or by cabothermic reduction. The product obtained in 8% H_2(g)+Ar(g) was a biphasic mixture of $BaMoO_3$(s) + $BaMoO_4$(s) and the carbothermic reduction leads to no chemical change of $BaMoO_4$(s). Pure $BaMoO_3$(s) was formed only when $BaMoO_4$(s) was loaded into a leak tight quartz-tube and heated at 1293 K under pure H_2(g) at a flow rate of 10 K min^{-1} for 20 h. The observed color of $BaMoO_3$ (s) and $SrMoO_3$ (s) were black and wine red, respectively. Hence, $Ba_{1-x}Sr_xMoO_3$(s) (x = 0, 0.2, 0.4, 0.5, 0.8, 1) solid solution was prepared from $Ba_{1-x}Sr_xMoO_4$(s)(x = 0, 0.2, 0.4, 0.5, 0.8, 1) by heating the mixture under pure H_2(g) at 1293 K for 20 h. The reduction of $Ba_{1-x}Sr_xMoO_4$(s) to $Ba_{1-x}Sr_xMoO_3$(s) can be described by the following reaction:

$$Ba_{1-x}Sr_xMoO_4\ (s) + H_2\ (g) \rightleftarrows Ba_{1-x}Sr_xMoO_3\ (s) + H_2O\ (g) \qquad (6.1)$$

6.2.2. XRD Analysis

The XRD pattern of pure $BaMoO_3$(s) and $SrMoO_3$(s) matches with the reported patterns **[186, 187]**. The computed room temperature lattice parameters, unit cell volume and density of cubic $BaMoO_3$(s) and $SrMoO_3$(s) are listed in **Table 6.2** and these values are in good agreement with that reported in the literature [**186, 187**].

Table.6.2: Crystal system and lattice parameter of $BaMoO_3$(s) and $SrMoO_3$(s)

Lattice parameters	**Tetragonal**			
	$SrMoO_3$(s)		**$BaMoO_3$(s)**	
	Present study	**Literature [187]**	**Present study**	**Literature [186]**
a /Å	3.9741(9)	3.974	4.0469(11)	4.040
V/Å^3	62.76(3)	62.76	66.28(3)	65.94
Z	1	1	1	1
ρ/g cm^{-3}	6.126	6.127	7.046	7.083

The 2θ positions obtained for $Ba_{1-x}Sr_xMoO_3$(s) (x = 0, 0.2, 0.4, 0.5, 0.8, 1) are shown in **Fig.6.1.** No new peaks were found. The color of $Ba_{1-x}Sr_xMoO_3$(s) (x = 0, 0.2, 0.4, 0.5, 0.8, 1) solid solutions prepared in this study, was found to change from blackish to wine reddish with decreasing barium content. Density of the unit cell was derived as per eqn 2.4. Similarly, the lattice parameters for $Ba_{1-x}Sr_x\ MoO_3$(s) (x = 0.2, 0.4, 0.5, 0.8) were refined by least square method using program by Wadhawan **[104].** The observed and calculated reflections for $Ba_{1-x}Sr_x\ MoO_3$(s) (x= 0, 0.2, 0.4, 0.5, 0.8, 1) along with their indices are given in **Table 6.3.**

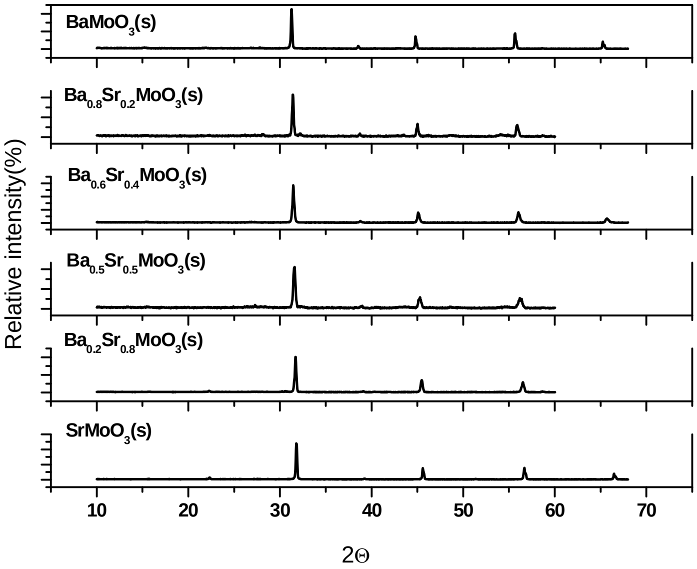

Fig.6.1. The XRD patterns of $Ba_{1-x}Sr_xMoO_3$ (s) (x = 0, 0.2, 0.4, 0.50, 0.8, 1) solid solutions.

The lattice parameters for these solid solutions were plotted as a function of concentration of $SrMoO_3$(s) and are shown in **Fig.6.2.** It shows a slight negative deviation from Vegard's law. The negative deviation was also predicted by Brixner **[72].** This negative deviation could be due to net attractive interaction between Ba and Sr as compared to the average Ba-Ba and Sr-Sr interactions **[93].**

The measured lattice parameters and unit cell volume of $Ba_{1-x}Sr_x MoO_3$(s) (x = 0, 0.2, 0.4, 0.5, 0.8, 1) were fitted as a function of mole fraction of $SrMoO_3$(s) and the resulting equations are given as:

$$a\ (\text{Å}) = 4.0421 - 0.0842\cdot x + 0.0175\cdot x^2 \qquad (6.2)$$

$$V\ (\text{Å})^3 = 66.0432 - 4.1119\cdot x + 0.0175\cdot x^2 \qquad (6.3)$$

Where ' *x*' is the mole fraction of $SrMoO_3$(s) in the solid solutions. The reported lattice parameters and unit cell volumes [72] of $Ba_{1-x}Sr_x MoO_4$(s) (x= 0, 0.25, 0.5, 0.75, 1) are also shown in **Fig.6.2.**

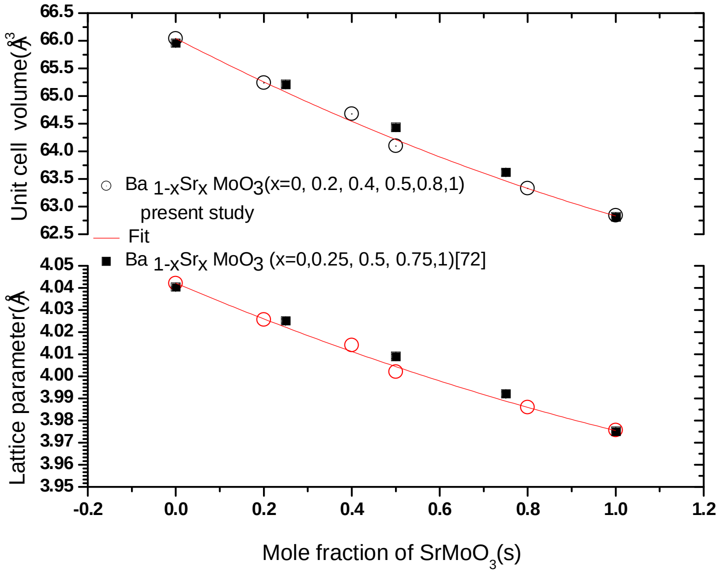

Fig.6.2. The plot of linear lattice parameters (*a)* and unit cell volume (*V*) as function of mole fraction of $SrMoO_3$(s) for $Ba_{1-x}Sr_x MoO_3$(s)(x = 0, 0.2, 0.4, 0.5, 0.8, 1) solid solutions.

Table.6.3. X-Ray powder diffraction data of $Ba_{1-x}Sr_xMoO_3$ (s) solid solutions

$BaMoO_3$(s)					**$Ba_{0.8}Sr_{0.2}MoO_3$(s)**					**$Ba_{0.6}Sr_{0.4}MoO_3$ (s)**					**$Ba_{0.5}Sr_{0.5}MoO_3$ (s)**					**$Ba_{0.2}Sr_{0.8}MoO_3$ (s)**					**SrMoO3(s)**				
d_{obs}	d_{cal}	*h*	*k*	*l*	d_{obs}	d_{cal}	*h*	*k*	*l*	d_{obs}	d_{cal}	*h*	*k*	*l*	d_{obs}	d_{cal}	*h*	*k*	*l*	d_{obs}	d_{cal}	*h*	*k*	*l*	d_{obs}	d_{cal}	*h*	*k*	*l*
2.857	2.858	1	1	0	2.848	2.846	1	1	0	2.838	2.839	1	1	0	2.830	2.830	1	1	0	3.982	3.986	1	0	0	3.982	3.976	1	0	0
2.333	2.334	1	1	1	2.323	2.324	1	1	1	2.317	2.318	1	1	1	2.308	2.311	1	1	1	2.821	2.819	1	1	0	2.812	2.811	1	1	0
2.022	2.021	2	0	0	2.012	2.013	2	0	0	2.007	2.007	2	0	0	2.001	2.001	2	0	0	2.302	2.301	1	1	1	2.295	2.295	1	1	1
1.650	1.650	2	1	1	1.643	1.643	2	1	1	1.639	1.639	2	1	1	1.635	1.634	2	1	1	1.994	1.993	2	0	0	1.988	1.988	2	0	0
1.429	1.429	2	2	0						1.419	1.419	2	2	0						1.627	1.627	2	1	1	1.623	1.623	2	1	1
																									1.405	1.406	2	2	0
Sys: Cubic, Space Group: Pm3m (221) , Cu K_α (λ=1.5406 Å), Filter:Ni																													
a = 4.042 Å, Z=1, Mwt: 281.27, Volume: 66.04Å^3, ρ =7.072 g cm^{-3}					a = 4.025 Å, Z=1, Mwt: 271.384, Volume: 65.21Å^3, ρ = 6.910g cm^{-3}					a =4.014 Å, Z= 1, Mwt: 261.384,Volume: 64.67 Å^3, ρ = 6.711g cm^{-3}					a =4.002 Å, Z=1, Mwt =256.413: Volume: 64.10 Å^3, ρ =6.642g cm^{-3}					a =3.986 Å, Z=1, Mwt: 241.50, Volume: 63.33 Å^3, ρ =6.332g cm^{-3}					a =3.976 Å, Z=1, Mwt: 231.56, Volume: 62.85Å^3, ρ =6.117g cm^{-3}				

6.2.3. SEM characterisation

The scanning electron micrographs for $SrMoO_3$(s) and $BaMoO_3$(s) are shown in **Fig.6.3 and 6.4.** The uniformity in the particle size is more in $SrMoO_3$(s) as compared to $BaMoO_3$(s) which might be due to high reactivity of Ba as compared to Sr. The particle sizes of both the samples are in micrometer range which could be due to the long annealing time.

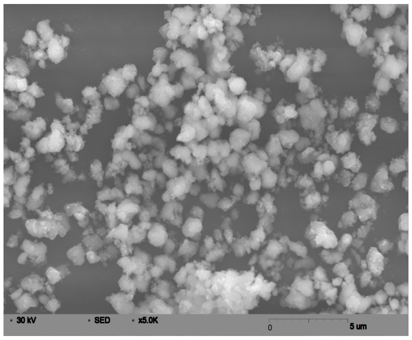

Fig.6.3. The scanning electron micrograph of $SrMoO_3$(s)

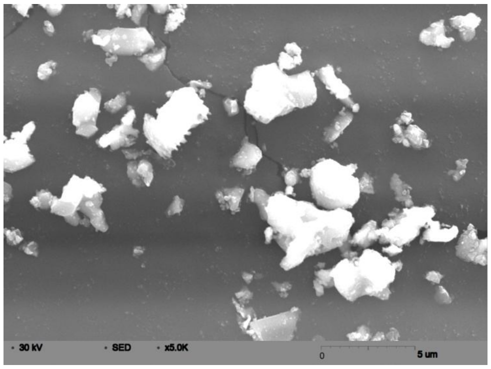

Fig.6.4. The scanning electron micrograph of $BaMoO_3$(s)

6.2.4. Thermal expansion of $Ba_{1-x}Sr_x MoO_3$(s) (x = 0, 0.4, 0.8 and 1)

The lattice parameters of $Ba_{1-x}Sr_x MoO_3$(s) (x = 0, 0.4, 0.8 and 1) were calculated from diffraction angles and the miller indices at different temperatures. The calculated linear lattice parameters and volume of $Ba_{1-x}Sr_x MoO_3$(s) (x = 0, 0.4, 0.8 and 1) were best fitted to the second order polynomial expressions. These expressions are:

Ba MoO_3(s)

$$a\ (\text{Å}) = 4.0403 + 1.72 \times 10^{-5}\ (T/\text{K}) + 1.779 \times 10^{-8}\ (T/\text{K})^2 \qquad (6.4)$$

$$V\ (\text{Å}^3) = 65.9986 + 5.88 \times 10^{-4}\ (T/\text{K}) + 1.329 \times 10^{-6}\ (T/\text{K})^2 - 2.459 \times 10^{-10}\ (T/\text{K})^3 \qquad (6.5)$$

$Ba_{0.6}Sr_{0.4} MoO_3$(s)

$$a\ (\text{Å}) = 4.0082 + 2.885 \times 10^{-5}\ (T/\text{K}) + 1.193 \times 10^{-9}\ (T/\text{K})^2 \qquad (6.6)$$

$$V\ (\text{Å}^3) = 65.1162 - 2.9 \times 10^{-3}\ (T/\text{K}) + 7.8970 \times 10^{-6}\ (T/\text{K})^2 - 4.4114 \times 10^{-9}\ (T/\text{K})^3 \qquad (6.7)$$

$Ba_{0.2}Sr_{0.8} MoO_3$(s)

$$a\ (\text{Å}) = 3.9883 + 2.733 \times 10^{-5}\ (T/\text{K}) + 1.187 \times 10^{-10}\ (T/\text{K})^2 \qquad (6.8)$$

$$V\ (\text{Å}^3) = 64.0075 - 2.05 \times 10^{-3}\ (T/\text{K}) + 6.1365 \times 10^{-6}\ (T/\text{K})^2 - 3.467 \times 10^{-9}\ (T/\text{K})^3 \qquad (6.9)$$

Sr MoO_3(s)

$$a\ (\text{Å}) = 3.9661 + 2.494 \times 10^{-5}\ (T/\text{K}) + 4.498 \times 10^{-9}\ (T/\text{K})^2 \qquad (6.10)$$

$$V\ (\text{Å}^3) = 62.6032 - 1.2700 \times 10^{-4}\ (T/\text{K}) + 2.636 \times 10^{-6}\ (T/\text{K})^2 - .380 \times 10^{-9}\ (T/\text{K})^3 \qquad (6.11)$$

The variation of lattice parameters and unit cell volume as a function of temperature for $Ba_{1-x}Sr_x$ MoO_3(s) (x=0, 0.4, 0.8 and 1) are given in **Table 6.4.**

Table.6.4. Lattice parameters (*a*),volume(*V*), linear(α_a) and volume(α_V) thermal expansion coefficients of $Ba_{1-x}Sr_xMoO_3$(s) (x=0, 0.4 and 1) solid solutions.

		$SrMoO_3$ (s)		
T/K	***a* (Å)**	***V* (Å^3)**	**$\alpha_a \times 10^6$**	**$\alpha_V \times 10^5$**
298.15	3.9741	62.76	4.03	1.21
373	3.9753	62.82	6.42	1.93
473	3.9788	62.99	8.56	2.57
573	3.9821	63.14	7.67	2.31
673	3.9849	63.28	7.93	2.39
773	3.9884	63.44	8.05	2.43
873	3.9913	63.58	7.30	2.21
		$Ba_{0.6}Sr_{0.4}MoO_3$ (s)		
298.15	4.0172	64.83	4.31	1.29
373	4.0185	64.89	6.39	1.92
473	4.0219	65.06	7.72	2.32
573	4.0247	65.19	8.46	2.55
673	4.0287	65.39	8.71	2.63
773	4.0317	65.53	6.60	1.99
873	4.034	65.65	5.73	1.73
		$Ba_{0.2}Sr_{0.8}MoO_3$ (s)		
298.15	3.997	63.86	3.67	1.10
373	3.9981	63.91	5.34	1.60
473	4.0009	64.04	7.63	2.29
573	4.0042	64.20	8.38	2.52
673	4.0076	64.37	7.01	2.11
773	4.0098	64.47	6.00	1.81
873	4.0124	64.60	6.50	1.97
		$BaMoO_3$ (s)		
298.15	4.0469	66.28	9.23	2.77
373	4.0497	66.42	7.58	2.28
473	4.0521	66.53	7.78	2.34
573	4.056	66.73	9.76	2.94
673	4.06	66.92	10.25	3.10
773	4.0643	67.14	10.87	3.29
873	4.0688	67.36	11.12	3.37

The values of the linear (α_a) and volume (α_V) thermal expansion coefficients at different temperatures were calculated and are also given in **Table 6.4.** The average linear (α_a) and volume (α_V) thermal expansion coefficients in the temperature range 298-873 K were best fitted to a polynomial equation as a function of the mole fraction of $SrMoO_3$(s) and are represented in **Fig.6.5.**

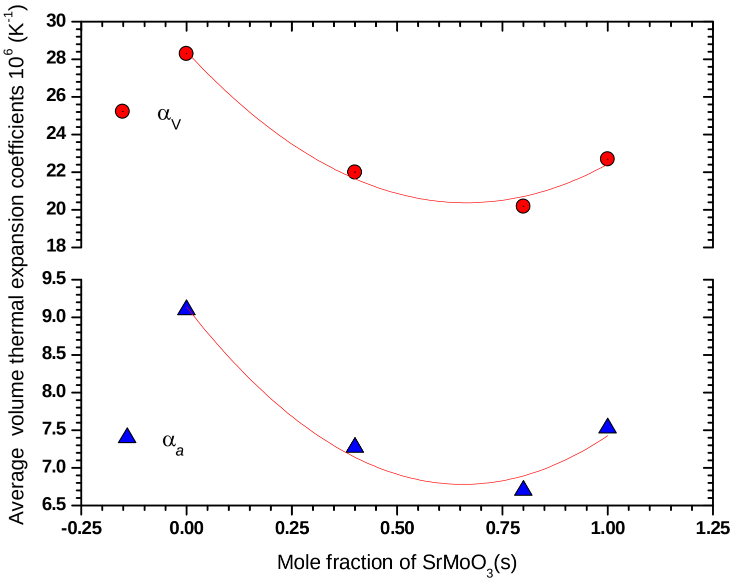

Fig.6.5. A plot of average linear and volume thermal expansion coefficient as a function of mole fraction of $SrMoO_3$(s) for $Ba_{1-x}Sr_x MoO_3$ (s) (x = 0, 0.4, 0.8, 1) solid solutions.

Expressions for the average linear (α_a) and volume (α_V) thermal expansion coefficients are given below:

$$\alpha_a = (9.14 - 7.18 \cdot x + 5.47 \cdot x^2) \times 10^{-6} \tag{6.12}$$

$$\alpha_V = (2.84 - 2.42 \cdot x + 1.82 \cdot x^2) \times 10^{-5} \tag{6.13}$$

where "*x*" is the mole fraction of $SrMoO_3$ (s) in the solid solutions. The values of average volume thermal expansion coefficient in the present study are close to that of ceramic nuclear fuels **[183-184].**

6.2.5. Heat capacity

Heat capacity was measured for $Ba_{1-x}Sr_x MoO_3$(s) (x=0, 0.4, 0.8 and 1) in the temperature range 290-870 K. The heat capacity of $BaMoO_3$ (s) and $SrMoO_3$ (s) are the mean values of four measurements. The error derived from the mean standard deviation for $BaMoO_3$(s) and $SrMoO_3$(s) was found to be within 1-2.5%, respectively. For each composition, the experimental molar heat capacity values in the complete temperature range were best fitted to $A + BT + CT^{-2}$ equation. A, B, *and* C are constants and T is absolute temperature. The values of these constants are given in **Table 6.5.**

Table.6.5.The coefficients of heat capacity, enthalpy increment, entropy and Gibbs energy function of Ba $_{1-x}$Sr$_{x}$ MoO3 (s) (x=0, 0.4, 0.8, 1).

Solid Solutions (Ba $_{1-x}$Sr$_{x}$ MoO3)	$C^{o}_{p,m}(T)$ $A+BT+CT^{-2}$ (Jmol^{-1}K$^{-1)}$ [300-870 K]			$H^{o}_{m}(T)-H^{o}_{m}(298.15)$ $=DT+ET^{2}+FT^{-1}+G$ (kJ mole^{-1}) [298.15-870 K]				$S^{o}_{m}(T)=$ $=Hlog(T)+IT+JT^{-2}+K$ (J mole^{-1}K^{-1}) [298.15-870 K]				$-\left(\frac{G^{o}_{m}(T)-H^{o}_{m}(298.15)}{T}\right)$ $=L\log(T)+MT+NT^{-2}+O$ (J mole^{-1}K^{-1}) [298.15-870 K]			
x	*A*	*B*	*C* × 10 $^{-6}$	*D*	*E* × 10^{5}	*F*	*G*	*H*	*I*	*J* × 10^{-6}	*K*	*L*	*M*	***N*** × 10^{-6}	*O*
0	123.25	0.03	-2.76	0.123	2.0	2760	-47.34	283.85	0.03	1.38	-624.56	67.65	0.074	2.41	-114.25
0.4	118.90	0.031	-2.25	0.119	2.0	2250	-44.35	73.83	0.031	1.12	-604.26	71.28	0.071	2.42	-129.62
0.8	116.39	0.034	-2.19	0.116	2.0	2190	-43.58	268.04	0.034	1.09	-598.0	69.02	0.072	2.39	131.19
1	115.09	0.031	-1.95	0.115	2.0	1952	-42.24	265.05	0.031	0.98	-591.89	72.13	0.068	2.40	-141.65

Heat capacity at 298.15 K for Ba $_{1-x}$Sr$_x$ MoO$_3$(s) (x= 0, 0.4, 0.8 and 1) was found to be 101.18, 102.68, 102.01 and 102.29 J K^{-1}mol^{-1}, respectively. The measured heat capacities of BaMoO$_3$(s) and SrMoO$_3$(s) along with that reported in the literature [**60, 61, 63**] and that estimated in this study using data from Barin et al.[**166**] are shown in **Figs. 6.6 and 6.7** respectively.

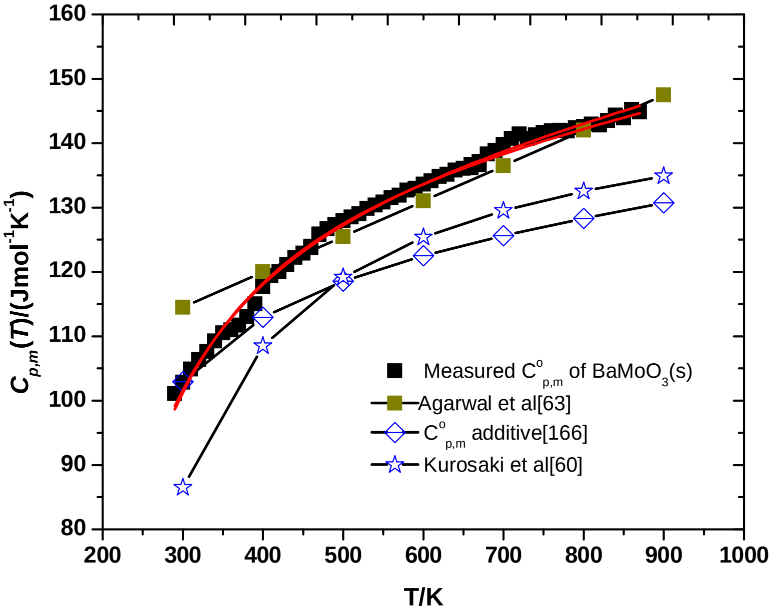

Fig.6.6. The heat capacity of BaMoO$_3$(s) as a function of temperature.

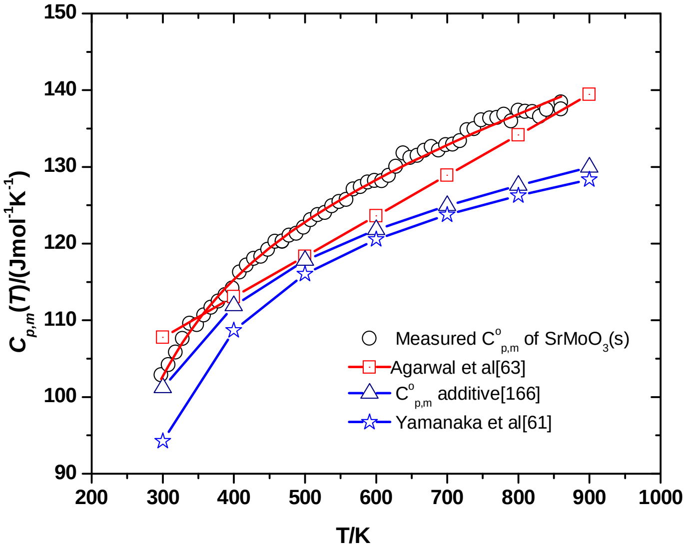

Fig.6.7. The heat capacity of SrMoO$_3$(s) as a function of temperature.

Fig.6.6 shows that the heat capacity data of $BaMoO_3$(s) measured in this study along with that reported values by Agarwal et al. **[63]** and Kurosaki et al. **[60].** It shows scattered heat capacity values reported by different authors, which might be due to use of different experimental methods and gas atmosphere. The standard errors of the polynomial fit for the heat capacity of $BaMoO_3$(s) is 0.77J K^{-1} mol^{-1} in the temperature range 290-870 K. It can be seen from Fig. 6.5 that present heat capacity data for $BaMoO_3$(s) are in good agreement with Agarwal et al **[63].** But the values deviate from Kurosaki et al. **[60]** and that estimated from Neumann–Kopp rule. However the room temperature heat capacity values are closer to Neumann-Kopp additive values.

Fig.6.7 shows the heat capacity data of $SrMoO_3$(s) measured in this study along with that reported by Maekawa et al. **[62]** and Agarwal et al. **[63].** The standard error of the polynomial fit for heat capacity of $SrMoO_3$(s) is 0.42 J K^{-1} mol^{-1}. The present data for $SrMoO_3$(s) are matching reasonably with that of Agarwal et al. [**63]**. But it deviates from the estimated as well as from Maekawa et al. **[62].**

The specific heat capacity of $Ba_{1-x}Sr_x MoO_3$(s) (x= 0, 0.4, 0.8, 1) solid solutions were plotted in **Fig.6.8.**

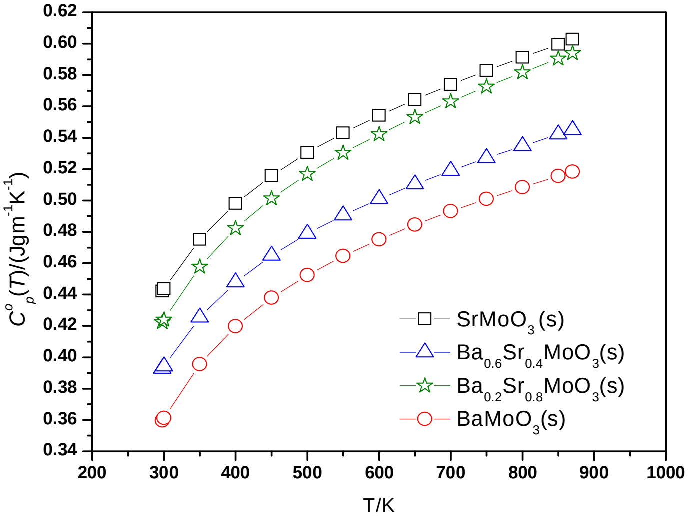

Fig.6.8. A comparison of specific heat capacity of $Ba_{1-x}Sr_x MoO_3$ (s) (x=0, 0.4, 0.8, 1) solid solutions as a function of temperature.

It was observed that specific heat of these solid solutions were increased with increased in the concentration of strontium from x = 0 to 1. This is attributed to the higher heat capacity of $SrMoO_3$(s) than that of $BaMoO_3$(s). From fitted equations of heat capacity and entropy at 298.15 K, other thermodynamic functions such as enthalpy increment $H_m^o(T) - H_m^o(298.15\,K)$, entropy $S_m^o(T)$ and Gibbs energy function $-\left(G_m^o(T) - H_m^o(298.15\,K)\right)/T$ were calculated in the temperature range of 298.15-870 K. Entropies of $Ba_{1-x}Sr_xMoO_3$(s)(x=0,0.18, 0.38, 0.60, 0.81,1) solid solutions were computed assuming ideal solution model. $S_m^o(Ba_{1-x}Sr_xMoO_{3,}\,s, 298.15\,)$ was estimated by taking $S_m^o(298.15\,K)$ for $SrMoO_3$ (s) and $BaMoO_3$ (s) in the stoichiometric ratio from Dash et al **[64, 65]** and ideal entropy of mixing ($\Delta S^{mix,id}$). The computed thermodynamic functions for $Ba_{1-x}Sr_x MoO_3$(s) (x= 0, 0.4, 0.8, 1) are given in **Table 6.5.**

6.3. Summary

1. $Ba_{1-x}Sr_xMoO_3$(s) (x=0, 0.2, 0.4, 0.5, 0.8, 1) solid-solutions were synthesized by reduction of $Ba_{1-x}Sr_x MoO_4$(s) (x=0, 0.2, 0.4, 0.5, 0.8, 1) and characterized using XRD.
2. Single cubic phase was observed for $Ba_{1-x}Sr_xMoO_3$(s) (x = 0 - 1) and the lattice parameter of solid solutions were found to deviate slightly (negative) from Vegard's law.
3. The average volume thermal expansion coefficient of $Ba_{1-x}Sr_x MoO_3$(s) (x=0, 0.4, 0.8 and 1) was calculated.
4. The specific heat capacity data of $Ba_{1-x}Sr_xMoO_3$(s) (x=0, 0.4, 0.8, 1) solid solutions were found to increase with increasing concentration of $SrMoO_3$(s). The specific heat capacity of perovskite oxides was found to be more than the corresponding scheelite oxides.
5. Thermodynamic functions of $Ba_{1-x}Sr_xMoO_3$(s) (x=0, 0.4, 0.8, 1) such as enthalpy increment, entropy and Gibbs energy functions were computed from the measured heat capacity for the first time

CHAPTER-7

A-Te-O (A=Cr, Fe, Ni) system

CHAPTER-7

Tellurium (Te) gets generated as one of the primary fission products with fission yield of about 1% and it is highly corrosive and mobile and forms compounds with various reactor components. During reactor operation, there is a possibility of interaction between clad and Te. The thermodynamic properties of compounds in A-Te-O (A=Cr, Fe, Ni) system need to be investigated. In this study, thermal expansion coefficients of Fe_2TeO_6(s) and Ni_3TeO_6(s) were measured by high temperature X-ray diffraction (HTXRD) in the temperature range 298-973 K and 298-923 K respectively. Heat capacity were measured for Cr_2TeO_6(s), Fe_2TeO_6(s) and Ni_3TeO_6(s) using temperature modulated differential scanning calorimeter (TMDSC) in the temperature range 300-870 K using TOPEM software. Gibbs energy of formation of Fe_2TeO_6(s) and Ni_3TeO_6(s) were measured using transpiration technique in the temperature range 940-1060 K. Self consistent thermodynamic functions for Cr_2TeO_6(s), Fe_2TeO_6(s) and Ni_3TeO_6(s) were derived in the temperature range 298.15–1100 K. Chemical potential diagram of Cr-Te-O, Fe-Te-O and Ni-Te-O systems were constructed.

7.1. Experimental

7.1.1. Synthesis of compounds in A-Te-O (A=Cr, Fe, Ni) system

Cr_2TeO_6(s), Fe_2TeO_6(s) and Ni_3TeO_6(s) were synthesized by solid-state reaction route. The starting materials Fe_2O_3(s) (99.9%), Cr_2O_3(s) (99.997%), NiO(s) (99.99%) and TeO_2(s) (99.99), obtained from M/s Alfa-Aesar (Lancaster) were used. The required oxides were mixed and pelletised for the synthesis of Cr_2TeO_6(s), Fe_2TeO_6(s) and Ni_3TeO_6(s). The pellet of these mixed oxides were kept in separate alumina boats and heated at 873 K for 12 h in air. For homogenization and pure phase formation, the reactant mixture was cooled intermittently and re-ground. The resulting powder was re-pelletised and heated at 923 K for 24 h in air.

7.1.2. Characterization using X-Ray Diffractometry

The purity and the formation of product was ascertained by X-ray diffractometry (XRD) using a STOE theta–theta X-ray diffractometer employing graphite monochromatic Cu K_{α}radiation (λ = 0.15406 nm). The XRD patterns were taken in the 2θ scans range: $10^{\circ} \leq 2\theta \leq 70^{\circ}$. XRD patterns of Cr_2TeO_6(s), Fe_2TeO_6(s) and Ni_3TeO_6(s) were found to match exclusively with that reported in the literature [188] with file nos.15-0696, 73-2238 and 74-1315, respectively and are shown in **Fig.7.1.**

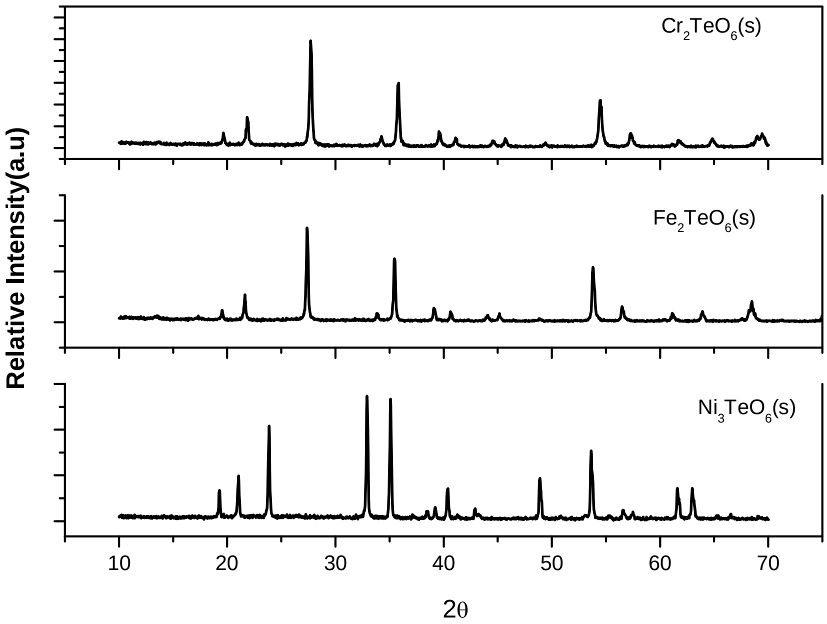

Fig.7.1. XRD Patterns of Cr_2TeO_6(s), Fe_2TeO_6(s) and Ni_3TeO_6(s).

Thermophysico-chemical Properties of A-Te-O (A=Cr, Fe, Ni) system

7.1.3..Thermal Expansion measurements using HT-XRD

The axial and volume thermal expansion measurements of Fe_2TeO_6(s) and Ni_3TeO_6(s) were carried out using STOE diffractometer following the procedure described in section 2.4.1.2.1. The high temperature XRD patterns were recorded for Fe_2TeO_6(s) and Ni_3TeO_6(s) in the temperature range 298-973 K and 298-923 K, respectively.

7.1.4. Heat capacity measurements using DSC

Heat capacity $C^{o}_{p,m}(T)$ measurements were carried out using a temperature modulated differential scanning calorimeter (TMDSC) (model number DSC 823^{e}/700 of M/s. Mettler Toledo GmbH, Switzerland) with TOPEM software for the first time. The detail procedure followed is given in section 2.5.1.4.

7.1.5. Measurement of Gibbs energy of formation of Fe_2TeO_6(s) and Ni_3TeO_6(s) by Transpiration technique

Transpiration apparatus shown in Fig. 2.28 consisted of a 20 mm inner diameter quartz reaction tube with ‘O’ ring sealed end couplings having provisions for carrier gas entry and insertion of a thermo-well at one side and a condenser at the other side. The condenser was made of quartz with an orifice of 0.5 mm. The biphasic sample mixture was kept in an alumina boat in the isothermal zone of the Kanthal wire-wound horizontal furnace. Prior to the transpiration measurements, the reaction tube was repeatedly evacuated and flushed with dry oxygen which was subsequently used as carrier gas. After attaining the stable furnace temperature, oxygen gas was flown over the equilibrium phase mixture from one side which gets saturated with $TeO_2(g)$ coming out of the sample. Subsequently, Carrier gas along with $TeO_2(g)$ was allowed to enter the condenser, where $TeO_2(s)$ was deposited in the cooler portion of the condenser, which was placed at the end of the isothermal zone of the furnace. The $TeO_2(g)$ was generated due to the following reactions:

$$Fe_2TeO_6(s) = Fe_2O_3(s) + TeO_2(g) + ½ O_2(g). \quad (7.1)$$

$$Ni_3TeO_6(s) = 3 NiO(s) + TeO_2(g) + ½ O_2(g). \quad (7.2)$$

Then the carrier gas was flown into the wet test meter for measurement of volume of $O_2(g)$ passed over equilibrium phase mixture at a required temperature. The mass of the condensate $TeO_2(s)$ per dm^3 of the carrier gas flown at each experimental temperature was measured and the carrier gas was collected at room temperature for the measurement of its volume. Prior to the experiment, transpiration apparatus was calibrated by measuring flow rate plateau for $TeO_2(g)$. The oxygen carrier gas was flown over pure $TeO_2(s)$ at different flow rates (0.03-0.1 $dm^3\ min^{-1}$) at 800 K. The mass of $TeO_2(s)$ collected inside condenser was measured for these flow rates. The mass of $TeO_2(s)$ collected per unit volume was found to be independent for the flow rate of 0.04 to 0.06 $dm^3\ min^{-1}$, which was the flow rate plateau region of $TeO_2(g)$. Thus, measurements were carried out with oxygen carrier gas flow rate of 0.045 $dm^3\ min^{-1}$.

7.1.6. Generation of chemical potential Diagram of A-Te-O system.

The chemical potential diagram for A-Te-O (A= Cr, Fe, Ni) system was established based on the minimization of Gibbs energy method. Factsage software [92] was used for the computation. Chemical potential diagram of Cr-Te-O, Fe-Te-O and Ni-Te-O systems were constructed using thermodynamic information of the various binary alloys in Cr-Te, Fe-Te, Ni-Te and binary oxide phases present in Cr-O, Fe-O, Ni-O, Te-O and ternary phases present in Cr-Te-O, Fe-Te-O and Ni-Te-O systems. These diagrams illustrate the stability of various compounds formed between tellurium and the different stainless steel components under various tellurium and oxygen potentials.

7.2. Results and Discussion

7.2.1. Thermal expansion

Fe_2TeO_6(s) can be indexed using tetragonal crystal structure with space group $P4_2/mnm$ whereas Ni_3TeO_6(s) can be indexed with rhombohedral crystal structure which is similar to hexagonal crystal structure. The lattice parameters were calculated from diffraction angles and the miller indices at different temperatures, while the density of the two tellurates was calculated using formula 2.4**.** For the calculation of density, the number of formula unit in the unit cell for Fe_2TeO_6(s) and Ni_3TeO_6(s) were taken as 2 and 3, respectively [**188**]. The calculated linear lattice parameters and unit cell volume were fitted to a second order polynomial equation. The measured lattice parameters (*a* and *c*), unit cell volume (*V*) and density at different temperatures for Fe_2TeO_6(s) and Ni_3TeO_6(s) are given in **Table 7.1.** The measured lattice parameters (*a* and *c*) and unit cell volume (*V*) of Fe_2TeO_6(s) and Ni_3TeO_6(s) along with that of Cr_2TeO_6(s) **[189]** are shown in **Fig.7.2.** The expressions for linear lattice parameters (*a* and *c*) and unit cell volume (*V*) of Fe_2TeO_6(s) and Ni_3TeO_6(s) are given as:

Fe_2TeO_6(s):

$$\boldsymbol{a}(\text{Å}) = \mathbf{4.595 + 1.98 \times 10^{-5}} \times (\mathrm{T/K}) + \mathbf{1.463 \times 10^{-8}} \times (\boldsymbol{T/K})^2 \qquad \mathbf{(7.3)}$$

$$\boldsymbol{c}(\text{Å}) = \mathbf{9.058 + 9.235 \times 10^{-5}} \times (\mathrm{T/K}) - \mathbf{1.685 \times 10^{-8}} \times (\boldsymbol{T/K})^2 \qquad \mathbf{(7.4)}$$

$$\mathrm{V}(\text{Å}^3) = 191.237 + 3.58 \times 10^{-3} \times (\mathrm{T/K}) + 9.1 \times 10^{-7} \times (\mathrm{T/K})^2 \qquad (7.5)$$

Ni_3TeO_6(s):

$$\boldsymbol{a}(\text{Å}) = \mathbf{5.088 + 6.344 \times 10^{-5}} \times (\mathrm{T/K}) - \mathbf{1.185 \times 10^{-8}} \times (\boldsymbol{T/K})^2 \qquad \mathbf{(7.6)}$$

$$\boldsymbol{c}(\text{Å}) = \mathbf{13.721 + 1.504 \times 10^{-4}} \times (\mathrm{T/K}) - \mathbf{4.577 \times 10^{-9}}(\boldsymbol{T/K})^2 \qquad \mathbf{(7.7)}$$

$$\mathrm{V}(\text{Å}^3) = 307.618 + 1.11 \times 10^{-2} \times (\mathrm{T/K}) - 1.462 \times 10^{-6} \times (\mathrm{T/K})^2 \qquad (7.8)$$

Table.7.1. Lattice parameters (a and c), volume (V), linear (α_a and α_c) and volume (α_V) thermal expansion coefficients of Fe_2TeO_6(s) in the temperature range 298-973 K and of Ni_3TeO_6(s) in the temperature range 298-923 K.

Fe_2TeO_6(s)							
T/K	**a (Å)**	**c (Å)**	**V (Å^3)**	**ρ(g/cm^3)**	**α_a (×10^6K^{-1})**	**α_c (×10^6K^{-1})**	**α_V (×10^6K^{-1})**
298	4.602	9.084	192.39	5.79	6.44	8.92	21.80
373	4.604	9.090	192.70	5.78	6.71	8.76	22.21
473	4.607	9.098	193.13	5.77	7.31	8.41	23.09
573	4.611	9.105	193.59	5.75	7.95	8.04	24.03
673	4.615	9.113	194.06	5.74	8.58	7.67	24.98
773	4.619	9.119	194.55	5.72	9.22	7.30	25.93
873	4.623	9.126	195.06	5.71	9.85	6.93	26.88
973	4.628	9.132	195.58	5.69	10.17	6.74	27.36
Ni_3TeO_6(s)							
298	5.106	13.764	310.75	6.41	10.87	13.10	34.33
373	5.110	13.778	311.57	6.39	10.66	12.13	32.45
473	5.115	13.793	312.57	6.37	10.23	10.48	31.86
573	5.121	13.806	313.50	6.35	9.77	9.59	29.28
673	5.125	13.819	314.39	6.33	9.30	9.63	27.67
773	5.130	13.833	315.26	6.32	8.84	10.61	28.32
873	5.134	13.848	316.16	6.30	8.43	12.18	32.02
923	5.137	13.857	316.63	6.29	8.26	13.01	37.33

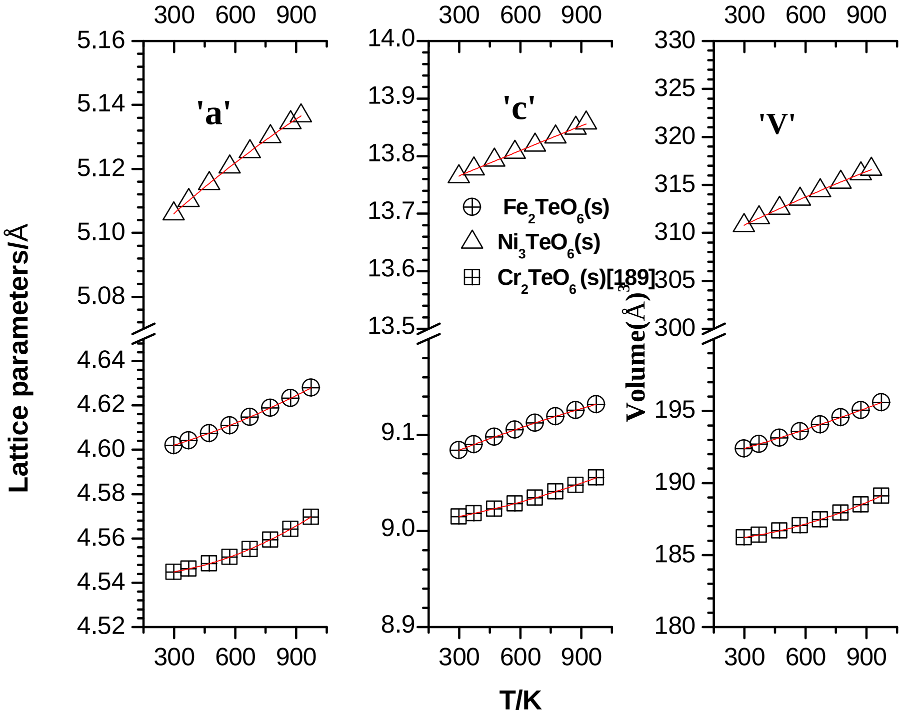

Fig.7.2. Lattice parameters and unit cell volume of Cr_2TeO_6(s), Fe_2TeO_6(s) and Ni_3TeO_6(s) as function of temperature.

The coefficient of linear thermal expansions α_a (along *a*-axis) α_c (along *c*-axis) and the coefficient of volume thermal expansion (α_V) were calculated for Fe_2TeO_6(s) and Ni_3TeO_6(s). These data are also given in **Table 7.1.**

The average coefficient of linear thermal expansion (α_a (along *a*-axis), α_c, (along *c*-axis)) and coefficient of volume thermal expansion (α_V) of Fe_2TeO_6(s) in the temperature range of 298–973 K were found to be 8.37×10^{-6}, 7.83×10^{-6} and 24.56×10^{-6} K^{-1}, respectively. Similarly, α_a, α_c and α_V of Ni_3TeO_6(s) in the temperature range of 298–923 K were found to be 9.71×10^{-6}, 10.81×10^{-6} and 30.23×10^{-6} K^{-1}, respectively.

7.2.2. Heat capacity

The measured heat capacities of Cr_2TeO_6(s), Fe_2TeO_6(s) and Ni_3TeO_6(s) were fitted to $A + BT + CT^{-2}$ in the temperature range 300-870 K. Where *A, B, and C* are constants and *T* is absolute temperature. Following heat capacity expressions were obtained, by least square analysis, for Cr_2TeO_6(s), Fe_2TeO_6(s) and Ni_3TeO_6(s):

$$C^{o}_{p,m}(Cr_2TeO_6,s,T)(Jmol^{-1}K^{-1}) = 207.257 + 23.85\times10^{-3}\times(T/K) - 4.781\times10^{6}\times(T/K)^{-2}$$

[300-870K] (7.9)

$$C^{o}_{p,m}(Fe_2TeO_6,s,T)(Jmol^{-1}K^{-1}) = 211.575 + 10.44\times10^{-3}\times(T/K) - 4.43\times10^{6}\times(T/K)^{-2}$$

[300-870K] (7.10)

$$C^{o}_{p,m}(Ni_3TeO_6,s,T)(Jmol^{-1}K^{-1}) = 226.365 + 48.33\times10^{-3}\times(T/K) - 4.338\times10^{6}\times(T/K)^{-2}$$

[300-870K] (7.11)

The measured heat capacity values as a function of temperature is given in **Table 7.2** and shown in **Fig.7.3.**

Table.7.2. Experimentally determined molar heat capacity data for Cr_2TeO_6(s), Fe_2TeO_6(s) and Ni_3TeO_6(s) in the temperature range 298-870 K

	Cr_2TeO_6(s)	**Fe_2TeO_6(s)**	**Ni_3TeO_6(s)**
***T*/K**	**$C^{o}_{p,m}(T)$/ $J{\cdot}K^{-1}{\cdot}mol^{-1}$**	**$C^{o}_{p,m}(T)$/ $J{\cdot}K^{-1}{\cdot}mol^{-1}$**	**$C^{o}_{p,m}(T)$/ $J{\cdot}K^{-1}{\cdot}mol^{-1}$**
300	160.94	164.88	191.72
350	177.45	180.01	208.25
400	186.57	188.35	219.82
450	194.05	193.96	227.17
500	199.57	198.43	234.41
550	205.33	202.65	238.89
600	208.67	205.64	242.03
650	211.82	207.82	244.65
700	213.07	209.66	249.82
750	216.54	211.87	255.84
800	218.89	213.32	260.05
850	220.65	214.19	261.79
870	222.27	214.62	262.60

Recently, Dawar et al **[86]** measured enthalpy increment of Cr_2TeO_6(s) using drop calorimeter and derived the heat capacities. These heat capacities are also compared in **Fig. 7.3.** It can be seen from **Fig.7.3** that the heat capacity values measured in present study are in good agreement in the temperature range 500-800 K , however, at 300 K $C_p(T)$ of present study is lower by 36 J K^{-1} mol^{-1} and is higher by 12 J K^{-1} mol^{-1} at 870 K from the Dawar et al **[86].** This could be due to the second constraint used during fitting of enthalpy increment by Dawar et al **[86].** The authors have assumed the derivative of enthalpy increment at 298.15 K is equal to the heat capacity of Cr_2TeO_6(s) at 298.15 K, which was estimated from the values of $C^{o}_{p,298K}$ of Cr_2O_3(s) and TeO_3(s) by applying Neumann–Kopp's molar additivity rule. For the calculation, Dawar et al have taken the reported $C^{o}_{p,298K}$ of TeO_3(s) from Agarwal et al **[190],** which was not experimentally determined but computed theoretically. Moreover, Agarwal et al **[190]** have assumed that the change in the heat capacity for the formation of every Te–O bond in TeO_2, from its constituent elements Te and O_2, remains same as in TeO_3(s) which may not correct.

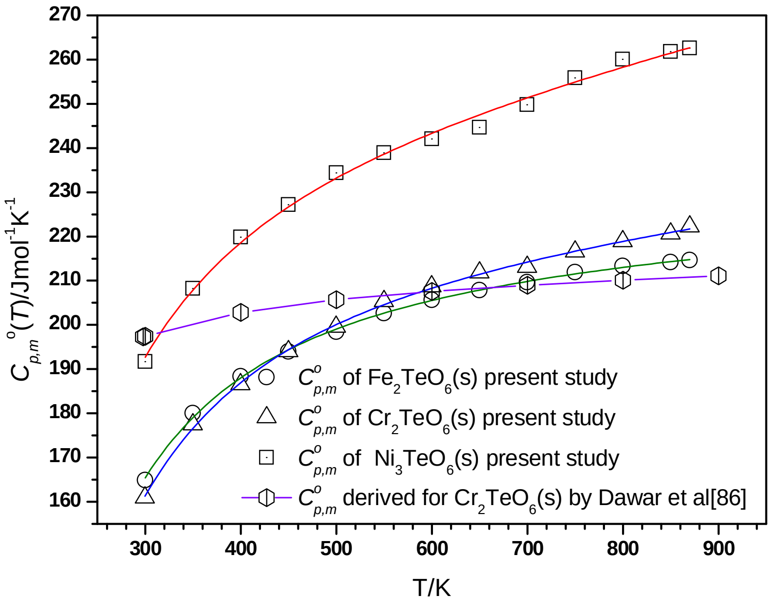

Fig.7.3. The measured molar heat capacity of Cr_2TeO_6(s), Fe_2TeO_6(s) and Ni_3TeO_6(s) as a function of temperature in the range 300-870 K.

Estimation of heat capacity of TeO_3(s)

From the above analysis, heat capacity contribution of TeO_3(s) to tellurium (VI) compounds was calculated from the presently measured heat capacity and that of various compounds reported in the literature **[86, 190-192]** and plotted as a function of temperature. Neumann–Kopp's molar additivity rule states that the heat capacity of ternary oxides is considered to be the summation of the heat capacity of binary oxides. Hence, the heat capacity contribution of TeO_3(s) to the of Te(VI) compounds, were calculated by subtracting heat capacity of metal oxides (A_xO_y) from that of corresponding metal tellurates and are plotted in **Fig.7.4.** Surprisingly, the values of $C^{o}_{p}(T)$ for TeO_3(s) calculated from various compounds showed reasonable overlap.

Thus, $C^{o}_{p}(T)$ of TeO_3(s) obtained from various experimentally measured $C^{o}_{p}(T)$ of Te(VI) compounds were least square fitted and is given as:

$$C^{o}_{p,m}(TeO_3,s,T)(\pm 7\,Jmol^{-1}K^{-1}) = 88.075 + 12.82\times10^{-3}\times(T/K) - 2.597\times10^{6}\times(T/K)^{-2} \qquad (7.12)$$

The estimated heat capacity value by Agarwal et a l**[190]** is found to be matching with the calculated heat capacity from Eq.(7.12) at higher temperature. But it is found to be 32% more than the calculated heat capacity at 300 K.

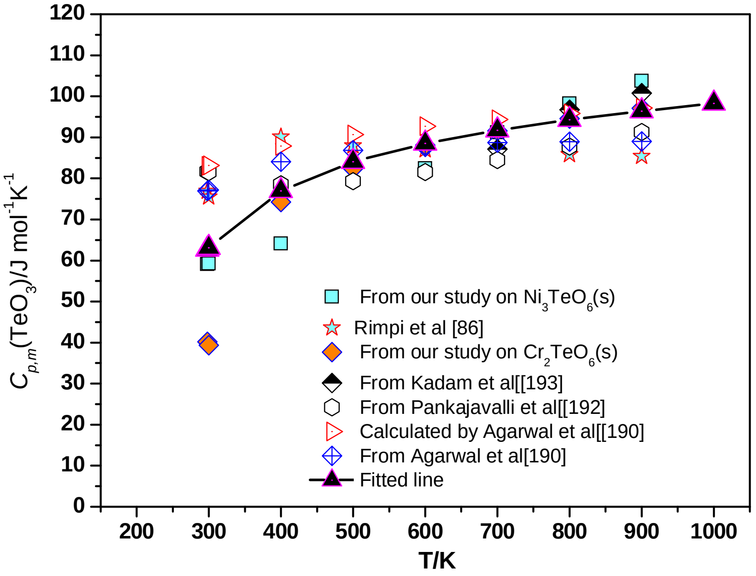

Fig.7.4. Heat capacity of TeO_3(s) derived from the tellurate containg Te(VI) using Newmann Kopp's rule

This could be one of the probable reasons in the variation of heat capacity of Cr_2TeO_6(s) between the present study and that of Dawar et al **[86].**

Heat capacity of Te(VI) compounds can be estimated by taking the $C_{p,m}(T)$ values of TeO_3**(s)** from Eq.(7.12) using Neumann–Kopp's molar additivity rule. The heat capacity data for Fe_2TeO_6(s) and Ni_3TeO_6(s) are being reported for the first time.

7.2.3. Gibbs energy using Transpiration method

The apparent equilibrium vapor pressure of TeO_2(g) at each experimental temperature was calculated for the Eq. 7.1 and 7.2. This equilibrium pressure is correlated with total pressure by equation given below:

$$p(TeO_2,g) = \frac{n(TeO_2,s)}{\{n(TeO_2,s) + n(O_2,g) + n(carrer\ gas)\}} \times P \qquad (7.13)$$

where P is the total pressure of the system ($p(O_2)$ =101.325 kPa), $n(TeO_2,s)$, $n(O_2,g)$ and n(carrier gas) are the respective number of moles. The value of $n(O_2,g)$ (due to reaction) can be calculated from those of $n(TeO_2,s)$ using the stoichiometry of reaction (Eq. 7.1 and 7.2) and n(carrier gas) can be calculated from volume of carrier gas $O_2(g)$ at STP (T = 273 K, P = 101.325 kPa).

7.2.3.1. (Fe_2TeO_6, s, T)

The vapour pressure of $TeO_2(g)$ over $\{Fe_2TeO_6(s) + Fe_2O_3(s)\}$ at each experimental temperature was calculated from Eq.(7.13). These values are plotted in **Fig.7.5** and given in **Table 7.3.**

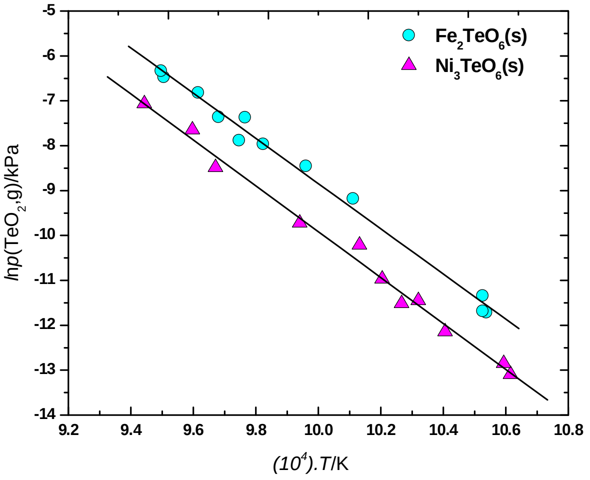

Fig.7.5. The vapour pressures of $TeO_2(g)$ over $\{Fe_2TeO_6(s) + Fe_2O_3(s)\}$ and $\{Ni_3TeO_6(s) + NiO(s)\}$ as a function of temperature.

Table 7.3. Pressures of TeO_2(g) over {Fe_2TeO_6(s)+Fe_2O_3(s)} and $\Delta_f G^o_m(Fe_2TeO_6,s,T)$ values as a function of temperature.

T/K	**Mass (TeO_2)·10^3 gm**	**$V(O_2)$ dm^3 at 298 K**	**$p(TeO_2)\cdot 10^5$ kPa**	**$\Delta_r G^o_m(T)$ kJ·mol^{-1}**	**$\Delta_f G^o_m(T)$ kJ mol^{-1}**
949	0.04	69.7	0.82	128.9	-765.5
950	0.1	119.8	1.19	126.0	-765.0
950	0.07	118.2	0.84	128.8	-765.0
989	0.91	126.0	10.28	113.5	-742.8
1004	2.01	134.1	21.32	109.1	-734.2
1018	2.84	116.0	34.85	106.5	-726.3
1024	2.95	66.8	62.80	102.1	-722.8
1026	3.8	143.4	37.70	106.6	-721.7
1033	5.05	113.0	63.61	102.9	-717.7
1040	7.91	103.0	109.28	98.9	-713.7
1052	7.49	69.1	154.24	97.0	-706.9
1053	14.64	117.1	177.83	95.9	-706.3

$V(O_2)$ is total volume of carrier gas (oxygen) collected at gas outlet temperature.

The least squares regression analysis of these data yielded following expression:

$$\{\ln (p(TeO_2,g) \pm 0.02/kPa\} = 41.5 - 50360\cdot(K/T) \qquad (7.14)$$

The standard molar Gibbs energy change for Eq.(7.1) is expressed by the equation:

$$\Delta_r G^o_m(T) = -R\cdot T\cdot \ln K = -R\cdot T\cdot \ln\left[\frac{a_{Fe_2O_3(s)}\, p_{TeO_2(g)}\, p_{O_2(g)}^{\;1/2}}{a_{Fe_2TeO_6(s)}}\right] \qquad (7.15)$$

where "a" represents thermodynamic activity. $a_{Fe_2O_3}$ and $a_{Fe_2TeO_6}$ were taken as unity and the Eq.(7.15) was simplified as follows:

$$\Delta_r G^o_m(T) = -R\cdot T\cdot \ln K = -R\cdot T\cdot \ln\left\{p_{TeO_2(g)}\, p_{O_2(g)}^{\;1/2}\right\} \qquad (7.16)$$

The value of $p(O_2)$ was taken as 101.325 kPa in Eq. (7.16) because the experiments were carried out at atmospheric pressure. Now, the standard molar Gibbs energy change for reaction (7.1) can be given as:

$$\Delta_r G^o_m(T) = -R\cdot T\cdot \ln p_{(TeO_2,g)} \qquad (7.17)$$

The standard molar Gibbs energy change of reaction (7.1) can also be expressed as:

$$\Delta_r G^o{}_m(T) = \Delta_f G^o{}_m(Fe_2O_3, s, T) + \Delta_f G^o{}_m(TeO_2, g, T) - \Delta_f G^o{}_m(Fe_2TeO_6, s, T) \qquad (7.18)$$

$\Delta_f G^o{}_m(Fe_2TeO_6, s, T)$ can be given as:

$$\Delta_f G^o{}_m(Fe_2TeO_6, s, T) = \Delta_f G^o{}_m(Fe_2O_3, s, T) + \Delta_f G^o{}_m(TeO_2, g, T) + R\cdot T\cdot \ln p(TeO_2) \qquad (7.19)$$

$\Delta_f G^o{}_m(Fe_2TeO_6, s, T)$ was calculated employing Eq.(7.19) by substituting value of $R\cdot T\cdot \ln p(TeO_2)$ from Eq.(7.14), $\Delta_f G^o{}_m(Fe_2O_3, s, T)$ and $\Delta_f G^o{}_m(TeO_2, g, T)$ values as reported by Barin **[166]** (as given in **Table 7.4**).

Table 7.4. The $\Delta_f G^o{}_m(T)$ of binary oxides used for computation of Gibbs energy of formation of Fe_2TeO_6(s) and Ni_3TeO_6(s).

Compounds/ Reference	$\Delta_f G^o{}_m(T)$/kJ mol^{-1} = A + B·(T/K)	
	A	B
Fe_2O_3(s) **[166]**	-807.6	0.2464
NiO(s) **[166]**	-234.8	0.0857
TeO_2(g) **[166]**	-79.5	0.0161

The following expression was obtained for $\Delta_f G^o{}_m(Fe_2TeO_6, s, T)$:

$$\{\Delta_f G^o{}_m(Fe_2TeO_6, s, T) \pm 9\}/\text{kJ}\cdot\text{mol}^{-1} = -1305.8 + 0.5693\cdot(T/\text{K}) \quad (949 \leq T/\text{K} \leq 1053) \qquad (7.20)$$

$\Delta_f G^\circ{}_m(T)$ values determined in this study were compared with those reported in the literature and is shown in **Fig. 7.6 and** given in **Table 7.5.** Krishnan et al. **[87]** have determined Gibbs energy of formation of Fe_2TeO_6(s) using Knudsen effusion mass-loss method in the temperature range 979–1052 K. $\Delta_f G^\circ{}_m(Fe_2TeO_6, s, 1000\text{ K})$ calculated from Eq. (7.20) and that from Krishnan et al. **[87]** are −736.5 and −761.4 kJ mol^{-1}, respectively. The difference of 24.9 kJ mol^{-1} between two measurements is considered to be high.

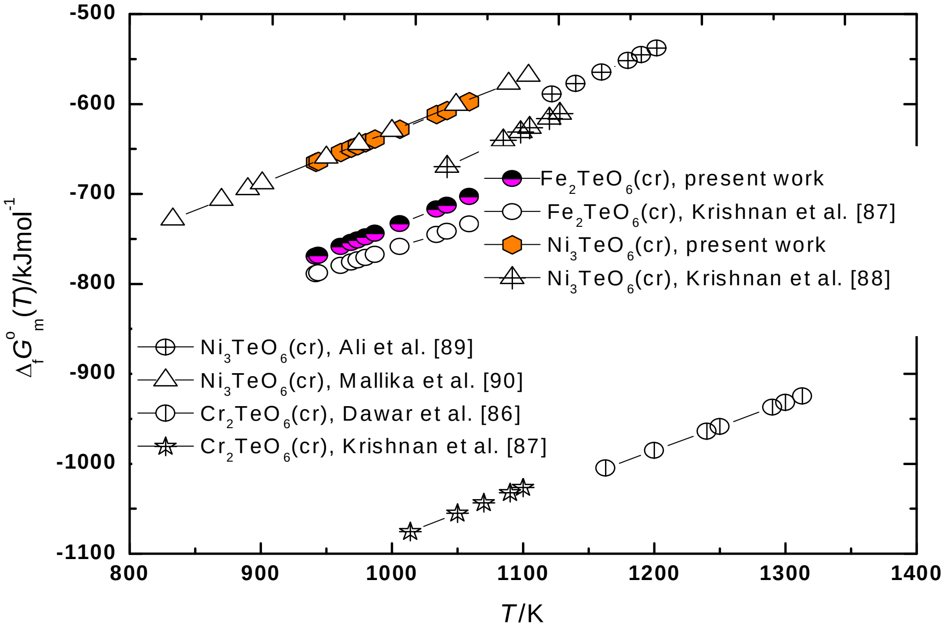

Fig.7.6. A comparison of Gibbs energy of formation of Cr_2TeO_6(s), Fe_2TeO_6(s) and Ni_3TeO_6(s) reported in the literature with that measured in this study.

Table 7.5. A comparison of $\Delta_f G^o{}_m(Fe_2TeO_6,s,T)$ and $\Delta_f G^o{}_m(Ni_3TeO_6,s,T)$ measured in this study and that reported in the literature. $\Delta_f G^o{}_m(Cr_2TeO_6,s,T)$ reported in the literature has also been given.

Compounds/ Reference	Temperature Range (K)	Method	$\Delta_f G^o{}_m(T)$/kJ·mol^{-1} = A + B·(T/K)		$\Delta_f G^o{}_m$(1000 K)/ kJ· mol^{-1}	$\Delta_f H^o{}_m$(298.15 K)/ kJ· mol^{-1}	$S^o{}_m$(298.15 K)/ J· K^{-1} · mol^{-1}
			A	B			
$Cr_2TeO_6(s)$							
Krishnan et al. **[87]**	1014-1100	KEML	-1651.6	0.5683	-1083.3	-1656.4	133.0
Dawar et al. **[86]**	1163-1313	Tra	-1625.6	0.5336	-1092.0	-1631.6	169.9
$Fe_2TeO_6(s)$							
Krishnan et al. **[87]**	979-1052	KEML.	-1234.3	0.4729	-761.4	-1230.8	247.7
Present study	949-1053	Tra	-1305.8	0.5693	-736.5	-1302.1	155.4
$Ni_3TeO_6(s)$							
Krishnan et al. **[88]**	1042-1129	KEML	-1386.7	0.688	-698.7	-1390.0	71.4
Ali et al. **[89]**	1122-1202	Tra.	-1307.0	0.640	-667.0	-1310.4	121.9
Mallika et al. **[90]**	624-964	e.m.f.	-1218.7	0.5884	-630.3	-1216.2	169.3
Present study	942-1059	Tra	-1208.8	0.5773	-631.5	-1211.7	179.9

7.2.3.2. Ni_3TeO_6(s)

TeO_2(g) pressures over {Ni_3TeO_6(s) +NiO(s)} was calculated from calculated from Eq.(7.13). These values are plotted in **Fig.7.5** and is given in **Table 7.6.**

These data were least squares fitted and to the expression:

$$\{\ln (p(TeO_2,g)) \pm 0.02\}/kPa = 41.2 - 51130\cdot(K/T). \qquad (7.21)$$

The $\Delta_f G^o{}_m(Ni_3TeO_6,s,T)$ was computed using Eq. (7.21) and $\Delta_f G^o{}_m(T)$ values for NiO(s) and TeO_2(g) from the Barin **[166]** (given in **Table 7.4**).

The corresponding $\Delta_f G^o{}_m(Ni_3TeO_6,s,T)$ expression is given as:

$$\{\Delta_f G^o{}_m\,(Ni_3TeO_6\,,s,T\,) \pm 8\}/kJ\square\ mol^{-1} = -1208.8 + 0.5773\cdot(T/K)\ (942 \leq T/K \leq 1059)\ (7.22)$$

$\Delta_f G^\circ{}_m(T)$ values determined in this study and those reported in the literature were compared in **Table 7.5** and shown in **Fig. 7.6.** Krishnan et al. **[88]** have determined Gibbs energy of formation of Ni_3TeO_6(s) using Knudsen effusion mass-loss method in the temperature range 1042–1129 K. Ali et al. **[89]** have studied thermodynamic stability of Ni_3TeO_6(s) using transpiration technique in the temperature range 1122 - 1202 K. Mallika et al. **[90]** measured Gibbs energy of formation of Ni_3TeO_6(s) by measuring e.m.f.s of the galvanic cells:

$$\text{Pt,C,Te(l),\{NiTeO}_3\text{(s),NiO(s) \}/15 YSZ/O}_2\ (P_{O2} = 0.2128\ \text{kPa) Pt}\ (833 \leq T/K \leq 1104) \qquad (7.23)$$

$$\text{Pt,C,\{NiTeO}_3\text{(s),Ni}_3\text{TeO}_6\text{(s),NiO(s) \}/15 YSZ/O}_2\ (P_{O2} = 0.2128\ \text{kPa),Pt}\ (624 \leq T/K \leq 964) \qquad (7.24)$$

where 15 YSZ=15 mass% yttria-stabilized zirconia. $\Delta_f G^\circ{}_m(Ni_3TeO_6,cr,1000\ K)$ calculated from Eq. (7.22), Krishnan et al. **[88],** Ali et al **[89]** and Mallika et al. **[90]** are -631.5 , −698.7 and −667.0, and -630.3 kJ mol^{-1}, respectively. **Fig 7.6** shows that Gibbs energy measured in this study found to match excellently with that reported by Mallika et al. **[90]** and around 35 kJ mol^{-1} more positive than Ali et al **[89]** and around 67 kJ mol^{-1} more positive than that of Krishnan et al. **[88].** The agreement of Gibbs energy data measured by two independent methods: transpiration and e.m.f. can be considered to be more reliable.

Table 7.6. Pressures of TeO_2(g) over {Ni_3TeO_6(s)+ NiO(s)} and $\Delta_fG^o{}_m(Ni_3TeO_6,s,T)$ values as a function of temperature.

T/K	Mass (TeO_2)·10^3 gm	$V(O_2)$ dm^3 at 298 K	$p(TeO_2)\cdot 10^6$ kPa	$\Delta_rG^o{}_m(T)$ kJ·mol^{-1}	$\Delta_fG^o{}_m(T)$ kJ·mol^{-1}
942	0.05	347.1	2.05	138.7	-665.0
944	0.04	216.3	2.63	137.1	-663.8
961	0.06	160.8	5.31	133.9	-654.0
969	0.17	226.9	10.66	129.4	-649.4
974	0.1	142.6	9.98	130.6	-646.5
980	0.21	173.6	17.21	127.0	-643.0
987	0.37	143.6	36.67	121.7	-639.0
1006	0.6	142.3	59.99	119.9	-628.0
1034	2.03	140.1	206.18	112.7	-611.9
1042	4.25	126.8	476.98	106.3	-607.3
1059	10.45	174.1	854.01	102.9	-597.4

7.2.4. Thermodynamic Functions

The heat capacity, enthalpy of formation and entropy at 298.15 K of Cr_2TeO_6(s), Fe_2TeO_6(s) and Ni_3TeO_6(s) are required to compute self-consistent thermodynamic functions such as Gibbs energy function (Φ), enthalpy($H^o{}_m(T)$), Gibbs energy ($G^o{}_m(T)$), Enthalpy of formation ($\Delta_fH^o{}_m(T)$) and Gibbs energy of formation ($\Delta_fG^o{}_m(T)$) of these tellurates (A_nTeO_6(s), A=Cr,Fe,Ni, n=2 for Cr & Fe, n=3 for Ni) in the temperature range 298.15-1100 K. The $\Delta_fH^o{}_m$ (298.15 K) and $S^o{}_m$ (298.15 K) values of Cr_2TeO_6(s), Fe_2TeO_6(s) and Ni_3TeO_6(s) are not reported directly in the literature. These values can be derived from the experimentally measured heat capacity and Gibbs energy formation data using second law method. The required heat capacity, entropy and phase transition energy data of Cr, Fe, Ni, Te, O_2 were taken from the literature **[166].**

Estimation of enthalpy of formation

The $\Delta_fH^o{}_m$ (298.15 K) and $S^o{}_m$ (298.15 K) values for Cr_2TeO_6(s), Fe_2TeO_6(s) and Ni_3TeO_6(s) have been calculated and compared in **Table 7.5.** It shows discrepancy in $\Delta_fH^o{}_m$(298.15 K) and $S^o{}_m$ (298.15 K) values of Fe_2TeO_6(s) and Ni_3TeO_6(s). In order to resolve this ambiguity, calculated $\Delta_fH^o{}_m$ (298.15 K) values of Cr_2TeO_6(s), Fe_2TeO_6(s) and Ni_3TeO_6(s) (given in **Table 7.5**) were plotted separately as a function of molecular weight as well as $\Delta_fH^o{}_m$ (298.15 K) of the respective transition metal oxides. A systematic variation of $\Delta_fH^o{}_m(A_nTeO_6,cr,298.15\ K)$ with enthalpy of formation of transition metal oxide was observed when enthalpy of transition metal oxides was normalized to 1.5 mole of oxygen as per the formation reaction of tellurate (**Eq.7.25**). For this estimation, the formation of $A_nTeO_6(s)$ was assumed by the following reaction:

$$a\ A_xO_y(s) + TeO_2(s) + 1/2O_2(g) = A_nTeO_6(s) \qquad (7.25)$$

where A= periodic table elements, “a” is the coefficient of $A_xO_y(s)$ oxide and n = 2, 3 and 6, the number of A elements in $A_nTeO_6(s)$. The second and third terms of the left hand side are common for all $A_nTeO_6(s)$. Hence, in order to make a general enthalpy of formation expression for $A_nTeO_6(s)$, enthalpy of formation of metal oxide (A_xO_y) per 1.5 mole of oxygen was considered. In $A_nTeO_6(s)$, n=3 implies a=3 and n=2 implies, a=1. The calculated enthalpy data for ternary tellurates (A_nTeO_6, cr, 298.15K) (and is given in **Fig.7.7**) were plotted against $\Delta_f H^{\circ}_m$(298.15K) of corresponding metal oxides($A_xO_y(s)$ normalized to 1.5 mole of oxygen. The data along with the data from Kadam et al **[193]** were least square analyzed to obtain a general expression for the estimation of enthalpy of formation of $A_nTeO_6(s)$ and is given as:

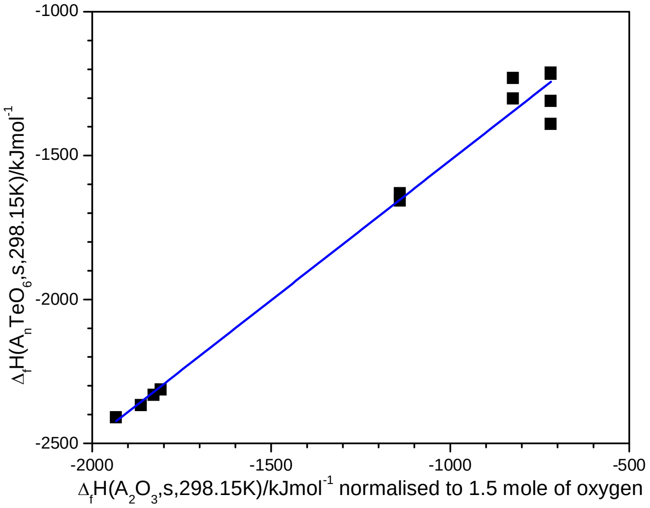

Fig.7.7. The plot of calculated enthalpy data for ternary tellurates (A_nTeO_6, s, 298.15K) against $\Delta_f H^{\circ}_m$(298.15K) of corresponding metal oxides($A_xO_y(s)$ normalized to 1.5 mole of oxygen.

$$\Delta_f H^{\circ}_m(A_nTeO_6,s,298.15\ K)\{(\pm 2.5\%)\ kJ\ mol^{-1}\} = -435.1 + 1.07098 \bullet \Delta_f H^{\circ}_m(A_xO_y,\ s,\ 298.15\ K) \qquad (7.26)$$

where $\Delta_f H^{\circ}_m(A_xO_y$,s,298.15 K) is the enthalpy of formation of metal oxide normalized to 1.5 mole of oxygen. $\Delta_f H^{\circ}_m(A_xO_y$ s,298.15 K) in **Eq.7.26** is the enthalpy of formation of one mole of $Fe_2O_3(s)$ and 3 mole of NiO(s) for $Fe_2TeO_6(s)$ and $Ni_3TeO_6(s)$, respectively. The calculated enthalpy of formation of $A_nTeO_6(s)$ (where A= Ba, Bi, Ca, Cd, Co, Cr, Cs, Cu, Dy, Er, Eu, Fe, Gd, Ho, K, La, Li, Lu, Mg, Mn, Na, Nd, Ni, Pb, Rb, Sm, Sr, Tb, Tl, Tm, Y, Yb, Pr and Sc) were given in **Table 7.7** and compared wherever experimental data exists **[191, 192, 193-196].**

Table 7.7 shows reasonable agreement between the calculated and reported experimental values. However, $\Delta_f H^\circ_m(Sc_2TeO_6, s, 298.15\ K)$ calculated from Pankajavalli et al **[196]** is ~ 200 kJ mol^{-1} more –ve than the value calculated from Eq. (7.26). The derived $S^o(Sc_2TeO_6, s, 298.15\ K)$ from the Gibbs energy expression is -ve (-18.0 J mol^{-1}K^{-1}), which is meaningless. Hence, the slope and intercept of Gibbs energy expression given by Pankajavalli et al **[196]** might be in error. The selected $\Delta_f H^\circ_m(298.15\ K)$ data from **Table 7.5** for Cr_2TeO_6(s), Fe_2TeO_6(s) and Ni_3TeO_6(s) are -1631.6, -1302.1 and -1216.2 kJ mol^{-1}, respectively. Similarly the selected $S^\circ_m(298.15\ K)$ data for Cr_2TeO_6(s), Fe_2TeO_6(s) and Ni_3TeO_6(s) are 169.9, 155.4 and 169.3 J K^{-1} mol^{-1}, respectively. Thermodynamic functions for Cr_2TeO_6(s), Fe_2TeO_6(s) and Ni_3TeO_6(s) were computed using measured heat capacity and selected enthalpy of formation and entropy at 298.15 K using the second law method. The corresponding thermodynamic functions for Cr_2TeO_6(s), Fe_2TeO_6(s) and Ni_3TeO_6(s) are given in **Tables 7.8-7.10**, respectively.

Table 7.7. A. comparison of $\Delta_f H^\circ_m$(A_nTeO_6,s, 298.15 K) values calculated in this study with that reported in the literature.

A_nTeO_6(s)	$\Delta_f H^o_m$(298.15 K)/ kJ ·mol^{-1}		A_nTeO_6(s)	$\Delta_f H^o_m$(298.15 K)/ kJ ·mol^{-1}	
	Calculated	Experimental		Calculated	Experimental
Ba_3TeO_6(s)	-2,212.5	-	Li_6TeO_6(s)	-2,357.8	-
Bi_2TeO_6(s)	-1,048.7	-	Lu_2TeO_6(s)	-2,445.7	-
Ca_3TeO_6(s)	-2,474.6	-	Mg_3TeO_6(s)	-2,365.9	-
Cd_3TeO_6(s)	-1,266.2	-	Mn_3TeO_6(s)	-1,671.8	-1710.0^{c}[194]
Co_3TeO_6(s)	-1,198.6	-	Na_6TeO_6(s)	-1,777.1	-
Cr_2TeO_6(s)	-1,654.7	-	Nd_2TeO_6(s)	-2,370.4	-2313.1^{a}[193]
Cs_6TeO_6(s)	-1,545.7	-	Ni_3TeO_6(s)	-1,204.3	-
Cu_3TeO_6(s)	-935.5	-	Pb_3TeO_6(s)	-1,134.7	-
		-			-
Dy_2TeO_6(s)	-2,429.5	2367.5^{a}**[193]**	Rb_6TeO_6(s)	-1,523.3	
		-	Sc_2TeO_6(s)	-2,478.2	-2680.16 [196]*
Er_2TeO_6(s)	-2,466.7				
		-			-2331.9^{d}**[193,**
Eu_2TeO_6(s)	-2,214.9		Sm_2TeO_6(s)	-2,390.8	**195]**
Fe_2TeO_6(s)	-1,316.9	-	Sr_3TeO_6(s)	-2,336.3	-
Gd_2TeO_6(s)	-2,390.7	-	Tb_2TeO_6(s)	-2,431.8	-
Ho_2TeO_6(s)	-2,448.3	-	Tl_6TeO_6(s)	-977.2	-
K_6TeO_6(s)	-1,595.6	-	Tm_2TeO_6(s)	-2,456.9	-
		-			-2389.3^{a}**[193]**
		2308.6^{b}**[193]**			-2521.8^{a}**[196]**
		-			
La_2TeO_6(s)	-2,355.2	2381.3^{a}**[191]**	Y_2TeO_6(s)	-2474.7	
Pr_2TeO_6(s)	-2,372.2	-2424.0^{d}			-
		[192]	Yb_2TeO_6(s)	-2,390.8	

^{a}= derived from Gibbs energy data, ^{b}= Enthalpy at experimental average temperature: 1076 K, ^{c}= Enthalpy from Gibbs energy data at experimental average temperature: 900 K, ^{d}= Enthalpy from Gibbs energy data, *= calculated S^{o} (Sc_2TeO_6,s,298K) from Gibbs energy of formation is –ve, which is not possible.

Table 7.8. Thermodynamic functions for $Cr_2TeO_6(s)$.

T/K	$C^{\mathrm{o}}_{\mathrm{p,m}}(T)$/ J·K^{-1}·mol^{-1}	$H^{\mathrm{o}}_{\mathrm{m}}(T)$-$H^{\mathrm{o}}_{\mathrm{m}}$(298.15 K)/ kJ·mol^{-1}	S$^{\mathrm{o}}_{\mathrm{m}}(T)$/ J·K^{-1}·mol^{-1}	$\phi^{\mathrm{o}}_{\mathrm{m}}(T)$ / J·K^{-1}·mol^{-1}	$H^{\mathrm{o}}_{\mathrm{m}}(T)$ kJ·mol^{-1}	$G^{\mathrm{o}}_{\mathrm{m}}(T)$ kJ·mol^{-1}	$\Delta_{\mathrm{f}}H^{\mathrm{o}}_{\mathrm{m}}(T)$ kJ·mol^{-1}	$\Delta_{\mathrm{f}}G^{\mathrm{o}}_{\mathrm{m}}(T)$ kJ·mol^{-1}
298.15	160.58	0.0	169.9	169.9	-1631.6	-1682.3	-1631.6	-1470.0
300	161.29	0.3	170.9	169.9	-1631.3	-1682.6	-1631.6	-1469.0
400	186.92	17.9	221.3	176.6	-1613.7	-1702.2	-1630.5	-1414.9
500	200.06	37.3	264.5	189.9	-1594.3	-1726.6	-1611.9	-1361.2
600	208.29	57.7	301.8	205.6	-1573.9	-1755.0	-1626.1	-1308.1
700	214.19	78.9	334.4	221.7	-1552.7	-1786.8	-1623.7	-1255.2
800	218.87	100.5	363.3	237.7	-1531.1	-1821.7	-1639.3	-1200.9
900	222.82	122.6	389.3	253.1	-1509.0	-1859.4	-1585.3	-1146.2
1000	226.33	145.1	413.0	267.9	-1486.5	-1899.5	-1635.2	-1091.8
1100	229.54	167.9	434.7	282.1	-1463.7	-1941.9	-1633.3	-1037.5

Table 7.9. Thermodynamic functions for Fe_2TeO_6(s).

T/K	$C^{o}_{p,m}(T)$/ $J \cdot K^{-1} \cdot mol^{-1}$	$H^{o}_{m}(T)-H^{o}_{m}(298.15\ K)$/ $kJ \cdot mol^{-1}$	$S^{o}_{m}(T)$/ $J \cdot K^{-1} \cdot mol^{-1}$	$\phi^{o}_{m}(T)$ / $J \cdot K^{-1} \cdot mol^{-1}$	$H^{o}_{m}(T)$ $kJ \cdot mol^{-1}$	$G^{o}_{m}(T)$ $kJ \cdot mol^{-1}$	$\Delta_f H^{o}_{m}(T)$ $kJ \cdot mol^{-1}$	$\Delta_f G^{o}_{m}(T)$ $kJ \cdot mol^{-1}$
298.15	164.80	0.0	155.4	155.4	-1302.1	-1348.4	-1302.1	-1134.0
300	165.43	0.3	156.4	155.4	-1301.8	-1348.7	-1302.1	-1132.9
400	188.03	18.1	207.6	162.4	-1284.0	-1367.0	-1301.2	-1076.7
500	199.06	37.5	250.8	175.8	-1264.6	-1390.0	-1283.1	-1020.8
600	205.52	57.8	287.7	191.4	-1244.3	-1416.9	-1298.0	-965.1
700	209.83	78.6	319.8	207.5	-1223.5	-1447.4	-1297.0	-909.8
800	213.00	99.7	348.0	223.4	-1202.4	-1480.8	-1314.3	-852.7
900	215.50	121.2	373.2	238.5	-1180.9	-1516.8	-1262.9	-794.8
1000	217.58	142.8	396.0	253.2	-1159.3	-1555.3	-1317.0	-737.0
1100	219.39	164.7	416.9	267.2	-1137.4	-1596.0	-1320.5	-678.8

Table 7.10. Thermodynamic functions for Ni_3TeO_6(s).

T/K	$C^{o}_{p,m}(T)$/ $J \cdot K^{-1} \cdot mol^{-1}$	$H^{o}_{m}(T)-H^{o}_{m}(298.15\ K)$/ $kJ \cdot mol^{-1}$	$S^{o}_{m}(T)$/ $J \cdot K^{-1} \cdot mol^{-1}$	$\phi^{o}_{m}(T)$ / $J \cdot K^{-1} \cdot mol^{-1}$	$H^{o}_{m}(T)$ $kJ \cdot mol^{-1}$	$G^{o}_{m}(T)$ $kJ \cdot mol^{-1}$	$\Delta_{f}H^{o}_{m}(T)$ $kJ \cdot mol^{-1}$	$\Delta_{f}G^{o}_{m}(T)$ $kJ \cdot mol^{-1}$
298.15	191.97	0.0	169.3	169.3	-1216.2	-1266.7	-1216.2	-1041.8
300	192.66	0.4	170.5	169.2	-1215.8	-1267.0	-1216.2	-1040.7
400	218.58	21.1	229.9	177.2	-1195.1	-1287.1	-1215.3	-982.3
500	233.18	43.7	280.4	193.0	-1172.5	-1312.7	-1197.2	-924.3
600	243.31	67.6	323.8	211.1	-1148.6	-1342.9	-1212.1	-866.5
700	251.34	92.3	361.9	230.0	-1123.9	-1377.2	-1210.5	-809.0
800	258.25	117.8	396.0	248.8	-1098.4	-1415.2	-1225.5	-750.0
900	264.51	143.9	426.8	266.9	-1072.3	-1456.4	-1170.8	-690.8
1000	270.36	170.7	454.9	284.2	-1045.5	-1500.4	-1219.9	-631.7
1100	275.94	198.0	481.0	301.0	-1018.2	-1547.3	-1216.9	-573.1

7.2.5. Chemical potential diagram of A-Te-O (A= Cr, Fe, Ni) system

The chemical potential diagram for A-Te-O (A= Fe, Cr, Ni) was generated assuming that ternary or binary compounds are formed from the reaction of one mole of A(s) (A = Cr, Fe, Ni) using the principle of minimization of Gibbs energy for various probable equilibrium mixture. Tellurium and oxygen potential were taken as axis variables. The formation of a typical ternary compound $A_kTe_mO_n$(s) can be written as:

$$A(s) + (m/k)Te(g) + 0.5(n/k)O_2(g) = (1/k)A_kTe_mO_n(s) \qquad (7.27)$$

The Gibbs energy of each compound in A-Te-O system at non-standard state can be written as a function of Standard Gibbs energy of formation and activities of species involved in Eq. (7.27). So Gibbs energy of ternary compounds in A-Te-O system can be calculated from Eq.(7.28).

$$\Delta G(A_kTe_mO_n) = \Delta G^o(A_kTe_mO_n) + (RT/k).\ln\{a(A_kTe_mO_n)/[(a(A))^k.(p(Te))^m.(p(O_2))^{0.5n}]\} \qquad (7.28)$$

where '*a*' is the activity. The calculation procedure of a stable species (minimum Gibbs Energy) for a given chemical potential is considerably tedious and complicated. FactSage software **[92]** was used for these calculations. The chemical potential diagram calculations by the software require the knowledge of various stable phases and their Gibbs energy of formation values. Hence, binary and ternary compounds present in A-Te-O system should be known clearly.

The compounds in A-O, Te-O, A-Te and A-Te-O (A = Cr, Fe, Ni) systems are well characterized. In general, the metal tellurides of A-Te systems are non-stoichiometric compounds. Chattopadhyay **[197]** have reported the phase diagram of Cr-Te system based on the investigations of Gunia **[198]** and Ipser et al **[199]**. The high temperature region of the phase diagram contains a disordered phase $Cr_{1-x}Te$(s). At intermediate temperature, the phase field is separated into $CrTe_{1.333}$(s), $CrTe_{1.5}$(s) and $CrTe_{1.6}$(s). A complex series of intermediate phases: $Cr_{4.14}Te_8$(s), $Cr_{4.33}Te_8$(s), $Cr_{2.01}Te_3$(s), CrTe(s), Cr_2Te_3(s), Cr_5Te_8(s), $CrTe_3$(s), Cr_3Te_4(s) have been reported in the literature **[197].** $CrTe_{1.1}$(s), Cr_3Te_4(s) ($CrTe_{1.33}$), Cr_2Te_3($CrTe_{1.5}$), Cr_5Te_8(s) ($CrTe_{1.6}$(s)) was taken for chemical potential diagram calculations at 900 K. Okamoto and Tanner **[200]** have assessed Fe-Te system. Most of the important features in the assessed diagram were based primarily on thermal and isopiestic experimental data by Ipser et al. **[201].** Lee and Nash [202] have assessed Ni-Te phase diagram based on literature data [203]. A number of binary tellurides: $FeTe_2$(s), $FeTe_{1.45}$(s), Fe_3Te_2(s),

$Fe_{2.25}Te_2$(s), $FeTe_{0.9}$(s),. FeTe(s), $FeTe_{1.1}$(s) and $FeTe_{1.5}$(s) are reported in the JCPDS files for Fe-Te system **[188].** Similarly, $Ni_{1.055}Te_2$(s), $NiTe_2$(s), $Ni_{2.86}Te_2$(s), NiTe(s),Ni_3Te_2(s), $Ni_3Te_{2.07}$(s), $Ni_{10.35}Te_{7.97}$(s) are reported binary tellurides in Ni-Te system **[202].** $FeTe_{0.9}$(s) ($Fe_{2.25}Te_2$(s)), $FeTe_{1.1}$(s), $FeTe_{1.45}$(s) and $FeTe_2$(s) in Fe-Te system and Ni_3Te_2(s), $NiTe_{0.775}$(s), $NiTe_{1.1}$(s), $NiTe_{1.5}$(s) and $NiTe_2$(s) in Ni-Te system were taken for chemical potential diagram calculations at 900 K. The binary phases of Cr-O, Fe-O, Ni-O, Te-O systems and ternary phases of Cr-Te-O, Fe-Te-O and Ni-Te-O systems reported in the JCPDS file **[188]** were taken for the calculations. The experimental Gibbs energy values of some of these compounds are reported in the literature **[86, 87-90, 166, 204-206]**.Wherever, experimental Gibbs energy of formation of binary telluride and ternary tellurates were not available, $\Delta_f G^\circ_m(T)$ values were calculated from the heat capacities, enthalpy of formation and entropy at 298.15 K using relation (7.29):

$$\Delta_f G^\circ_m(T) = \Delta_f H^\circ_m(298.15\text{K}) - T.\ \Delta_f S^\circ_m(298.15\ \text{K}) \tag{7.29}$$

The experimental $\Delta_f H^\circ_m$(298.15K), S°_m(298.15 K) and heat capacity values of binary telluride [**197, 207-218**] in A-Te system and ternary tellurate **[205, 206]** in A-Te-O system were used for the calculations of respective $\Delta_f G^\circ_m(T)$. Wherever, experimental data for the heat capacities, enthalpy of formation and entropy at 298.15 K have not been reported these values were estimated in this study using methods given in the literature **[193, 204, 219].** The Gibbs energy values obtained in this study along with that reported in the literature for A-Te and A-Te-O systems are given in **Table 7.11.** The predominant module and FactPS database along with data reported in **Table 7.11** were used in the FactSage programme to construct the chemical potential diagrams of A-Te-O which are shown in **Figs 7.8-7.10.** These diagrams show the possible stable phases over the specified ranges of the chemical potentials. At any point on the diagram (**Figs.7.8-7.10**) the chemical potential of elemental species Te(g) or O_2(g) can be determined from the y and x co-ordinates. The invariant point (three phase field) is independent of the choice of chemical potential of species (Te, TeO_2 or O_2) for the axis. The calculated invariant points (three phase field) for A-Te-O system along with their tellurium and oxygen potential is given in **Table 7.12.** The calculated chemical potential diagram can be related to the Gibbs phase diagram of A-Te-O system. The line represented with sign '+' on **Figs.7.8-7.10** corresponds to reaction pathway at the P(total) = 1 bar. Hence, along this line the sum of the partial pressures of all the gaseous species, $p(O) + p(O_2) + p(O_3) + p(Te) + p(Te_2)$

+... $p(TeO_2)$ + ..., is 1 bar. On Fig. **7.8-7.10** P(total) is greater than 1 bar above the '+' line, and P(total) < 1 bar below the line.

The tellurate of stainless steel component (Fe, Cr, Ni) with less negative Gibbs energy of formation results in less cladding corrosion. But in a nuclear reactor both the oxygen and tellurium potential play an important role. **Table 7.12** gives required oxygen and tellurium potential for different equilibrium phase fields in A-Te-O system. The oxygen potentials and tellurium potentials in the fuel-clad gap of MOX fuel of PFBR at 900 K is $\Delta\mu(O_2)$ =-550 kJ mol^{-1} and -460 kJ mol^{-1} and $\Delta\mu(Te)$ = -250 kJ mol^{-1}, -115 kJ mol^{-1} for O/M= 1.9998 and 2.0000, respectively **[194]. Figs 7.8-7.10** reveal that at lower $\Delta\mu(O_2)$ binary telluride are stable and at higher oxygen potential ternary tellurates are stable. However, tellurium potential required for ternary tellurates are lower than the binary tellurides. From the **Figs 7.8-7.10**, the oxygen potential required for the formation of Cr_2O_3(s), FeO(s) and NiO(s) were found to be -597, -412 and -315 kJ mol^{-1}, respectively. For minimum oxygen and tellurium potential, $Cr_2Te_3O_9$(s), Fe_2TeO_5(s) and $NiTeO_3$(s) are the stable ternary tellurate in equilibrium with respective metal oxides in Cr-Te-O, Fe-Te-O and Ni-Te-O systems, respectively. Similarly, the minimum $\Delta\mu(O_2)$ and $\Delta\mu(Te)$ for the formation of $Cr_2Te_3O_9$(s) is -272 and -122 kJ mol^{-1}, that for Fe_2TeO_5(s) is -212 and -171 kJ mol^{-1} and that for $NiTeO_3$(s) are -206 and -290 kJ mol^{-1}, respectively. The tellurium potential required for the formation of $CrTe_{1.1}$(s), $FeTe_{0.9}$(s) and $NiTe_{0.67}$(s) are -175, -126 and -155 kJ mol^{-1}, respectively at 900 K. $CrTe_{1.1}$(s) requires least tellurium potential amongst all binary telluride of stainless steel components. **Fig.7.8** shows that the reaction between stainless steel clad and tellurium can only take place to form $CrTe_{1.1}$(s) before the formation of Cr_2O_3(s). The calculations of $\Delta\mu(Te)$ for the reaction between fission products (Mo,Cs,Zrand Sr) and tellurium show that $\Delta\mu(Te)$ of Cs_2Te(s) and SrTe(s) are minimum and around -320 kJ mol^{-1}. As the vapour pressure of Cs is more than that of Sr, so Cs_2Te(s) will be formed first in the reactor. As $\Delta\mu(O_2)$ increases during irradiation of fuel, Cs forms stable oxides and tellurium gets free to react with stainless steel **[220].**

Table 7.11: Constants of the fit equations of heat capacity and Gibbs energy of formation data of binary and ternary compounds in A-Te-O system. The enthalpy of formation and entropy at 298.15 K are also included.

Ternary compounds	$\Delta_f H^o_m$(298.15 K) /kJ.mol^{-1}	S^o_m(298.15 K) /J.K^{-1}.mol^{-1}	$C^o_{p,m}(T)$/J.K^{-1}. mol^{-1}= a + b.(T/K) + c.(K/T)^2			$\Delta_f G^o_m(T)$/kJ.mol^{-1} = A+B.(K/T)	
			a	b.10^3	- c.10^{-5}	A	B
$Cr_2Te_3O_9$(s)	-2117.4 ^{e}	306.1 ^{e}	316.20	51.84	33.039 ^{e}	-2157.2	0.8253 ^{e}
$Cr_2Te_4O_{11}$(s)	-2440.8 ^{e}	381.0 ^{e}	381.39	66.40	38.060 ^{e}	-2476.3	1.0222 ^{e}
$CrTe_{1.1}$(s)	-78.4 **[213]**	77.68 ^{e}	57.6	13.59	0.282 ^{e}	-94.5	0.0225 **[207]**
$CrTe_{1.33}$(s)	-90.0 ^{e}	94.0 ^{e}	46.67	41.0	1.167 ^{e}	-88.1	0.0076 **[207]**
$CrTe_{1.5}$(s)	-105.0 ^{e}	78.3 ^{e}	49.79	0.042	0.42 ^{e}	-104.2	0.0215 **[207]**
$CrTe_{1.6}$(s)	-85.0 ^{e}	107.2 ^{e}	51.67	0.047	1.114 ^{e}	-110.3	0.0290 ^{e}
$Fe_2Te_3O_9$(s)	-1802.1 ^{e}	301.2 ^{e}	312.0	68.10	32.0 **[205]**	-1809.6	0.8476 ^{e}
$Fe_2Te_4O_{11}$(s)	-2127.5 ^{e}	371.6 ^{e}	370.0	424.0	-7.14 **[205]**	-2037.8	0.8243 ^{e}
Fe_2TeO_5(s)	-1151.2 ^{e}	160.3 ^{e}	196.20	74.92	48.520 **[205]**	-1140.2	0.4304 ^{e}
$FeTe_{0.9}$(s)	-24.2 **[87]**	80.1 **[92]**	52.86	4.23	3.958 **[92]**	-43.5	0.0174 **[92]**
$FeTe_{1.1}$(s)	-29.4 ^{e}	89.9 ^{e}	56.6	8.74	3.919 ^{e}	-51.9	0.0218 ^{e}
$FeTe_{1.45}$(s)	-39.0 ^{e}	98.7 ^{e}	63.16	16.653	3.851 ^{e}	-74.9	0.0551 ^{e}
$FeTe_2$(s)	-72.4 **[87]**	100.2 **[92]**	72.32	20.55	4.192 **[92]**	-113.2	0.0819 **[92]**
$Ni_2Te_3O_8$(s)	-1679.0 ^{e}	306.1 ^{e}	278.92	65.23	-24.506 ^{e}	-1693.5	0.8677 **[206]**
$NiTe_2O_5$(s)	-949.3 ^{e}	381.0 ^{e}	172.05	39.90	9.743 ^{e}	-1000.7	0.5029 **[206]**
$NiTeO_3$(s)	-602.1 ^{e}	112.05 ^{e}	106.90	25.40	14.79 ^{e}	-577.3	0.2669 **[90]**
$NiTe_{0.67}$(s)	-42.3 ^{e}	62.4 ^{e}	39.06	12.605	-5.356 ^{e}	-55.3	0.0176 ^{e}
$NiTe_{0.775}$(s)	-50.2 ^{e}	62.92 ^{e}	39.33	12.64	-5.201 ^{e}	-66.7	0.0275
$NiTe_{1.1}$(s)	-57.3 ^{e}	84.06 ^{e}	57.18	7.11	4.011 ^{e}	-79.212	0.0306 **[92]**
$NiTe_{1.5}$(s)	-72.4 ^{e}	100.4 ^{e}	57.78	25.10	-0.903 ^{e}	-105.81	0.0502 **[92]**
$NiTe_2$(s)	-87.86 ^{e}	120.3 ^{e}	67.14	36.39	0.196 ^{e}	-131.7	0.0693 **[92]**

^{e}= estimated in this study

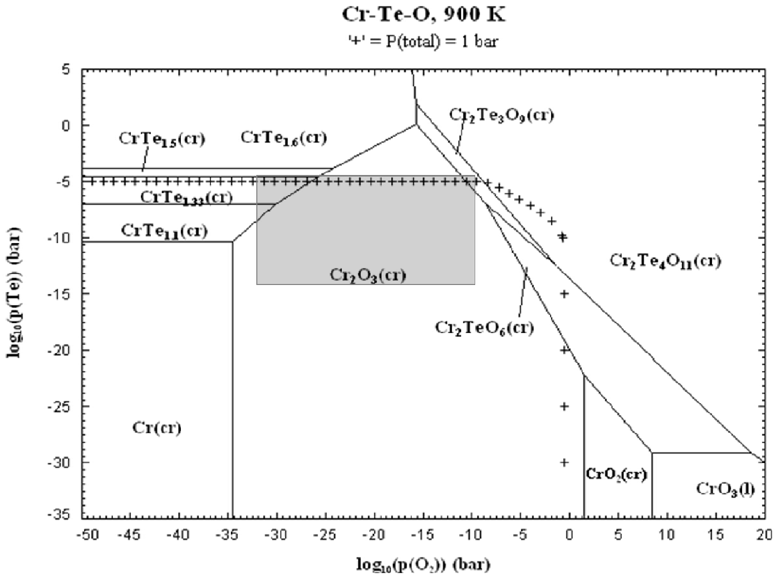

Fig.7.8. The chemical potential diagram of Cr-Te-O system at 900 K. The shaded region in the figure represent a typical $\Delta\mu(O_2)$ and $\Delta\mu(Te)$ in the operating mixed oxide fuel.

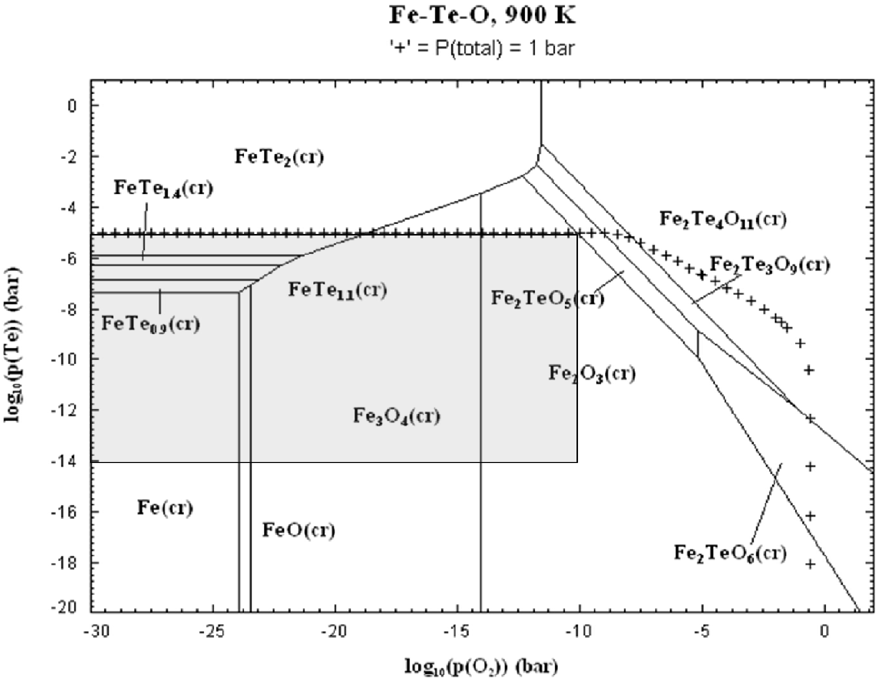

Fig.7.9. The chemical potential diagram of Fe-Te-O system at 900 K. The shaded region in the figure represent a typical $\Delta\mu(O_2)$ and $\Delta\mu(Te)$ in the operating mixed oxide fuel.

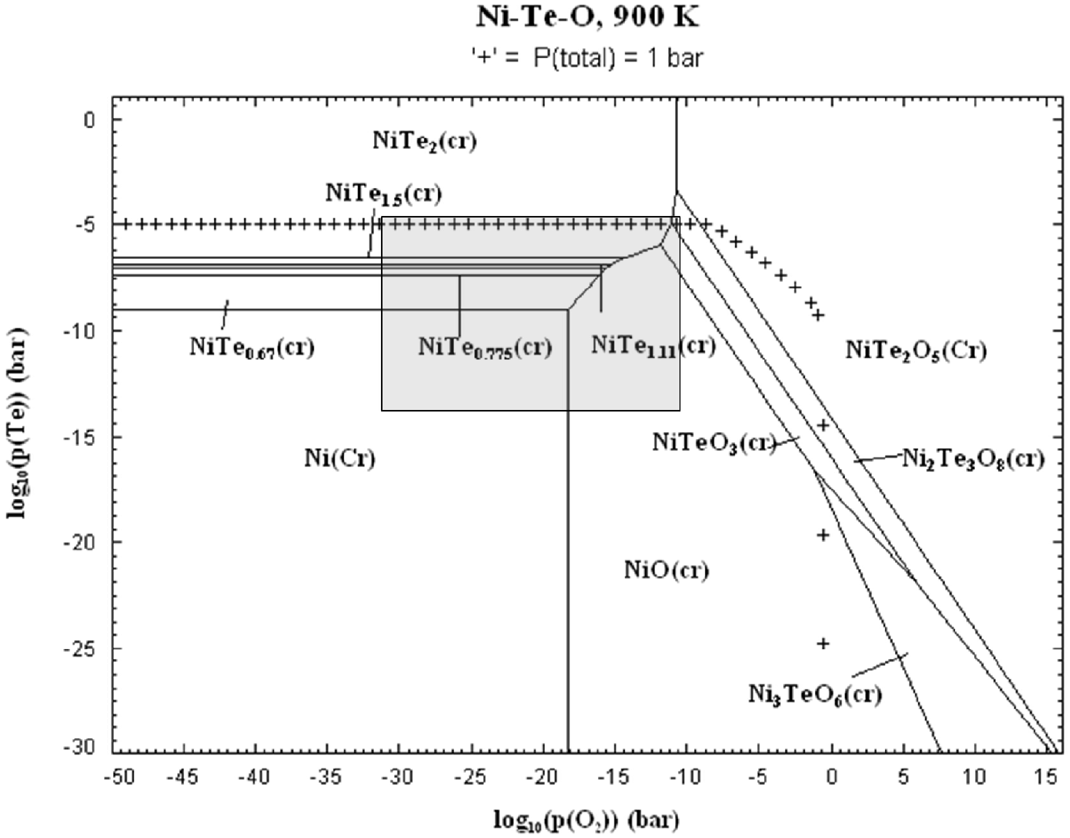

Fig.7.10. The chemical potential diagram of Ni-Te-O system at 900 K. The shaded region in the figure represent a typical $\Delta\mu(O_2)$ and $\Delta\mu(Te)$ in the operating mixed oxide fuel.

Table 7.12: The chemical potentials of Tellurium and oxygen at invariant points at 900K.

Phases at Invariant points	**$\Delta\mu(O_2)^*$ /kJ.mol^{-1}**	**$\Delta\mu(Te)^*$ /kJ.mol^{-1}**
$Cr(s) + Cr_2O_3(s) + CrTe_{1.1}(s)$	-594.7	-177.7
$Cr_2O_3(s) + CrTe_{1.1}(s) + CrTe_{1.333}(s)$	-519.8	-121.5
$Cr_2O_3(s) + CrTe_{1.333}(s) + CrTe_{1.6}(s)$	-436.1	-74.4
$Cr_2O_3(s) + Cr_2TeO_6(s) + Cr_2Te_3O_9(s)$	-150.2	-120.1
$Cr_2TeO_6(s) + Cr_2Te_3O_9(s) + Cr_2Te_4O_{11}(s)$	-22.7	-215.7
$Fe(s) + FeO(s) + FeTe_{0.9}(s)$	-412.4	-127.0
$Fe_3O_4(s2) + FeO(s) + FeTe_{0.9}(s)$	-404.7	-122.8
$Fe_3O_4(s2) + FeTe_{0.9}(s) + FeTe_{1.1}(s)$	-398.9	-118.5
$Fe_3O_4(s2) + FeTe_2(s) + FeTe_{1.1}(s)$	-375.2	-104.1
$Fe_2O_3(s) + Fe_3O_4(s2) + FeTe_2(s)$	-242.6	-59.9
$Fe_2O_3(s) + FeTe_2(s) + Fe_2TeO_5(s)$	-219.9	-51.4
$FeTe_2(s) + Fe_2TeO_5(s) + Fe_2Te_3O_9(s)$	-212.7	-45.4
$FeTe_2(s) + Fe_2Te_3O_9(s) + Fe_2Te_4O_{11}(s)$	-209.8	-32.2
$Fe_2O_3(s) + Fe_2TeO_5(s) + Fe_2TeO_6(s)$	-69.7	-201.6
$Fe_2TeO_5(s) + Fe_2TeO_6(s) + Fe_2Te_3O_9(s)$	-69.7	-188.5
$Fe_2TeO_6(s) + Fe_2Te_3O_9(s) + Fe_2Te_4O_{11}(s)$	-5.0	-237.0
$NiO(s) + Ni(s) + NiTe_{0.666}(s)$	-315.6	-155.5
$NiO(s) + NiTe_{0.666}(s) + NiTe_{7.9}(s)$	-277.8	-127.2
$NiO(s) + NiTe_{1.11}(s) + NiTe_{7.9}(s)$	-270.4	-122.3
$NiO(s) + NiTe_{1.5}(s) + NiTe_2(s)$	-246.2	-113.4
$NiO(s) + NiTe_2(s) + NiTeO_3(s)$	-205.6	-103.3
$NiTe_2(s) + NiTeO_3(s) + Ni_2Te_3O_8(s)$	-193.1	-84.6
$NiTe_2(s) + NiTe_2O_5(s) + Ni_2Te_3O_8(s)$	-186.5	-58.3
$NiO(s) + NiTeO_3(s) + Ni_3TeO_6(s)$	-22.2	-286.6

$\Delta\mu(X)^*$ where X=Te, O_2 are the relative potentials with respect to standard potentials for the equilibrium phase field.

7.3. Summary

1. Cr_2TeO_6(s), Fe_2TeO_6(s) and Ni_3TeO_6(s) were synthesized by solid state reaction method using metal oxides and characterized by XRD technique.
2. The coefficient of thermal expansion measurements of A_nTeO_6(s) revealed that α_{av} increased in the order Cr_2TeO_6(s) < Fe_2TeO_6(s) < Ni_3TeO_6(s). Heat capacity also followed similar trend.
3. This study resolved the ambiguity in Gibbs energy data reported in the literature for Fe_2TeO_6(s) and Ni_3TeO_6(s) by devising an independent theoretical method for estimation of enthalpy of formation of A_nTeO_6(s).
4. The experimental enthalpy of formation data on tellurates is scarce in the literature due to experimental difficulty in handling corrosive tellurium compounds; hence this estimation will help in computing the enthalpy of formation of tellurates.
5. The heat capacity contribution of TeO_3(s) to Te(VI) compounds was calculated, which can be used for the estimation of the heat capacity of various tellurium(VI) compounds using Newmann Kopp's rule.
6. The two dimensional chemical potential diagrams have been constructed to evaluate the reaction between components of stainless steel clad and fission product tellurium. These diagrams illustrate stable phases under different $\Delta\mu(O_2)$ and $\Delta\mu(Te)$. The species of corrosion products can be determined from these diagrams at different burn up ($\Delta\mu(O_2)$, $\Delta\mu(Te)$, O/M ratio) and plutonium content of fuel $U_{1-q}Pu_qO_2$ (q=Pu fraction).
7. Thermodynamic data reported in **Tables 7.8-7.10** will also be helpful for computation of multi-component systems.

Chapter-8

Conclusion and Suggestions for further studies

Chapter-8

Conclusion

The thermodynamic and physiochemical properties of RE-U-O, Sr-Ce-O, Ba-Sr-Mo-O and A-Te-O (A= Cr, Fe, Ni) systems have been investigated in this thesis. The only RE_6UO_{12}(s) compound present in RE-U-O system is important from the point of view of chemical interactions between 4f and 5f elements.The measured physico-chemical properties of these compounds will give an insight into the chemical bonding between rare earth and actinide oxides. The physiochemical properties of RE_6UO_{12}(s) showed diverse from the regularity. $SrCeO_3$(s) present in Sr-Ce-O system showed an oxygen non stoichiometric phase in reducing atmosphere due to change in oxidation state of Ce^{4+} to Ce^{3+}. The thermal expansion versus composition plot of perovskite $Ba_{1-x}Sr_xMoO_3$(s) solid solution showed minima. An estimation method for enthalpy of formation of Te^{6+} containing tellurate was derived which could be a significant contribution to the literature as experimental data was difficult to obtain for corrosive tellurates. The detailed conclusion derived on different systems is given below.

RE-U-O system

The method of synthesis of RE_6UO_{12}(s) and its characterization have been standardized. As Er_6UO_{12}(s) was not reported in the JCPDS file. This compound was synthesized and its XRD peaks were indexed with hexagonal unit cell and its lattice parameters and theoretical density were determined for the first time. The lattice parameter of Er_6UO_{12}(s) in hexa coordination was found to fall on the linear plot of lattice parameter of RE_6UO_{12}(s) versus ionic radii of RE^{+3}.

The thermal expansion measurements of RE_6UO_{12}(s) (RE = La, Pr, Sm, Eu, Gd, Tb, Dy, Ho, Er, Tm, Yb, Lu) revealed these compound as high expansion materials and also regular trend was not observed along the series. However, the average linear thermal expansion coefficients (α_a and α_c) and volume thermal expansion coefficients (α_V) of RE_6UO_{12}(s) (RE= La, Gd, Lu) as a function of RE^{+3} were found to follow linear relation, which might be due to the empty, half filled and full filled 4 f orbital in La^{+3}, Gd^{+3} and Lu^{+3} ions, respectively. The expansion coefficients of La_6UO_{12}(s), Gd_6UO_{12}(s) and Lu_6UO_{12}(s) were contributed by lattice phonon only and hence dependent on the size of the rare earth ions. As the bond strength increases with reduction in size of trivalent rare earths ions (RE^{+3}), the expansion coefficient reduces along the series. The thermal expansion of RE_6UO_{12}(s) (RE = La, Pr, Sm, Eu, Gd, Tb, Dy, Ho, Er, Tm, Yb, Lu) have been reported for the first time and these compounds are categorized as high expansion materials.

The heat capacities of RE_6UO_{12}(s) (RE= La, Pr, Nd, Sm, Eu, Gd, Tb, Dy, Ho, Er, Tm, Yb, Lu) as a function of RE^{3+} ionic radii do not follow any regular trend. This irregularity in C^{o}_{p} might be due to excess heat capacity (difference between measured and lattice C^{o}_{p}) which could be due to excess electronic contribution from f-shell electrons. Heat capacity of RE_6UO_{12}(s) containing $La^{3+}(f^{0})$, Gd^{3+} ($f^{7)}$ and $Lu^{3+(}f^{14}$) is due to phonon vibrations only and related to volume of the rare earth element and C^{o}_{p} follows $La^{3+}> Gd^{3+} >Lu^{3+}$. The plot of C^{o}_{p} versus RE^{3+} (La^{3+}, Gd^{3+}, Lu^{3+}) varies linearly with RE^{3+}. From this plot lattice contribution of C^{o}_{p} to the total heat capacity was obtained for RE_6UO_{12}(s) (RE= Pr, Nd, Sm, Eu, Tb, Dy, Ho, Er, Tm, Yb). The excess heat capacities for these compounds were calculated separately by subtracting lattice part from the corresponding calorimetric measured heat capacity.

Standard molar Gibbs energy of formation of RE_6UO_{12}(s) (RE=La, Nd, Sm, Eu, Gd, Tb, Dy, Ho, Tm, Yb, Lu) was measured using e.m.f. technique. The ΔH_f^{o}(298.15 K) and S^{o}(298.15K) were derived from the measured Gibbs energy data. These thermodynamic functions for RE_6UO_{12}(s) have been reported for the first time. The second law and third law data treatment were carried out for $\Delta H_f^{o}(RE_6UO_{12}$,s,298.15 K).

The e.m.f. measurements on {RE_6UO_{12}(s) + U_3O_8(s) + RE_2O_3(s)} revealed that its $\Delta\mu(O_2)$ is lower than {Ni(s)+NiO(s)}for RE= La, Pr, Nd, Sm, Eu, Gd, Tb, Dy} and higher than {Ni(s)+NiO(s)}for RE= Ho, Tm, Yb, Lu. This observation corroborate with the $\Delta\mu(O_2)$ versus temperature plot of RE_6UO_{12}(s) (RE=La, Nd, Sm, Eu, Gd, Tb, Dy, Ho, Tm, Yb, Lu). It showed that La_6UO_{12}(s) to have maximum stability amongst rare earth uranates and its oxygen potential lied between UO_2(s) and U_3O_8(s). The stability order was found to be UO_2(s) > La_6UO_{12}(s) >Tm_6UO_{12}(s) ~Ho_6UO_{12}(s)> >Lu_6UO_{12}(s) > U_3O_8(s). The probability of formation of La_6UO_{12}(s) in the reactor environment depends on its fission yield, O/M ratio and the oxygen potential of the fuel.

The phase transition was observed in Nd_6UO_{12}(s), Sm_6UO_{12}(s) and Yb_6UO_{12}(s) and their transition temperatures were determined by more than one technique such as thermal expansion, heat capacity, e.m.f and conductivity. However, RE_6UO_{12}(s) (RE = La, Pr, Eu, Gd, Tb, Dy, Ho, Er, Tm, Lu) showed stable crystal structure up to 1300 K.

Sr-Ce-O System

This study found $SrCeO_3(s)$ to unstable in reducing atmosphere. Hence, the reported heat capacities of $SrCeO_3(s)$ in the argon atmosphere are not reliable. The heat capacity of $SrCeO_3(s)$ and $Sr_2CeO_4(s)$ were measured in oxygen atmosphere in this study for the first time.

The volume expansion coefficient of $Sr_2CeO_4(s)$ was found to be higher than that of $SrCeO_3(s)$. This could be due to the less rigid structure of $Sr_2CeO_4(s)$ compared to $SrCeO_3(s)$. The study of average coefficient of volume expansion and heat capacity of $Sr_2CeO_4(s)$ confirmed the presence of second order phase transition at 637 K. Thermodynamic functions generated in this study along with required literature data will help in establishing the phase relations in the Sr- Ce-O system.

Ba-Sr-Mo-O System

$Ba_{1-x}Sr_x MoO_4(s)$ and $Ba_{1-x} Sr_xMoO_3(s)$ solid-solutions

The lattice parameters of $BaMoO_4(s)$-$SrMoO_4(s)$ and $BaMoO_3(s)$-$SrMoO_3(s)$ systems were found to follow Vegard's law and formed complete range of solid solutions. However, $Ba_{1-x}Sr_xMoO_3(s)$ solid solution showed slight negative deviation from Vegard's law. The thermal expansion coefficient of $Ba_{1-x} Sr_xMoO_3(s)$ as a function of $SrMoO_3$ followed a polynomial relation and that of $Ba_{1-x} Sr_xMoO_4(s)$ as a function of $SrMoO_4(s)$ followed a linear relation. However, specific heat capacity of both the systems increased with Sr content in the solid solutions.

Enthalpy increment, entropy and Gibbs energy functions were computed for $Ba_{1-x}Sr_x MoO_4(s)$ and $Ba_{1-x} Sr_xMoO_3(s)$ solid-solutions. These data could be useful for the assessment of performance of nuclear reactors operating with high burn up oxide fuels. The perovskite-type oxide $(Ba,Cs, Sr)(U,Pu,Zr,RE,Mo)O_3(s)$ phase has been observed by the post irradiation study of the MOX fuel. Therefore the physic-chemical data determined on $Ba_{1-x} Sr_xMoO_3(s)$ might be used as input for the designing of reactor code.

Cr-Te-O, Fe-Te-O and Ni-Te-O system

The coefficient of volume thermal expansion and molar heat capacity of $A_nTeO_6(s)$ increases in the order $Cr_2T_eO_6(s) < Fe_2T_eO_6(s) < Ni_3T_eO_6(s)$. This study resolved the ambiguity in Gibbs energy data reported in the literature for $Fe_2T_eO_6(s)$ and $Ni_3T_eO_6(s)$. An estimation method with reasonable accuracy was devised for the enthalpy of formation of $A_nT_eO_6$(**s**) for the first time. The experimental enthalpy of formation data on Te^{6+} tellurates are scarce in the literature due to difficulty in handling corrosive tellurium compounds; hence this estimation will help in computing the enthalpy of formation of Te^{6+} tellurates.

In addition, the heat capacity contribution of TeO_3(s) to Te^{6+} tellurates was also computed which could be used for estimation of heat capacity of $A_nT_eO_6$(**s**) (A= periodic table element) using Newmann Kopp's rule.

The two dimensional chemical potential diagrams for A-Te-O (A=Cr, Fe, Ni) was computed for the first time. These diagrams will help to evaluate the reaction between stainless steel clad and fission product tellurium. The species of corrosion products can be determined from these diagrams at different burn up ($\Delta\mu(O_2)$, $\Delta\mu$(Te), O/M ratio) and plutonium content of fuel$U_{1-q}Pu_qO_2$ (q=Pu fraction).

$CrTe_{1.1}$(s) was found to require least tellurium potential amongst all binary telluride of stainless steel components. Therefore, the reaction between stainless steel clad and tellurium can only take place to form $CrTe_{1.1}$(s) before the formation of Cr_2O_3(s). The calculations of $\Delta\mu$(Te) for the reaction between fission products (Mo,Cs,Zrand Sr) and tellurium showed that $\Delta\mu$(Te) of Cs_2Te(s) and SrTe(s) are minimum and as the vapour pressure of Cs is more than that of Sr, so Cs_2Te (s) will be formed first in the reactor. As $\Delta\mu(O_2)$ increases during irradiation of fuel, Cs forms stable oxides and tellurium gets free to react with components of stainless steel clad. Thermodynamic data reported for Cr_2TeO_6(s), Fe_2TeO_6(s) and Ni_3TeO_6(s) may help in computation of phase diagram involving multi-component systems

Suggestions for further studies

The high temperature heat capacity of the solid solutions between UO_2 and $REO_{1.5}$(s) and that for Er_6UO_{12} have not been reported, hence it is essential to determine their physicochemical properties to bridge gap in the literature on RE-U-O system. The various contributions to the excess heat capacity of rare earth actinide compounds should be resolved from magnetic and spectroscopic measurements. The Schottky contribution to heat capacity can be derived by finding the energy levels and degeneracy from spectroscopy. The type of second order phase transition in Nd_6UO_{12}(s), Sm_6UO_{12}(s) and Yb_6UO_{12}(s) should be determined. The Gibbs energy of formation of Er_6UO_{12}(s) and Pr_6UO_{12} (s) need to be determined to bridge the gap existed in this thesis.

References:

1. H. Kleykamp, The chemical state of the fission products in oxide fuels, J. Nucl. Mater. 131 (1985) 221-246.
2. F.T. Ewart, R.G. Taylor, J.M. Horspool, G. James, J. Nucl. Mater. 61 (1976) 254-270.
3. H. Kleykamp, J.O. Paschoal, R. Pejsa, F. Thummler, J. Nucl. Mater. 130 (1985) 426-433.
4. D.R. O'boyle, F.L. Browm, A.E. Dwight, J. Nucl. Mater. 35 (1970) 257-266.
5. I. Sato, H. Furuya, T. Arima, K. Idemitsu, K. Yamamoto, J. Nucl. Mater. 273 (1999) 239-247.
6. M.G. Adamson, E.A. Aitken, T.B. Lindemer, J. Nucl. Mater. 130 (1985) 375.
7. W.B. Wilson, C.A. Alexander, A.F. Gerds, J. Inorg. Nucl. Chem. 20(3–4) (1961) 242–251.
8. E.A.C. Crouch, Report-AERE-R-6056, 1969
9. Y. Zheng, K. Kurosaki, K. Tokushima, Y. Ohishi, H. Muta, S, Yamanaka, J. Nucl. Mater. 419 (2011) 357–36.
10. M. Amaya, K. Une, M. Hirai, J. Nucl. Sci. Tech. 41(2) (2004) 108 – 115.
11. R.J. Beals, J. H. Handwerk, B. J. Wrons, J. Am. Ceram. Soc. 48 (5) (1965) 271-274.
12. U. Berndt, R. Tanamas, C. Keller, J. Solid State Chem. 17 (1976) 113.
13. Y. Hinatsu, N. Masaki, T. Fujino, J. Solid State Chem. 73 (1988) 567.
14. E.A. Aitken, S.F. Bartram, E.F. Juenke, Inorg. Chem. 3 (1964) 949.
15. H.G. Diel, C. Keller, J. Solid State Chem. 3 (1971) 621.
16. H. Jena, R. Asuvathraman, K.V. Govindan Kutty, J. Nucl. Mater. 280 (2000) 312.
17. R. Venkata Krishnan, P. Manikandan, H. Jena, K. Nagarajan, Thermochim. Acta 472 (1-2) (2008) 95-98.
18. M. V. Krishnaiah, G. Seenivasan, P. Srirama Murti, C.K. Mathews, J. Nucl. Mater. 306 (2002)10.
19. R. Venkata Krishnan, R. Babu, G. Panneerselvam, K. Ananthasivan, M.P. Antony, K. Nagarajan, Ceramics International 38 (6)(2012) 5277–5280.
20. R. Venkata Krishnan, Hrudananda Jena, K. V. Govindan Kutty, K. Nagarajan, J. of Therm.Anal. Calorim. 101 (2010) 371-377.
21. M. Stan, T.J. Armstrong, D.P. Butt, T.C. Wallace, Y.S. Park, C.L. Haertling, T. Hartmann, R.J. Hanrahan, J. Am. Ceram. Soc. 85 (2002) 2811–2816.
22. L.M. Lopato, V.N. Pavlikar, L.I. Lugin, Russ. J. Inorg. Chem. 14 (3) (1969) 449–450.
23. H. Iwahara, T. Esaka, H. Uchida, N. Maeda, Solid State Ionics 3/4 (1981) 359–363.
24. H. Iwahara, Solid State Ionics 86–88 (1996) 9–15.

25. H. Matsumoto, S. Hamajima, H. Iwahara, J. Electrochem. Soc. 148 (10) (2001) D121–D124.
26. H. Iwahara, Solid State Ionics 77 (1995) 289–298.
27. F. Shimojo, Solid State Ionics 179 (2008) 807–810.
28. Z. Yongqing, Z. Xueling, Y. Guozhong, M. Yuan, Y. Sumei, G. Zaihong, J. Rare Earths 24 (2006) 281–284.
29. E. Danielson, M. Devenney, D.M. Giaquinta, J.H. Golden, R.C. Haushalter, E.W. McFarland, D.M. Poojary, C.M. Reaves, W.H. Weinberg, X.D. Wu, Science 279 (1998) 837–839.
30. E. Danielson, M. Devenney, D.M. Giaquinta, J.H. Golden, R.C. Haushalter, E.W. McFarland, D.M. Poojary, C.M. Reaves, W.H. Weinberg, X.D. Wu, J. Mol. Struct. 470 (1998) 229–235.
31. S. K. Gupta, M. Sahu, K. Krishnan, M. K. Saxena, V. Natarajan and S. V. Godbole, J. Mater. Chem. C 1 (2013) 7054-7063.
32. S. Gopalan, A.V. Virkar, J. Electrochem. Soc. 140 (1993) 1060–1065.
33. R. Pankajavalli, K. Ananthasivan, S. Anthonysamy, P.R. Vasudeva Rao, J. Nucl. Mater. 336 (2005) 177–184.
34. A.N. Shirsat, K.N.G. Kaimal, S.R. Bharadwaj, D. Das, J. Solid State Chem. 177 (2004) 2007–2013.
35. S. Yamanaka, K. Kurosaki, T. Oyama, H. Muta, M. Uno, T. Matsuda, S. Kobayashi, J. Am. Ceram. Soc. 88 (6) (2005) 1496–1499.
36. S. Yamanaka, K. Kurosaki, T. Matsuda, S. Kobayashi, , J. Alloys Compd. 352 (2003) 52–56.
37. R. Saha, R. Babu, K. Nagarajan, C.K. Mathews, J. Nucl. Mater. 167 (1989) 271–277.
38. E.H.P. Cordfunke, A.S. Booij, M.E. Huntelaar, J. Chem. Thermodyn. 30 (1998) 437– 447.
39. J. Goudiakasa, R.G. Haire, J. Fuger, J.Chem. Thermodyn. 22(6)(1990) 577–587.
40. A.N. Shirsat, K.N.G. Kaimal, S.R. Bharadwaj, D. Das, Thermochim. Acta 447 (2006) 101–105.
41. S.K. Rakshit, S.C. Parida, Mohini, Z. Singh, B.K. Sen, J. Alloys Compd. 505 (2010) 302–308.
42. Z. Singh, Smruti Dash, R. Prasad, V. Venugopal, J. Alloys Compd. 279 (1998) 287– 294.
43. K. Kurosaki, K. Tanaka, M. Osaka, Y. Ohishi, H. Muta, M. Uno, S. Yamanaka, Prog.Nucl.Sci.Tech. 2(2011)5-8.
44. J.B. Goodenough, J. Appl. Phys. 37 (1966) 1415-1422.

45. S. Hayashi, R. Aoki, Mat. Res. Bull. 14(1979) 409-413.
46. Y.M. Zhang, F.D. Yang, J. Yang, Y. Tang, P. Yuan, Solid State Commun. 133(2005) 759–763.
47. M. Ishii and M. Kobayashi, Prog. Crys. Growth Charact. 23 (1991)245.
48. N. Faure, C. Borel, M. Couchaud, G. Basset, R. Templier and C. Wyon, Appl. Phys. B: Laser and Optics 63 (1996) 593.
49. J.H. Ryu, J.W. Yoon, C.S. Lim, W.C. Oh, K.B. Shim, J. Alloys Compd. 390 (2005) 245.
50. P. Jena, S. K. Gupta, V. Natarajan, M. Sahu, N. Satyanarayana, M. Venkateswarlu, J. Lumin. 158 (2015) 203–21.
51. X. Li, L. Guan, M. Sun, H. Liu, Z. Yang, Q. Guo, G. Fu, J. Lumin. 131(5) (2011)1022–1025.
52. K. K. Aruna, R. Manoharan, Int. J. Hydrogen Energ. 38(29)(2013)12695–12703.
53. J. Kubo, W. Ueda, Mater. Res. Bull. 44 (2009) 906-912.
54. Z. Singh, S. Dash, R. Prasad, V. Venugopal, J. Alloys Compd. 279 (1998)287-294.
55. Z. Singh, S. Dash, R. Prasad, V. Venugopal, J. Alloys Compd. 266 (1998)77–80.
56. Z. Singh, S. Dash, R. Prasad, D.D. Sood, J. Alloys Compd. 215(1994) 303–307.
57. S. Hayashi, R. Aoki, Mater. Res. Bull. 14 (1979) 409–413
58. S.I. Ikeda, N. Shirakawa, Physica C 341–348 (2000) 785–786.
59. V. Nassif, R.E. Carbonio, J.A. Alonso, J. Solid State Chem. 146 (1999) 266–270.
60. K. Kurosaki, T. Oyama, H. Muta, M. Uno, S. Yamanaka, J. Alloys Compd. 372(2004) 65–69.
61. S. Yamanaka, K. Kurosaki, T. Maekawa, T. Matsuda, S. Kobayashi, M. Uno, J.Nucl. Mater. 344 (2005) 61–66.
62. T. Maekawa, K. Kurosaki, H. Muta, M. Uno, S. Yamanaka, J. Alloys Compd. 390(2005) 314–317.
63. R. Agarwal, Z. Singh, V. Venugopal, J. Alloys Compd. 282 (1999) 231–235.
64. S. Dash, Z. Singh, R. Prasad, D.D. Sood, J. Alloys Compd. 201 (1993) 99–102.
65. S. Dash, Z. Singh, R. Prasad, D.D. Sood, J. Nucl. Mater. 207 (1993) 350–352.
66. S. Dash, Z. Singh, R. Prasad, V. Venugopal, High Temp.–High Press. 32 (2)(2000) 215–225.
67. S. Dash, Z. Singh, V. Venugopal, D.D. Sood, High Temp. High Press. 31 (2) (1999) 153–161.
68. O. Kubaschewski, High Temp.–High Press. 4 (1972) 1–12.
69. B. Lindblom, E. Rosen, Acta Chem. Scand. Ser. A 40 (1986) 452–458.

70. L.A. Zharkova, T.N. Rezukhina, Zhur. Fiz. Khim. 32 (1958) 2233–2235.
71. T.N. Rezukhina, Thesis, University of Moscow, 1968.
72. L.H. Brixner, J. Inorg. Nucl. Chem. 14 (3–4) (1960) 225–230.
73. S. Ukai, Y. Yamazaki, N. Oono, S. Hayashi, J. Nucl. Mater. 440**(**2013)39–45.
74. A.M. Azad, O.M. Sreedharan, J. Nucl. Mater. 167**(**1989) 89-93.
75. B. Saha, R. Viswanathan, M, Saibaba, D. Darwin Albert Raj, R, Balasubramanian, D. Karunasagar, C.K. Mathews, J. Nucl. Mater. 130**(**1985) 316-325.
76. C.K. Mathews, J. Nucl. Mater. 201**(**1993) 99-107.
77. R. Viswanathan, M. Saibaba, D. Darwin Albert Raj, R. Balasubramanian, B. Saha and C.K. Mathews, J. Nucl. Mater. 167**(**1989) 94- 104.
78. R. Viswanathan, M. Sai Baba, T.S. Lakshmi Narasimhan, R. Balasubramanian, D. Darwin Albert Raj, C.K. Mathews, J. Alloys Compd. 206**(**1994) 201-210.
79. S.C. Chetal, P. Chellapandi, P. Puthiyavinayagam, S.Raghupathy, V.Balasubramaniyan, P. Selvaraj, P. Mohanakrishnan, B. Raj, Energy Procedia. **7(**2011) 64–73.
80. Y.N.Shyr, G.L. Price, Ind.Eng.Chem.Prod.Res.Dev. 23**(**1984) 536-541.
81. M. Yamaguchi, M. Ishikawa, J. Phys. Soc. Jpn. 63 (1994) 1666.
82. T. Birchall, J. Solid State Chem. 27(1979) 293-298.
83. K.D. Singh Mudher, K. Krishnan, I.K. Gopalakrishnan, Darshan C. Kundaliya, S.K. Malik, J. Alloys Compd. 392 (2005) 40–43
84. R. Sankar, G. J. Shu, B. Karunakara Moorthy, R. Jayaveld, F. C. Chou, Dalton Trans. 42(2013) 10439-10443
85. PDF-2 Database, International Centre for Diffraction Data, Pennsylvania, 1997.
86. R. Dawar, R. Pankajavalli, J. Joseph, S. Anthonyswamy, V. Ganesan, J. Therm. Anal. Calorim. 112**(**2013) 95-102.
87. K.Krishnan, K.D.Singh Mudher, G.A. Rama Rao, V.Venugopal, J. Alloys Compd. 316**(**2001) 264-268.
88. K.Krishnan, G.A. Rama rao, K.D.Singh Mudher, V.Venugopal, J. Alloys Compd. 288**(**1999) 96-101.
89. M. Ali, R. Mishra, A.S. Kerkar, S.R. Bharadwaj, D. Das, J. Nucl. Mater. 301(2002)183-186.
90. C.Mallika, O.M. Sreedharan, Thermochim. Acta. 190**(**1991) 217-224.
91. G. Chattopadhyay, J.M. Juneja, J. Nucl. Mater. 202**(**1993)10-28.

92. FactSage, Version 5.4.1, the Integrated Thermodynamic Data Bank System, GTT-Technologies, GmbH, Germany, 1976–2006.
93. A. R West, Solid State Chemistry and its Applications, John Wiley & Sons, Singapore (2008).
94. K. C. Patil, S. T. Aruna, S. Ekambaram, Current Opinion in Solid State and Materials Science, 2 (1997) 158.
95. M. Pechini, U.S. Patent No. 3,330,697, July 11 (1967)
96. W. Hume-Rothery and H. M. Powell, Z. Krist. 91 (1935) 23.
97. W. Hume-Rothery, Atomic Theory for Students of Metallurgy, The Institute ofMetals, London, 1969 (fifth reprint).
98. W. Hume-Rothery, R. W. Smallman and C. W. Haworth, The Structure of Metals and Alloys, The Institute of Metals, London, 1969.
99. H. Cottrell, An Introduction to Metallurgy, Edward Arnold (publishers), London, 1967, p.192.
100. K. Janghorban, J. S. Kirkaldy and G. C. Weatherly, J. Phys. (Condensed Matter) 13 (2001) 8661
101. P. Tsai, MRS bulletin, November 1997.
102. B. D. Cullity, Elements of X-ray Diffraction, Addison–Wesley Publishing Co., Reading, Massachusetts (1956).
103. C. Whiston, X-ray Methods, Analytical Chemistry by Open Learning, John Wiley & Sons, (1987).
104. LATPAR, A least squares program written by V.K. Wadhawan, Neutron Physics Division, Mumbai, India.
105. D.J. Gardiner, Practical Raman spectroscopy. Springer-Verlag (1989).
106. D. A. Skoog, F. J. Holler, T. A. Nieman, Principles of Instrumental Analysis, Saunders College Pub., (1998)
107. K. Nakamoto, Infrared and Raman Spectra of Inorganic and Coordination Compounds: Theory and Applications in Inorganic Chemistry (Volume A), John Wiley & Sons Inc.(2009).
108. P. J. Goodhew, J. Humphreys, R. Beanland, Electron Microscopy and Analysis, Tayor and Francis, London (2000),
109. N. Yao, Z. L. Wang,Handbook of microscopy for nanotechnology, New York, Springer Science (2005).
110. O.H. Krikorian and D.Y. Lai, J. Nucl. Mater. 167 (1989) 14.
111. M. Sahu, K. Krishnan, M.K. Saxena, K.L. Ramkumar, J. alloys compd. 482(2009) 141.

112. Jr E.F. Westrum. Thermal and electronic properties of rare earth oxides. In: Kleber EV, editor. Rare earth research, New York: Macmillan Company, 1961. p. 69-80.
113. E.S.R. Gopal, Specific heats at low temperatures, Plenum Press, New York, (1966).
114. J. D. Blaise, Phy. 40 (1979) 4.
115. R. Szwarc, J. Phys. Chem. Solids 30 (1969) 705.
116. R. Bahadur, P.K. Sharma, Solid State Comm. 15 (1974) 621.
117. N.F. Uvarov and E.F. Hairetdinov, J. Therm. Anal. 33 (1988) 279.
118. G. Höhne, W. Hemminger, H.J. Flammersheim, Differential Scanning Calorimetery – An Introduction for Practitioners, Springer – Verlag, Berlin, 1995.
119. M. Sorai, Comprehensive Handbook of Calorimetry and Thermal Analysis, (2004).
120. M. E. Brown, Handbook of Thermal Analysis and Calorimetry, Vol. I, Principles and Practice, (1998).
121. R. F. Speyer, Thermal Analysis of Materials, Marcel Dekker, New York, (1993).
122. B.Wunderlich, Thermal Analysis. New York: Academic Press. (1990) pp. 137.
123. E.Gmelin, S.M.Sarge, Calibration of Differential Scanning Calorimeters, Pure Applied Chemistry.67 (1995)1789-1800.
124. J.E.Callanan, S.A.Sullivan, Rev, Sci.Instu.57 (1986) 2284.
125. G.H.W.Hohne, E.Gloggler, Thermochim. Acta. 151 (1989) 295.
126. C.Y.Ho (Ed) Specific heat of solids, Hemisphere Publishing Corp, Taylor and Francis Group, 1988.
127. W.Hemminger, S.M.Sarge, Thermochim Acta 245 (1994)181.
128. I. Fraga, S. Montserrat, J. M. Hutchinson, J. Therm. Anal. Calorim., 87 (2007) 119– 124.
129. S. L Simon, Thermochim. Acta. **374(**2001) 55-71.
130. J.E.K. Schawe, T. H¨utter, C. Heitz, I. Alig and D. Lellinger, Thermochim. Acta. 446(2006**)** 147–155**.**
131. Z. Jiang, C.T. Imrie, J. M. Hutchinson, Thermochim. Acta. 387 **(**2002) 75–93.
132. http://in.mt.com/in/en/home/products/Laboratory_Analytics_Browse/TA_Family_Browse/TA_software_browse/STARe_Software_Option_TOPEM.html.
133. Y. Sun, Z.Li, C.Xie, W.Chen and C.Zhang, Front. Chem. Sci. Eng. 7(1)(2013)110-115.
134. E. C. Subba Rao, Solid Electrolyte and their Applications, Plenum Press, New York,(1980).
135. S. Geller, Solid Electrolyte, Spinger-Verlag, Berlin Heidelberg New York (1977).
136. T.A. Ramanarayan, and W.L. Worrell, Can. Metall. Quart. 13 (1974) 325.

137. P.J. Meschter and W.L. Worell, Metall. Trans. A, 7A (1976) 299.

138. S.G. Foord, J. Sci. Inst., 11 (1934) 126.

139. I. Langmuir, J. Am. Chem. Soc., 35 (1913) 105.

140. W.J.H. Moll and H.C. Burger, Z. Tech Phys., 21 (1940) 199.

141. M. Pirani, Verhandl. Deut. Phys. Ges., 8 (1906) 686.

142. J.L.Margrave, Physico-Chemical Measurements at High Temperatures, editors Bockris, White and Mackenzie, (Butterworth Scientific Publications, London, 1959.

143. R. Rapp, editor, “Physicochemical measurements in metals research”, Vol IV, Part 1 of Techniques of metal research, Wiley Interscience, 1970, Chapters 1-5.

144. M.W. Chase, Jr., J. Phys. Chem. Ref. Data, Monograph 9, JANAF Thermochemical Tables, (4th Ed.), 1995.

145. H.Yokokawa, T.Kawada and M.Dokiyo, J.Am.ceram.Soc.72(11)(1989) 2104-10.

146. H.Yokokawa, J.Phase.Equil. 20(3)(1999)258-87.

147. J. R. Mc Donald, Impedance Spectroscopy, John Wiley & Sons, New York (1987).

148. J.B. Holt, Z.A. Munir, J. Mater. Sci. 21(1986) 251.

149. Z.A. Munir, Am. Ceram. Soc. Bull. 67 (1988) 342.

150. C.R. Brown and B.Derby, Brit. Ceram. Trans. 96 (1997) 25.

151. H.C.Yi, A. Pertric, J.J. Moore, J. Mater. Sci. 27 (1992) 6797.

152. C.C.Hwang, T.Y. Wu, J. Wan, J. S. Tsai, Mater. Sci. Engg. B 111 (2004) 49.

153. PDF-2 Database, Powder Diffraction File, No. 84-1583, International Centre for Diffraction Data, Pennsylvania, 1997.

154. PDF-2 Database, Powder Diffraction File, No. 19-1020, International Centre for Diffraction Data, Pennsylvania, 1997.

155. PDF-2 Database, Powder Diffraction File, No. 19-0830, International Centre for Diffraction Data, Pennsylvania, 1997.

156. PDF-2 Database, Powder Diffraction File, No. 20-1357, International Centre for Diffraction Data, Pennsylvania, 1997.

157. H. Jena, R. Asuvathraman, M. V. Krishnaiah, and K. V. G. Kutty, Powder Diffr., 16(4)2001 (Eu_6UO_{12} & Dy_6UO_{12}).

158. PDF-2 Database, Powder Diffraction File, No. 20-1335, International Centre for Diffraction Data, Pennsylvania, 1997.

159. PDF-2 Database, Powder Diffraction File, No. 20-1359, International Centre for Diffraction Data, Pennsylvania, 1997.

160. PDF-2 Database, Powder Diffraction File, No. 19-0567, International Centre for Diffraction Data, Pennsylvania, 1997.
161. PDF-2 Database, Powder Diffraction File, No. 20-1360, International Centre for Diffraction Data, Pennsylvania, 1997.
162. PDF-2 Database, Powder Diffraction File, No. 20-1366, International Centre for Diffraction Data, Pennsylvania, 1997.
163. PDF-2 Database, Powder Diffraction File, No. 20-1339, International Centre for Diffraction Data, Pennsylvania, 1997.
164. B.D. Cullity, S.R. Stock, Elements of X-Ray Diffraction, 2001
165. Shannon RD, Prewitt CT, Acta. Cryst. B 25 (1969) 925.
166. I. Barin, Thermochemical Data of Pure Substances, Vol. 1, VCH, Weinheim, 1995.
167. I. Hashimoto, M. Yoshinaga, Y. Ueda, K. Komazaki, K. Asaoka, S. Wang. J. Therm. Anal. Calorim. 69(2002)909–17.
168. N. Nakajima, Y. Yamamura, T. Tsuji, J. Therm. Anal. Calorim. 70(2002)337–44.
169. M. Rodova´, J. Brozek, K. Knizek, K. Nitsc., J. Therm. Anal. Calorim. 71(2003)667–73.
170. J.L. Drummond and R.A. Grant, Talanta 13 (1966) 477-488..
171. PDF-2 Database, Powder Diffraction File, No. 47-1689, International Centre for Diffraction Data, Pennsylvania, 1997.
172. PDF-2 Database, Powder Diffraction File, No. 01-089-5546, International Centre for Diffraction Data, Pennsylvania, 1997.
173. J. Ranløv, K. Nielsen, J. Mater. Chem. 4(6) (1994) 867-868.
174. I. Riess, M. Ricken and J. Nölting, J. Solid State Chem. 57 (1985) 314-322.
175. A. P. de A. Marquesa, D.M.A. de Meloa, C. A. Paskocimasb, P.S. Pizanic, M. R. Joyac, E. R. Leited, E. Longo, J. Solids State Chem. 179 (2006) 671-678.
176. PDF-2 Database, Powder Diffraction File, No. 8-0482, International Centre for Diffraction Data, Pennsylvania, 1997.
177. PDF-2 Database, Powder Diffraction File, No. 29-0193, International Centre for Diffraction Data, Pennsylvania, 1997
178. Harold P. klug, Leroy E. Alexander, X-Ray Diffraction Procedures, 2nd ed., John Wiley and Sons, New York, 1974, pp. 687-690.
179. D.K. Smith, G.J.McCarthy, Penn State Univ., University park, Pennsylvania, USA, ICDD- Grant- in-Aid (1978) JCPDF card No. [30-0157].

180. D.K. Smith, G.J.McCarthy, Penn State Univ.,university park, Pennsylvania, USA, ICDD- Grant- in-Aid (1978) JCPDF card No. [28-1207].
181. T.T.Basiev, A.A.Sobol, Y.U.K.Voronko, P.G.Zverev,Opt.Mater.15(2000)205-216.
182. J. F. Scott, J. Chem. Phys. 49(1968)98-100.
183. K.H. Kang, H.J. Ryu, K.C. Song, M.S. Yang, J. Nucl. Mater. 301 (2002) 242-244.
184. A.K.Tyagi, M.D.Mathews, B.R.Ambekar, R.Ramachandran, Thermochim.Acta 421 (2004) 69-71.
185. P. S. Ramanjaneyulu, A. S. Kulkarni, Komal Chandra, C. S. Yadav, M. K. Saxena, B. S. Tomar, K. L. Ramakumar, Accred. Qual. Assur. 18 (2013) 525–531.
186. PDF-2 Database, Powder Diffraction File, No. 34-0324, International Centre for Diffraction Data, Pennsylvania, 1997.
187. PDF-2 Database, Powder Diffraction File, No. 24-1224, International Centre for Diffraction Data, Pennsylvania, 1997.
188. PDF-2 Database, International Centre for Diffraction Data, Pennsylvania, 1997.
189. B. G. Vats, R. Phatak, K.Krishnan and S.Kannan, Mat. Res. Bull. 48(2013) 3117–3121.
190. R. Agarwal and Z. Singh, J. Alloys Compd. 414(2006) 230–234.
191. R. Pankajavalli, A Jain, R. Babu, K. Ananthasivan S. Anthonysamy and V. Ganesan, J. Nucl. Mater. 397(2010)116–121.
192. R. Pankajavalli, A. Jain, R. Babu, S. Anthonysamy, K. Ananthasivan, V. Ganesan and K. Nagarajan, J. Therm. Anal. Calorim. 111(2013)1609–1614.
193. A.Kadam, S.Dash, Z. Singh, B.K.Sen and V.Venugopal, J. Alloys Compd. 496(1-2)(2010) 20- 24.
194. T.S. Lakshmi Narasimhan, M. Sai Baba, S. Nalini and R. Viswanathan, Thermochim. Acta., 410(2004) 149–159.
195. S. Balakrishnan, R. Pankajavalli, K. Ananthasivan and S. Anthonysamy, Thermochim. Acta. 467(2008) 80–85.
196. R. Pankajavalli, A. Jain, A. Sharma, S. Anthonysamy and V. Ganesan, J. Therm. Anal. Calorim. 112(2013) 83–93.
197. G.Chattopadhyay, J. Phase Equil. 15(4)(1994)431-40.
198. P.Gunia,thesis,Gesamthochschule Siegenin in German ,1979.

199. H.Ipser, K.L.Komarek and K.O.Klepp, J.Less-Common Met. 92(1983) 265-282.
200. H.Okamoto and L.E.Tanner, Bull. Alloy Phase Diagrams, 11(4) (1990)371-376
201. H.Ipser,K.L.Komarek and H.Mikler, Monatsh. Chem. 105(6)(1974)1322-1334.
202. S.Y.Lee, P.Nash, Phase Diagram of Binary Nickel Alloys,1991.
203. J.Barstard, F.Gronvold, E.Rost and E.Vestersjo, Acta Chem.Scand. 20(10) (1966) 2865-2879.
204. O.Kubaschewski, C.B.Alcock and P.J.Spencer, Materials Thermochemistry, 6th ed., Pergamon Press, England, 1993.
205. G. Gospodinov and L. Atanasova, J. Therm. Anal. Calorim. 91(2)(2008)655–657.
206. A. Lesar, A. Popovie and J. Marsel, J. Less-Common .Met. 143(1988)151 – 157.
207. A.M. Azad and O.M. Sreedharan, J. Nucl. Mater. 167(1989) 89-93.
208. B. Saha, R. Viswanathan, M, Saibaba, D. Darwin Albert Raj, R, Balasubramanian, D. Karunasagar and C.K. Mathews, J. Nucl. Mater. 130(1985) 316-325.
209. C.K. Mathews, J. Nucl. Mater. 201(1993) 99-107.
210. R. Viswanathan, M. Saibaba, D. Darwin Albert Raj, R. Balasubramanian, B. Saha and C.K. Mathews, J. Nucl. Mater. 167(1989) 94- 104.
211. R. Viswanathan, M. Sai Baba, T.S. Lakshmi Narasimhan, R. Balasubramanian,D. Darwin Albert Raj and C.K. Mathews, J. Alloys Compd. 206(1994) 201-210.
212. T. Tsuji, T. Kato and K. Naito, J. Nucl. Mater. 201(1993)120-125.
213. E. F. Westrum, C. Chou, F. Gronvold, J. Chem. Phys. 30(1959)761-764.
214. E. F. Westrum, C. Chou, R. E. Machol and F. Grønvold, J. Chem. Phys. 28(1958) 497-503.
215. E. F. Westrum and R. E. Machol, J. Chem. Phys. 29(1985) 824-828.
216. R. Viswanathan, M. Saibaba, D. Darwin Albert Raj, R. Balasubramanian, B. Saha, C.K. Mathews, J. Nucl. Mater. 149(1987)302-311.
217. B. Saha, R. Viswanathan, M. Saibaba and C.K. Mathews, High Temp- High Press., 20(1) (1988)47-58.
218. M. Saibaba, R. Viswanathan and C.K. Mathews, Rapid Commun. Mass Spectrom.10 (6)(1996) 691-698.
219. S. Dash, Z. Singh, S.C. Parida and V. Venugopal, J. Alloys Compd. 398(2005) 219–227.
220. O.Götzmann, J. Nucl. Mater .84(1979)39-54.